DISSERTATION

The Microstructure of Nb₃Sn Superconductors for the Future Circular Collider Project and its Impact on the Performance

Ausgeführt zum Zwecke der Erlangung des akademischen Grades
eines Doktors der technischen Wissenschaften
unter der Leitung von

Priv.Doz. Dipl.-Ing. Dr.techn. Michael Stöger-Pollach, MInstP

E057-02 - Universitäre Service-Einrichtung
für Transmissions-Elektronenmikroskopie
und
E138 - Institut für Festkörperphysik

eingereicht an der Technischen Universität Wien
Fakultät für Physik
von

Dipl.-Ing. Stephan Pfeiffer

00925168
Ferdinand-Raimund-Gasse 401
3034 Maria Anzbach, Österreich

Wien, am 20.07.2020

Kurzfassung

Das Future Circular Collider (FCC) Projekt befasst sich mit dem konzeptionellen Design und der Planung eines zukünftigen Teilchenbeschleunigers am Europäischen Kernforschungszentrum CERN. Dieser stellt den Nachfolger des Large Hadron Colliders (LHC) dar. Geplant ist die Unterbringung des Beschleunigerringes in einem 100 km langen Tunnel, in welchem Kollisionsenergien von bis zu 100 TeV erreicht werden sollen. Um die zu kollidierenden Teilchen auf ihrer Bahn zu halten, sind Magnete basierend auf Supraleitern notwendig, welche magnetische Felder von 16 T erzeugen müssen. Für die Herstellung dieser Magnete sind Nb_3Sn-Supraleiter vorgesehen, welche derzeit jedoch noch nicht die dazu nötige kritische Stromdichte von 1500 A mm^{-2} bei dieser Feldstärke und einer Temperatur von 4.2 K erreichen. Um die Performance auf das angestrebte Niveau zu erhöhen, ist ein tiefgründiges Verständnis des Einflusses der Mikrostruktur notwendig, welches Voraussetzung für die Optimierung des Herstellungsprozesses ist.

Die vorliegende Arbeit beschäftigt sich mit der Untersuchung der Mikrostruktur von Nb_3Sn-Supraleitern des neuesten Standes der Technik, welche einen wesentlichen Einfluss auf die makroskopischen supraleitenden Eigenschaften hat. Ein spezieller Fokus wird auf drei Möglichkeiten gelegt, wie die kritische Stromdichte erhöht werden kann. Erstens kann eine verbesserte Homogenität in der elementaren Zusammensetzung zu einer Erhöhung der kritischen Temperatur T_c und des oberen kritischen Feldes B_{c2} führen, was die kritische Stromdichte J_c positiv beeinflusst. Zweitens wird durch neue Herstellungsverfahren und verbesserte Wärmebehandlungen eine Verringerung der Korngröße dieser polykristallinen Drähte erzielt. Die resultierende Erhöhung der Korngrenzen-Dichte erhöht die Verankerungskraft der magnetischen Flusslinien und somit J_c. Drittens kann die Einführung von zusätzlichen Verankerungszentren für die Flusslinien zu einer weiteren Erhöhung der Verankerungskraft beitragen und somit J_c verbessern. Diese Verankerungszentren liegen in den untersuchten Proben in zwei verschiedenen Formen vor: einerseits Defekte im Kristallgitter, welche durch die Bestrahlung mit schnellen Neutronen erzielt wurden, andererseits in Form von Nanopartikeln, die durch ein neues Herstellungsverfahren durch interne Oxidation gebildet wurden.

Die resultierende Mikrostruktur von verschiedenartigen Nb_3Sn-Drähten wurde mithilfe von Raster- und Transmissions-Elektronenmikroskopie untersucht und verglichen. Die elementare Zusammensetzung wurde mithilfe von energiedispersiver Röntgenspektroskopie analysiert, wodurch Gradienten in der A15-Phase und innerhalb von

Körnern bestimmt wurden. Die Korngrößenverteilung wurde durch Transmissions-Kikuchi-Beugung bestimmt, zusammen mit Informationen über die Korn-Geometrie und -Orientierung. Informationen über die Größenverteilungen und Dichten der verschiedenen künstlichen Verankerungszentren wurden durch den Einsatz verschiedener Techniken der Transmissions-Elektronenmikroskopie erlangt und verglichen. Es wurde beobachtet, dass die künstlichen Verankerungszentren in neutronenbestrahlten und ternären Drähten der neuen Generation, die Nanopartikel enthalten, vergleichbare Eigenschaften in Bezug auf ihre Mikrostruktur aufweisen.

Die Ergebnisse der Mikrostruktur-Untersuchung wurden mit lokalen magnetischen Eigenschaften korreliert, welche mit Raster-Hall-Sonden-Mikroskopie bestimmt wurden, wodurch sich erhebliche Unterschiede in der Performance zwischen den Subelementen zeigten, ebenso wie Inhomogenitäten innerhalb individueller Subelemente. Der kombinierte Einsatz von Elektronenmikroskopie, energiedispersiver Röntgenspektroskopie und Raster-Hall-Sonden-Mikroskopie erbrachte Informationen über kritische Stromdichte von individuellen Subelementen und die Abhängigkeit der kritischen Temperatur vom Zinngehalt.

Abstract

The Future Circular Collider (FCC) project deals with the conceptual design and planning of a future particle accelerator at the European Organization for Nuclear Research CERN, which represents the successor to the Large Hadron Collider (LHC). It is planned to house the accelerator ring in a $100\,\mathrm{km}$ long tunnel, in which collision energies of up to $100\,\mathrm{TeV}$ are aspired to be achieved. To keep the particles to be collided on their path, magnets based on superconductors are necessary, which are required to generate magnetic fields of $16\,\mathrm{T}$. Nb_3Sn superconductors are intended for the production of these magnets, which currently do not reach the required critical current density J_c of $1500\,\mathrm{A\,mm^{-2}}$ at this field and a temperature of $4.2\,\mathrm{K}$. To increase the performance to the intended level, a thorough understanding of the impact of the microstructure is necessary, which is a requirement for the optimization of the manufacturing process.

The present work deals with the investigation of the microstructure of state-of-the-art Nb_3Sn superconductors, which has an essential impact on the macroscopic superconducting properties. A special focus is placed on three options of how the critical current density can be increased. Firstly, an improved homogeneity in the elementary composition can lead to an increase in the critical temperature T_c and the upper critical field B_{c2}, which benefits the critical current density J_c. Secondly, through novel manufacturing processes and improved heat treatments a reduction in the grain size of these polycrystalline wires is achieved. The resulting increase in the grain boundary density increases the pinning force of the magnetic flux lines and therefore J_c. Thirdly, the introduction of additional pinning centres for the flux lines can contribute to a further increase in the pinning force and therefore improve J_c. These pinning centres are present in the examined wires in two different forms: on the one hand defects in the crystal lattice, which were introduced by the irradiation with fast neutrons, on the other hand in the form of nano-precipitates created by a novel manufacturing process through internal oxidation.

The resulting microstructure of various types of Nb_3Sn wires was investigated and compared using scanning and transmission electron microscopy. The elementary composition was analysed using energy-dispersive X-ray spectroscopy, where gradients across the A15 phases as well as inside grains were determined. The grain size distributions were determined by transmission Kikuchi diffraction, together with information about the grain geometry and orientation. Information about the size distributions and densities of the different artificial pinning centres was obtained

using various techniques of transmission electron microscopy and compared. It was observed that the artificial pinning centres in neutron irradiated and new generation ternary wires containing nano-precipitates exhibit comparable properties regarding their microstructure.

The results of the microstructural investigation were correlated with local magnetic properties that were assessed using scanning Hall probe microscopy, where considerable differences in the performance between sub-elements became apparent, as well as inhomogeneities inside individual sub-elements. The combined use of electron microscopy, energy-dispersive X-ray spectroscopy and scanning Hall probe microscopy yielded information about the critical current density of individual sub-elements and the dependency of the critical temperature on the Sn content.

Contents

Contents

Contents

List of Figures

List of Tables

1 Introduction

This chapter aims to provide information about the Future Circular Collider project, the superconducting compound Nb_3Sn, wires based on Nb_3Sn as well as the methods and goals of this work. As outlined in a collaboration agreement between CERN and TU Wien, the microstructure of state-of-the-art Nb_3Sn wires was investigated and the results were related to the superconducting properties. This knowledge is required in order to improve the performance of future Nb_3Sn wires, which is necessary to meet the requirements of the Future Circular Collider, whose parameters are outlined in Section 1.1. The crystal structure of Nb_3Sn is shown in Section 1.5.

1.1 The Future Circular Collider study

The Standard Model of Particle Physics describes the fundamental particles that form the visible universe as well as most of their interactions. The recent discovery of the Higgs boson further confirmed the validity of the Standard Model, yet several observations remain unexplained, such as the evidence for dark matter, the prevalence of matter over antimatter and the neutrino masses. The Future Circular Collider (FCC) study aims to design a post-LHC (Large Hadron Collider) particle accelerator at CERN, the European Organization for Nuclear Research. The increased precision and collision energy of the FCC will enable examination in yet unexplored territory, potentially aid in answering those unresolved questions and further increase our understanding of the universe [17, 18, 19].

In 2019, CERN released four volumes of conceptual design reports that outline the designs and opportunities of possible FCC machines [20, 17, 18], including a proton-proton collider (FCC-hh), an electron-positron collider (FCC-ee) and an electron-proton collider (FCC-eh). The fourth volume describes the HE-LHC (high energy LHC) project [19], which aims to upgrade the LHC to a proton-proton collider with a collision energy of 27 TeV and a luminosity more than 3 times higher than the HL-LHC (high luminosity LHC).

The FCC project aims achieve significantly higher centre-of-mass collision energies of 100 TeV for proton-proton collisions, compared to the 14 TeV of the LHC. The machine will be located in a circular tunnel of around 100 km circumference. The FCC dipole magnets necessary to reach the foreseen beam energy are required to generate a magnetic field of 16 T. Since magnets based on NbTi superconductors are not capable

of achieving such high fields, the dipole magnets of the FCC accelerator will be based on Nb_3Sn superconductors. The 16 T dipole program is addressing the development of high field Nb_3Sn accelerator magnets, including the performance enhancement of the superconductor as well as the design and assembly of demonstrator magnets. Different magnet design options are considered, including Cosine-Theta, Canted Cosine-Theta and Block type designs. The conductor development program revolves around the manufacture and characterization of Nb_3Sn superconductors with the main target of increasing the critical current density J_c. Superconductors of the two manufacturing technologies Internal-Tin and Powder-In-Tube are considered as possible candidates for the magnets and are being focused on during the conductor development program [153, 159]. Figure 1.1 shows the planned layout of the 100 km long tunnel in Geneva and Table 1.1 gives an overview of the design parameters of the LHC and the FCC-hh.
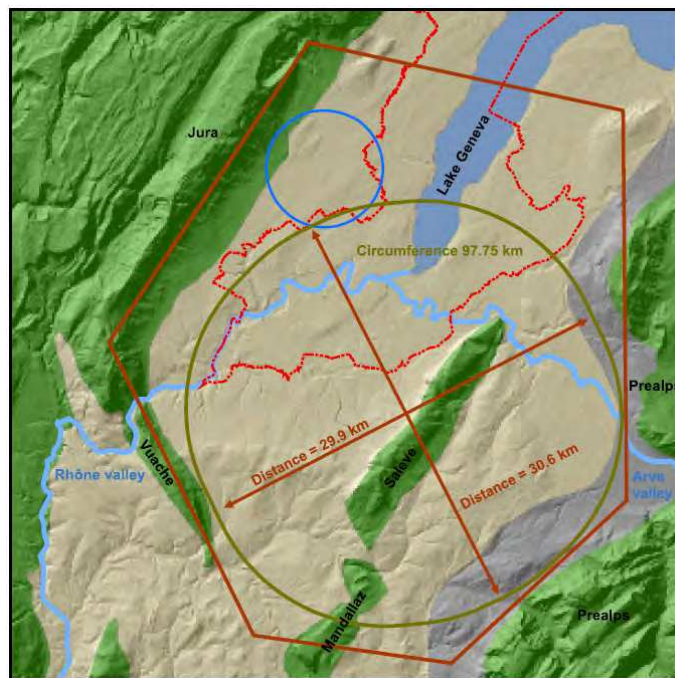
Figure 1.1: Planned size and location of the Future Circular Collider. Blue line: LHC tunnel, olive line: FCC tunnel [17].

The current target baseline for FCC-hh accelerator dipole magnets based on Nb_3Sn superconductors is a non-Cu critical current density J_c of $1500\,A\,mm^{-2}$ at 16 T and 4.2 K. State-of-the-art Nb_3Sn wires do not reach this performance yet [7]. A further increase in the critical current density J_c of at least 40 %–45 % is required for the planned FCC with respect to the currently best performing RRP conductors [171]. In order to improve the manufacturing of Nb_3Sn wires, a deep understanding of the microstructure and its impact on the performance is necessary. Figure 1.2 shows a comparison between the critical current density J_c of Nb_3Sn wires that are used for the High Luminosity upgrade of the LHC and the required values for the FCC.

Parameter	LHC	FCC-hh
Centre of mass collision energy [TeV]	14	100
Peak dipole field [T]	8.33	16
Circumference [km]	26.7	97.75
Synchrotron radiation power per beam [kW]	3.6	2400
Stored energy per beam [GJ]	0.392	8.4

Table 1.1: Comparison between LHC and FCC-hh parameters [18, 19].
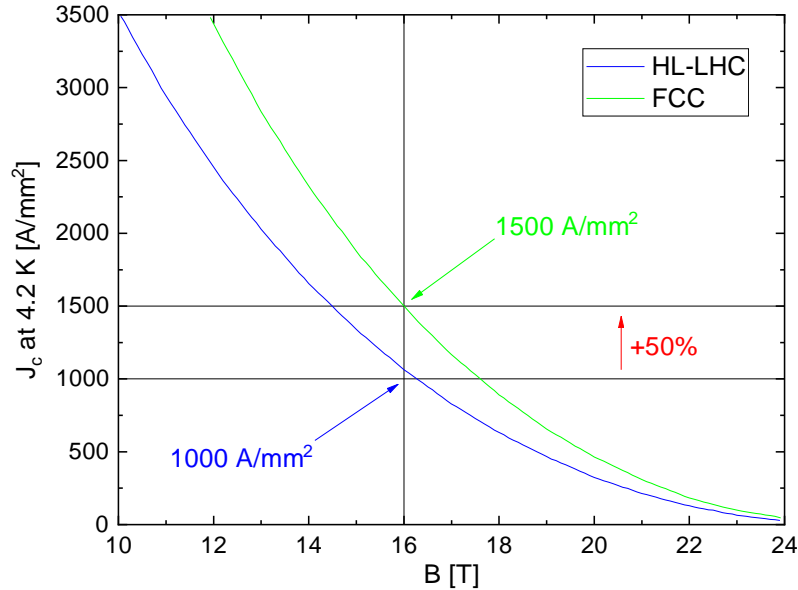
Figure 1.2: Comparison between J_c of HL-LHC wires and the target of wires for the FCC [5].

The CERN FCC conductor development program is a worldwide effort of industries and laboratories with the ultimate goal of achieving Nb_3Sn wires with a non-Cu critical current density J_c of $1500\,\mathrm{A\,mm^{-2}}$ at $16\,\mathrm{T}$ and $4.2\,\mathrm{K}$. This performance would enable the production of $16\,\mathrm{T}$ dipole magnets needed for a $100\,\mathrm{TeV}$ post-LHC hadron collider in a $100\,\mathrm{km}$ long tunnel as proposed by the FCC conceptional design reports. Such a project would require the fabrication of about 4800 dipole magnets based on Nb_3Sn, while demanding challenging targets for both the performance and the cost of the superconductors [7]. 8000 tons of Nb_3Sn would be required for the superconducting magnets of the FCC operating at a field of $16\,\mathrm{T}$ in order to bend the particles beams and achieve higher collision energies [171].

The development targets of the FCC conductor development program are summarized in Table 1.2. TU Wien is contributing to the program by a correlated characterization of the microstructure and the superconducting properties. As example, assessments of compositional gradients in sub-elements and grains are conducted since the stoichiometry majorly affects the intrinsic properties and therefore the macroscopic performance of the wire as discussed in this chapter.

Parameter	Value
Wire diameter [mm]	$0.7 - 1.1$
Cu/non-Cu ratio	~ 1
Non-Cu J_c, 16 T and 4.2 K [A mm^{-2}]	≥ 1500
$\mu_0 \Delta M$, 1 T and 4.2 K [mT]	≤ 150
d_{eff} [µm]	≤ 20
RRR	≥ 150
Unit length [km]	≥ 5
Price, 16 T and 4.2 K [Euro kA^{-1} m^{-1}]	≤ 5

Table 1.2: Development targets for Nb$_3$Sn wires [7].

Similar to the FCC conductor development program, the HE-LHC program also requires superconducting magnets based on Nb$_3$Sn providing a magnetic field of 16 T in order to achieve collision energies of 27 TeV. For that program, also a variety of magnet designs such as cos–theta, block-type, common-coil, and canted–cos–theta are considered [125].

Remarkable progress in the development of high performance Nb$_3$Sn wires has been made over the years. In [87], the milestones achieved between 1999 and 2008 are described, which include the achievement of a non-Cu critical current density J_c of 3000 A mm^{-2} at 12 T and 4.2 K in internal tin wires at long wire lengths. Prototype magnets achieving peak fields higher than 16 T have been fabricated, the reduction of radial Sn gradients across the A15 layers to an average of 0.1 at.% µm^{-1} was reported and progress was made towards reducing effective sub-element diameters to less than 40 µm.

Further goals of the Nb$_3$Sn conductor development include the reduction of the sub-element diameter to less than 20 µm in order to suppress persistent currents and the reduction of the Cu/Nb$_3$Sn ratio, requiring an even more evaluated quench protection [130].

1.2 Scope of this thesis

Current state-of-the-art Nb_3Sn conductors have not yet reached the performance necessary to meet the FCC requirements. Ongoing efforts around the world aim to improve the performance to the target value. This can only be achieved through an optimization of the manufacturing process and a deep understanding of the correlation between the microstructure and the macroscopic performance [7, 171].

The FCC study is a worldwide collaboration of over 140 institutes in 34 countries. In a collaboration between CERN and TU Wien, the microstructural and superconducting properties are investigated in order to gain a better understanding about the impact of the microstructure on the local superconducting properties and ultimately the macroscopic performance of the superconductor. Two institutes of TU Wien are working on the characterization of Nb_3Sn wires. At the University Service Centre for Transmission Electron Microscopy (USTEM), the investigation of the microstructure is being performed, including grain size distribution, compositional gradients and defect structure. At Atominstitut (ATI), the superconducting properties are being examined using scanning Hall probe microscopy (SHPM) and SQUID (superconducting quantum interference device) magnetometry. Correlations between the microstructural and superconducting properties are established in order to disclose potentials for enhancing the performance of Nb_3Sn wires and achieve the FCC J_c target.

The work described in this thesis mainly focused on the microstructural investigations and was carried out under a collaboration agreement between CERN and TU Wien titled KE3194, which is categorized into work units and deliverables that are described in the addendum FCC-GOV-CC-0061. The results of each category were summarized in internal progress reports, deliverable reports and a final report which were submitted to CERN. This thesis describes the methods, results and conclusions in greater detail as well as a large number of additional results that were not included in the reports. Some preliminary measurements may have been extended or re-evaluated and might differ from the results described in the reports.

The procedures for preparing samples for microstructural and magnetic investigations are described in Chapter 2. Analyses of sub-element inhomogeneities using scanning electron microscopy are presented in Chapter 3. Chapter 4 deals with the analysis of the local microstructure using transmission electron microscopy. The elemental composition is investigated by energy-dispersive X-Ray spectroscopy in Chapter 5. The technique of transmission Kikuchi diffraction is applied in Chapter 6 in order to gain information about grain geometry and orientation. Irradiation experiments using fast neutrons are presented in Chapter 7, where the resulting defect structure is investigated. Chapter 8 describes magnetic measurements using scanning Hall probe microscopy and their correlation with the microstructure is discussed in Chapter 9. The main results are summarised in Chapter 10, which also provides an outlook for future experiments.

1.3 Superconductivity and flux pinning

1.3.1 Superconductivity and classification of superconductors

This section gives a brief overview of the phenomenon of superconductivity and is mainly based on information taken from [130]. Superconductors are materials that show two remarkable properties under certain conditions:

1. Current transport with 0 resistance

2. Perfect diamagnetism

In the superconducting state, magnetic fields are expelled from the inside of the superconductor. Screening currents on the surface produce a magnetic field with equal magnitude, which oppose the applied field. These currents do not decay as a result of the resistance being zero. For applications it is important to note that the thermal conductivity in the superconducting state can be orders of magnitude lower compared to the normal state. The conditions that need to be fulfilled in order to maintain the superconducting state are:

1. Temperature below the critical temperature T_{c}

2. Current density below the critical current density J_{c}

3. Magnetic field below the critical field B_c

The conditions mentioned above are valid for type I superconductors, while type II superconductors exhibit a different behaviour with respect to the last two conditions, which will be explained below. The superconducting state is characterized by an energy gap in the order of 3.5 $k_{\mathrm{B}}T_c$. This gap reaches its maximum at 0 K, decreases with increasing temperatures and becomes zero when the temperature reaches the critical temperature T_{c}. The transition to the normal conducting state occurs as soon as one of the critical parameters is exceeded. These parameters are not independent of each other, the dependency of B_c on T_{c} is described by

$$B_c(T) = B_c(0) \left[1 - (T/T_c)^2 \right],$$ (1.1)

where $B_c(0)$ is the maximum critical field at a temperature of 0 K. External magnetic fields penetrate the superconductor for small distances and decay exponentially. The flux inside the material is described by

$$B(x) = B_c(0)e^{-(x/\lambda)},$$ (1.2)

where x is the distance from the sample surface and λ is the penetration depth, which is dependent on the temperature and usually in the order of $10\,\mathrm{nm}$–$100\,\mathrm{nm}$ for most pure metals at $0\,\mathrm{K}$ and increasing sharply near T_c. Magnetic flux inside superconductors is found to be always quantized and multiples of the flux quantum ϕ_0, which is defined as

$$\phi_0 = \frac{h}{2e} = 2.067\,833 \times 10^{-15}\,\mathrm{T\,m^2}. \tag{1.3}$$

Aside from the penetration depth λ, another fundamental parameter describing superconductors is the coherence length ξ, which describes the distance over which the order parameter changes. The minimum of the coherence length is reached at $0\,\mathrm{K}$, increases with increasing temperature and diverges at T_c. The temperature independent Ginzburg-Landau parameter κ is defined as:

$$\kappa = \lambda/\xi. \tag{1.4}$$

Superconductors can thus be classified by their magnetic properties in type I and type II superconductors:

1. $\kappa < \frac{1}{\sqrt{2}}$: type I superconductor

2. $\kappa > \frac{1}{\sqrt{2}}$: type II superconductor

Type II superconductors only show perfect diamagnetism up to the lower critical field B_{c1}, but can sustain the superconducting state until the upper critical field B_{c2} is reached. Above B_{c1}, magnetic flux starts to penetrate the superconductor in the form of flux lines, where each flux line carries a flux quantum ϕ_0. The flux lines are parallel to the applied field, arrange themselves in a triangular lattice and consist of normal conducting cores that are surrounded by circulating currents that flow in the opposite direction than the screening currents on the surface. Their diameter is in the order of 2ξ. The current is able to flow through the whole cross section in type II superconductors. At B_{c2}, the material is fully penetrated by the magnetic flux and the transition to the normal state occurs. B_{c1} generally shows rather small values, while B_{c2} shows significantly higher values than the thermodynamic critical magnetic field B_c. For that reason, only type II superconductors are relevant for technological applications, where large currents are required to be transported through the conductor while sustaining large magnetic fields.

Another categorization of superconductors is by their critical temperature T_c into low-temperature superconductors (LTS) and high-temperature superconductors (HTS). HTS possess a critical temperature of over $77\,\mathrm{K}$ and can therefore be kept in the superconducting state by cooling with liquid nitrogen, given J_c and B_c2 are not exceeded. LTS on the contrary need to be cooled by cryogenic liquids with lower boiling points, for example liquid helium.

The theory of magnetic hysteresis in high-field superconductors was developed by Bean [16], who assumed that the critical current density is independent of the magnetic field. According to Bean, an increasing applied field leads to an increased penetration of the superconductor until at a certain field H^* the entire conductor is fully penetrated. Current flows at the value of the critical current density J_c near the surface and penetrates the conductor at increasing fields, in a depth that is required for reducing the internal fields to zero, while inside regions that experience no magnetic field carry zero current. At H^*, currents at the value of J_c are induced in the whole volume. After the removal of the applied field, the surface currents reverse and a remanent field is left in the sample, together with trapped currents.

1.3.2 Flux pinning and critical current

In type II superconductors, magnetic flux enters the material in the form of flux lines, which are normal conducting tubes confined by shielding currents that flow along their surface. A current trough the conductor induces a Lorentz force on the flux lines. Flux lines, however, are capable of pinning onto pinning centres in the crystal structure, in which case the pinning force counteracts the Lorentz force. Below the critical current density J_c, the flux lines are pinned and no dissipation occurs. Figure 1.3 show a schematic of flux lines entering a type II superconductor, together with the occurring forces.
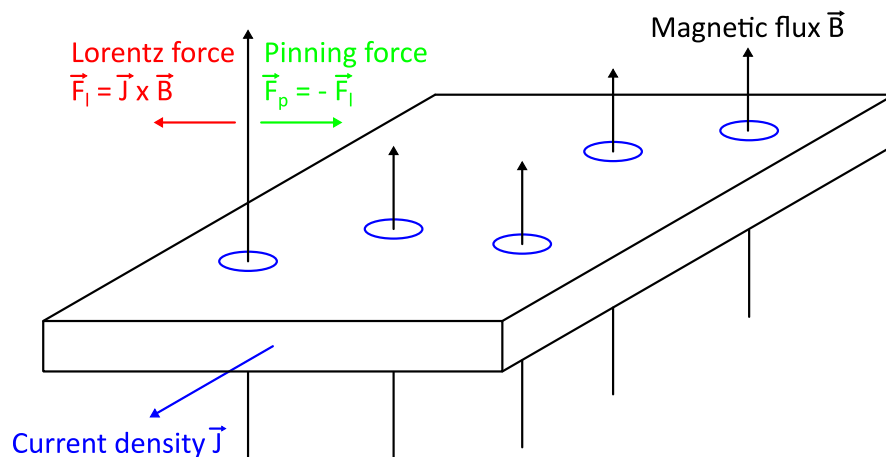
Figure 1.3: Flux pinning in type II superconductors, drawn after [131].

Once the critical current density J_c is exceeded, the Lorentz force overtakes the pinning force, causing a drift of the flux lines through the conductor, which induces a voltage and the transition to dissipative current transport. The critical current density J_c can therefore be increased by the introduction of additional pinning centres, such as defects, dislocations, impurities and grain boundaries. The superconducting state is lost at the depairing current density J_d.

An overview of flux pinning mechanisms in type II superconductors was given by Dew-Hughes [32]. The volume pinning force is influenced by various factors such as: the nature of the pinning sites, since the local interaction strength is defined by the variation in the superconducting properties, the size and spacing of the pinning centres in relation to the penetration depth λ and the spacing of the flux lattice as well as the flux lattice rigidity. The interaction between flux lines and pinning centres is caused by the difference in the superconducting properties compared to the surrounding superconducting regions. The main microstructural factors contributing to the pinning force were found to be grain boundary pinning and point pinning trough precipitates.

Scaling laws for the flux pinning force density F_p were described by Kramer [83] as a function of a reduced magnetic field $h = H/H_{c2}$. F_p corresponds to the critical Lorentz force $\vec{J_c} \times \vec{B}$ per volume. A chance in temperature does not alter the value of the reduced field at which the peak maximum of F_p occurs. Further detailed descriptions of flux pinning mechanisms in superconductors are given in [94].

The optimal pinning centre density for maximum flux pinning corresponds to the fluxon spacing, which in a triangular lattice is given by [5]:

$$d = \left(\frac{2\phi_0}{\sqrt{3}B} \right)^{1/2} , \tag{1.5}$$

where a single flux quantum ϕ_0 was defined in Equation 1.3. At a field of $16\,\text{T}$, the flux line spacing d and therefore the optimal flux pinning site spacing results in about $12.2\,\text{nm}$.

Different types of pinning centres in Nb_3Sn were investigated in [118]. Through correlation of the microstructure with J_c values, it was determined that grain boundaries are responsible for flux pinning in this material. Regarding standard Nb_3Sn wires, the most important pinning centres are therefore in the form of grain boundaries. In this work, the following possibilities of further increasing the pinning centre density will be analysed and discussed in detail:

1. The introduction of nano-precipitates by internal oxidation in Chapter 4.

2. The increase of the grain boundary density by grain refinement in Chapter 6.

3. The introduction of artificial defects by neutron irradiation in Chapter 7.

1.4 Superconductors for accelerator magnets

1.4.1 Technical requirements

Experiments using the Large Hadron Collider (LHC) have started in 2009 and in November of 2012 the existence of the Higgs boson with a mass of $125\,\mathrm{GeV}\,{c_0}^{-2}$ has been confirmed. More than 1600 dipole and quadrupole magnets based on superconducting wires are installed in the LHC. The superconducting magnets in particle accelerators are responsible for controlling and focusing the beam. The particles travelling close to the speed of light in circular accelerators emit synchrotron radiation, leading to the loss of significant amounts of energy, which is proportional to E^4. For that reason it is beneficial to increase the size of the machine. Heavy particles like protons are less prone to energy losses by synchrotron radiation and are therefore suited for the use in circular colliders, while lighter particles such as electrons are preferably accelerated in linear accelerators [130].

The beam energy determines the energy region in which new physics can potentially be investigated and discovered and is therefore one of the most important parameters of particle colliders. The relativistic particle energy E in GeV of particles with charge q in units of the electron charge is governed by the magnetic field B of the dipole magnets in T and the radius r of the circular collider in m [124]. The maximum obtainable beam energy in a circular particle accelerator can roughly be described by

$$E \approx 0.3qBr. \tag{1.6}$$

It can therefore be seen, that in order to achieve high collision energies, high magnetic fields and an appropriate size of the accelerator are essential [130].

One of the most important parameters of superconducting Nb_3Sn wires is the critical current density J_c, which is usually defined as the critical current over the non-Cu area of the wire. It heavily impacts the performance of the superconducting magnets and depends on the microstructure of the superconductor, such as grain size, inhomogeneities and precipitates, which determine the flux pinning properties of the material. Thus an examination thereof as conducted in this work is of great importance for the production of high-performance wires in the future. Further parameters that influence the performance of the conductor include the wire diameter D, the magnetization M, the effective filament diameter d_{eff}, filament twist pitch l_{p}, superconductor fraction λ or Cu/non-Cu ratio, axial and transverse resistivity ρ_{n} and ρ_{e} and the Residual Resistivity Ratio RRR [10].

The critical current density J_c not only defines the current-carrying capability, but also other important parameters such as magnetization and stability, and therefore the design and the performance of the superconducting magnets [124]. Ongoing

efforts aim to improve the performance of current Nb_3Sn wires and cables to the ultimate goal of creating 16 T magnets for an eventual future 100 TeV proton-proton collider [10].

Superconductors are generally inhibited by their low thermal conductivity and low electrical conductivity in the normal state, leading to thermal and electro-magnetic instabilities. These instabilities can result in the quenching of superconducting magnets, during which T_c is exceeded locally, the transition to the normal state occurs and a large amount of energy is released, potentially damaging the magnet. In order to counteract this, superconductors for practical applications are consisting of thin superconducting filaments, so called sub-elements, that are embedded in a matrix of a material with high thermal and electrical conductivity, most frequently copper. In the event of a quench, the generated heat and the current can drain off through the matrix. In the past, NbTi has been used for generating fields up to 9 T in magnets used for particle accelerators and fusion reactors, since it is ductile and relatively easily manufactured. New projects such as the FCC, which require the operation at higher fields, demand the exploration of new materials [130].

The cause for quenches is the abrupt movement of the magnetic flux penetrating the superconductor, which is called flux jump effect. Flux jump is a process in which the magnetization suddenly collapses due to the magnetic energy stored in shielding currents becoming too large. Attempts of reducing this effects led to the definition of stability criteria, which limit the spacial extent of the superconductor and thus its maximum diameter. Since superconductors in the normal state show high values of the resistivity, they have to be embedded into a normal conducting matrix of low resistance and high thermal diffusity, in order to minimize the heating during a quench, conduct away the heat and absorb a large fraction due to a high specific heat. These requirements to stability and protection have led to the development of multifilamentary superconducting wires, where fine filaments are surrounded by a normal conducting matrix. For additional stability against flux jumps and the reduction of coupling currents between filaments, these filaments are twisted along the axis of the wire. Due to protection against flux jumps, not only the diameter of the superconducting filaments is limited, but also the diameter of the multifilamentary wire itself [21, 124].

The two parameters essential for the electromagnetic stability of superconductors are the sub-element diameter d_{sub} and the thermal conductivity of the matrix, which is described through the residual resistance ratio (RRR), commonly defined as the ratio of the electrical resistance at 273 K to the one at 20 K [171]. A small sub-element size is desired to reduce AC losses and magnetic fields produced by screening currents.

In order to avoid flux jumps, it is essential to keep the sub-element diameter as small as possible. The maximum stable diameter of a filament that is embedded in a matrix is given by

$$d \leq \frac{2}{J_c} \left(\frac{3\gamma C(\theta_c - \theta_o)}{\mu_0} \right)^{1/2}, \qquad (1.7)$$

where γ is the density, θ_c the critical temperature and C the specific heat of the matrix. This leads to filament diameters of typically around $50\,\mu\text{m}$ [5].

A small sub-element size is generally to be preferred since it reduces low field magnetization and helps to avoid thermo-magnetic instability [2, 124]. Nb$_3$Sn wires with sub-element numbers as high as 1248 and sub-element diameters as low as $12\,\mu\text{m}$ have already been fabricated [108].

Applying a magnetic field to a superconductor induces a field opposed to the applied field. The sum of the opposed and applied fields results in the total field. Responsible for generating the induced field are local coupling currents between the filaments that are flowing through the resistive matrix. The coupling currents between filaments in a wire are determined by the time constant

$$\tau = \frac{\mu_0}{2\rho_{eff}} \left(\frac{l_t}{2\pi} \right)^2, \qquad (1.8)$$

where l_t is the twist pitch length of the filaments and ρ_eff the effective transverse resistivity of the matrix. The ohmic loses due to the coupling currents lead to a temperature increase and are able to cause the transition to the normal state [114]. From this it becomes apparent that un-twisted conductors are useless for applications in accelerator magnets and that it is essential to reduce the twist pitch length in order to reduce coupling currents [5].

The sub-elements in multi-filamentary superconducting wires are embedded in a normal-conducting low resistance matrix, commonly Cu, in order to protect the superconductor in case of transition to the normal state (quench). Due to its high thermal conductivity and high specific heat it is able to conduct heat away from the superconducting filaments and absorb a fraction of it. Additionally, the filaments are twisted along the wire axis in order to improve the stability with respect to flux jumps [10].

The addition of Cu to the precursor materials has proven to lead to additional advantages aside from protection and stabilization. It prevent the formation of non-superconducting phases, even at lower temperatures and therefore lowers the necessary temperature for the Nb$_3$Sn phase formation from $930\,°\text{C}$ to about $650\,°\text{C}$. It furthermore contributes to limiting grain growth, which is beneficial for increased flux pinning [124].

The Cu barrier between sub-elements is also helpful in preventing a merging during reaction and possible deformation which could lead to increased local instabilities

[155]. The Cu/non Cu ration of wires used for accelerator magnets is typically between 1.5 and 2 [5].

Aside from optimal superconducting properties, practical materials demand further parameters for the use in superconducting magnets, which include the possibility of manufacturing wires of long lengths and in large amounts, while retaining an acceptable cost [124].

In order to reach a high current through the magnets, multiple wires are connected, twisted and transposed to form cables. The most common type of cable that is used in accelerator magnets is the Rutherford cable with a mostly rectangular or keystoned cross section. The Rutherford cable design is suitable for Nb_3Sn wires, albeit the formation of the wires to such cables without degrading the superconducting properties of the delicate precursor material is challenging and necessitates dedicated optimization. The use of such cables based on multiple superconducting wires reduces the number of turns per coil and therefore the magnetic inductance [124].

1.4.2 Magnets based on NbTi and Nb_3Sn

In the past 40 years, NbTi has been the most frequently used superconductor for accelerator magnets for HEP (high energy physics) applications, which has been optimized over the years and has reached close to its maximum potential. Particle accelerators like the LHC that are based on NbTi superconductors have reached their performance limit. In order to reach past the operating limit of NbTi of 10 T at 1.9 K, the use of a new material is necessary. Due to the recent progress in improving the manufacturing techniques of Nb_3Sn it has been the most promising candidate for replacing NbTi so far, which can operate at fields of 16 T at 4.2 K and is now considered for the first time to be used in accelerator magnets with fields up to 12 T. Nb_3Sn is currently the only material that can realistically offer the required high field performance in order to achieve higher beam luminosity, as aspired in the HL-LHC, and higher beam energy as planned for the FCC. The High-Luminosity LHC (HL-LHC) project aims to increase the LHC rate of collision, denoted as luminosity, in the next years by a factor of five, which will require dipole magnets of 11 T and quadrupole magnets of 12 T–13 T based on Nb_3Sn. Recently a design study for a The Future Circular Collider (FCC) has been started which aims to outline the options for a post-LHC particle accelerator with a centre-of-mass collision energy of 100 TeV, which is 7 times as high as currently achievable with the LHC. The first designed configuration foresees the necessity of 16 T Nb_3Sn dipole magnets in a 100 km tunnel [6, 10, 21].

In the course of the High Luminosity upgrade of the Large Hadron Collider at CERN, some NbTi dipole magnets are being replaced by superconducting magnets based on Nb_3Sn with peak fields over 11 T. This will be the first time ever that Nb_3Sn superconductors will be used in High Energy Physics accelerator magnets and a

particle collider operating by the use of high-field Nb_3Sn magnets. Fields up to $16\,T$ are not only of interest for the use in the HL-LHC, the High Energy LHC (HE-LHC) and the FCC, but could also find application in the Super Proton-Proton Collider, a Very Large Hadron Collider or in muon colliders. Aside from Nb_3Sn, such high fields could also be achieved by the use of two other superconductors: $Bi_2Sr_2CaCu_2O_8$ and $REBa_2Cu_3O_7$. The cost of these alternative conductors is at present much higher than Nb_3Sn, therefore Nb_3Sn is at the moment the most efficient option for achieving the current density target of the FCC [2, 124].

While for the HL-LHC project, the operation in a field range of up to $12\,T$ appears realistic, the operation of magnets at fields up to $16\,T$ provide additionally major challenges, many of which still have to be explored and overcome efficiently [124].

Different designs of dipole magnets for future accelerators based on Nb_3Sn are in consideration. The most common design types are the Cos-Theta, Block-Type and Common-Coil dipole magnets. A comprehensive overview of these types of magnets is given in [124]. The cos-theta and block coil type magnets are more efficient than their contractants, since the largest fraction of the magnet cost is determined by the cost of the conductor. Other magnet types, however, show less stress sensitivity.

Aside from particle accelerators, another field which will require large amounts of magnets based on of Nb_3Sn superconductors in the future is nuclear fusion, especially in the ITER (International Thermonuclear Experimental Reactor) that is currently under construction. The requirements of fusion reactors inherently differ from those of particle accelerators in regard to stability and magnitude of magnetic fields, which results in different layouts and demands of the Nb_3Sn conductors [130].

1.5 The compound Nb$_3$Sn and Nb$_3$Sn wires

1.5.1 General properties

Nb$_3$Sn is the material of choice for producing high magnetic fields up to 16 T magnets that are required for FCC-hh dipole magnets. It is a brittle intermetallic compound and a type II superconductor. Modern multi-filamentary Nb$_3$Sn wires possess a diameter of around 1 mm with sub-elements of 60 µm in size. Commonly, the ternary compounds (NbTi)$_3$Sn and (NbTa)$_3$Sn are formed by adding 1 at.%–2 at.% Ti or 2 at.%–4 at.% Ta. By doing so, B_{c2} is enhanced by increasing the resistivity ρ_n without sacrificing T_c [5, 10]. The highest upper critical field B_{c2} in ternary Nb$_3$Sn wires was found to be in the order of (29.5 ± 0.3) T and the highest critical temperature T_c (17.8 ± 0.3) K [53]. Other sources cite a T_c of up to 18.3 K [130].

The Nb$_3$Sn crystal structure is A15 and it belongs to the space group P$_{m3n}$(O$_h^3$), where the Nb atoms are located at $(0, \frac{1}{4}, \frac{1}{2})$ and the Sn atoms at (000) and $(\frac{1}{2}, \frac{1}{2}, \frac{1}{2})$. The Sn atoms are located on bcc sites while the Nb atoms are located on the sides of the unit cell in the form of chains that are orthogonal to each other [102]. The Nb$_3$Sn lattice parameter is 0.529 nm [130]. The crystal structure of a Nb$_3$Sn unit cell is schematically displayed in Figure 1.4.
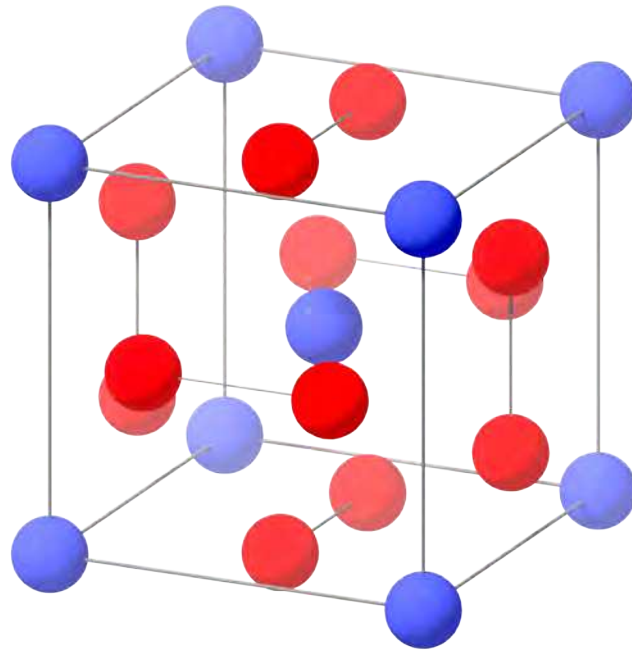
Figure 1.4: Nb$_3$Sn crystal structure. Red: Nb atoms, blue: Sn atoms. Graphic drawn by and used with permission of Stefan Löffler.

The Nb$_3$Sn phase will often be referred to as A15 phase in this thesis. The A15 phase range corresponds to a Sn content of about 18 at.%–25 at.% [10, 52]. Other sources suggest a possible wider composition range of around 17 at.%–27 at.% [26]. Below 43 K, a phase transformation occurs from the cubic A15 phase to the tetragonal phase [130]. A phase diagram of the binary Nb-Sn system including the tetragonal phase range can be found in [52].

Since standard Nb$_3$Sn wires consist of different phases such as Nb$_3$Sn, Nb and Cu, the critical current density J_c can be defined in different ways [171]:

1. The engineering J_c is defined by the average critical current density over the entire wire cross section, including the Cu and the A15 phase, as well as the Nb barrier and the residual Cu and Sn in the centre of the sub-elements.

2. The layer J_c is defined by the critical current density of the A15 phase only.

3. The non-Cu J_c is defined by the average critical current density of the A15 phase, the Nb barrier and the residual Cu and Sn in the centre of the sub-elements. The FCC target J_c of 1500 A mm^{-2} refers to the non-Cu J_c value.

1.5.2 Variations, dependencies and scaling of the superconducting properties

The Nb$_3$Sn layer J_c depends on the pinning force density F_p provided by the pinning centres at a certain field: $J_c = F_p/B$, where F_p is a function of B [171]. A common procedure of determining B_{c2} is the linear extrapolation of $J_c^{0.5}B^{0.25}$ over B, denoted as Kramer rule or Kramer plot [44, 45]. Experimental data was fitted using the relationship

$$J_c(B) \propto \left(\frac{B_{c2}}{B} \right)^{1-p} \left(1 - \frac{B}{B_{c2}} \right)^q. \tag{1.9}$$

For PIT and internal tin wires, no considerable amounts of columnar grains exist in the A15 layer. In this case of mainly equiaxed grains, the parameters of $p = 0.5$ and $q = 2$ yield a good fit to the data.

A detailed summary of the property variations with composition, morphology and strain state in Nb$_3$Sn are given in [52]. Nb$_3$Sn commonly occurs off-stoichiometric in the form Nb$_{1-\beta}$Sn$_\beta$ with $0.18 \leqslant \beta \leqslant 0.25$. Since the critical temperature T_c is dependent on the composition, it ranges from about 6 K to 18 K. The phase transformation to the tetragonal structure occurs below 43 K at a phase range of $0.245 \leqslant \beta \leqslant 0.252$. At the stoichiometric composition, the lattice parameter of Nb$_3$Sn is about 0.529 nm. The Nb chains are of great importance for the high T_c, since it is related to the long range crystallographic ordering, which can be described

trough the Bragg-Williams long range atomic order parameters S_a for the chain sites and S_b for the cubic sites:

$$S_a = \frac{r_a - \beta}{1 - \beta} \qquad S_b = \frac{r_\beta - (1 - \beta)}{1 - (\beta)}, \tag{1.10}$$

where r_a and r_b are respective factors of the occupation for A atoms at chain sites and B atoms at cubic sites in the system $A_{1-\beta}B_\beta$ and β the atomic Sn content. The stoichiometric composition leads to $S = 1$ and complete disorder is described by $S = 0$. Variations of the superconducting properties are related to changes of the lattice parameter, the normal state resistivity, the long range order and the atomic Sn content, which are dependent on each other and can thus be expressed by one of these variables, most commonly either by the resistivity or the Sn content. A higher Sn content leads to an expansion of the lattice parameters in Nb₃Sn, while in all other A15 compounds, the contrary was observed. Knowledge of the dependence of the superconducting properties on the composition are important since Nb₃Sn is formed by solid-state diffusion, inevitably leading to compositional gradients in the wires. The dependency of T_c on the Sn content was described by two fits to literature data, one linear in the form of

$$T_c(\beta) = \frac{12}{0.07}(\beta - 0.18) + 6 \tag{1.11}$$

and one described by a Boltzmann function identical to

$$T_c(\beta) = \frac{-12.3}{1 + exp\left(\frac{\beta - 0.22}{0.009}\right)} + 18.3, \tag{1.12}$$

where a maximum T_c of 18.3 K is assumed, which is the record value of Nb₃Sn. The experimental data of $H_{c2}(\beta)$ was described by the function

$$\mu_0 H_{c2}(\beta) = -10^{-30} exp\left(\frac{\beta}{0.00348}\right) + 577\beta - 107. \tag{1.13}$$

The dependencies of T_c and B_{c2} on the Sn content described by the functions in Equation 1.11, Equation 1.12 and Equation 1.13 are displayed in Figure 1.5.

The phase boundary between field and temperature is independent of morphology, strain and composition and thus constant, therefore only $H_{c2}(0)$ and $T_c(0)$ are necessary to describe the phase boundary. The highest Sn contents lead to the upper phase boundary of 29 T and 18 K in ternary wires. The average of the compositional range in a wire leads to a lower phase boundary, which influences the critical current density. Additions of Cu were found to lower the formation temperatures of the A15 phase, thus reducing grain growth and achieving a higher grain boundary density,
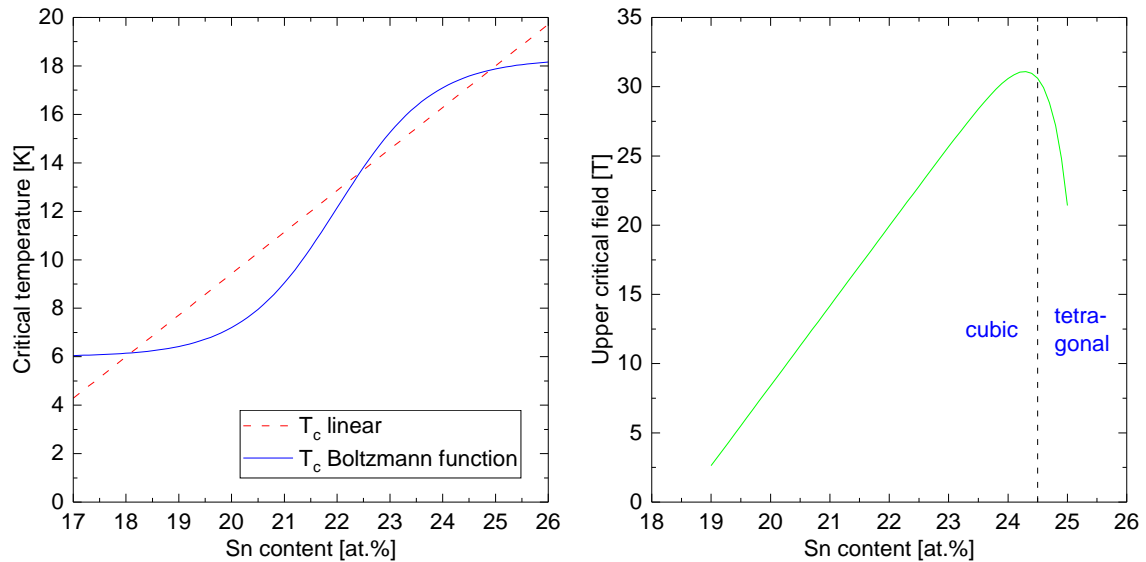
Figure 1.5: Dependency of T_c (left) and B_{c2} (right) on the Sn content in binary Nb$_3$Sn described by functions listed in [52].

beneficial for flux pinning. Precise data about the Cu influence and phase diagrams of the Nb-Sn-Cu system are required to be established in the future, although it is known that Cu contributes to the destabilisation of the phases NbSn$_2$ and Nb$_6$Sn$_5$. It is believed that Cu is only located at grain boundaries and not inside Nb$_3$Sn grains, thus the presence of Cu does not considerably alter the superconducting properties of the wires. When introducing Ti and Ta doping in Nb$_3$Sn wires, these elements are cited in [52] to occupy Nb lattice sites. At contents of over 2.8 at.% for Ta and 1.3 at.% for Ti, they suppress the transition from the cubic to the tetragonal phase at low temperatures. The value of $H_{c2}(4.2K)$ was found to increase with these additions, where the maximum is found at around 4 at.% for Ta and 1.5 at.% for Ti, after which a reduction occurs at higher contents. The maximum of the critical temperature is found at 2 at.% for Ta and 1 at.% for Ti, a substantial reduction is observed above 3.5 at.% for Ta and 1.5 at.%. The suppression of the tetragonal phase thus leads to an increase in $H_{c2}(0K)$, where elemental contents over 3.5 at.% for Ta and 1.5 at.% for Ti reduce $H_{c2}(0K)$ and $T_c(0)$ due to increased resistivity, which is equivalent to a reduction in the Sn content. The current carrying capabilities of a conductor is determined by the bulk pinning force

$$\vec{F}_p \equiv -\vec{J}_c \times \vec{B}, \tag{1.14}$$

where the maximum lies between about 0.1 and 0.4 of H_{c2}. The dominant pinning centres in Nb$_3$Sn are believed to be grain boundaries, where the reciprocal grain size and therefore the grain boundary density are related to the maximum pinning force. The exact underlying mechanisms of the pinning at Nb$_3$Sn grain boundaries are yet unknown, for which reason an investigation of the composition and morphology at

grain boundaries is relevant. A function is presented in order to describe the relation between the pinning force and the grain size, which yields a good fit to existing literature data:

$$F_{p,max} = 22.7 \ln\left(\frac{1}{d_{av}}\right) - 10,$$ (1.15)

where $F_{p,max}$ is in units of $\mathrm{GN\,m^{-3}}$ and d_{av} is the average grain size in µm. The optimum grain size is achieved when one pinning site exists for each flux line. The grain size thus has to be in the order of the spacing of the flux lines, which depends on the field. For a triangular lattice, the spacing of the flux lines can be described by

$$a_\triangle(H) = \left(\frac{4}{3}\right)^{1/4}\left(\frac{\phi_0}{\mu_0 H}\right)^{1/2},$$ (1.16)

yielding a value of 14 nm at a field of 12 T. Since grain sizes of present Nb₃Sn wires are in the order of 100 nm–200 nm, it becomes apparent that there is still great potential for optimisation of the pinning force through grain refinement, contrary to NbTi wires, where the optimal pinning site density was achieved through the introduction of alpha-Ti precipitates. The effects of strain on the superconducting properties can be understood as instabilities in the lattice that can lead to tetragonal distortions and as influences on the interactions between electrons. It was suggested that strain sensitivity can be attributed to the degree of ordering and is thus dependent on the A15 composition in Nb₃Sn. At increasing magnetic fields and temperatures, the strain sensitivity of the critical current density increases. The composition might have an influence on the strain sensitivity, where an increase in the Sn content might possibly result in an enhancement thereof, which could lead to this undesired effect in new generation wires, where performance enhancements through higher Sn contents are strived for. Experimental results showed that the strain dependence of $H_{c2}(0)$ is three times as high as the one of $T_c(0)$. In summary, the close spacing of the Nb chains in the A15 lattice results in a high critical temperature due to an increase in the density of states around the Fermi level. The impact of variations from stoichiometry can be described through the lattice parameter, long range ordering, resistivity and Sn content, where these parameters can be considered equivalent. The Sn content has a substantial impact on the phase boundary between field and temperature due to deviations from stoichiometry and the tetragonal phase, which occurs close to stoichiometry. The critical current density is determined by the maximum bulk pinning force, strain effects and the phase boundary between field and temperature [52].

In practical high field superconductors, the flux pinning force per unit length obeys the unified scaling law (USL) [35, 36, 37]

$$F_p = I_c(B, T, \epsilon)B = K(t, \epsilon_0)f(b) = K(t, \epsilon_0)b^p(1 - b)^q, \qquad (1.17)$$

where $K(t, \epsilon_0)$ is a pre-factor dependent on temperature and strain, $b = B/B_{c2}^*(t, \epsilon_0)$ and $t = T/T_c^*(\epsilon_0)$ the reduced magnetic field and temperature, respectively, with $B_{c2}^*(t, \epsilon_0)$ and $T_c^*(\epsilon_0)$ being effective scaling fields, ϵ_0 describes the intrinsic strain and p and q are constant scaling parameters. According to the USL, neither strain nor temperature influence the shape of the pinning force curve when represented by the dimensionless scaling variables b and t. For simplification, the USL can be parametrised by separate functions for intrinsic strain ϵ_0, reduced temperature t and reduced magnetic field b, leading to the separable form of the USL

$$F_p = Cg(\epsilon_0)h(t)f(b), \qquad (1.18)$$

with C being a constant. $f(b)$ is often denoted as pinning force function and, as seen above, $f(b) = b^p(1 - b)^q$. This leads to the division of the scaling law into five scaling functions, that are dimensionless and have values between 0 and 1: $b_{c2}(\epsilon_0), b_{c2}(t), g(\epsilon_0), h(t) and f(b)$. These functions are again determined by a few scaling parameters.

In [54], a scaling relation is proposed for the upper critical field in Nb$_3$Sn in the form of

$$H_{c2}(t)/H_{c2}(0) \cong 1 - t^{1.52}, \qquad t = T/T_c. \qquad (1.19)$$

The relation of $H_c(t)/H_c(0)$ was determined at $(1 - t^{2.07})$. Longitudinal compressive strain leads to a linear degradation of the superconducting properties in Nb$_3$Sn wires, while longitudinal leads to an increase of the critical parameters up to a certain point, after which a linear reduction occurs. Due to a higher thermal contraction of the matrix compared to Nb$_3$Sn, axial compression occurs when cooling from the reaction temperature to a low temperature where superconductivity occurs. For the critical current density the strain dependency was considered and the relation

$$J_c(H, T, \epsilon) \cong (C/\mu_0 H)s(\epsilon)(1 - t^{1.52})(1 - t^2)h^{0.5}(1 - h)^2 \qquad (1.20)$$

was derived, where C is a constant, s describes the normalizes strain dependence of $H_{c2}^*(0)$ and $h = H/H_{c2}^*(T, \epsilon)$, with H_{c2}^* representing the inhomogeneity averaged critical field where the critical current density extrapolates to 0. The main mechanism for de-pinning of the flux lines was assumed to be shearing of the flux lines.

The effects of Sn concentration gradients on pinning force scaling in Nb$_3$Sn wires is analysed in [15]. It was shown that in real wires that exhibit gradients in the elemental composition inside sub-elements of Nb$_3$Sn wires, scaling behaviours can occur that differ considerably from expectations. The Sn content and gradient in that work was modelled after the real RRP-Ti-108 wire that was investigated in this thesis. The concentration gradient of the Sn content led to a variation in T_c in the linear region of 1.7 K and a distribution of B_{c2} with a maximum in the centre of the A15 layer.

The effects of neutron irradiation on pinning force scaling in Nb$_3$Sn was investigated in [12], where wires were subjected to fast ($E > 0.1$ MeV) neutron fluences of up to 1.6×10^{22} m^{-2}. It was found that there are significant differences in the pinning force functions compared to expected values for pinning purely by grain boundaries. The contribution of point pinning centres induced by radiation to the pinning force was included in a function consisting of two components and its dependence on the fluence was found to be universal for all types of wires. At a fast neutron fluence of about 10^{22} m^{-2}, the pinning force of the unirradiated state and the contribution by the radiation defects were found to be relatively equal. It was found that wires alloyed with Ti or Ta show deviations from the expected grain boundary pinning, presumably due to differences in composition and grain boundary thickness. The irradiation with fast neutrons led to an increase of the maximum pinning force and shifted the peak position of the normalised pinning force to higher fields. The upper critical field B_{c2} was found to only increase slightly after irradiation.

The pinning force function was extended for irradiated samples and described by two components [13]

$$f(b) = \alpha b^{p_1}(1 - b)^{q_1} + \beta b^{p_2}(1 - b)^{q_2}, \tag{1.21}$$

where the first term describes the unirradiated state that is dominated by grain boundary pinning and the second term the change in the pinning behaviour induced by radiation. The contributions between both pinning mechanisms are weighted by the factors α and β. The parameter β was found to increase with increasing neutron fluence. The expected exponents for grain boundary pinning are $p = 0.5$ and $q = 2$, while for point pinning $p = 1$ and $q = 2$. The type of damage created by fast neutron irradiation was cited to be in the form of disordered regions with sizes of a few nm, which were stated to be responsible for point pinning contributions additional to the pinning by grain boundaries.

1.5.3 Manufacturing processes

Standard processes

The manufacture of Nb₃Sn wires can be conducted by various different processes. Modern Nb₃Sn wires are produced by mainly three manufacturing techniques: the bronze process, the internal tin (IT) process including the Restacked Rod Process (RRP) variant and the powder-in-tube (PIT) process [124, 10].

The similarity of the all production methods is the final high-temperature heat treatment during which the Nb₃Sn phase is formed, which includes several steps with varying duration and temperatures up to around 700 °C as described in Subsection 1.5.4.

In the bronze process, thin Nb filaments are stacked into a bronze matrix, which leads to a small filament size of around 2 µm–3 µm. The critical current density of bronze route wires is rather low, since the formation of Nb₃Sn is limited by a low Sn content in bronze [124].

Due to the requirements of a high J_c as well as the possibility of the manufacture in large quantities, only Internal Tin (IT), including Restacked Rod Process (RRP) which falls under the IT process, and Powder-in-Tube (PIT) wires Nb₃Sn wires are currently in consideration for the application in high energy physics to reach the desired performance for high-field accelerator magnets [5, 6, 124]. The standard Nb₃Sn wires investigated in this work were manufactured using the IT and PIT techniques, therefore these techniques will be described in detail.

The IT process includes multiple variations which show differences in the design of the Nb filaments, the position of the diffusion barrier, the distribution of Sn and the processing. The Restack Rod Process (RRP), which was developed by OST (now Bruker-OST), is one of these and held the record for the best performance for several years, until it was overtaken by PIT wires with artificial pinning centres, that achieved the J_c specifications of the FCC design in short samples in early 2019 [124].

In the IT RRP process, Nb filaments and pure Sn or Sn-alloy rods are stacked into a Cu matrix. The Sn or a Sn alloy is placed in a central hole in the matrix and the entire composition is formed into hexagonal rods that are easily stackable. Diffusion of Sn into the Cu matrix is prevented by a thin diffusion barrier of Nb or Ta. Multiple of those sub-elements are placed in a copper tube, followed by cold drawing to the final wire size. During the heat treatment, the Sn is diffusing outwards to the Nb rods and forms the Nb₃Sn phase. Wires produced by this method possess the highest J_c values due to an optimal Sn content, but the minimal sub-element size is limited to 40 µm–50 µm [2, 124, 130].

As for all Nb_3Sn wires, the parameters of sub-element size, elemental ratios, heat treatment, purity of Cu and J_c have to be balanced and optimized with respect to each other. The doping or RRP wires is done by inserting Ti or Ta rods between the Nb filaments inside sub-elements. The use of Ti in RRP wires has led to the lowering of the optimal heat treatment temperatures compared to Ta wires, and by that to the improvement of J_c at high fields and other important parameters [124].

A detailed compilation of the PIT manufacturing technique as well as the phase formation processes are given in [55]. Tubes made of Nb or Nb-alloys are filled with fine $NbSn_2$ powder and a few at.% of Cu, which contributes to a fast A15 phase formation below a temperature of 700 °C. The filled tubes are then stacked into a Cu matrix and the wire is drawn to its final size. The last step involves a heat treatment at a temperature of typically around 675 °C for the duration of a few days. This method results in small filament sizes of less than 50 µm and J_c values almost as high as in IT wires with the disadvantage of double their cost [2, 124].

Due to the fabrication process, two different A15 grain morphologies are present in PIT Nb_3Sn wires: a fine grained region with grain sizes of around 100 nm–200 nm, and a coarse grained region with grains of 1 µm–2 µm. It was found that the two phases in PIT wires show different values of the superconducting properties. The coarse grained region possess a higher critical temperature T_c but a lower critical field B_{c2} compared to the fine grained region due to a higher Sn content [129].

Coarse grains in PIT wires are caused by intermediate phase formations during the heat treatment and do not contribute to carrying supercurrent. Only the fine grains in Nb_3Sn carry supercurrent and are formed by the diffusion reaction between Nb and Sn. The fraction of fine grains in RRP wires was found to be much higher than in PIT wires. The coarse grain region in Nb_3Sn is commonly stoichiometric, while the fine grain region shows Sn contents of around 22 at.%–24 at.% [171].

While PIT wires are generally characterized by a smaller A15 fraction and lower non-Cu J_c than RRP wires, the fabrication technique makes it possible to achieve smaller sub-element diameters. It was found that the coarse grains in the A15 phase of PIT wires possess the highest T_c, but have no contribution to the transport current at high fields. The small transport properties defining A15 grains showed a maximum T_c of 17.7 K. While the fine grains in the centre of the A15 phase are generally equiaxed, the outmost grains near the Nb barrier often show columnar character. Since a considerable amount of Sn gets consumed by the formation of large grains that could otherwise fuel the creation of fine grains, the suppression of large grains is highly desirable [147].

Tube type conductors generally show lower magnetization due to a smaller sub-element diameter and therefore better stability in the low field region, while having lower J_c values at 12 T compared to RRP wires. This discrepancy was attributed to a lower fine grain A15 area fraction in the tube conductors, rather than a difference in grain size [165].

In modern Nb_3Sn wires, additional diffusion barriers consisting of Nb are often added before the heat treatment. The Nb barrier is important for preventing Sn from diffusing into the Cu matrix, as well as separating the sub-elements from each other to prevent their coupling [130].

There are variations of the standard RRP and PIT manufacturing processes in existence that have been explored with the goal of primarily reducing the cost of the conductor, whose performance has not reached the desired values and exploited their full potential yet [59, 61].

Aside from the already mentioned techniques, it is in principle possible to manufacture Nb_3Sn wires using other techniques, such as the Jelly Roll (JR) Process and the In Situ Process [130]. There have also been a few attempts of alternative fabrication methods, for example based on Sn-B and Sn-Ta alloys, which, while showing promising results, have to be considered non-standard and have not achieved the performance of the best standard wires so far [144].

The two main manufacturing techniques for industrial Nb_3Sn wires regarding performance and availability have been the IT RRP by Oxford Superconducting Technology (OST) and PIT by Bruker European Advanced Superconductors (Bruker EAS) [10]. OST reported steady progress over the years, already achieving a non-Cu J_c of $2900\,A\,mm^{-2}$ at $12\,T$ and $4.2\,K$ in the year 2003 [106]. A non-Cu J_c of over $3000\,A\,mm^{-2}$ at $12\,T$ and $4.2\,K$ was reported in [33]. So far the IT wire with the highest performance was manufactured by the Restacked Rod Process of OST, which has reached non-Cu J_c values of $3300\,A\,mm^{-2}$ at $4.2\,K$ and $12\,T$ and values of B_{c2} of around $25\,T$ at $4.2\,K$. The PIT wire with the highest J_c has been produced by Bruker-EAS with values of around $2700\,A\,mm^{-2}$ at $4.2\,K$ and $12\,T$ and B_{c2} of about $25.7\,T$ [6].

While it can be said that the present state-of-the-art Nb_3Sn wires confidently fulfil the requirements for the planned HL-LHC upgrade, even leaving some margin, the performance is still insufficient for a collider with the magnitude of the FCC. The target value for the minimum non-Cu J_c was determined to be $1500\,A\,mm^{-2}$ at $4.2\,K$ and $16\,T$, about $50\,\%$ higher than for the HL-LHC. Aside from the performance requirement, two other challenges that also need to be resolved for the FCC are the reduction cost of the conductor and the magnetization by reduction of the effective filament diameter to $20\,\mu m$. Increasing J_c even further and pushing it towards its performance limit will require an increase in the pinning force by a more elaborate grain refinement and possibly the introduction of artificial pinning centres (APC) [6].

As already mentioned, RRP wires are produced by stacking small filaments which then form to sub-elements, while PIT wires consist of tubes in a matrix, in which case filament would be the correct denotation for each tube. For clarity reasons, the term sub-element will be applied to all wires in this thesis, including PIT wires.

Figure 1.6 shows SEM images of sub-elements of a final wire cross section where the different phases are marked.
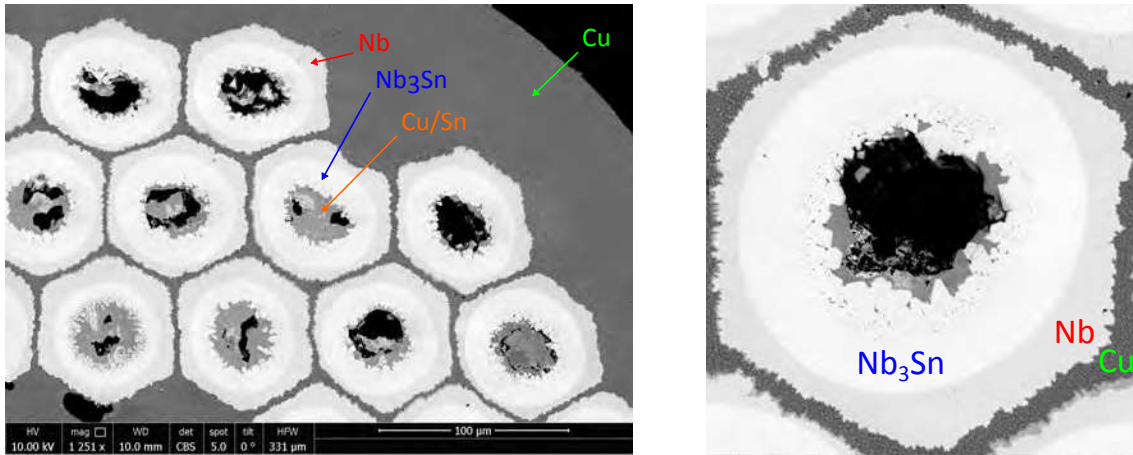
Figure 1.6: SEM images of sub-elements of a final Nb$_3$Sn wire cross section showing the different phases.

As a result of the manufacturing process, during which a Sn source diffuses from the core of the sub-elements outside to a Nb layer where the Nb$_3$Sn phase is formed, the Sn content in the Nb$_3$Sn phase usually exhibits a gradient. The Nb$_3$Sn phase is limited to a Sn content between about 18 at.% and 25.5 at.%. The Sn content highly impacts the critical temperature T_c, leading to the fact that the gradient in elemental composition results in a gradient of T_c, where the sub-elements in Nb$_3$Sn show a T_c range from about 6 K to slightly above 18 K. The Sn content furthermore highly affects the upper critical field B_{c2}, which shows a maximum at around 24.5 at.% [14]. Sn concentrations gradients in PIT wires were found to be commonly in the order of 0.1 at.% µm^{-1}–0.2 at.% µm^{-1}, leading to differences in the local superconducting properties [171].

The manufacturing of Nb$_3$Sn wires therefore has to be adjusted in respect to various compromises that have to be accounted for such as the optimization of the superconducting properties, the maximization of the A15 fraction, the minimization of compositional gradients inside sub-elements and achieving a high critical current density J_c through refinement of the grain size and increasing the flux pinning. The homogeneity of the A15 phase can be improved by an increase of the temperature and duration of the heat treatment, which on the other hand results in an increase of the grain growth [146].

Internal oxidation

Recently a milestone in Nb$_3$Sn grain refinement was achieved by the addition of Zr and O to Nb and Sn before the heat treatment, leading to the internal oxidation of Zr

and formation of ZrO_2 precipitates, consequently reducing the grain size of the A15 phase. While 1 at.% Zr is alloyed with Nb, O is supplied by adding SnO_2 powder. The authors of the study claimed to have achieved grains with less than half the size of conventional Nb_3Sn wires [167]. It was also suggested that intra-granular ZrO_2 precipitates could potentially act as pinning centres and contribute to the increase in the pinning force in these wires [174].

Figure 1.7 shows the comparison between the manufacturing methods of standard PIT and internal oxidized Nb_3Sn wires using Zr and O to form ZrO_2 nano-precipitates during the heat treatment, which are principally very similar. In this thesis, the Nb_3Sn wires produced by the internal oxidation method will be referred to as APC (artificial pinning centres) wires. The wires irradiated with fast neutrons technically also contain artificial pinning centres in the form of defects but will simply be denoted as irradiated wires.
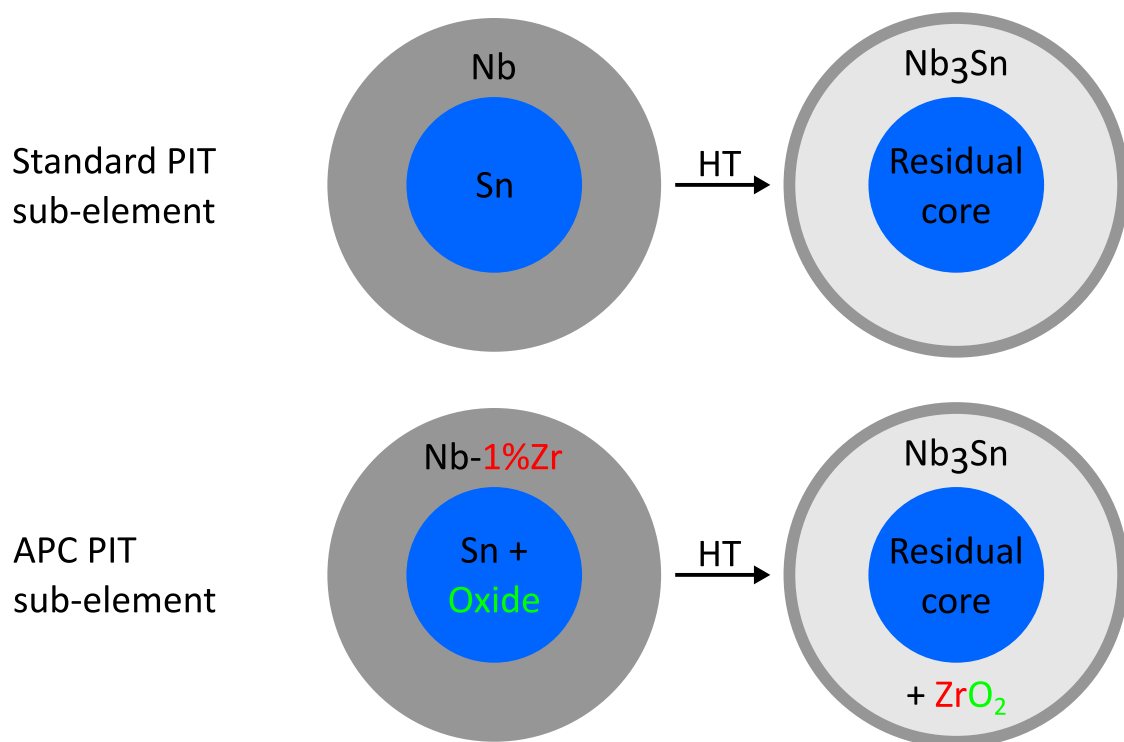
Figure 1.7: Comparison between manufacturing methods of standard PIT and internal oxidized Nb_3Sn wires. Graphic drawn after concept by Xingchen Xu, e.g. [171].

For the use of internal oxidation in Nb_3Sn wires, a Nb-Zr alloy is often used due to the fact that the affinity of Zr to O is much stronger than the affinity of Nb to O. The O required to oxidise the Zr atoms during the heat treatment is usually supplied in the form of oxide powders located inside the sub-elements. The ZrO_2 precipitates were found to be located intra- and inter-granularly with diameters of around 3 nm–15 nm.

It was suggested that these precipitates are capable of contributing to point pinning and thus shifting the peak of the pinning force curve to higher fields. At grain sizes lower than around 50 nm, not only the maximum pinning force increases, also the peak shifts to higher fields, additionally benefiting the high field J_c. Currently, the development of PIT wires with improved pinning through grain refinement is in progress, which aims to also achieve the other requirements of a small sub-element diameter, a high RRR and larger wire lengths. The optimisation of the fine grained fraction of Nb$_3$Sn and B_{c2} additionally can not be neglected. It is thus proposed that in order to achieve the FCC J_c target, focus should be laid upon the improvement of the flux pinning, especially through the introduction of artificial pinning centres [171].

The mechanisms of the grain refinement by ZrO$_2$ precipitates are not fully understood yet, though it is presumed that either the particles serve as nucleation centres or they are pinning the Nb$_3$Sn grain boundaries during the Nb$_3$Sn formation reaction. Most recently an average grain size of 36 nm was reported to be achieved in internally oxidized Nb$_3$Sn wires, leading to a significant increase of J_c, being nearly double as high as in conventional Nb$_3$Sn wires [173].

Aside from the addition of Zr, the internal oxidation manufacturing process has also been conducted with Hf instead of Zr, since both elements show a high affinity to O. Both routes were furthermore employed with and without an O source in the form of SnO$_2$, where the highest vortex pinning performance was achieved using a Nb4Ta1Hf alloy without SnO$_2$. The samples containing Hf without O source showed the best performance of a layer J_c of roughly 3700 A mm^{-2} at 16 T and 4.2 K, which corresponds to a non-Cu J_c of about 2200 A mm^{-2} in RRP wires. The Ta–Hf based wires therefore showed layer J_c values that were about three times higher than in standard Ta and Ta–Zr based wires. The resulting grain size of the Ta–Hf wire was determined at (68 ± 25) nm, the one for the Ta–Hf–SnO$_2$ wire at (55 ± 10) nm. It was thus concluded that the addition of Hf is more effective than Zr, and that the FCC target can be achieved without the addition of internal oxygen sources. It might thus be the best option to use Hf additions to Nb4Ta for grain refinement in internal tin or PIT wires without internal oxidation [4].

A PIT approach of producing Nb$_3$Sn wires with ZrO$_2$ nano-precipitates is presented in [98], where SnO$_2$ powder is added to Cu$_5$Sn$_4$ in the PIT core, while the Nb on the outside is alloyed with 1 wt.% Zr. The authors stated the achievement of an average A15 grain size of 38 nm, but the volume of this fine grained Nb$_3$Sn produced was very limited. The pinning force curves where separated into contributions from grain boundaries and point-pinning centres, where the point-pinning component showed a much higher impact of up to 89 %. The peak shift of the pinning force curves to higher fields was stated to be comparable to the ones resulting from irradiation experiments.

The addition of Ti to internal oxidized Nb$_3$Sn wires has been explored already with success, and based on this technique, PIT wires with ~25 μm small sub-elements

have been manufactured [174].

In the newest generation of APC wires with ZrO_2 nano-precipitates, the addition of Ta has been explored, achieving upper critical field B_{c2} values of 28 T. In [170], non-Cu J_c values of 1200 A mm^{-2} at 16 T and 4.2 K were reported as well as Nb_3Sn layer J_c values of 4710 A mm^{-2}, where the fine grain Nb_3Sn fraction and the average grain size of 70 nm–80 nm were stated to be not yet fully optimized.

New generation APC wires produced by Hyper Tech Research Inc. have already achieved J_c values close to the FCC target of 1500 A mm^{-2} at 16 T in short samples in 2019, corresponding to a J_c of 3600 A mm^{-2} at 12 T [124].

1.5.4 Heat treatment

The multi-stage heat treatment that is required for the formation of Nb_3Sn during all manufacturing techniques involves temperatures up to 650 °C–700 °C and treatment times of 50 h–100 h [124]. The fabrication method as well as the heat treatment have to be chosen and optimized particularly for the desired application, each demanding different requirements [60].

One disadvantage of magnets based on Nb_3Sn over NbTi superconductors is the high brittleness of Nb_3Sn in the reacted form. The unreacted wires on the other hand, are ductile enough to be formed into coils. For that reason, winding of Nb_3Sn magnets is done before the heat treatment, which then leads to the formation of the Nb_3Sn phase [130].

The heat treatment to form the Nb_3Sn phase involves multiple steps at different temperatures and durations and impacts the final grain size and stoichiometry [178]. Detailed studies of Nb_3Sn phase growth during heat treatment and the resulting effects on the superconducting properties have been conducted in the past [9].

During the heat treatment of typical tube type wires, the Sn and Cu inside the tube becomes molten and reacts with the tube that is made out of Nb. This leads to the formation of $NbSn_2$, followed by Nb_6Sn_5. At later stages of the heat treatment, both of those phases are converted to Nb_3Sn. While a Nb-Sn reaction results in a fine grain region of Nb_3Sn, the conversion of Nb_6Sn_5 to Nb_3Sn leads to a coarse grain structure with grain sizes of around 1 µm–2 µm. The proportion of these regions has an important impact on the superconducting properties of the conductor, because the coarse grains carry less current than the fine grains in the superconducting state. The addition of Cu before reaction is important because it decreases the production of the Nb_6Sn_5 phase and therefore the the ratio of the coarse grain region. The amount of Cu in the starting alloy that was found to be optimal for maximizing the amount of the fine grain region is when the Sn content is ∼27 at.% [166].

An in-situ study of the phase formation during the heat treatment of RRP Nb_3Sn wires can be found in [123], where it was observed that these wires show less formation of

Nb_6Sn_5 during the heat treatment. Coarse grains were also observed in the RRP wires, which only occupied a very limited fraction of the A15 phase, which was suggested to be related to the low amount of Nb_6Sn_5 formed. Furthermore, microtomographic investigations showed in increased void formation at higher reaction temperatures.

The different phases that form in PIT sub-elements during the heat treatment were investigated by synchrotron diffraction in [97]. At increasing temperatures, pure Sn forms phases in the order Cu_6Sn_5, a ternary Cu-Nb-Sn phase with a high Sn content, $NbSn_2$ and Nb_6Sn_5 before forming into Nb_3Sn.

The crystal structure of this ternary Cu-Nb-Sn phase that occurs during the phase formation in the course of the heat treatment was unknown for a longer time and recently investigated by means of EDX, EBSD and X-ray diffraction [91]. The authors determined the composition of this phase to be approximately $(Nb_{0.75}Cu_{0.25})Sn_2$.

A higher amount of Cu inside the tube reduces the formation of coarse grains, but at the same time lowers the Sn content in the fine grain region, thus limiting J_c [172]. It has also been shown that the addition of only a few at.% of Ti dramatically increases the Nb_3Sn layer growth during heat treatment [164].

The Cu distribution between the Nb filaments in RRP wires is beneficial for the sub-elements, due to the diffusion rate of Sn in Cu-Sn being much higher than the growth rate of Nb_3Sn [171].

Cu was shown to contribute to the Nb_3Sn phase formation at lower temperatures [171]. An increase in the Cu/Sn ratio also led to an increase in the fine grained Nb_3Sn fraction due to a reduction in the amount of intermediate phases and coarse grains. On the other hand, a higher Cu/Sn ratio has negative consequences on the stoichiometry, B_{c2} and the maximum pinning force of the Nb_3Sn phase. The Nb_3Sn layer growth rate was furthermore found to be the highest for wires with the highest Cu/Sn ratio. Although not common in RRP and PIT wires, columnar grains are sometimes present in these types of wires too. An increase in the Cu/Sn ratio leads to a thicker layer of columnar grains, which shows large gradients in the Sn content, resulting in low B_{c2} values. Furthermore, due to columnar grains showing lower pinning efficiency, the presence of larger fractions of such grains leads to a lower maximum pinning force.

A higher reaction temperature leads to an increase in the final Nb_3Sn grain size and a decrease of the maximum pinning force. From this result it was concluded that grain boundaries are the primary flux pinning centres in Nb_3Sn [118]. In [85], it is described how a high temperature heat treatment can lead to a decrease in the Sn gradient and thus benefiting the high field J_c, however leading to an increase in grain size and thus a reduction in the flux pinning site density and therefore J_c. A higher reaction temperature not only leads to a better high-field (over 20 T) performance due to a higher Sn content in the A15 phase, but also decreases the performance at medium fields (12 T–15 T) due to increased grain growth and therefore lower grain

boundary flux pinning [21]. For that reason superconductors need to be optimized for the best performance at either high or medium fields.

Efforts and discussions are ongoing about the optimal temperatures and annealing times for wires of different manufacturing techniques [43]. It has also been shown that the optimal values of these parameters change depending on the alloying elements Ti and Ta used [51] and on the targeted operating field [50].

It was furthermore found that the heat treatment conditions also affect the mechanical properties of the reacted Nb_3Sn wire. A lower temperature leads to higher ductility, proof stress and stability. Additionally, a longer heat treatment resulted in a higher brittleness [66].

1.5.5 Doping

In modern Nb_3Sn wires, further elements are often alloyed to the precursor materials that dissolve into the Nb_3Sn layer and improve the superconducting properties. An addition of $1\,at.\%$–$2\,at.\%$ Ti has led to an increase of T_c, H_{c2} and a significant J_c improvement of one magnitude in high fields [3]. Considering the addition of Ti, multiple methods of doing so are also available, including alloying with Nb, the matrix, as well as with Sn as described in [58] and the references therein.

In [171] it was suggested that the dominating mechanism for diffusion of Sn in Nb_3Sn is grain boundary diffusion, due to the diffusivity of Sn at Nb_3Sn grain boundaries being orders of magnitudes higher than for bulk diffusion. A high Sn diffusion rate relative to the reaction rate is beneficial for a homogeneous Sn distribution and a low gradient, thus a high diffusion rate is important for improving the stoichiometry. Ti doping was found to contribute to an acceleration of the Nb_3Sn layer growth rate was furthermore found to lead to a more uniform Sn content of the Nb_3Sn layer, possibly explaining the enhancement of B_{c2}. Additionally, it is believed to be responsible for a higher diffusivity at grain boundaries, which results in higher layer growth rates and reduced Sn gradients due to higher diffusion rates.

While both Ta and Ti doping have been applied to Nb_3Sn wires in the past, a recent study has shown that doping with Ti achieves a greater homogeneity of the superconducting and chemical properties, presumably due to a fast Ti and improved Sn diffusion. Additionally, the wires with Ti have shown a narrower T_c distribution, resulting in a higher upper critical field B_{c2} [148].

A comprehensive compilation of the most influential microstructural parameters such as the composition and the correlations with the superconducting properties of Nb_3Sn superconductors is given in [45]. The dependency of T_c on the Sn content was described by a linear fit up to around $24\,at.\%$, after which saturation occurs. The addition of Ti and Ta was shown to enhance B_{c2} and T_c due to atomic substitution and compositional changes and thus changes in the atomic ordering. Wires containing

Ti furthermore showed a lower T_c values than those containing Ta. The maximum B_{c2} values of up to 30 T were observed at Sn contents around 24 at.% in alloyed Nb$_3$Sn wires. The maximum values for T_c occurred at a Ti content of around 1 at.% and a Ta content of around 3 at.%, while the maximum B_{c2} values were obtained at 1 at.%–2 at.% Ti and at 3 at.%–4 at.% Ta. Ti showed higher diffusion rates than Ta, leading to a lower required temperature of the heat treatment. The phase transformation to the tetragonal state occurs at a temperature of 43 K in binary Nb$_3$Sn, but depends on the composition and additives. The transformation was observed at Sn contents near stoichiometry values and low additive contents.

While it has been known for a while that the addition of Ti and Ta to Nb$_3$Sn conductors can have a beneficial influence on J_c by increasing H_{c2}, the underlying mechanisms and the site occupancy of Ti and Ta in the Nb$_3$Sn lattice have remained a frequently discussed topic with contradictory hypotheses as also later discussed in Chapter 5.

Recent Extended X-ray Absorption Fine Structure (EXAFS) experiments contributed to a better understanding of these mechanisms, showing that Ti atoms substitute only on the Nb sites in the lattice, while Ta atoms occupy not only Nb places but also a substantial amount of Sn sites [69]. These results gave rise to the discussion if Ti could be more beneficial for a homogeneous Nb$_3$Sn phase, since it does not inhibit the Sn diffusion, while Ta might compete with Sn for the lattice sites, thus limiting its diffusion ability.

1.5.6 Strain and voids

Another important factor to consider that influences the performance is intrinsic and applied strain which generally leads to degradation of the superconducting properties. During magnet assembly, the stress in the conductor reaches levels of up to 150 MPa and up to 200 MPa during operation at low temperatures [124]. Multiple groups have investigated the dependence of the critical properties under strain in Nb$_3$Sn wires before [89, 151]. A comprehensive study of strain effects on J_c can also be found in [150].

One of the main reasons why Nb$_3$Sn superconductors have not been used in accelerator magnets so far is its brittleness, which can lead to permanent degradation even under low strain [27]. During the fabrication of Nb$_3$Sn magnets, the delicate processing, stress and strain sensitivity and brittleness of the wires and cables all have to be accounted for. For that reason Nb$_3$Sn magnets are produced by the wind-and-react technology, where the ductile precursor material is wound to coils, followed by the reaction heat treatment for several days, during which the superconducting Nb$_3$Sn phase is formed. Stress and strain that occurs during the heat treatment due to coil expansion leads to the degradation of the critical current density of Nb$_3$Sn, which can be reversible or irreversible, depending on the severity [2, 124].

Induced strain on Nb_3Sn superconductors can lead to degradation of their properties that results in a limited performance of the high field magnets. Irreversible degradation of J_c can be caused by cracks in Nb_3Sn due to its brittleness. It was determined by neutron diffraction that the preferred grain orientation is $\langle 110 \rangle$ parallel to the wire axis. The grain orientation generally does not highly impact the critical properties, but might have be of great importance when considering strain induced degradation of J_c [119].

Indications were found that stress due to voids and in the centre of sub-elements contribute to early cracking of the Nb_3Sn phase [79]. A past study suggested a correlation between the presence of so called Kikendall voids and the formation of micro-cracks in their vicinity, which can have a significant impact on the degradation of the critical current [27]. Simulations have also shown that voids in the wire can lead to increased stress and therefore possibly cracking of the sub-elements [177].

These voids in the centre of sub-elements form in internal tin Nb_3Sn wires during the reaction heat treatment and are mainly caused by density changes due to the formation of Cu_3Sn. Slowly ramping the temperature before Nb_3Sn phase formation and temperature holding steps have shown to be ineffective in reducing the void volume [119].

In [111], it is even suggested that, additionally to Kirkendall voids, there are multiple types of voids in Nb_3Sn wires, such that result from solid state formations and such that origin from liquid phase formations. The latter can lead to local inhomogeneities in the elemental composition trough local depletion and accumulation of Sn, which should therefore be avoided by a heat treatment at low temperatures.

The presence of Kirkendall voids becomes especially apparent in intern tin wires, which often use hexagonal filament stacking, frequently leading to six Kirkendall voids at the contact points between filaments and surrounding each individual filament. They can most frequently found near the outer diffusion barrier. The presence of Kirkendall voids did not suppress the Sn diffusion outwards, even when no solid Cu-Sn matrix was present. For the Nb_3Sn layer formation at lower temperatures, a Cu content of around $5\,at.\%$ is required, which was not denied by voids. Additionally, insufficient Cu contents prevent the formation of Cu-Sn phases that possess higher melting temperatures and thus lead to the formation of a liquid phase during the heat treatment. This can lead to building up pressure and tin bursting into the Cu matrix, which impacts the stability performance of the wire. In summary, it was found that the diffusion mechanisms of Cu play a critical role in the development of phases inside the cores of sub-elements. The distribution of Kirkendall voids was correlated with the distribution of coarse Nb_3Sn grains. Cu diffusion strongly influences the microstructure of Nb_3Sn wires and is thus relevant for optimizing the critical current density [112].

To summarize, during the manufacturing process of Nb$_3$Sn wires, a multitude of parameters has to be optimized [130], including:

1. The heat treatment has a major influence on the superconducting properties of the final Nb$_3$Sn wires. A longer duration of the heat treatment leads to a higher volume of the fine grain region. In order to achieve a fine grain size and therefore a high J_c, the temperature during the reaction has to be kept low. On the other hand, a high temperature heat treatment results in an improved stoichiometry of the Nb$_3$Sn phase, which also benefits B_{c2} and J_c. For that reason the heat treatment of Nb$_3$Sn wires of often divided into several stages, starting with a low temperature treatment for a long duration, followed by a treatment at a higher temperature.

2. The diameter of the sub-elements should be kept as small as possible in order to counteract thermal and electric instabilities. Small sub-element diameters furthermore require heat treatments for a lower duration.

3. The absolute value of the Sn content in the final sub-elements impacts the superconducting properties and should therefore be optimized.

4. Elemental additions to the precursor materials have shown to be capable of optimizing the grain size or B_{c2}, both of which lead to an improvement of J_c.

1.6 Performance enhancing capabilities

Efforts of improving the performance of Nb_3Sn wires by increasing the critical current density J_c have been made in a multitude of ways. A comprehensive review of the development of Nb_3Sn superconductors is given in [171]. The non-Cu J_c of Nb_3Sn conductors is influences by three main factors: the fraction of the Nb_3Sn phase that is capable of carrying current, the upper critical field B_{c2} and the capacity of pinning the flux lines. It was shown that the limit for the current-carrying fraction of the Nb_3Sn phase is around 65%. In a practical long wire, the weakest segment is responsible for limiting J_c. The given parameters are determined by microstructural factors, as B_{c2} is dependent on the stoichiometry of the Nb_3Sn phase and doping and the maximum pinning force on the density of flux pinning centres. Higher temperatures during the heat treatment results in a higher Sn content beneficial for B_{c2}, but lead to larger grain sizes and thus a reduction of the maximum pinning force. Larger grain aspect ratios are also undesirable, since it was shown that boundaries of such grains exhibit lower pinning efficiency than the boundaries of equiaxed grains [171].

The most prevalent vortex pinning mechanism in Nb_3Sn is grain boundary pinning [171] for which reason it is important to achieve the finest possible grain size in order to maximize vortex pinning and therefore increase J_c. Grain size refinement and optimization of the heat treatment are therefore important factors for the optimization of Nb_3Sn wires. The grain size of state-of-the-art Nb_3Sn wires is in the order of $150\,nm$, and since the vortex spacing at $16\,T$ is around $12\,nm$, there is considerable room for improvement in order to match the pinning sites density to the vortex density. Grain refinement can be achieved by lowering the heat treatment temperature but this counteracts the formation of a stoichiometric Sn composition of the A15 phase, demanding the right balance between grain boundary density and compositional homogeneity [5]. Aside from that, avoiding composition gradients to achieve a stoichiometric A15 phase and using the entire Nb and Sn precursor material to maximize the A15 phase are to be aspired.

The flux line spacing at fields of $12\,T$–$20\,T$ is in the order of $10\,nm$–$15\,nm$, much larger than the average grain sizes of present Nb_3Sn wires [171]. The maximum pinning force is inversely proportional to the grain size, for which reason a reduction in the grain size would shift the maximum pinning force to higher field values. A reduction of the heat treatment temperature can result in a decrease in the grain size, but also inhibits the stoichiometry and Nb_3Sn. A more promising approach to increase the pinning force in Nb_3Sn was stated to be by artificial pinning centres. This optimal pinning has been achieved in NbTi, where precipitates of Ti were distributed at distances of less than $10\,nm$. On the other hand, it was found that at high magnetic fields, a substantial increase in J_c cannot be achieved by defects in the crystal structure alone and it is necessary to maximise the thermodynamic critical field through optimisation of the heat treatment and doping [83]. In order to

achieve a high B_{c2}, both a high Sn content in Nb_3Sn as well as the correct doping by additions of for example Ti and Ta is necessary. A high Sn content is related to a high heat treatment temperature, which should be avoided, since the grain size increases exponentially with the temperature. A higher Sn content of the Sn source was also found to increase the rate of the Nb_3Sn layer growth [171].

While current state-of-the-art conductors achieve the J_c requirement of the HL-LHC upgrade with a margin of 3 %, a further increase by about 45 % is required to meet the FCC target. The most recent generation of ternary APC wires with Ta addition was reported to show B_{c2} values of up to 27.8 T and thus higher than those of standard PIT and RRP wires. Lowering the heat treatment temperatures from 700 °C to 685 °C resulted in significantly higher non-Cu J_c values. At a field of 21 T, the FCC target was exceeded in short samples by 29 % and at 16 T by 16 %, which is around 30 % higher than the record of RRP wires. Additionally, it was found that APC wires produced by internal oxidation exhibit a higher Sn content in the layers with fine grains compared to standard wires, by about 1 at.%–1.5 at.%. It was believed that this occurred due to a lower reaction rate at the interface of Nb_3Sn and Nb, which is beneficial for a higher Sn content in the Nb_3Sn layer. Since the value of B_{c2} is dependent on doping and Sn content, it was suggested that the higher B_{c2} in these APC wires can be related to the higher Sn content in the fine grained Nb_3Sn layer. The main reason for the improvement of J_c compared to older generation APC wires was stated to be the higher fraction of fine grains in the Nb_3Sn layer. A lower heat treatment temperature was related to a higher flux pinning, resulting in a higher non-Cu J_c. SEM analyses revealed that the area fraction occupied by fine grains in the APC wires are still lower than those in standard wires due to the Sn/Nb ratio being too low in the precursors. It it thus expected that by adjusting the wire recipe, a higher fraction of fine grains and thus even higher non-Cu J_c values can be achieved. The authors stated that also the heat treatment and wire design requires further optimization in order to achieve the highest performance possible. The APC wires presented in that study are of the same batch number than some of those investigated in this thesis, although the elemental ratios in the precursors and heat treatments differ slightly [169].

Summarizing, a large amount of parameters has to be considered and optimised in order to achieve a J_c increase to the FCC target value. In this thesis the focus will be laid upon the following factors, that will be investigated in Nb_3Sn wires produced by different manufacturing techniques:

1. The reduction of inhomogeneities in the A15 phase, where those in the geometry will be analysed in Chapter 3, specifically Sn gradients that impact T_c and B_{c2} will be investigated in Chapter 5 and the impact of the inhomogeneities on the superconducting properties in Chapter 8 and Chapter 9.

2. Grain refinement, which aims to decrease the grain size by an optimization of the heat treatment and novel manufacturing processes, leading to an increase in the pinning force. The assessment of the grain geometry will be presented in Chapter 6.

3. The introduction of artificial pinning centres in the form of ZrO_2 nano-precipitates that can contribute to an increase the pinning force, where their microstructural analysis will be shown in Chapter 4.

4. The increase in the pinning force through the introduction of artificial pinning centres by means of fast neutron irradiation, which will be investigated in Chapter 7.

1.7 Overview of investigated Nb₃Sn wires

In this work various types of multifilamentary as well as two monofilamentary Nb₃Sn wires were investigated, which differ in terms of production process including heat treatment, composition and geometric layout. Common to all wires is the Nb diffusion barrier which surrounds their Nb₃Sn sub-elements and the copper matrix that they are embedded in. The wire denotation was chosen in the format [type]-[additive]-[number of sub-elements], for example RRP-Ti-108 is referring to the Restack Rod Processed wire alloyed with Ti that possesses 108 Nb₃Sn sub-elements. In the case of the APC wires, the denotation follows the format APC-[wire number]-[number of sub-elements]. Two APC wires with the number 3912 possess the same amount of sub-elements and are therefore denoted by using the format APC-3912-[wire diameter]. The wire APC-3657-48 was originally denoted with the number 3757, for reason of consistency the notation APC-3657-48 was chosen to be maintained.

For the manufacturing of all multifilamentary APC wires, a Nb tube alloyed with 1 at.% Zr or Hf was used. In this thesis, binary as well as ternary APC wires were investigated. In the case of ternary wires, an additional 4 at.% Ta was added to the Nb tube. SnO_2 was used in the form of powder as the oxygen source in all cases. The wire IT-3736-54 is a tube-type wire. Table 1.3 gives an overview of all investigated wires and their main properties.

Wire	Type	Add.	Subel. No.	Diam. [mm]	Manufact.
BIN-246	IT	none	246	1.25	Alstom
RRP-Ti-108	RRP	Ti	108	0.8	Bruker-OST
RRP-Ta-54	RRP	Ta	54	0.8	Bruker-OST
PIT-Ta-114	PIT	Ta	114	0.7	Bruker-EAS
PIT-Ta-192	PIT	Ta	192	1.0	Bruker-EAS
APC-3607-1	APC	Zr, O	1	0.25	Hyper Tech
APC-3680-1	APC	Zr, O	1	0.25	Hyper Tech
APC-3657-48	APC	Zr, O	48	0.72	Hyper Tech
APC-3682-48	APC	Zr, O	48	0.52	Hyper Tech
APC-3912-071	APC	Zr, O, Ta	48	0.71	Hyper Tech
APC-3914-48	APC	Hf, O, Ta	48	0.71	Hyper Tech
APC-3912-084	APC	Zr, O, Ta	48	0.84	Hyper Tech
PIT-31284-192	PIT	Ta	192	0.78	Bruker-EAS
IT-3736-54	IT	Ta	54	1.0	Hyper Tech

Table 1.3: Overview of the parameters of the investigated Nb₃Sn wires.

As mentioned in Section 1.5, the heat treatment plays an important role in the manufacturing process of Nb$_3$Sn wires, since it influences the grain size and elemental composition, and has to be conducted after winding the wire to its final form due to its brittleness. Table 1.4 gives an overview of the applied heat treatment on the investigated wires.

Wire	Heat treatment
BIN-246	215 °C (24 h), 340 °C (24 h), 400 °C (24 h), 645 °C (50 h)
RRP-Ti-108	210 °C (48 h), 400 °C (48 h), 665 °C (50 h)
RRP-Ta-54	695 °C (17 h)
PIT-Ta-114	620 °C (120 h), 640 °C (120 h)
PIT-Ta-192	625 °C (250 h)
APC-3607-1	unknown
APC-3680-1	unknown
APC-3657-48	650 °C (250 h)
APC-3682-48	640 °C (300 h)
APC-3912-071	675 °C (317 h)
APC-3914	700 °C (91 h)
APC-3912-084	685 °C (236 h)
PIT-31284	675 °C (110 h)
IT-3736	675 °C (110 h)

Table 1.4: Overview of the heat treatment of the investigated Nb$_3$Sn wires.

Different techniques of examination were employed on the wires listed in Table 1.3, which are described in Section 1.8. Not every method was conducted on every sample, Table 1.5 summarizes the applied techniques on each given wire.

Wire	SEM	TEM	EDX SEM	EDX TEM	TKD	SHPM	IRR
BIN-246	✓	✓	✓	✓	✓	✗	✗
RRP-Ti-108	✓	✓	✓	✓	✓	✓	✓
RRP-Ta-54	✓	✓	✓	✓	✓	✗	✓
PIT-Ta-114	✓	✓	✓	✓	✓	✓	✗
PIT-Ta-192	✓	✓	✓	✓	✓	✗	✓
APC-3607-1	✓	✓	✓	✓	✓	✗	✗
APC-3680-1	✓	✓	✓	✓	✗	✗	✗
APC-3657-48	✓	✓	✓	✓	✓	✗	✗
APC-3683-48	✓	✓	✓	✓	✓	✗	✗
APC-3912-071	✓	✓	✓	✓	✓	✗	✗
APC-3914	✓	✓	✓	✓	✓	✗	✗
APC-3912-084	✓	✓	✓	✓	✓	✗	✗
PIT-31284	✓	✓	✓	✓	✗	✗	✗
IT-3736	✓	✓	✓	✓	✗	✗	✗

Table 1.5: Summary of the applied methods of investigation on the different Nb$_3$Sn wires. SEM = scanning electron microscopy, TEM = transmission electron microscopy, EDX = energy-dispersive X-ray spectroscopy, TKD = transmission Kikuchi diffraction, SHPM = scanning Hall probe microscopy, IRR = irradiation of wires.

1.8 Experimental methods

The microstructure and the magnetic properties of the Nb$_3$Sn wires in Table 1.3 were investigated using a wide range of analytical techniques which are described in detail in the corresponding chapters. This section aims to give an overview of the main principles of scanning and transmission electron microscopy.

1.8.1 Scanning electron microscopy

Scanning electron microscopy (SEM) investigations were carried out using the model FEI Quanta 250 FEG. The device is equipped with a detector for energy-dispersive X-ray spectroscopy (EDX) analyses as described in Chapter 5 as well as a camera for electron backscatter diffraction (EBSD) and transmission Kikuchi diffraction as described in Chapter 6.

1.8.2 Transmission electron microscopy

The theory of transmission electron microscopy (TEM) is described in detail in [162]. TEM was conducted using a FEI TECNAI F20 for microstructural investigations such as the ones described in Chapter 4 and Chapter 7. This TEM can be operated in two different modes that are described in the following.

TEM mode

When operating in the TEM mode, the magnetic lenses that steer the electrons are excited in such a way that the beam is nearly parallel when penetrating the specimen. This operation mode offers imaging under BF (bright field) and DF (dark field) conditions as well as imaging the diffraction pattern by selecting the corresponding apertures. By increasing the magnification, imaging of the crystal planes and their defects is possible provided the sample is thin enough and its orientation allows their visibility. Imaging under such high magnification conditions will be referred to as HRTEM (high resolution TEM).

STEM mode

In STEM mode the excitation of the magnetic lenses lead to a convergent beam geometry, where each sample point is scanned in a similar fashion to SEM. For imaging, the HAADF (high angle annular dark field) detector is used. Based on the chosen camera length, which defines the magnification of the diffraction pattern and the angles of the beams that fall onto the bright field and the annular dark

field detector, different forms of contrast can be achieved. At high camera angles, ADF (annular dark field) conditions are achieved where the contrast is based on Bragg scattering and arises due to different crystal orientations, so called diffraction contrast. A suitable camera length for this condition was found to be in the order of 970 mm, where individual grains could clearly be identified. At even higher camera lengths, the un-diffracted beam partly impinges onto the HAADF detector, leading to ABF (annular bright field) conditions. At a low camera angle of less than 100 mm, HAADF conditions are achieved and contrast arises due to Rutherford scattering and differing atomic number of the elements, called Z-contrast.

Techniques for characterising radiation damage

The experiments described in Chapter 7 revolve around the examination and analysis of defects in the crystal structure caused by the impact of fast neutrons. A comprehensive overview of imaging techniques for the characterisation of radiation damage using TEM is given in [77], from which the information presented in this section was mainly taken. In general, three different contrast mechanisms are used to assess radiation damage: diffraction/strain contrast, structure factor contrast and phase contrast.

The most common method used is diffraction contrast, where strain fields around the defects lead to contrast based on local changes in the diffracting conditions. Depending on the diffraction conditions, the following distinctions can be made:

1. In 2-beam dynamical conditions, certain diffracting planes corresponding to a $\vec{g}$-vector are satisfying the Bragg condition, therefore the deviation parameter s_g is exactly or very close to zero. The objective aperture can then be placed around the un-diffracted $\vec{0}$ -beam or the diffracted $\vec{g}$-beam, resulting in either a bright field or a dark field image. Dark field images are frequently preferred, since they show higher contrast. In order to reduce effects of the spherical aberration, the diffracted beam is often centred in the optical axis by tilting. Since both the diffraction spots $\vec{0}$ and $\vec{g}$ are excited under these conditions, they are referred to as 2-beam conditions.

2. In bright field kinematical conditions, the deviation parameter s_g is slightly increased, resulting in weakening of the $\vec{g}$ diffraction spot and the contrast being simplified and more limited to the real cluster size. Such conditions can also be achieved by imaging near a zone axis, where multiple beams will be excited and therefore a high fraction of defects will be visible.

3. The third type of condition when using diffraction contrast is known as weak-beam dark field, which was frequently applied in this thesis. Here, lattice strain near the defect cores are responsible for forming the contrast. In this case the deviation parameter s_g is large for the chosen $\vec{g}$-reflection, which shows weak intensity and therefore leads to a low intensity of the final dark field image.

Local strain fields near defects, however, may lead to high relative intensity peaks locally by bending reflecting planes back and thus fulfilling the Bragg condition. For weak-beam dark field, the electron beam is frequently tilted to shift an excited $\vec{g}$-reflection (two-beam case) into the optical axis, which then loses intensity and is used to form the image.

Figure 1.8 shows a comparison of the different beam geometry settings used for bright field (BF), dark field (DF) and weak-beam dark field (WBDF) imaging. In Figure 1.9, a schematic is displayed showing the principle of weak-beam dark field imaging. While the Bragg condition is not fulfilled for the main lattice, the deformed lattice around the defect leads to locations where it is fulfilled, which are visible with high contrast in the weak-beam image.
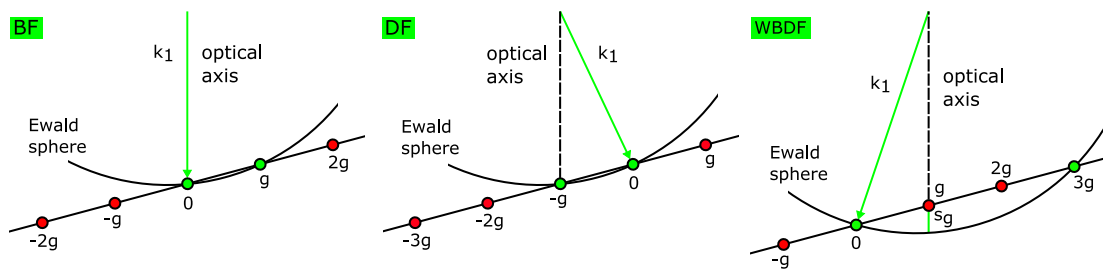
Figure 1.8: Comparison of the beam geometry settings used for BF, DF and WBDF TEM imaging. Drawn after [162].
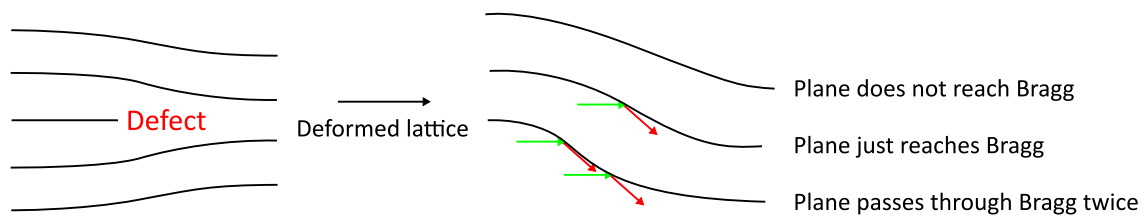
Figure 1.9: Schematic showing the principle of weak-beam dark field imaging. Drawn after [162].

In weak-beam imaging, the diffraction condition of the used $\vec{g}$-reflection determines the resulting image contrast. The image is acquired using a weak reflection, where the Bragg condition is not fulfilled. The parameter s_g states the deviation from the exact Bragg condition in nm^{-1}. The absolute value of the deviation parameter that is often cited in order to achieve true weak-beam conditions is $s_g \geq 2 \times 10^{-1}\,\mathrm{nm}^{-1}$. Images acquired using lower values of s_g are often denoted as semiweak-beam images. In weak-beam dark field imaging the highest possible deviation parameter s_g should be used in order to achieve the best image resolution. For optimal weak-beam dark field conditions, a value for s_g of over $2 \times 10^{-1}\,\mathrm{nm}^{-1}$ is often cited [77, 162].

The point at which the Ewald sphere intersects the array of systematic reflections is often described by $n\vec{g}$. In the case of n being integral, the corresponding bright Kikuchi line will intersect the diffraction spot $n\vec{g}$ and lead to its excitation. This should be avoided, since it leads to a loss of intensity in the image and potentially image artefacts, therefore a non-integral value of n should be chosen. From the formula

$$s_g = (n-1)g^2/2k \tag{1.22}$$

the minimum value of n can be calculated, which is necessary in order to achieve $s_g = 2 \times 10^{-1}\,\text{nm}^{-1}$. Here, $g = 1/d$ denotes the absolute value of the lattice vector $\vec{g}$ that corresponds to the planes with spacing d. The radius of the Ewald sphere is given by $k = 1/\lambda$ with λ being the wavelength of the electrons in nm. The condition, where the reflection $n\vec{g}$ is then satisfied is denoted as $(\vec{g}, n\vec{g})$. The $\vec{g}$-reflection of number n that needs to be excited to reach the desired value of s_g can thus be calculated by

$$n = 2ks_g/g^2 + 1. \tag{1.23}$$

For the calculation of the wavelength λ, the relativistic speed of the electrons needs to be considered [162]:

$$\lambda_{rel} = \frac{h}{\sqrt{2meU(1 + \frac{eU}{2mc^2})}}, \tag{1.24}$$

which results in a value of $2.5 \times 10^{-3}\,\text{nm}$ for an acceleration voltage U of $200\,\text{keV}$.

When conducting weak-beam dark field microscopy or other dark field techniques using TEM, precise knowledge of the crystal structure and lattice parameters is required in order to chose the desired reflection and determine the used diffraction conditions correctly. Table 1.6 gives an overview of the most important reflections resulting of the Nb_3Sn crystal structure and their corresponding lattice plane spacings and $\vec{g}$-vectors. The necessary value for n to obtain s_g larger than $2 \times 10^{-1}\,\text{nm}^{-1}$ was calculated for each reflection and the results are displayed in the same table.

It can thus be seen that for low order reflections, the sample needs to be tilted away from the zone axis by a large amount. The required calculated values for n are often so large, that the respective diffraction spots are outside the field of view and exhibit a very low intensity due to their distance from the optical axis. Aside from the small grain size, which made setting exact diffraction conditions a challenging task, this is another reason why the conical weak-beam dark field technique described in Section 1.8.2 was deemed useful for the investigation of irradiation damage in Nb_3Sn. It is more straightforward to record a series of weak-beam images and determine

Reflection (hkl)	Plane spacing d [nm]	g [nm^{-1}]	n
110	0.37	2.68	23.24
200	0.26	3.79	12.12
210	0.24	4.24	9.89
211	0.22	4.65	8.41
220	0.19	5.37	6.56
222	0.15	6.57	4.71
400	0.13	7.59	3.78
420	0.12	8.48	3.22

Table 1.6: Overview of some important reflections used for dark field imaging of Nb$_3$Sn including the value of n necessary to obtain s_g larger than $0.2\,\text{nm}^{-1}$. Crystallographic data taken from ICSD database, plane spacings calculated by JEMS.

the exact diffraction conditions afterwards, instead of rigorously trying to set exact conditions beforehand.

From Equation 1.22 it furthermore becomes apparent that a high acceleration voltage of 200 keV is in fact detrimental for achieving high values of s_g, leading to the necessity for using reflections with higher n values. An interesting future experiment would therefore consist of lowering the acceleration voltage of the TEM and subsequently comparing the resulting images obtained under the same weak-beam conditions. The quality of weak-beam images depends also on the specimen thickness, which should generally be less than 50 nm.

Aside from diffraction contrast, structure factor and phase contrast are used for analysing radiation damage. Differences in structure factor between the damaged regions and the surrounding matrix lead to different extinction distances and therefore different contrast. This type of contrast therefore appears due to differences in the effective specimen thickness and intensity changes between a perfect crystal and defective regions. Imaging by phase contrast includes the growing field of high resolution imaging, which is commonly conducted without the use of an objective aperture to maximise the intensity and collect information from multiple diffracted beams. Especially the newer generations of TEMs are focusing on high resolution imaging and aiming to reduce the spherical aberration by the use of additional quadrupole lenses, leading to higher resolutions close to atomic levels [77].

In the STEM mode, the use of ADF and HAADF detectors can additionally be helpful to characterise radiation damage, by analysing changes in the atomic density through Z-contrast and associated strain fields through diffraction contrast.

Analysis of irradiation damage

When analysing radiation defects using TEM imaging, it has to be considered that the visibility of defects is not only dependent on the diffraction conditions, but also the specimen thickness and the depth of the defects within the specimen. The detailed characterisation of defects becomes increasingly difficult for sizes less than about 5 nm. Weak-beam dark field is best suited for analysing defects larger than around 10 nm. For defects smaller than around 10 nm, analysis based on black-white contrast is recommended. The connection between the centres of the white and the black area is defined as the $\vec{l}$-vector. In the case of symmetrical strain fields, the $\vec{l}$-vector is parallel to the $\vec{g}$-vector. Therefore the $\vec{l}$-vector is parallel to the $\vec{g}$-vector for isotropic defects. This black-white contrast is generally visible for defects close to the sample surfaces, defects located in deeper layers appear as black dots. As will become apparent in this thesis, defects produced by neutron irradiation in Nb_3Sn are mostly below 10 nm in size, making the use of some of the conventional analysis techniques extremely difficult, albeit still being able to yield useful information [77].

A literature review of ion irradiation damage in metals led to the general agreement that the type of defects produced in displacement cascades are vacancy in nature. A past study of neutron irradiation damage in Cu showed that all defects smaller than 4 nm consisted of vacancies, while larger defects often showed interstitial character. It was thus suggested that cascade collapse was responsible for forming vacancies, while homogeneous nucleation resulted in interstitial defects. It was stated that in all previous studies of neutron irradiation defects, black-white contrast was observed in only half of the visible defects. Compressive strain can influence the type of defect by increasing the likelihood of vacancies nucleating in clusters, while dilatation more likely leads to nucleating of clusters made of interstitials.

The determination of dislocation sizes smaller than 10 nm was stated to be extremely challenging, since it is dependent on the sample thickness and the depth of the defect in the sample. A good estimate for the defect size was stated to be the length of the border between the black and the white contrast regions. Black-white contrast is observed under dynamical conditions, while kinematical conditions lead to black dot contrast. When determining the density of defects, a number of factors can contribute to the uncertainty: defects might be too small to be resolved, or they might show too weak contrast to be visible due to their location or the diffraction condition. For that reason, it is beneficial to image the same region using different conditions and diffraction vectors and compare the results. Artefacts can likely be excluded when when a defect is visible with similar contrast under multiple different conditions. Other uncertainty factors during the density evaluations include the fact that defects hight migrate to the sample surface and get lost, as well as errors in the measurement of the sample thickness and the irradiation dose.

Displacement cascades can result in disordered regions, in which the long range order

is locally reduced. This leads to a reduction in structure factor of the superlattice reflections in comparison with the surrounding ordered matrix. For analysing the cascade fine structure and imaging the disordered regions, superlattice reflections are therefore useful for dark field imaging. When applying dark field imaging to strongly excited superlattice reflections, disordered regions can be made visible. While structure contrast is generally dominant over strain contrast arising from cascade collapse, strain contrast can be achieved by the use of fundamental reflections. All cascade sites lead to the production of disordered regions, regardless of the fact if dislocation loops are formed or not. At the cores of cascades, it is believed that local melting is occurring. Structure factor contrast can also be used to image defects at cascade sites by imaging at a zone axis. The best contrast can generally be found at thin specimen areas. Amorphous zones showed better contrast under bright field conditions in the (110) zones axis than under strongly excited dark field conditions.

For high resolution TEM imaging, the specimen thickness should again be as thin as possible to increase the fraction of the thickness that the defects occupy. This technique can be useful to investigate cascade sites in superconductors, where melting, amorphization and recrystallisation might occur [77].

Conical weak-beam dark field microscopy

While weak-beam dark field conditions can be obtained by shifting the beam in x and y directions, the use of the conical dark field option has proven to be a more accessible and straightforward technique. The main reason for this is the small grain size of Nb_3Sn, as will be assessed in Chapter 6, which caused setting specific diffraction conditions by tilting the beam and the specimen to be an exceptionally challenging task. For conical weak-beam dark field imaging, the smallest objective aperture is centred in the optical axis. The beam is then tilted so that the desired rings of the ring diffraction pattern of the polycrystalline Nb_3Sn is shifted into the optical axis and thus the objective aperture. Under these conditions, the beam can then be rotated, leading to the shift of the diffraction pattern along the diffraction rings inside the aperture until weak-beam conditions are achieved. This principle is illustrated in Figure 1.10, where the aperture is located at a fixed position in the optical axis. This method allows for a rapid setting of the desired beam geometry, which can be used to investigate multiple grains simultaneously. The disadvantage is that the exact conditions and deviations from the Bragg condition are not known at the time of image acquisition and are determined by imaging the diffraction pattern afterwards.
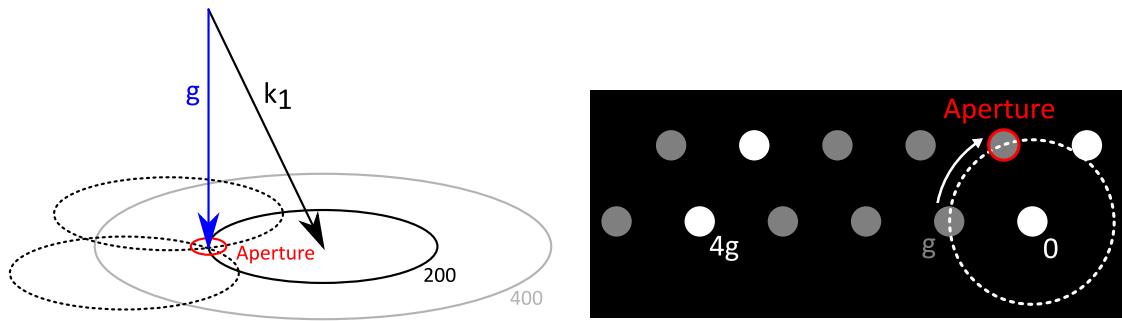
Figure 1.10: Schematics showing the principle of conical weak-beam dark field imaging. The aperture is located at a fixed position in the optical axis, while the beam is rotated and therefore the diffraction pattern is shifted along the diffraction rings.

In order to choose the desired diffraction rings for imaging, knowledge of the corresponding reflections is required. The ring diffraction pattern of polycrystalline Nb_3Sn was simulated using the JEMS software and is displayed in Figure 1.11. The smallest objective aperture of the employed TEM covers the range of about three diffraction rings and it is thus not possible to distinguish between the used reflections beforehand. Most commonly, the rings of the (200), (210) and (211) diffraction spots were tilted into the optical axis and used for weak-beam imaging. These rings show the highest intensity, as can also be seen in the experimentally obtained ring diffraction pattern of a Nb_3Sn specimen that is displayed in Figure 1.12.
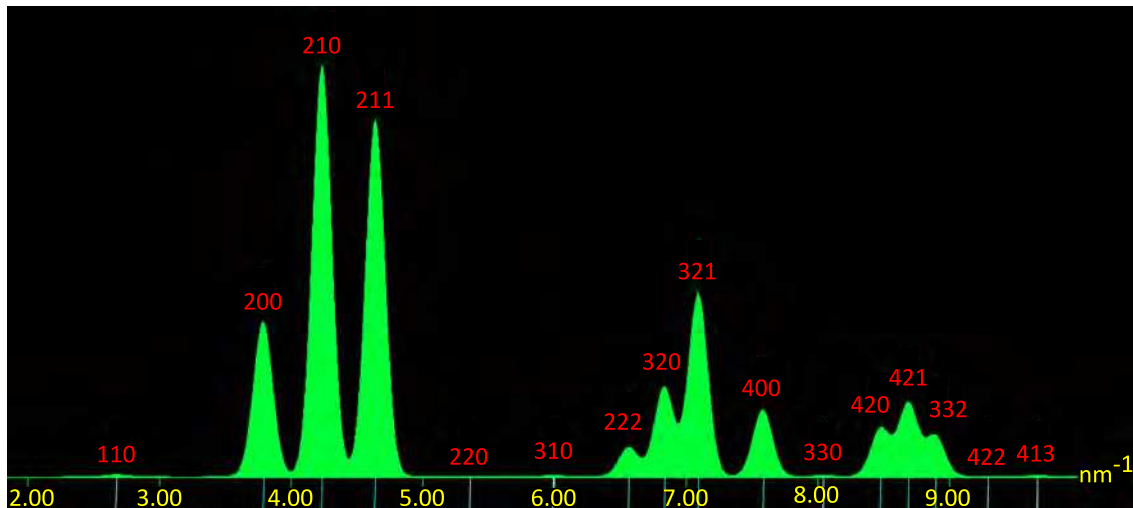
Figure 1.11: Simulated diffraction pattern with intensity of the diffraction spots of polycrystalline Nb_3Sn.
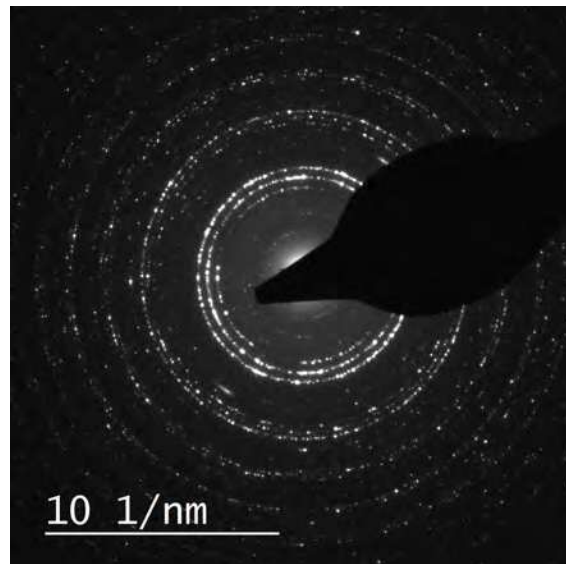
Figure 1.12: Experimental ring diffraction pattern with intensity of the diffraction spots of polycrystalline Nb$_3$Sn.

The Kikuchi lines viewed in the diffraction pattern yield information about the closest zone axis and thus the orientation of the investigated grains. Simulations were conducted in order to gain information about the appearance of the Kikuchi lines to be expected when viewing the specimen along certain zone axes. The images of the Kikuchi bands of Nb$_3$Sn were constructed using the PTCLab program [63] and are displayed in Figure 1.13.
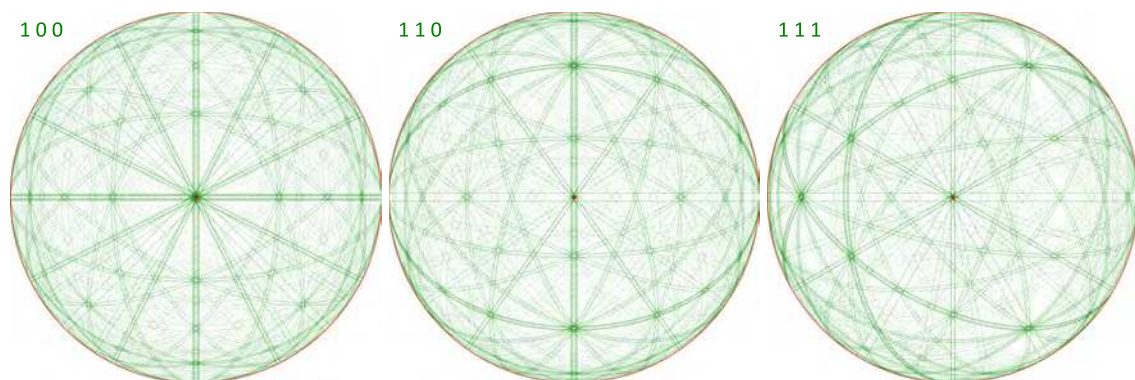
Figure 1.13: Kikuchi patterns of Nb$_3$Sn at different zone axes.

Weak-beam dark field in the STEM mode

Even though the analysis of defects using the technique of weak-beam dark field microscopy is often conducted in the TEM mode using a rather parallel beam, it can also be done in the STEM mode using convergent beam imaging. The diffraction contrast resulting from STEM imaging of dislocations was described in [110], where various diffraction conditions were explored and where it was shown that the rules for diffraction contrast in conventional TEM imaging are also applicable in STEM. Contrary to the parallel beam geometry in conventional TEM imaging, the beam in the STEM imaging mode forms a convergent cone. The image contrast is strongly dependent on a variable parameter called camera length, which describes the distance between the detector plane and the sample and controls the angles of the beams that fall onto the bright field and the annular dark field detectors. The application of weak-beam dark field in the STEM mode for imaging dislocations was also demonstrated in [76]. The stated advantages of STEM imaging of defects over TEM include the ability to investigate specimens of a greater thickness and the simultaneous accessibility of analytical techniques such as EDX and EELS. The chosen camera length has to be large enough to select a specific diffraction disk, corresponding to a small objective aperture in the TEM mode, otherwise the diffraction conditions are unclear due to both diffracted and transmitted disks falling onto the detector. Additionally, the value of s_g is not unique, instead due to the convergent beam geometry it exhibits a diversity. In that study, weak-beam dark field imaging in the STEM mode was employed using the $(\vec{g}, 3\vec{g})$ diffraction condition. While in the TEM mode, a small objective aperture is centred around the $\vec{g}$-reflection to form the image, in the STEM mode this is achieved by setting a high camera length and shifting the $\vec{g}$-reflection to the detector centre. WBDF imaging in the STEM mode was furthermore employed in [96], where an objective aperture was centred around the $\vec{g}$-reflection disk and the annular dark field detector was used for imaging, reducing the uncertainties in the image interpretation caused by overlapping of the disks of the transmitted and diffracted beams. One advantage of imaging in the STEM mode was stated to be the possibility of imaging areas where the specimen possesses a higher thickness. The application of this technique in the STEM mode also led to the suppression of bend contours compared to conventional weak-beam dark field TEM imaging.

1.8.3 Energy-dispersive X-ray spectroscopy

Energy-dispersive X-ray spectroscopy (EDX) is a method of examining the distribution of the chemical elements in a sample by exciting the electrons of the atoms with an electron beam and analyse the characteristic X-rays that are emitted by the excited electron during the transition back to the ground state. EDX is best suited for the investigation of heavy elements and thus was the main technique used in this study for the investigation of the elemental composition, which is described in Chapter 5.

1.8.4 Electron energy loss spectroscopy

Electron energy loss spectroscopy (EELS) yields information about elemental composition and other properties of a TEM sample by determining the energy loss of the transmitted electrons. It is best suited for the investigation of light elements. In the present study, EELS was most commonly used for the determination of the sample thickness, which is required for the estimation of the defect density of precipitates described in Chapter 4 and of irradiation defects described in Chapter 7.

1.8.5 Transmission Kikuchi diffraction

The analysis of grain geometries and orientations was conducted by the use of transmission Kikuchi diffraction (TKD) in the SEM, which represents a variation of conventional electron backscatter diffraction (EBSD), where TKD is performed in transmission mode on thin lamellae, leading to a higher spatial resolution. The technique and its application on the investigated Nb_3Sn wires is described in detail in Chapter 6.

1.8.6 Scanning Hall probe microscopy

Information about local magnetic and superconducting properties was acquired by scanning Hall probe microscopy (SHPM), which was conducted on polished cross sections of the wires at low temperatures and after applying external magnetic fields. The technique and the acquired results of SHPM are described in detail in Chapter 8, their correlation with the microstructure is investigated in Chapter 9.

2 Sample preparation

This chapter describes the findings related to the sample preparation processes beneficial to structural investigations by electron microscopy and magnetic characterizations by scanning Hall probe microscopy. It is divided into sections describing the respective techniques of preparing samples for TEM, SEM and SHPM investigations. At the end of the chapter, insights into alternative techniques are provided, which were explored and are potentially useful for future studies.

2.1 Sample preparation for TEM of pristine wires

For preparing specimens for structural TEM investigations of the A15 phase in Nb_3Sn wires, FIB (focused ion beam) using the model FEI Quanta 200 3D DBFIB was employed. A sample area of around $25\,\mu m \times 3\,\mu m$ was chosen to be cut out. To protect the sample from beam damage, one $300\,nm$ layer of Pt was deposited using a current of $0.3\,nA$ and one $3\,\mu m$ layer with a current of $0.5\,nA$. For lifting out lamellae, different techniques have been explored, but the one that has proven to be best suited was cutting out a wedge shape by tilting the stage by 8° in both directions. The accelerating voltage of the ion beam used was $30\,kV$, the first cuts were done using a current of $20\,nA$. Further thinning to a thickness of about $2\,\mu m$–$3\,\mu m$ was done using a current of $7\,nA$. This fabrication step can be seen in Figure 2.1.

Using a micro-manipulator, the lamella was connected to a needle by tungsten deposition, and the sample was lifted out and mounted to a half ring of $3\,mm$ in diameter. For this sample holder, three different materials were explored: Cu, Mo and Si. Using Cu has led to sputtering onto the sample and partly contamination during post-FIB thinning using ion milling. Mo has shown a much better behaviour in this regard, which is why mainly this material was used. Si holders are much more expensive and only used for mounting specimens which are subject to be included in irradiation steps after preparation and investigation. Mo is not suited for irradiation experiments because of a high activation during irradiation.

After the specimen was mounted to the sample holder, it was separated from the needle and further thinning was applied using currents of $3\,nA$ down to around $0.3\,nA$. At a thickness of $200\,nm$–$300\,nm$, final thinning was either done in the FIB using low currents, or by using the Gatan PIPS ion mill. The most frequent parameters used for ion milling were an accelerating voltage of $1\,kV$–$2\,kV$, a current of about $5\,\mu A$, a
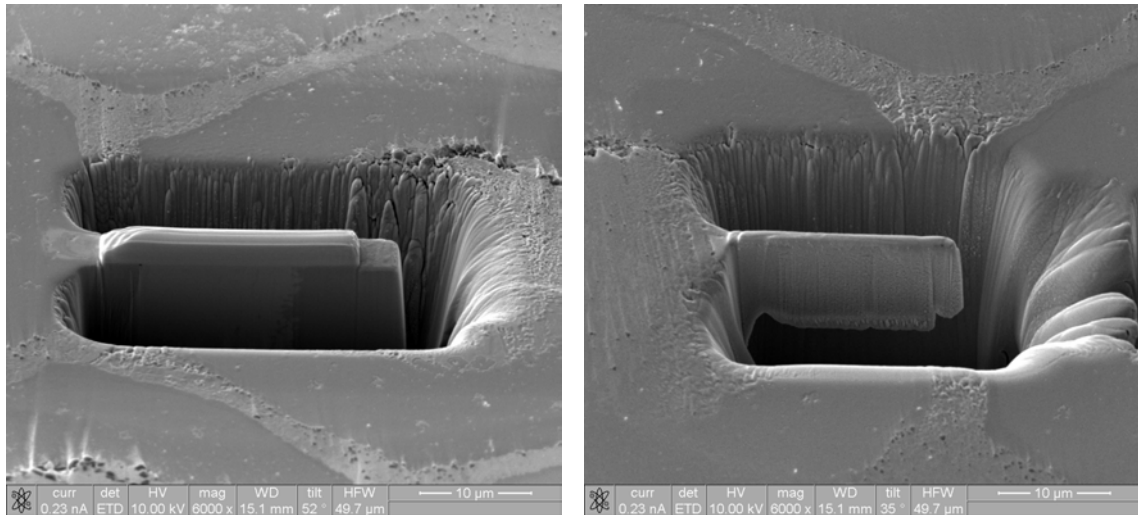
Figure 2.1: Cutting and thinning lamellae before lift-out using FIB.

tilt angle of 8°–10° and a duration of 30 min–60 min. Generally, higher angles and lower voltages have led to better results, as well as cooling the stage during milling using liquid nitrogen. Figure 2.2 shows a SEM image of a TEM sample after the last thinning step using FIB and a STEM image of a finished sample after ion milling.
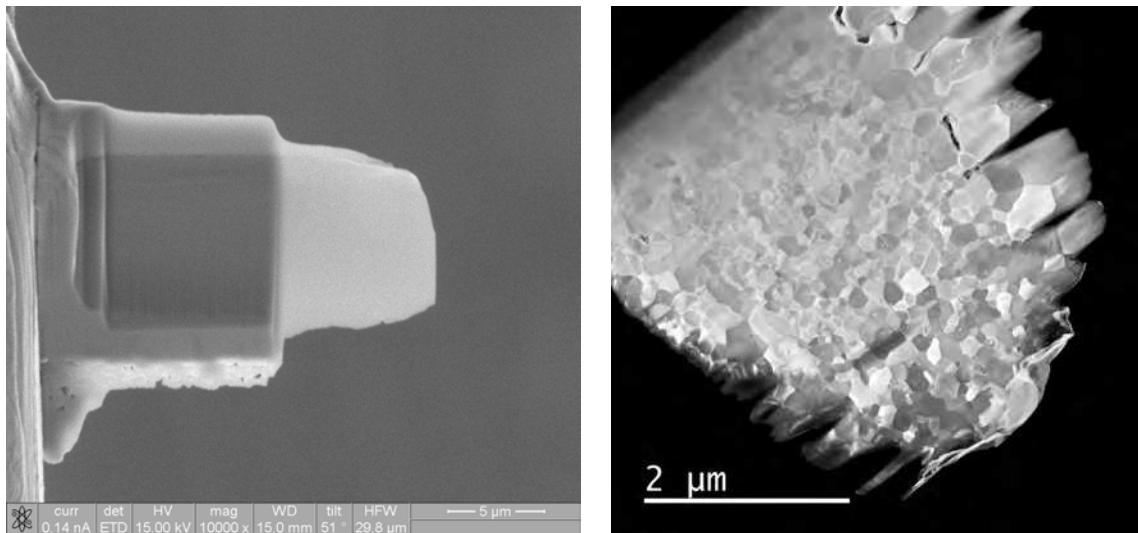
Figure 2.2: SEM image of a TEM sample after the last thinning step using FIB (left) and STEM image of a finished sample after ion milling (right).

A useful tool for evaluating grain size distribution is TKD (transmission Kikuchi diffraction) which is conducted in the SEM at an operating voltage of around 25 kV as described in Chapter 6. The samples used for this technique are required to be as

thin as TEM specimens to be electron transparent, the optimal thickness was found to be in the order of 100 nm. Since the prepared TEM samples already fulfil this requirement, they were also being used for TKD investigations.

In the present study, the microstructure of pristine as well as neutron irradiated wires was investigated as described in Chapter 4 and Chapter 7, respectively. Two different methods for preparing specimens before starting FIB processing have been explored which both have led to success and were used:

1. Polishing the cross section of a wire, then lifting lamellae out of the polished surface as seen in figure Figure 2.3. This method provides the advantage of being able to precisely choose the desired area which leads to samples where ideally the entire A15 region can be investigated. Therefore, gradients of for example grain size and elemental composition can be examined more easily. Since for SEM investigations, there is need to polish the wires anyway, this method was most frequently used for preparing samples of pristine wires.

2. Etching out single sub-elements by completely removing the Cu matrix using a mixture of 50 % HNO_3 and 50 % distilled water as seen in figure Figure 2.4. The advantage in this case is that most of the specimen area consists of the Nb and A15 phase and no special care needs to be taken to select a specific area where the lamellae are lifted out. Additionally, since there is no need to polish the wire, no material is wasted and less time is used doing so. This method was most frequently used for preparing samples of irradiated wires since the etching can be done before irradiation and greatly reduces the amount of material and therefore the residual radiation. Further details about the preparation of lamellae of irradiated wires are provided in the following section.
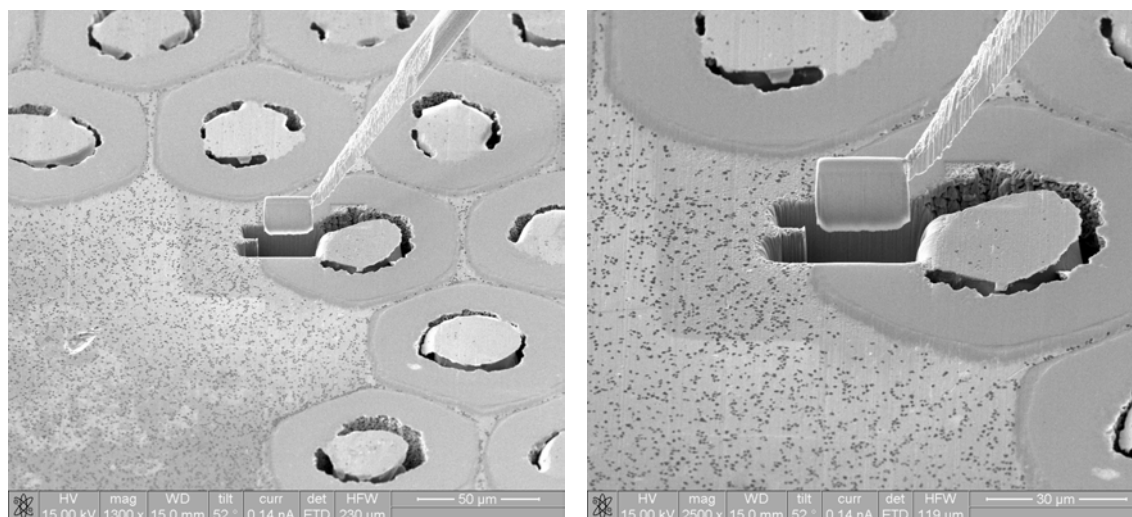
Figure 2.3: Lifting TEM lamellae out of polished wire cross sections.
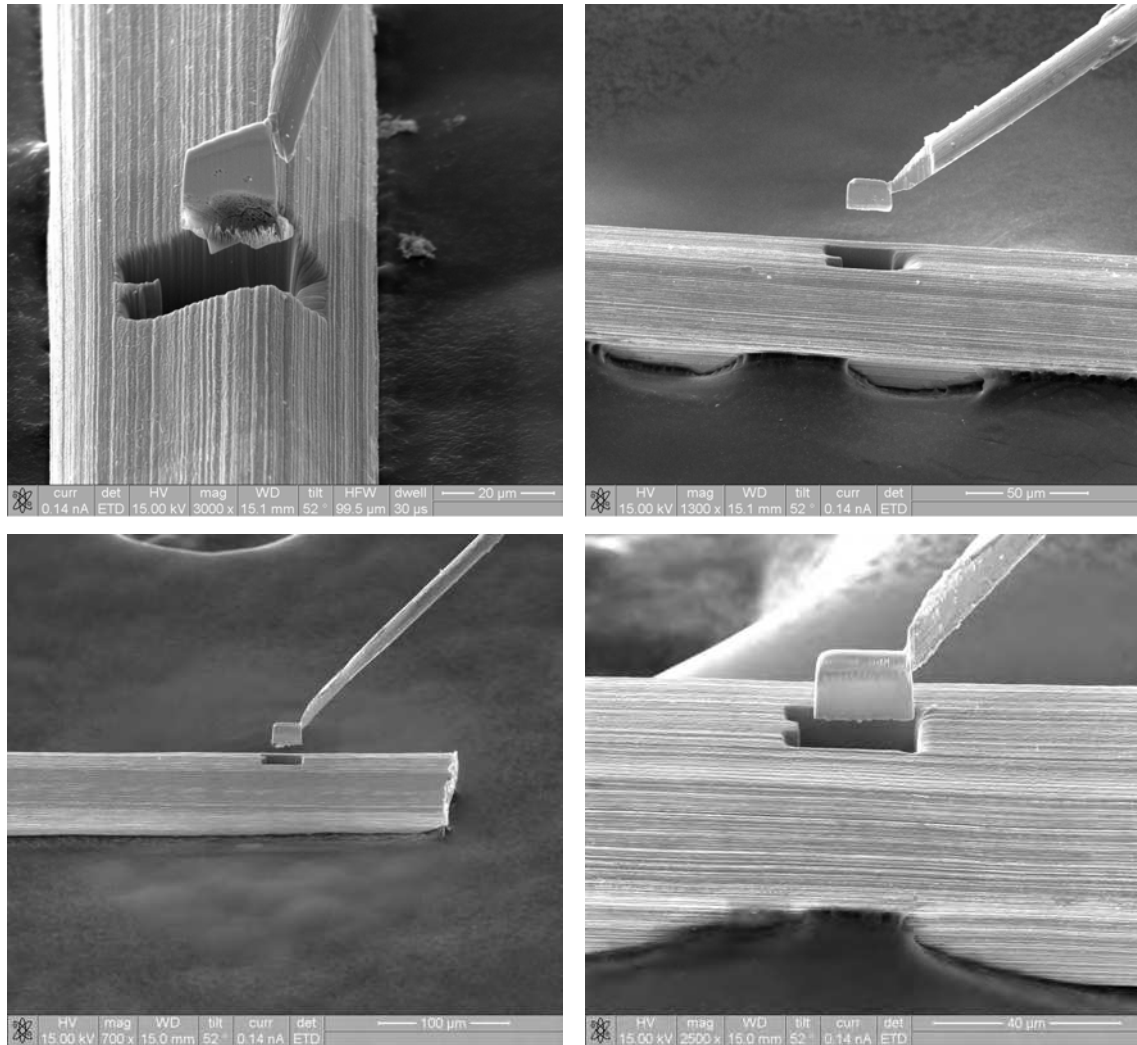
Figure 2.4: Lifting TEM lamellae out of single sub-elements. The Cu matrix was etched away.

2.2 Sample preparation for TEM of irradiated wires

Part of this thesis revolves around the investigation of irradiated Nb_3Sn wires by TEM as described in Chapter 7. Due to radiation protection precautions and protection of the samples during the irradiation process, specific sample preparation methods had to be employed for irradiated wires. The following methods for sample preparation of irradiated wires have been explored:

1. Preparing thin samples to investigate and compare the same area before and after irradiation. This option was conducted by using Si sample holders which are sealed in silica glass capsules before irradiation as seen in Figure 2.5. As atmosphere inside the capsules air, helium and vacuum were explored. The air atmosphere has led to contamination and destruction of samples, while helium and vacuum have led to good results as seen in Figure 2.6. Since the procedure of using vacuum is in addition considerably easier to handle, it was deemed to be the best option and should also be used in future experiments.

2. Preparing samples with a thickness of $3\,\mu m$ and thinning them after irradiation. This option has been explored in case the surface would deteriorate due to irradiation but has not proven to lead to any advantage compared to the other methods while retaining the risk of damaging the fragile lamellae during transportation and irradiation.

3. For the third option, individual sub-elements were etched out of the wire using $50\,\%$ HNO_3, and were used to cut out TEM samples after irradiation. This method has proven to be the most reliable, since it provides clean samples and basically unlimited material to work with when there is a need to produce new samples. The disadvantage of this method is that it is not possible to compare the same sample area before and after irradiation.
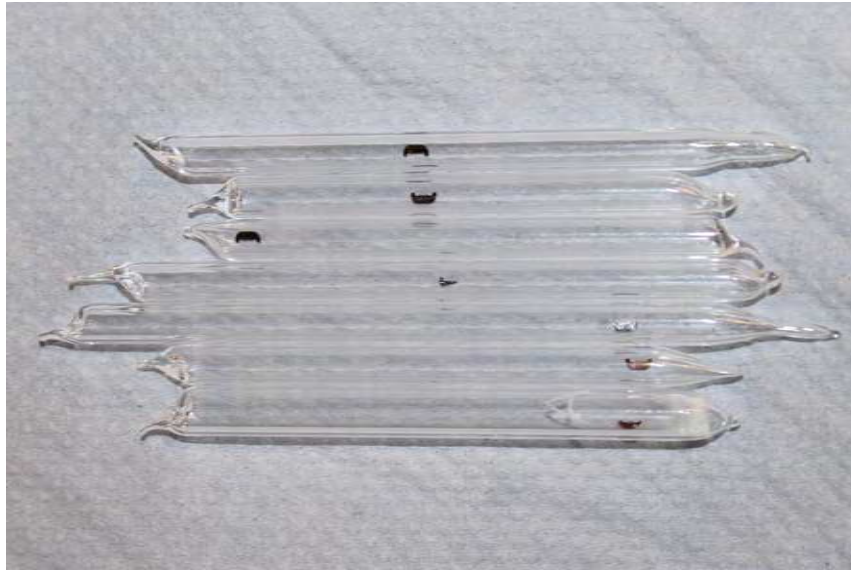
Figure 2.5: TEM samples sealed in silica glass tubes before irradiation.
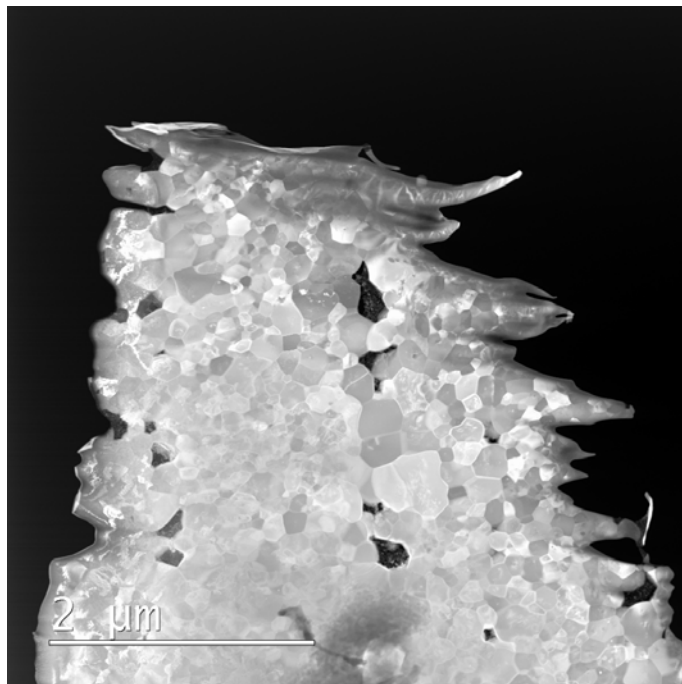
Figure 2.6: STEM image of an irradiated TEM sample that was mounted on a Si holder and sealed in helium atmosphere. Most of the thin region suited for investigation remained uncontaminated.

2.3 Sample preparation for SEM

For SEM investigations including high-resolution imaging and EDX, the cross section of wires was mechanically polished using an Allied Multiprep polishing machine. Firstly, the sample holder made of glass was polished using a coarse diamond or aluminium oxide polishing disk with grains of 9 μm or more in order to achieve an even surface. The wire was mounted on the holder using acetone-soluble wax. The cross section of the first side of the wire was then polished with the 9 μm or a finer disk at 125 RPM (rotations per minute), again for an even surface. Care had to be taken to apply as little force as possible, since the small wire diameter of under 1 mm provides little sturdiness. The wire was then detached from the holder, turned around and mounted on the polished side. The cross section of the second side was polished using disks with grains of 9 μm at 125 RPM, 6 μm at 100 RPM, 3 μm at 75 RPM and 1 μm at 50 RPM. Final polishing using 0.5 μm and 0.1 μm disks at 10–30 RPM with lubricants has been explored but has generally not led to better results than using the 1 μm disk. The reason thereof is the differing hardness of Nb, the A15 phase and the Cu matrix which causes varying ablation rates that can lead to Cu smearing over the surface and inducing scratches. Additionally, the presence of voids in the centre region of the sub-elements increases the likelihood for material to break out and decrease the surface quality during polishing. After polishing, the sample was detached, cleaned and mounted on a SEM sample holder using a conductive carbon-based adhesive tape. Final cleaning in the plasma cleaner removed any residual contamination. This procedure can also be applied to wires that were embedded using epoxy resin after stacking them into a holder, which is shown in Figure 2.7, together with a final sample for SEM investigations. In the case of embedded wires, polishing was conducted using various SiC disks with increasing fineness, followed by fabric disks with 3 μm and 1 μm grained diamond suspensions.
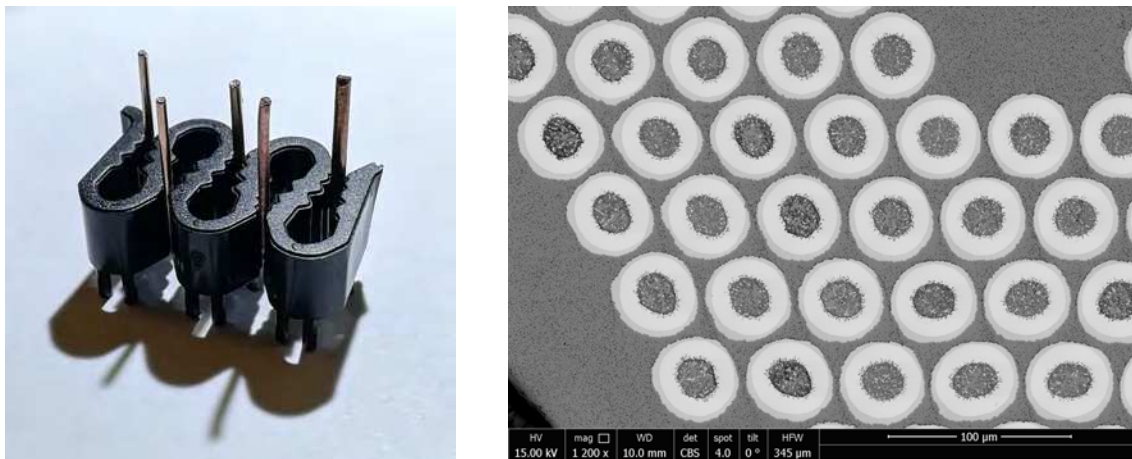
Figure 2.7: Embedding of Nb$_3$Sn wires in preparation for polishing (left) and SEM image of polished PIT wire cross section (right).

2.4 Sample preparation for SHPM

The preparation procedure for SHPM specimens is in principle very similar to the preparation for SEM investigations. For samples with a thickness of more than 1 mm, the only difference is the requirement of an adhesive capable of withstanding temperatures as low as 4 K. For this purpose, the Allied M-Bond adhesive was used to mount the polished wire sections directly onto polished Ti-6Al-4V sample holder disks which should be less than 3 mm in height and 10 mm in diameter in order to fit into the employed scanner. After the adhesive dried for 1 h at 175 °C, the sample was firmly attached to the holder.

2.5 Alternative sample preparation methods

In this chapter, the most reliable sample preparation methods were introduced and described in detail. However, various other methods for the different investigations have been explored in order to determine the most suited methods for optimal results. In the following, preparation methods that have been explored but have not led to satisfactory results are briefly presented, since these insights might be useful for future projects.

2.5.1 Alternatives for SHPM sample preparation

For inversion of the Biot-Savart law, determination of the critical current density and assessing of J_c inhomogeneities, slices of wires with a thickness of less than 10 µm are ideal. The procedure is the same as for thicker samples, except that both sides have to be polished carefully with fine-grained disks. At this thickness the wires start to break apart as seen in Figure 2.8 and the effect of Cu smearing and material breaking out as described in the section of the SEM preparation becomes increasingly problematic. For that reason, cutting off slices of etched sub-elements using FIB was explored as seen in Figure 2.9, which has proven to be less effective. The edges of the slices have sustained damage and achieving an even slice thickness was found to be very challenging. Furthermore, because of the size of around 50 µm, cutting a single sub-element and mounting it consumes several hours of time. Ion milling has also been attempted, but does not provide an accurate way of controlling the thickness of the specimen, which is why mechanical polishing was found to be the most reliable method. SHPM scans and SQUID measurements of thin slices of wires have shown different behaviours than those of a thickness of 1 mm or more. The critical temperature T_c seems to be suppressed in such samples, which could be due to damage induced by polishing or stoichiometry variations along the wire axis. Therefore, thicker samples were found to be preferable in terms of SHPM-related investigations.
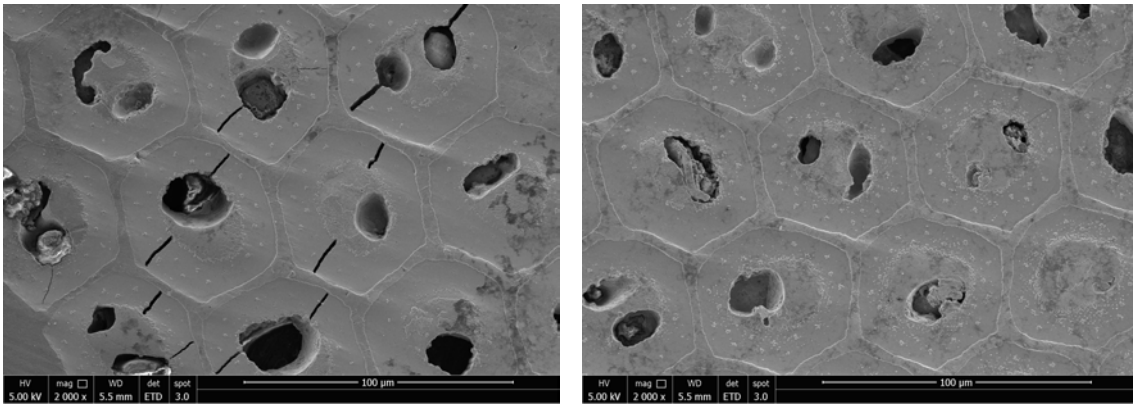
Figure 2.8: Mechanical polishing of less than 10 µm thin wire cross sections induced damage on samples and rendered some of them unusable for investigation (left). Successfully polished wire cross section of less than 10 µm thickness that was investigated by scanning Hall microscopy (right).
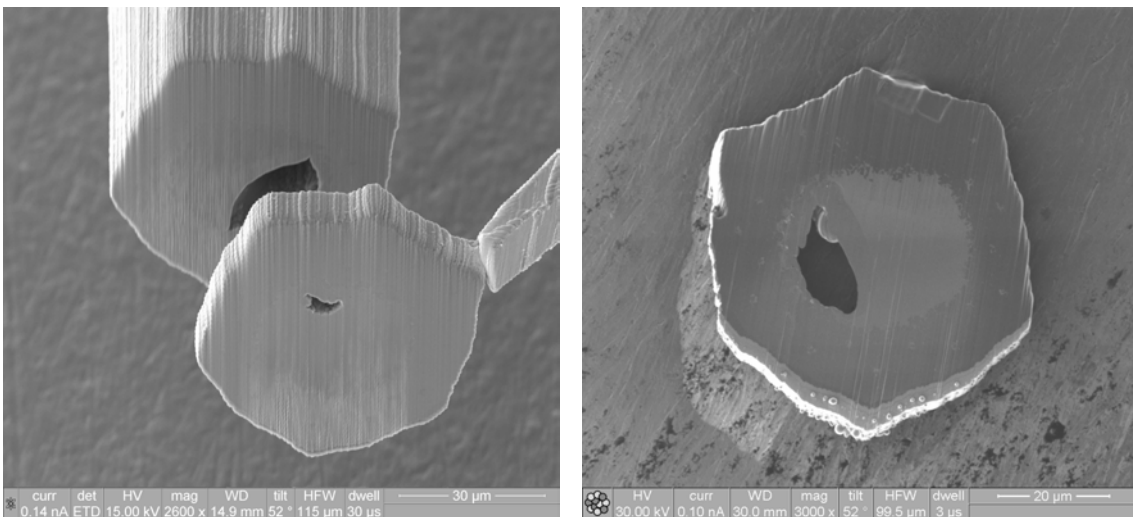
Figure 2.9: Cutting off slices of etched sub-elements for scanning Hall microscopy using FIB has not proven to be effective due to beam damage, uneven resulting slice thickness and time consumption.

2.5.2 Alternatives for TEM sample preparation

For the preparation of thin lamellae for TEM investigations, the option of mounting single filaments of Nb_3Sn wires on sample holder disks and ion milling them in the PIPS using beam energies of 4 kV–5 kV was explored, but has not lead to satisfying results consistently.

Another method used for TEM sample preparation aside from conventional FIB lift-out, which has proven to be effective, was mounting single filaments on the sample holder before FIB preparation and performing the H-Bar technique. This implies cutting small windows of 10 μm in size into the filament and thinning them as much as possible as seen in Figure 2.10. This methods provides the advantage of not needing to use the micro manipulator needle and thus being less time consuming and easier to handle. The disadvantage is that final ion milling becomes more of a challenge due to shadowing of the edges of the specimen, but H-Bar was found to be the best technique of pre-thinning samples before flash electro-polishing that is described in the following. The additional stability of two side walls also ensured better survivability during immersion in the etchant solution.
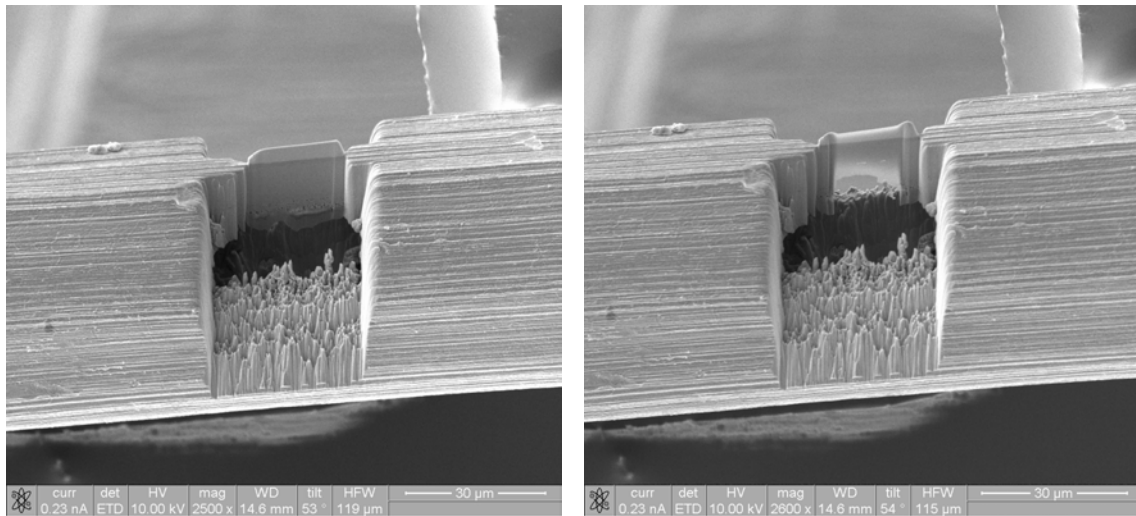
Figure 2.10: H-bar technique of thinning a sample by FIB for TEM investigations.

Aside from FIB and ion milling, alternative sample preparation routines for the investigation of neutron irradiated Nb_3Sn were explored, since specimen preparation for TEM investigations using ion milling can lead to significant beam damage on the surface and thus complicate the evaluation of neutron defects. An alternative method of TEM specimen preparation that often finds use on other materials is electro-polishing. Conventional jet electro-polishing is done by releasing a jet of an etchant solution onto the sample. However, Nb_3Sn wires with only around 1 mm in diameter cannot be mounted properly in such a machine, and this method would be too destructive for fragile TEM lamellae. In [71], lamellae of neutron irradiated W were prepared by flash electro-polishing using 0.5 % NaOH, which lead to a good surface quality of the samples.

In order to explore the use of flash electro-polishing on Nb_3Sn lamellae, a suitable flash electro-polishing setup was assembled as seen in Figure 2.11. During flash electro-polishing, TEM specimens with a thickness of around 200 nm–300 nm that were prepared using FIB and mounted onto a sample holder were immersed into

an aqueous etchant solution. The sample holders were mounted using stainless steel tweezers which were then contacted to a power source to act as an anode. As cathode, a steel plate was contacted to the negative exit of the power source and also immersed into the etchant solution. A high precision timer allowed to apply current for the short time period of $1\,ms$. Different possibilities for etchant solutions of Nb_3Sn can be found in literature, yet the one component almost all sources mention is HF acid, e.g. [67]. A mixture of H_2SO_4 and HF with 10:1 ratio was used for flash electro-polishing and proved to be very effective. The first experiment was conducted without cooling at room temperature, which led to amorphization of the samples. For the second experiment, the etchant was pre-cooled for $15\,min$ in the freezer. This had the consequence of a more gentle etching progress and resulted in an improved sample quality compared to the first experiment. Following that, the setup was adjusted in a way that made cooling the etchant possible using liquid nitrogen. However, flash electro-polishing has not led to improvements compared to ion milling, since a multitude of parameters has to be optimized for achieving good results, such as temperature, voltage and duration. Furthermore, in the case of Nb_3Sn, HF acid is required for electro-polishing, which poses a considerable health hazard. For these reasons it was refrained from exploring the use of this method further within this study. The assembled flash electro-polishing setup, however, was shown to be working as intended and can be useful for TEM sample preparations in the future, provided that the optimal parameters are explored in greater detail, which warrants a separate study itself.

Figure 2.11: Flash electro-polishing setup.

3 SEM analysis of the sub-element geometry

This chapter presents the results of the scanning electron microscopy (SEM) analyses of the investigated Nb_3Sn wires, including overview images of the wire geometry and sub-element layout, together with higher magnification images of single sub-elements. The SEM investigations were conducted on polished cross sections of the Nb_3Sn wires in order to gain information about the geometry and inhomogeneities between different and inside individual sub-elements. The CBS (circular backscattered electron) detector was used for achieving higher contrast between the different phases of the samples, which is based on their respective atomic numbers and thus yield differing contrast created by the backscattered electrons. This allows for a clear distinction between the Nb, A15 and Cu phase and leads to an easier identification of the A15 area. The resulting images were used for determining the area and aspect ratio distributions of the sub-elements. Additionally, information about other inhomogeneities such as longitudinal thickness variations of the A15 phase, unreacted sub-elements and Sn leakage was acquired.

3.1 Introduction

The geometry of sub-elements of multi-filamentary superconducting Nb_3Sn wires can have a great impact on their performance as later seen in Chapter 8 and Chapter 9. As outlined in Chapter 1, smaller sub-elements are desired for improved thermal and magnetic stability.

In [126], it was found that an increase in the sub-element aspect ratio is associated with a reduction of the minimum diffusion barrier thickness, which most frequently occurs in the outer sub-elements in PIT wires. A breach of the diffusion barrier can lead to Sn leakage into the Cu matrix and a substantial degradation of the Residual Resistance Ratio (RRR), which is needed for protection and electromagnetic stabilization. Therefore an assessment of the sub-element size distribution and distortion is of great importance for understanding this performance-limiting factor and improving the manufacturing process in the future.

While in undeformed wires, the outmost sub-elements generally show higher aspect ratios than the ones close to the centre of the wire as shown in this chapter, a different study that analysed the distortion of sub-elements in PIT and RRP wires due to deformation found that in that case, preferably the inner sub-elements become distorted [22].

3.2 Analysis of sub-element geometry

Inhomogeneities between the sub-elements over the wire cross section were investigated by assessing the sub-element area and aspect ratio distribution from SEM images. Overview SEM images with high contrast values were taken of different wire types using the CBS detector, Figure 3.1 showing an example. The image processing software ImageJ was used to threshold the images based on the strong contrast of the A15 phase as seen in the same figure. Corrections were applied manually in areas with weak contrast and poor image signal due to surface contamination on the sample and holes due to lifted out lamellae for TEM investigations. Such locations of FIB lift-outs can frequently be seen in the overview SEM images of the wires. Single sub-elements, in which the evaluation was too inhibited due to weak contrast or contamination on the sample surface that could not be corrected were removed and excluded from the statistics. Clean-up procedures such as despeckeling were applied to remove isolated pixels. The resulting images were used to analyse the area and aspect ratio of the A15 area and including the inner parts of the sub-elements, which were measured by pixel counting. The sub-element area is therefore defined as the sum of the A15 phase area and the central area. The sub-element aspect ratio is defined as the length of the major axis of an elliptical sub-element divided by its minor axis.
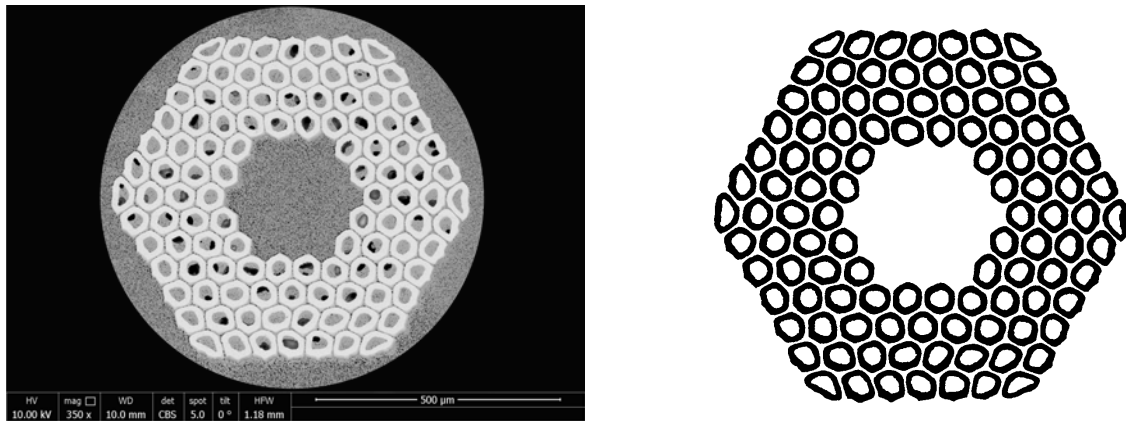
Figure 3.1: SEM image of the polished cross section of the RRP-Ti-108 wire taken with the CBS detector, yielding high contrast (left) and A15 area of RRP-Ti-108 sub-elements after thresholding the SEM image (right).

3.3 Results of sub-element geometry

Figure 3.2 to Figure 3.25 show SEM images of the different wire types as well as the areas and aspect ratios of the sub-elements and the corresponding statistics. The displayed overview images do not necessarily correspond to the images used for the analysis. The sub-elements were coloured according to the measured values using the ROI Colour Coder plug-in for the ImageJ software [40]. The range of the colour bar spans from the minimum to the maximum of the measured values. The aspect ratios of the RRP wires are exceptions to this case due to the hexagonal layout of the sub-elements in the Cu matrix and the 6 outmost sub-elements at the corners being outliers, which exhibit a significantly greater aspect ratio than the rest of the sub-elements. In order to better visualize the inner sub-elements, the upper limit of the colourbar was rescaled accordingly and set to a fixed value for the aspect ratios of the RRP wires. The coloured overlay possessed an opacity of 80 % in order for the A15 phase to be visible in the background, where the colour in the centre of the sub-elements corresponds to the value displayed by the colour bar. The sub-element area distributions can approximately be described by fits using Gaussian functions, where the best fitting functions are superimposed by red lines in the graphs.

3.3.1 BIN-246
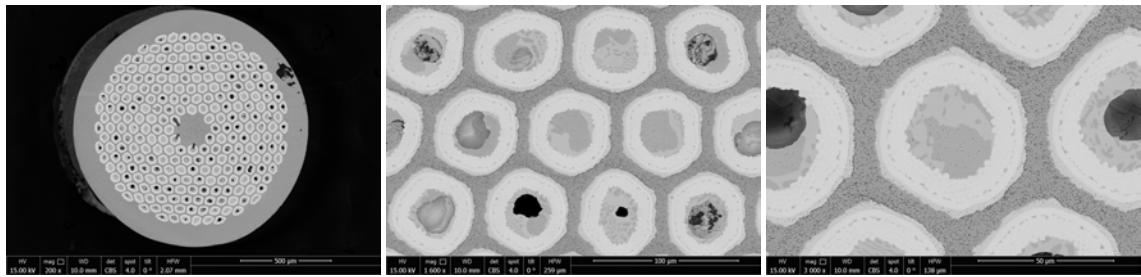
Figure 3.2: SEM images of the polished cross section of the BIN-246 wire. Overview of the whole wire (left) and single sub-elements.
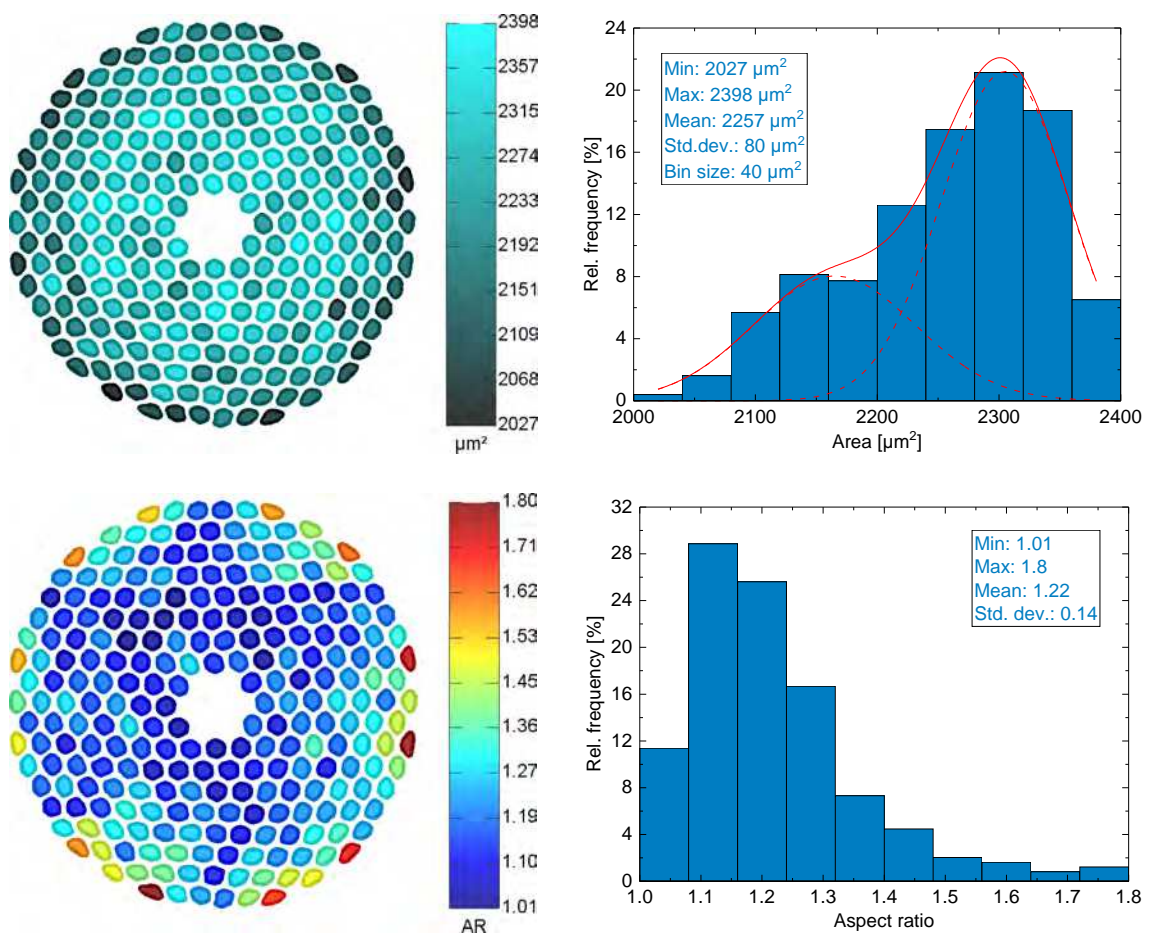
Figure 3.3: Sub-element areas (top) and aspect ratios (bottom) of the BIN-246 wire with corresponding statistics.

3.3.2 RRP-Ti-108
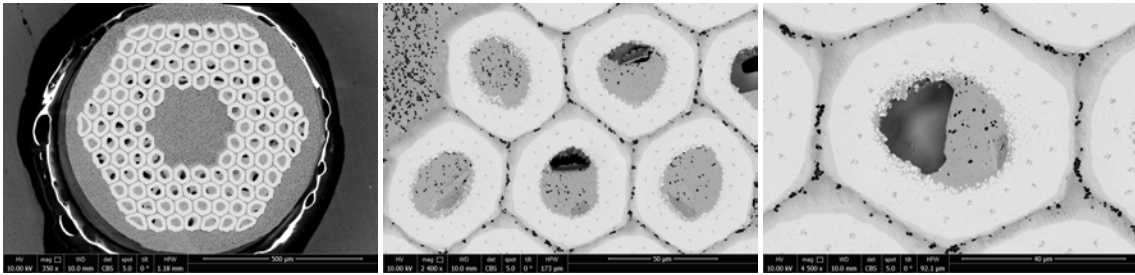
Figure 3.4: SEM images of the polished cross section of the RRP-Ti-108 wire. Overview of the whole wire (left) and single sub-elements.
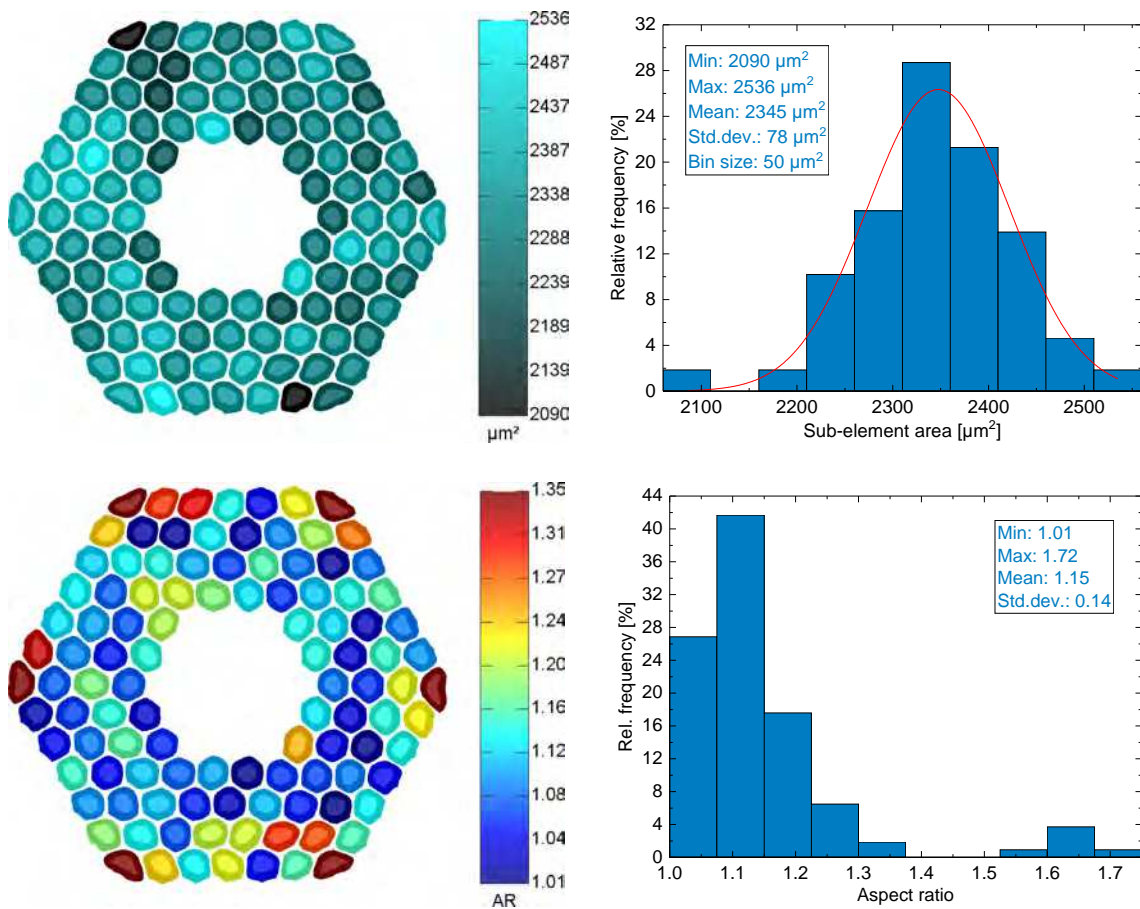
Figure 3.5: Sub-element areas (top) and aspect ratios (bottom) of the RRP-Ti-108 wire with corresponding statistics.

3.3.3 RRP-Ta-54
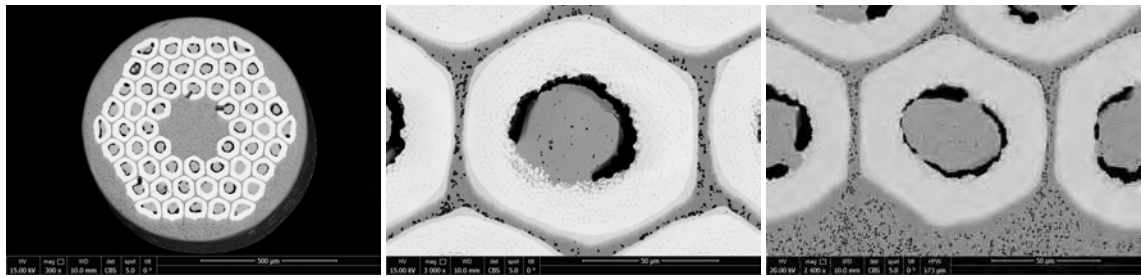
Figure 3.6: SEM images of the polished cross section of the RRP-Ta-54 wire. Overview of the whole wire (left) and single sub-elements.
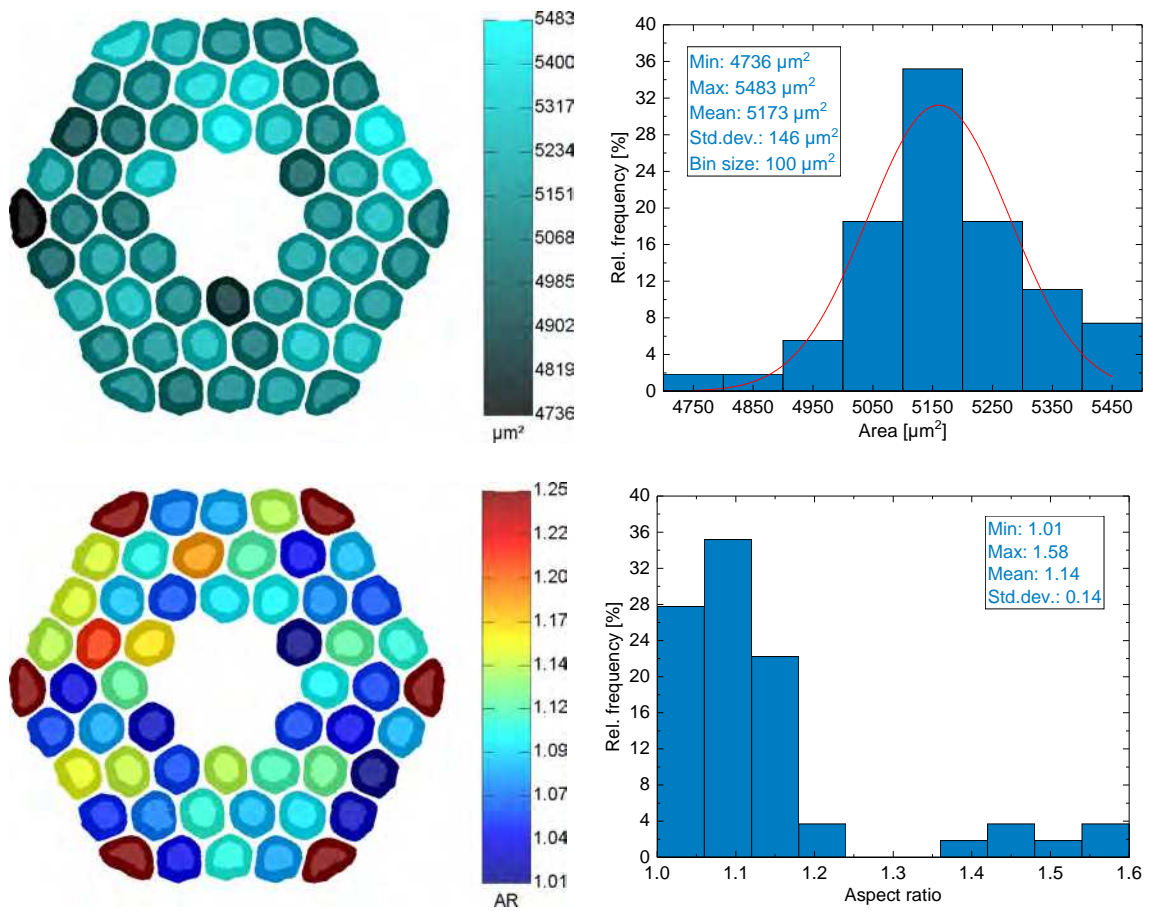
Figure 3.7: Sub-element areas (top) and aspect ratios (bottom) of the RRP-Ta-54 wire with corresponding statistics.

3.3.4 PIT-Ta-114
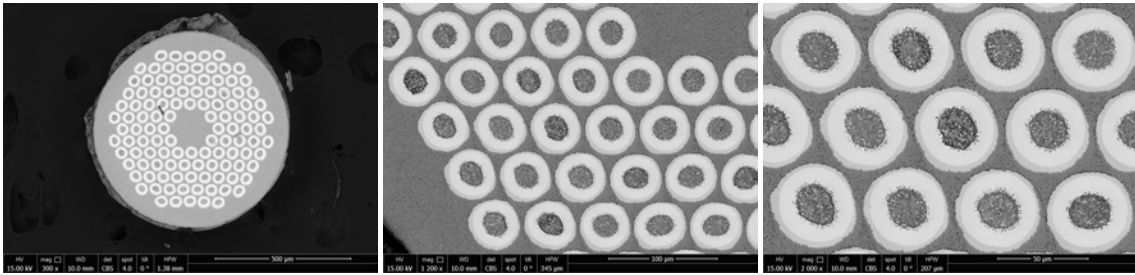
Figure 3.8: SEM images of the polished cross section of the PIT-Ta-114 wire. Overview of the whole wire (left) and single sub-elements.
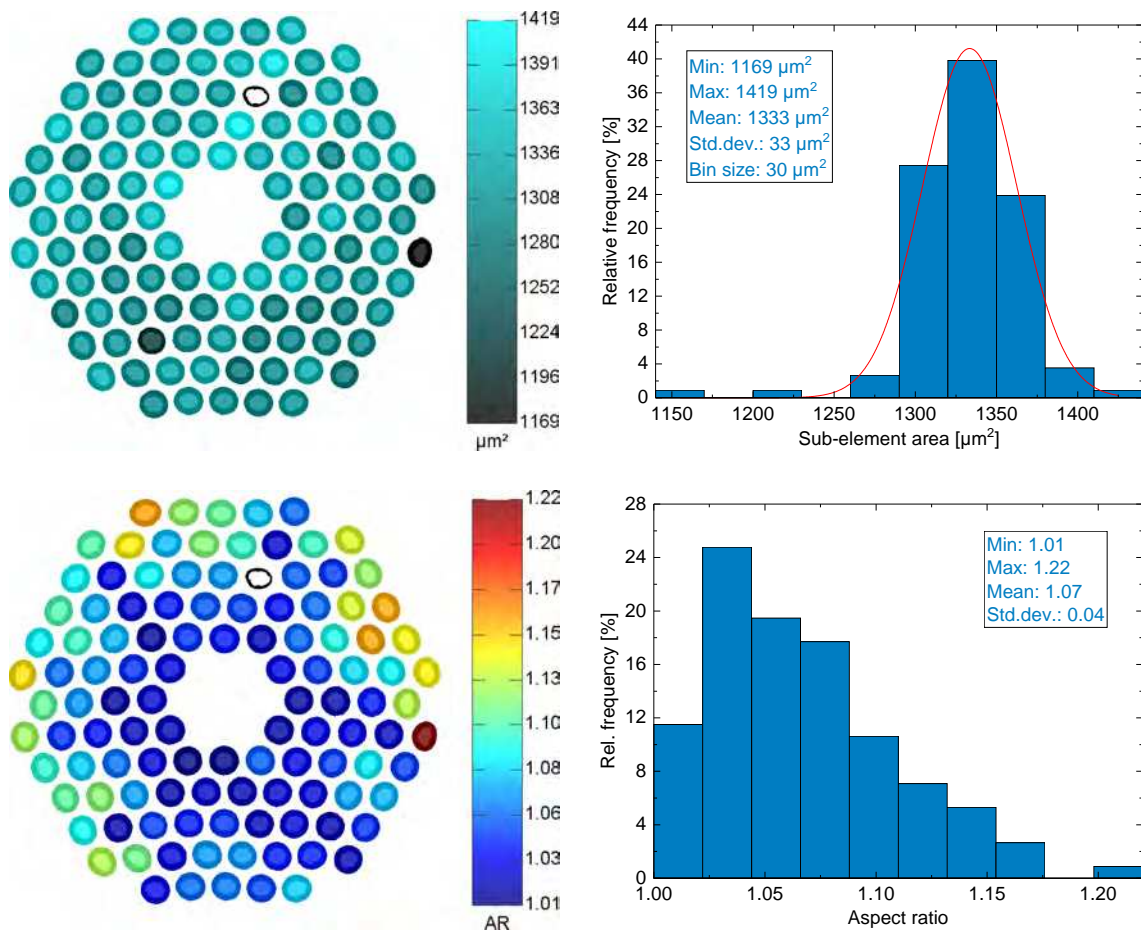
Figure 3.9: Sub-element areas (top) and aspect ratios (bottom) of the PIT-Ta-114 wire with corresponding statistics.

3.3.5 PIT-Ta-192
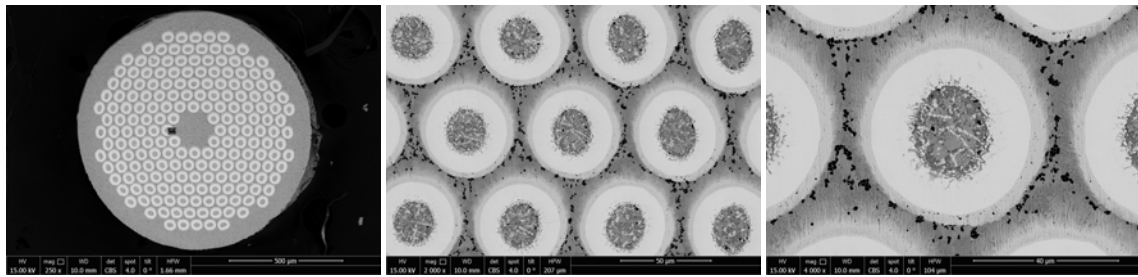
Figure 3.10: SEM images of the polished cross section of the PIT-Ta-192 wire. Overview of the whole wire (left) and single sub-elements.
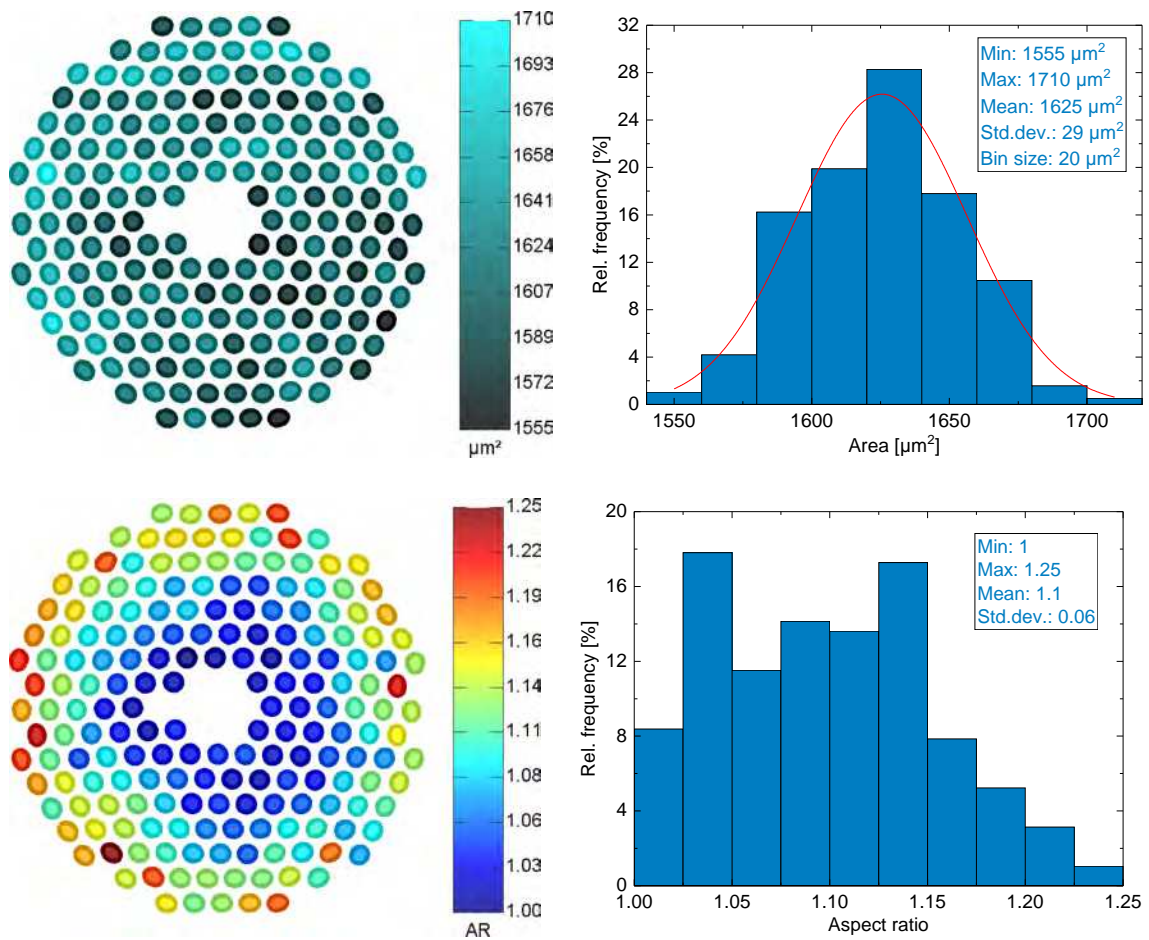
Figure 3.11: Sub-element areas (top) and aspect ratios (bottom) of the PIT-Ta-192 wire with corresponding statistics.

3.3.6 APC-3657-48
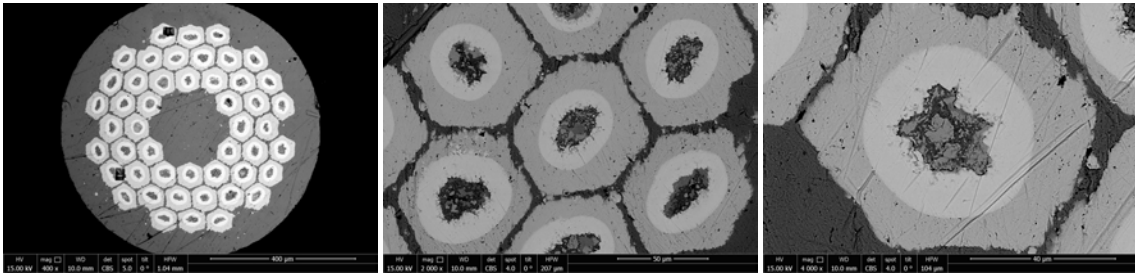
Figure 3.12: SEM images of the polished cross section of the APC-3657-48 wire. Overview of the whole wire (left) and single sub-elements.
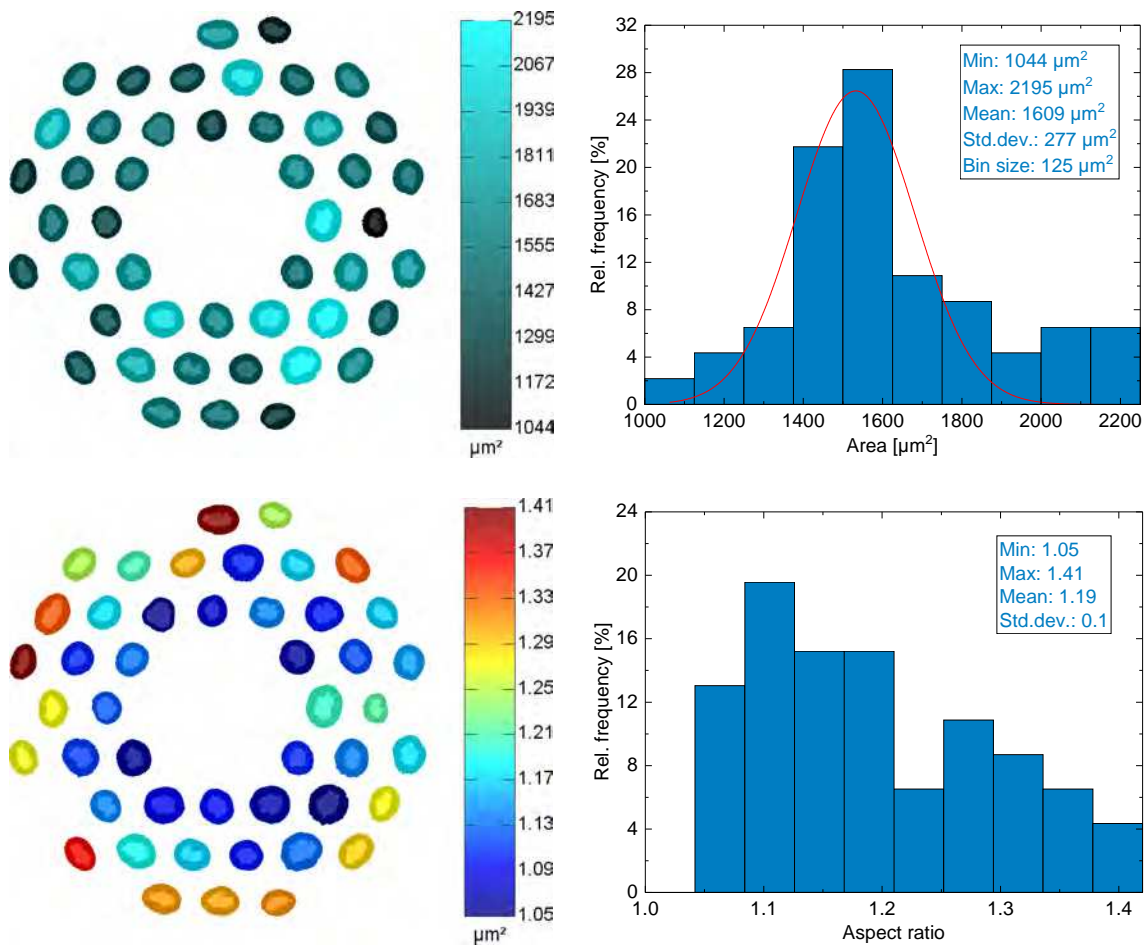
Figure 3.13: Sub-element areas (top) and aspect ratios (bottom) of the APC-3657-48 wire with corresponding statistics.

3.3.7 APC-3682-48
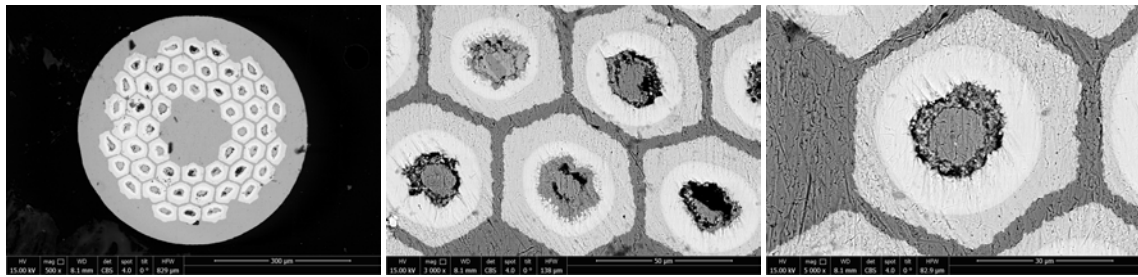
Figure 3.14: SEM images of the polished cross section of the APC-3682-48 wire. Overview of the whole wire (left) and single sub-elements.
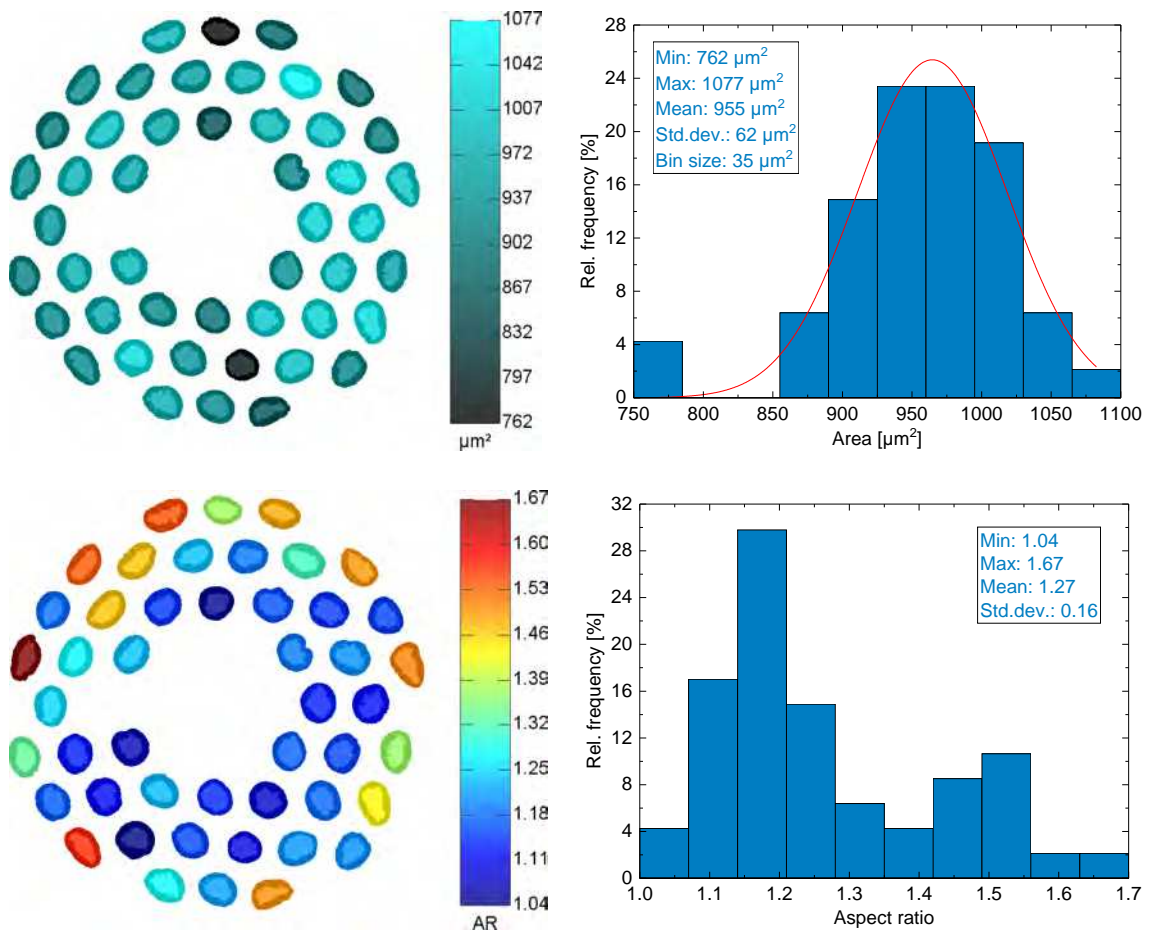
Figure 3.15: Sub-element areas (top) and aspect ratios (bottom) of the APC-3682-48 wire with corresponding statistics.

3.3.8 APC-3912-071
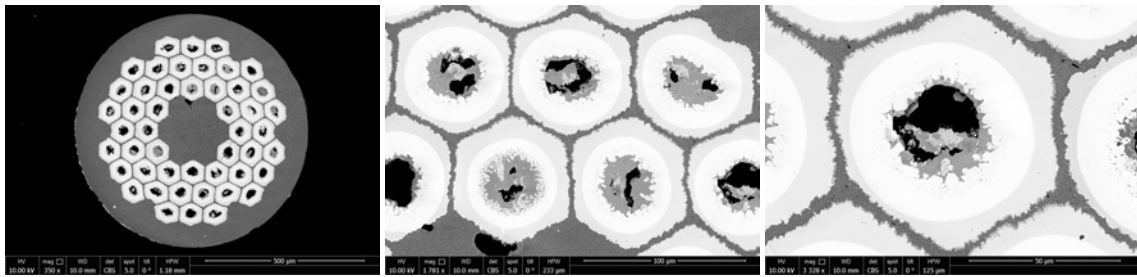
Figure 3.16: SEM images of the polished cross section of the APC-3912-071 wire. Overview of the whole wire (left) and single sub-elements.
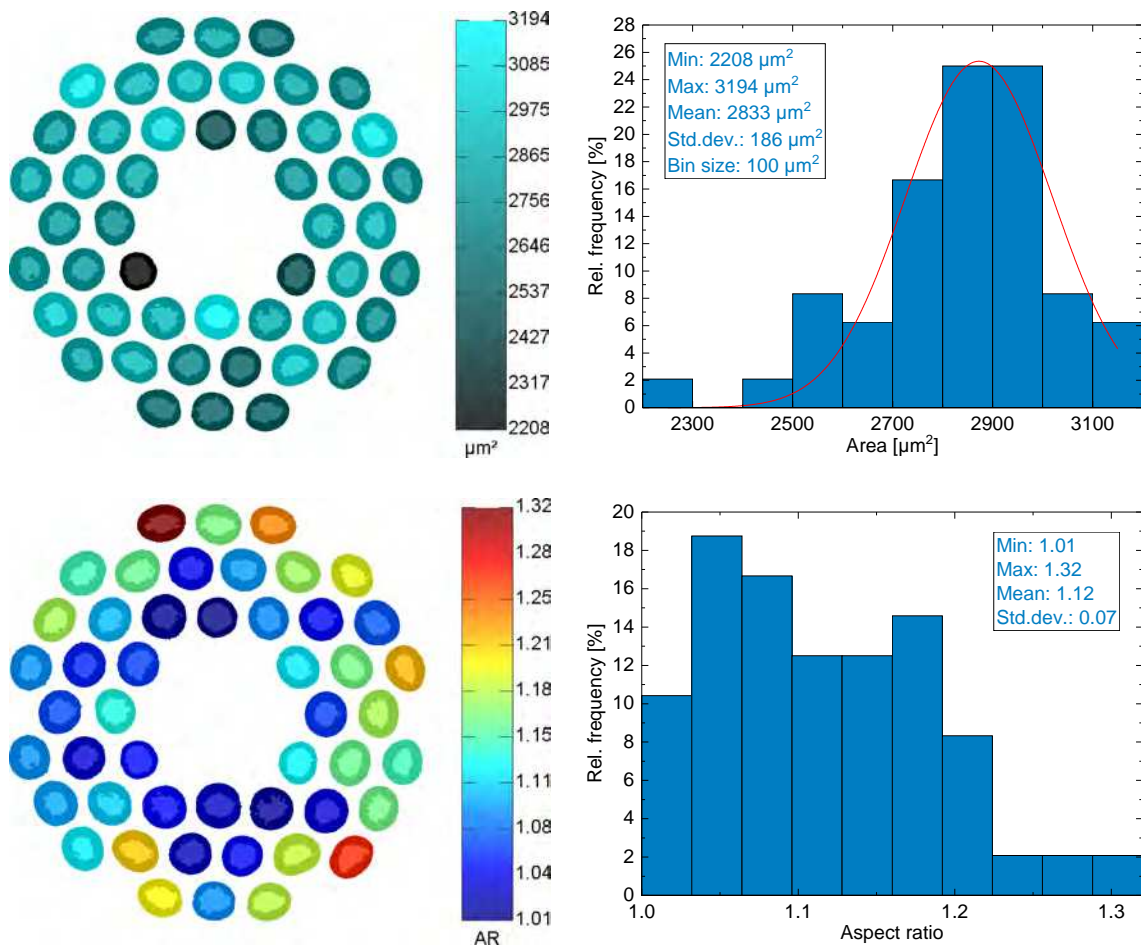
Figure 3.17: Sub-element areas (top) and aspect ratios (bottom) of the APC-3912-071 wire with corresponding statistics.

3.3.9 APC-3914-48
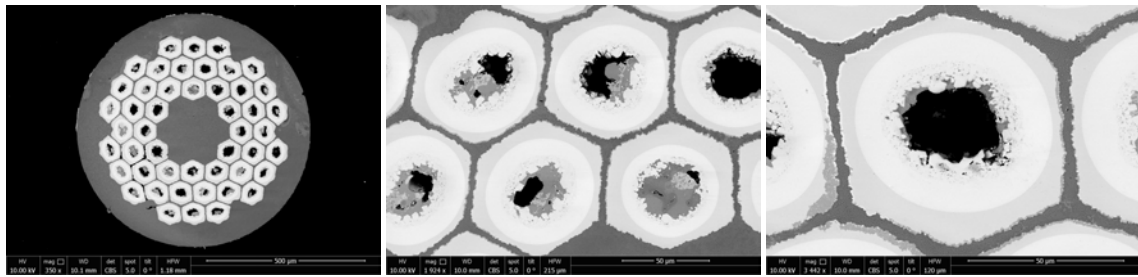
Figure 3.18: SEM images of the polished cross section of the APC-3914-48 wire. Overview of the whole wire (left) and single sub-elements.
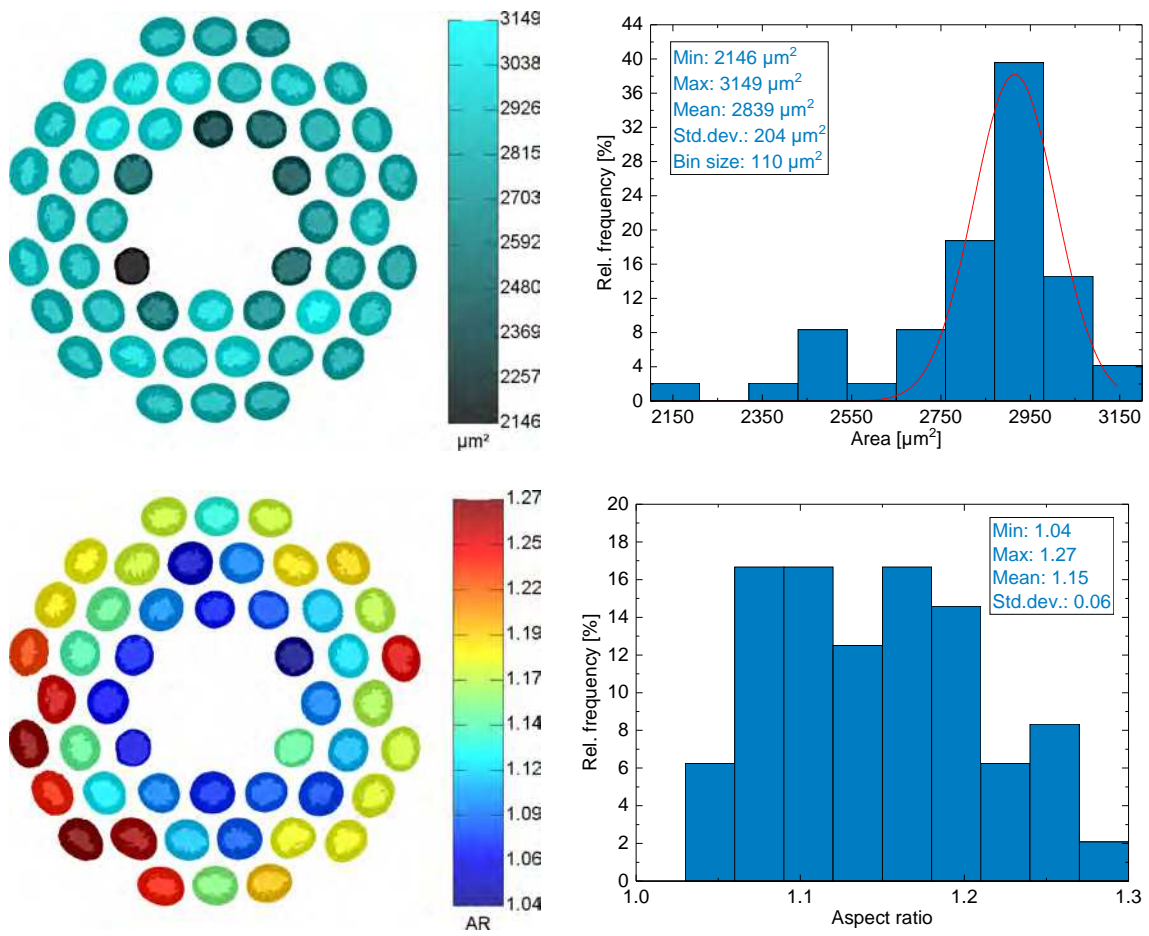
Figure 3.19: Sub-element areas (top) and aspect ratios (bottom) of the APC-3914-48 wire with corresponding statistics.

3.3.10 APC-3912-084
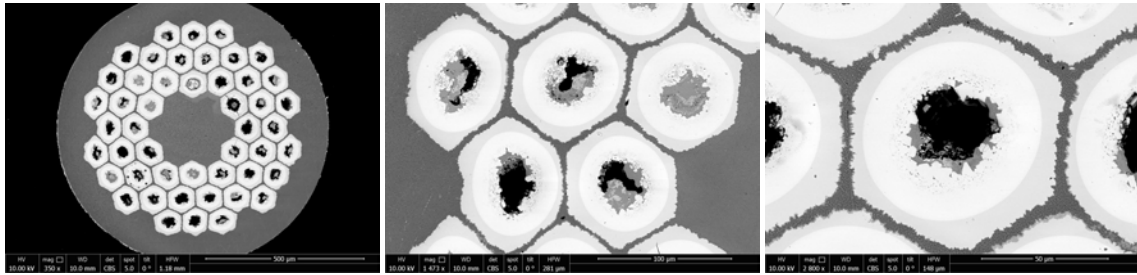
Figure 3.20: SEM images of the polished cross section of the APC-3912-084 wire. Overview of the whole wire (left) and single sub-elements.
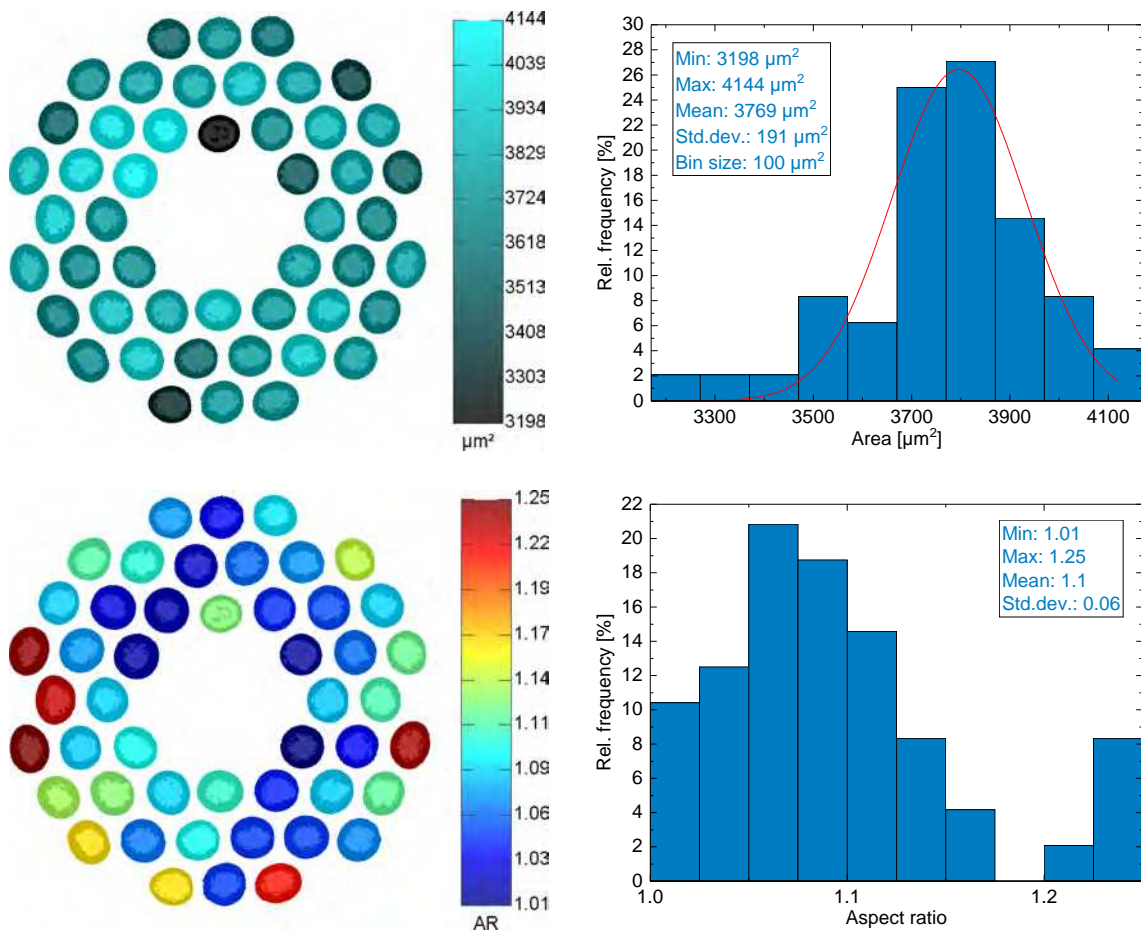
Figure 3.21: Sub-element areas (top) and aspect ratios (bottom) of the APC-3912-084 wire with corresponding statistics.

3.3.11 PIT-31284-192
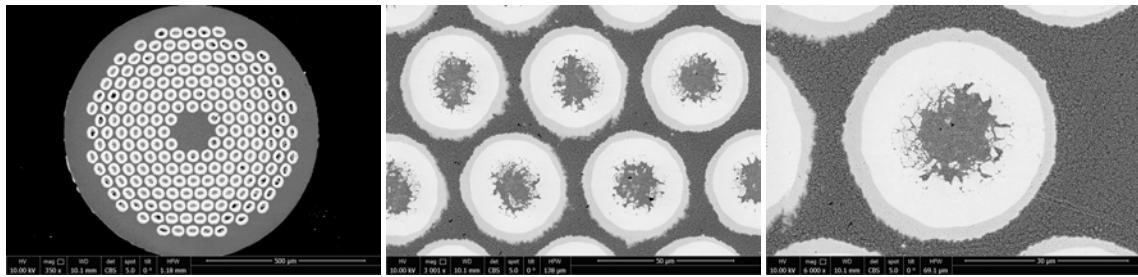
Figure 3.22: SEM images of the polished cross section of the PIT-31284-192 wire. Overview of the whole wire (left) and single sub-elements.
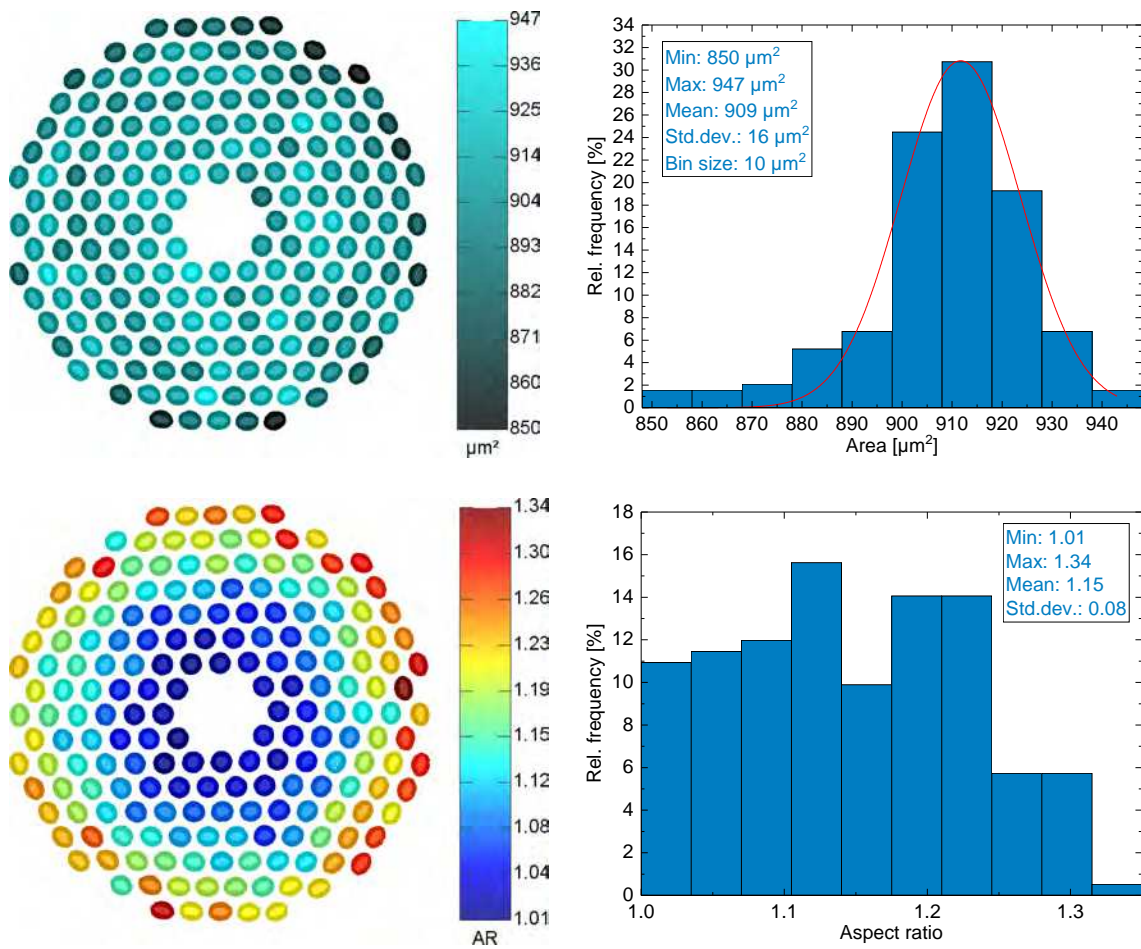
Figure 3.23: Sub-element areas (top) and aspect ratios (bottom) of the PIT-31284-192 wire with corresponding statistics.

3.3.12 IT-3736-54
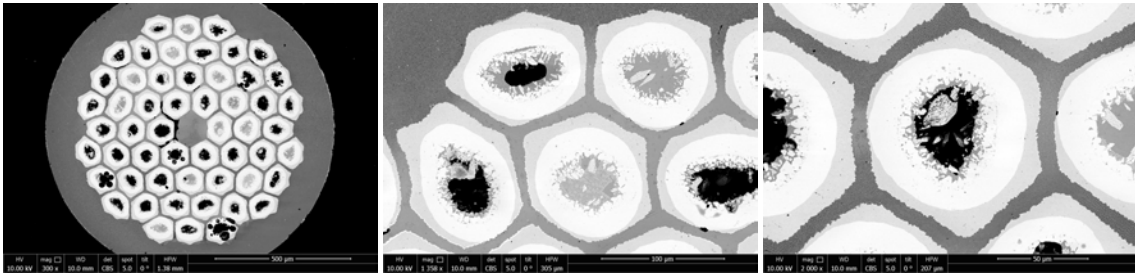
Figure 3.24: SEM images of the polished cross section of the IT-3736-54 wire. Overview of the whole wire (left) and single sub-elements.
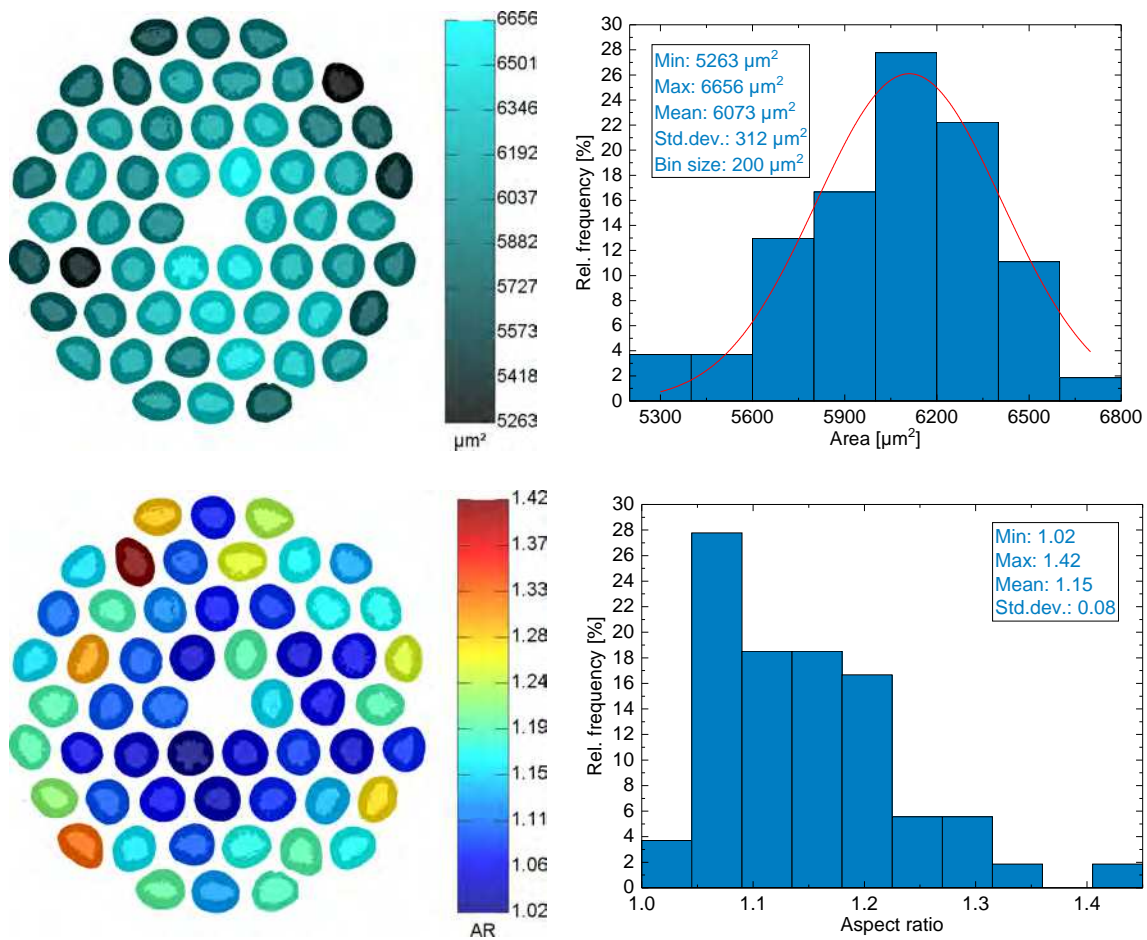
Figure 3.25: Sub-element areas (top) and aspect ratios (bottom) of the IT-3736-54 wire with corresponding statistics.

While the results of most of the investigated wires show no clear correlation between distance from the wire centre and area of the sub-elements, in case of the BIN-246 wire the inner sub-elements are generally larger than the ones on the outside. The sub-element area distribution for this wire can approximately be described by fitting two normal distributions, one for the inner sub-elements and one for the outer ones. It also becomes apparent that the outmost sub-elements are typically of a more elliptic shape than the ones in the centre, with aspect ratios up to 1.8, compared to the mean value of 1.22.

The sub-elements of the RRP-Ti-108 wire are rather uniformly distributed with respect to their area and aspect ratio, with the 6 outmost sub-elements being an exception and showing aspect ratios of up to 1.72, while the mean value is 1.15.

The RRP-Ta-54 wire shows similar results compared to the RRP-Ti-108 wire, where the 6 outmost sub-elements possess aspect ratios of up to 1.58. A notable difference of the RRP-Ta-54 wire compared to most other wires is the substantially larger average sub-element area of $5173\,\mu m^2$ with a standard deviation of $146\,\mu m^2$.

The analysis of the PIT-Ta-114 wire revealed a single sub-element that did not react properly during heat treatment, possibly due to insufficient amounts of Sn, which was not included in the statistics. The rest of the sub-elements of this wire show a rather narrow distribution with two sub-elements being an exception and featuring a much smaller area. The aspect ratios of the sub-elements of the PIT-Ta-114 wire generally tend to show larger values with increasing distance to the centre of the wire with a maximum of only 1.22.

The areas of the sub-elements of the PIT-Ta-192 wire are uniformly distributed across the wire section and show similar results to the PIT-Ta-114 wire in regard to the sub-element aspect ratio where the outer sub-elements show higher values than the ones in the centre of the wire, with a maximum of 1.25.

The investigation of the sub-elements of the APC-3657-48 wire reveals no correlation between location and area, but shows a very broad distribution with a standard deviation of $277\,\mu m^2$, where the largest sub-elements are more than double the size of the smallest ones. The trend of more elliptic sub-elements on the outer rows of the wire can also observed in the APC-3657-48 wire due to the fabrication process of APC wires being similar to that of PIT wires, with a maximum aspect ratio of 1.41.

The APC-3682-48 wire shows a more uniform sub-element area distribution than the APC-3657-48 wire with single sub-elements being exceptions. The aspect ratios of this wire also show higher values on the outmost areas of the wire section with a maximum value of 1.67, compared to the average value of 1.27.

The sub-element areas of the newer generation ternary APC-3912-071 wire were found to be much larger in size compared to the older generation ones of up to

$3194\,\mu m^2$ and a mean value of $2833\,\mu m^2$. The aspect ratios show a lower standard deviation of 0.07, a lower maximum value of 1.32 and a lower mean value of 1.12.

The analysis of the APC-3914-48 wire shows very comparable results of area and aspect ratio distribution compared to the APC-3912-071 wire. The outmost sub-elements in this wire seem to exhibit a slighter higher aspect ratio on one side of the cross section than on the opposing side which could be a result of applied stress during fabrication or preparation.

The APC-3912-084 wire shows even higher values of the sub-element areas than the other newer generation ternary APC wires, up to $4144\,\mu m^2$. The aspect ratios of the sub-elements, on the other hand, are very comparable.

The PIT-31284-192 wire exhibits an exceptionally small standard deviation of the sub-element area distribution of only $16\,\mu m^2$, and at the same time the smallest sub-element areas of all wires with a mean value of $909\,\mu m^2$. The distribution of the sub-element aspect ratios clearly show increasing values with increasing distance from the wire centre.

The IT-3736-54 wire shows the highest values of the sub-element areas of all wires with a mean value of $6073\,\mu m^2$ and also the highest standard deviation of $312\,\mu m^2$. The sub-element aspect ratios were found to be rather independent of their location in the matrix, with slightly smaller values near the wire centre. The maximum aspect ratio of sub-elements in this wire was found to be 1.42.

3.4 Summary of sub-element geometry

The analysis of the sub-element geometry in this chapter revealed considerable differences between sub-elements over the wire cross sections. The smallest and most elliptical sub-elements are frequently located at the outside of the wire cross sections. RRP wires show no such clear correlation between geometry and location of the sub-elements inside the cross sections, with the exception of the sub-elements in the corners, which show the highest aspect ratios. Table 3.1 shows a summary of selected results of the sub-element geometry investigation of the different Nb_3Sn wires. The mean sub-element areas are displayed together with their absolute and relative standard deviations, as well as the mean and maximum values of the aspect ratios. It becomes apparent that the relative standard deviations of the sub-element areas is larger for the APC wires compared to the standard RRP and PIT wires, where PIT wires show the smallest absolute and relative deviations. The mean aspect ratios show comparable values across all types of wires, while the maximum aspect ratios differ considerably between the wires with values between 1.22 and 1.80.

The results of the sub-element geometry analysis furthermore show that while most sub-element area distributions can be described by fits using Gaussian functions,

Wire	Mean area [μm²]	Abs. area SD [μm²]	Rel. area SD [%]	Mean AR	Max AR
BIN-246	2257	80	3.5	1.22	1.80
RRP-Ti-108	2345	78	3.3	1.15	1.72
RRP-Ta-54	5173	146	2.8	1.14	1.58
PIT-Ta-114	1333	33	2.5	1.07	1.22
PIT-Ta-192	1625	29	1.8	1.10	1.25
APC-3657-48	1609	277	17.2	1.19	1.41
APC-3682-48	955	62	6.5	1.27	1.67
APC-3912-071	2833	186	6.6	1.12	1.32
APC-3914-48	2839	204	7.2	1.15	1.27
APC-3912-084	3769	191	5.1	1.10	1.25
PIT-31284-192	909	16	1.8	1.15	1.34
IT-3736-54	6073	312	5.1	1.15	1.42

Table 3.1: Summary of selected results of the sub-element geometries of the investigated Nb$_3$Sn wires. SD = standard deviation, AR = aspect ratio.

single sub-elements show values that greatly differ from the mean value and do not follow the Gaussian distribution. PIT wires generally show a much narrower distribution than the other types of wires, while also possessing a smaller average sub-element area. Figure 3.26 shows a comparison of the sub-element area distributions of the investigated wires described by Gaussian functions. These distributions were calculated by using the corresponding mean values and standard deviations of the data shown in Table 3.1, assuming that all sub-elements follow a Gaussian distribution that can be described by the probability density function of the form

$$f(x) = \frac{1}{\sigma\sqrt{2\pi}}e^{-\frac{1}{2}\left(\frac{x-\mu}{\sigma}\right)^2}, \tag{3.1}$$

where μ denotes the mean value and σ the standard deviation of the distribution.
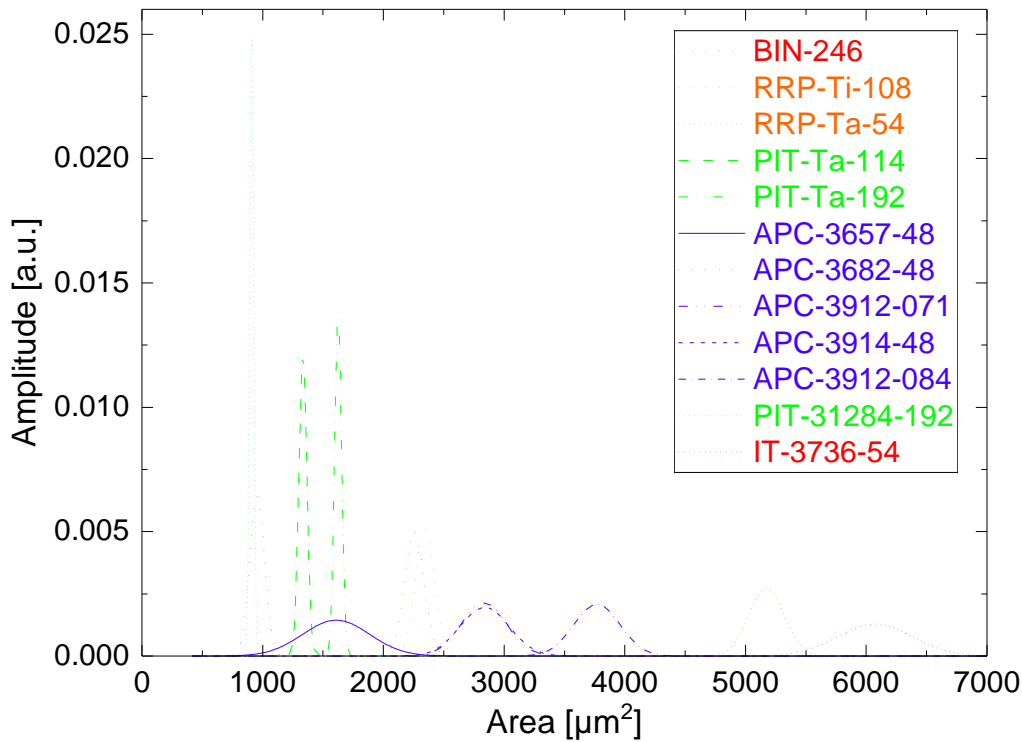
Figure 3.26: Sub-element area distributions of the investigated wires described by Gaussian distributions calculated by using the mean values and standard deviations of the data.

3.5 Other Inhomogeneities

This section shows exemplary data of additional inhomogeneities that were observed during the SEM investigations of the different Nb_3Sn wires. These inhomogeneities were mostly found in specific wires and do not occur regularly. Nevertheless, they can potentially have a significant impact on the superconducting performance, for which reason their assessment and discussion is not to be neglected.

3.5.1 Longitudinal variations of the A15 geometry

Two of the Nb_3Sn wires that are investigated in this study are older generation monofilamentary binary APC wires, whose transversal cross sections are seen in Figure 3.27. Since they only consist of one single large sub-element, an analysis of their sub-element area and aspect ratio distributions is obsolete. However, these types of wires were found to be suitable for investigations of longitudinal variations of the A15 phase along the wire axis. Specimens for such examinations were prepared by mechanically polishing the wires along the axis until the wire centre was reached. SEM

imaging of these longitudinal cross sections revealed considerable variations of the A15 geometry along the axis as seen in Figure 3.28. These longitudinal inhomogeneities could potentially have an impact on the superconducting performance by limiting the available A15 layer thickness locally.
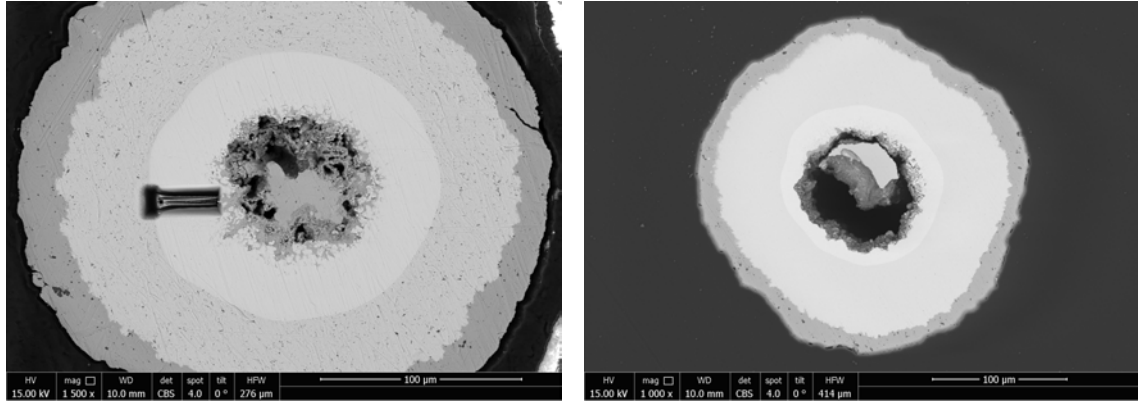
Figure 3.27: SEM images of the polished transversal cross sections of the APC-3607-1 wire (left) and the APC-3680-1 wire (right).
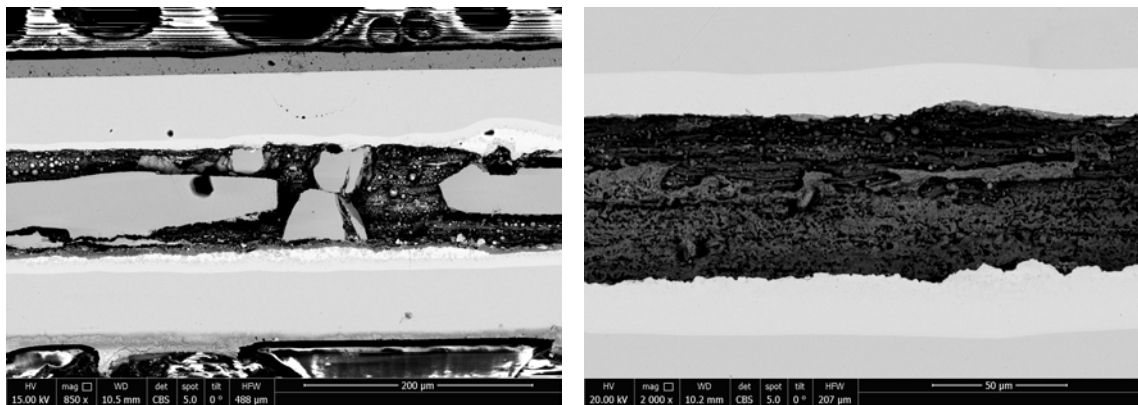
Figure 3.28: SEM images of the polished longitudinal cross section of the APC-3680-1 wire.

3.5.2 Un-reacted sub-elements

During the investigation of the sub-elements of the PIT-Ta-114 wire, one sub-element was found to not have reacted properly during the heat treatment and shows a significantly reduced area of the A15 phase as seen in Figure 3.29. A possible explanation for this occurrence is an insufficient amount of Sn prior to the reaction heat treatment. Such improper sub-elements inhibit the overall wire performance by limiting the overall current carrying capability.
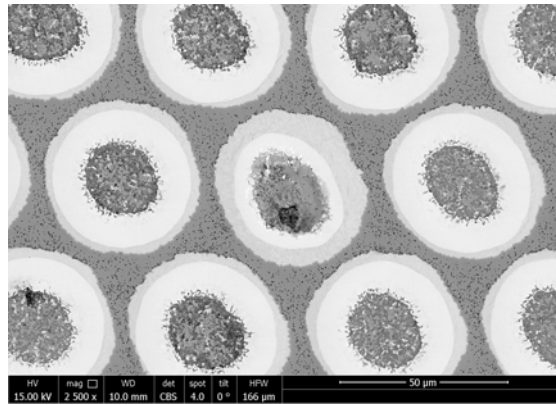
Figure 3.29: SEM image of the unreacted sub-element of the PIT-Ta-114 wire.

3.5.3 Sn leakage

During the manufacturing of Nb_3Sn wires, Sn might leak into the Cu matrix due to locations with a reduced or damaged Nb barrier. A possible cause is a too long duration of the heat treatment, due to which the A15 phase expands to a larger radius than the Nb barrier. This can lead to the loss of Sn content in the A15 phase and thus resulting in a degradation of the superconducting properties [126]. For that reason care should be taken to avoid Sn leakage during the manufacturing process.

SEM images were taken of all wires in order to analyse locations of possible Sn leakage into the Cu matrix, but only in one of the wires hints of Sn leakage were determined. In the wire IT-3736-54 manufactured by Hyper Tech, about 50% of the sub-elements showed locations where the A15 phase was in contact with the surrounding Cu matrix due to the reduced thickness of the Nb barrier as seen in Figure 3.30.
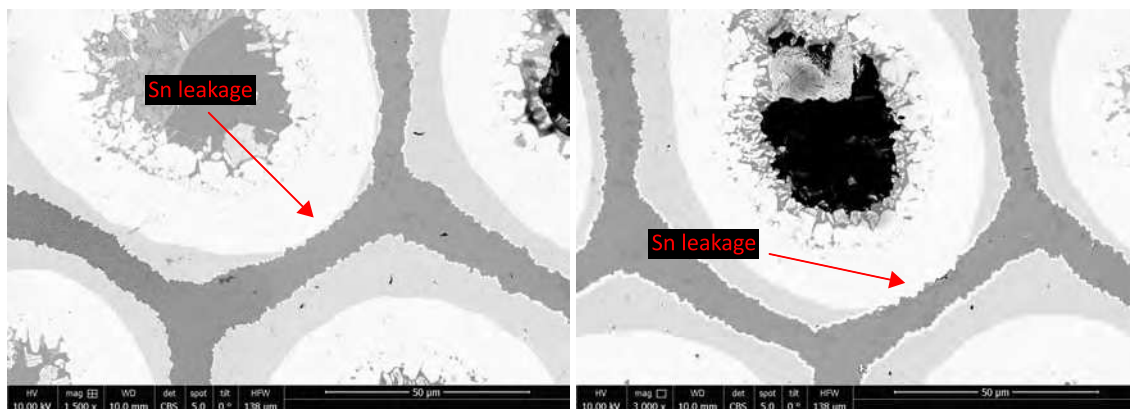
Figure 3.30: SEM images of the IT-3736-54 wire show sub-elements where Sn is leaking into the Cu matrix.

4 TEM investigation of the A15 microstructure

This chapter describes the results of the transmission electron microscopy (TEM) investigations of the different Nb_3Sn wires. Some of the findings occur in a similar form in all wires, while others were only observed in specific wires. The first section deals with the analysis of the general microstructure of the wires, including local inhomogeneities, and shows overview images as well as the local microstructure with a focus on the internal oxidized APC wires and their nano-precipitates. Thereafter, an analysis of the size distribution and density of the precipitates in the different APC wires is presented and compared, which are important for refining the grain size and increasing the pinning force.

4.1 Local microstructure

The local microstructure of the A15 phase was investigated on thin lamellae by means of TEM and STEM imaging. Numerous precipitates of around 10 nm in diameter were found in specimens of all wires as displayed in Figure 4.1 by STEM imaging under diffraction contrast. EDX line scans across the precipitates of the BIN-246 wire and the RRP-Ti-108 wire were conducted in order to assess their elemental composition. The resulting statistics can be found in Figure 4.2. For the BIN-246 wire, a single line scan is shown, while the statistics for the RRP-Ti-108 wire consist of 7 line scans across different precipitates. The EDX analyses revealed a higher Nb/Sn ratio compared to the surrounding A15 area. The Sn content decreases by about 10 %–15 % at the centre of these precipitates. Since they are relatively small compared to the specimen thickness and can be located in deeper sample layers, the EDX spectrum in these areas contains information of the surrounding A15 area as well. Thus, assumptions can be made that the precipitates most likely consist of pure residual Nb which originates from the heat treatment during the manufacturing process. Since they naturally exhibit different superconducting properties due to differing elemental composition and crystal structure, they might potentially act as additional pinning centres and could therefore contribute to the pinning force. High resolution TEM imaging was conducted on the precipitates in Figure 4.3, where the Fourier transform revealed a different crystal orientation in these areas.
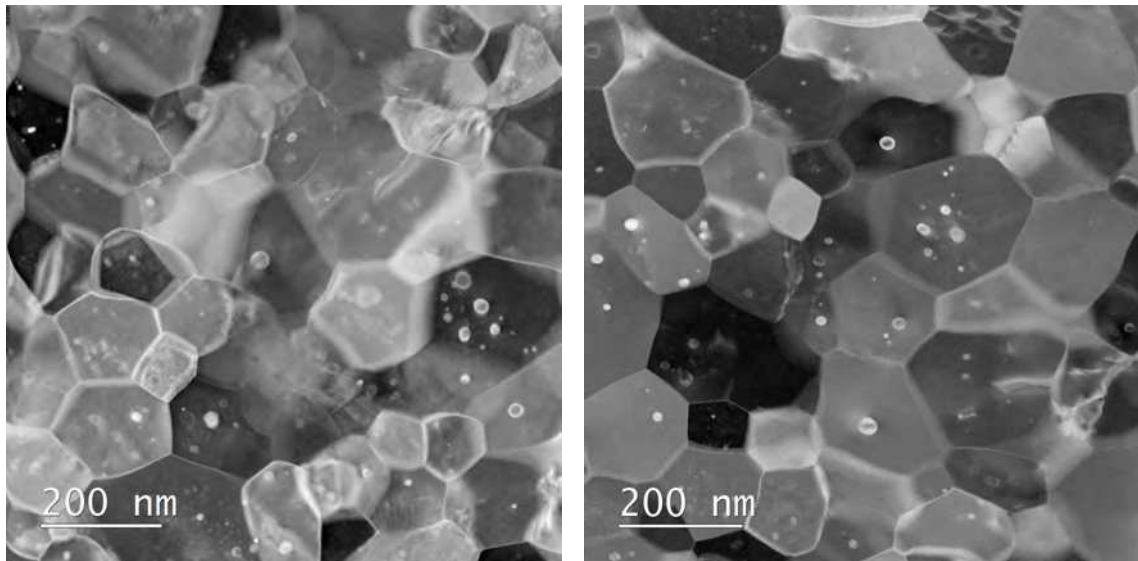
Figure 4.1: STEM annular dark field images of precipitates in various Nb₃Sn wires. The precipitates appear as bright spots in diffraction contrast.
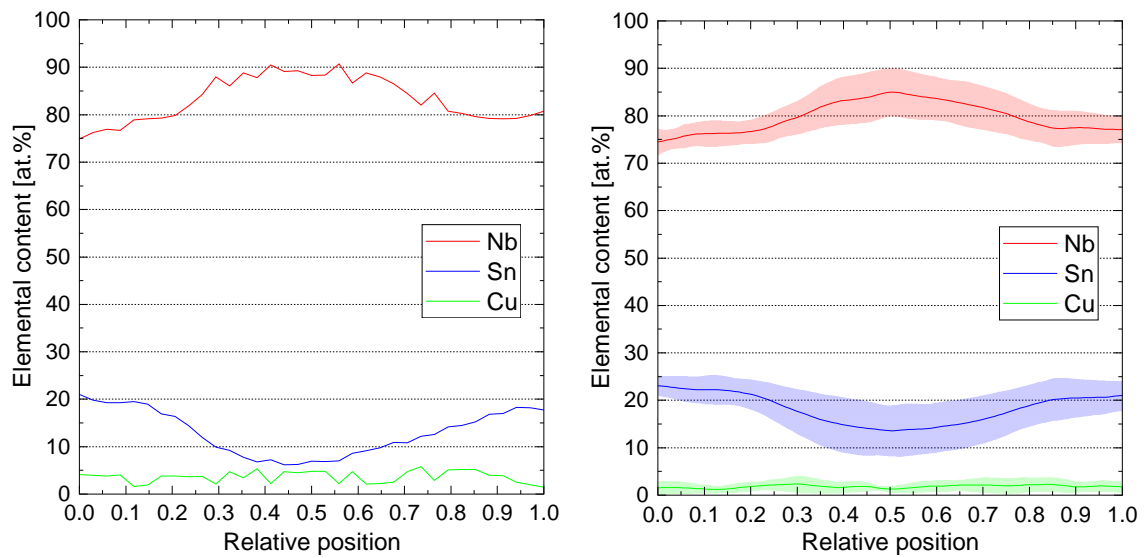
Figure 4.2: EDX line scans over precipitates in the BIN-246 (left) and RRP-Ti-108 (right) wires.
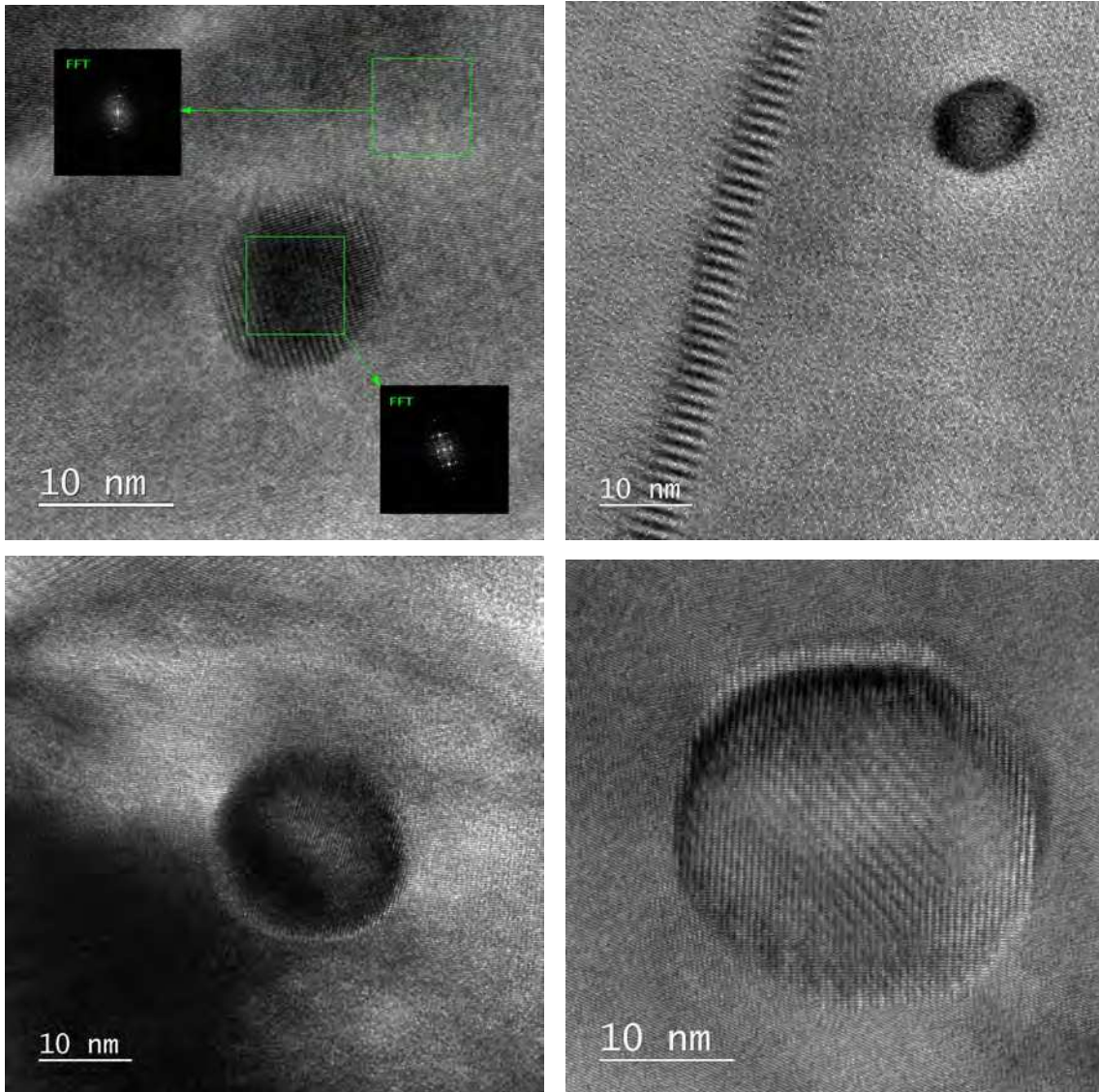
Figure 4.3: HRTEM images of precipitates in various Nb₃Sn wires. The Fourier transform shows a different crystal orientation in the precipitates compared to the surrounding area.

While the different types of Nb$_3$Sn wires show differences in grain size and orientation as later shown in Chapter 6, the microstructure of the Nb$_3$Sn phase is generally very comparable. In the following, some exemplary findings during the TEM investigation of the wires are shown, which are not necessarily unique to a specific wire type. After a short discussion of the standard wires, the focus will be laid upon the APC wires and the analysis of their nano-precipitates.

4.1.1 BIN-246

It is common knowledge that due to their manufacturing process as described in Chapter 1, PIT type Nb$_3$Sn wires exhibit two types of grains in the A15 phase: coarse grains near the sub-element centre and fine grains towards the outside barrier. While not as dominant, a similar behaviour was also observed in the BIN-246 wire, where multiple rows of altering fine and coarser grains are present as seen in Figure 4.4.
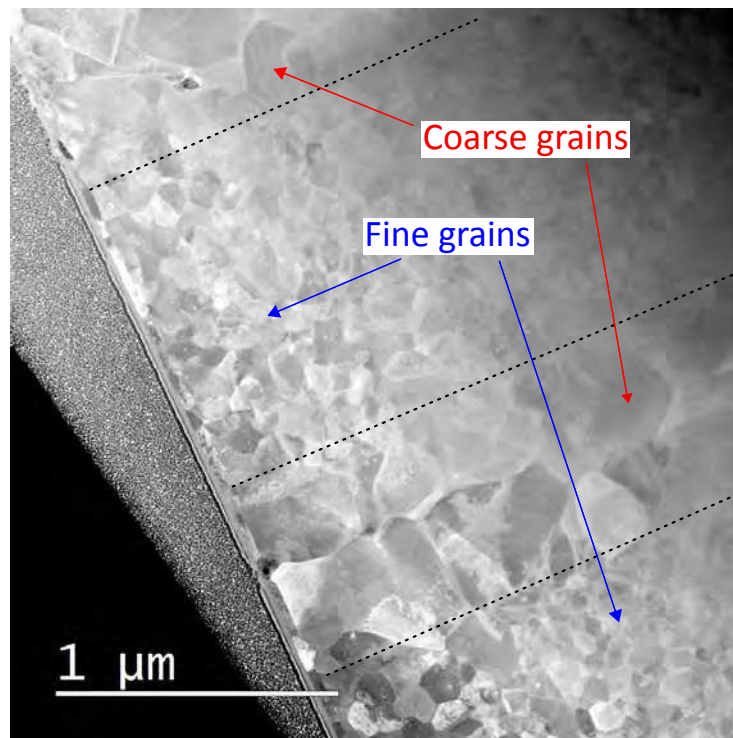
Figure 4.4: STEM image of BIN-246 wire shows regions of coarse and fine grains.

Since APC wires are manufactured in principle by the same process as PIT wires, their microstructure also exhibits the separation between a coarse grained and a fine grained region, as shown later as an example for the APC-3657-48 wire in Figure 4.8.

4.1.2 APC-3607-1

STEM and HRTEM images were taken of the APC wires in order to investigate the grain structure and the precipitates. STEM images of the APC-3607-1 wire are shown in Figure 4.5 and Figure 4.6 with varying camera length, leading to different types of contrast. A high camera length leads to ADF diffraction contrast and grains showing contrast due to differing orientations, while a small camera length leads to HAADF contrast based on the atomic number of the elements. ZrO_2 precipitates appear bright under diffraction contrast and dark under Z-contrast due to a lower atomic number of 18.67 compared to Nb_3Sn with 43.25. The average atomic number of the HfO_2 precipitates is 29.33 and therefore closer to that of Nb_3Sn, leading to weaker contrast between these phases. HRTEM images of the precipitates in the APC-3607-1 wire are shown in Figure 4.7.
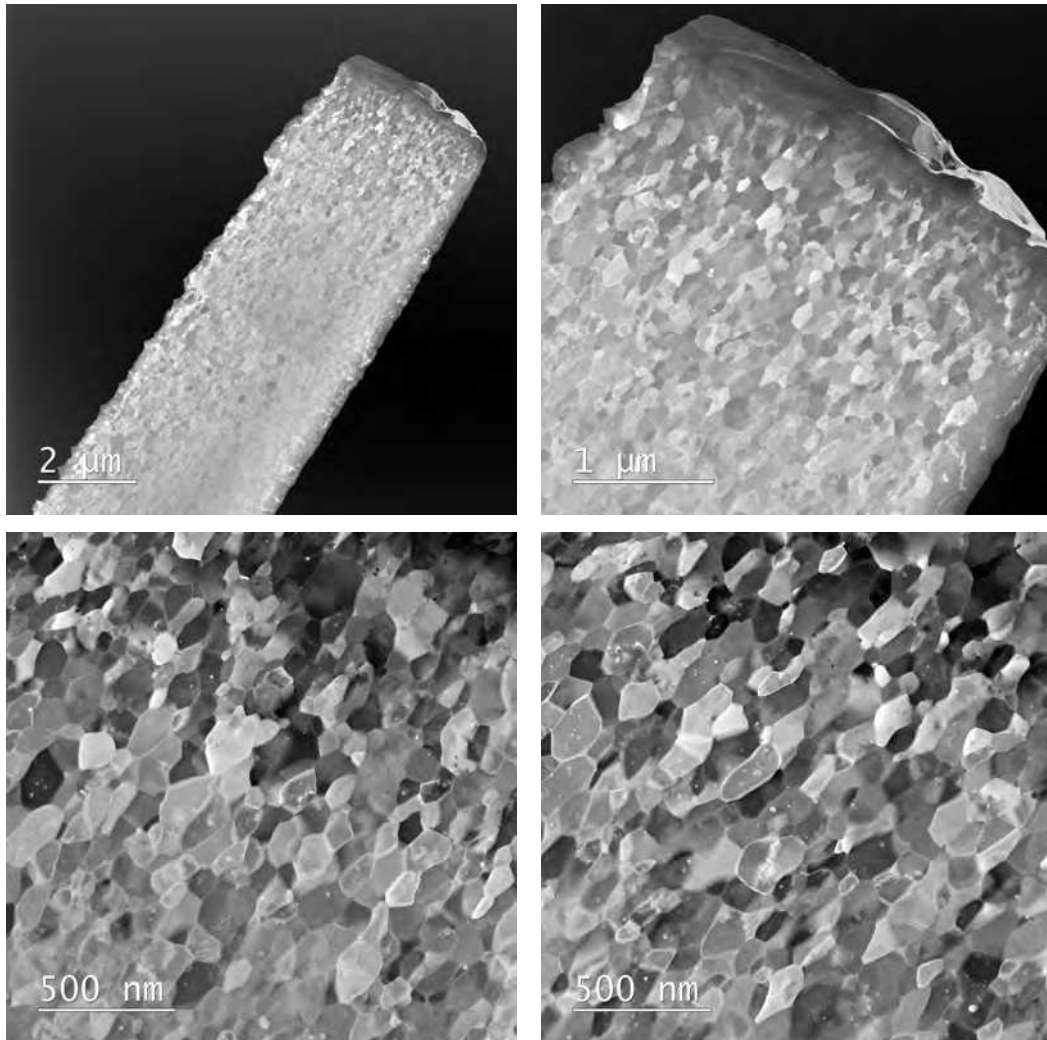
Figure 4.5: Annular dark field STEM images of the APC-3607-1 wire. Diffraction contrast arises due to different orientation of grains. Precipitates appear typically as bright spots.
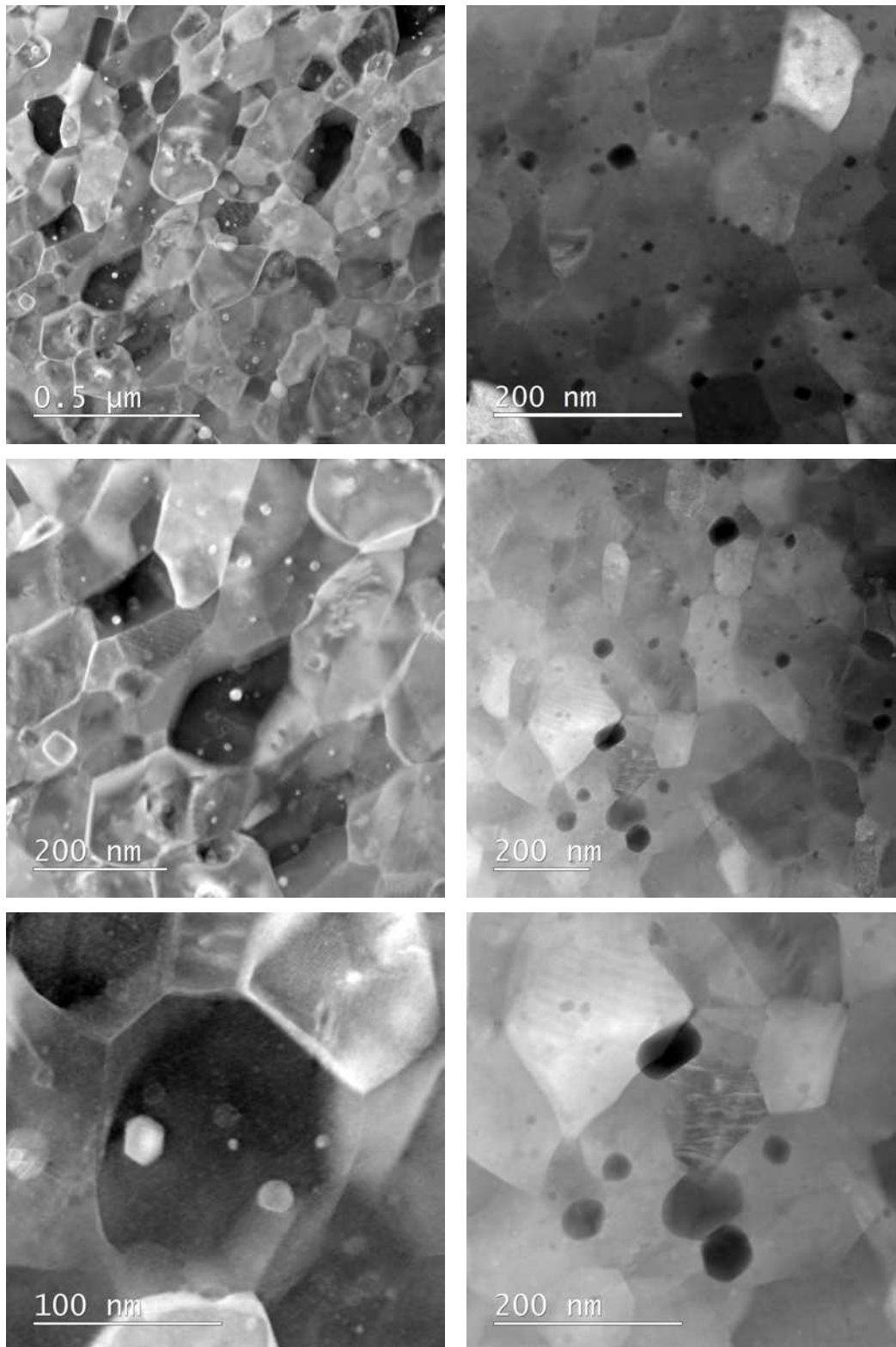
Figure 4.6: STEM images of precipitates embedded in A15 phase of the APC-3607-1 wire. Precipitates appear as bright spots in ADF diffraction contrast (left) and as dark spots due to Z-contrast in HAADF images (right).
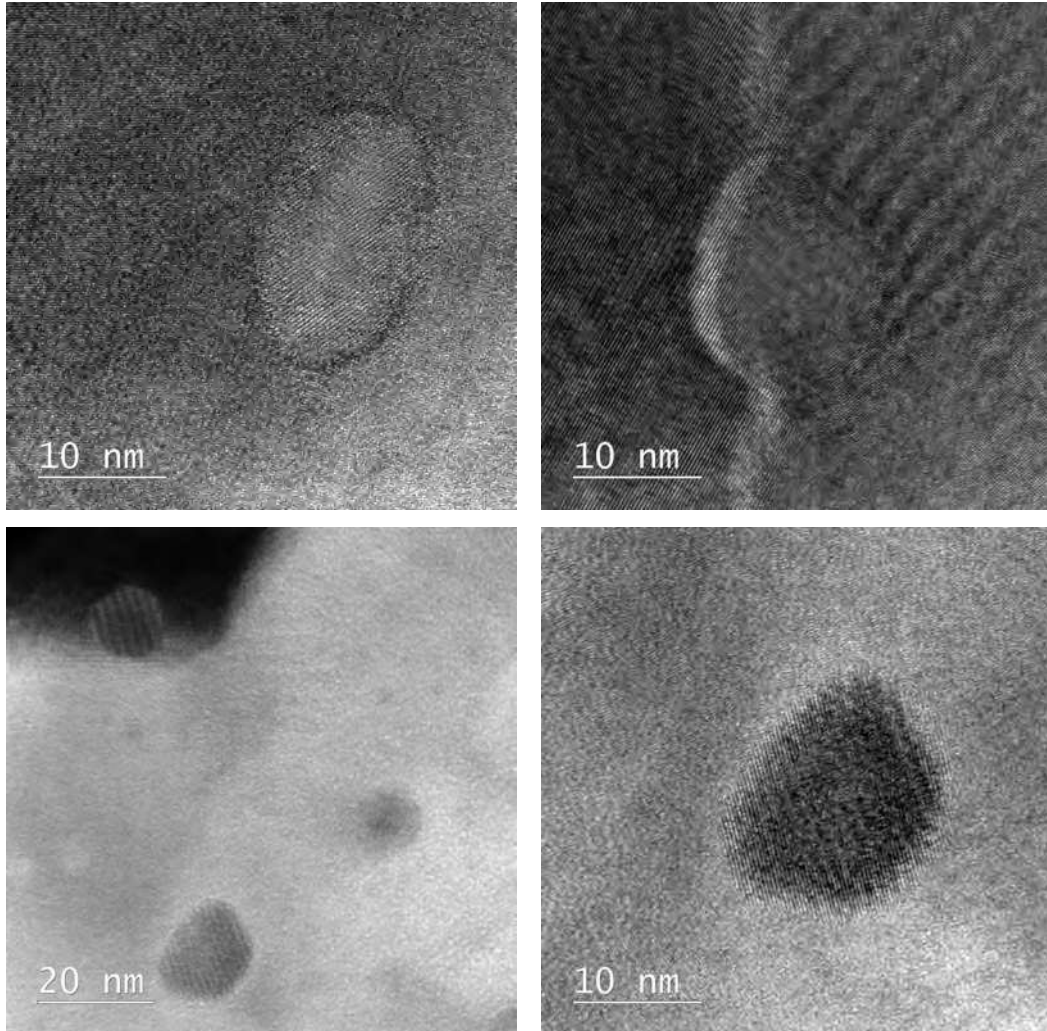
Figure 4.7: HRTEM images of precipitates embedded in A15 phase of the APC-3607-1 wire. Precipitates were found inside grains (top left) and at grain boundaries (top right).

4.1.3 APC-3657-48

Similar to PIT wires, the A15 phase of internally oxidized Nb$_3$Sn wires are divided into a coarse-grained region near the sub-element centre and a fine-grained region towards the outside. The images in Figure 4.8 show a sharp border between coarse grains and fine grains in the A15 area of the APC-3657-48 wire. The coarse grained area is located near the centre of the sub-element with a thickness of 3 µm, where the largest coarse grain found was 2.7 µm in diameter. The fine grained region is located on the outside of the A15 area and showed a thickness of 5.5 µm, leading to a total A15 phase thickness of 8.5 µm. Aside from the separation of the A15 phase into coarse and fine grains, no significant gradient of grain size between the inside and outside of the filament was found in any of the investigated wires.
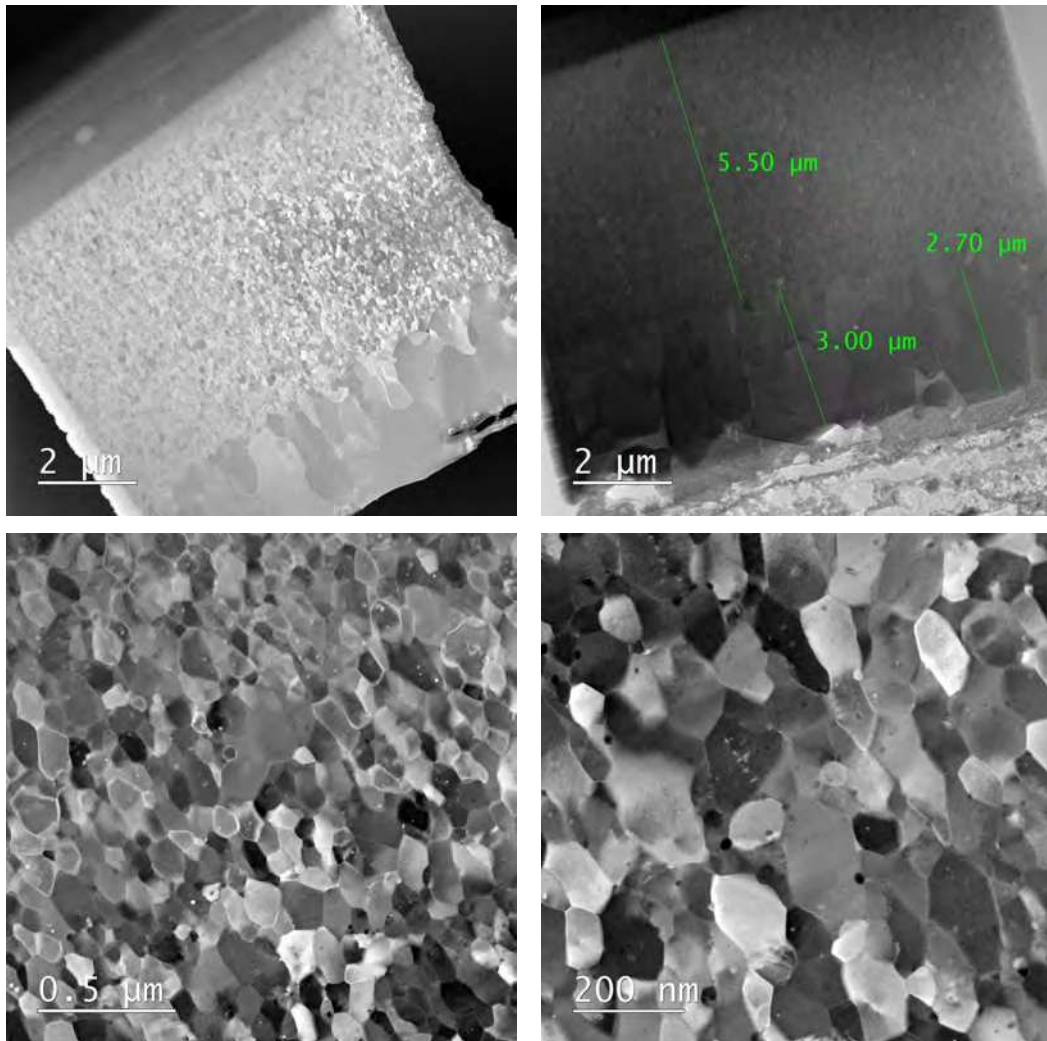
Figure 4.8: STEM annular dark field images of the APC-3657-48 wire showing coarse and fine grains under Z-contrast (top right) and diffraction contrast (remaining images).

4.1.4 APC-3682-48

A high resolution TEM image of the APC-3682-48 wire can be found in Figure 4.9, which shows precipitates that are located at grain boundaries and inside grains, which confirms that the precipitate location in the A15 phase is not restricted to grain boundaries.
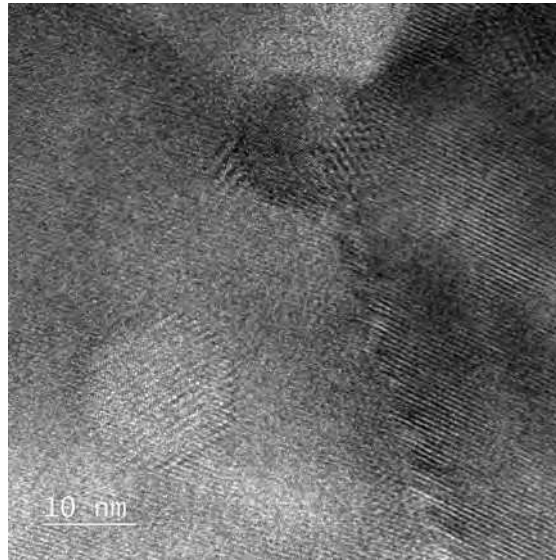
Figure 4.9: HRTEM images of the APC-3682-48 wire showing nano-precipitates located at grain boundaries and inside grains.

4.1.5 APC-3914-48

TEM images of the APC-3682-48 wire taken with a small objective aperture can be found in Figure 4.10, from which it becomes apparent that a large amount of small grains is present in the A15 phase. Furthermore, a high amount of dislocations is present that likely formed during the reaction process, but part of which could be related to the sample preparation process. A TEM image taken at an increased magnification is displayed in the same figure, where the HfO_2 nano-precipitates can be seen. Figure 4.11 shows high resolution TEM images of these precipitates.
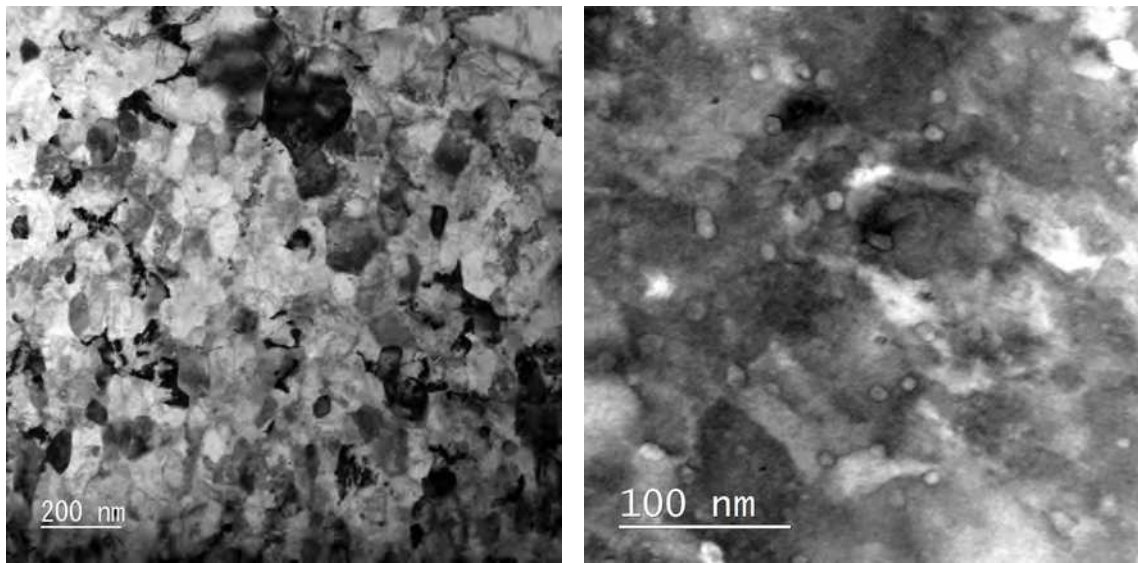
Figure 4.10: TEM images of the APC-3914-48 wire showing small grains with dislocations (left) and nano-precipitates (right).
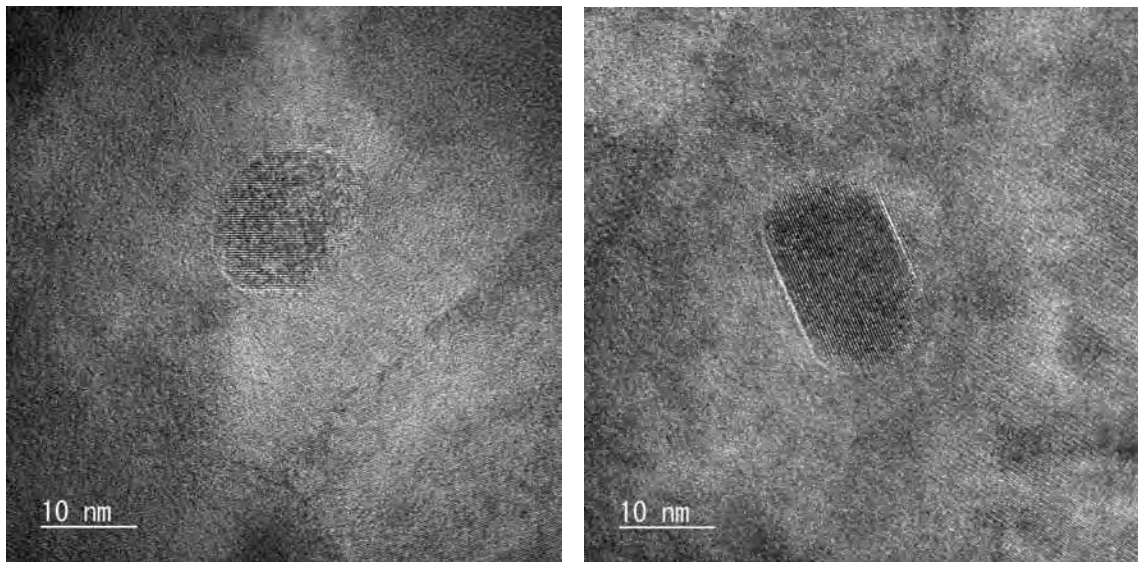
Figure 4.11: HRTEM images of nano-precipitates in the APC-3914-48 wire.

4.1.6 APC-3912-084

TEM images of the APC-3912-084 wire are shown in Figure 4.12, where the majority of precipitates are found to be located at grain boundaries. However, as seen in the same figure, a number of precipitates is also present inside the grains.
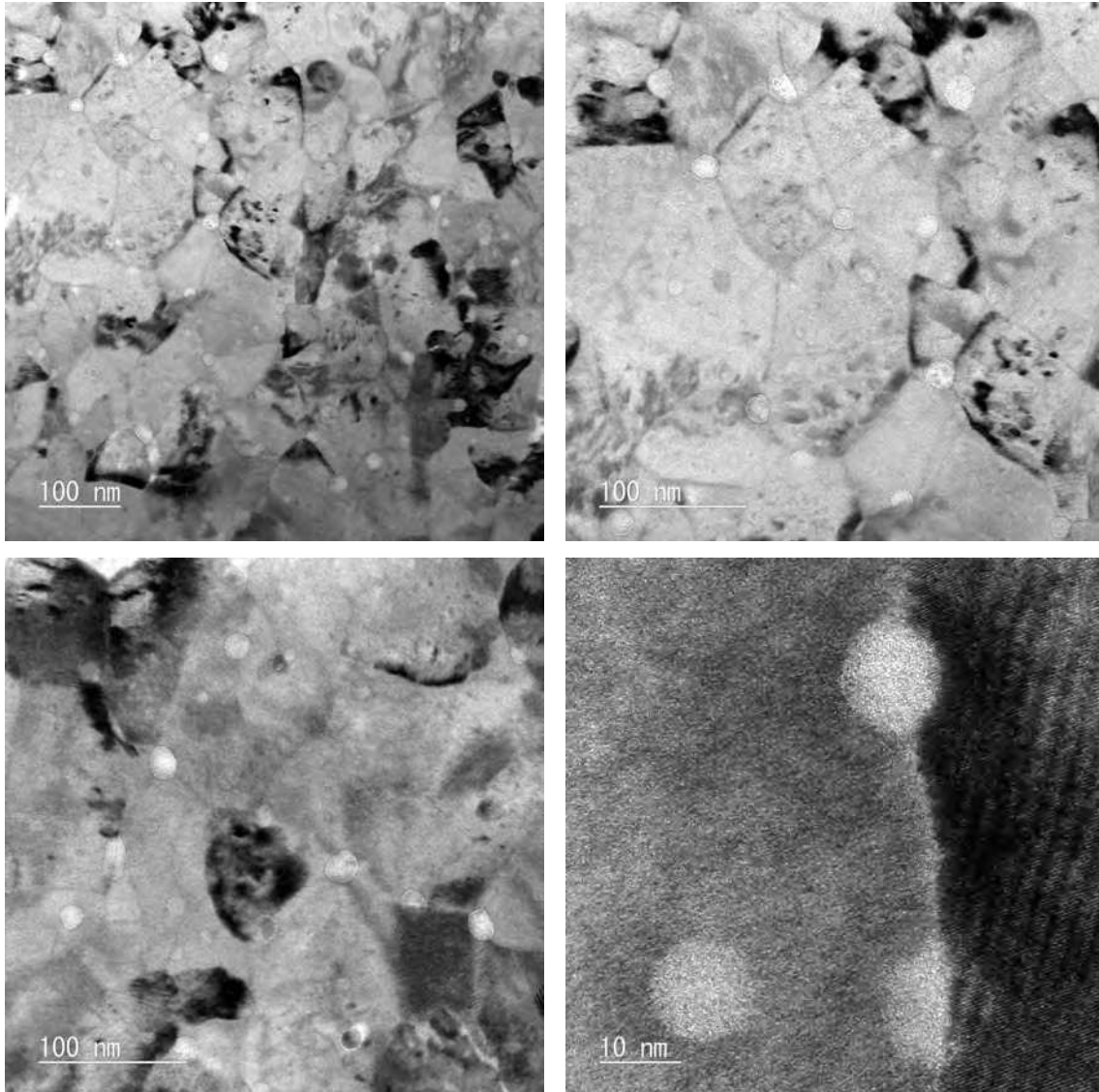
Figure 4.12: TEM images of nano-precipitates in the APC-3912-084 wire located at grain boundaries and inside grains.

4.2 Analysis of precipitate size distribution and density

While the main advantage of the internal oxidation manufacturing method is the pinning force increase through refinement of the grain size as analysed in Chapter 6, it is believed that the produced nano-precipitates contribute significantly to the pinning force [171, 174]. In order to gain a better understanding of their impact on the pinning, an evaluation of their size distribution and density is of great relevance.

The analysis of the precipitate size distribution and density was conducted by STEM imaging under HAADF conditions with a small camera length, leading to contrast based on the atomic number of the elements in the imaged area. Since the average atomic number of ZrO_2 is with a value of 18.67 lower than that of Nb_3Sn with 43.25, the ZrO_2 precipitates appear darker than the surrounding Nb_3Sn. Precipitates consisting of HfO_2 have an average atomic number of 29.33 therefore appear with less contrast in the Nb_3Sn phase.

The precipitate size distribution was determined by drawing lines across the diameter of all visible precipitates in an imaged area and evaluating their lengths. This method of evaluation is associated with errors due to the shape of the precipitates. While most of the precipitates are in good approximation of circular shape, particularly the largest ones are often times elliptical, which affects the determined diameters and leads to small errors in the size determination. Since the largest precipitates most frequently constitute outliers, this circumstance does not have a considerable impact on the overall size distribution. The determined density and size distribution of the nano-precipitates might also be dependent on potential gradients across the A15 phase, which are not accounted for in these statistics. However, the comparison of precipitate densities at different locations inside the A15 phase did not lead to an obvious correlation.

The density was calculated by counting the amount of precipitates in the imaged area and determining the average sample thickness in this area by EELS (electron energy loss spectroscopy) measurements in different locations. For each wire, multiple areas were imaged and analysed, since the precipitate density could potentially be dependent on the analysed location within the A15 phase. A bin size of 1 μm was used for graphically visualising the statistics of the precipitate size distributions of all wires.

Contrary to the investigation of neutron irradiation defects as described in Chapter 7, the visibility of nano-precipitates in APC wires using TEM is a less restricting factor, since the contrast in HAADF imaging is based on the atomic number of the elements and not on the diffraction conditions. Only the smallest precipitates are sometimes not clearly identified due to their size and potentially being located in deeper sample layers and are thus affected with the largest number error.

4.2.1 APC-3607-1

The analysis of the precipitate size distribution of the APC-3607-1 wire can be found in Figure 4.13. The size of the first imaged area in which precipitates were counted was $655\,nm \times 655\,nm$, the amount of precipitates in this area was counted at 125. The modal precipitate size interval of the distribution was determined to be $6\,nm$–$7\,nm$. The average specimen thickness in the given area was determined to be $55\,nm$, which leads to a precipitate density of $5297\,\mu m^{-3}$.

The size of the second area in which precipitates were counted was $914\,nm \times 914\,nm$, the amount of precipitates in this area was 295. The modal precipitate size interval of the distribution was determined to be $5\,nm$–$6\,nm$. The average specimen thickness in the given area was determined to be $55\,nm$, which leads to a precipitate density of $6420\,\mu m^{-3}$.

No clear indication for a preferred precipitate location at grain boundaries was found, leading to a higher number fraction being located inside grains. In the first investigated area in Figure 4.13, roughly one third of the detected precipitates were located at grain boundaries.

4.2.2 APC-3657-48

The analysis of precipitate size distribution of the APC-3657-48 wire can be found in Figure 4.14. The size of the first area in which precipitates were counted was $655\,nm \times 655\,nm$, the amount of precipitates was 392. The modal precipitate size interval of the distribution was determined to be $4\,nm$–$5\,nm$. The average specimen thickness in the given area was determined to be $76\,nm$, which leads to a precipitate density of $12\,022\,\mu m^{-3}$.

The size of the second area in which precipitates were counted was $655\,nm \times 655\,nm$, the amount of precipitates was 217. The modal precipitate size interval of the distribution was determined to be $8\,nm$–$9\,nm$. The average specimen thickness in the given area was determined to be $90\,nm$, which leads to a precipitate density of $5620\,\mu m^{-3}$.

The amount of precipitates located in the first area was more than double than in the second area as seen in Figure 4.14. This hints towards the existence of varying densities of precipitates between the A15 boundaries.
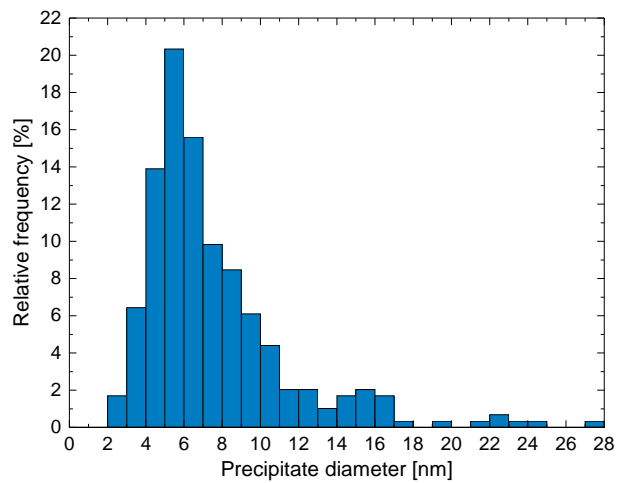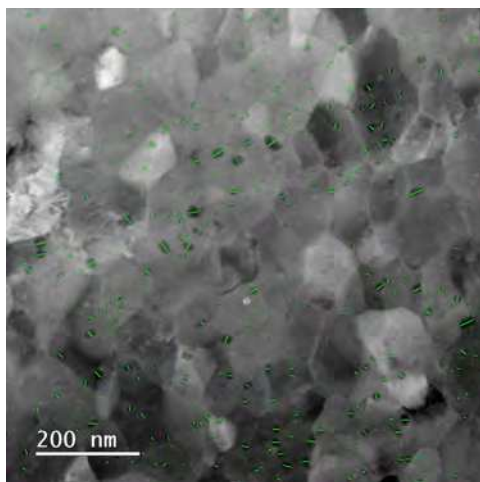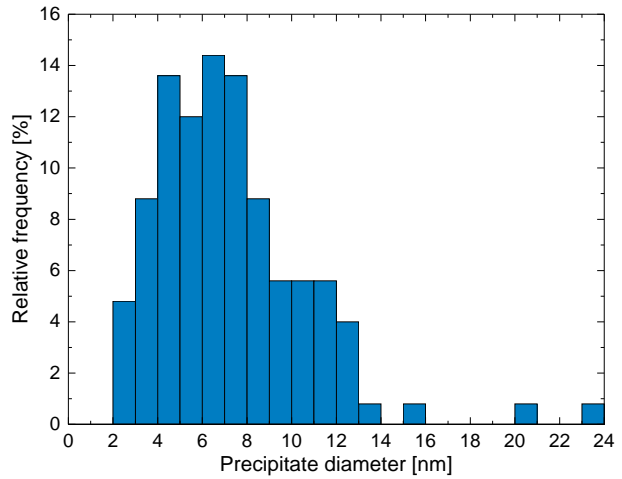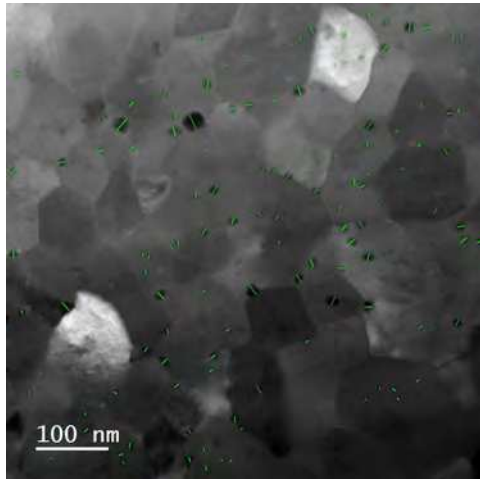
Figure 4.13: Precipitate size distribution of the APC-3607-1 wire in area 1 (top) and area 2 (bottom). The left column shows how the precipitate size was determined by drawing lines across their diameter, the right column the statistics of the distributions.
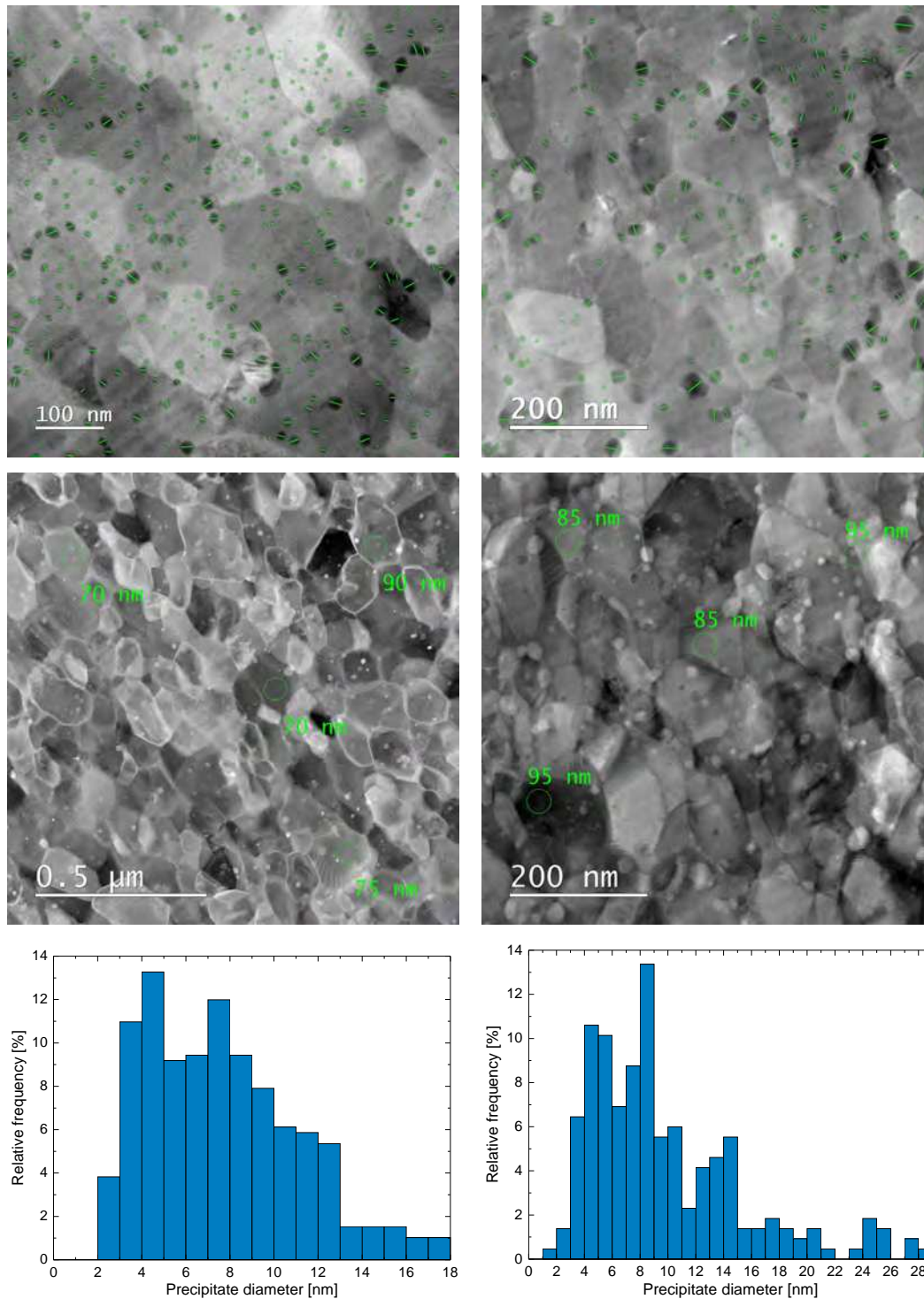
Figure 4.14: Precipitate size distribution analysis of the APC-3657-48 wire in area 1 (left column) and area 2 (right column). The first row shows how the precipitate size was determined by drawing lines across their diameter, the second row shows the sample thickness measurements and the third row the statistics of the distributions.

4.2.3 APC-3682-48

The same procedure was continued for the remaining APC wires. The analysis of the precipitate size distribution of the APC-3682-48 wire can be found in Figure 4.15. In this wire, the largest precipitates were observed. Both investigated areas contained multiple precipitates of over 30 nm in size and at least one precipitate with a diameter of over 50 nm.
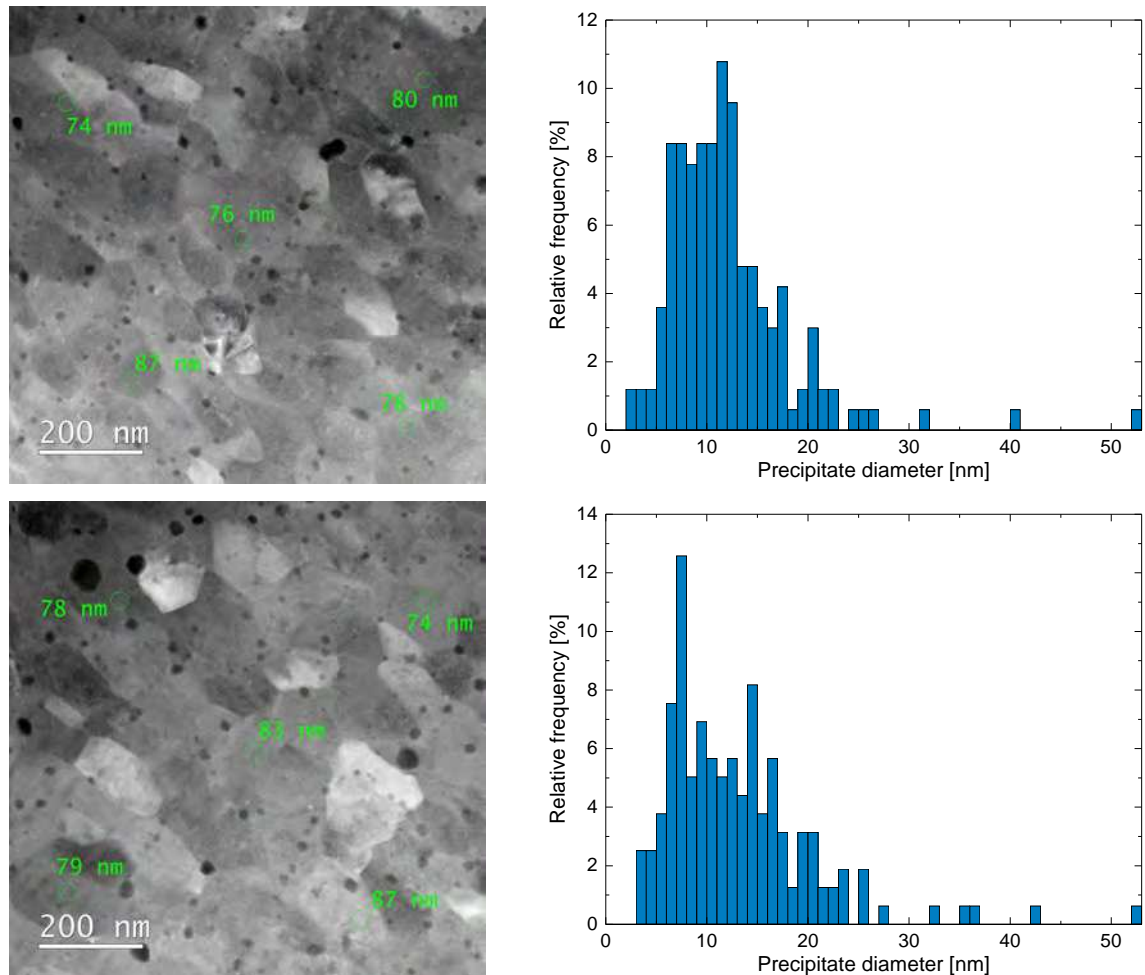
Figure 4.15: Precipitate size distribution of the APC-3682-48 wire. Sample thickness measurements (left) and statistics of the distributions (right).

4.2.4 APC-3912-071

The results of the precipitate size distribution analysis of the APC-3912-071 wire is shown in Figure 4.16 and Figure 4.17. The results for the APC-3914-48 wire are displayed in Figure 4.18 and Figure 4.19, the ones for the APC-3912-084 wire in Figure 4.20. A summary of all parameters of the investigated areas including number of precipitates, specimen thickness, modal precipitate size and precipitate density is presented in Section 4.3.
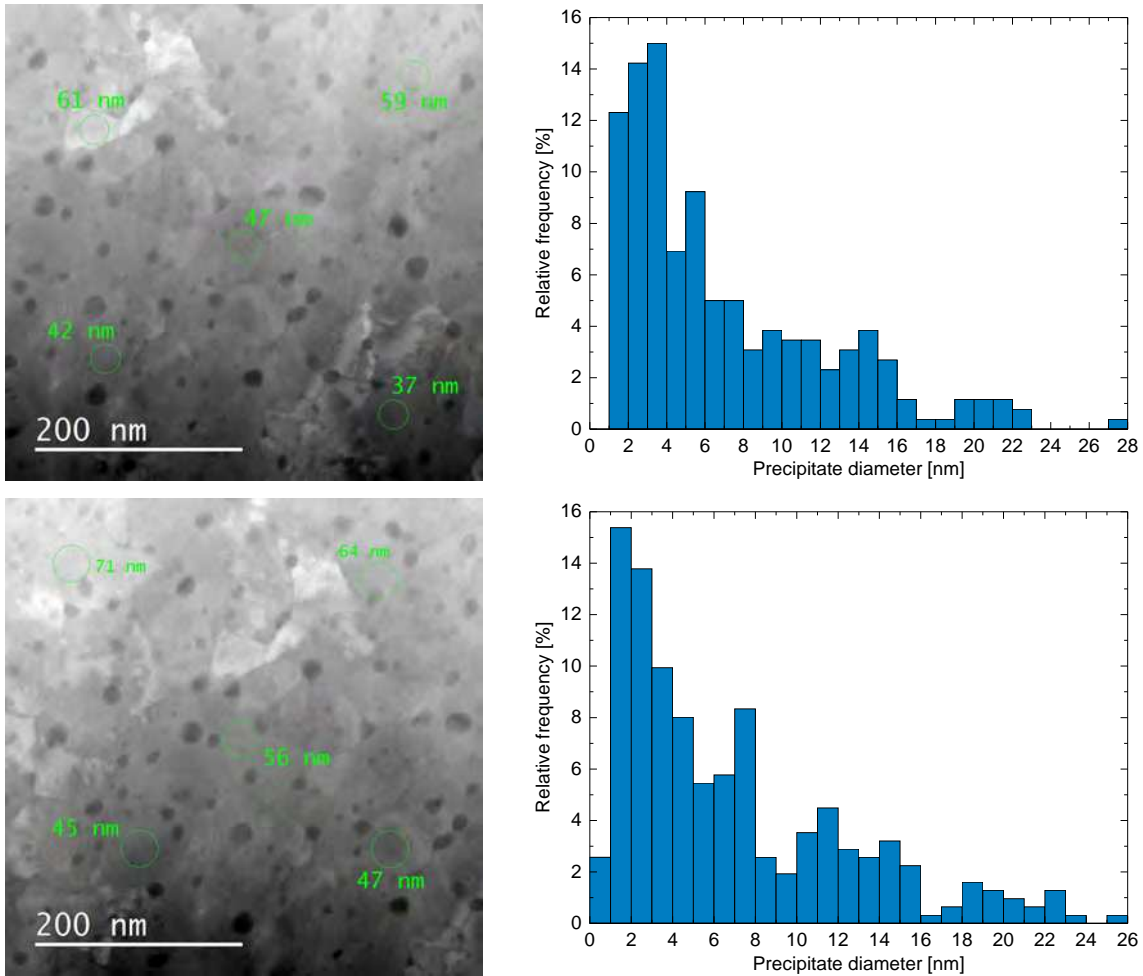
Figure 4.16: Precipitate size distribution of the APC-3912-071 wire. Sample thickness measurements (left) and statistics of the distributions (right).
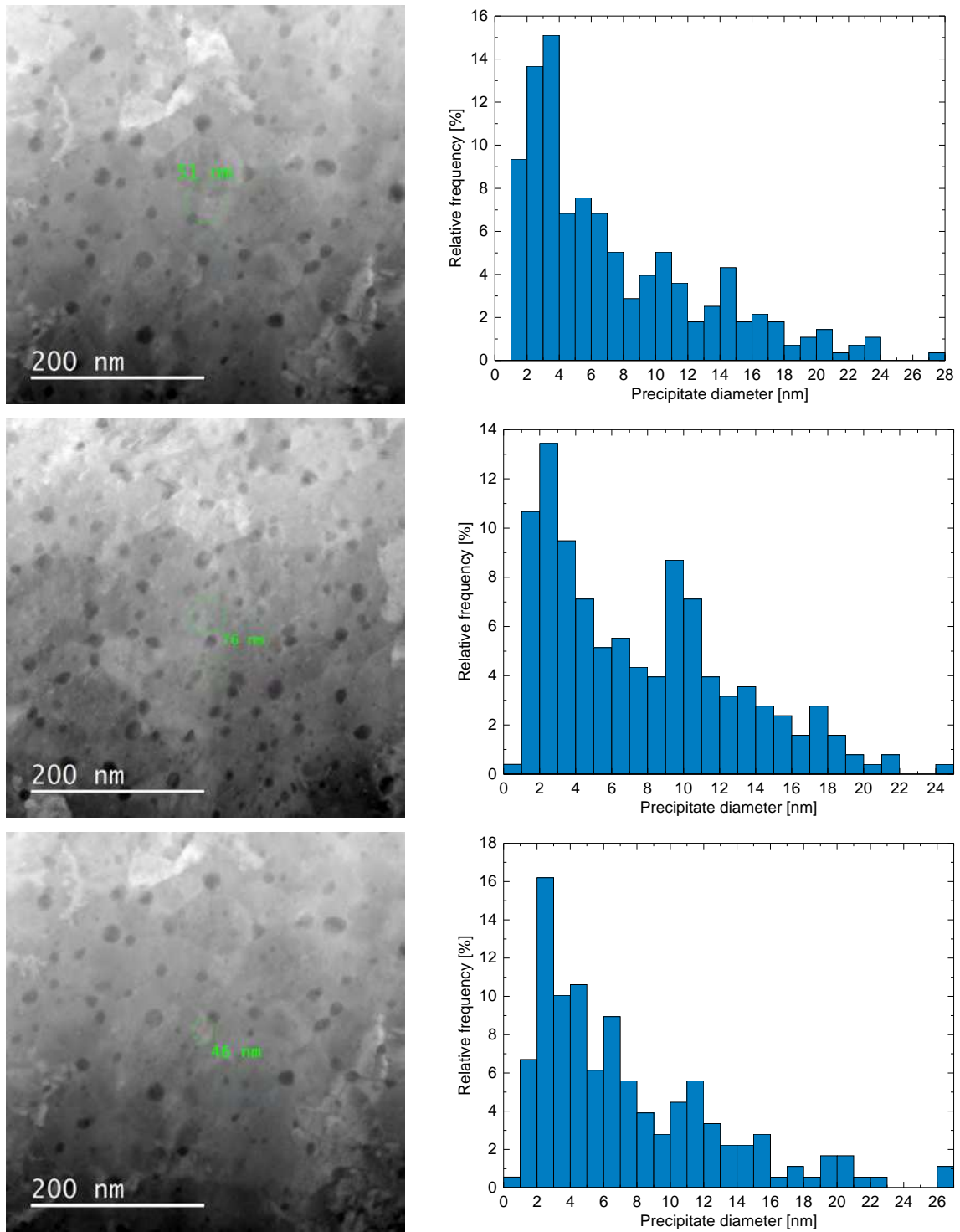
Figure 4.17: Precipitate size distribution of the APC-3912-071 wire. Sample thickness measurements (left) and statistics of the distributions (right).

4.2.5 APC-3914-48
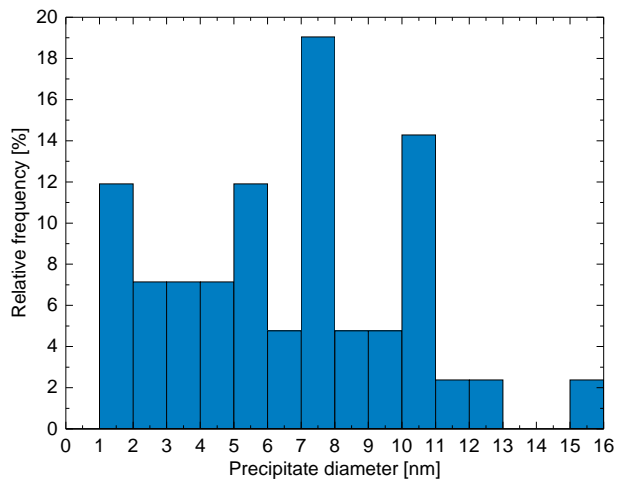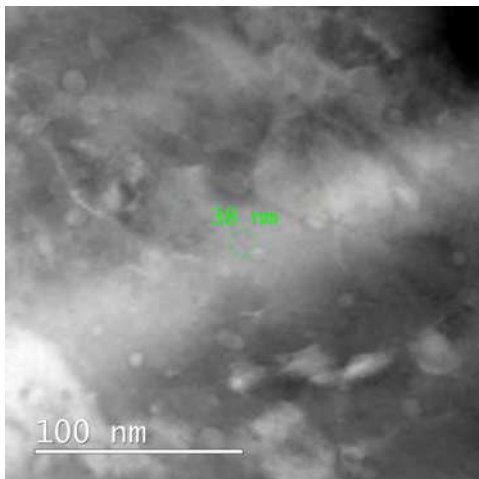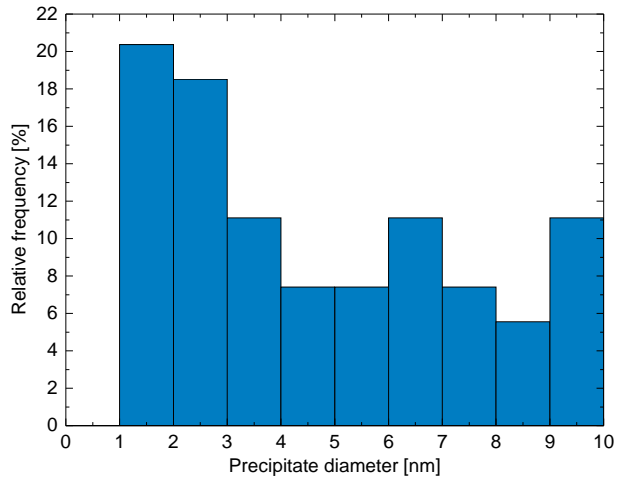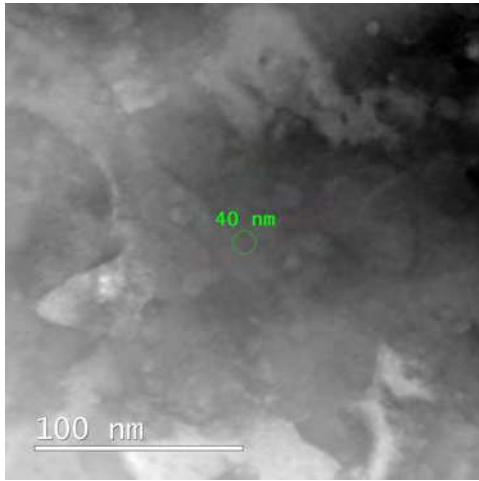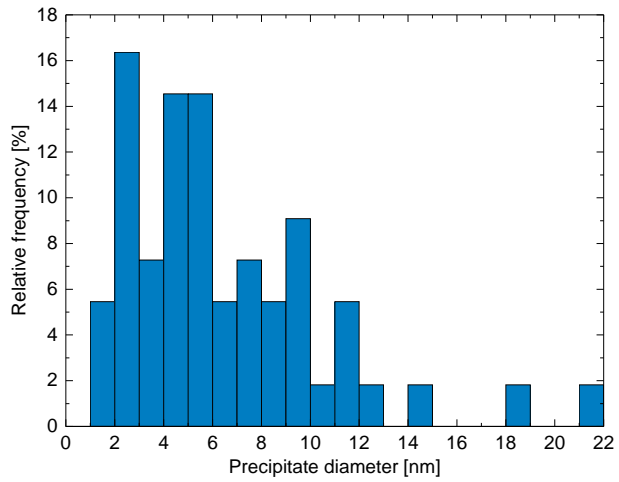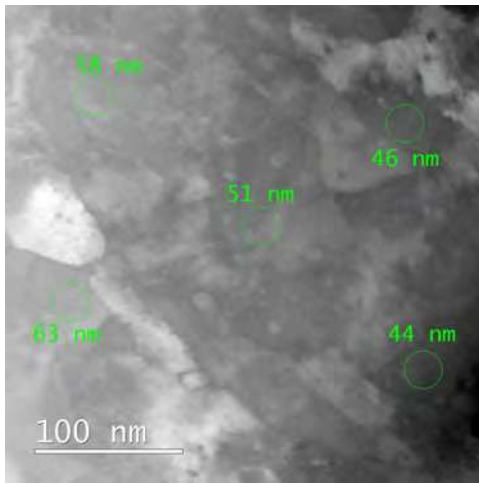
Figure 4.18: Precipitate size distribution of the APC-3914-48 wire.
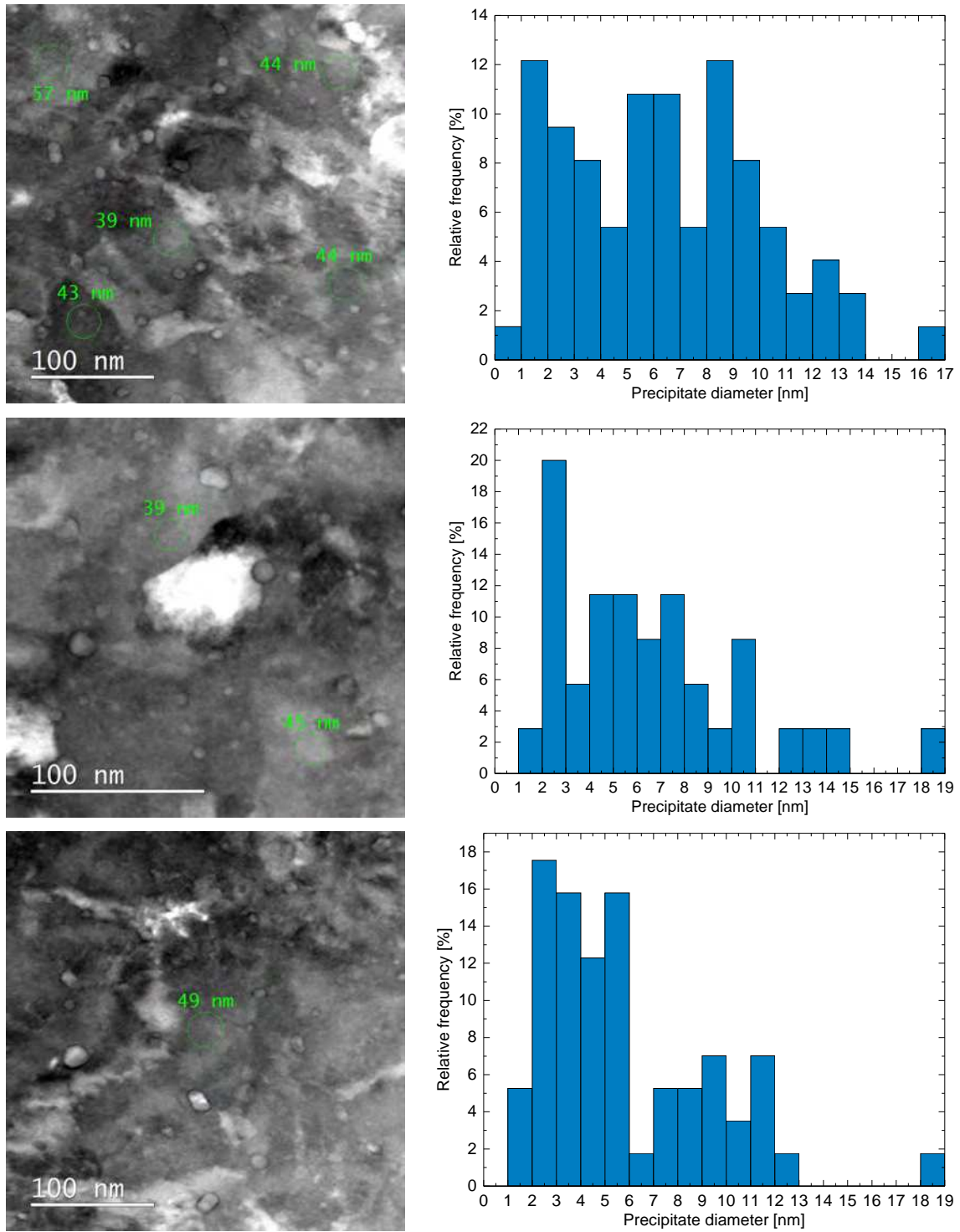
Figure 4.19: Precipitate size distribution of the APC-3914-48 wire.

4.2.6 APC-3912-084
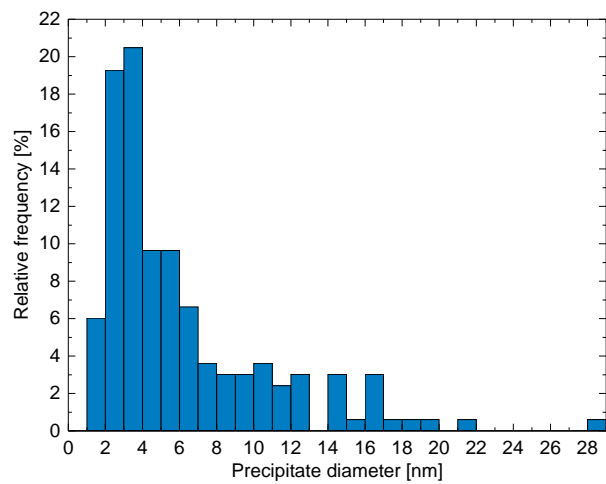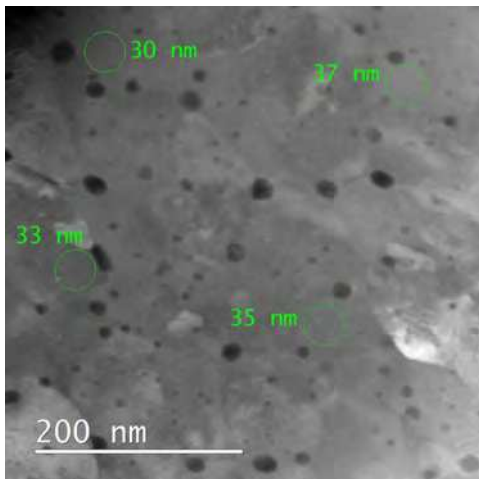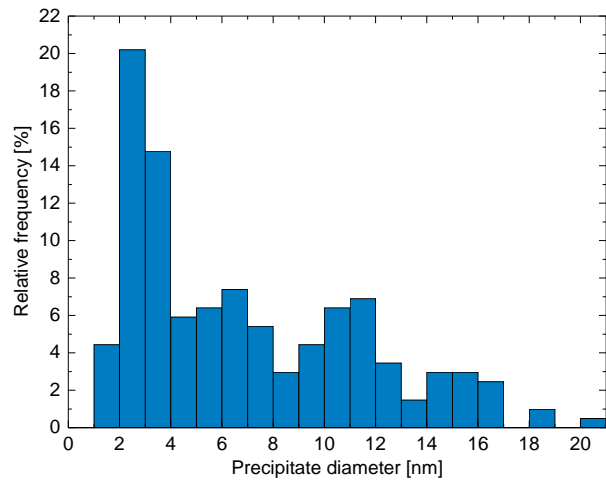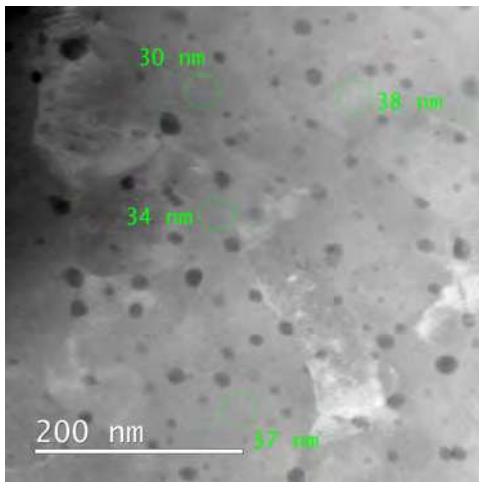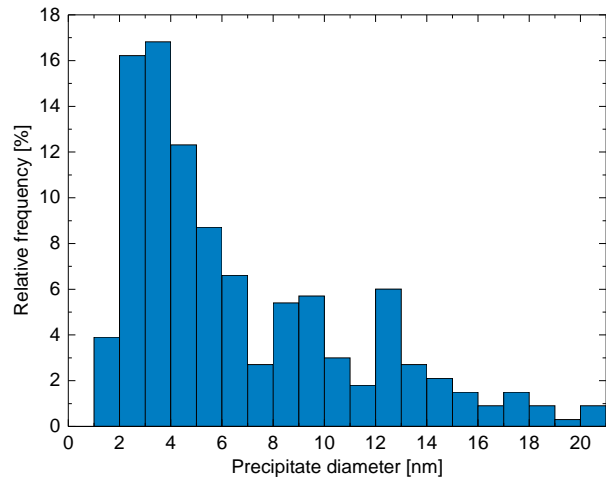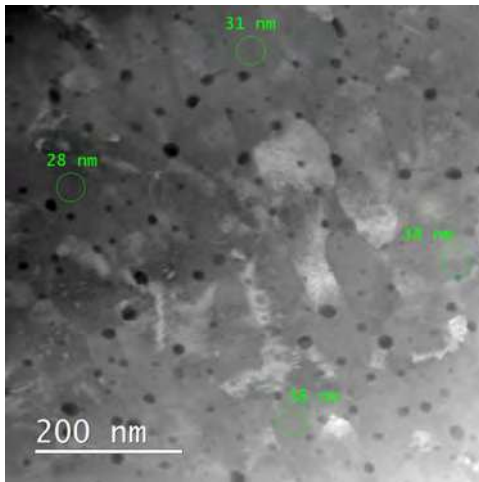
Figure 4.20: Precipitate size distribution of the APC-3912-084 wire.

4.3 Summary of precipitate size distribution and density

This section summarises the precipitate size and density analysis of the APC Nb$_3$Sn wires. The results of the older generation 3600-series binary APC wires are shown in Table 4.1, Table 4.2 and Table 4.3, the results of the newer generation 3900-series ternary APC wires are shown in Table 4.4, Table 4.5 and Table 4.6.

It becomes apparent that the density of precipitates is much higher in the newer generation ternary APC wires. While in the 3600-series wires, the precipitate density is generally in the region of $5000\,\mu m^{-3}$, in the 3900-series wires, it frequently reaches values over $20\,000\,\mu m^{-3}$, corresponding to $2 \times 10^{22}\,m^{-3}$. The observed density of HfO$_2$ precipitates is slightly lower in the APC-3914-48 wire than the density of ZrO$_2$ precipitates in the APC-3912-071 and APC-3912-084 wires, however as already mentioned the visible contrast of the HfO$_2$ precipitates is less pronounced due to their lower atomic number, which might have impacted the evaluation.

Additionally, the sizes of the precipitates show lower values in the newer generation wires, where a modal value of 3 nm is often observed. A comparison of the precipitate size distributions between the APC-3682-48 and the APC-3912-084 wire is displayed in Figure 4.21, where all investigated precipitates of the respective wires were included. A clear reduction of the average precipitate size is observed in the APC-3912-084 wire compared to the APC-3682-48 wire. The graph furthermore shows the existence of precipitates with sizes of over 50 nm in the APC-3682-48 wire, which were the largest observed precipitates of all wires.

It can thus be expected that the newer generation APC wires show in increase in the pinning force due to a higher density of precipitates, in case the precipitates are capable of contributing to the pinning force. It is anticipated that in Chapter 6, it will be shown that also the grain refinement is much improved in the newer generation wires, leading to an increase in the pinning force through grain boundary pinning. Since the purpose of the nano-precipitates is the refinement of the grain size, presumably due to the provision of nucleation centres for grain boundaries as stated in Chapter 1, a direct correlation between precipitate density and grain refinement could potentially be established in the future.
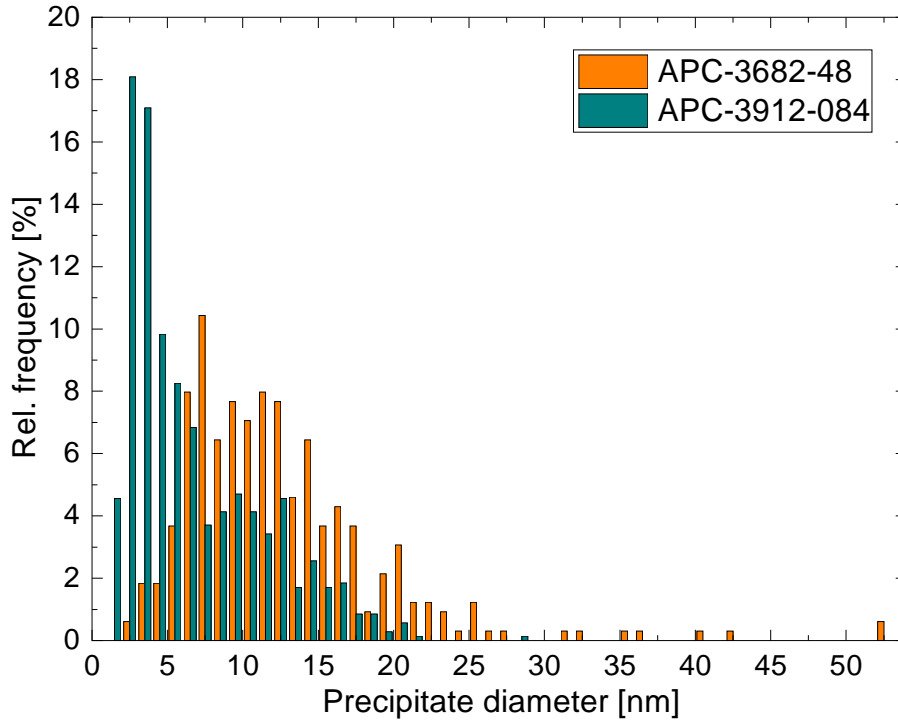
Figure 4.21: Comparison of the precipitate size distributions of the APC-3682-48 and the APC-3912-084 wire.

Image	Av. sample thickness [nm]	Area [nm × nm]	Number of precipitates	Modal size [nm]	Precipitate density [μm^{-3}]
1	55	655 × 655	125	6–7	5297
2	55	914 × 914	295	5–6	6420

Table 4.1: Summary of the precipitate size and density analysis of the APC-3607-1 wire.

Image	Av. sample thickness [nm]	Area [nm × nm]	Number of precipitates	Modal size [nm]	Precipitate density [μm^{-3}]
1	76	655 × 655	392	4–5	12022
2	90	655 × 655	217	8–9	5620

Table 4.2: Summary of the precipitate size and density analysis of the APC-3657-48 wire.

Image	Av. sample thickness [nm]	Area [nm × nm]	Number of precipitates	Modal size [nm]	Precipitate density [µm^{-3}]
1	79	914 × 914	167	11–12	2530
2	80	914 × 914	159	7–8	2379

Table 4.3: Summary of the precipitate size and density analysis of the APC-3682-48 wire.

Image	Av. sample thickness [nm]	Area [nm × nm]	Number of precipitates	Modal size [nm]	Precipitate density [µm^{-3}]
1	49	460 × 460	260	3–4	25076
2	57	460 × 460	312	1–2	25868
3	51	460 × 460	278	3–4	25761
4	76	460 × 460	253	2–3	15732
5	46	460 × 460	179	2–3	18390

Table 4.4: Summary of the precipitate size and density analysis of the APC-3912-071 wire.

Image	Av. sample thickness [nm]	Area [nm × nm]	Number of precipitates	Modal size [nm]	Precipitate density [µm^{-3}]
1	52	323 × 323	55	2–3	10138
2	40	230 × 230	54	1–2	25520
3	38	230 × 230	42	7–8	20893
4	45	323 × 323	74	1–2, 8–9	15762
5	42	230 × 230	35	2–3	15753
6	49	323 × 323	57	2–3	11150

Table 4.5: Summary of the precipitate size and density analysis of the APC-3914-48 wire.

Image	Av. sample thickness [nm]	Area [nm × nm]	Number of precipitates	Modal size [nm]	Precipitate density [µm^{-3}]
1	34	647 × 647	333	3–4	23397
2	35	460 × 460	203	2–3	27410
3	34	460 × 460	166	3–4	23074

Table 4.6: Summary of the precipitate size and density analysis of the APC-3912-084 wire.

5 Elemental composition analysis by EDX

The formation of the Nb$_3$Sn phase by a diffusion process during the heat treatment results in gradients in the elemental composition, which has a major influence on the superconducting properties as will be discussed in this chapter. Using Energy-dispersive X-ray spectroscopy (EDX), the elemental composition of the different Nb$_3$Sn wires was assessed by mapping and line scans across the A15 regions as well as individual grains and compared.

5.1 Introduction

A theory describing the variation of the superconducting properties with the composition of the A15 phase of Nb$_3$Sn wires was presented in [88], showing that inhomogeneities have a significant influence. Compositional inhomogeneities and deviations from the stoichiometry may lead to defects and disorders in the lattice and thus electron scattering by impurity. H_{c2} is therefore related to the electron mean free path and the superconducting properties such as the coherence length and the London penetration depth. These parameters cannot be directly observed through experiments, hence they were derived by fitting experimental data of macroscopic properties such as the critical temperature T_c. Figure 5.1 shows a fit of the dependency of T_c on the Sn content that was derived by the authors from experimental data. It was further shown that Sn gradients also impact the upper critical field B_{c2}, where a higher Sn content up to around 24 at.% leads to an increase in B_{c2} in the cubic phase and shifts the peak of the pinning force curve to higher fields. In the tetragonal phase, the opposite behaviour is observed. Sn gradients thus impact the critical current density J_c, especially at lower fields, where a high Sn content with a homogeneous Sn distribution across the A15 phase would result in the highest J_c values.

It was shown that Sn concentration gradients in Nb$_3$Sn wires lead to significant reductions in J_c and performance gains might be achieved by avoiding strong gradients. A perfect stoichiometric composition in the A15 phase can not be obtained due to the fact that both the time and the temperature during the reaction are limited in order to maintain a small grain size, which is essential for good flux pinning and therefore
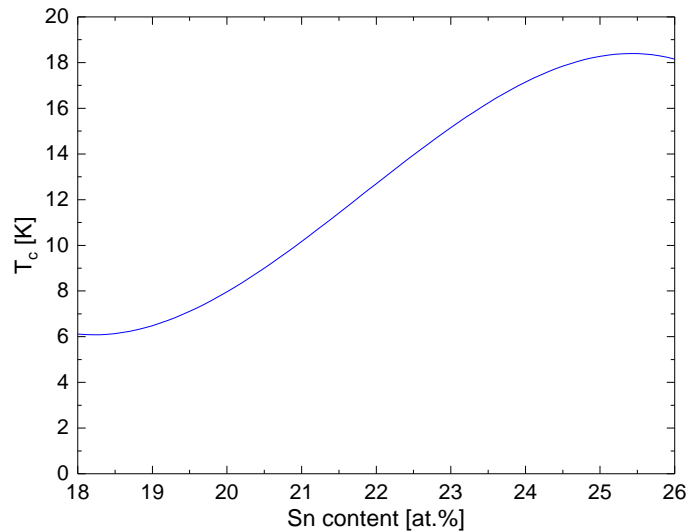
Figure 5.1: Dependency of T_c on the Sn content derived from experimental data [88].

high J_c values. As mentioned in Chapter 1, one has to find a compromise regarding the heat treatment. A short heat treatment leads to a small grain size which leads to an increased pinning force but has the disadvantage of strong compositional gradients, while a longer heat treatment lowers these gradients at the cost of a larger grain size. It is predicted that a significant increase in J_c can be achieved by reducing the compositional gradients in the A15 phase under the premise that a small grain size can be maintained simultaneously [29].

A longer heat treatment of Nb_3Sn wires leads to a larger A15 area and simultaneously to a smaller change in the Sn content per µm, since a longer diffusion time increases the homogeneity in the Sn distribution [68]. In the same publication the radial T_c distribution was assessed using DC SQUID magnetometry. The radial Sn and T_c gradients were stated to be approximately linear and in good agreement with each other. In [99] it was shown that increasing the initial Sn content in Nb_3Sn precursors has no effect on the Sn content in the resulting fine grained A15 layer. The initial composition also had no considerable influence on the morphology and fine grain size.

The T_c distribution inside Nb_3Sn wires due to Sn gradients was also confirmed by other techniques such as calorimetric specific heat measurements. The Sn content was also found to have an influence on the morphology of the grains and therefore on the grain boundary induced flux pinning properties. Wires with higher fractions of equiaxed grains have shown higher values of non-Cu J_c [128].

The importance of grain boundaries for the flux pinning in Nb_3Sn is due to variations of the electronic mean free path. On the one hand, a higher grain boundary density leads to increased electron scattering, on the other hand variations in the elemental

composition near grain boundaries enhance the Ginzburg-Landau parameter κ in these areas. Deviations from stoichiometry near grain boundaries lead to the local decrease in the mean free path, causing an increase in the residual resistivity ρ_0 and the upper critical field B_{c2}. Therefore, the assessment of the grain boundary density and the composition at grain boundaries and inside grains is highly important for understanding the pinning mechanisms in Nb_3Sn. Aside from the elements constituting the A15 phase, the assessment of the local Cu concentration is as relevant, since it can contribute to scattering and pinning at the grain boundaries. Previous studies of the composition inside Nb_3Sn grains have found gradients where the concentrations of Sn and Cu decreased near the grain centre compared to the grain boundaries, while the behaviour of Nb was the opposite. In Ta doped wires it was found that Ta decreases near grain boundaries, showing a very similar behaviour to Nb, and was therefore believed to substitute Nb, even near boundaries. Near grain boundaries were the only locations at which Cu was located. The Ti concentration in Ti doped wires was found to increase rapidly in this region due to the strong affinity to Cu and presumably replacing both Nb and Sn atoms. The distribution of Cu was furthermore found to be dependent on the heat treatment and the thickness of the A15 layer. Near the grain boundaries, the elements were found to exhibit a nearly exponential variation. The higher Sn concentration at boundaries is likely due to Sn diffusion along the boundaries during the formation of the A15 grains. While it remains unclear, what the exact influence on the pinning mechanisms the elements Cu, Ti and Ta near the boundaries have, variations of the superconducting properties due to compositional variations in these areas appear obvious [115].

Another study that investigated the chemical composition around grain boundaries in Nb_3Sn fabricated by the bronze route is presented in [139]. In this case, the composition was analysed using Auger electron spectroscopy, which confirmed higher Sn and Cu contents at the grain boundaries compared to inside the grains. It was suggested that the presence of Cu creates disordered regions at grain boundaries, which could contribute to an enhancement of the Sn diffusion at the boundaries and the Nb_3Sn layer growth. These investigations were stated to be important for understanding both flux pinning and diffusion mechanisms in Nb_3Sn.

In ternary Nb_3Sn wires, the replacement of Nb atoms by Ta is well established, but considering the site occupancy of Ti, controversial results can be found. A previous EDX study of bulk Nb_3Sn with Ti and Ta additions suggested that Nb atoms are replaced by Ta and Sn atoms are replaced by Ti in the A15 phase. This was achieved through comparison of the local Nb-Sn ratios and Ti or Ta concentrations. It was found that the addition of Ta leads to a decrease of the Nb to Sn ratio, while the addition of Ti leads to leads to an increase of the Nb to Sn ratio. The additions of Ti and Ta have lead to a significant increase in H_{c2}, while the strain sensitivities remained unchanged [95].

In a recent study [149], Extended X-Ray Absorption Fine Structure Spectroscopy (EXAFS) studies revealed that Ti atoms are always located at Nb lattice sites,

independent of the heat treatment. The site occupancy of Ta atoms, on the other hand, is dependent from the heat treatment temperature and split between Nb and Sn sites. A temperature increase leads to a decrease of the fraction of Ta atoms on Sn sites. It was thus concluded that an increase in the heat treatment temperature of wires doped with Ta is beneficial for improving the chemical homogeneity and providing additional site disorder, leading to a higher H_{c2} at low temperatures. It was further found that the Kramer extrapolation to high fields is not reliable for wires containing Ti and Ta doping.

Energy-dispersive X-ray spectroscopy (EDX) enables the option to obtain information about the elemental composition with a spacial resolution by inducing X-rays that are characteristic of each element. In this chapter, EDX analyses were performed on the different Nb_3Sn wires listed in Table 1.3. Mapping was conducted to assess compositional inhomogeneities and line scans were used to acquire information about compositional gradients. Measurements across sub-elements on polished cross sections of wires were conducted using the SEM and investigations of gradients inside grains were performed on thin lamellae inside the TEM. When discussing the results of EDX analyses, it is important to note the inherent limited accuracy of the quantification of EDX spectra, which is inhibited by various factors including the overlap of elemental peaks in the spectra [162].

5.2 Elemental composition maps of sub-elements

EDX mapping was performed on sub-elements of different wires. The net intensity maps of the elements Nb, Sn, Cu and the additive Ti or Ta of sub-elements of the respective wires are shown in this section. Some of the EDX maps were post-processed by altering the contrast and brightness levels in an external image processing software to improve the visibility, especially for elements with low concentrations inside the wire such as Ti and Ta.

The EDX maps of the RRP-Ti-108 wire are shown in Figure 5.2 with the net intensity maps of the elements Nb, Sn, Cu and Ti. Some examples for locations of the Ti filaments in this wire before the heat treatment are marked by circles, where the same locations are marked in all elemental maps. The EDX maps reveal a higher Ti intensity in the EDX spectrum in these areas due to residual Ti. It was found that these locations at the same time show a high Cu accumulation and lower intensities of Nb and Sn. These results potentially hint to a worse diffusion rate of Ti during the heat treatment, leading to a non-uniform Ti distribution in this wire.

EDX maps of sub-elements of the RRP-Ta-54 wire can be found in Figure 5.3, where net intensity maps of the elements Nb, Sn, Cu and Ta are shown. No locations with exceptionally high Ta concentrations were found. While the Sn and Ta distributions appear rather uniform, in the intensity maps of Nb and Cu, the layout of the stacked
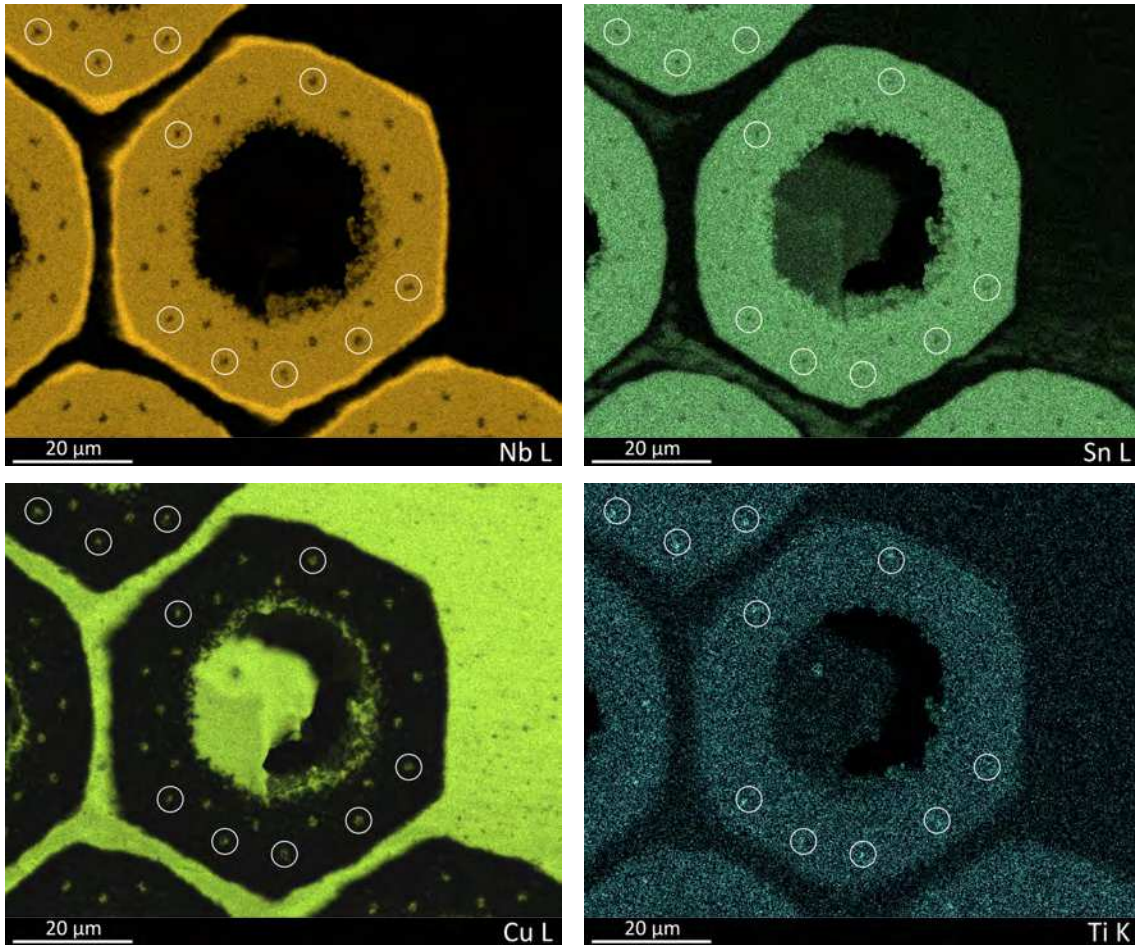
Figure 5.2: Net intensity EDX maps of the RRP-Ti-108 wire.

filaments before the heat treatment become apparent. Between the filaments, a higher Cu intensity and lower Nb intensity can be found. These results show that the heat treatment procedure did not lead to a perfect stoichiometry in the A15 phase of this wire. On the other hand, Cu can have a beneficial impact on the diffusion rate of Sn as discussed in Subsection 1.5.4.

It becomes apparent that to the manufacturing technique of RRP wires by stacking filaments into a matrix leads to inherent inhomogeneities of the elemental composition in the reacted wires. Due to the differing layout of PIT wires, where Nb tubes instead of filaments are used, no comparable inhomogeneities arise in these wires. However, all Nb$_3$Sn wires are manufactured by a diffusion process during the heat treatment and thus show gradients of the elemental composition across the A15 phase, which will be discussed in the following.
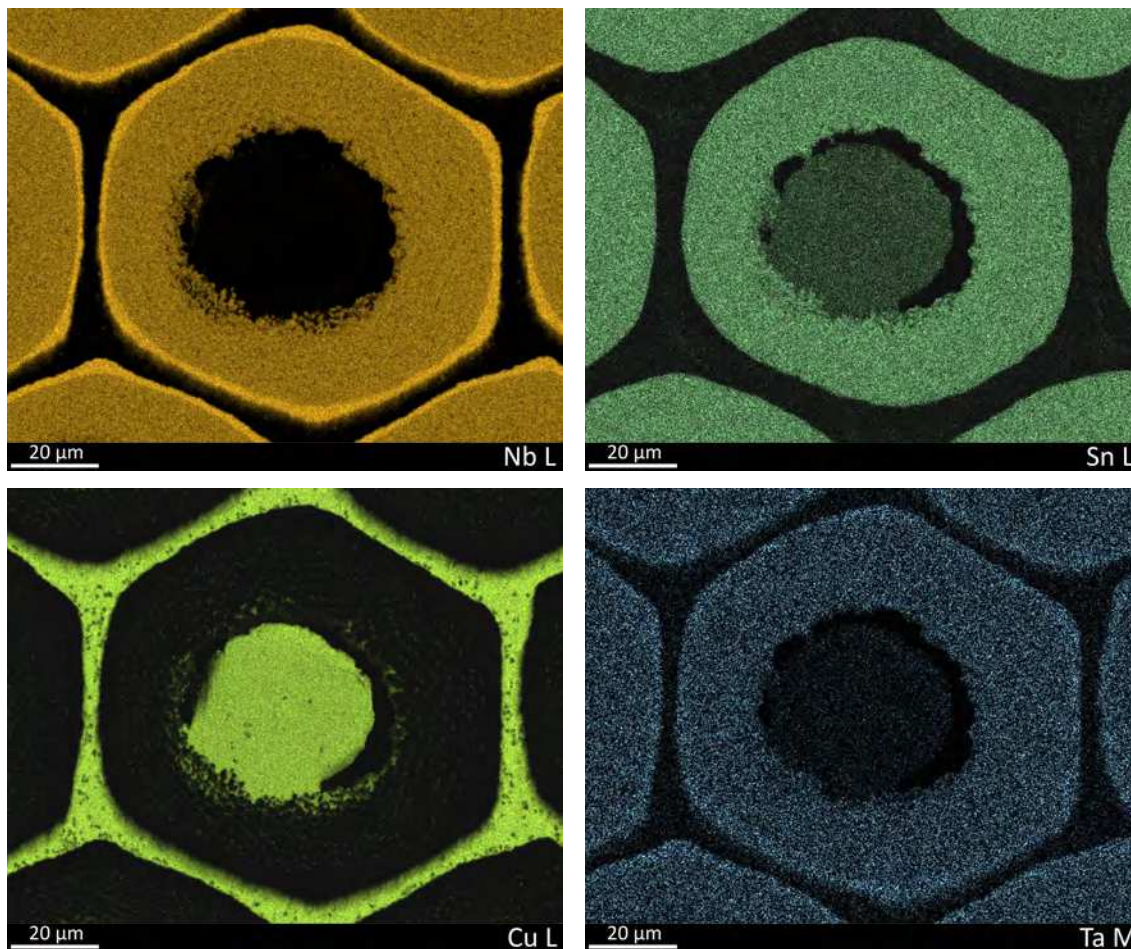
Figure 5.3: Net intensity EDX maps of the RRP-Ta-54 wire.

5.3 Elemental composition maps of grains

EDX maps were acquired of grains of various wires on thin lamellae in the TEM, in order to gain information about the elemental distribution at grain boundaries and inside grains. Particularly the preferential distribution of Cu becomes apparent through the elemental maps acquired of the grains by TEM.

A net intensity map of the BIN-246 wire is shown in Figure 5.4, which shows the elemental distribution of Cu. It becomes apparent that an increased content of Cu is located at the grain boundaries, between grains of the A15 phase. A net intensity map of Cu of the PIT-Ta-114 wire can be found in Figure 5.5, where an inclusion of Cu can be seen between the grains of the Nb_3Sn phase. The EDX maps were post-processed in order to better visualise intensity differences.
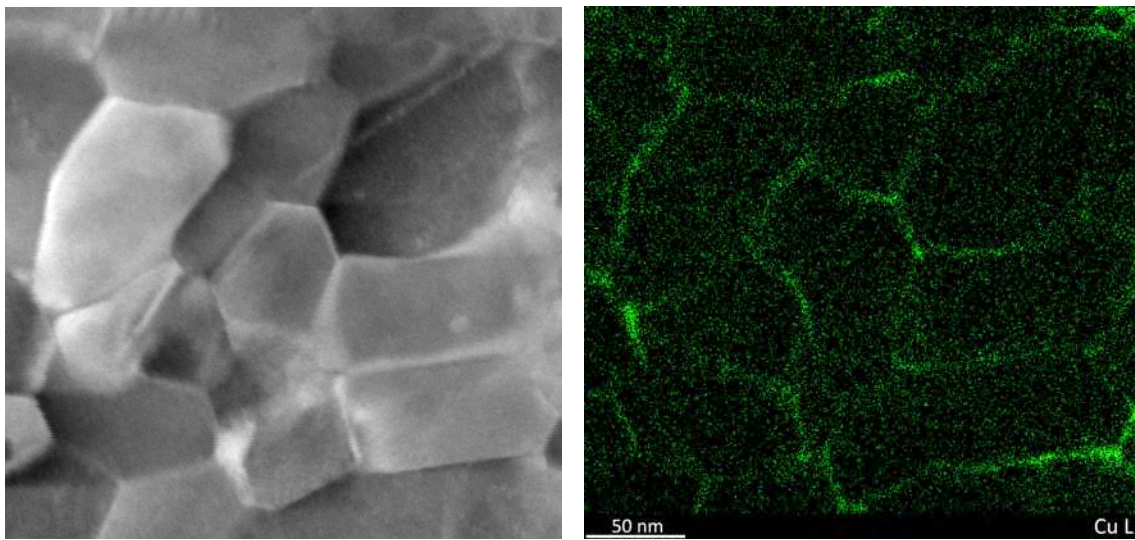
Figure 5.4: STEM image of grains of the BIN-246 wire (left) and corresponding Cu net intensity EDX map (right).
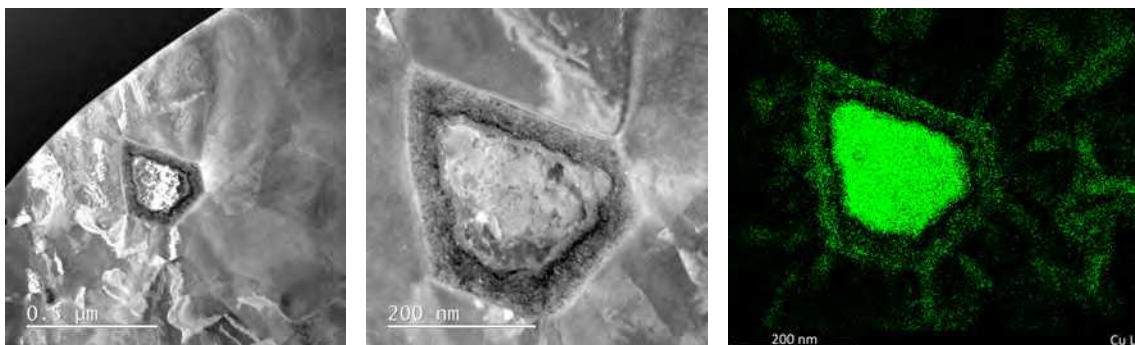
Figure 5.5: STEM image of Cu inclusions in the PIT-Ta-114 wire (left and middle) and corresponding Cu net intensity EDX map (right).

5.4 Elemental gradients inside sub-elements

5.4.1 Experimental

The correlations between Sn content and upper critical field B_{c2} have been investigated in numerous studies and Nb_3Sn wires in the past which also have confirmed a Sn gradient with increasing Sn content towards the centre of sub-elements of internal tin and tube type Nb_3Sn superconductors, although with lower precision than in the present study [107].

The compositional gradients of the A15 phase between the inner and outer border of the sub-elements were analysed using EDX in the SEM. EDX line scans were performed across the A15 area of sub-elements of polished cross sections of the investigated wires using a step width of 100 nm–200 nm between two points where a spectrum was acquired, depending on the A15 layer thickness, in order to reduce the acquisition times and therefore the potential influence of sample drift. Figure 5.6 shows a SEM image of a Nb_3Sn sub-element where the location of an EDX line scan across the A15 phase is marked.
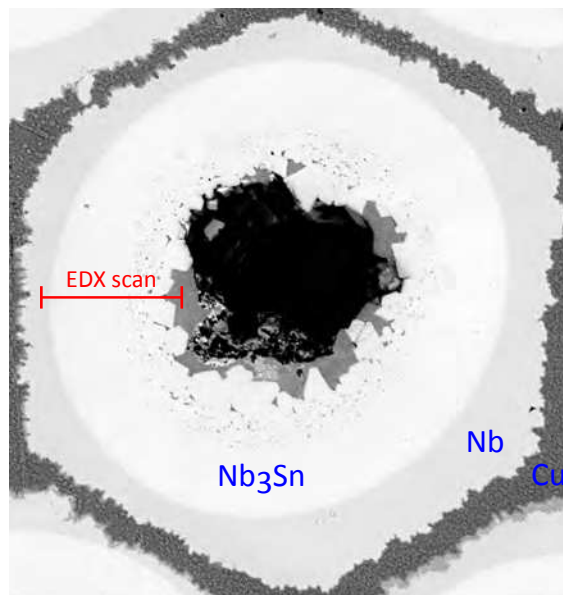
Figure 5.6: SEM image of a Nb_3Sn sub-element showing the location of an EDX line scan across the A15 phase.

Setting the high voltage to high values yields more counts, which is helpful for an accurate quantification, but simultaneously leads to a lower resolution due to a larger activation area from which X-ray are originating. Most of the measurements were conducted using a high voltage of 10 kV–15 kV which offers a good compromise for the investigation of Nb_3Sn. The EDX signal at this accelerating voltage originates

from up to a few hundred nm below the sample surface in Nb_3Sn [113]. The spectrum was collected for a dwell time of 5 s–10 s at every point to ensure sufficient counts for an accurate quantification.

Multiple sub-elements of each wire were investigated in order to produce accurate statistics. For each multifilamentary wire, around 10 line scans were acquired on different sub-elements. On the monofilamentary wires, around 4 scans were conducted. The total atomic content of the elements Nb, Sn, Cu and potential additives such as Ti or Ta was normalized to 100 % and the fraction of the atomic content of these elements was calculated.

When comparing the absolute values of the atomic Sn content, some factors have to be considered. The concentration of the elements Nb, Sn, Cu and Ti or Ta are not independent of each other, since they represent the fraction of the atomic content. Specifically in the BIN and RRP wires, frequent Cu inclusions were found, which impact the measured Sn content due to the normalisation of the elements. Parts of the measurements that exceeded a Cu content of 10 at.% were excluded from the statistics.

The atomic contents of the additives vary between different wire types, thus affecting the resulting value of the atomic Sn content. The site occupancy of Ti and Ta in the Nb_3Sn crystal structure also influences the absolute value of the Sn content, dependent on if Sn atoms or Nb atoms are replaced. For this reason, the comparison of the absolute Sn values between the different wires has to be conducted with respect to the content and possible site occupancy of the doping elements.

Since the site occupancy of Ti and Ta in the Nb_3Sn crystal structure has been controversial as stated in Chapter 1 and in the introduction of this chapter, the elemental contents of Sn, Ti and Ta were plotted separately in all figures of this chapter, rather than showing cumulative values of Sn and the additives or the ratio between these values to the Nb content.

Figure 5.7 shows an exemplary line scan across the A15 phase of a Nb_3Sn sub-element of the PIT-Ta-192 wire, where the relevant elements are plotted. The different phases and the border between the fine grain and coarse grain region are marked. From this graph it furthermore becomes apparent that the transition between the fine grain region with lower Sn contents and the coarse grain region with higher Sn contents is afflicted with an accumulation of Cu at the boundary. Such regions with coarse grains are primarily present in PIT and APC wires as described in Chapter 1 and Chapter 4.

The length of the line scans between the outer and the inner border of the A15 area was normalized because of varying lengths between different sub-elements and even inside individual sub-elements and average values were computed for each point. The outer border was defined at the position where the Sn content reached about 18 at.%, since according to the Nb_3Sn phase diagram the A15 phase begins at this point. The inner border was defined through the same criterion if possible at the point where the
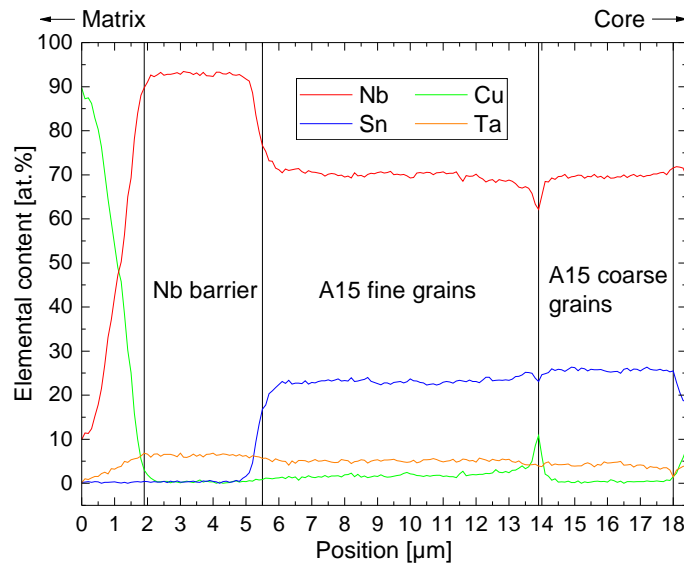
Figure 5.7: Example of an EDX line scan across the A15 layer where an increase in Sn content towards the sub-element centre becomes apparent.

Sn content reaches its maximum (within the atomic phase limit of 26 at.%). After normalisation and averaging of the measurements, the inner border was redefined if necessary at the point where the Sn content reaches the maximum near the steep fall-off in the centre of the sub-elements, and the length of the averaged line scans was re-normalized. This was done in order to compare the results of the different wires more accurately.

The averaged length of the line scans of each wire was used to calculate the real distance of the normalized statistics and plotted on the x-axis on the graphs in this section. The graphs show the behaviour of the Sn gradients between the outer border at the Nb barrier and the inner border to the core of the sub-elements. Fits through the regions where the Sn concentration varies approximately linearly were applied to calculate the change in Sn content in at.% μm^{-1}, which heavily depends on the fitted area since the Sn content shows a non-linear behaviour near the A15 phase borders. The plots in this section show the average Sn content at each position, the standard deviation of the measurements and the fits through the linear regions and are labelled with the type of the wire and the resulting Sn gradient in at.% μm^{-1}.

5.4.2 Results

The graphs in Figure 5.9 show the Sn gradients across the A15 phases of investigated binary wires. In the case of the BIN-246 wire, it was not possible to accurately approximate the entire region using one linear fir, instead two different linear fits were used to approximate the Sn content change in different regions. In

the first, steeper region near the barrier, the Sn content change was determined at $(1.425 \pm 0.025)\,\text{at.\%}\,\text{µm}^{-1}$ and in the second region the incline of the Sn content is very small at $(0.041 \pm 0.012)\,\text{at.\%}\,\text{µm}^{-1}$. Noteworthy is the appearance of multiple peaks in the Sn gradient across the A15 area of the sub-elements that likely origin from the coarse filament stacking before the heat treatment. Figure 5.8 shows a SEM image of an un-reacted BIN-246 sub-element before the heat treatment in which the stacked filament structure is visible. From this layout a correlation with the peaks in the Sn gradient can be deduced. This could hint towards and insufficient Sn diffusion to the filaments, thus resulting in an inhomogeneous Sn distribution inside the A15 phase. The RRP wires also showed inhomogeneities in the EDX maps in Section 5.2, however in the statistics of the EDX line scans in this section, such large variations as in the BIN-246 wire are not observable, likely due to a larger stacked filament count in the precursors.
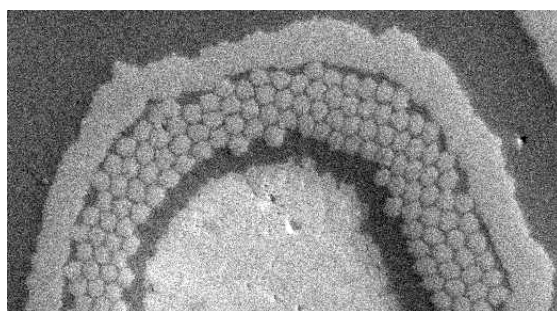
Figure 5.8: SEM image of an un-reacted BIN-246 sub-element showing the layout of the stacked filaments before the heat treatment. Data provided by CERN.

Figure 5.9 also shows the Sn gradients of older generation binary APC wires, where almost no gradient can be found over a longer distance in the centre region of the A15 phases. The Sn content in these multi-filamentary APC wires is around $24\,\text{at.\%}$, while in the mono-filamentary wires it is slightly higher at $25\,\text{at.\%}$. In case of the mono-filament wire APC-3607-1, the Sn content in the fine-grained region was determined at around $24.5\,\text{at.\%}$, while in the coarse-grained region it reached $26\,\text{at.\%}$. A fit through the fine grained region of the mono-filamentary APC-3607-1 wire with approximately linear Sn content change results in a Sn gradient that does not significantly differ from 0.

The Sn gradients over the A15 phases of the ternary internal tin wires are displayed in Figure 5.10, together with the gradients of the additives. Using the statistic of the Sn gradient in the RRP-Ti-108 wire, a fit through the linear region of the Sn gradient yields a Sn content change of $(0.046 \pm 0.004)\,\text{at.\%}\,\text{µm}^{-1}$. Using the statistic of EDX line scans of the RRP-Ta-54 wire, the Sn gradient was determined by a fit through the linear region at $(0.041 \pm 0.002)\,\text{at.\%}\,\text{µm}^{-1}$. The gradient of the additives is almost constant with only a minimal decrease towards the sub-element centre. The comparison between the different RRP type wires reveals that the Ti content in

the RRP-Ti-108 wire is at about 1.5 at.%, while the Ta content in the other RRP type wires lies around 5 at.%.

The Sn and Ta gradients over the A15 phases of the ternary PIT wires can be found in Figure 5.11. As common in PIT wires, the PIT-Ta-114 wire possesses a coarse grained region near the centre of the sub-element and a fine grained region on the outside towards the barrier. The Sn content in the coarse grained region averages roughly 26 at.%, while in the fine grained region it lies around 23.5 at.%. Since the coarse grains are less relevant due to a lower grain boundary density and thus reduced flux pinning compared to the fine grained region, a linear fit was applied through the fine grained region where the Sn content varies approximately linear. This results in a Sn content change of (0.041 ± 0.006) at.% μm^{-1}. The same can be said about the results of the PIT-Ta-192 wire, where the Sn content in the coarse grained region averages roughly 25.5 at.%, while in the fine grained region it lies around 23 at.%. A linear fit was applied through the fine grained region where the Sn content varies approximately linear. This results in a Sn content change of (0.079 ± 0.004) at.% μm^{-1}. While the Ta content in the fine grained regions of the PIT wires was found to be rather constant at around 5 at.%, the coarse grained regions shows a significant decrease in the Ta content.

The Sn contents of the ternary standard wires were in summary found to be in the order of 23 at.% with gradients of around 0.04 at.% μm^{-1}.

Figure 5.12 shows the Sn and Ta gradients of newer generation ternary APC wires. The Sn content of these APC wires show the highest values of all wires at nearly 26 at.% with varying gradients up to 0.07 at.% μm^{-1}. The gradients in the Ta content become more apparent in these wires compared to the others, where the content near the outer barrier is in the order of 6 at.% and drops to about 4 at.% near the sub-element centres.

The Sn content in the ternary APC wires were found to be slightly higher than reported in [169], where wires of the same batch number but with different heat treatments were investigated and the internally oxidized samples reached Sn contents of up to 25 at.%. Differences in the Sn content can be related to differences in the heat treatment, but also to the limited accuracy of the EDX quantification. It was stated that the ternary APC wires showed Sn contents that were higher than in standard wires, which is in agreement with the results shown here. It was suggested that the higher Sn content in the APC wires originated from a lower reaction rate at the interface between Nb_3Sn and Nb, from which the Sn content in the A15 layer benefits.

Binary standard and APC wires
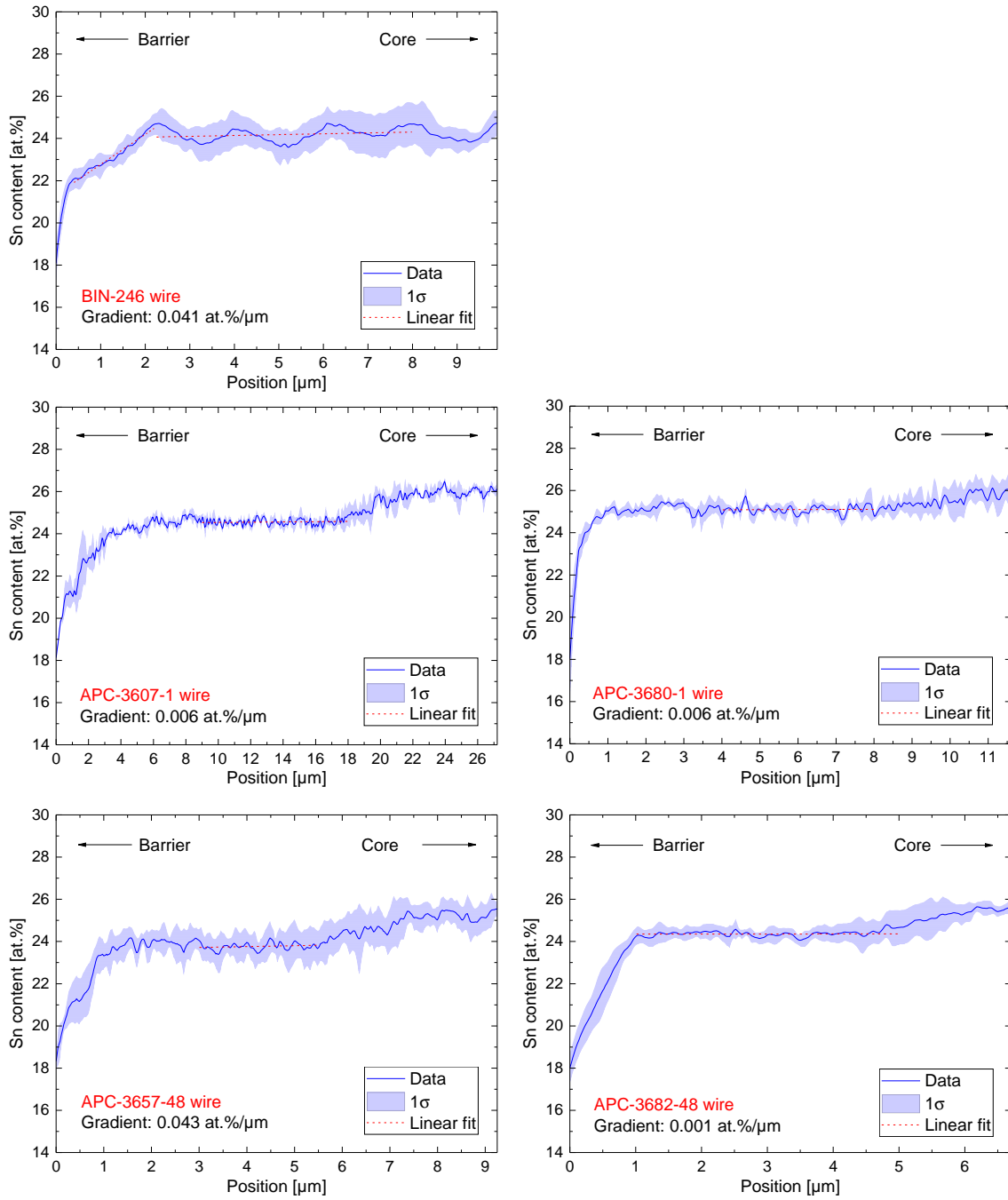
Figure 5.9: Statistics of the elemental gradients across the A15 phase of the binary standard and APC wires.
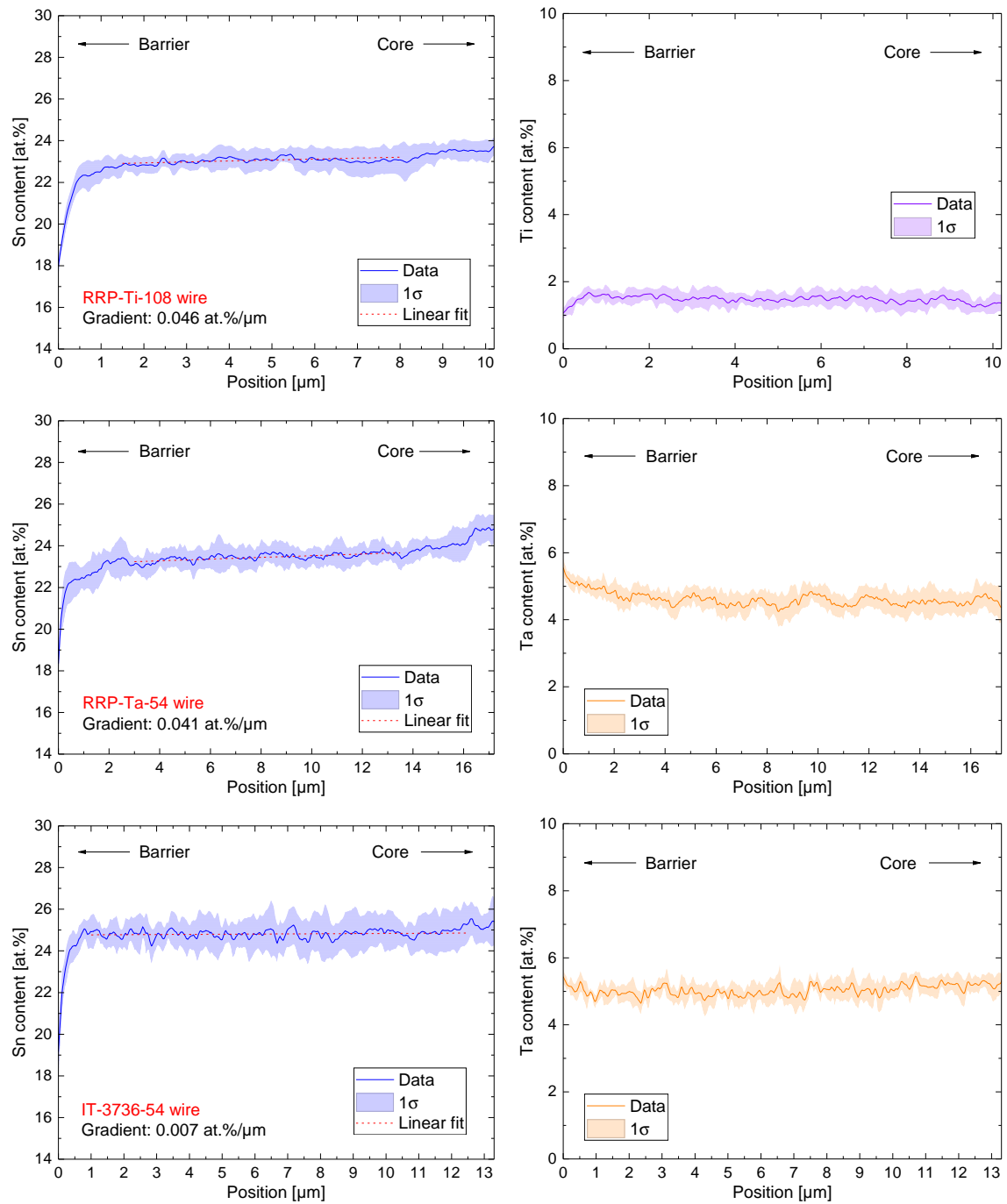
Ternary IT wires

Figure 5.10: Statistics of the elemental gradients across the A15 phase of the ternary IT wires.
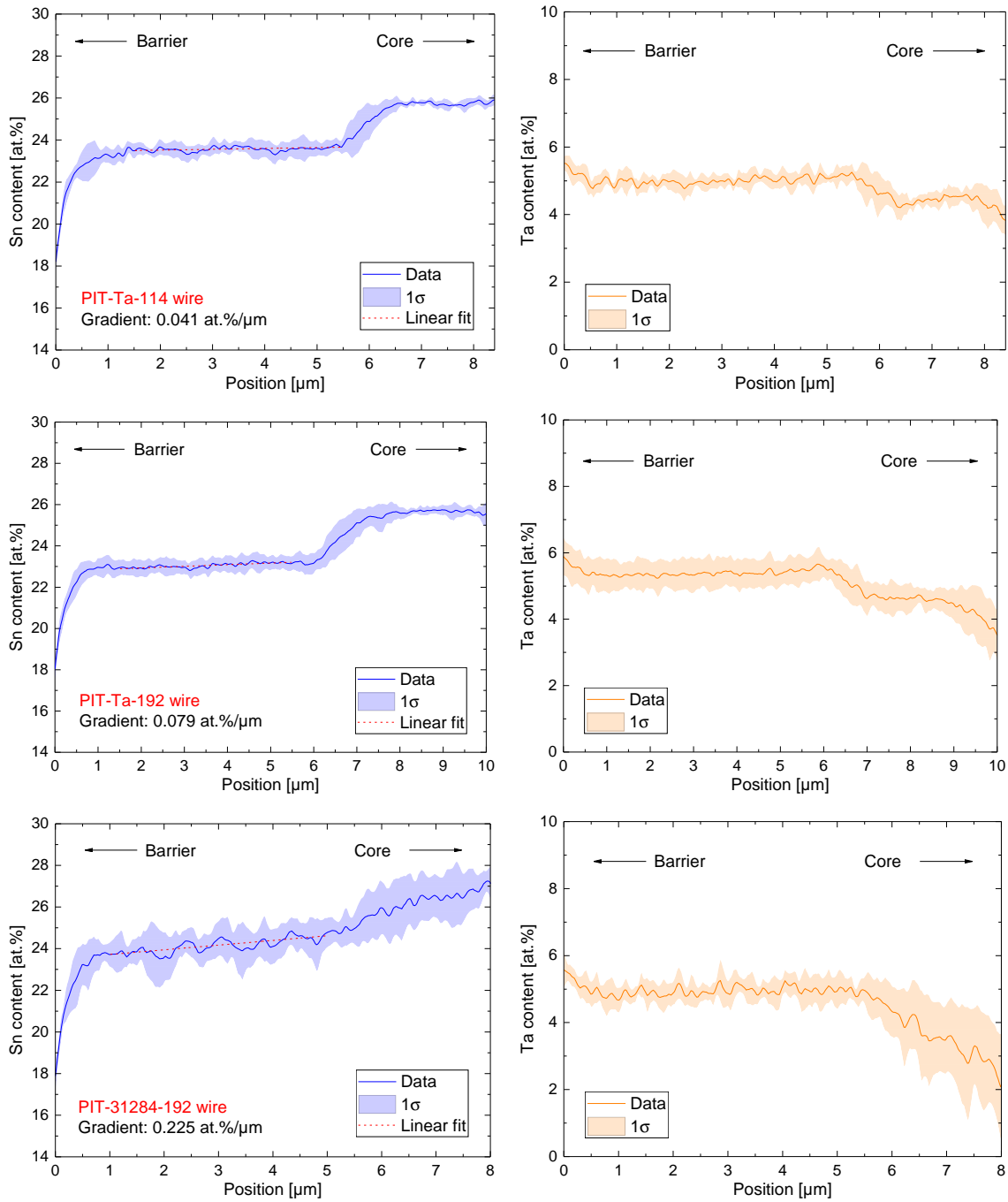
Ternary PIT wires

Figure 5.11: Statistics of the elemental gradients across the A15 phase of the ternary PIT wires.
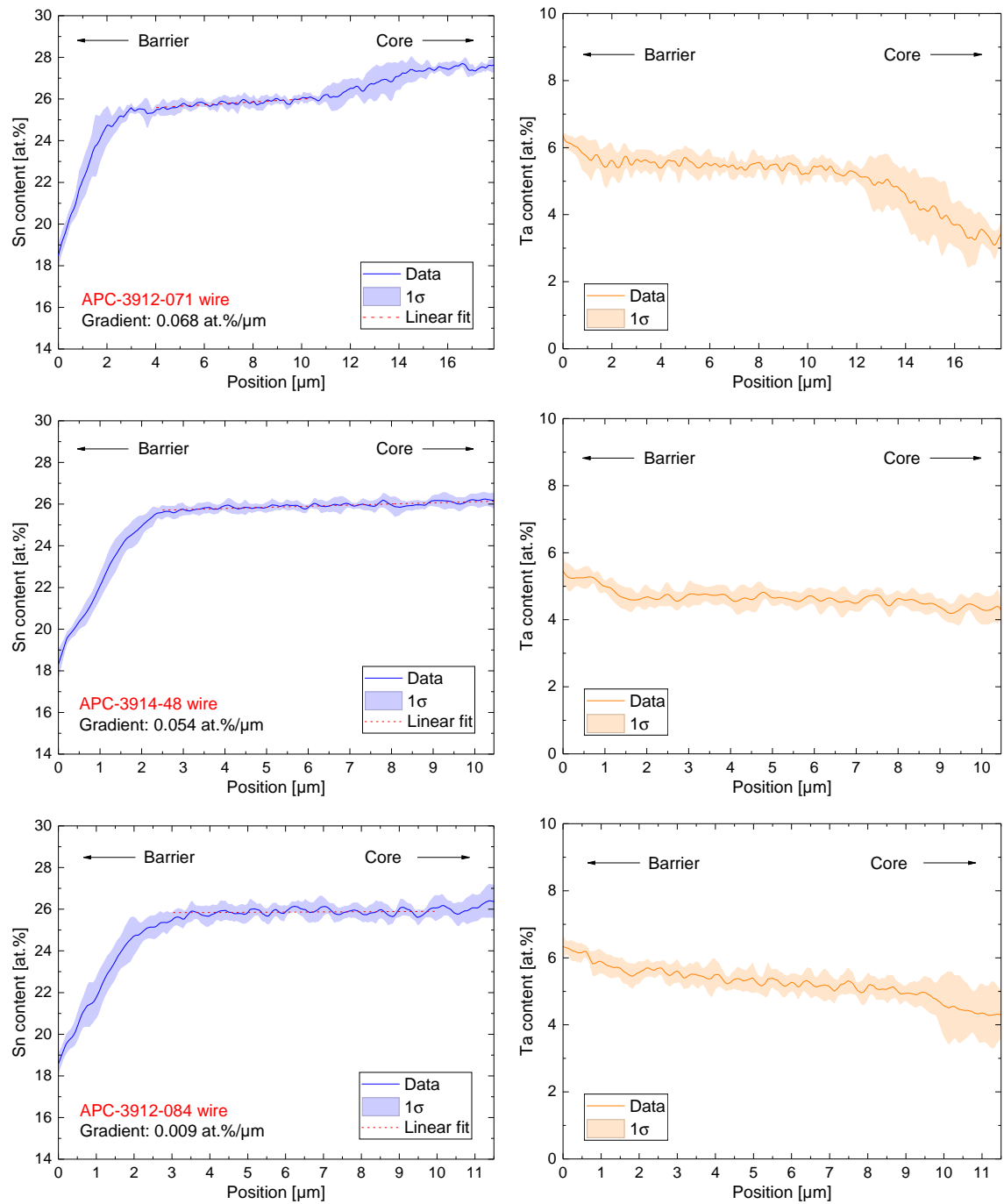
Ternary APC wires

Figure 5.12: Statistics of the elemental gradients across the A15 phase of the ternary APC wires.

A summary of the analyses of the elemental composition across the A15 phases of the investigated Nb_3Sn wires can be found in Table 5.1, where the average fine grained (FG) A15 layer thickness, the average Sn content of the linear fit and the Sn gradients in the linear regions and their standard errors are displayed. It can clearly be seen that the average Sn content is lowest in the standard RRP and PIT wires and highest in the ternary APC wires. The Sn gradients were found to be below $0.08\,\mathrm{at.\%\,\mu m^{-1}}$ in all wires except the PIT-31284-192 wire, where it reaches over $0.22\,\mathrm{at.\%\,\mu m^{-1}}$. Noteworthy is also the high average thickness of the fine grained A15 layer in the ternary APC wires of at least $10.5\,\mathrm{\mu m}$, which is roughly double the value compared to the standard PIT wires.

Wire	Average FG A15 thickness [μm]	Average Sn content [at.%]	Gradient [at.% μm^{-1}]
BIN-246	9.9	24.2	0.041 ± 0.012
RRP-Ti-108	10.1	23.1	0.046 ± 0.004
RRP-Ta-54	16.1	23.5	0.041 ± 0.002
PIT-Ta-114	5.5	23.6	0.041 ± 0.006
PIT-Ta-192	5.7	23.1	0.079 ± 0.004
APC-3607-1	18.0	24.6	0.006 ± 0.003
APC-3680-1	8.0	25.1	0.006 ± 0.012
APC-3657-48	5.7	23.8	0.043 ± 0.021
APC-3682-48	5.0	24.4	0.001 ± 0.009
APC-3912-071	10.7	25.8	0.068 ± 0.003
APC-3914-48	10.5	25.9	0.054 ± 0.002
APC-3912-084	11.0	25.9	0.009 ± 0.005
PIT-31284-192	5.5	24.2	0.225 ± 0.012
IT-3736-54	12.6	24.8	0.007 ± 0.002

Table 5.1: Summary of the EDX investigations across the A15 phases of the different Nb_3Sn wires.

5.5 Elemental gradients inside grains

5.5.1 Experimental

In [14], the T_c distribution of a PIT wire was assessed by AC magnetometry and compared with simulations. It was found that for a reasonable agreement between the experimental data and the results of the simulations, it is necessary to assume an intra-granular Sn gradient of 1.5 at.% between the grain boundary and the grain centre. This chapter revolves around validating this assumption by investigation Sn gradients in different wires by applying EDX line scanning across grains of thin TEM lamellae and evaluating the change of the elemental composition between the grain boundaries and the grain centres.

The Sn gradient of a PIT-Ta Nb_3Sn wire has been investigated in a previous study which found that the gradient inside single grains is larger than the one across the A15 phase of the sub-element. While the Sn gradient across sub-elements was in the order of 0.2 at.% μm^{-1}, the gradient inside single grains was reported to cover the entire Sn composition range of the Nb_3Sn phase with a roughly estimated gradient of 0.02 at.% nm^{-1}. An increased concentration of Cu and Sn was found at grain boundaries. From these results it was concluded that grain boundary diffusion is the major factor considering the Sn transport through the fine grained Nb_3Sn region. It was suggested that because of this reason, small grains not only improve the flux pinning, but also play an important role in achieving a higher homogeneity in elemental distribution of the Nb_3Sn phase [24].

A similar procedure to the EDX analyses on sub-elements using SEM was furthermore applied on thin lamellae using TEM. The elemental composition was analysed across individual grains on lamellae with a thickness of about 100 nm that were prepared using FIB. EDX line scans were performed across the grains to gain information about compositional gradients inside them. Figure 5.13 shows a schematic of the location of an EDX line scan across a single grain where relevant points such as grain boundaries and grain centre are marked. The step width used was 1 nm–2 nm for most of the measurements, depending on the grain diameter, in order to reduce the acquisition times and therefore the potential influence of sample drift. The line scans across grains were acquired using an operating voltage of 200 keV with an acquisition dwell time of around 5 s.

For each wire, around 10 EDX line scans were acquired on different grains that were randomly distributed in the A15 layer. The total atomic content of the elements Nb, Sn, Cu and potential additives such as Ti or Ta was normalized to 100 % in the same way as the scans acquired in the SEM and the fractions of the atomic contents were calculated. The absolute Sn was determined by normalizing the present elements, for which reason it is also dependent on the doping. Since the atomic contents of Ti and Ta differ between the respective wires, this results in different values of
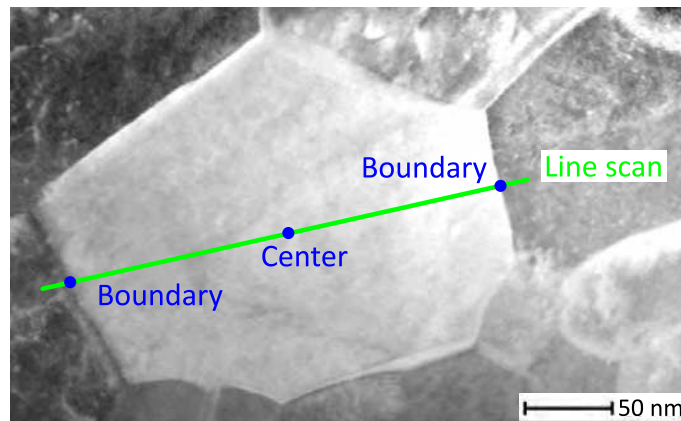
Figure 5.13: TEM image showing the location of an EDX line scan across a single grain.

the Sn content. The different site occupancy of Ti and Ta furthermore influences the values of the Sn and Nb concentrations in different ways. In some cases it was necessary to exclude the Cu content from the normalisation due to external influences such as sputtering of Cu onto the sample or Cu content in the sample holder that influence the measured Sn content. In the case of the APC-3680-1, APC-3682-48 and APC-3912-071 wires, the EDX signal was influenced by Cu that was sputtered onto the sample surface during preparation, for that reason the Cu content was factored out for the evaluation of the measurements of these wires. Since Cu is normally included in the normalisation, this led to a slight increase in the content of the remaining elements, however the Cu content inside the grains is generally very low, therefore this procedure did not drastically affect the results of these wires. Multiple grains of each wire were investigated and the results averaged.

Similar to the investigation of sub-elements and because the grain size inside a single sample varies greatly, the length of the line scans were normalized before producing the statistics. In the case of scans across grains, the distance between the grain boundary and the centre of the grain was normalized and the measurements averaged. Contrary to the line scans across the entire A15 phase, the definition of these boundaries for the scans across grains are not as straightforward.

Frequent inclusions of Cu were found at grain boundaries, which led to a reduction of the Sn content fraction at these locations. The grain boundary can thus often times most easily defined by an increased Cu content, after which the Sn content reaches its maximum towards the inside of the grain before decreasing near the centre. In case of a lower Sn concentration near the grain boundary due to increased Cu content, the point of highest Sn concentration close to the grain boundary was defined as the outer border, where the Cu content has decreased again.

The grain centre was defined as the point where the Sn content inside a grain reached its minimum value. This was justified because it was found that for most grains the

Sn content decreases near the centre of the grains and that point of lowest Sn content was frequently located near the geometric centre of the respective grain. An EDX line scan across an entire grain can thus yield two lines, from which the gradient between the grain boundary and the grain centre can be evaluated. An exemplary measurement of an EDX line scan across an individual grain of the RRP-Ti-108 wire can be found in Figure 5.14, where the relevant elements are plotted from which the decrease in Sn content towards the grain centre becomes apparent.
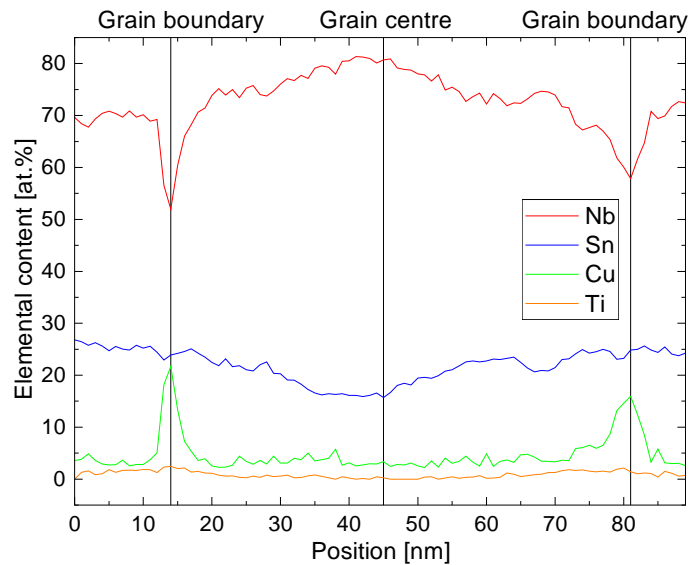
Figure 5.14: Example of an EDX line scan across a single grain where a decrease in Sn content towards the grain centre becomes apparent.

As described above, the Sn content was found to frequently reach its minimum near the grain centre, where most grains showed one minimum of the Sn content along the line scan. Some grains showed multiple minima of the Sn content which might be attributed to an inhomogeneous Sn diffusion into the grains or small inclusions of Nb or Cu. In some other grains, especially larger ones, no significant gradient was determined.

The absolute value of the Sn content acquired by EDX on thin samples in the TEM can be influenced by various factors such as sample thickness and the location at which grains are analysed. The absolute Sn concentrations within the grains are not easily comparable due to the existence of global Sn gradients across the A15 phase as shown in Section 5.4, leading to the fact that the Sn concentration within the grains depends on the position of the examined grains within the A15 phase. The conditions can not be guaranteed to be equal, since different wires also show different sub-element geometries and thicknesses of the A15 layer. Additionally, the investigation of the elemental composition using the TEM is more sensitive compared to the SEM due to contamination and the sample holder material potentially influencing the measurements. The measurements which could not be evaluated properly due to

factors such as bad signal, contamination or inclusions were not included in the statistics.

Another factor that impacts the absolute value of the measured Sn content inside the grains is the global Sn gradient across the A15 layer of the sub-elements as analysed in Section 5.4. The Sn content inside the grains is thus dependent on the locations inside the A15 layer, from which the TEM lamellae were lifted out by the use of FIB. The statistics consist of a limited amount of grains inside the lamellae that were analysed and are therefore potentially not representative for the entire wire. Furthermore, the grain sizes show significant variations as shown in Chapter 6, which might also impact the behaviour of their Sn gradients.

For these reasons it is not trivial to compare the absolute values of Sn gradients inside grains between different wires and samples. Such a comparison has to be conducted with great caution and consideration of these factors. Regardless, the analysis of the variation in the Sn content across grains of each individual sample, on the other hand, can be conducted independent of these factors. Grains with a gradient in Sn concentration were found in all wires, which often covers the entire Nb_3Sn phase range of about 18 at.%–26 at.% in Sn content.

5.5.2 Results

The graphs in this section show the statistics of the Sn gradients and additive contents inside grains of the different wires. The statistics of the binary standard and APC wires are displayed in Figure 5.15, the ones of the ternary IT wires in Figure 5.16, the graphs of the ternary PIT wires can be fount in Figure 5.17 and the ones for the ternary APC wires in Figure 5.18. As already mentioned, since the length of the line scans showed great variations due to differing grain sizes, they were normalised and the relative distance between grain boundary and grain centre was plotted on the x-axis of the graphs in this section. The graphs show the average behaviour of the Sn gradients and the additives between the grain boundary and the grain centre of the different wires. The plots are labelled with the type of the wire and show the average elemental content at each relative position and the standard deviation of the measurements. The phase range of Nb_3Sn between a Sn content of about 18 at.% and 26 at.% is marked by horizontal lines in the graphs.

As already mentioned, the severity of the gradients varies between individual grains. In each wire, grains with almost no gradients as well as very substantial gradients can be found. Smaller grains generally seem to exhibit stronger compositional gradients, which is in consistency with the observations of past studies [29]. The graphs in this section show the statistics of the grains that exhibit significant gradients. In some graphs for each wire type, additionally the statistics of the grains with no significant gradient are included as examples. In the case of the PIT-Ta-114 and PIT-Ta-192 wires, the distinction between the coarse and fine grains is visualised. Aside

from the fact that the coarse grains possess a higher overall Sn content, which was already confirmed in Section 5.4, it becomes apparent that they exhibit practically no gradients in the Sn content, while large gradients can be observed in the fine grains. The Ta content, on the other hand, shows slightly higher values in the fine grains.

A similar behaviour of the Sn content in grains with a significant gradient is found in all wires, where it often covers the entire Nb_3Sn phase range. The gradients are non-linear, where a steeper fall-off is observed towards the grain centres. Since the gradients inside grains are non-linear, stating a gradient per distance is not reasonable, however if a linear approximation and an average grain size of around $100\,nm$ is assumed, a gradient in the Sn content between $26\,at.\%$ at the boundary and $18\,at.\%$ at the centre corresponds to a gradient of $0.16\,at.\%\,nm^{-1}$.

From the statistics of the RRP-Ti-108 wire, it becomes apparent that the Ti content decreases towards the grain centres. In the wires doped with Ta, the Ta content increases towards the centres of the grains, where the grains with stronger Sn gradients exhibit higher values in the absolute atomic Ta content.

The results of the EDX analyses across grains of the different Nb_3Sn wires can be summarised as follows: The absolute values can not easily be compared as already described, the difference between these values represents the total Sn gradient that occurs on average in grains of the respective wires. It was found that a majority of the grains showed gradients in the Sn content. The Sn gradients across grains are non-linear, a steeper fall-off is observed towards the grain centres. The Sn gradients showed a similar behaviour in all wires, the maximum Sn content was found near grain boundaries and the minimum near the centre of the grains. The Sn content across grains were found to often cover the entire Nb_3Sn phase range. The Ti content was found to decrease towards the grain centre, while the Ta content increased with increasing distance from the grain boundary. Grains with a higher Sn gradient generally showed higher Ta contents than those with lower gradients.

Binary standard and APC wires
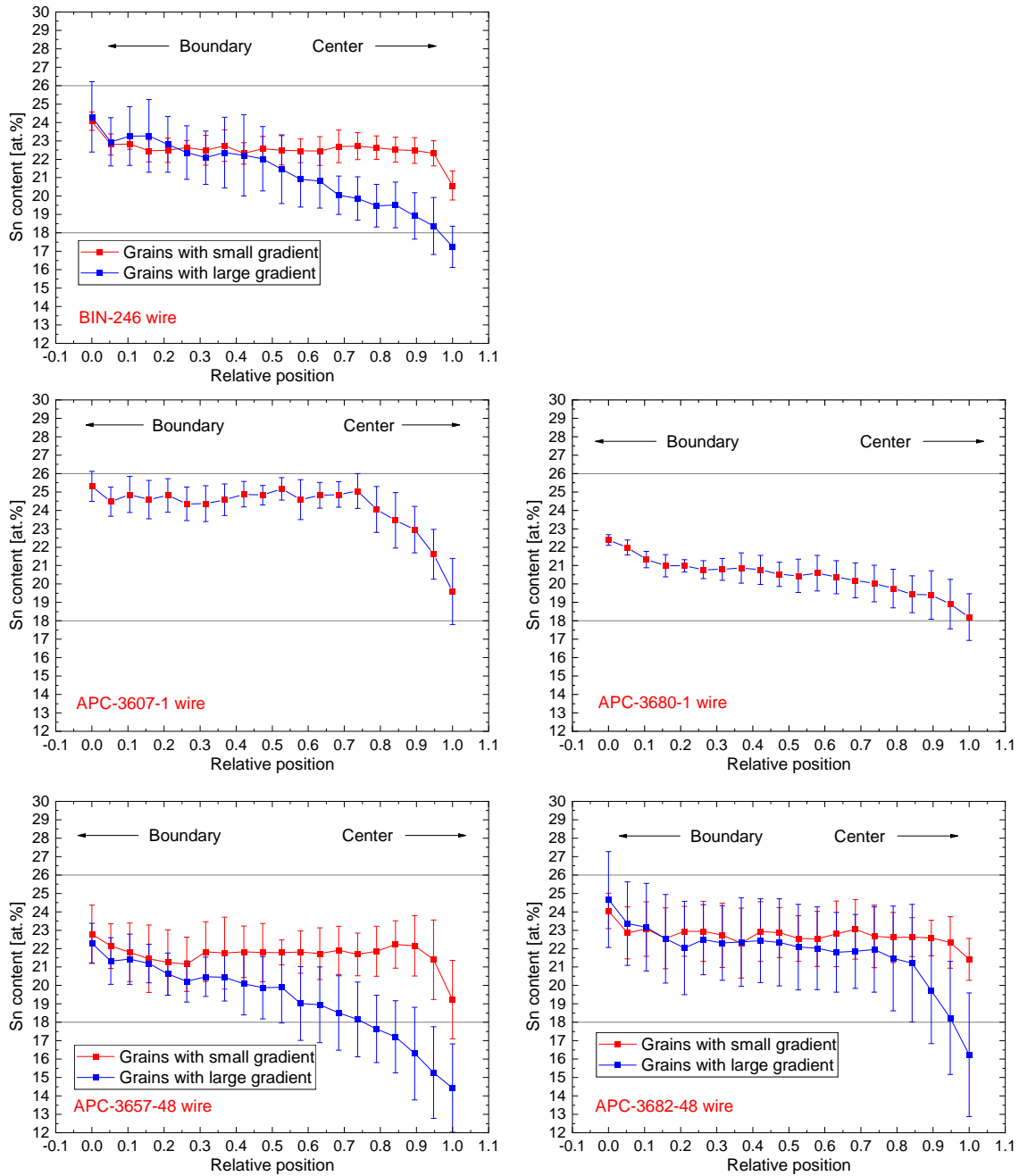
Figure 5.15: Statistics of the elemental gradients across grains of the binary standard and APC wires.
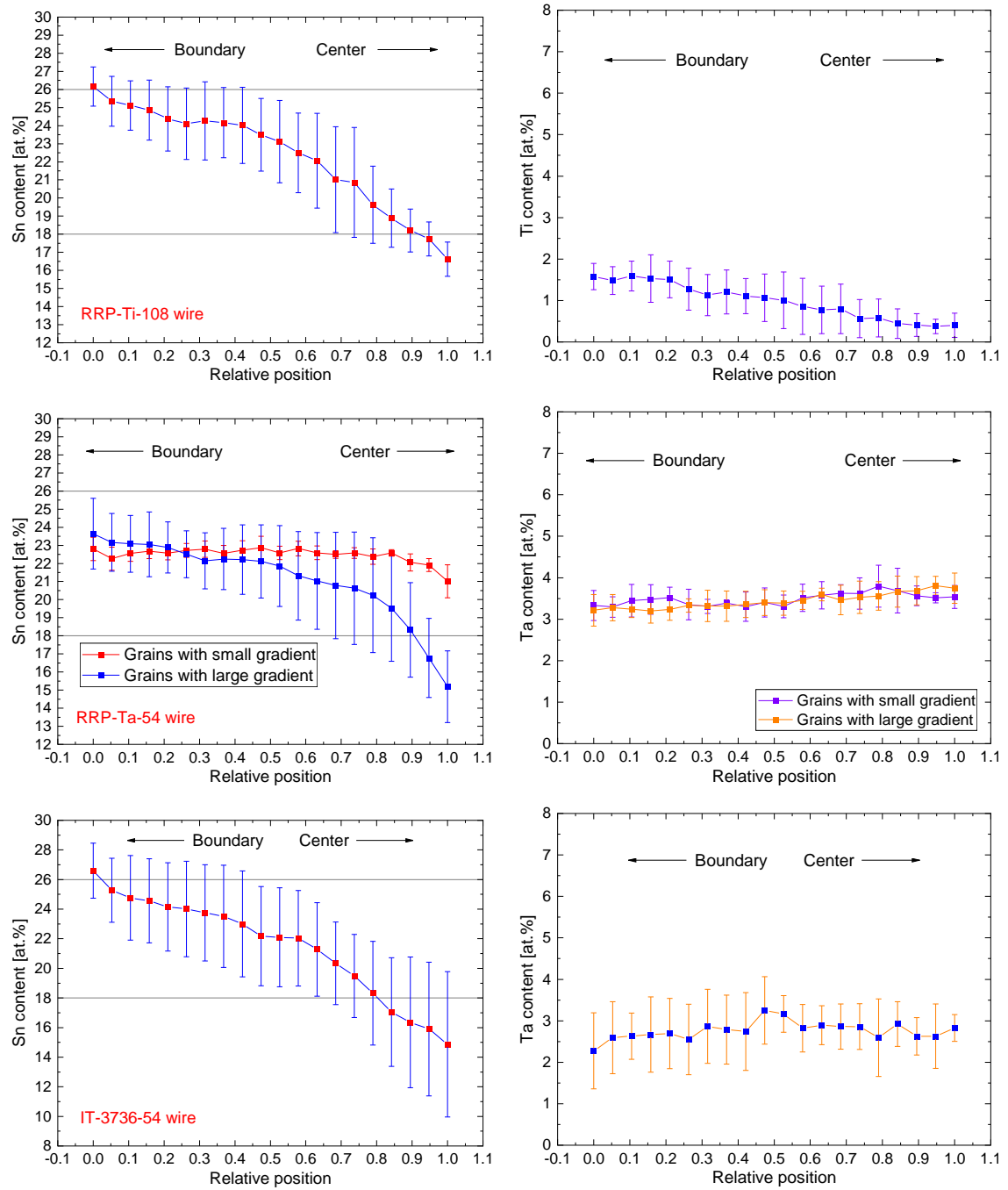
Ternary IT wires

Figure 5.16: Statistics of the elemental gradients across grains of the ternary IT wires.
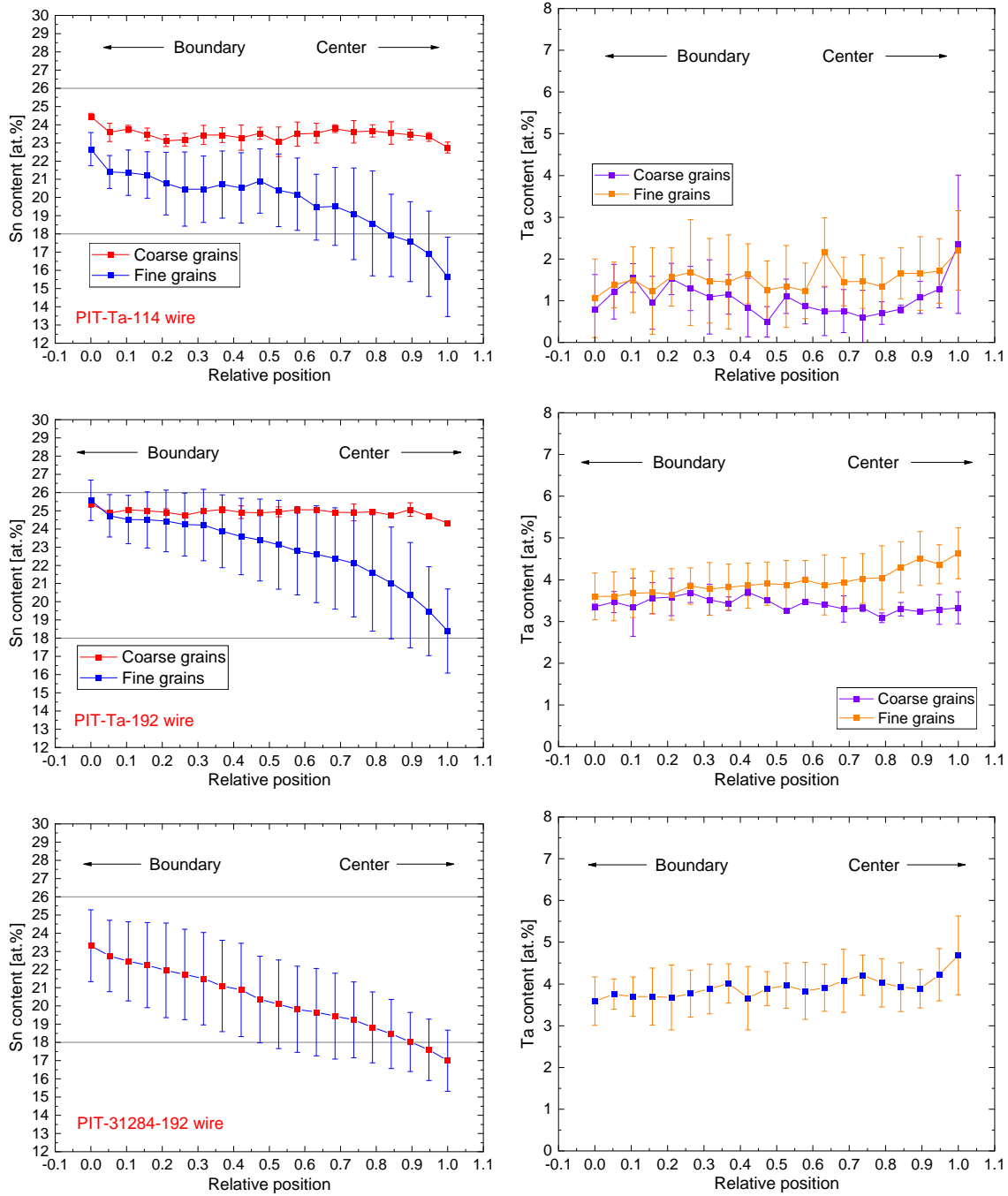
Ternary PIT wires

Figure 5.17: Statistics of the elemental gradients across grains of the ternary PIT wires.
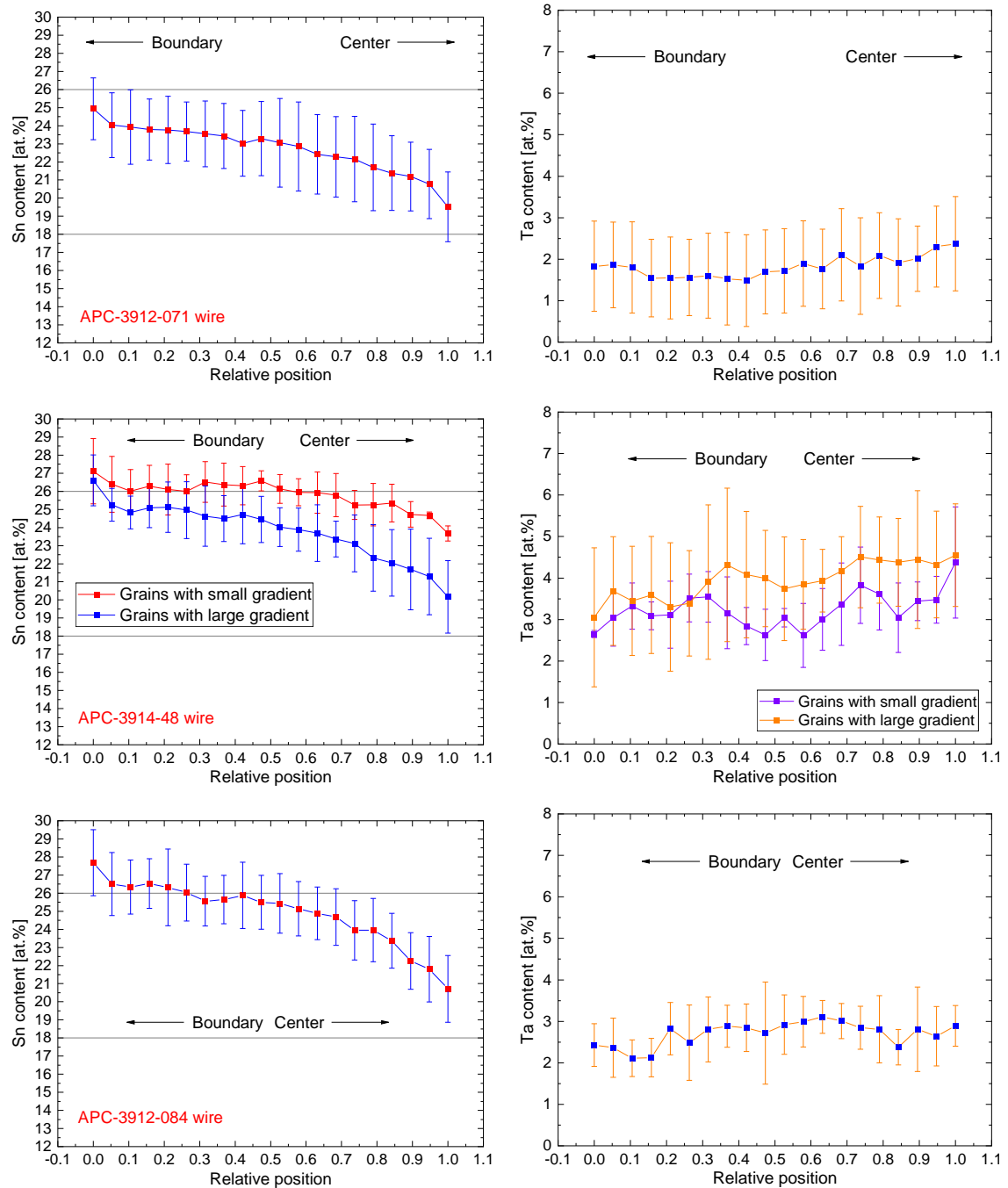
Ternary APC wires

Figure 5.18: Statistics of the elemental gradients across grains of the ternary APC wires.

5.6 Elemental composition at grain boundaries

The investigation of the elemental composition at grain boundaries is important because stoichiometry variations at grain boundaries can contribute to flux pinning. Another reason is the fact that Cu has a positive impact on the formation of the Nb_3Sn phase during the diffusion reaction. The addition of Ti also affects the formation of the Nb_3Sn phase. Previous studies reported an increased Cu and Ti concentration at grain boundaries of bronze processed Nb_3Sn wires. This can improve the diffusion of Sn along the grain boundaries [117].

During the heat treatment the Sn atoms are diffusing along gain boundaries. A detailed mathematical and experimental study of grain boundary diffusion is given in [38]. It was found that the formation of the Nb_3Sn layer thickness shows a time dependence of $t^{0.35}$.

Statistics of EDX line scans across grain boundaries of the APC-3607-1 wire can be found in Figure 5.19. It becomes apparent that while the changes of the Sn content at grain boundaries are small, the changes of the Nb and Cu content are substantial. A higher content of Cu is located at grain boundaries, where the increase of the Cu content and the decrease of the Nb content is in the order of 15 at.%.
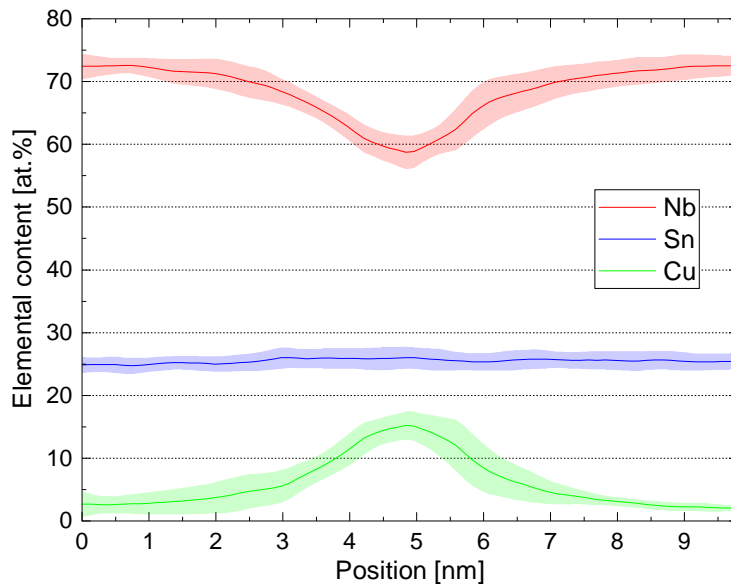
Figure 5.19: Statistic of EDX line scans across grain boundaries of the APC-3607-1 wire.

5.7 Elemental composition gradients along wire axis

In Chapter 3, it was shown that the A15 geometry varies considerably along the wire axis, raising the suspicion of possible longitudinal variations in the elemental composition. An EDX analysis was performed on a longitudinally polished wire sub-element in order to examine possible longitudinal gradients in the elemental composition. The RRP-Ti-108 wire was polished to the wire centre and a central sub-element was investigated, which showed practically no twisting, in contrast to the outer sub-elements. Care was taken to measure parallel to the wire axis to obtain information of the change in Sn content along the wire axis only, without any influence from radial gradients. The results are shown in Figure 5.20, where the data were smoothed by FFT filtering as marked by the lines in order to reduce the noise of the signal. Variations in the elemental composition become apparent that are clearly larger than the noise. It can be concluded that there are significant changes in the elemental concentration of the A15 phase along the wire axis, in the present case over 1.5 at.% within a short distance of less than 30 μm.
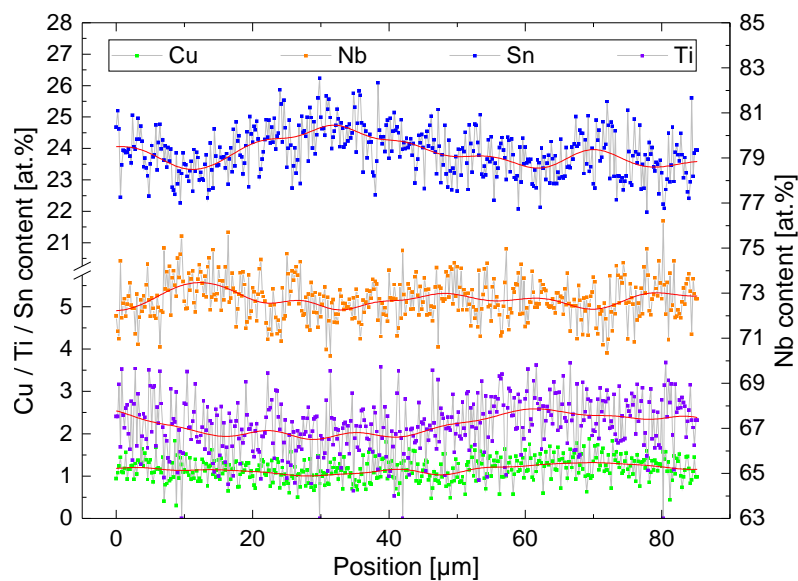
Figure 5.20: EDX line scan along the RRP-Ti-108 wire axis showing longitudinal variations in the elemental composition. The data were smoothed by FFT filtering as marked by the lines in order to reduce the noise of the signal.

The EDX analyses led to the validation of radial and longitudinal variations of the Sn content inside the A15 phase of Nb_3Sn wires, which impact the distribution of T_c and other superconducting properties as discussed in Chapter 1 and later shown in Chapter 9. The determined longitudinal variations in the elemental content along

the wire axis can potentially limit the superconducting properties locally and thus impact the performance of the wire. The inhomogeneities were determined in wires within short distances of a few µm. Since the superconducting properties of wires are determined by their worst performing region, it can be expected that in longer wires the inhomogeneities can have a considerable impact.

5.8 Conclusions of elemental composition analyses

The results of the EDX investigations of the different Nb$_3$Sn wires can be summarised as follows:

1. EDX mapping of sub-elements of the standard RRP wires revealed residual Ti at the locations of the Ti rods, together with an accumulation of Cu. The Ta content was more uniform, but Cu was still present between filaments.

2. EDX mapping of grains of different wires revealed the preferential location of Cu at the grain boundaries as well as locations with larger Cu inclusions.

3. The Sn gradient across the A15 phase of all wires can be described by a fit through the linear region. A steep fall-off is observed near the outer barrier of the sub-elements.

4. The change in Sn content per µm across the A15 phase in the linear region that was determined by a linear fit is comparable for most of the wires and were generally found to be below $0.08\,\mathrm{at.\%\,µm^{-1}}$ in all but one wire.

5. The Sn content in standard wires was generally found to be around $23\,\mathrm{at.\%}$, while in new generation APC wires it often reaches up to $26\,\mathrm{at.\%}$.

6. The contents of the additives Ti and Ta decreased slightly between the outer barrier and the inner border of the sub-elements. The Ti content was found to be in the order of $1.5\,\mathrm{at.\%}$, while the Ta contents lied at around $4\,\mathrm{at.\%}$–$6\,\mathrm{at.\%}$.

7. Most of the grains showed gradients in the Sn content. The Sn gradients across grains were found to be non-linear, where a steeper fall-off is observed towards the centre of the grains.

8. The Sn gradients across grains showed a similar behaviour in all wires, where the maximum Sn content was found near grains boundaries and the minimum near the centre of the grains.

9. The Sn content across grains often covers the entire Nb$_3$Sn phase range between around $18\,\mathrm{at.\%}$ and $26\,\mathrm{at.\%}$.

10. The content of Ti was found to decrease towards the grain centre, while the content of Ta increased with increasing distance from the grain boundary. Grains with a higher Sn gradient generally showed higher values of the Ta content than those with lower gradients.

11. The investigation of the elemental composition at grain boundaries revealed a reduction of the Nb content by around 15 at.% due to Cu inclusions between grains, while the Sn content was less affected.

12. The investigation of longitudinal gradients in the elemental composition along the wire axis revealed variations in the Sn content of around 1.5 at.% over a distance of only 30 µm.

6 Transmission Kikuchi diffraction analysis of the grain geometry

This chapter deals with the assessment of the grain geometry and orientation by the use of transmission Kikuchi diffraction. The introduction presents literature data of existing EBSD (electron backscatter diffraction) experiments on Nb_3Sn, followed by outlining the advantages of TKD compared to EBSD. The experimental section described in detail the employed setup and used parameters. After the discussion and comparison of the grain size and aspect ratio distribution of the investigated wires, the results are compared with conventional evaluation methods and potential error factors are discussed. The chapter concludes with further analyses of grain shape orientation, phase distribution, grain boundary misorientation and texture, where a focus is laid upon the newest generation APC wires.

6.1 Introduction

A critical target of the FCC conductor development programme [7] is the refinement of the grain size as recently demonstrated by a novel production method of wires containing APCs (artificial pinning centres) using internal oxidation and the formation of nano-precipitates [167]. The reason for the importance of the grain size in Nb_3Sn lies in the pinning capability of grain boundaries. Reducing the grain size leads to a higher grain boundary density and consequently to an increase of the pinning force, thus increasing the critical current density. Additionally, the produced nano-precipitates are believed to contribute significantly to the increase in the pinning force. The ternary APC wires of the newest generation that are investigated in this study have already achieved the FCC J_c specification in short samples, based on the assessment of their superconducting properties reported in [169].

A recurring issue during the measurement and evaluation of the grain size distributions stems from the inconsistency between the methods used. Different research groups might make use of different evaluation methods, leading to a low reproducibility and comparability of the results. Common evaluation methods include the use of SEM imaging of fracture surfaces, where wires are broken in half and the grain size is measured directly from the image, for example by drawing lines across the grains and counting the number of intersections. Such methods have the disadvantage of

only measuring a small subset of grains and not taking into account the grain shape. Grains in Nb_3Sn are commonly elongated as can be seen from the results in this chapter, leading to a major difference between the length of the major and the minor axes. Furthermore, it is often not clear if the given values of grain size correspond to the average, median or modal values of the distributions and if number fractions or area fractions were calculated.

In principle, it is possible to investigate the grain size distribution in Nb_3Sn by electron backscatter diffraction (EBSD). Not many studies of EBSD measurements of Nb_3Sn wires have been published so far. EBSD investigations of Nb_3Sn wires that were produced by the bronze process were published in [116] and [117]. The grain boundary misorientation angle distribution was found to follow a distribution of randomly oriented grains, while the Nb_3Sn grain themselves were preferably oriented in a $\langle 110 \rangle$ direction parallel to the wire axis.

An EBSD study of PIT and RRP Nb_3Sn wires is presented in [121]. In the PIT wire, a preferred $\langle 110 \rangle$ orientation with respect to the wire axis was confirmed resulting from the drawing process before the heat treatment, while in the RRP wires, the grains were mainly oriented in a $\langle 100 \rangle$ direction. The PIT wire showed an average grain diameter of $(161 \pm 87)\,nm$, the grains in the Ta-alloyed RRP wire had very similar values of $(166 \pm 74)\,nm$. However, the spatial resolution of EBSD is limited to $20\,nm$–$50\,nm$, depending on the material. The samples are usually tilted by $70°$ towards the detector, further limiting the resolution [132].

Neutron diffraction experiments also found that the grains in PIT wires are preferably oriented along $\langle 110 \rangle$ parallel to the wire drawing axis as a result of the Nb-Ta phase that forms during the drawing process before the heat treatment [119].

In this chapter, the use of transmission Kikuchi diffraction (TKD), also known as transmission electron backscatter diffraction (t-EBSD), is demonstrated in the SEM. This evaluation method is useful for the assessment of grain size distributions of fine grained superconducting wires. The technique as well as the comparison to conventional EBSD is described in [132] and in the references therein. In TKD, the sample has to be thin enough to be electron transparent. The electron beam transmigrates through the sample and is diffracted by the crystal planes, resulting in a diffraction pattern that is recorded by the standard EBSD camera. The TKD technique can be conducted in standard SEM systems with an EBSD camera and only requires the use of a dedicated sample holder that is suited for holding small lamellae. TKD offers the advantage of automatically determining the grain size distribution by counting the number of measured points in each grain. The effective diameter of the grains is then calculated from the measured area assuming circular shape. Furthermore, information about grain aspect ratio, phase distribution and orientation can easily be extracted from the dataset. Another important advantage of TKD is the use of a small specimen tilt angle, where the sample is tilted away from the detector by $0°$–$40°$, leading to a smaller diffraction volume and smaller projected beam diameter, and therefore a higher spatial resolution compared to

conventional EBSD. Depending on the imaging parameters used, TKD is able to achieve a resolution of 5 nm–10 nm [132]. Such a high resolution is required to resolve the smallest grains in Nb_3Sn, especially in the newest generation APC wires, which can be of the order of only 20 nm.

The TKD diffraction pattern benefits from a short working distance (the distance between the pole piece and the sample) and a small distance between the sample and the detector. A higher specimen tilt can lead to higher indexing rates of the diffraction pattern, but on the other hand worsens the spatial resolution due to a higher effective sample thickness. Regarding the optimal specimen thickness, one has to consider the grain size which is in the order of 100 nm in Nb_3Sn. In order to avoid overlapping grains, the specimen thickness should be lower than that number for the investigation of Nb_3Sn. It was also found that for a lower specimen thickness is better suited for materials with lower atomic number [132].

In [154], it was shown that the best diffraction pattern quality for an Al-alloy was obtained in areas with a sample thickness of around 100 nm at an accelerating voltage of 22 kV. It was also stated that too thick samples are more problematic for acquiring good quality patterns than samples that are too thin. Given that the average atomic number of Nb_3Sn is 43.25, much higher than the more frequently investigated materials such as aluminium and copper, a specimen thickness of less than 100 nm is desirable, as well as a higher accelerating voltage. The disadvantage of TKD compared to EBSD is the need of electron-transparent specimens and thus a more complicated sample preparation process, but since specimen had to be prepared for TEM investigations of this study too, those could also be used for TKD.

6.2 Experimental

The grain size distribution, aspect ratio, phase distribution, grain boundary misorientation, grain shape orientation and texture of the different types of Nb_3Sn wires was investigated. An overview of the investigated Nb_3Sn wires and some relevant parameters was given in Table 1.3. Three of the listed wires were not subjected to TKD analyses, since a sufficient amount of wires for each manufacturing technique was investigated for a comparison of the results.

In [168], it was found that the maximum pinning force increases linearly with $1/d$, where d denotes the grain size, until it becomes saturated at small d values, potentially due to a columnar grain shape. Grains with larger aspect ratios might exhibit larger fractions of lower angle boundaries and thus have less pinning efficiency than higher angle boundaries. A reaction temperature of 650 °C led to grain aspect ratios of around 1.8, while a temperature of 700 °C led to equiaxed grains and aspect ratios less than 1.5. It was also shown that the heat treatment of the wires has a critical influence on the grain size of the A15 phase. The grain sizes were found

to increase exponentially with heat treatment temperature. As the heat treatment temperature increased from 625 °C to 750 °C, the grain size doubled. For that reason the specification of the heat treatment is important when comparing grain sizes and is displayed in Table 1.4. A good trade-off between high field J_c and low field stability was found at a temperature of around 700 °C, where non-Cu J_c values of over 3000 A mm^{-2} at a field of 12 T can still be achieved.

TKD is conducted in transmission mode at an accelerating voltage of 25 keV–30 keV. Since electrons of this energy need to traverse the entire specimens, the final sample thickness needs to be in the order of 100 nm. FIB was used for preparing specimens for TKD investigations. Lamellae were cut and lifted out of polished cross sections of the Nb$_3$Sn wires, followed by mounting them onto 3 mm wide grids and final thinning with the ion beam. A SEM image of the lift-out process showing the sample orientation relative to the wire cross section is displayed in Figure 6.1, together with a finalized sample. The TKD maps were generally and whenever possible acquired in such a way that the horizontal axis corresponds to the radial direction of the sub-elements. One thing to note about grain size analyses using TKD is the fact that this technique only allows for the investigation of a small specimen area at a time, corresponding to a few µm^2. The resulting values thus depend on the location inside the A15 layer, from which the specimen was lifted out by means of FIB and on which area of this specimen was analysed. This area can not always be chosen at will, since only the areas with adequate sample thickness offer an acceptable signal quality. Potential gradients in grain size over the A15 layer are not accounted for, since the determined grain size values result from the averaging over all mapped grains. However, the number of examined grains usually is in the order of hundreds to thousands, and should thus provide accurate statistics that are valid for the majority of all grains inside the A15 layer.

This is consistent with [68], where it was shown that the microstructure of PIT wires does not significantly change over most of the fine grained A15 layer, except close to the outer barrier, where an increase in grain size and grain aspect ratio was observed. It was also stated that a higher aspect ratio is related to a lower nucleation rate of the grains and therefore a lower Sn content in the A15 phase.

For TKD investigations in the employed FEI Quanta 250 FEG SEM, the samples were mounted onto a dedicated TKD specimen holder produced by TSL Solutions. The principle of TKD is visualised in Figure 6.2, which displays an image of the TKD setup in the SEM. The TKD sample holder is mounted on the SEM stage, which is tilted away from the EBSD camera. Table 6.1 summarizes the parameters of the experimental setup that were found to be optimal for the investigation of the given samples.

A step width of 10 nm–20 nm was chosen depending on the sample size. After the acquisition of the TKD maps, a clean-up routine was applied to the data in order to reduce the amount of incorrectly and unallocated pixels, since the signal near grain boundaries is often inhibited due to overlapping crystal lattices.
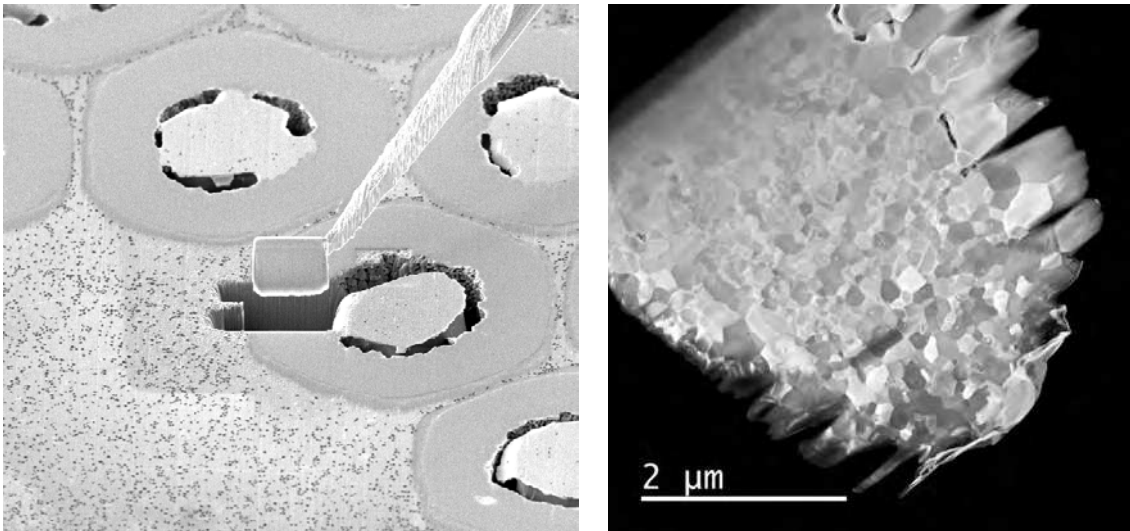
Figure 6.1: Lifting a lamella out of a polished transversal cross section of a Nb$_3$Sn wire (left) and a final TKD sample (right).
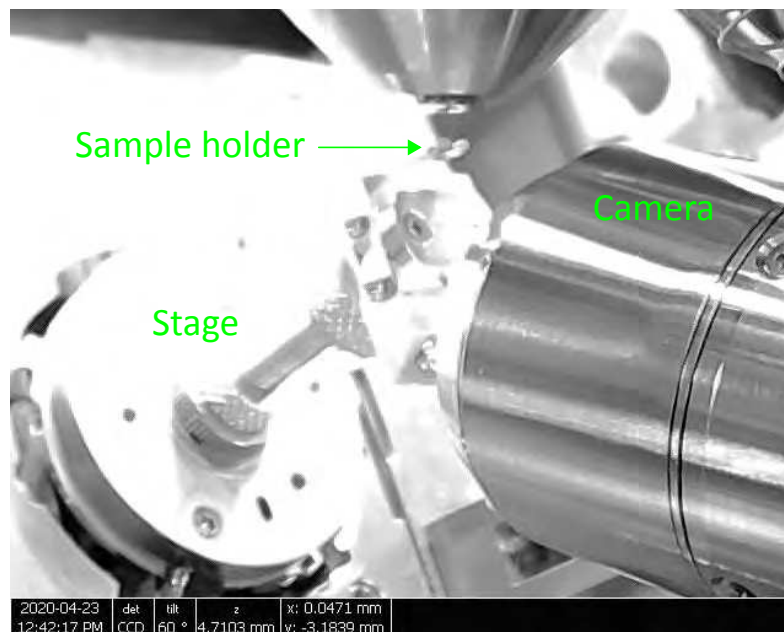
Figure 6.2: TKD setup in the SEM with TKD sample holder, SEM stage and EBSD camera.

Neighbour Pattern Averaging and Re-indexing (NPAR) was applied during rebuilding the acquired maps in the EDAX Texture and Elemental Analytical Microscopy (TEAM) software, which averages the intensity of the diffraction pattern between neighbouring points. If the data is collected on a square grid, the intensity of the diffraction pattern of every point in a scan is averaged with the patterns of the four neighbouring scan points. The TKD maps described in this work were acquired using

Parameter	Value
Working distance	4 mm–5 mm
Accelerating voltage	25 kV
SEM stage tilt angle	60°
Holder plate pre-tilt angle	90°
Resulting specimen tilt angle	−30°
Spot size	4.5–5
Aperture	50 µm
Camera binning	4 × 4
Step size	10 nm–20 nm
Specimen thickness	100 nm

Table 6.1: Summary of the optimized parameters for TKD investigations.

a hexagonal grid. In this case the averaging procedure contains the pattern of the point of interest and the patterns of the six nearest neighbours. NPAR has proven to clearly improve the pattern indexing success rate and quality of the given TKD maps.

The data were then exported to the TSL Orientation Imaging Microscopy (OIM) Analysis Software, where one iteration of grain dilation was applied, which changes the orientation of unallocated pixels and reallocates them to adjacent grains. There are two reasons for the existence of such unallocated points: Either they could not be indexed due to too poor quality of the diffraction pattern or they belong to a grain group that has fewer members than the minimum grain size which has to be specified by the user. By applying grain dilation, the orientation of a point that fulfils the requirement is changed to match the grain that contains the majority of the neighbours of the given point. Otherwise, the orientation is changed randomly to match any of the neighbouring grains. Theoretically, this process can be continued until all unallocated points are reallocated to grains, but since this process leads to a significant increase in grain size, only one iteration of grain dilation was performed.

During the clean-up procedure, a minimum grain size has to be specified, which was chosen depending on the used step size of each measurement and so that the noise becomes minimal. This noise appears as a peak at very small grain sizes in the statistics when using number fractions and originates from isolated pixels. Only grains and pixels with sufficiently high image quality and confidence index were included in the statistics. The areas in which the signal quality does not fulfil the required specifications were coloured in black in all graphs and not included in the statistics.

6.3 Grain size and aspect ratio of standard wires

The graphs in this section show the acquired TKD maps together with the statistics of grain size distribution and aspect ratio. The grain size was determined by counting the measured points in each grain and the diameter was calculated based on circles of equivalent area. Only grains with diameters up to 400 nm were included in the statistics of all investigated Nb$_3$Sn wires, since larger grains were considered outliers and not relevant for the superconducting properties. The radial direction of the sub-elements and therefore the A15 layer direction corresponds to the horizontal axis of most TKD maps, except for the RRP-Ti-108, APC-3914-48 and APC-3912-084 wires, where it corresponds to the vertical axis due to map or sample rotation.

6.3.1 RRP-Ti-108

TKD was conducted on a lamella of the RRP-Ti-108 wire and grain size distributions and aspect ratios were analysed. Figure 6.3 shows the resulting map after clean-up, where each grain is displayed in a different colour. In the same figure, a grain size map is shown in which the grains were coloured according to their diameter. Figure 6.4 shows the statistics of the grain size distribution of the RRP-Ti-108 wire. The distinction between number fraction and area fraction that describe grains of a certain diameter is visualized. As the critical current density is determined by the grain boundary density across the current-carrying area, it is proposed that using the area fraction, which describes the proportion of the total sample area occupied by grains of the given diameter, yields the more relevant statistics. It reveals information about the fraction of the sample area which possesses fine grains and therefore the best flux pinning capabilities, thus the fraction of the sample area that is relevant for contributing to improved superconducting properties. For example, if the sample area contains many very fine grains but one large grain occupies the majority of the sample area, this large grain will hardly be visible in the statistics when using number fractions, even though the majority of the sample exhibits poor flux pinning capabilities.

The aspect ratio distribution of the RRP-Ti-108 wire is displayed in Figure 6.4, which is defined as the ratio of the minor grain axis to the major axis. In this case, the distinction between number fraction and area fraction does not lead to considerable differences in the resulting distribution, indicating no grain shape dependence on the grain size. The analysis of grain size distributions and aspect ratios was conducted in the same manner on the remaining standard RRP and PIT Nb$_3$Sn wires, the results are shown in this section and a summary of the results is shown in Table 6.2. The results for the BIN-246 wire can be found in Figure 6.5 and Figure 6.6, for the RRP-Ta-54 wire in Figure 6.7 and Figure 6.8, for the PIT-Ta-114 wire in Figure 6.9 and Figure 6.10 and for the PIT-Ta-192 wire in Figure 6.11 and Figure 6.12.
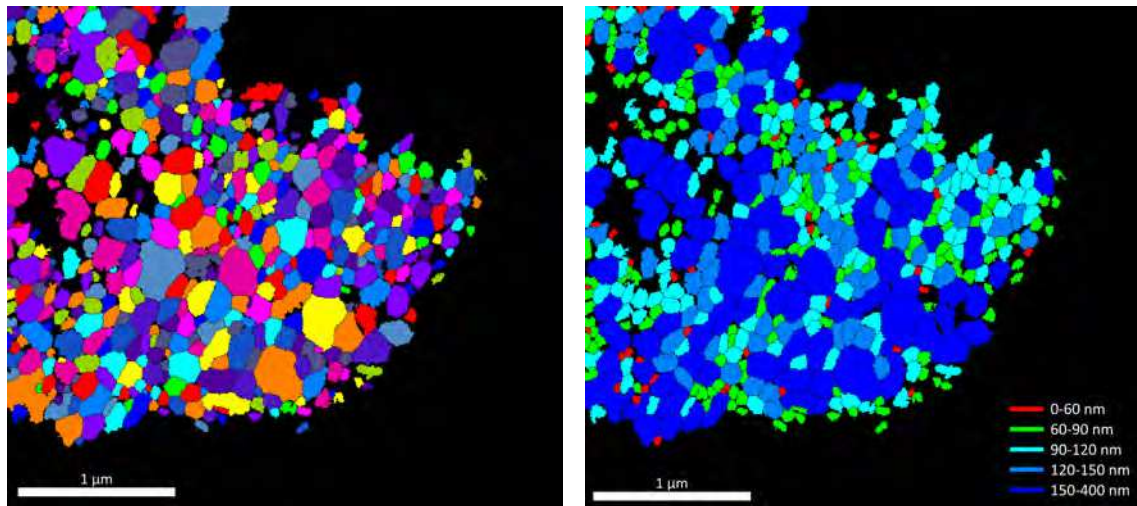
Figure 6.3: TKD map of the RRP-Ti-108 wire where each grain was allocated a different colour (left) and grain size map of the same area (right).
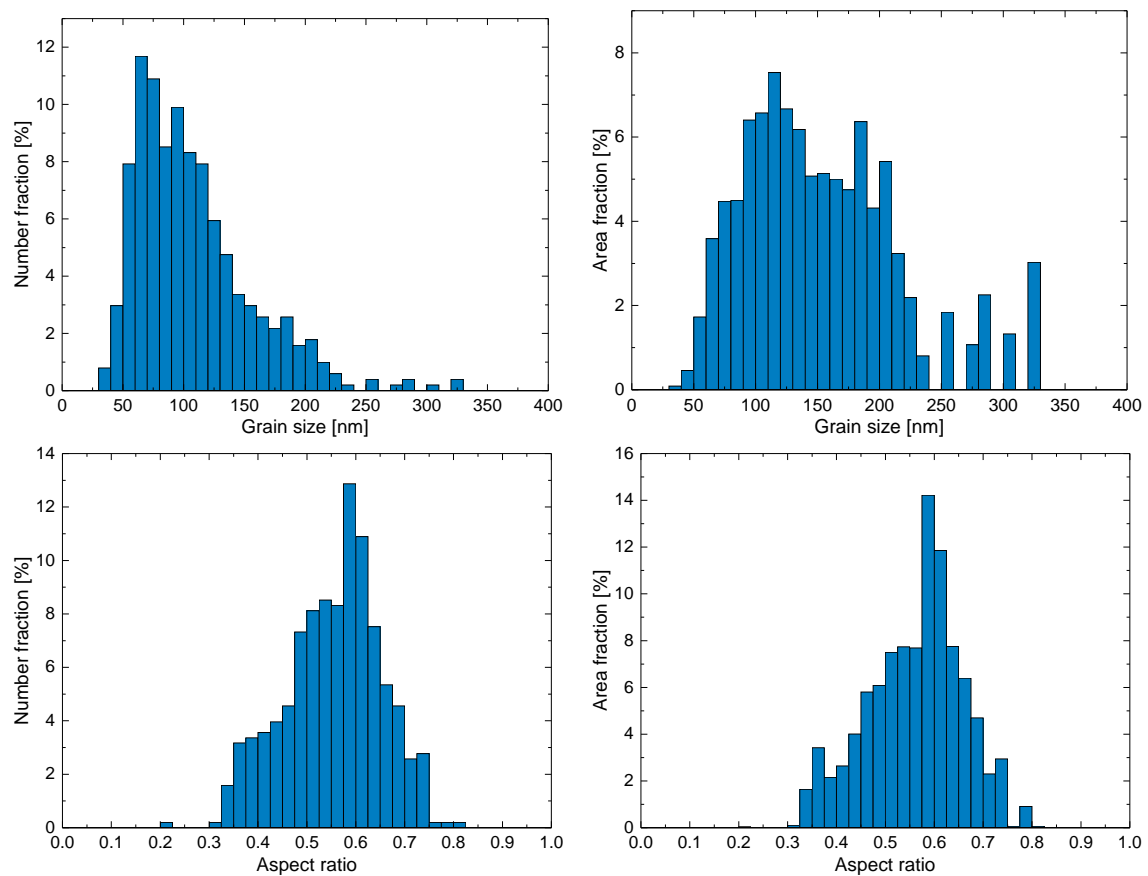
Figure 6.4: Grain size and aspect ratio distribution of the RRP-Ti-108 wire: grain size number fractions (top left), grain size area fractions (top right), aspect ratio number fractions (bottom left) and aspect ratio area fractions (bottom right).

6.3.2 BIN-246
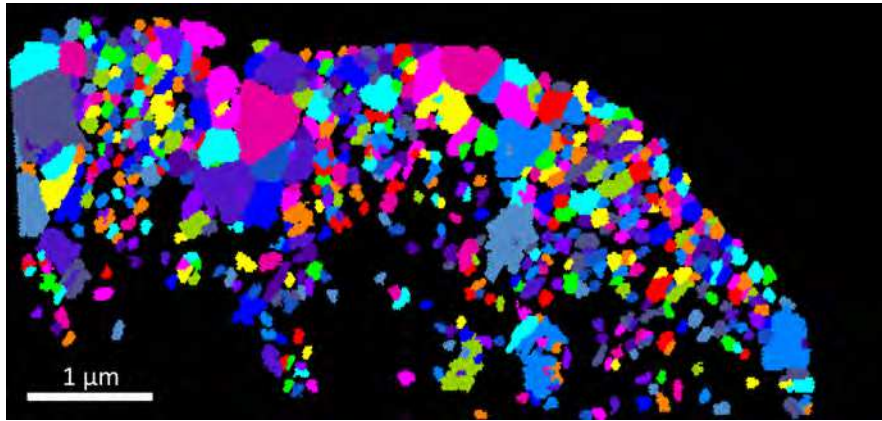
Figure 6.5: TKD map of the BIN-246 wire.
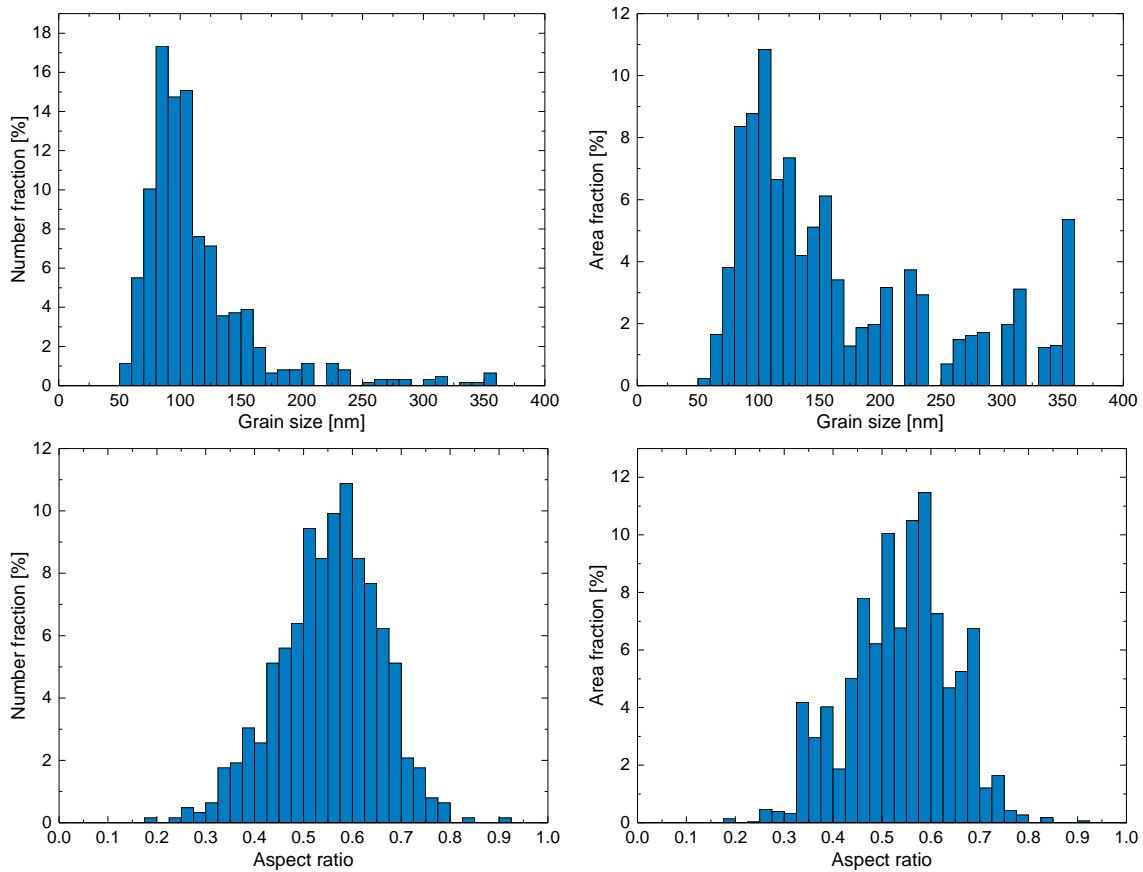
Figure 6.6: Statistics of grain size (top) and aspect ratio (bottom) distribution of the BIN-246 wire.

6.3.3 RRP-Ta-54
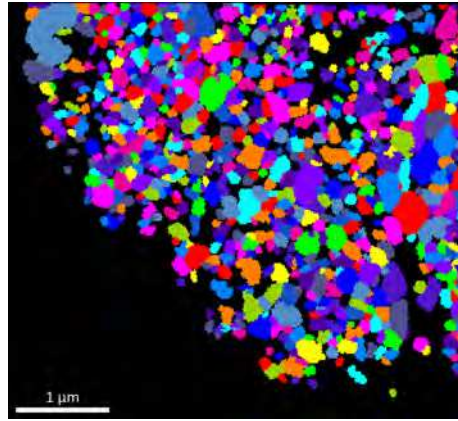
Figure 6.7: TKD map of the RRP-Ta-54 wire.
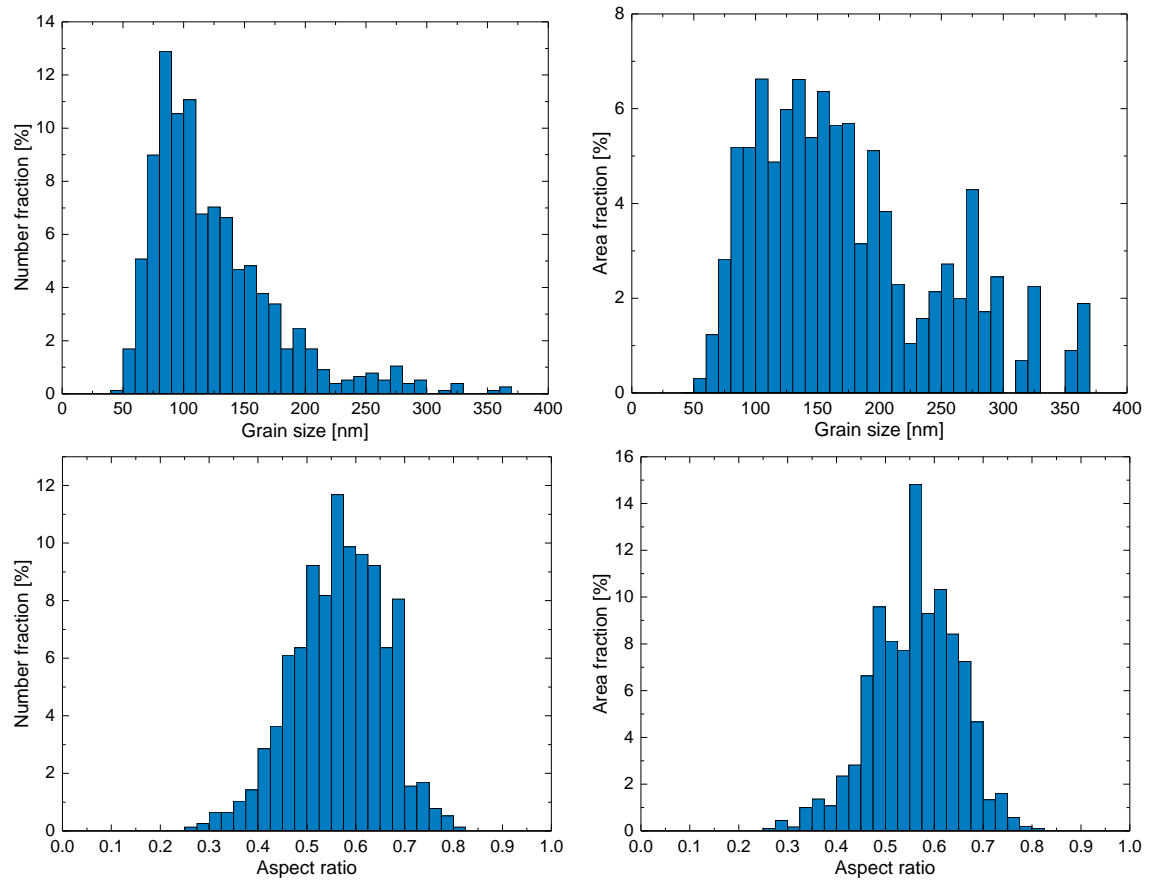
Figure 6.8: Statistics of grain size (top) and aspect ratio (bottom) distribution of the RRP-Ta-54 wire.

6.3.4 PIT-Ta-114
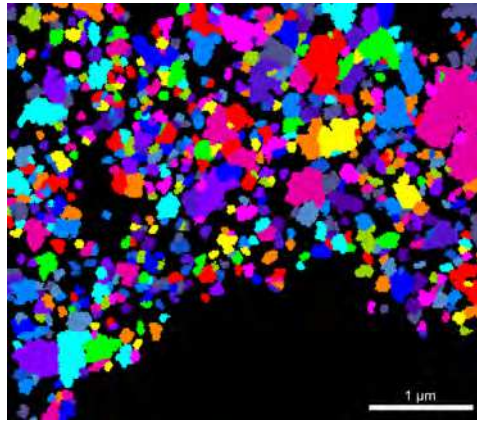
Figure 6.9: TKD map of the PIT-Ta-114 wire.
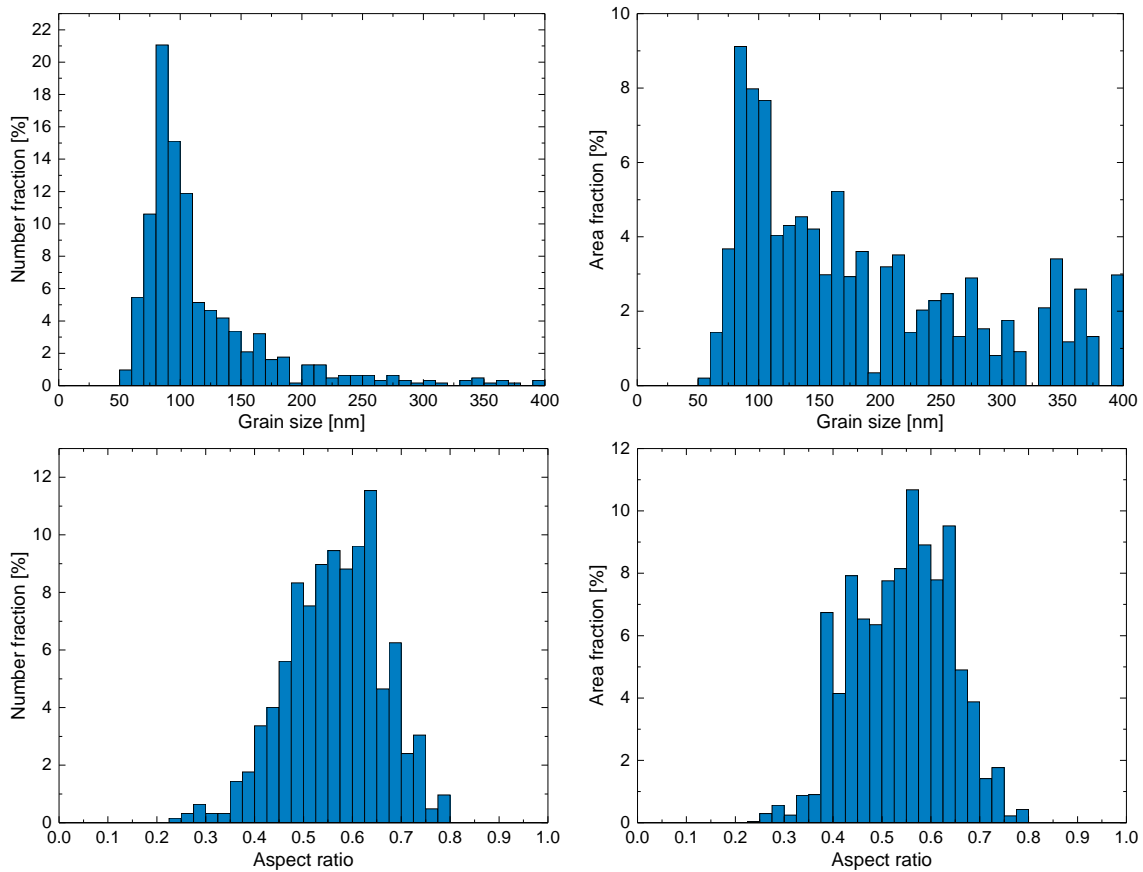
Figure 6.10: Statistics of grain size (top) and aspect ratio (bottom) distribution of the PIT-Ta-114 wire.

6.3.5 PIT-Ta-192
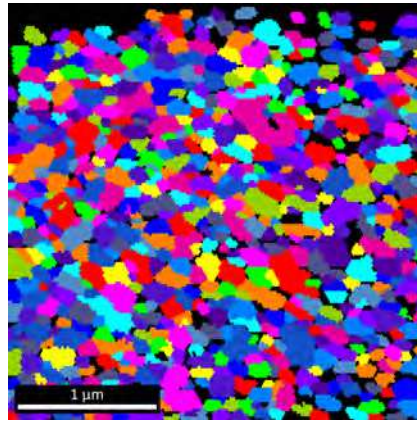
Figure 6.11: TKD map of the PIT-Ta-192 wire.
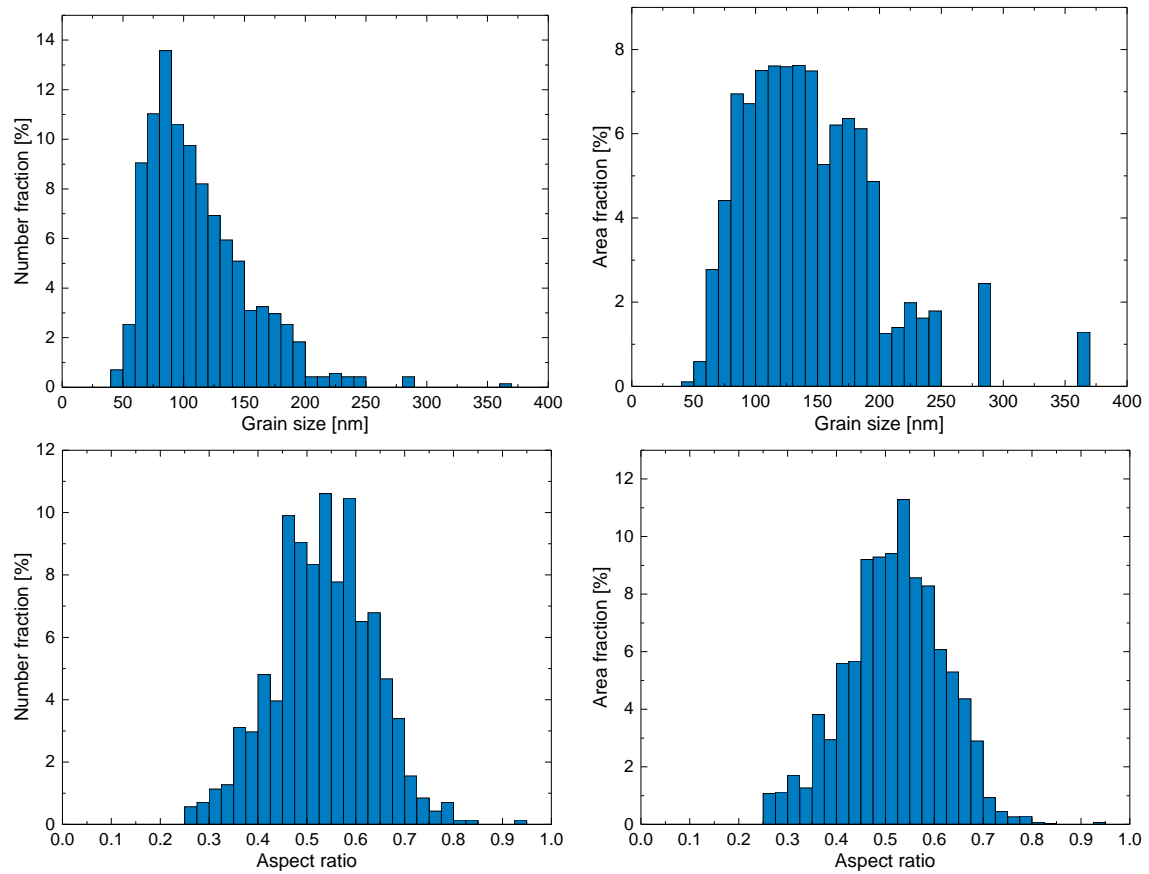
Figure 6.12: Statistics of grain size (top) and aspect ratio (bottom) distribution of the PIT-Ta-192 wire.

6.4 Grain size and aspect ratio of old generation APC wires

TKD investigations were furthermore carried out on Nb_3Sn wires that were manufactured by the novel internal oxidation process which leads to the formation of nano-precipitates. This process can lead to grain refinement, an increase in the flux pinning capabilities and thus the critical current density of the final Nb_3Sn wires. The detailed manufacturing process was described in Chapter 1, together with the literature review. This section shows the results of the investigation of the older generation binary 3600-series APC wires without Ta or Ti additives. Figure 6.13 shows the TKD map of the APC-3607-1 wire, the corresponding statistics can be found in Figure 6.14. The TKD maps of the APC-3657-48 and the APC-3682-48 wires can be found in Figure 6.15 and Figure 6.17, respectively, the corresponding statistics of the respective wires are displayed in Figure 6.16 and Figure 6.18. The results are summarized and compared with the other wires in Table 6.2.

6.4.1 APC-3607-1
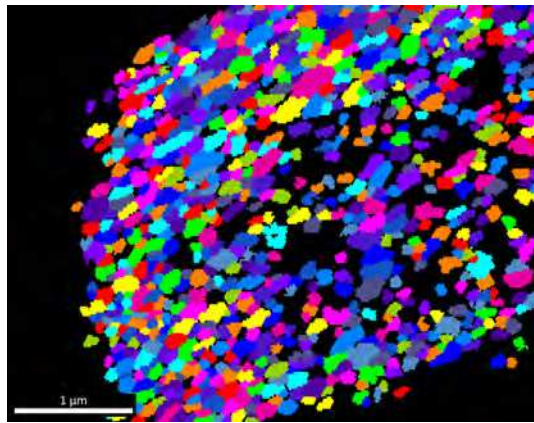
Figure 6.13: TKD map of the APC-3607-1 wire.
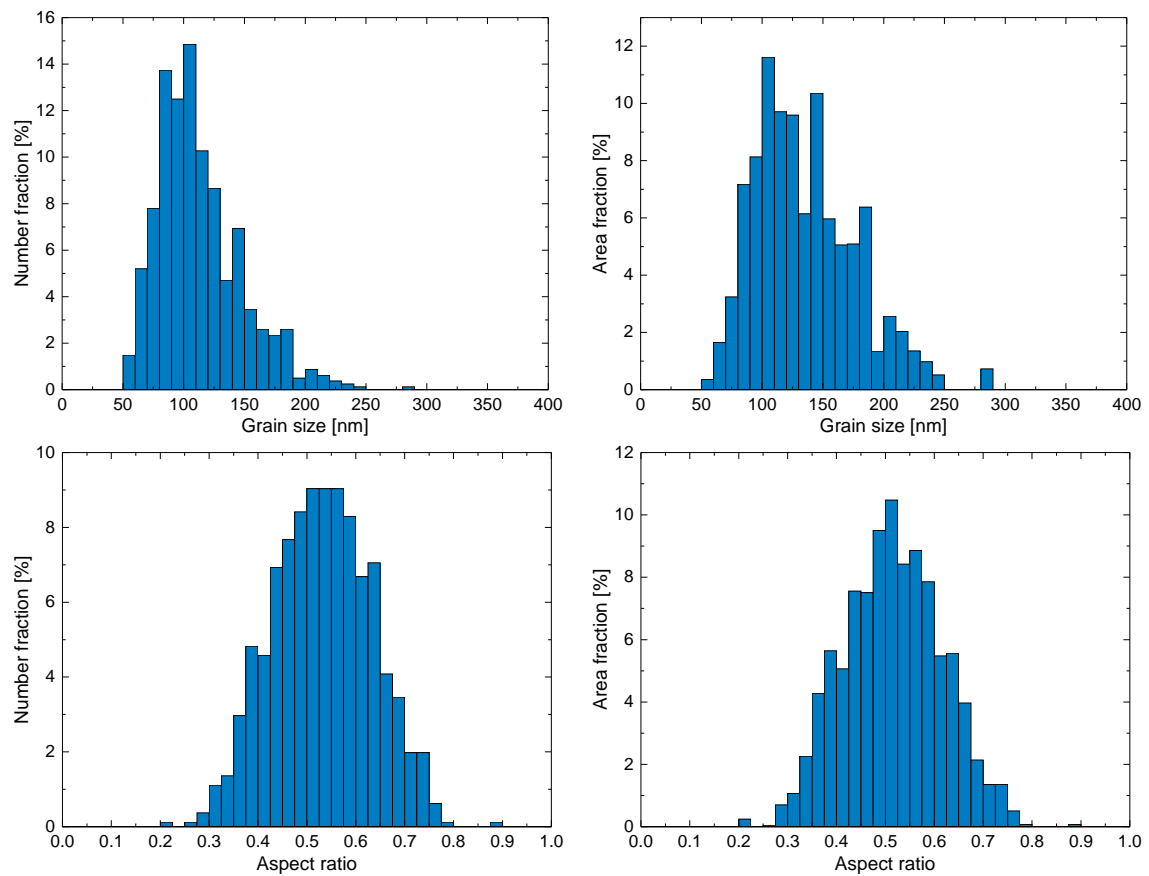
Figure 6.14: Statistics of grain size (top) and aspect ratio (bottom) distribution of the APC-3607-1 wire.

6.4.2 APC-3657-48
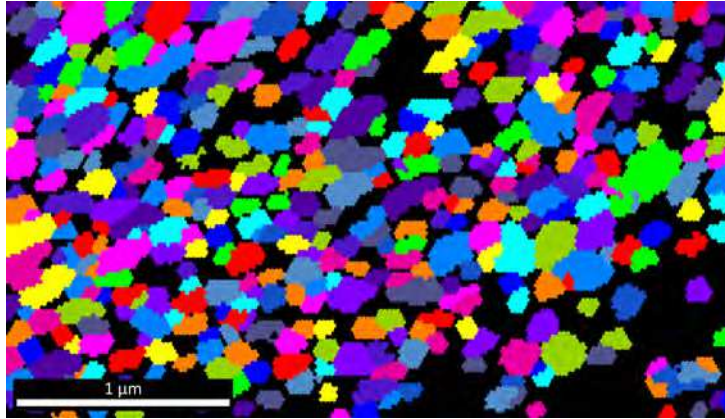
Figure 6.15: TKD map of the APC-3657-48 wire.
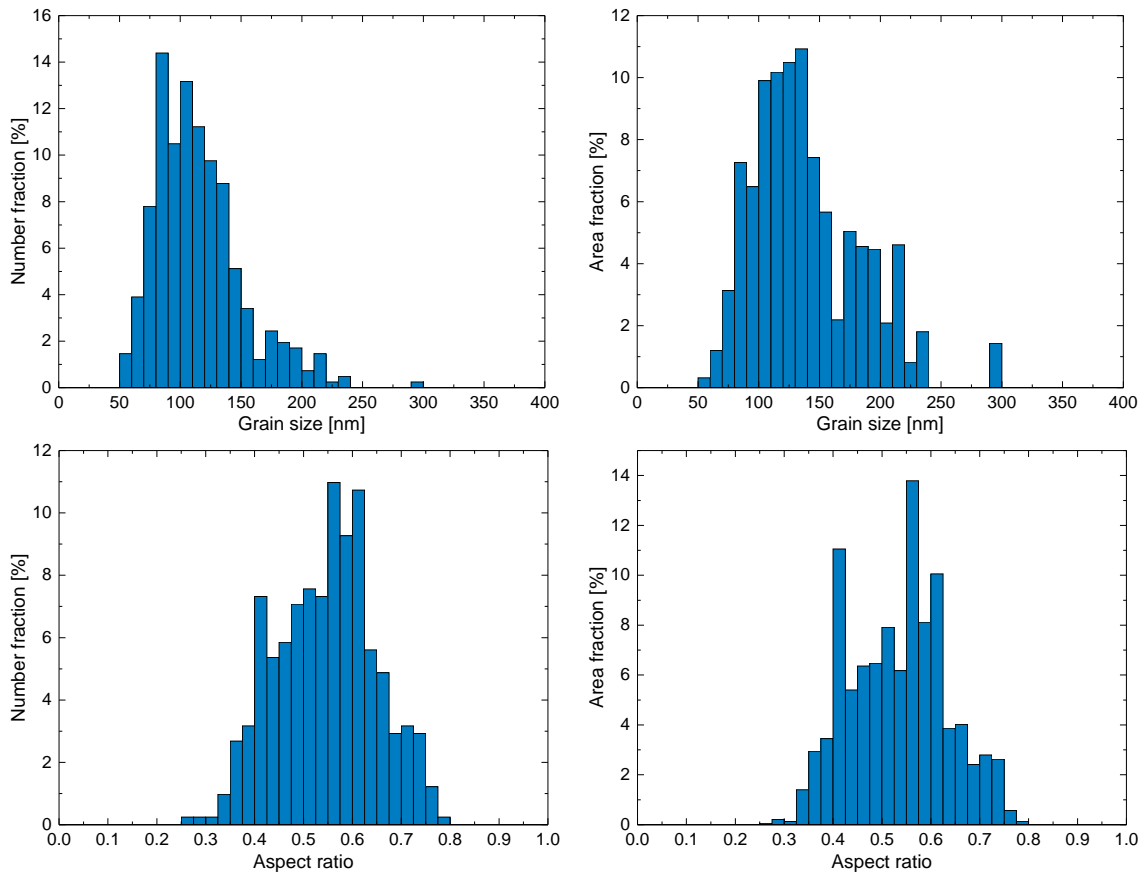
Figure 6.16: Statistics of grain size (top) and aspect ratio (bottom) distribution of the APC-3657-48 wire.

6.4.3 APC-3682-48
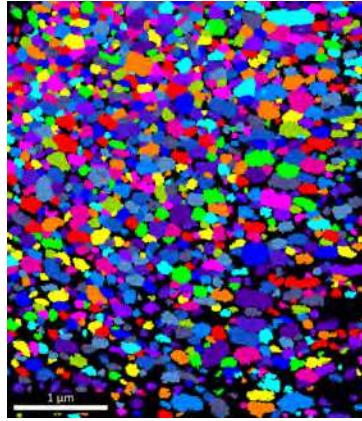
Figure 6.17: TKD map of the APC-3682-48 wire.
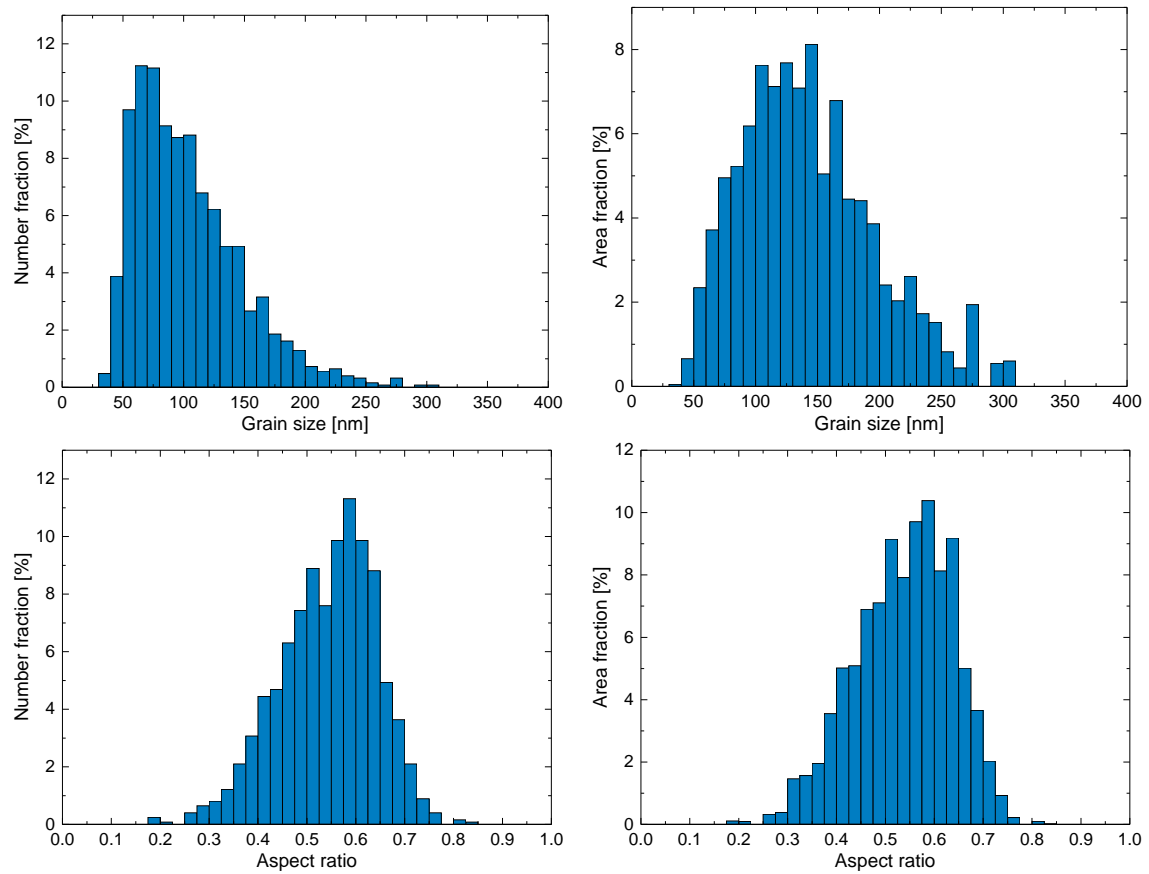
Figure 6.18: Statistics of grain size (top) and aspect ratio (bottom) distribution of the APC-3682-48 wire.

6.5 Grain size and aspect ratio of new generation APC wires

This section shows the results of the TKD investigations on the newer generation ternary 3900-series APC wires that contain Ta additions. A TKD map of the APC-3912-071 wire can be found in Figure 6.19 where each grain was coloured differently. The same figure shows a grain size map where the grains were coloured according to their diameter. While some large grains can be found, the majority of the grains possess small diameters of around 45 nm as can be seen in the grain size distribution shown in Figure 6.20. In comparison with Figure 6.3, it becomes apparent that the population of fine grains with diameters below 90 nm in the APC-3912-071 wire is much higher than in the RRP-Ti-108 wire. The aspect ratios are displayed in Figure 6.20, in which the grains are slightly more elongated compared to the standard RRP-Ti-108 wire. This can be a result of the location of the measured area, since grains near the outside Nb barrier are frequently more elongated as seen in Figure 6.27.

The same investigations were carried out on a sample of the APC-3914-48 wire and the resulting maps of unique grain colour, grain size and misorientation are shown in Figure 6.21. The grain size and aspect ratio distributions of the APC-3914-48 wire can be found in Figure 6.22.

The data of the APC-3912-084 wire can be found in Figure 6.23 and Figure 6.24, the comparison of all investigated APC and standard wires is shown in Table 6.2.

6.5.1 APC-3912-071
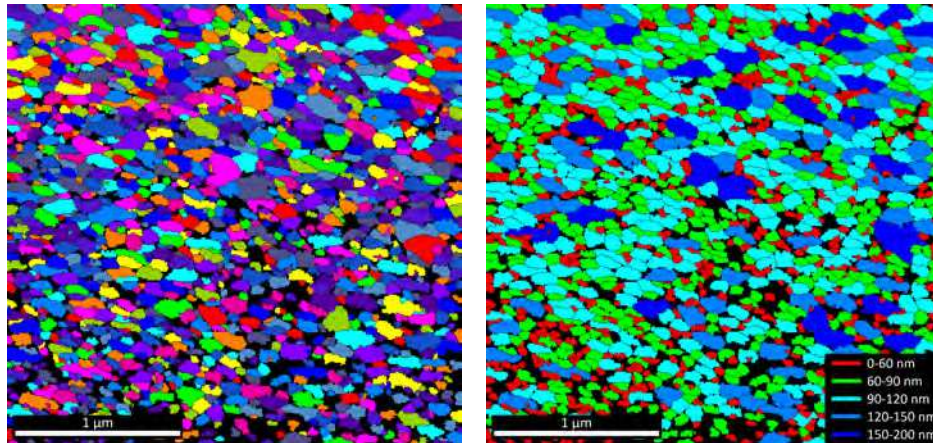
Figure 6.19: TKD map of the APC-3912-071 wire where each grain was allocated a different colour (left) and grain size map of the same area (right).
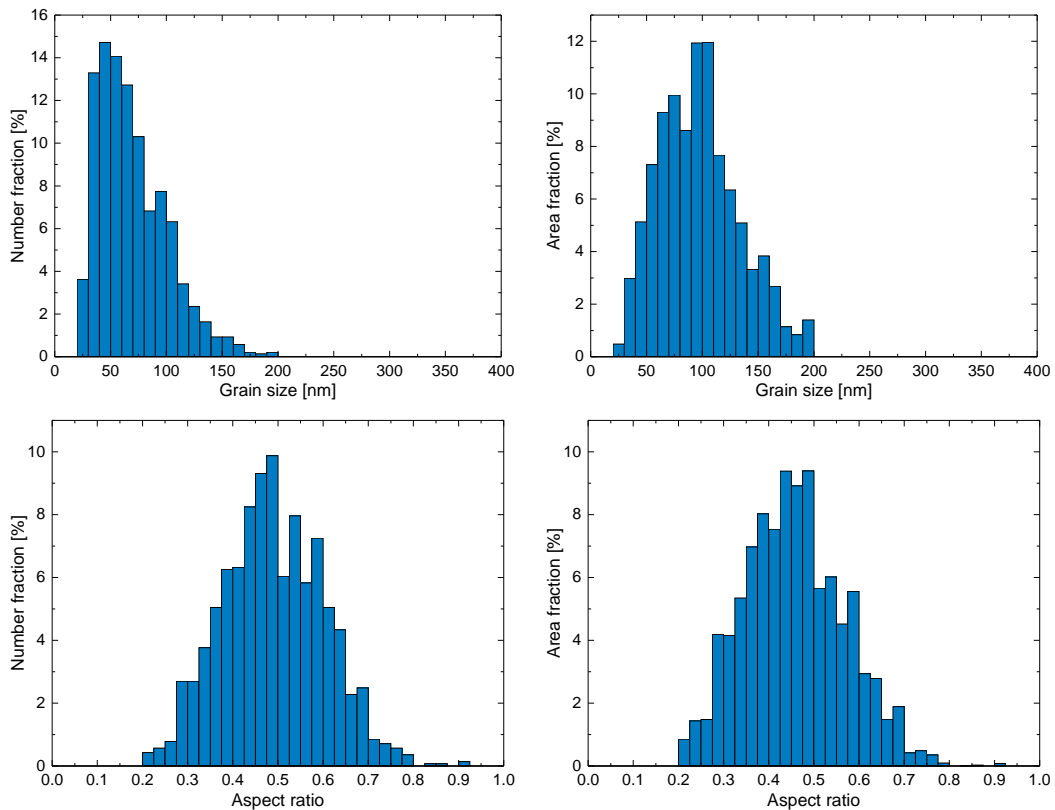
Figure 6.20: Grain size and aspect ratio distribution of the APC-3912-071 wire: grain size number fractions (top left), grain size area fractions (top right), aspect ratio number fractions (bottom left) and aspect ratio area fractions (bottom right).

6.5.2 APC-3914-48
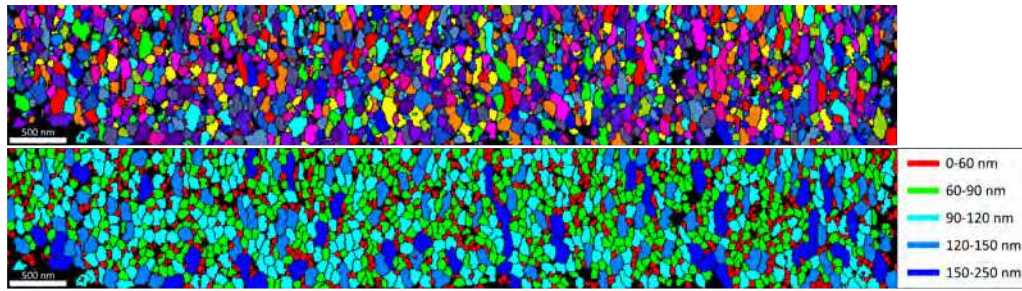
Figure 6.21: TKD map of the APC-3914-48 wire where each grain was allocated a different colour (top) and grain size map of the same area (bottom).
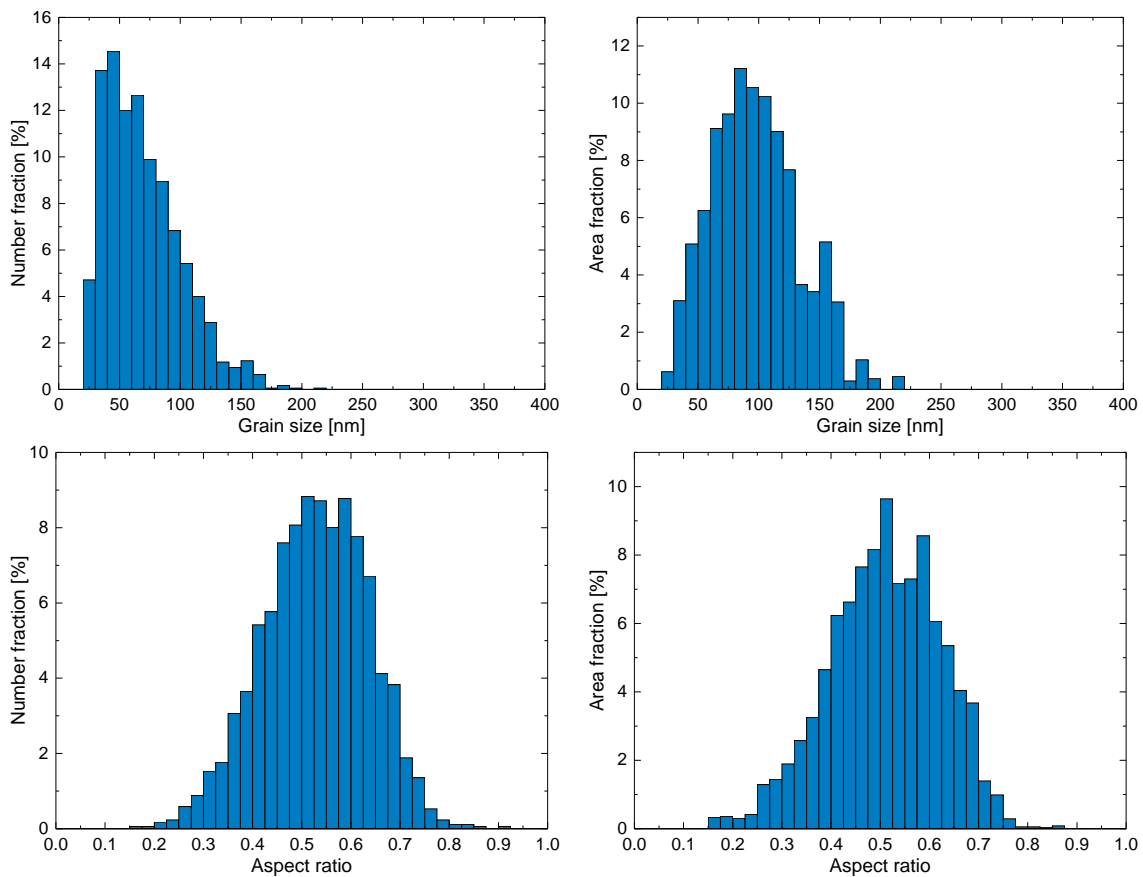
Figure 6.22: Grain size and aspect ratio distribution of the APC-3914-48 wire: grain size number fractions (top left), grain size area fractions (top right), aspect ratio number fractions (bottom left) and aspect ratio area fractions (bottom right).

6.5.3 APC-3912-084
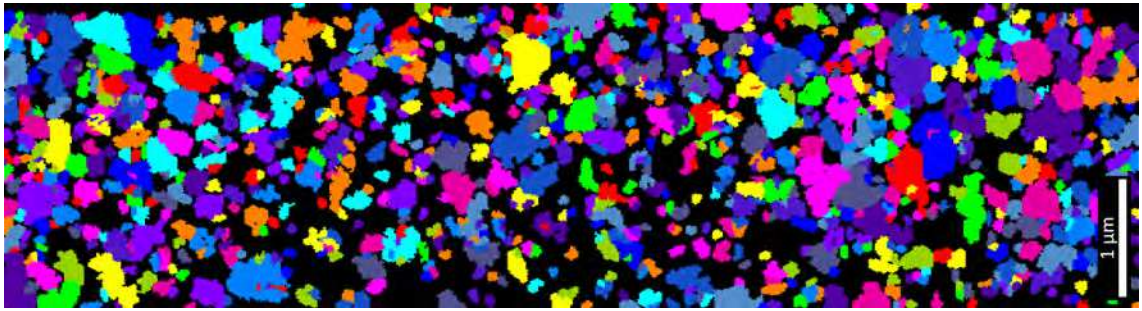
Figure 6.23: TKD map of the APC-3912-084 wire.
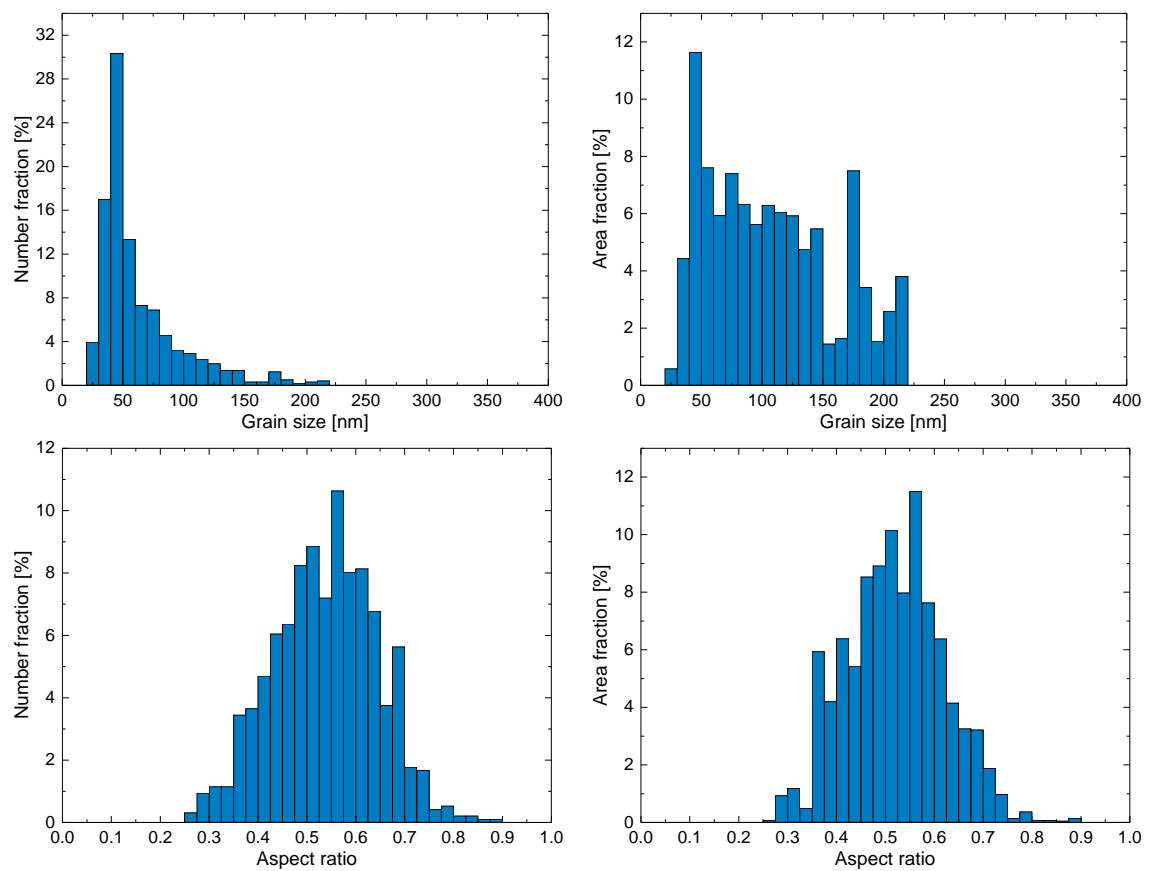
Figure 6.24: Statistics of grain size (top) and aspect ratio (bottom) distribution of the APC-3912-084 wire.

6.6 Summary and comparison between standard and APC wires

A summary of the results of the TKD investigations performed on the different wire types is shown in Table 6.2, where the numerical average (NA) and the area weighted average (AWA) of the grain size is displayed. These averages were calculated according to the formulae

$$GS_{NA} = \frac{1}{N} \sum_{i=1}^{N} d_i, \qquad GS_{AWA} = \frac{\sum_{i=1}^{N} A_i d_i}{\sum_{i=1}^{N} A_i}, \tag{6.1}$$

where N denotes the total number of grains, d_i the diameter of grain i and A_i the area of grain i. In the realistic case of a non-uniform grain size these averages can show significant differences. The area weighted average values of the grain size distributions of the standard wires were found to be in the order of 150 nm–200 nm. The older generation APC wires showed only a minor grain refinement compared to the values of the standard wires, with area weighted average values around 140 nm. In the new generation APC wires, a clear refinement in grain size was determined, where the area weighted average values of the grain size distributions are in the order of 100 nm. The modal values of the number fractions of the APC wires show that the largest fraction of the grains in these wires possess a diameter of about 45 nm, compared to 65 nm in the RRP-Ti-108 wire. Figure 6.25 shows a comparison of the grain size distributions between the standard RRP-Ti-108 and PIT-Ta-192 wires and new generation APC wires, where a clear shift towards smaller values is visible in the APC wires. Another set of wires is compared in Figure 6.26.

The average values of the aspect ratios were calculated in the same manner as the grain sizes in Equation 6.1, by replacing the grain diameters by the aspect ratios, and are displayed in Table 6.2. The average aspect ratios of the grains were found to be comparable in all wires, where most grains are elongated with average aspect ratios of around 0.5. The aspect ratios of the grains in the APC-3912-071 wire showed slightly smaller values. Generally, the average aspect ratio number fractions do not significantly differ from the area fractions, therefore the grain shape appears to be independent of the grain size.

Wire	GS_{NA} [nm]	GS_{AWA} [nm]	AR_{NA}	AR_{AWA}
BIN-246	114 ± 48	166 ± 84	0.55 ± 0.10	0.54 ± 0.11
RRP-Ti-108	108 ± 48	154 ± 64	0.55 ± 0.10	0.56 ± 0.10
RRP-Ta-54	125 ± 52	174 ± 72	0.57 ± 0.09	0.56 ± 0.09
PIT-Ta-114	117 ± 56	185 ± 95	0.56 ± 0.10	0.54 ± 0.10
PIT-Ta-192	112 ± 41	145 ± 55	0.53 ± 0.10	0.52 ± 0.10
APC-3607-1	113 ± 35	136 ± 42	0.53 ± 0.10	0.52 ± 0.10
APC-3657-48	115 ± 36	139 ± 44	0.55 ± 0.10	0.53 ± 0.10
APC-3682-48	104 ± 44	143 ± 54	0.54 ± 0.10	0.54 ± 0.10
APC-3912-071	70 ± 31	97 ± 36	0.49 ± 0.11	0.46 ± 0.11
APC-3914-48	70 ± 31	98 ± 36	0.53 ± 0.11	0.51 ± 0.11
APC-3912-084	63 ± 35	107 ± 53	0.54 ± 0.11	0.52 ± 0.10

Table 6.2: Summary of the TKD results of the investigated Nb_3Sn wires. GS = grain size, AR = aspect ratio, NA = numerical average, AWA = area weighted average. The standard deviations of the distributions are shown.
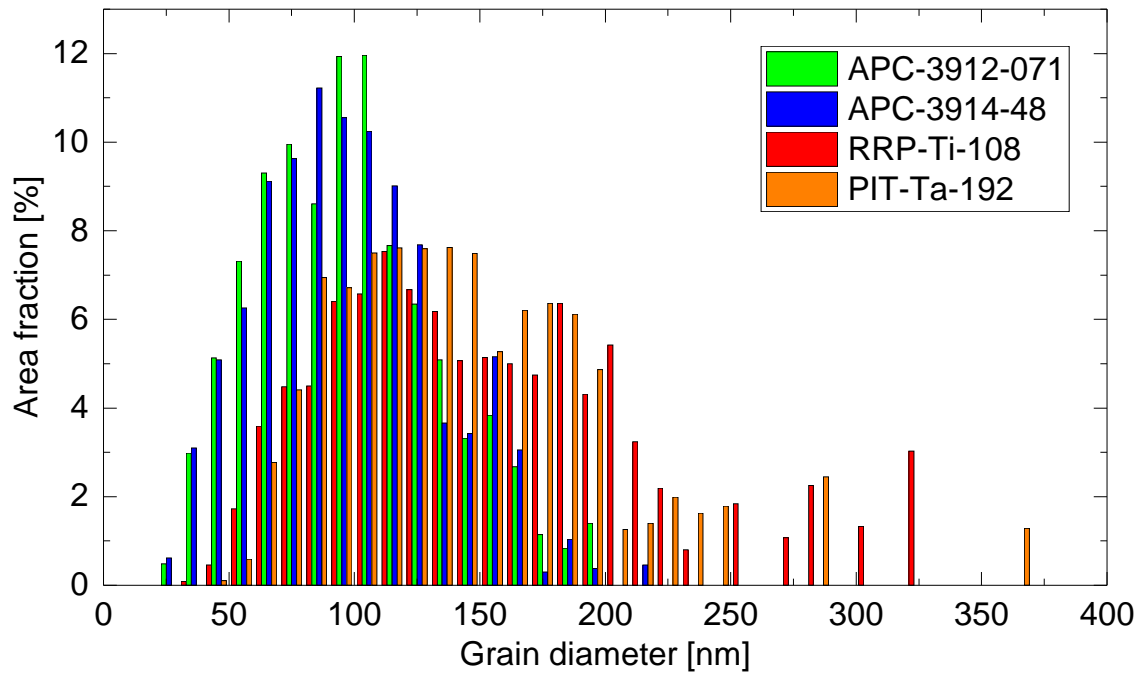
Figure 6.25: Comparison of the grain size distributions of standard and new generation APC wires.
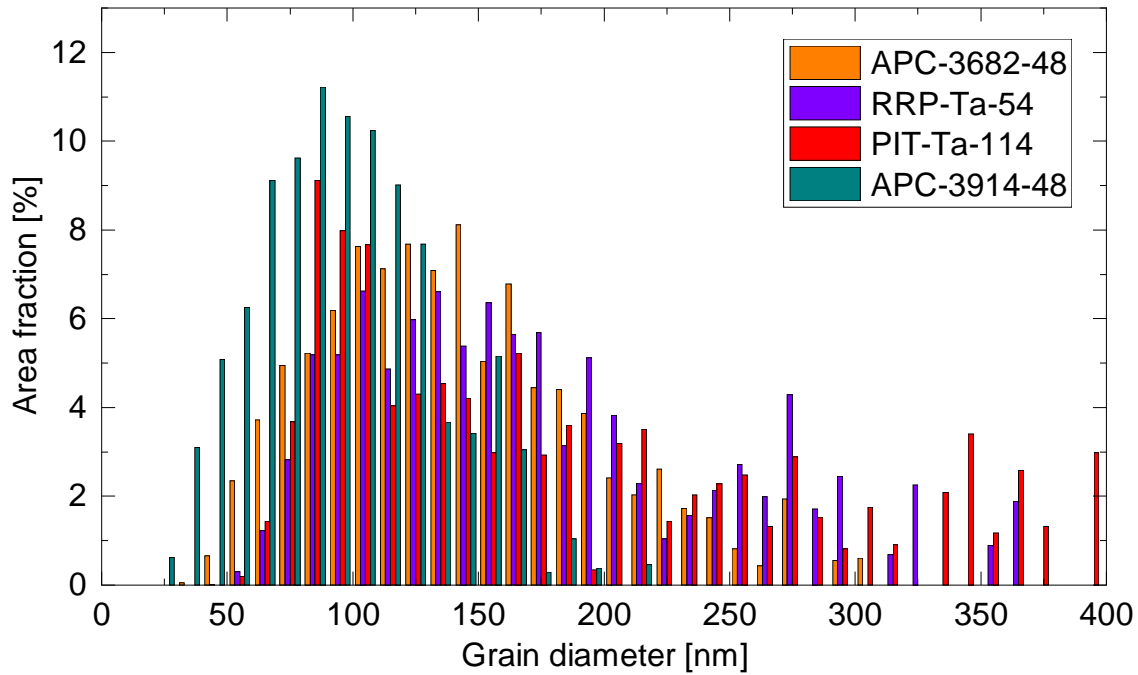
Figure 6.26: Comparison of the grain size distributions of standard, old generation and new generation APC wires.

The results of the investigation of the grain size and aspect ratio distribution in the Nb$_3$Sn wires can be summarized as follows:

1. The grain shape was found to be comparable in all wires, where a majority of the grains are elongated with modal values of the aspect ratios of around 0.5.

2. The grain size distributions of the standard wires showed area weighted average grain sizes in the order of 150 nm–200 nm.

3. Only a minor grain refinement was observed in the older generation APC wires compared to the values of the standard wires.

4. A clear refinement in grain size was determined in the new generation APC wires, where the area weighted average grain size was reduced to about 100 nm.

6.7 Comparison between TKD and conventional methods

The results of the TKD investigations were compared with the standard grain size determination methods as described by the ASTM international standard under designation E112 [75]. Using the linear intercept method, lines of a well defined length are drawn over the grains of an imaged area. The length is divided by the number of counted interceptions by grain boundaries to yield the average grain diameter. Aside from the fact that these conventional methods do not take into account the shape of the grains, another disadvantage is that they simply yield an average grain size value and no information about the distribution.

In the case of non-equiaxed grains, this standard furthermore suggest the preparation of three cross sections per sample, one in each plane, in order to gain holistic knowledge of the grain geometry. Considering the large amount of investigated samples in this thesis, this approach was deemed unreasonable from a time-allocating viewpoint.

The linear intercept procedure was conducted on SEM and transmission electron microscopy (TEM) images acquired of the APC-3912-071 wire that was analysed by TKD. Figure 6.27 shows examples of such images. The application of the linear intercept method on multiple areas of different SEM images of the APC-3912-071 wire yielded an average grain diameter of $(81.5 \pm 5.5)\,\text{nm}$, while the same procedure applied to multiple TEM images of the same thin sample of the same wire that was investigated by TKD in this study led to $(54.8 \pm 2.6)\,\text{nm}$. The corresponding value of the number fraction of this wire obtained by TKD was $(70 \pm 31)\,\text{nm}$ as seen in Table 6.2 and therefore lies between the results of the evaluation from SEM and TEM images. The standard deviation of the intercept method results from the averaging of multiple images, while the standard deviation of the TKD measurements results from the distribution of values, hence the difference in magnitude. One possible explanation for the discrepancy of the average grain size results between the used methods is the fact that the resolution achievable by SEM is lower than by TEM. Small grains might easily be overlooked in SEM images. Additionally, fracture cross sections of wires usually show the whole grain diameters, since the wire preferably breaks along grain boundaries. In samples prepared by FIB, the grains are often not cut through their centre, leading to a potential underestimation of their diameter. Clean-up processes after TKD acquisition might lead to grain growth and therefore larger grain sizes compared to values obtained from TEM images. The results can also depend on the sampled area within the Nb_3Sn layer, which might differ between SEM and TKD investigations.

It has to be noted that the determination of the grain size using all mentioned methods is based on evaluations of two-dimensional cross sections through the samples. In this case, the small grains are underweighted compared to the larger
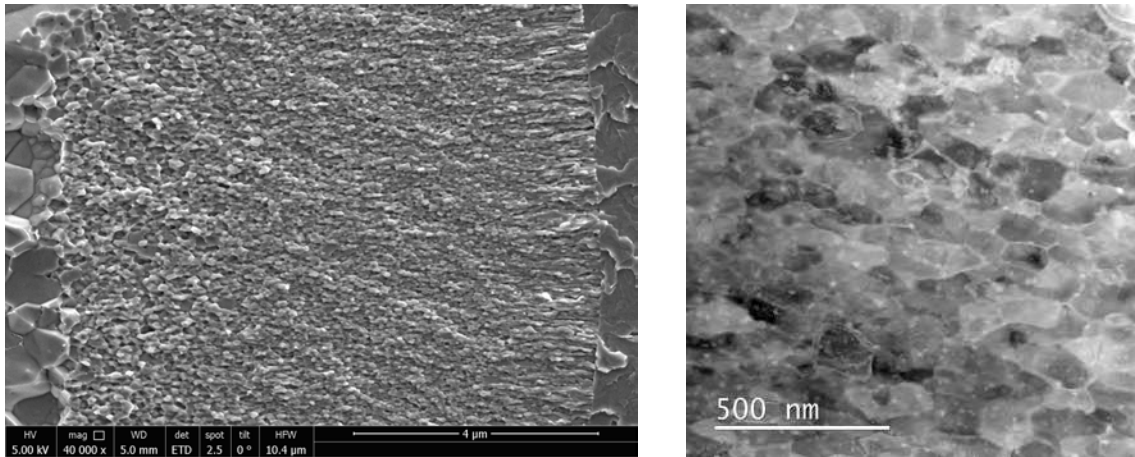
Figure 6.27: SEM image of the fractured cross section (left) and TEM image of the investigated sample (right) of the APC-3912-071 wire.

grains with respect to a three-dimensional distribution. In order to achieve the real three-dimensional distribution, the two-dimensional distribution would have to be additionally weighted by $1/d_i$, although it has to be considered that the grains are not equiaxed.

These results show that while specific methods applied to different areas and images lead to consistent results, the comparison between different methods lead to inconsistent results of the final grain size values, therefore the same method has to be employed for a good comparability between different samples.

6.8 Phase distribution

It was shown that the diffusion mechanisms of Cu during the heat treatment influence the distribution of Kirkendall voids in the wires [112]. This is a result of faster Cu diffusion into the sub-element cores than the Sn diffusion outwards to the Nb. For that reason, the Cu diffusion can be linked to the coarse and fine grained Nb_3Sn formation, even though Cu is not a constituent of the superconducting A15 phase. Thus, the Cu diffusion during heat treatment has a major impact on the microstructure of the final Nb_3Sn wires and a microstructural assessment of the Cu distribution is highly relevant. The segregation of elements of bronze-processed Nb_3Sn wires was studied by atom probe tomography [117], where an increased Cu content was determined at grain boundaries.

The identification of the elemental Cu phase and the analysis of its distribution is also possible using TKD and was conducted on the RRP-Ti-108 wire. Figure 6.28 shows a phase map of this wire, where the Nb_3Sn and Cu phases are displayed in different colours. It becomes apparent that frequent elemental Cu inclusions are located between grains of the Nb_3Sn phase. While single pixels of the Cu phase could be attributed to an inhibited signal quality near grain boundaries, areas of the Cu phase that consist of multiple pixels clearly stem from Cu inclusions.

For evaluation of the grain sizes of the A15 layer, the question arises, if the distinction between the A15 and the Cu phases between the grains has to be accounted for. However, the identification of the Cu phase is often times not unambiguous, since it frequently corresponds to a few pixel at a time and can be mistaken for a bad signal quality at A15 grain boundaries, which are the locations at which Cu inclusions occur. Anyhow, since these Cu inclusions in most cases occupy only a very small area of the specimen, the grain size distribution of the A15 grain is only very minorly affected, thus the influence of the Cu phase on the Nb_3Sn grain size determination can be neglected.

The following sections deal with the evaluation of the grain shape orientation, grain boundary misorientation and texture of the Nb_3Sn wires. The results are shown and discussed particularly for the newest generation ternary APC-3912-071 and APC-3914-48 wires, since they show a significant grain refinement as reported in this chapter are thus highly relevant for technological applications in the future.
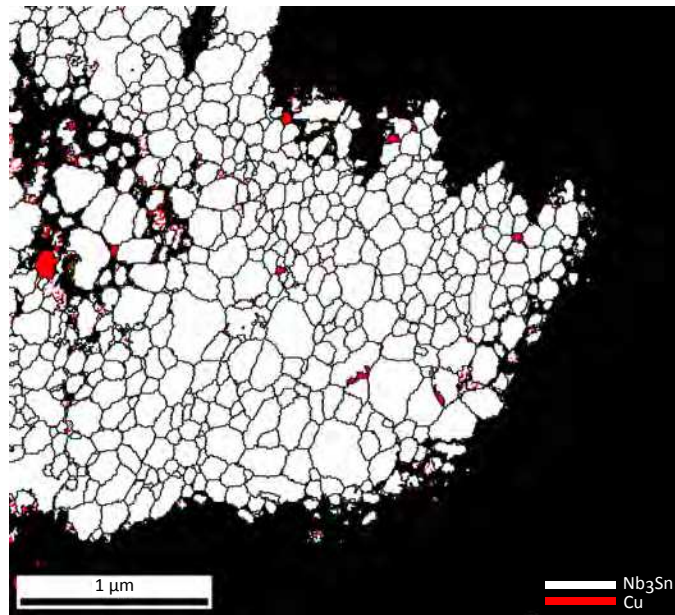
Figure 6.28: Phase map of the RRP-Ti wire.

6.9 Grain shape orientation

The investigation of the grain aspect ratios in this chapter revealed that the grains are commonly elongated with aspect ratios in the order of 0.5. Following this result, the question arises, in which direction with respect to the A15 layer the elliptical grains are oriented. An analysis of the grain shape orientation of the APC-3912-071 and the APC-3914-48 wires is shown in Figure 6.29 and Figure 6.30, respectively. These graphs show the distribution of the angles between the horizontal axis, which corresponds to the radial direction of the sub-elements, and the major axis of the grains. It becomes apparent that the majority of the grains exhibit orientations close to either 0° or 180°, meaning their elongation is parallel to the radial direction of the sub-elements and normal to the wire axis. This direction corresponds to the direction of the diffusion reaction from the centre of the sub-element to the Nb barrier. The distinction between the number fraction and the area fraction for the respective wires does not lead to considerable differences in the distributions, leading to the conclusion that the grain shape orientation is independent of the grain size.
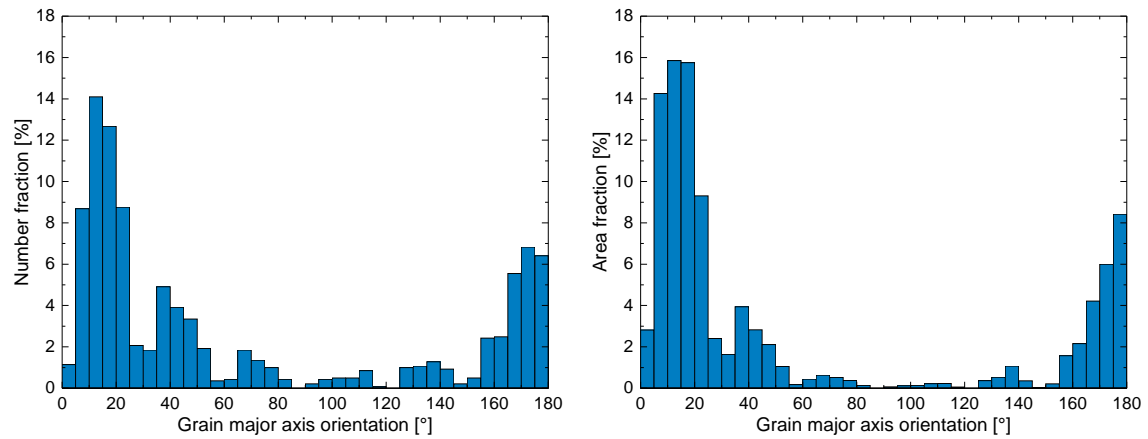
Figure 6.29: Grain shape orientation of the APC-3912-071 wire: number fractions (left) and area fractions (right).
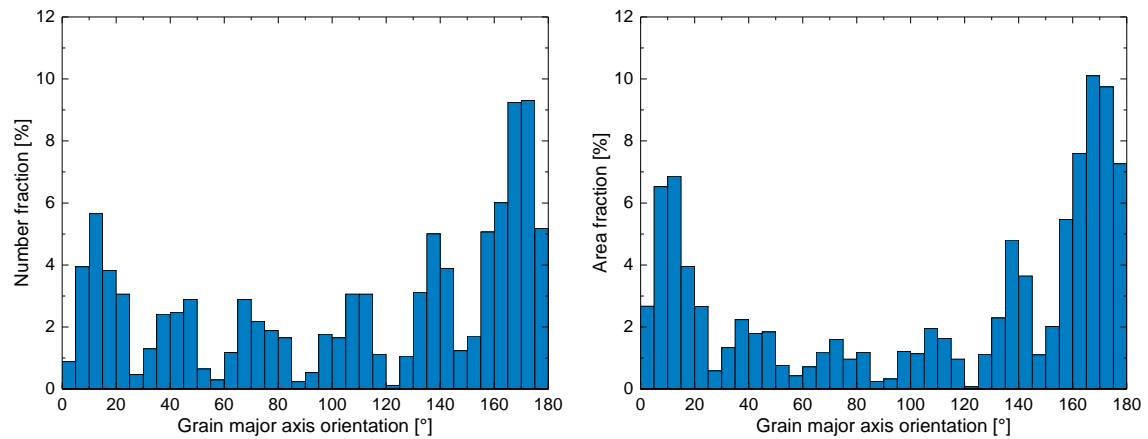
Figure 6.30: Grain shape orientation of the APC-3914-48 wire: number fractions (left) and area fractions (right).

6.10 Grain boundary misorientation

It was suggested that larger grain boundary misorientation angles in Nb_3Sn lead to a higher pinning force at the grain boundaries [152]. Therefore, an orientation distribution with many high-angle boundaries might be beneficial for improving grain boundary pinning and achieving a higher J_c. An analysis of the grain boundary misorientation of the RRP-Ti-108 wire is shown in Figure 6.31, where the grain boundaries were coloured based on their misorientation and from which it can be concluded that the misorientations span a wide range. Figure 6.31 also shows the distribution of the correlated grain boundary misorientation of the RRP-Ti-108 wire.
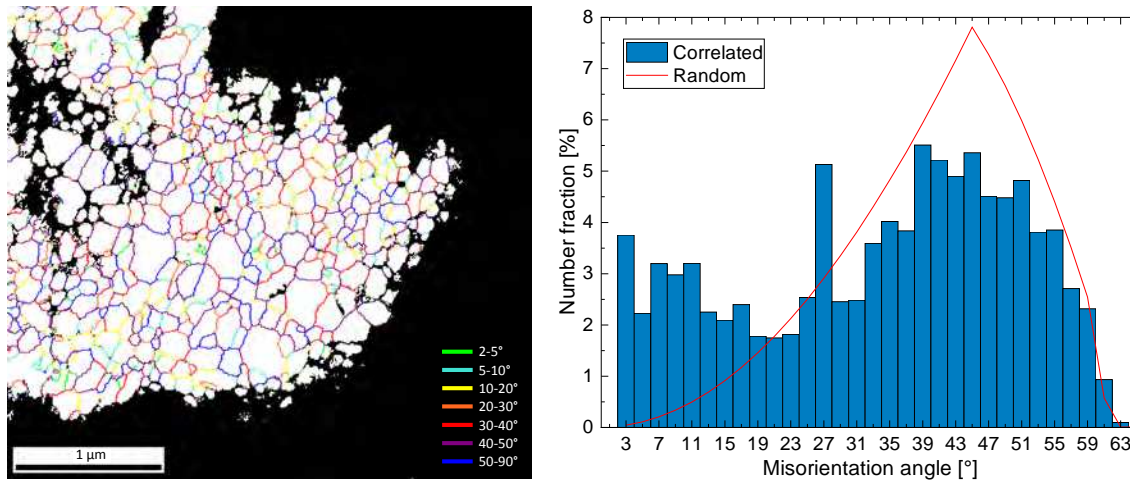
Figure 6.31: Grain boundary misorientation map (left) and distribution of the grain boundary misorientation (right) in the RRP-Ti-108 wire.

The grain boundary misorientation map of the APC-3912-071 wire is shown in Figure 6.32, the one for the APC-3914-48 wire in Figure 6.33. The distributions of misorientation angles in the APC-3912-071 and APC-3914-48 wires are displayed in Figure 6.34, where the correlated and uncorrelated data of the experiments are plotted as well as the distribution of randomly oriented grains in a cubic system that was derived by Mackenzie [90, 93]. In the correlated statistics, only the orientation between grains that share a boundary is considered, while in the uncorrelated statistics, the orientation between all grains in the mapped sample area is calculated. It is clearly visible that the uncorrelated statistics are reasonably well described by the random distribution, while the correlated statistics show a sharp peak at a misorientation angle of around 27°. The same peak was observed in all our investigated Nb_3Sn wires, including the RRP-Ti-108 wire, and in an EBSD investigation of Nb_3Al in [145], where the authors attributed this peak to the coincidence site lattice (CSL) Σ 13b boundary, which corresponds to a misorientation angle of 27.8°. When comparing with known CSL boundary tables of cubic systems [62], the other boundaries that fit the observed peak reasonably well are the Σ 17a boundary with an angle of 28.1°, the Σ 43b boundary with an angle of 27.9° and the Σ 45a boundary with an angle of 28.6°. The analysis of these CSL boundaries using the OIM software revealed that while all those boundaries contribute to our observed peak near 27°, the highest fraction belongs to the Σ 17a boundary. The peak near 38° stems from the contributions of the Σ 7 boundary at 38.2° and the Σ 9 boundary at 38.9°, the peak near 44° from the Σ 21b boundary at 44.4°. The peaks at very low angles partly stem from the small grain tolerance angle of 1° that was chosen for the evaluation of these measurements. This parameter influences the grain size, where higher values lead to larger grain sizes, since neighbouring grains are then often merged to one larger grain.

It was suggested that stacking faults are responsible for the CSL boundary forming

during the heat treatment process [145]. The correlated misorientation distribution of a bronze processed wire on the other hand, was shown to follow the random distribution without such a peak [116].
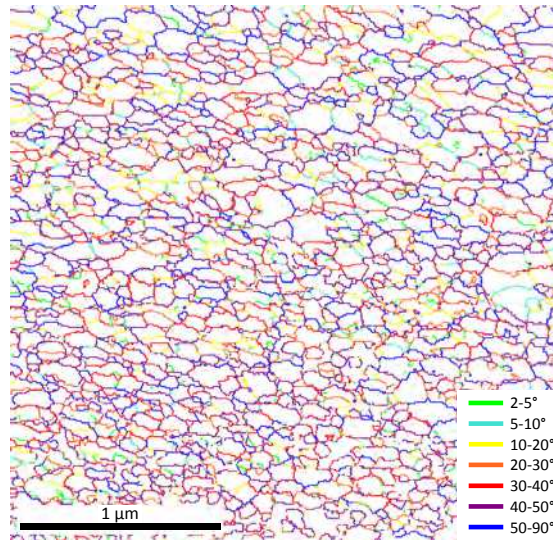
Figure 6.32: Grain boundary misorientation map of the APC-3912-071 wire.
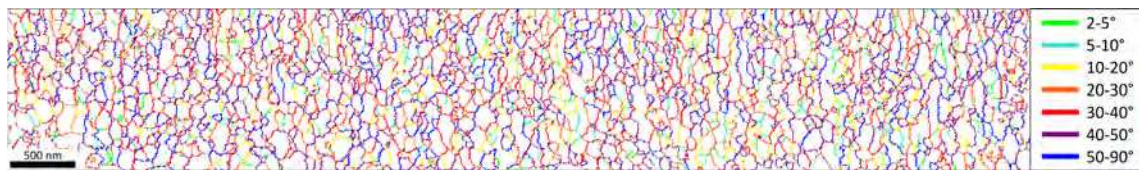
Figure 6.33: Grain boundary misorientation map of the APC-3914-48 wire.
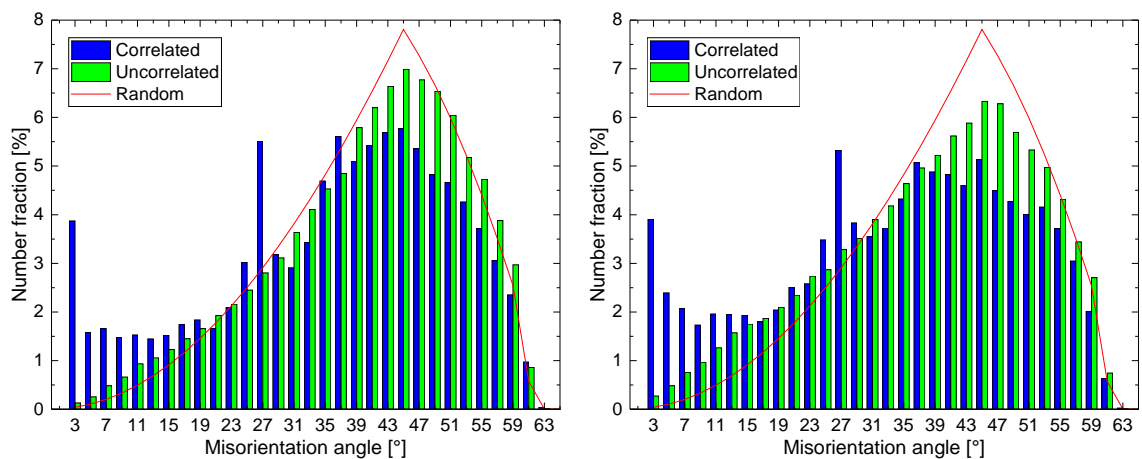
Figure 6.34: Distribution of the grain boundary misorientation in the APC-3912-071 wire (left) and the APC-3914-48 wire (right).

6.11 Texture

The texture of PIT and RRP wires was investigated by EBSD in [121]. Due to the differences in the manufacturing process, the grains in the PIT wire were preferably oriented in a ⟨110⟩ direction with respect to the wire axis, while in the RRP wire, a preferred ⟨100⟩ orientation parallel to the axis was observed. It was suggest that the grain orientation might impact the dependence of J_c on the strain sensitivity and thus explain the differences between the processing routes. Additionally, different grain orientations lead to different stress after applied strain and therefore influence the irreversible strain limit.

These results of the preferred grain orientations were confirmed in the present study on different PIT and RRP wires (not shown here). The investigation of the APC wires, however, revealed differences in the orientation compared to standard wires. Figure 6.35 shows the stereographic pole figures of the APC-3912-071 wire and Figure 6.36 the ones of the APC-3914-48 wire, where the ⟨100⟩, ⟨110⟩ and ⟨111⟩ directions are plotted. These pole figures were rotated so that the Nb$_3$Sn wire axis corresponds to the axis that lies normal to the plane of the pole figure. It becomes apparent that in APC wires the majority of the grains show a preferential ⟨111⟩ orientation along the wire axis, contrary to the results of the RRP and PIT wires. The grains of the APC-3912-071 wire that are oriented in a ⟨100⟩ direction additionally seem to exhibit a preferential in-plane orientation, which might result from a lack of statistics due to a limited number of investigated grains.
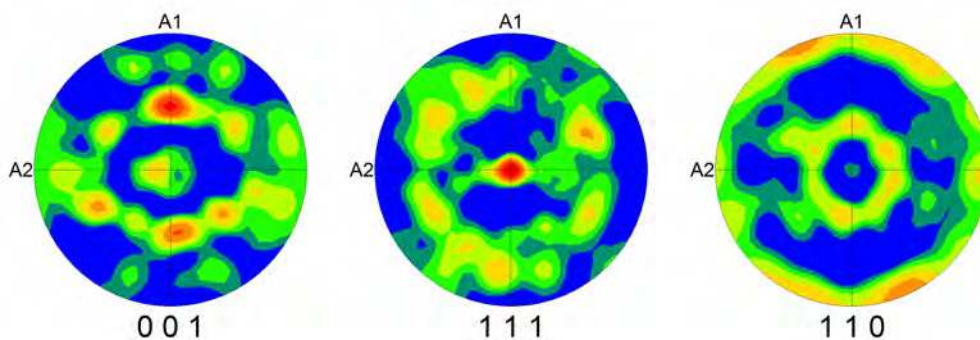
Figure 6.35: Stereographic pole figures of the Nb$_3$Sn grains in the APC-3912-071 wire showing a preferential ⟨111⟩ orientation. Blue: low intensity of <0.78 times random. Red: high intensity of >3.48 times random. Maximum intensity: 4.46 times random.
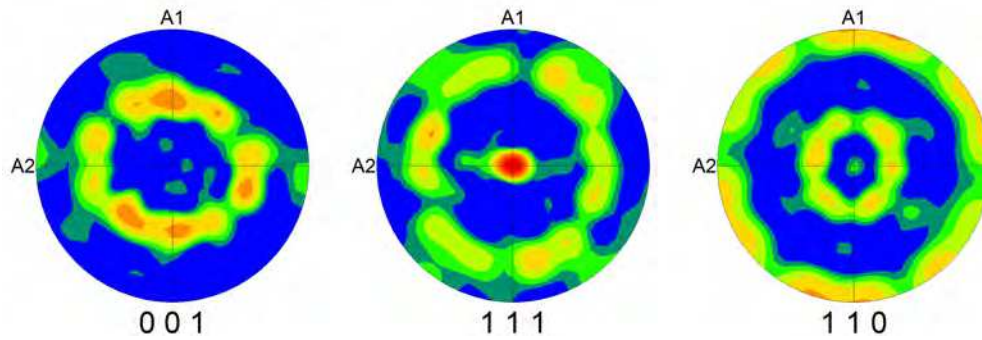
Figure 6.36: Stereographic pole figures of the Nb$_3$Sn grains in the APC-3914-48 wire showing a preferential $\langle 111 \rangle$ orientation. Blue: low intensity of <0.72 times random. Red: high intensity of >5.34 times random. Maximum intensity: 7.46 times random.

6.12 Conclusions of TKD analyses

The application of transmission Kikuchi diffraction for the assessment of the grain geometry of various Nb$_3$Sn wires was demonstrated. The obtained grain size distributions of the different wires were compared to each other as well as to the values assessed by conventional grain size determination methods from SEM and TEM images.

The advantages of TKD include the comparability of the results, creating a solid foundation for the grain size analyses in Nb$_3$Sn wires. Additionally, the extraction of additional information about phase distribution, grain aspect ratio, grain boundary misorientation and grain orientation is straightforward and was demonstrated in this study. Finally, TKD provides the advantage of a high spatial resolution of 5 nm–10 nm, offering the possibility of resolving extremely small grains as present in new generation APC Nb$_3$Sn wires.

The drawback of TKD is among others the time-consuming specimen preparation which requires the fabrication of 100 nm thin lamellae. Moreover, the investigation is limited to rather small specimen areas at a time and involves long mapping times. The analysed plane through the sample in most cases does not cut through the centres of the grains, potentially underestimating the grain size. Clean-up routines on the other hand may introduce artefacts and lead to an overestimation of the grain size due to the reallocation of unindexed pixels.

The results of the TKD investigations on Nb$_3$Sn wires can be summarized as follows:

1. The area weighted average grain size value was found to be in the order of 150 nm–200 nm in standard wires.

2. The analysis of old generation APC wires revealed only a minor grain refinement compared to standard Nb$_3$Sn wires.

3. The comparison between standard and new generation APC wires showed a clear refinement of the grain size in the APC wires. A much higher density of fine grains below 90 nm in size was found in these APC wires, where the area weighted average value is about 100 nm. The modal value of the number fraction revealed that the highest population of grains possess a diameter of around 45 nm in the newer APC wires.

4. The grain aspect ratios showed similar values in all wire types of about 0.5 and were found to be largely independent of the grain size.

5. The investigation of the phase distribution in the RRP-Ti-108 wire revealed frequent Cu inclusions between grains of the Nb$_3$Sn phase.

6. The evaluation of the grain shape orientation made apparent that the major axes of the elliptical grains are often orientated along the diffusion direction of the sub-elements, normal to the wire axis.

7. The analysis of grain boundary misorientation angles showed the same peak at around 27° in all investigated wires when using the correlated statistics, which deviates from the random distribution and can mainly be attributed to the Σ 17a coincidence site lattice boundary. When using uncorrelated statistics, the distribution follows the random Mackenzie distribution.

8. Pole figures of the APC wires revealed a preferential $\langle 111 \rangle$ grain orientation along the wire axis, which differs from the results of the RRP and PIT wires, where grains were oriented in the $\langle 100 \rangle$ and $\langle 110 \rangle$ directions, respectively.

This study demonstrates that transmission Kikuchi diffraction is a suitable method for microstructural grain investigations of Nb$_3$Sn superconductors, which allows for a better comparability of grain size distributions and furthermore provides additional useful statistics about phase distribution, grain aspect ratio, grain boundary misorientation and preferred grain orientation. The application of the TKD technique on Nb$_3$Sn superconductors is especially useful for the investigation of new generation APC wires and thus supporting the FCC project, where a pinning force increase through grain refinement is required and grain sizes show values close to the resolution limit of conventional methods.

In Chapter 4 it was shown that the density of precipitates is much higher in the newer generation APC wires compared to the older generation ones. From the results of the TKD analysis in this chapter it became apparent that also the grain

refinement is much improved in the newer generation wires. The superconducting properties of 3900-series APC wires were recently investigated [169]. Due to both the grain refinement and presumably also the increase in precipitate density, the newer generation APC wires show a great increase in J_c and achieved the FCC specification in short samples. Additionally, the 3900-series wires contain the addition of Ta, contributing to the increase in B_{c2}, and therefore J_c.

7 Irradiation experiments and resulting defect structure

This chapter revolves around the investigation of artificial pinning centres in Nb_3Sn that were created by irradiation with high-energy particles. At the beginning, an extensive literature review will be presented, where the influence of various forms of irradiation on Nb_3Sn wires will be discussed. Subsequently, the conducted irradiation experiments and examination of the induced defects will be shown. In the present study, Nb_3Sn wires were irradiated with fast neutrons in a research reactor and the resulting microstructure was investigated by means of TEM in order to gain information about the nature, size and density of the pinning sites and their correlation with the macroscopic J_c.

7.1 Introduction

The study of irradiation effects in superconductors is important for various reasons. The wires used for accelerator magnets in the future will be subjected to substantial irradiation doses. In order to be able to predict the degradation of the superconducting properties over the accelerator lifetime, an understanding of the behaviour under these circumstances is of great relevance. Furthermore, irradiation of superconductors can have a positive impact on the J_c performance, up to a certain value [136]. Understanding the underlying mechanisms could allow for improved manufacturing techniques of high-performance wires in the future.

The investigation of the behaviour of Nb_3Sn wires after exposure to radiation is relevant to technological applications such as particle accelerators and nuclear fusion magnets. This knowledge is for instance required in order to estimate the life time of new HL-LHC quadrupole magnets which are expected to be exposed to substantial radiation doses [12].

The irradiation of metals and compounds frequently leads to pairs of interstitials and vacancies, which are denoted as Frenkel pairs. Various mechanisms of displacing atoms can occur that include replacement collisions and disordering, which are especially important in compounds, and the recombination of interstitials with vacancies [82].

Most commonly, the amount of radiation damage in irradiated materials is quantified by the unit Displacement Per Atom (*dpa*). It describes the average amount that each atom was displaced from its lattice site, independent of the displacing source [39]. The value of *dpa* is defined as

$$dpa = \frac{A}{V N_A \rho} N_F, \tag{7.1}$$

where ρ is the mass density in $\mathrm{g\,cm^{-3}}$, A the molar mass in $\mathrm{g\,mol^{-1}}$, V the volume in $\mathrm{cm^3}$, N_A the Avogadro number in $\mathrm{mol^{-1}}$ and N_F the number of Frenkel pairs. A Frenkel pair describes a pair of defects, where an interstitial atom and the vacancy are located in close proximity to each other. It is formed when an atom dislocates off its lattice site, forming a vacancy and relocates at an interstitial site.

In case of the *dpa* value being lower than 1, it describes the fraction of atoms that have been displaced once from their lattice site. Equation 7.1 therefore describes the total number of Frenkel defects, in the present case in Nb_3Sn [48].

The advantage of referring to *dpa* over fluence when considering irradiation damage is that it takes into account the damage energy and with that the effectiveness of different particles at inducing damage in the crystal structure. At an energy of 1 MeV, a neutron fluence of $1 \times 10^{22}\,\mathrm{m^{-2}}$ corresponds to a *dpa* of 1×10^{-3} [136].

The wires and magnets based on Nb_3Sn superconductors used for the high luminosity upgrade of the LHC and in FCC machines will be subjected to substantial high energy irradiation of different kinds, such as neutron, proton, electron and photon irradiation, where the neutron irradiation contributes up to $90\,\%$ of the *dpa*. The effects of this irradiation on the superconducting properties over the accelerator lifetimes was analysed in [48]. The changes in T_c, the parameter of atomic order S and the lattice parameter a as well as J_c were described in dependency of the *dpa* value. The increase in J_c at 10 T after irradiation with neutrons by $70\,\%$ and after irradiation with protons by $100\,\%$ was attributed to an increased number of Frenkel pairs that create additional point pinning centres. The distinction between two different types of Frenkel defects was made: Stable Frenkel defects can form to defect clusters with high concentrations of Frenkel defects, while mobile Frenkel defects are caused by single Nb atoms being displaced and causing the movement of adjacent Nb atoms. The total *dpa* values that the quadrupole magnets will be subjected to during the first FCC run at a planned luminosity of $5000\,\mathrm{fb^{-1}}$ and the second run at $30\,000\,\mathrm{fb^{-1}}$ were calculated at 5×10^{-4} and 3×10^{-3}, respectively. The predicted changes of T_c during run 1 and run 2 are in the order of $-0.4\,\mathrm{K}$ and $-1.5\,\mathrm{K}$, respectively, while a J_c increase of around $60\,\%$ is expected during both runs.

The defect density at which J_c is optimized is achieved when the value of the spacing of the defects is close to the spacing of the flux line lattice [49]. It was

found in previous studies that while the change of the critical properties of Nb_3Sn under irradiation depend on the initial state of strain, they are insensitive to the temperature during irradiation [64].

The effect of neutron irradiation on the critical temperature T_c is well known and documented in several publications. According to Sweedler [143], the effect on various A15 compounds is very comparable. The authors quote three different mechanisms that occur due to neutron irradiation in these materials: the interchange of atoms between their lattice sites, the creation of pairs of interstitials and vacancies, and the formation of different elements. As another evidence for this reasoning it was stated that neutron irradiation effects on T_c are small in superconductors that are insensitive to atomic ordering. The largest consequence of the irradiation was stated to be the exchange of lattice sites between atoms. Thus, the critical temperature T_c can directly be related to the Bragg-Williams long range order parameter S, where T_c depends exponentially on S and S depends exponentially on the neutron fluence n.

7.1.1 Studies on neutron irradiation of other materials

Neutron irradiation studies have been performed in the past on different superconducting materials that showed an increase in critical current density due to introduced defects in the crystal structure that are capable of pinning magnetic flux vortices [176].

Neutron irradiation studies on Nb_3Ge were performed in [30], where a decrease in T_c from $20.9\,K$ to $4.4\,K$, a decrease in the long range order parameter S and an increase in the lattice parameter a_0 was reported for a fast ($E > 1\,MeV$) neutron fluence of $3.4 \times 10^{23}\,m^{-2}$. The main reason for the decrease in T_c after irradiation was stated to be atomic disorder on the lattice sites. Similar analyses were conducted in [142], where Nb_3Al was irradiated with fast neutrons. A fast ($E > 1\,MeV$) neutron fluence of $1.4 \times 10^{23}\,m^{-2}$ led to a reduction in T_c from $18.7\,K$ to $1.4\,K$. The irradiation also led to a decrease in S and an increase in a_0. Therefore it was suggested that the highest T_c is achieved in a completely order compound. It was thus stated that the behaviour of different A15 compounds based on Nb under irradiation is very comparable, while the A15 structure remains intact during the reduction in T_c.

Neutron irradiation of MgB_2 has led to amorphous defects the size of around $3\,nm$–$4\,nm$ where a fluence of $1.4 \times 10^{20}\,cm^{-2}$ caused a defect density of $1.63 \times 10^{-2}\,nm^{-2}$. The amorphous regions were surrounded by strain contrast that was induced locally due to lattice deformation and amorphization [92].

Fast neutron irradiation of $YBa_2Cu_3O_{7-\delta}$ single crystals has been conducted in previous studies [49], which has produced defect cascades with sizes between $1\,nm$ and $5\,nm$. The irradiation with fast ($E > 0.1\,MeV$) neutrons at a fluence of $2 \times 10^{21}\,m^{-2}$

resulted in a defect density of $10^{22}\,\mathrm{m}^{-3}$. The irradiation to a fluence of $3 \times 10^{22}\,\mathrm{m}^{-2}$ led to a defect density of about $10^{23}\,\mathrm{m}^{-3}$.

The defects appeared as lobes with black/white contrast parallel or anti-parallel to the $\vec{g}$-vector under dark field diffraction conditions. The defect size was defined as the length of the border between the black and white contrast lobes. It was found that the contrast and visibility of the defects are strongly dependent on the chosen diffraction conditions. In that study, defects showing the black/white contrast were counted as one defect, while those showing weaker or only black dot contrast were counted as half.

The $\vec{g}$-vector (200) was used always used for determining the defect densities in that study, since all visible defects appeared under this condition. The determined defect density was found to increase linearly with neutron fluence. Furthermore, the defect density did not significantly depend on the irradiation temperatures or differences in the neutron spectra. The mean diameter of the neutron defects was stated at $2.5\,\mathrm{nm}$, while the strain fields were found to be about $6\,\mathrm{nm}$ in diameter on average. The defects that were determined after irradiation were still visible 3 months later, leading to the conclusion that the defect cascades show no significant annealing at room temperature.

A comparison between ion and neutron irradiated samples led to the conclusion that neutron irradiation defects are more difficult to verify due to a smaller size compared to the defects produced by ion irradiation. Defects resulting from neutron irradiation were stated to be of a smaller average size than those from ion irradiation and thus not as easily imaged. The defect cascades produced by ion irradiation were previously believed to be amorphous, where also hints were detected that suggest the cascade regions melting and recrystallizing during irradiation. In past ion irradiation experiments, it was found that only about half of the produced defects were visible by TEM imaging due to coherent recrystallization of the others.

It was suggested that the defect structure resulting from ion and neutron irradiation is very comparable in nature. About the nature of the defects induced by neutron irradiation it was suggested that for between $70\,\%$ and $90\,\%$ of the visible defects the atomic structures are amorphous or heavily disordered, consisting of vacancies.

It was concluded that defect cascades are responsible for creating defects that are visible by TEM. Only half of the calculated cascades were observed by TEM due to the defect regions often recrystallizing coherently. The defect density per fluence thus resulted in a value of $5\,\mathrm{m}^{-3}/\mathrm{m}^{-2}$ [49].

Another group reported regions of $2\,\mathrm{nm}$–$7\,\mathrm{nm}$ in size that induced strain contrast in $\mathrm{YBa_2Cu_3O_{7-\delta}}$ after irradiation with fast neutrons. The defect clusters were found to be homogeneously distributed and appeared as dark, strain induced contrast with approximately circular shape under bright field conditions. It was further stated that the effects of neutron irradiation in $\mathrm{YBa_2Cu_3O_{7-\delta}}$ and A15 superconductors show high similarity [84].

The irradiation of Bi-2212 single crystals with fast neutrons led to the formation of cascades with diameters of 3.5 nm and associated strain fields of 5 nm–7 nm that induce diffraction contrast around the disordered regions. In that work, the disordered regions are believed to be amorphous. The cascade density was stated to be $3.7 \times 10^{22} \, \mathrm{m}^{-3}$ per neutron fluence of $10^{22} \, \mathrm{m}^{-2}$ (E > 0.1 MeV). The cascade size was defined as the length of the intersection between the white and black lobes that arise due to the strain field around the defect when using fundamental reflections for imaging. The visibility of the defects was stated to be dependent on the sample thickness and their location along the thickness of the sample [1].

7.1.2 Studies on neutron and proton irradiation of Nb$_3$Sn

Considering Nb$_3$Sn, the effects of neutron as well as proton irradiation on T_c and J_c have been examined. After calculating the *dpa* (displacements per atom), it was found that the decrease in T_c is independent from the particles that were used for irradiation as well its their energy, leading to the conclusion that the alteration of T_c is only dependent on the variation of atomic ordering. The increase in J_c, that stated to be caused by enhanced point pinning due to irradiation-induced defects, showed a similar behaviour regarding *dpa*, albeit through a more complex relationship than for T_c [136].

Fähnle [41] suggested that neutron irradiation of Nb$_3$Sn leads to small defects such as vacancies, interstitials and Frenkel pairs as well as clusters of defects that for example can be caused by displacement spikes or are agglomerates of interstitials. Such clusters may act as additional pinning sites for the magnetic flux lines. An interchange of Nb and Sn caused by a collision can lead to the breaking of the Nb chains, thus leading to atomic disorder and altering the superconducting properties. At low doses of less than $2 \times 10^{22} \, \mathrm{m}^{-2}$ (E > 1 MeV) two types of radiation damage were predicted: defect clusters that act as pinning sites and determine the behaviour of J_c, and atomic disordering that leads to a reduction in the long range order parameter and a change of the superconducting properties. It was calculated that single atomic defects do not have a direct contribution to the total pinning force, but can reduce the length of the Nb chains which influences the superconducting properties.

In another paper Fähnle [42] stated that the division of the linear chains between the Nb atoms is the only mechanism that leads to a reduction of T_c after irradiation. Furthermore, atomic disorder has a high impact on the superconducting properties, strongly depressing T_c, H_{c2} and J_c at fluences greater than $2 \times 10^{22} \, \mathrm{m}^{-2}$ (E > 1 MeV). A homogeneous distribution of defects was found to describe the experimental data better than an inhomogeneous distribution. Additionally, in order to achieve an increase in J_c, it is important that dopants are introduced interstitially instead of substitutionally onto Nb sites in order to avoid a subdivision of the linear Nb chains.

In [134], it was shown that the J_c increase in Nb_3Sn after proton irradiation is comparable between different proton energies. In Ti doped wires, a greater J_c increase was observed compared to the Ta doped wires. It was further found that the same amount of damage is caused in Nb_3Sn wires that are irradiated with protons and neutrons when the neutron fluence is one magnitude higher than the proton fluence.

Proton irradiation of Nb_3Sn wires led to an increase in both J_c and B_{c2} without showing a direct correlation between these parameters, since the J_c enhancement is related to the introduction defect clusters that serve as point-pinning centres and therefore an increase in the pinning force. T_c was found to decrease linearly with proton fluence. The J_c enhancement in Ta alloyed wires was found to be independent of their fabrication techniques and Ti wires showed a higher increase in J_c [135].

In [46], Nb_3Sn was irradiated with protons with an energy of $12\,MeV$ and the change in lattice parameter a, atomic order parameter S and the critical temperature T_c due to the irradiation was determined and compared with data of neutron irradiation studies. It was found that there are large differences between proton and neutron irradiation when only considering the total fluence. However, after replacing the fluences of both irradiation types with the corresponding *dpa* values, the variation of all of those parameters in dependency of the *dpa* after irradiation can reasonably well described by the same curves. Therefore, the number of Frenkel defects in the Nb_3Sn phase induced by irradiation and consequently the variation of a, S and T_c can be considered as independent of the type of irradiation and can be calculated through the *dpa* value. It was furthermore found that higher fluences led to an increase in microstrain and lattice parameter and a decrease in T_c and S.

Neutron irradiation studies of Nb_3Sn irradiated in the TRIGA Mark-II reactor in Vienna are presented in [65]. It was cited that damage due to neutron irradiation occurs in the form of displaced atoms and displacement cascades. The reduction in the long range order leads to a decrease in T_c. The increase in the resistivity leads to an increase in B_{c2}. The critical current density is influenced by both of these mechanisms. A fluence of $5 \times 10^{21}\,m^{-2}$ led to an increase in J_c by $14\,\%$ and a fluence of $10^{22}\,m^{-2}$ achieved a J_c increase by $38\,\%$.

Irradiation studies on the wires examined in this work have been carried out previously. It was found that the pinning force shifted towards higher values after irradiation and the resulting pinning force function can be described by two components, a contribution of the grain boundary pinning and a point-pinning contribution due to irradiation induced pinning centres [12].

The irradiation of a Ti-alloyed RRP Nb_3Sn wire to a fast neutron fluence of $8.9 \times 10^{21}\,m^{-2}$ has led to an increase of the critical current density J_c by around $60\,\%$ compared to the unirradiated wire. It was concluded that this change in J_c was caused by the introduction of point-pinning centres which increase the volume pinning force and shift the peak towards higher fields [13].

A previous irradiation study of binary and ternary RRP and PIT Nb$_3$Sn wires that were irradiated in the TRIGA reactor in Vienna can be found in [47], where the maximum neutron fluence was $1.4 \times 10^{22}\,\mathrm{m}^{-2}$. The peak of the critical current density J_c was not reached at this fluence and therefore located at much higher fluences than in previously investigated Bronze Route wires, presumably due to a difference in the additives and the Sn content. The reason for the increase in J_c was stated to be the formation of defect clusters, which occur at a higher frequency at higher fluences. The increase in J_c due to neutron irradiation was stated to be lower than expected in these wires, which on the other hand translates to a higher lifetime of accelerator magnets based on Nb$_3$Sn.

7.1.3 Studies of irradiation effects by X-ray diffraction

X-ray diffraction can deliver complimentary information to the investigation about irradiation defects in Nb$_3$Sn. Numerous X-ray diffraction studies on irradiated Nb$_3$Sn have been conducted in the past and are discussed in this section.

X-ray diffraction spectra can yield information about crystallite size, dislocation structure and their character. The underlying mechanism is the broadening of X-ray diffraction peaks due to in imperfect crystal lattice. A broadening of the X-ray diffraction peaks can be caused by a small crystallite size and by a high number of lattice defects. The crystallize size in this case is defined as the average of the smallest regions in the crystal that are undistorted. Stress in the lattice can lead to peak broadening and peak shift, while dislocations and point defects can also influence the shape of the peaks [156, 157, 158].

A global stress can lead to the shift of Bragg peaks, while a decreasing crystallite size and increasing defect density leads to in increase of the peak width. Information about the density of point defects can be gained from analysing background scattering, since they are partly responsible for diffuse background scattering. The evaluated crystallite size is rarely equal to the grain size since it describes the smallest perfect crystal volume with coherent scattering [81].

A common method of analysing X-ray diffraction spectra is by the Williamson-Hall analysis, according to which lattice strain can lead to a broadening of the peaks in the spectrum [163]. By plotting the breadth of the peaks against their distance from the origin, it is possible to distinguish between broadening caused by particle size and strain. A small particle size alone leads to a horizontal line while strain leads to a line with a slope in the case of an isotropic strain distribution.

As a result, the Williamson-Hall plot visualizes the order dependence of the peak broadening by plotting the full width at half maximum (FWHM) or the integral breadth over the corresponding diffraction vector. The modified version of the Williamson-Hall plot furthermore takes into account different contrast factors if strain broadening is caused by dislocations. The average crystallite size can be

calculated by extrapolating a linear fit to the intersection with the Y-axis. The presence of dislocations generally leads to anisotropic peak broadening in the modified Williamson-Hall plot. The slope of linear curves in the modified Williamson-Hall plot is proportional to the density of dislocations [81].

High energy X-ray diffraction studies of Nb_3Sn carried out in an synchrotron are presented in [120], where the phase formations during heat treatment and the elastic strain in the finalized wires was investigated. The growth of voids during the heat treatment was observed by synchrotron micro-tomography. X-ray diffraction offer the advantage of monitoring changes of the Nb_3Sn wire properties during the reaction process in-situ.

Stress and strain on Nb_3Sn wires can lead to lattice distortions, which are investigated by synchrotron X-ray diffraction in [122]. The examined PIT and RRP and bronze route wires showed very similar lattice parameter of 0.5275 nm–0.5277 nm in the stress free state at 4.2 K. The grain orientation, however, was found to be dependent on the manufacturing process. The PIT wire showed a preferential $\langle 110 \rangle$ orientation due to the Nb drawing texture, while the grains in the RRP wire showed a growing direction of $\langle 100 \rangle$ in the direction of the wire drawing.

A previous X-ray study of radiation damage induced by He particle radiation in Nb_3Sn found evidence of antisite defects and displacements of the Nb as well as the Sn atoms. In that study no broadening of the peaks was observed, instead the peaks were shifted due to an increase in the lattice parameter. It was stated that the displacements of the atoms from their original positions are associated with a decrease of T_c. It was suggested that the radiation leads to a destruction of the covalent bonds between the Nb atoms, leading to metallic bonds and an increase in the lattice parameter. The displacements of the atoms leads to an increased electron scattering and thus a degradation of the superconducting properties [23].

In another X-ray study that investigated neutron irradiated Nb_3Sn, the authors found increased small-angle scattering that they attributed to the presence of small regions with different scattering ability than the surrounding matrix. The half-width of fundamental reflections did not change at an increasing irradiation dose, confirming that the crystal structure is kept in disordered regions that appear during irradiation. The authors suggested an inhomogeneous disordering in Nb_3Sn and that in irradiated samples local melting and recrystallization of small regions takes place. These regions are completely disordered but keep the crystal structure of the surrounding matrix. The consequence is a decrease in the long range order parameter and small angle scattering. The variation of the long range order parameter depends on the irradiation dose due to a higher number of disordered regions at higher doses. The critical temperature T_c also depends on the dose since T_c is smaller in these disordered regions. At high doses T_c decreases to a value that is determined by the properties of the disordered regions [80].

Other studies of X-ray diffraction in neutron irradiated Nb_3Sn found that X-ray line broadening took place at high fluences, while at low and medium fluences no line broadening was observed. Additionally, a weakening in fundamental and superlattice lines was observed, hinting to significant amounts of displacements and the decrease of the long range order parameter. The lattice constant was found to have increased in the same way for all A15 compounds, up to 1.25 % [104].

In [46], X-ray measurements of Nb_3Sn irradiated with protons with an energy of 12 MeV were performed. It was found that an increased proton fluence leads to a broadening of the diffraction peaks, which the authors attributed to increased microstrain. Irradiation at a fluence of $10^{22}\,m^{-2}$ led to an increase of the microstrain by up to almost 0.4 %. The long range order parameter S and T_c decreased with increasing fluence and the investigated parameters were found to be described by the same curve as the one that originates from neutron irradiation when plotted as a function of dpa.

7.1.4 Microstructural investigations of irradiation damage in Nb_3Sn

The compound Nb_3Sn has been known and studied for over 50 years, yet the exact processes that occur in the material when subjected to irradiation with high-energy particles and the resulting defect structure are still not fully understood. Not much literature can be found about microstructural investigations of the defect structure of Nb_3Sn irradiated with fast neutrons or other particles, and the results published by different authors differ considerably from each other.

Holdway et al. [70] performed investigations of fast (E > 0.7 MeV) neutron irradiated Nb_3Sn at fluences between $3.7 \times 10^{21}\,m^{-2}$ and $5.4 \times 10^{23}\,m^{-2}$ under strong two-beam diffraction conditions with s, the deviation from the Bragg condition, being zero or very small. For dark field TEM, the reflections (110), (200) and (400) were used. The authors reported the finding of different types of contrasts after irradiation. Black dot contrast was observed under (200) and (400) dark field conditions and in bright field TEM under fundamental conditions. Black/white contrast was also found using bright field conditions. Regions of high disorder were stated to be located in a matrix of less disorder. The disordered regions were determined to be 2 nm–10 nm in size. The black dot contrast was stated to be less than 1 nm. Assumptions were made that this black dot contrast stems from the sample preparation process by ion milling at 5 kV. Additionally, dislocation loops with diameters between 15 nm and 30 nm were found. From the correlation between the microstructure and T_c it was concluded that only the small disordered regions have a significant impact on the change of the superconducting properties after irradiation.

Degtyarenko et al. [31] investigated Nb_3Sn irradiated with protons with energies of 12.4 MeV and 12.8 MeV and fluences of $5 \times 10^{21}\,m^{-2}$ and $1 \times 10^{22}\,m^{-2}$ and found thin

particles of Nb with random orientation and a size of 0.1 μm–0.5 μm. Dislocations were found inside the particles that origin from the lattice mismatch at the Nb-Nb$_3$Sn interface.

Pande [101] explains the decrease in T_c of irradiated A15 materials through the creation of disordered regions that possess a much lower T_c than the surrounding matrix. The neutron irradiation induced disordered regions were imaged by means of TEM using (110) superlattice reflections, which led to structure factor contrast. The observed regions were found to be 2 nm–6 nm in size with an average of around 4 nm.

In [102], Pande detected highly disordered regions between 2 nm and 6 nm, which retain A15 structure, in fast neutron irradiated Nb$_3$Sn (E $\geqslant$ 1 MeV). According to the author, antisite defects and strain fields are contained in these regions. The techniques used by them include diffraction contrast, weak-beam dark field and structure factor contrast. In that work the same reflections were used as described by Holdway et al. [70]: (110), (200) and (400). The superlattice reflection (110) used in dark field imaging leads to contrast mainly due to a different structure factor between ordered and disordered regions, as by variations of the Bragg-Williams long range atomic order parameter S, while the fundamental reflections (200) and (400) produce contrast due to strain, as by the displacement of atomic planes. In unirradiated specimen, a few disordered regions of around 10 nm as well as faint black dots of 1 nm due to ion milling were observed, most clearly under weak-beam conditions. In irradiated specimen, a higher concentration of black dots was found under (110) dark field conditions, which, according to the author, were disordered regions due to neutron irradiation. These disordered regions were also found under bright field fundamental (200) and (400) conditions and in weak-beam dark field using (200) and (g,3g) and (g,4g) conditions, leading to the conclusion that neutron irradiation also induces localized strain due to displaced atoms. Under bright field, the disordered regions appear black, and in weak-beam dark field they are seen in white. Black spots were also observed in dark field. A comparison of images under different conditions evidenced that most of the disordered regions contained strain or atomic displacements. Inside the disordered regions, a high concentration of vacancies was expected. In that study, no dislocation loops were found in irradiated specimens due to most disordered regions not showing the expected characteristic black and white contrast. In specimens irradiated with lower fluences than 10^{22} m^{-2}, faint black and white contrast was observed under dark field conditions due to strain contrast, with the $\vec{g}$-vector joining both parts. In specimen that were irradiated at higher fluences, the spacing between the disordered regions was too small to differentiate between the black and white parts of the contrast changes. It was further stated that in order to achieve a good contrast, the specimen thickness has to be less than 100 nm and fluences higher than 1.5×10^{23} m^{-2} also lead to a stronger contrast. The A15 structure was retained in most specimen parts even at such high irradiation levels, hence it is assumed that the largest part of the disordered regions also keep that structure, instead of becoming amorphous. The contrast of the images was found

to be dependent on the size of the disordered regions and the specimen thickness, where thinner specimens and larger disordered regions led to better contrast. A higher fluence also led to an increased contrast. In summary it was stated that point defects and a high density of antisite defects are present in cascades in Nb_3Sn after irradiation. The disordered regions are surrounded by a less disordered matrix, while the A15 structure is kept in both. The presence of antisite defects reduces the long range order parameter S.

Pande [103] also described in a different publication the imaging of regions of reduced long range order parameter S using superlattice reflections in A15 compounds. In this case such regions appear as dark dots in the image due to a different structure factor between the disordered regions and the ordered surrounding matrix. Generally no dislocation loops were found in A15 compound after irradiation with fast neutrons. The size of the disordered regions was found to be between $2\,nm$ and $6\,nm$. Most of the defects in irradiated Nb_3Sn were found to be located inside these disordered regions. The volume fraction of disordered regions at a fluence of $1 \times 10^{22}\,m^{-2}$ was found to be over $1\,\%$.

The distortion of the lattice of Nb_3Sn due to neutron irradiation has also been investigated in TEM using the imaging of moire fringes. The origin of moire fringes is the overlap two crystals that are slightly misoriented or have different lattice constants. This leads to a magnification and better visibility of small distortions. It was found that in irradiated samples large bending of the moire fringes occurred. Important to note is the fact that also other factors, such as thickness variations, can lead to distortions and bending of the moire fringes and should not be confused with irradiation induced effects. The authors believe the observed distortions are cause by small disordered regions the size of around $3.5\,nm$ that are coherent with the surrounding matrix but contain a higher density of antisite defects, that can furthermore lead to increased strain [105].

Jenkins at el. [78] investigated Au^{++} ion irradiation damage in Nb_3Sn using superlattice and fundamental reflections in dark field imaging. Under superlattice reflections, dark spots were observed while fundamental reflections led to black-white contrast antiparallel to the $\vec{g}$- vector. Irradiations leads to antisite defects in the unit cell, which are distributed uniformly in the irradiated material. The displacement of the Nb atoms leads to a reduction of the long range order, leading to a decrease in T_c and an intensity loss of superlattice reflections. Electron scattering due to defects leads to reduction in the density of states and thus in T_c. Using superlattice reflections, the defect size was determined around $3\,nm$–$10\,nm$, with an average of around $7\,nm$. The author reported best contrast when using the reflections (440) and (444). (110), (200) and (400) were also used for imaging defects. It was stated that under fundamental dark field reflections, isotropic displacement fields will exhibit a black-white vector parallel to the $\vec{g}$-vector, while lightly anisotropic displacement fields will lead to a black-white contrast that does not perfectly align with the $\vec{g}$-vector. The size of the defects was defined as the length of the border between the black and white

parts of the contrast changes. Using fundamental reflections, all previously observed defects imaged in superlattice reflections were visible. On the other hand, some defects were visible in fundamental images, but not in superlattice ones. Under exact (200) conditions with s, the parameter of the deviation from the Bragg condition, being close to 0, only weak contrast was observed, but by increasing s slightly and therefore satisfying the (400) reflection, a stronger contrast could be achieved by imaging (200). Increasing s over a value of $0.08\,\text{nm}^{-1}$ led to a gradual diminishing of the contrast. No defects could be imaged under real weak-beam conditions with high s. Calculations have shown that due to the similar atomic numbers of Nb and Sn, the intensity of the superlattice reflection (110) is very low in Nb_3Sn, which has also been observed in the present study. The authors stated that no dislocation loops were found in irradiated Nb_3Sn and that strain fields could arise due to a high concentration of Frenkel pairs which lead to an expansion of the lattice. Another factor might be anti-site exchange that causes displacements of atoms from their lattice sites, and therefore lead to an expansion of the lattice volume. The latter option was stated to likely be the the most dominant factor. It is thus assumed that a high number of antisite defects are produced inside the experimentally observed cascade regions. The lattice expands locally in these regions in order for the A15 structure to be retained, leading to strain fields in the TEM images. The antisite defects furthermore might lead to electron scattering and thus the degradation of the superconducting properties.

When attempting a quantification of the defects per volume, one has to consider a multitude of factors that have an impact on the visibility of the contrast, which is influenced by the diffraction conditions, the sample thickness, the size of the defects and their position within the sample as described in Chapter 1 and in [1, 77, 102].

Attempts of investigating the same TEM sample before and after irradiated have been hindered in the past due to deteriorating of the sample surface during the irradiation process [175].

7.2 Simulations

7.2.1 Damage per atom

In order to estimate the excepted amount of displaced atoms at a given fluence, simulations were performed using the programme FISPACT-II [138]. The simulations of the expected *dpa* using the FISPACT-II programme described here were conducted in collaboration with Jack Haley from the Department of Materials of the University of Oxford. The neutron spectrum of the TRIGA Mark-II reactor shown in Figure 7.3 was used as input file for the calculation of the *dpa*. Since a given neutron fluence most commonly refers to fast neutrons with an energy above $0.1\,\mathrm{MeV}$, it needs to be scaled over the entire spectrum to calculate the total fluence. The samples in this study were irradiated with fast (E>$0.1\,\mathrm{MeV}$) neutrons up to a cumulative fluence of $2.82 \times 10^{22}\,\mathrm{m^{-2}}$. A fast neutron fluence of $2.82 \times 10^{22}\,\mathrm{m^{-2}}$ corresponds to a total neutron flux of $7.01 \times 10^{22}\,\mathrm{m^{-2}}$ when scaling over the spectrum of the TRIGA Mark-II reactor. The parameters used for the simulation are summarized in Table 7.1 and the results are displayed in Table 7.2.

Trough the simulations it becomes apparent that at a fluence of $2.82 \times 10^{22}\,\mathrm{m^{-2}}$, a total *dpa* of 2.2×10^{-3} is produced. Since fine grains in Nb_3Sn are commonly in the order of $100\,\mathrm{nm}$ as analysed in Chapter 6, a single grain was approximated by a cube of $100\,\mathrm{nm}$ side length in order to estimate the amount of produced vacancies per grain. It was found that at this fluence, 1.18×10^5 atoms are on average displaced in a single grain.

Variable	Value	Unit
Lattice parameter of Nb_3Sn	0.53	nm
Atoms per unit cell	8	atoms
Atomic density	5.37×10^{10}	atoms $\mathrm{\mu m^{-3}}$
Atoms in a cube of $100\,\mathrm{nm}$ side length	5.37×10^7	atoms

Table 7.1: Parameters used for the simulation of the expected amount of vacancies using FISPACT-II.

Produced	Value	Unit
total at fast fluence of $2.82 \times 10^{22}\,\mathrm{m^{-2}}$ (E>0.1 MeV)	2.2×10^{-3}	dpa
per total fluence	3.14×10^{-26}	dpa
per total fluence $\times\ 10^{22}$	3.14×10^{-4}	dpa
per fast fluence (E>0.1 MeV)	7.81×10^{-26}	dpa
per fast fluence (E>0.1 MeV) $\times\ 10^{22}$	7.81×10^{-4}	dpa
per μm^3 at fast fluence of $2.82 \times 10^{22}\,\mathrm{m^{-2}}$ (E>0.1 MeV)	1.18×10^{8}	vacancy
per $(100\,\mathrm{nm})^3$ at fluence of $2.82 \times 10^{22}\,\mathrm{m^{-2}}$ (E>0.1 MeV)	1.18×10^{5}	vacancy

Table 7.2: Results of the the simulation of the expected amount of vacancies using FISPACT-II.

7.2.2 Image contrast

To be able to compare the experimental results of the high resolution STEM investigation of neutron irradiated samples with theoretical expectations, image simulations were performed using the JEMS program. These high resolution STEM images shown in Section 7.5 were acquired with the use of a JEOL JEM-ARM 200F microscope. For simulation of the HAADF image contrast, the convergence angle of the microscope is a required input, which has the value of 31.5 mrad.

Figure 7.1 shows the simulated HAADF image contrast of Nb_3Sn in a $\langle 100 \rangle$ zone axis with the marked unit cell. At the lowest thickness, different contrast between Nb and Sn atoms can be seen due to their difference in atomic number and density.

Figure 7.2 shows the results of the HAADF image simulation with different parameters. In subfigures 1 to 3 the contrast of the lattice with defects is shown at different samples thicknesses. The differing contrast between the elements only becomes significant at a very low sample thickness. The remaining subfigures were simulated using this sample thickness of 1.6 nm. Subfigures 4 to 10 show the resulting contrast when one atom is displaced. In subfigure 4, the displacement of one Nb atom in x- and y-direction leads to a reduction of the intensity at the original position while simultaneously leading to image blur due to the atom being dislocated. In subfigure 5, a Nb atom is displaced in x-direction to the position of a Sn atom, increasing the contrast at the final position while lowering the contrast at the original position. In subfigure 6, one Sn atom is displaced in x-direction to the position of a Nb atom, evening out the contrast between the two atomic sites. In subfigure 7, one Nb atom and one Sn atom are displaced in y-direction, leading to the impression of a deformed unit cell. In subfigure 8, one Nb and one Sn atom are displaced to the same location in x-direction, resulting in image blur which makes it difficult to distinguish between different atoms. In subfigure 9, these atoms are additionally displaced in y-direction. Subfigure 10 shows the weak resulting contrast difference of a Nb and a Sn atom switching atomic sites.
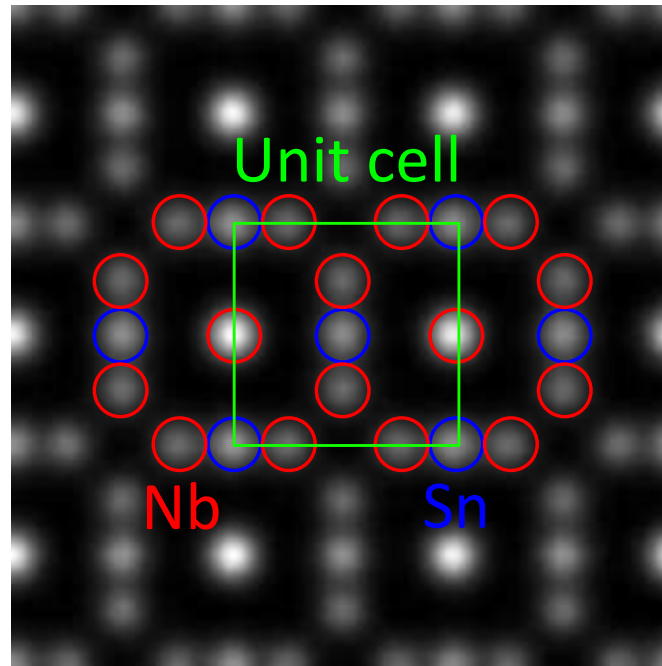
Figure 7.1: Simulated HAADF image contrast and Nb₃Sn unit cell.

When using realistic TEM lamellae thicknesses of tens of nm for the simulations, a single displaced atom does not lead to visible contrast differences. Differing contrast in high resolution STEM contrast therefore only arises due to the displacement of multiple atoms.
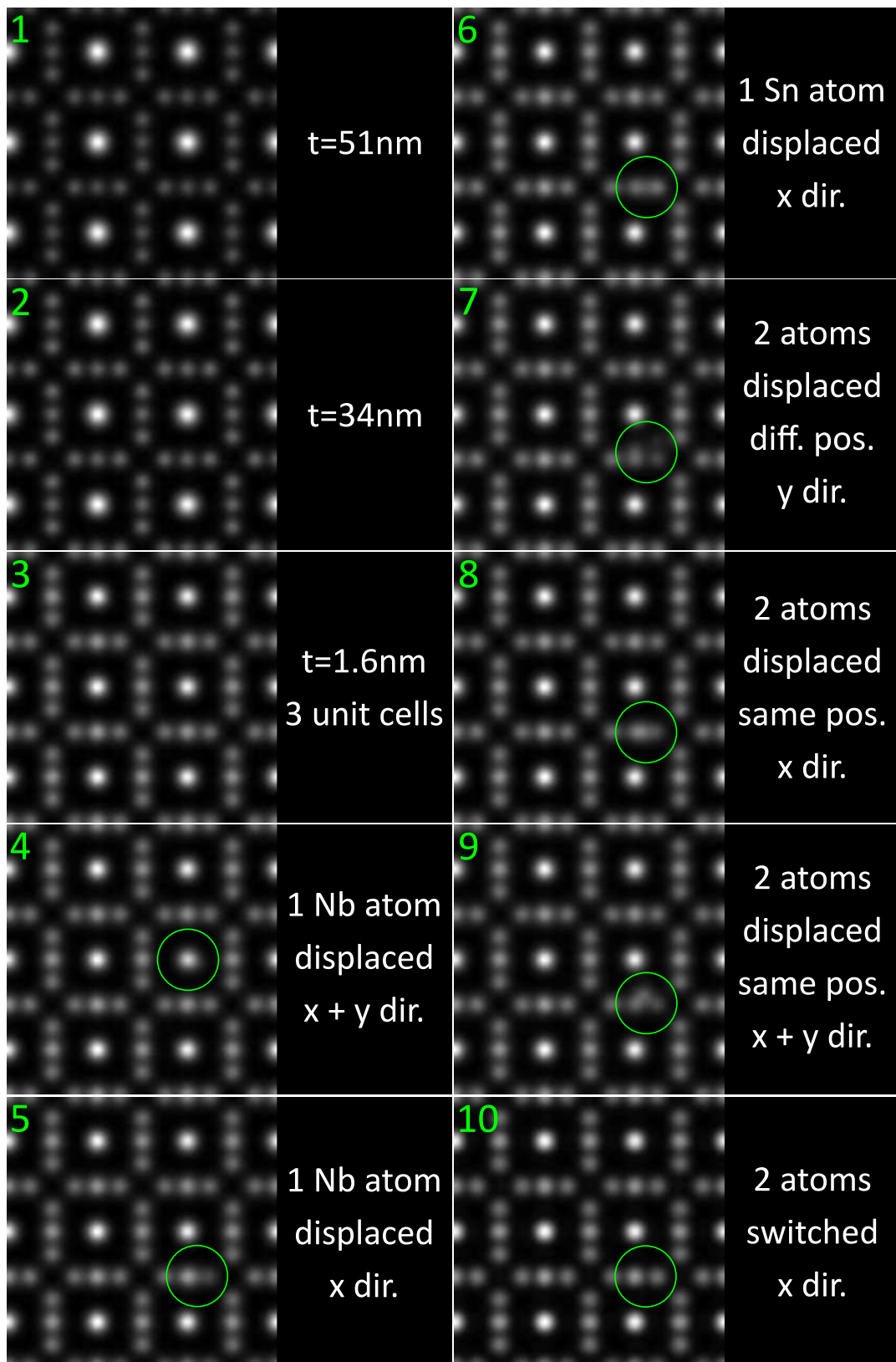
Figure 7.2: Simulated HAADF image contrast of displaced atoms.

7.3 Irradiation procedure

The irradiation of samples was carried out in the central irradiation pipe of the Triga Mark-II reactor of TU Wien which yields a total neutron flux density of $2.1 \times 10^{17} \, \text{m}^{-2} \, \text{s}^{-1}$ at the maximum power level of $250 \, \text{kW}$. The thermal neutron flux is $6.1 \times 10^{16} \, \text{m}^{-2} \, \text{s}^{-1}$, the amount of fast neutrons with energies above $0.1 \, \text{MeV}$ is $7.6 \times 10^{16} \, \text{m}^{-2} \, \text{s}^{-1}$ and with energies above $1 \, \text{MeV}$ $4 \times 10^{16} \, \text{m}^{-2} \, \text{s}^{-1}$. The displacements per atom (dpa) has been calculated at 2.81×10^{-3} for Nb and 2.01×10^{-3} for Sn at a fast neutron flux of $4 \times 10^{22} \, \text{m}^{-2}$, which is equivalent of a total neutron flux of $1.1 \times 10^{23} \, \text{m}^{-2}$. The above values of absolute neutron flux density were determined in the 1980s and have changed since then, but the energy distribution is assumed to be nearly unchanged [161]. The neutron spectrum of the TRIGA Mark-II reactor in Vienna shown in Figure 7.3. In this chapter the given neutron fluences are generally referring to fast fluences of neutrons with energies above $0.1 \, \text{MeV}$, unless stated otherwise.
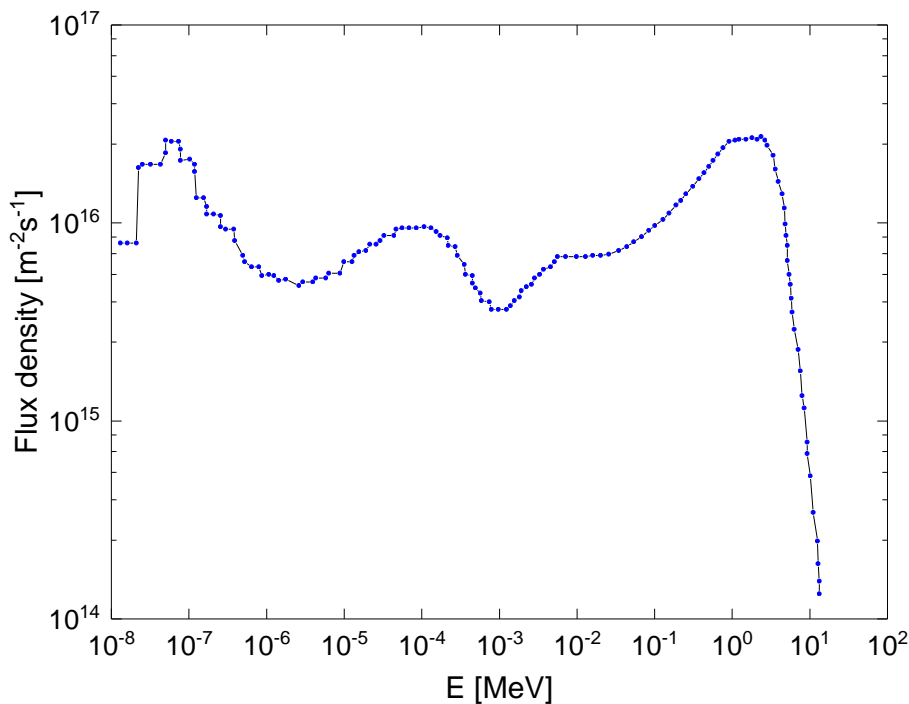
Figure 7.3: Spectrum of the TRIGA Mark-II reactor in Vienna [161].

Two irradiation steps were carried out containing TEM specimen as well as sub-elements that were etched out of the copper matrix as described in Chapter 2. The samples were sealed into silica glass tubes under different atmospheres during the irradiation process. After irradiation, the samples cooled off for about two weeks before further processing them in order to reduce the radiation exposure. After that time, the dose rate of the samples was measured and found to be negligible, thus allowing safe transportation and handling.

The first irradiation process was carried out with a fast neutron fluence of $3.8 \times 10^{21}\,\mathrm{m}^{-2}$. Six TEM lamellae of the RRP-Ti-108 wire as well as several sub-elements of the same wire type were included. The reasoning for preferably including sub-elements of this wire is fact that the activation of Ti during irradiation leads to far lower dose rated compared to the wires with Ta additives, leading to lower cool-off times before safe handling and transportation of the samples was ensured. The TEM samples were prepared using FIB to lift out lamellae from a polished cross section of the wire. Two of the samples were thinned and investigated before irradiation, the remaining four were left at a thickness of $3\,\mu\mathrm{m}$ in case the surface would deteriorate due to irradiation, and were thinned afterwards. For two samples helium was used as protective gas inside the silica glass capsule, while the others were sealed in air atmosphere before irradiation. Additionally, individual sub-elements were etched out of the wire using $50\,\%$ HNO_3, and were used to cut out TEM samples after irradiation. Table 7.3 gives an overview of the properties of the pre-prepared samples that were included in the first irradiation process as well as the results and usability status of the samples after irradiation.

Sample	Thickness	Atmosphere	Result	Usable
U1	$< 150\,\mathrm{nm}$	air	oxidized	✗
U2	$< 150\,\mathrm{nm}$	He	contaminated	✗
U3	$3\,\mu\mathrm{m}$	He	intact, thinned afterwards	✓
U4	$3\,\mu\mathrm{m}$	air	destroyed	✗
U5	$3\,\mu\mathrm{m}$	air	oxidized, destroyed	✗
U6	$3\,\mu\mathrm{m}$	air	oxidized, thinned afterwards	✓

Table 7.3: Overview of samples included in the first irradiation step.

Copper rings were used to mount the lamellae of all samples that were included in the first irradiation step, which heavily oxidized when no protective gas was used. This led to the destruction of some samples and rendered others unusable for TEM investigation. Figure 7.4 shows the oxidation of samples without protective gas.

Nevertheless, a few of the prepared samples survived the irradiation process and were investigated further. The investigation of sample U2, which was irradiated under helium atmosphere, revealed a web-like structure which formed mainly in the copper area, and was identified as Cu_2O on the surface, most likely from sputtering or oxidation due to residual oxygen in the protective gas atmosphere. The structure was gone after removing a few nm of material from the surface using ion milling. Dark spots and round structures were also observed and believed to be surface contamination. Figure 7.5 shows a comparison of the same sample before and after irradiation.
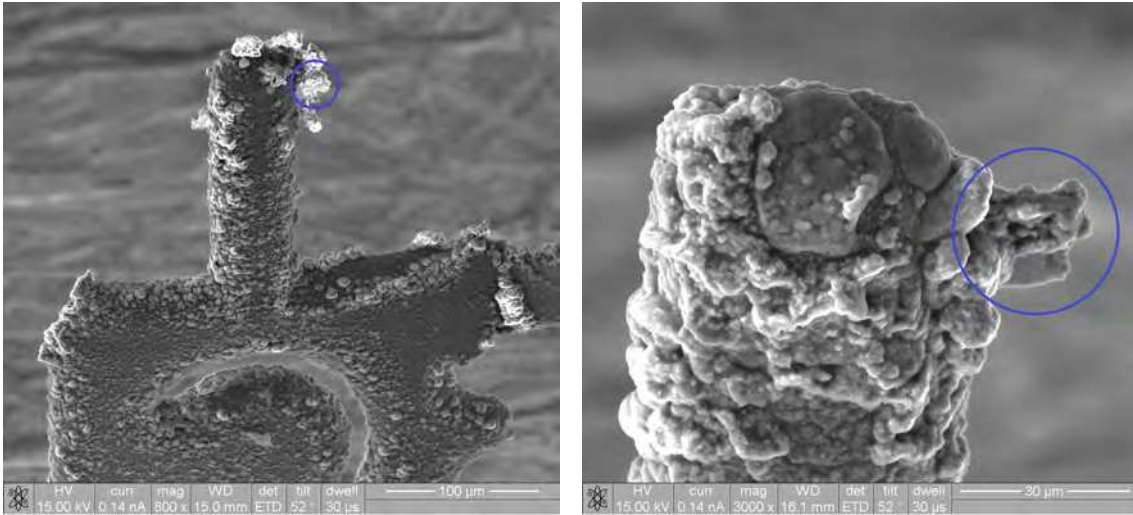
Figure 7.4: Oxidized Cu sample holders after irradiation under air atmosphere. Circles mark the positions of destroyed TEM samples.
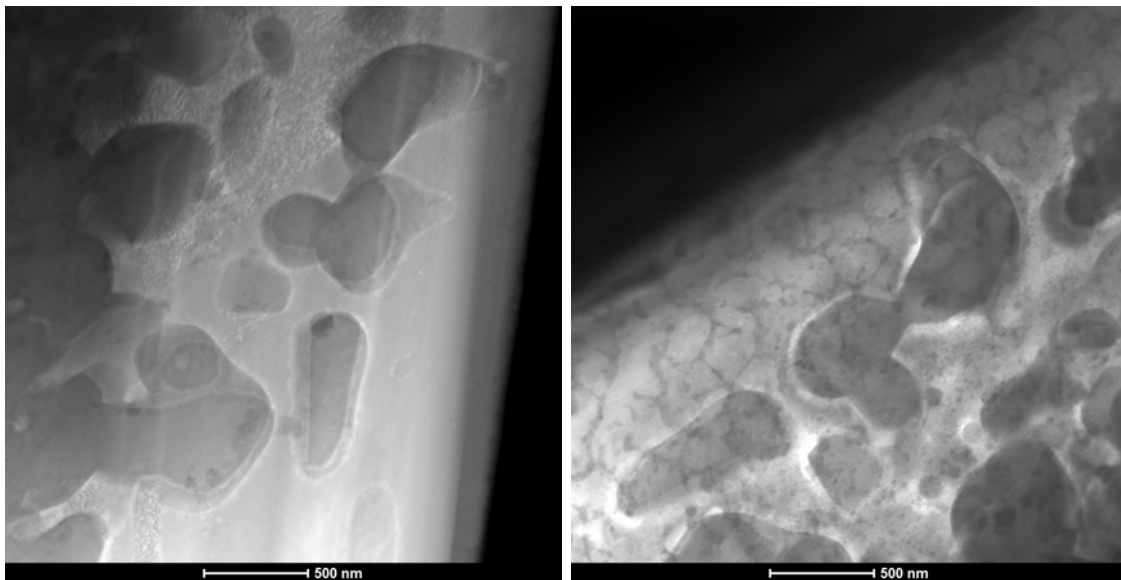
Figure 7.5: Comparison of sample U2 before (left) and after irradiation (right).

The main insights gained from the first irradiation procedure can be summarized as follows: Irradiating finalized TEM specimens was proven to be difficult due to the deterioration of the surface during irradiation, specifically air atmosphere leads to heavy oxidation of copper based sample holders and destruction of the lamellae. In order to avoid oxidation, it is necessary to use a protective gas atmosphere. Furthermore, a different sample holder material than copper should be utilized.

In the second irradiation step, a few extracted sub-elements of the PIT-Ta-192 wire, two highly stoichiometric large-grained bulk samples, and seven TEM lamellae were exposed to a fast neutron fluence of $3.9 \times 10^{21}\,\mathrm{m}^{-2}$. Details on the TEM samples and their status after irradiation are given in Table 7.4, and a photograph was shown in Figure 2.5. Except for U13, which was cut from a large-grained bulk, all of them were taken from the RRP-Ti-108 wire. Different sample holder materials (Si and Cu) as well as different atmospheres (He and vacuum) were used to investigate the optimal conditions preferable in terms of surface degradation.

Sample	Thickness	Holder	Atmosphere	Result	Usable
U7	$< 150\,\mathrm{nm}$	Cu	vacuum	contaminated	✗
U8	$< 150\,\mathrm{nm}$	Cu	He	contaminated	✗
U9	$< 150\,\mathrm{nm}$	Si	vacuum	contaminated	✗
U10	$3\,\mathrm{\mu m}$	Si	vacuum	destroyed	✗
U11	$3\,\mathrm{\mu m}$	Si	He	contaminated, destroyed	✗
U12	$< 150\,\mathrm{nm}$	Si	He	intact	✓
U13	$< 150\,\mathrm{nm}$	Si	vacuum	destroyed	✗

Table 7.4: Overview of samples included in the second irradiation step.

A large fraction of TEM samples that were prepared before irradiation and included in the irradiation steps was destroyed or rendered useless during the process. Nevertheless, the use of different atmospheres, especially vacuum, coupled with the use of Si sample holders has allowed a number of TEM lamellae to survive the irradiation procedure. While most of the TEM lamellae showed surface contamination, the sample U12 is the only sample that remained intact with sufficiently clean surfaces for further investigations, which will be shown in this chapter.

Overall, it was found that the irradiation of pre-prepared lamellae is associated with a high risk of contamination and destruction and thus an inefficient method for the preparation and investigation of irradiation damage by TEM. The most reliable method was found to be etching away the Cu matrix, and lifting out TEM lamellae of sub-elements after irradiation, since and this method ensured enough material to work with. Table 7.5 lists the irradiated sub-elements of the investigated wires and the corresponding fast neutron fluences. As already mentioned, most of the prepared and investigated specimens stem from RRP-Ti-108 wire sub-elements, since Ti is less prone to activation during the irradiation than Ta and thus safer in handling. The samples irradiated at the lower fluence received a fluence of around $3.8 \times 10^{21}\,\mathrm{m}^{-2}$, while the samples of the RRP-Ti-108 wire irradiated at a higher fluence were exposed to about $2.8 \times 10^{22}\,\mathrm{m}^{-2}$.

The microstructure of the different types of $\mathrm{Nb_3Sn}$ wires is generally comparable, since it is in principle the same material with potentially slightly different grain sizes and different forms of doping. The most important difference with regard to changes

Sample	Fast neutron fluence	Unit
RRP-Ti-108	3.83×10^{21}	m^{-2}
RRP-Ti-108	2.82×10^{22}	m^{-2}
RRP-Ta-54	3.68×10^{21}	m^{-2}
PIT-Ta-192	3.92×10^{21}	m^{-2}

Table 7.5: Irradiated sub-elements of the investigated wires and the corresponding fast neutron fluences.

during neutron irradiation is the variation in additives between the different wires. As discussed in Chapter 1 and Section 7.1, the addition of Ti and Ta significantly impacts the superconducting properties. However, due to the low at.% values of the dopants in the wires, it can be expected that the defect structure after irradiation does not show considerable differences between the different wires types.

7.4 Investigation of irradiated wires by TEM

Samples of Nb_3Sn wires that were irradiated at different neutron doses were investigated by means of transmission electron microscopy (TEM). A large amount of TEM images was acquired of neutron irradiated wires using a wide range of techniques such as scanning transmission electron microscopy (STEM), dark field TEM (DF TEM), weak-beam dark field TEM (WBDF TEM) and high resolution TEM (HRTEM). The different techniques are described in Section 1.8. For some images shown in this chapter, the contrast, brightness and gamma values might have been adjusted for a better visibility.

Most specimens of irradiated wires for TEM investigations were prepared after irradiation by lifting lamellae out of etched filaments using FIB as described in Chapter 2. A few finalized samples that were investigated before irradiation and sealed into silica glass tubes under vacuum during irradiation were sufficiently intact after this process, which enabled the direct comparison of the same sample regions before and after irradiation.

Setting the optimal diffraction conditions that are required for analysis of the Nb_3Sn damage structure by means of weak-beam dark field TEM has proven to be an extremely challenging task because of the small grain size. The method of setting weak-beam conditions by the use of conical dark field has proven to drastically reduce the required time to achieve weak-beam conditions are described in Section 1.8. The beam was tilted so that the (200), (210) and (222) diffraction rings located in the optical axis, where the smallest objective aperture was applied. The beam was then rotated until weak-beam conditions were achieved, after which the image and the corresponding diffraction pattern was acquired. The disadvantage of this method

is that the exact diffraction condition can not be chosen before imaging, but it has proven to lead to considerably better image results.

When interpreting the images of neutron irradiated wires, the largest factor of uncertainty stems from the fact that the specimens were prepared using FIB and ion milling, where the impact of ions can lead to substantial damage in the crystal structure that can be mistaken for damage caused by the neutron irradiation. Aside from damage induced by the sample preparation process, an additional challenge of evaluating irradiation damage is risen by the presence of defects and dislocations already present in the samples before irradiation. For that reason a careful comparison between samples of different preparation parameters and neutron fluences is necessary and the interpretation should be handled with great caution.

7.4.1 Comparison before and after irradiation

This section shows the comparison of images of the sample U12 prepared by PIPS ion milling from the RRP-Ti-108 wire before and after irradiation to a neutron fluence of $3.9 \times 10^{21}\,\mathrm{m}^{-2}$. After investigation of the un-irradiated state, the sample was sealed in a silica glass tube under vacuum for protection during the irradiation process as shown in in Table 7.4. Scanning transmission electron microscopy (STEM) images of this same sample before and after irradiation can be found in Figure 7.6 and Figure 7.7.

The analysis of the sample U12 irradiated at $3.9 \times 10^{21}\,\mathrm{m}^{-2}$ does not show considerable differences compared to the un-irradiated state. Dislocations were found during analysis before the irradiation, which were also present at the same locations thereafter. These locations are marked by circles in Figure 7.6 and Figure 7.7. No additional locations with defects stemming from the irradiation were found at this magnification and under these imaging conditions. The critical current density, however, shows a slight increase at this fluence [13], leading to the conclusion that the defects responsible for increased flux pinning must be smaller than resolvable at this magnification, not visible under the used STEM conditions or too sparsely distributed to become apparent.

HRTEM images of an unirradiated sample of the RRP-Ti-108 wire can be found in Figure 7.8, which show regions where no significant damage in the crystal lattice becomes apparent.

Figure 7.9, Figure 7.10 and Figure 7.11 show HRTEM images of the sample U12 after irradiation that were acquired at a higher magnification. Sparsely distributed defects were indeed located in the crystal structure with a size of a few nm that are marked by circles.
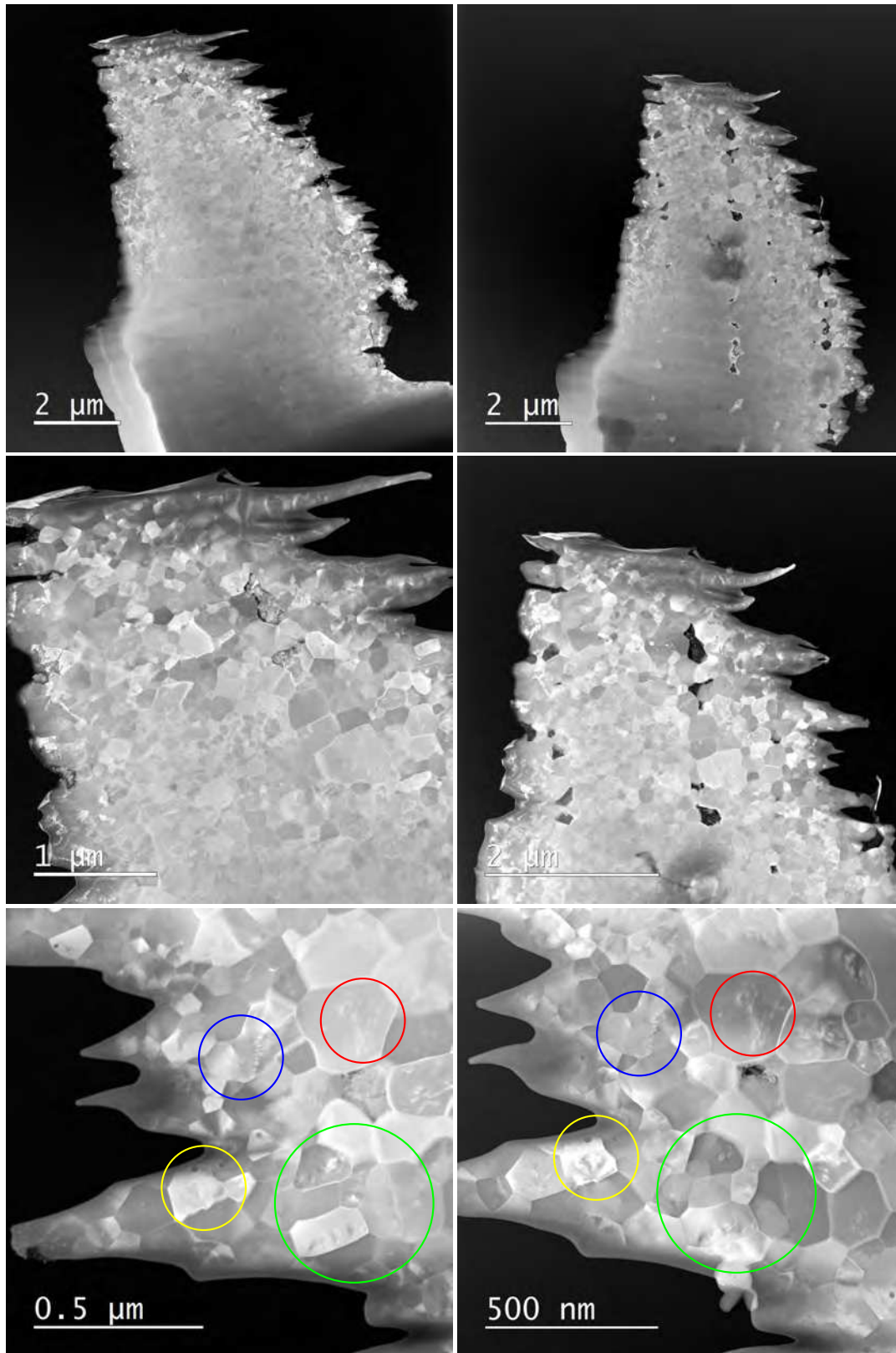
Figure 7.6: STEM images of the same sample regions before (left) and after irradiation (right).
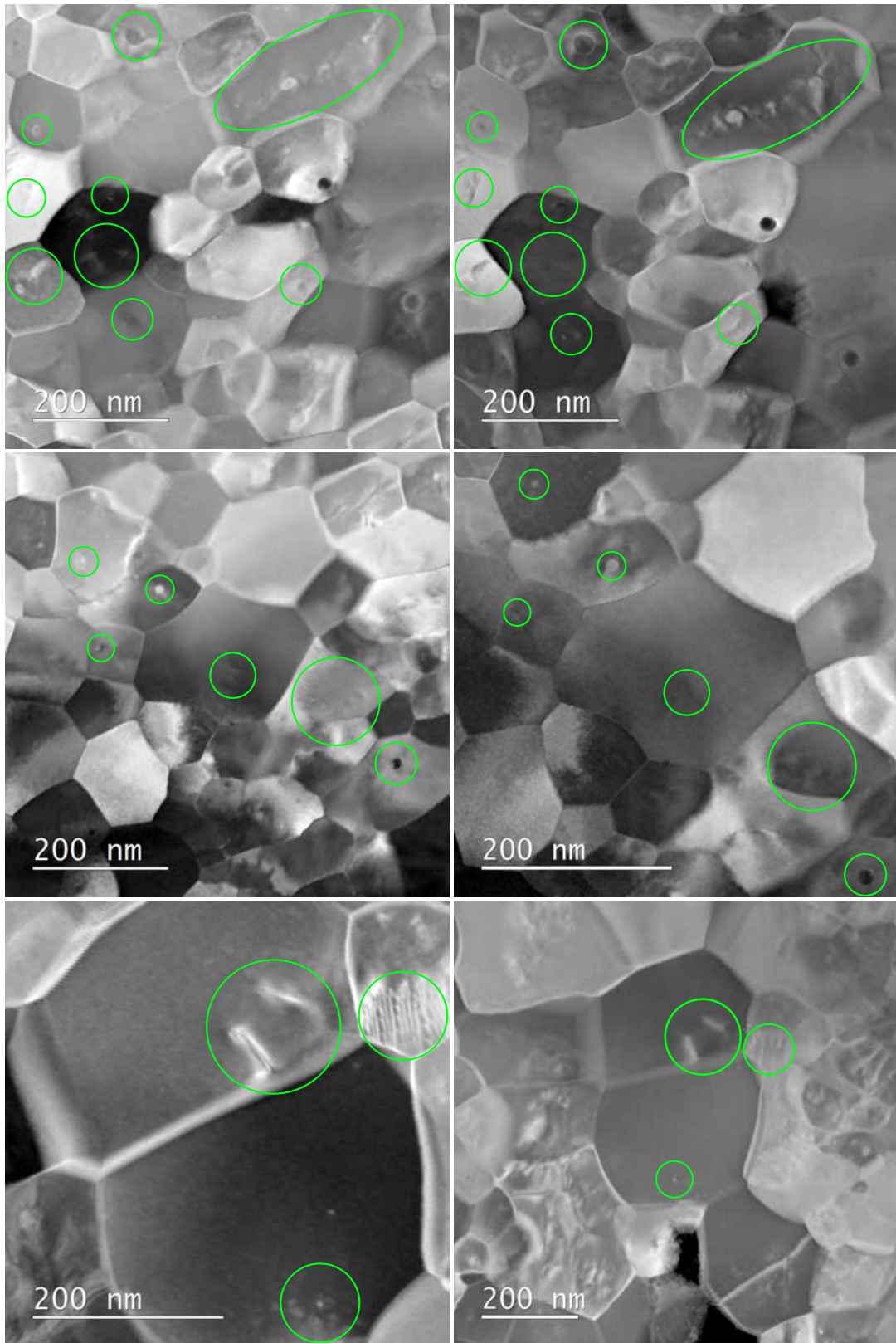
Figure 7.7: STEM images of the same sample regions before (left) and after irradiation (right).
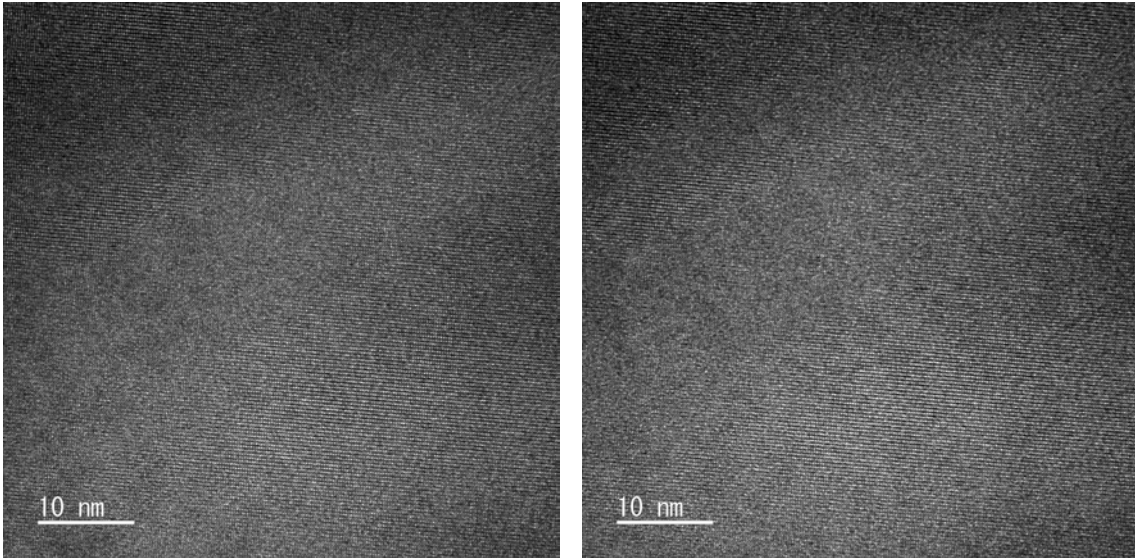
Figure 7.8: HRTEM images of an unirradiated sample.
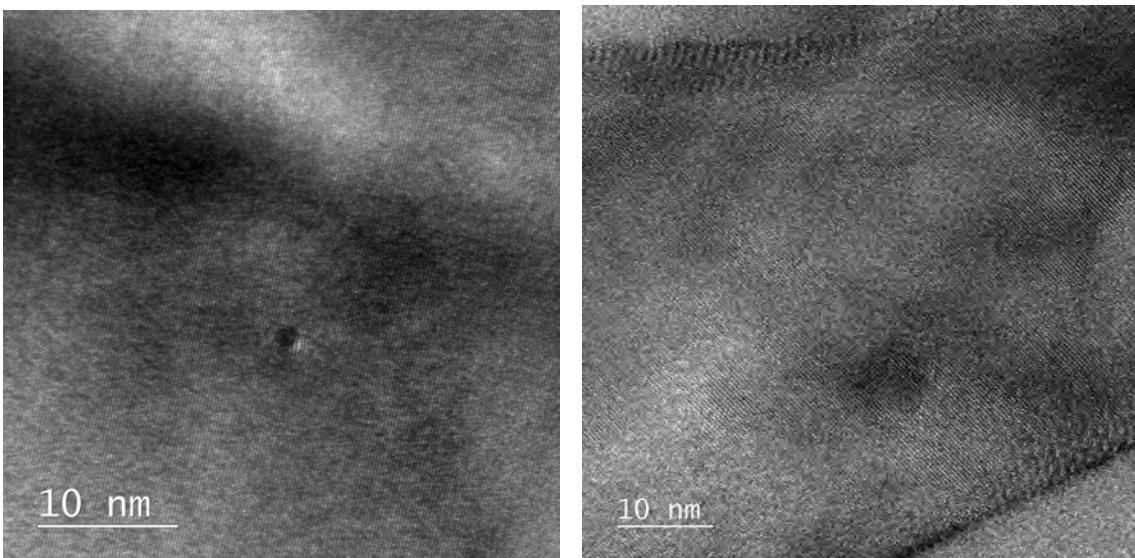
Figure 7.9: HRTEM images of a sample irradiated at a low dose.
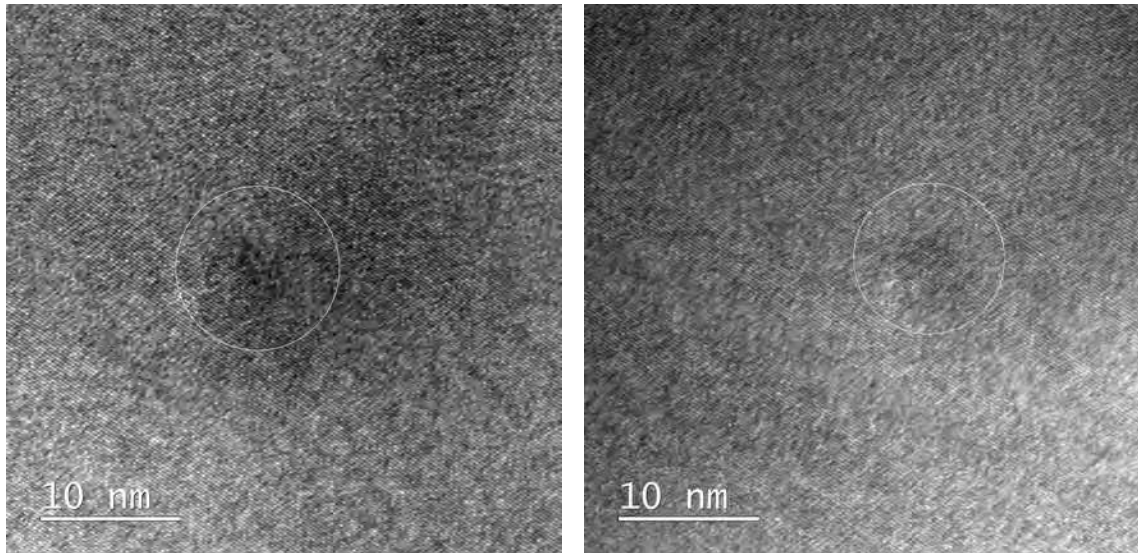
Figure 7.10: HRTEM images of a sample irradiated at a low dose.
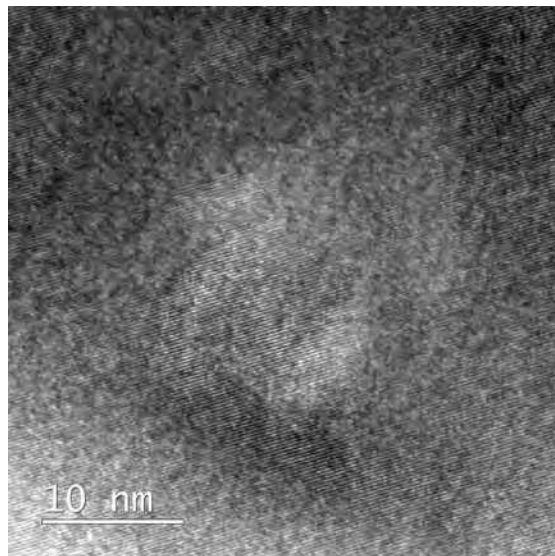
Figure 7.11: HRTEM images of a sample irradiated at a low dose.

7.4.2 Samples irradiated at a low dose

Aside from the sample described in the last section, the irradiation of pre-prepared TEM specimens generally did not lead to satisfying results since most of them became contaminated or destroyed during the irradiation process. As described in Chapter 2, most specimens for investigation of neutron impact sites were prepared by lifting lamellae out of etched and irradiated sub-elements. Bright field (BF), weak-beam dark field (WBDF) and high resolution TEM (HRTEM) images of irradiated sub-elements of different Nb_3Sn wires irradiated at different fluences as outlined in Table 7.5 are shown in this section.

Figure 7.12 shows images of the PIT-Ta-192 wire that was irradiated at a fast fluence of $3.92 \times 10^{21}\,m^{-2}$. Images of the RRP-Ta-54 wire irradiated at a fast fluence of $3.68 \times 10^{21}\,m^{-2}$ can be found in Figure 7.13 to Figure 7.15. The samples of the PIT-Ta-192 and RRP-Ta-54 wire were prepared by FIB only and show sparsely distributed regions with a high defect density, likely resulting from incident ions during the sample preparation process.

The sample of the RRP-Ti-108 wire was irradiated at a fluence of $3.83 \times 10^{21}\,m^{-2}$, the corresponding images are displayed in Figure 7.16. This sample was post-processed using the ion mill and shows sparsely distributed defects with diameters of a few nm, which occurred with a too low density for quantification.
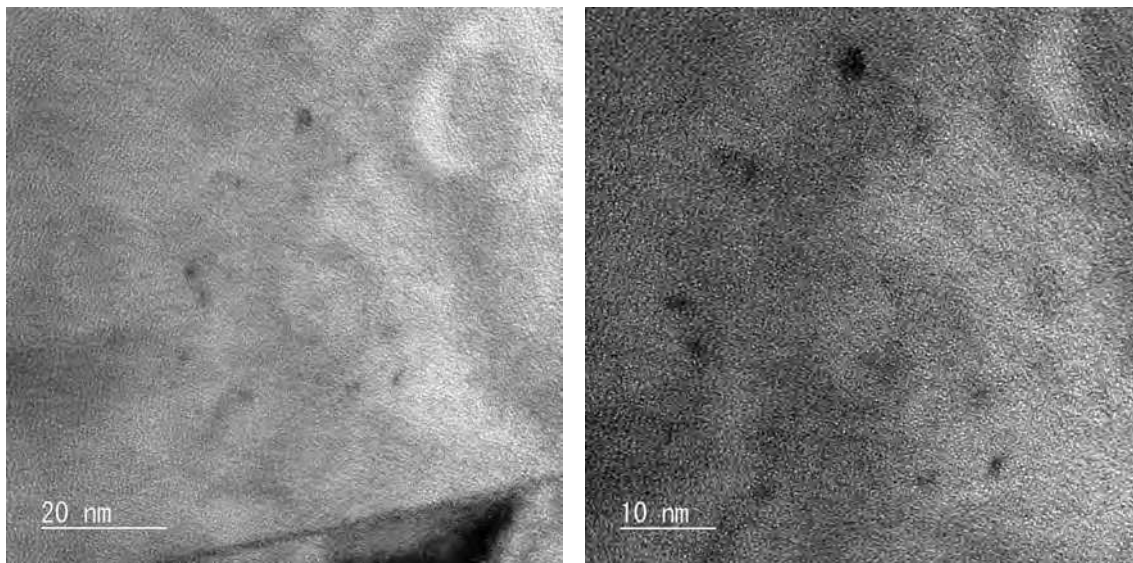
Figure 7.12: TEM images of the same grain of the PIT-Ta-192 wire irradiated at a low dose showing defects.
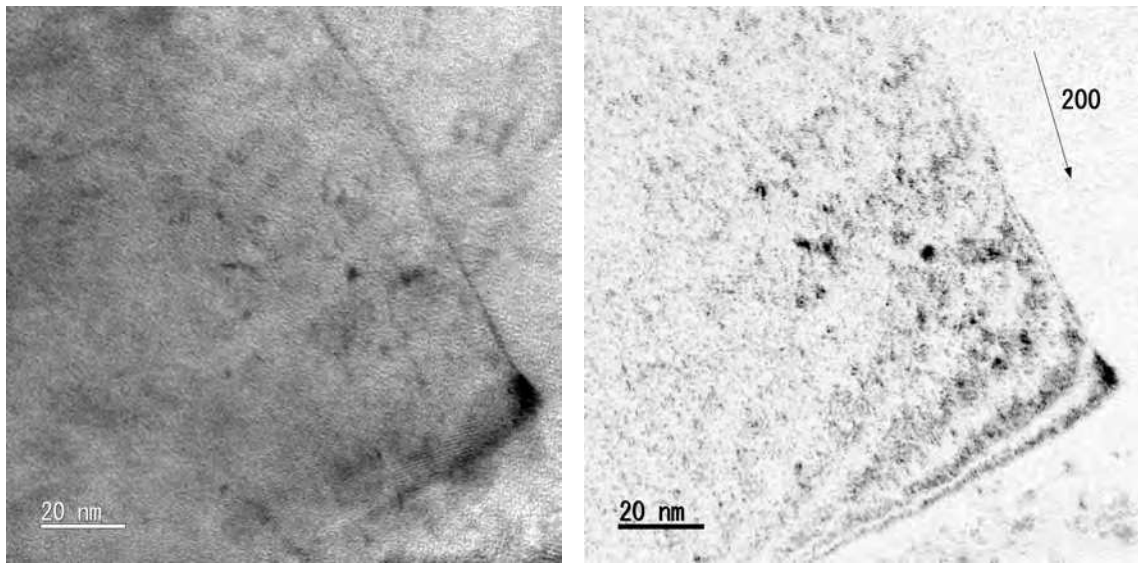
Figure 7.13: Bright field image (left) and inverted WBDF image (right) of the irradiated RRP-Ta-54 wire showing defects.
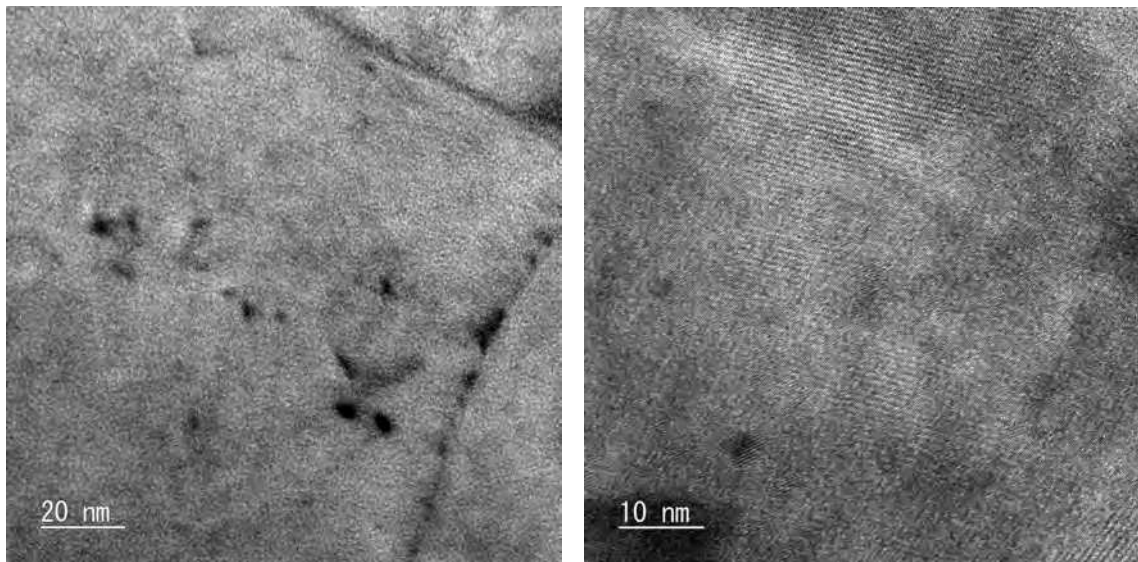
Figure 7.14: TEM images of the irradiated RRP-Ta-54 wire showing defects.
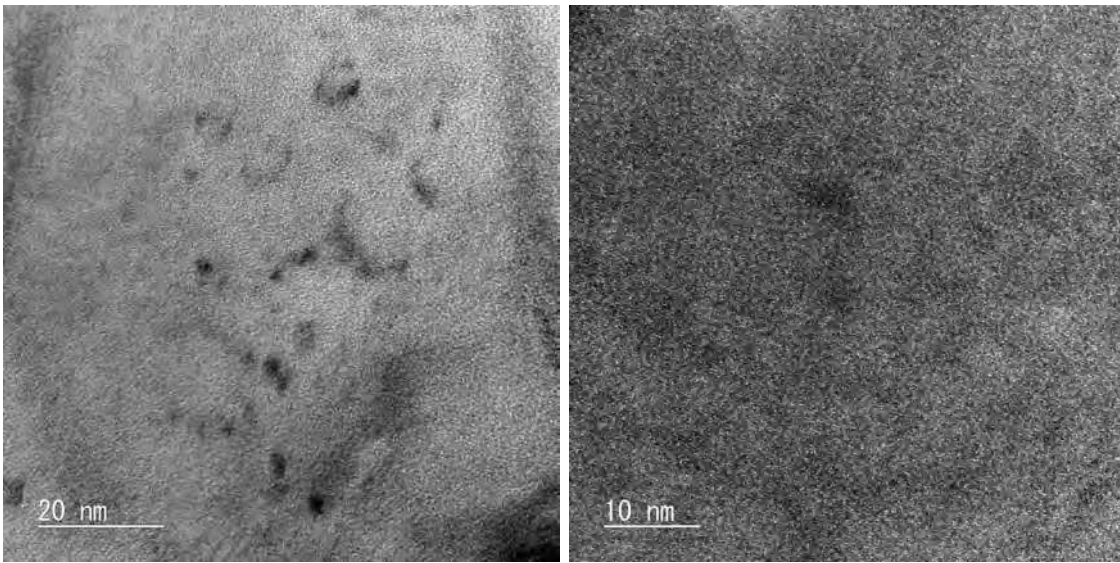
Figure 7.15: TEM images of the irradiated RRP-Ta-54 wire showing defects.
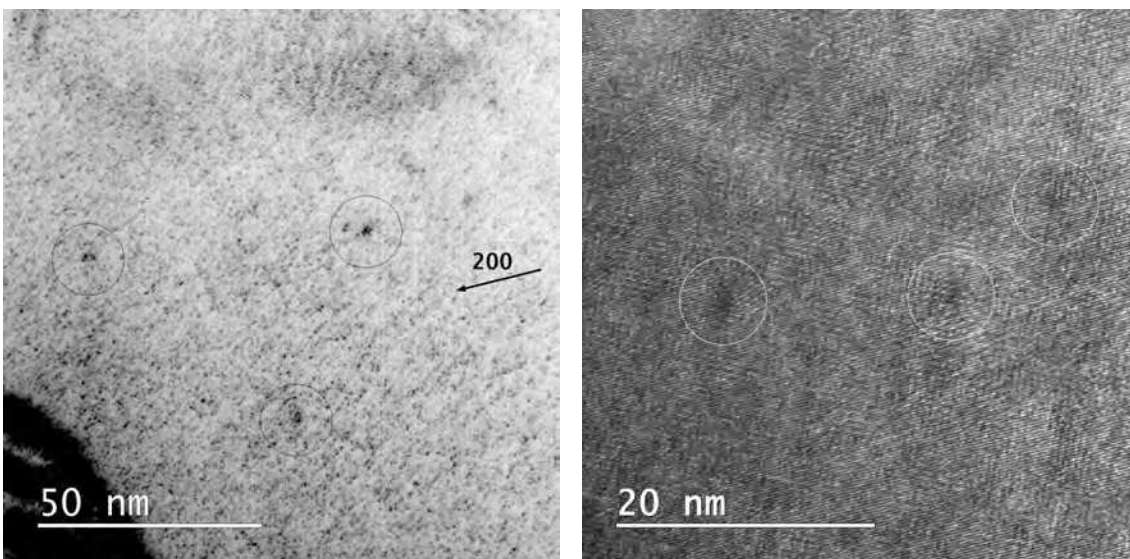
Figure 7.16: Inverted WBDF image (left) and HRTEM image (right) of the irradiated RRP-Ti-108 wire.

7.4.3 Samples irradiated at a high dose

Small pieces of the RRP-Ti-108 wire were subjected to further irradiation steps to a total fast neutron fluence of $2.82 \times 10^{22}\,\mathrm{m}^{-2}$. Some samples were prepared using FIB followed by thinning and cleaning using ion milling at around $2\,\mathrm{kV}$, while others were prepared using only FIB in order to evaluate the influence of ion damage on the microstructure.

Samples prepared by FIB only

This section describes the images acquired of RRP-Ti-108 wire samples that were irradiated at a fast neutron fluence of $2.82 \times 10^{22}\,\mathrm{m}^{-2}$ and prepared using FIB without any additional treatment. The bright field and dark field images in Figure 7.17 to Figure 7.20 show locations with a high density of nm sized defects, most of which can likely be attributed to ion damage that was caused by the sample preparation process. A HRTEM image of such a defect is shown in Figure 7.21.
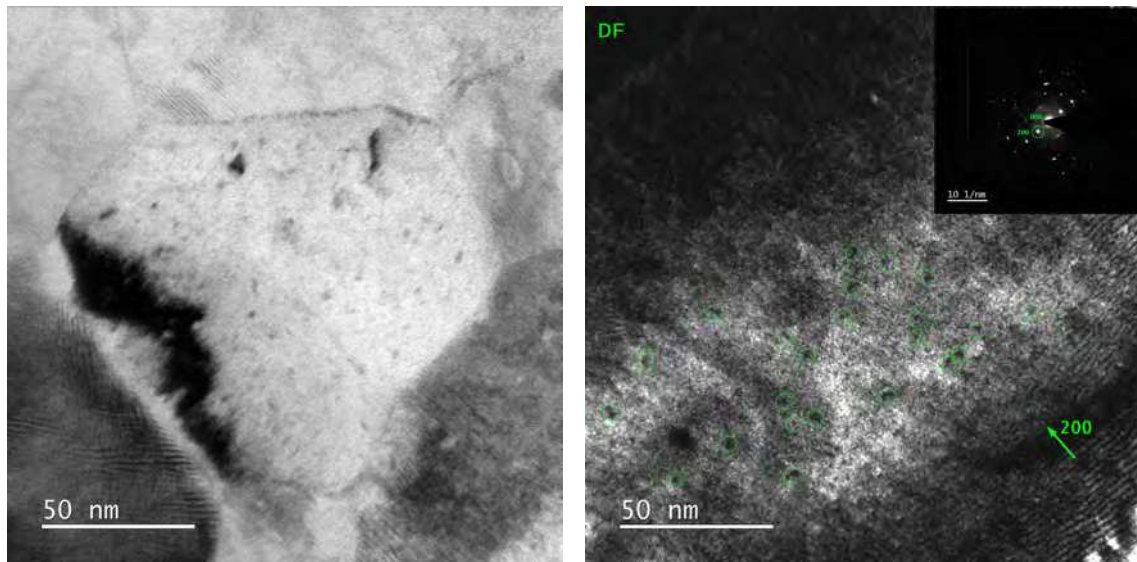
Figure 7.17: Bright field (left) and dark field (right) images of irradiated samples showing high density of nano-meter sized defects which partly stem from the preparation process using FIB.
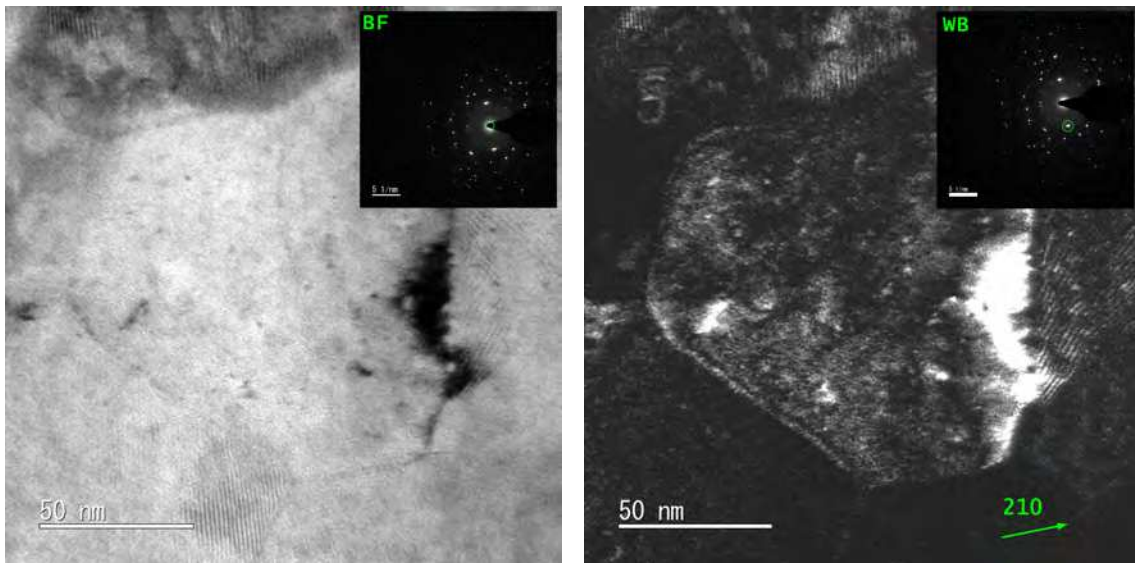
Figure 7.18: Bright field (left) and WBDF (right) images of irradiated samples showing high density of nano-meter sized defects which partly stem from the preparation process using FIB.
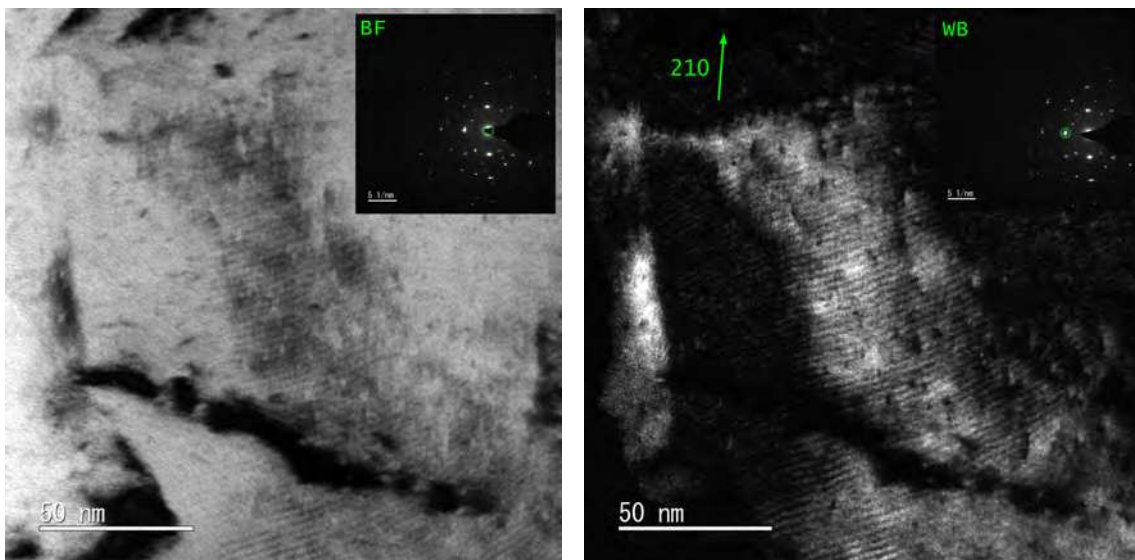
Figure 7.19: Bright field (left) and WBDF (right) images of irradiated samples showing high density of nano-meter sized defects which partly stem from the preparation process using FIB.
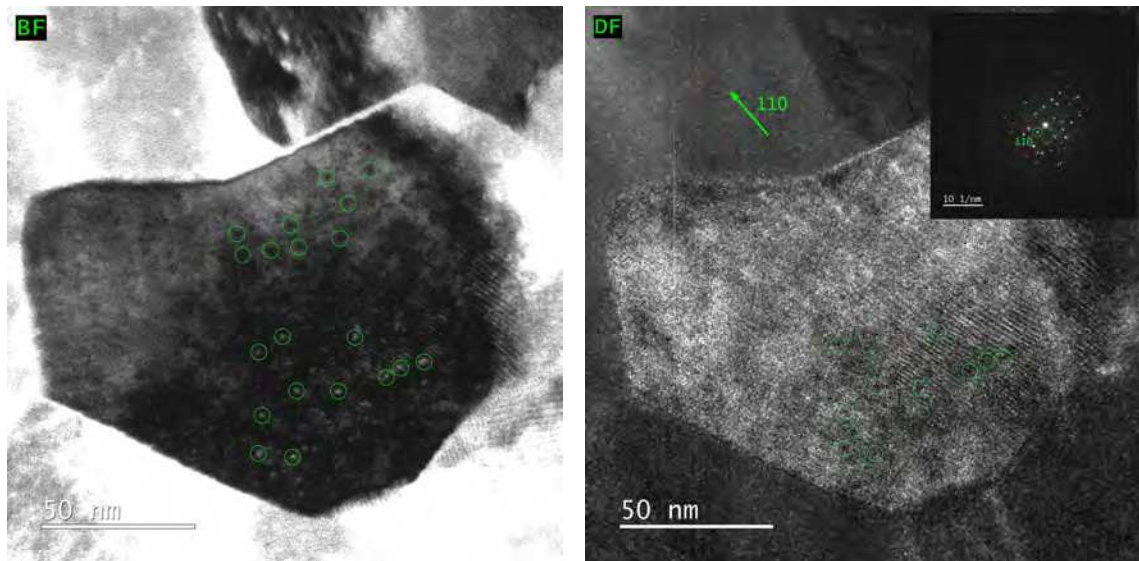
Figure 7.20: Bright field (left) and dark field (right) images of irradiated samples showing high density of nano-meter sized defects which partly stem from the preparation process using FIB.
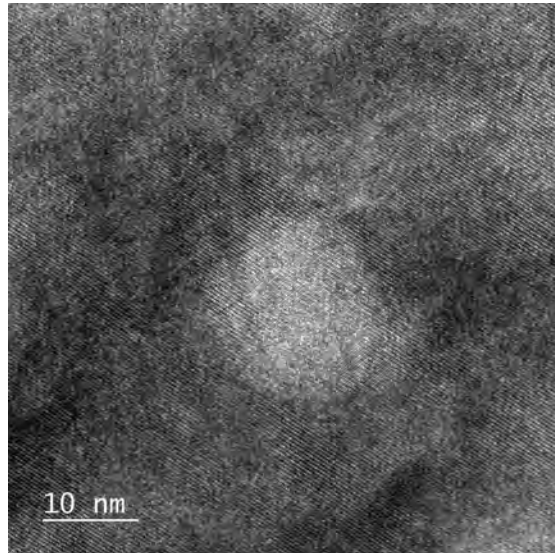
Figure 7.21: HRTEM image showing a sample region in which the crystal lattice is distorted, possibly originating from an inclusion or FIB induced damage.

Samples prepared by PIPS cleaning

This subsection shows a selection of images of RRP-Ti-108 wire samples that were irradiated at a fast neutron fluence of $2.82 \times 10^{22} \, \mathrm{m}^{-2}$ and prepared using FIB and ion milling. Descriptions of the applied TEM techniques and the visible defects can be found in the figure captions. Figure 7.22 shows a BF and WBDF image of the same area, where different defects are visible. The larger defects visible in the BF image are caused by inclusions in the wire that were present before irradiation, which show fringe contrast due to overlapping crystal lattices and were investigated in Chapter 4. These defects are not visible in the WBDF image, instead frequent small defects of a few nm in size become apparent.

Figure 7.22 shows images of the same grain under BF, DF and WBDF conditions, where black-white contrast changes in the direction of the $\vec{g}$-vector become apparent due to diffraction contrast, hinting towards defects with strain fields surrounding them.

The HRTEM images in Figure 7.24 to Figure 7.29 frequently show locations in the crystal lattice with contrast changes in regions of a few nm in diameter. These regions are indicated by circles in the images.
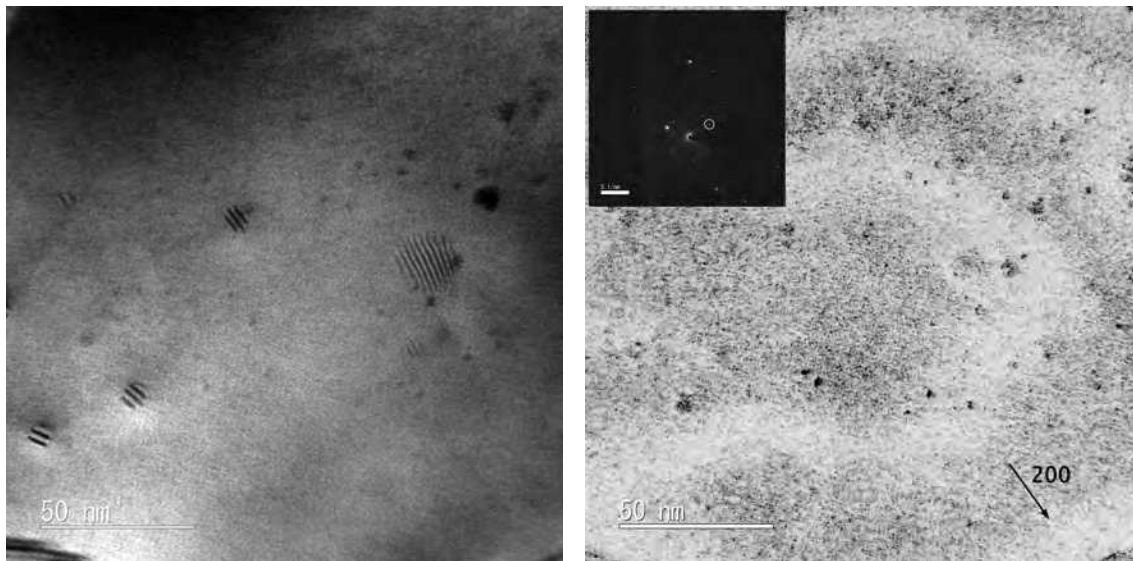
Figure 7.22: Bright field image (left) and inverted WBDF image (right) of the same irradiated sample region. The bright field images shows inclusions with fringe contrast, which are not visible in the WBDF image. In the WBDF image, small disordered regions with the size of a few nm are visible, which only partly can be found in the bright field image.
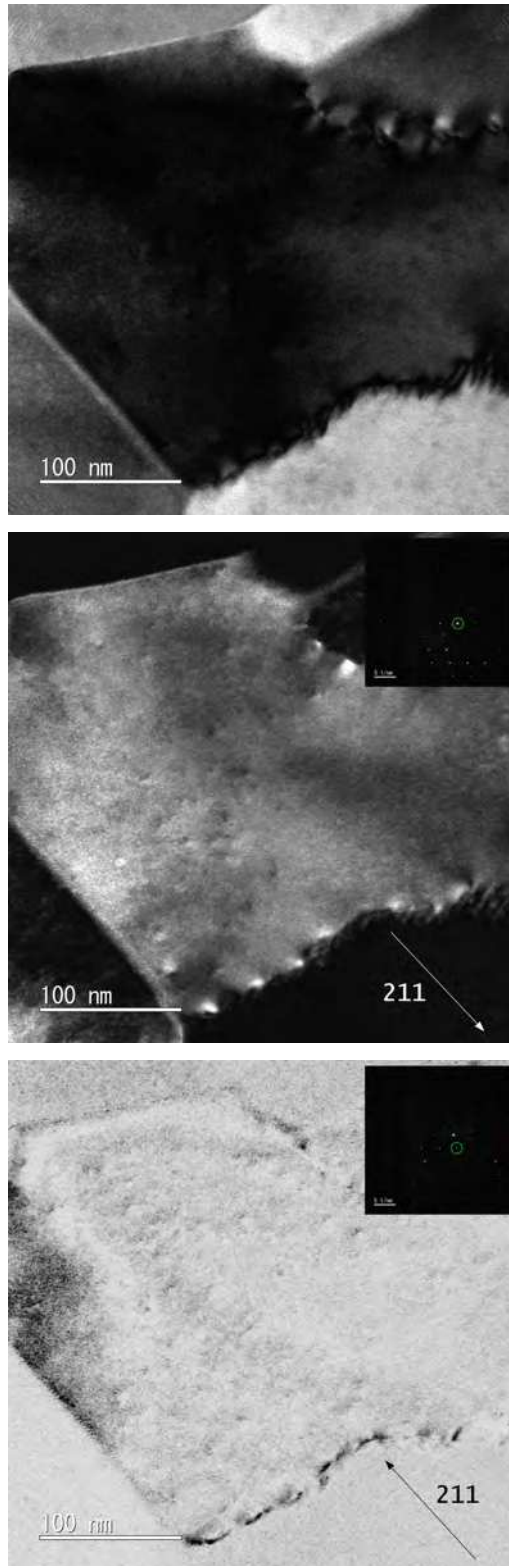
Figure 7.23: Bright field (top), dark field (middle) and inverted weak-beam dark field (bottom) images of an irradiated sample.
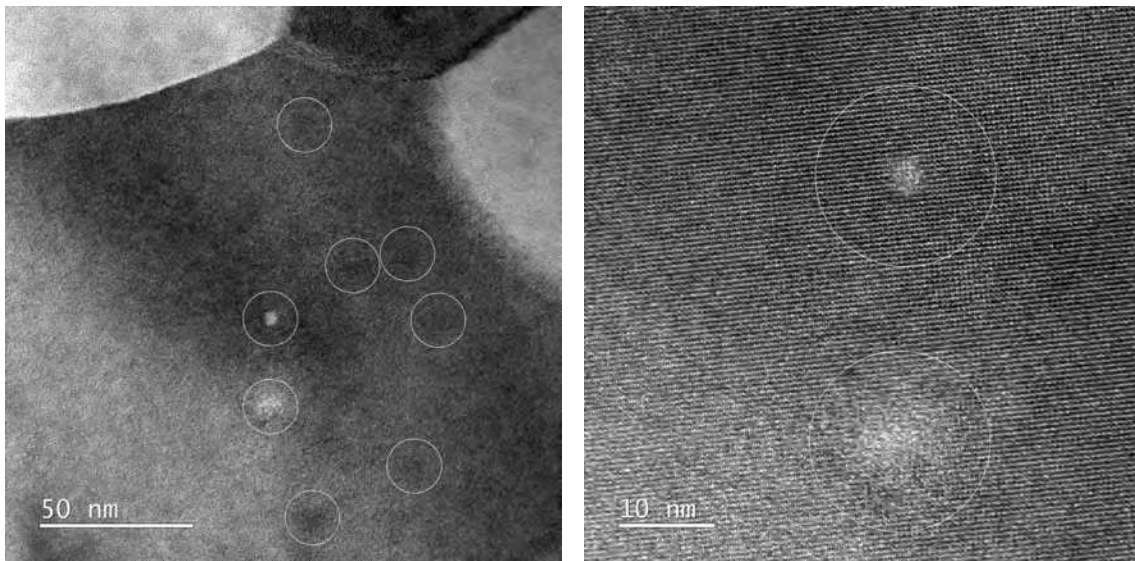
Figure 7.24: HRTEM images of the irradiated samples showing nano-meter sized locations in which the crystal structure is distorted (marked by circles).
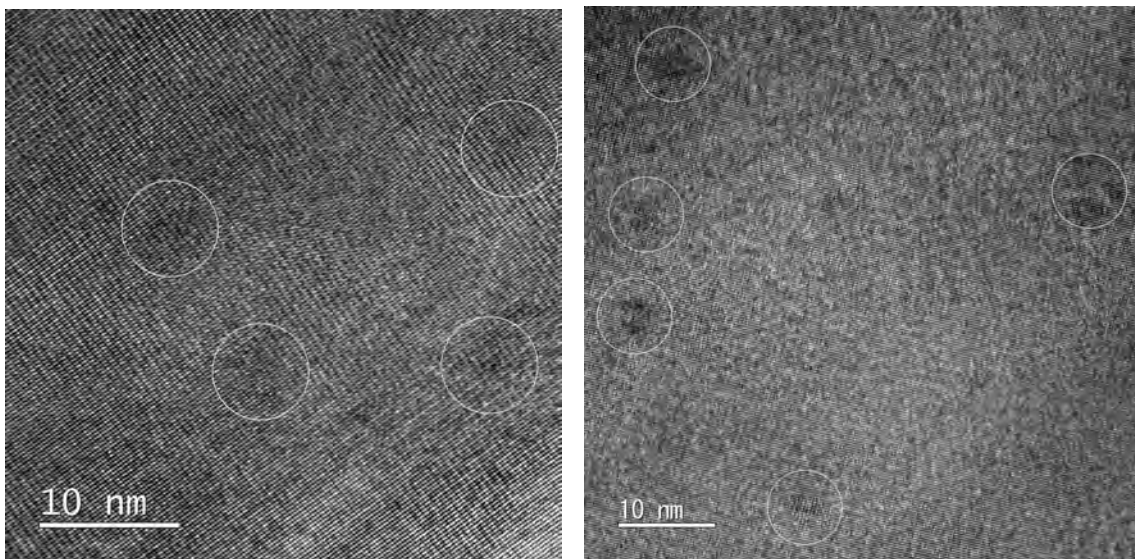
Figure 7.25: HRTEM images of the irradiated samples showing nano-meter sized locations in which the crystal structure is distorted (marked by circles).
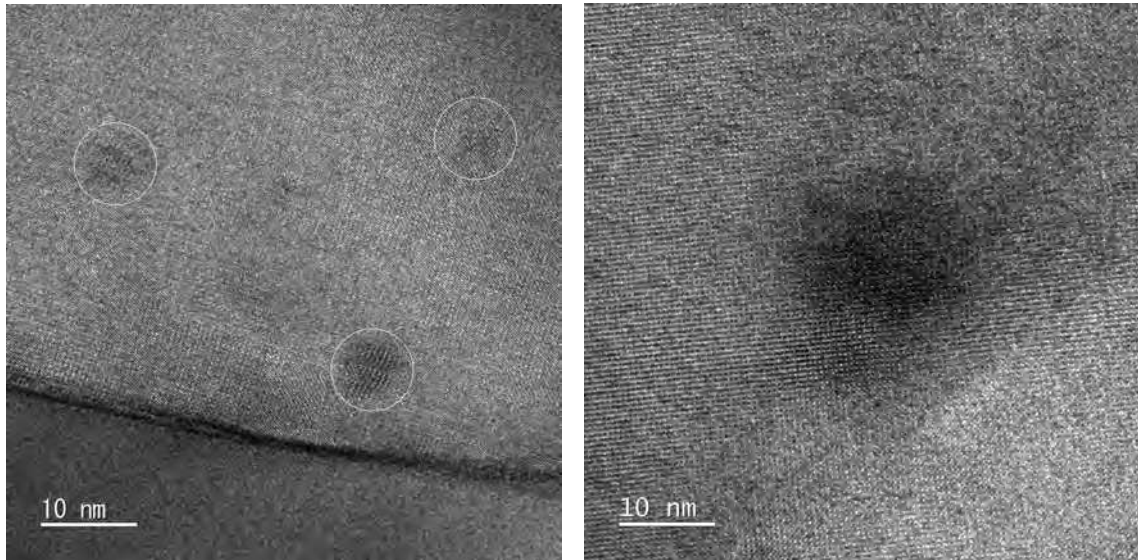
Figure 7.26: HRTEM images of the irradiated samples showing nano-meter sized locations in which the crystal structure is distorted (marked by circles).
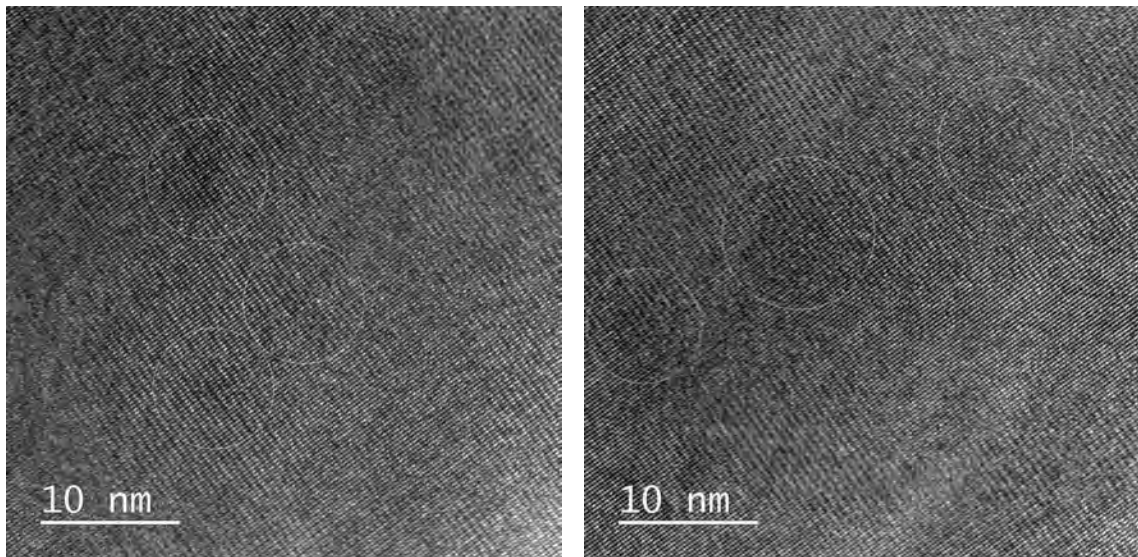
Figure 7.27: HRTEM images of the irradiated samples showing nano-meter sized locations in which the crystal structure is distorted (marked by circles).
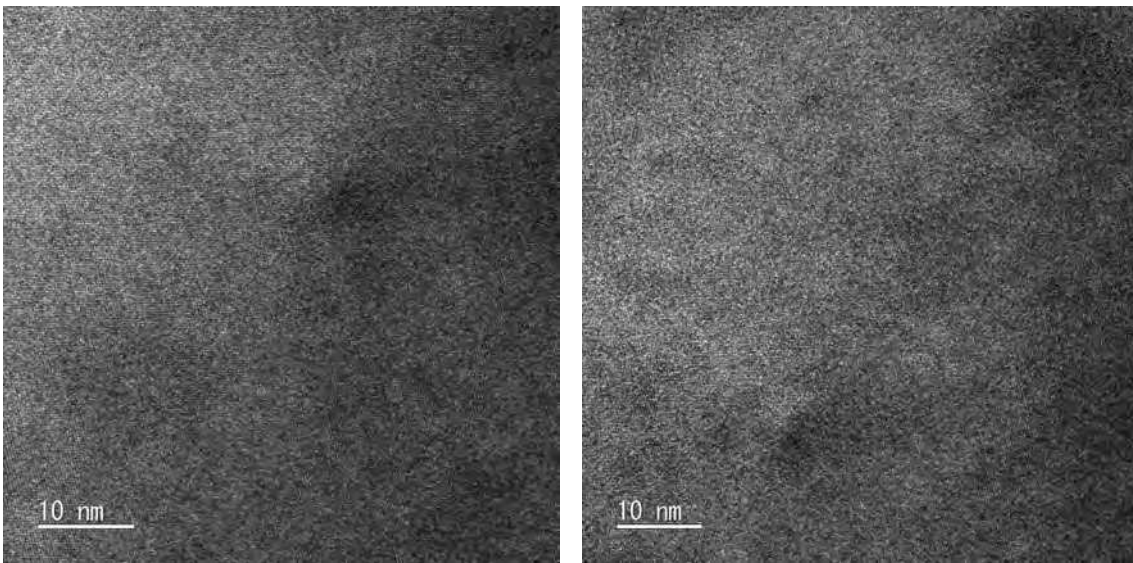
Figure 7.28: HRTEM images of the irradiated samples showing nano-meter sized locations in which the crystal structure is distorted.
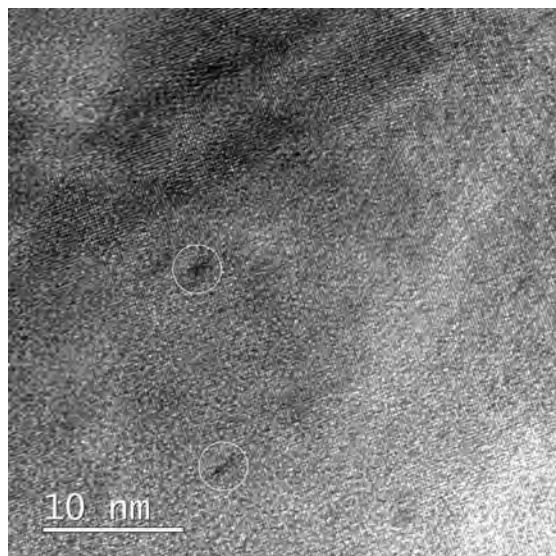
Figure 7.29: HRTEM images of the irradiated samples showing nano-meter sized locations in which the crystal structure is distorted (marked by circles).

7.5 Investigation of irradiated wires by HRSTEM

High resolution STEM (HRSTEM) imaging was conducted using a JEOL JEM-ARM 200F microscope in the course of a research visit at the Department of Materials, University of Oxford. This new generation TEM possesses additional magnetic quadrupole lenses that are able to correct the spherical aberration C_s, leading to a higher achievable resolution. The operation of the JEOL JEM-ARM 200F microscope for acquiring the results shown in this section was conducted by Jack Haley from the Department of Materials of the University of Oxford. While in the TEM mode, a small objective aperture was used to select the desired diffraction spot for dark field imaging in Section 7.4, in the STEM mode used in this section this was achieved by choosing a small camera length and shifting the corresponding diffraction disk onto the BF detector. Due to an overlap of the diffraction disks, the neighbouring disks may contribute to the information contained in the resulting image.

HRSTEM images of RRP-Ti-108 wire samples were acquired of un-irradiated wires and those irradiated at a fast neutron fluence of $2.82 \times 10^{22}\,\mathrm{m}^{-2}$. In the following, a comparison of un-irradiated and irradiated samples is shown. All samples shown in this section were post-processed using ion milling, unless stated otherwise.

7.5.1 Un-irradiated samples

High resolution STEM images of un-irradiated samples of the RRP-Ti-108 wire taken in a $\langle 100 \rangle$ zone axis are displayed in Figure 7.30 and Figure 7.31. Image taken of the same sample near a $\langle 110 \rangle$ zone axis is displayed in Figure 7.32, the ones shown in Figure 7.33 were taken in a $\langle 111 \rangle$ zone axis. No locations with considerable damage in the crystal structure were determined, except inclusions of Nb that are present in all wires as described in Chapter 4.
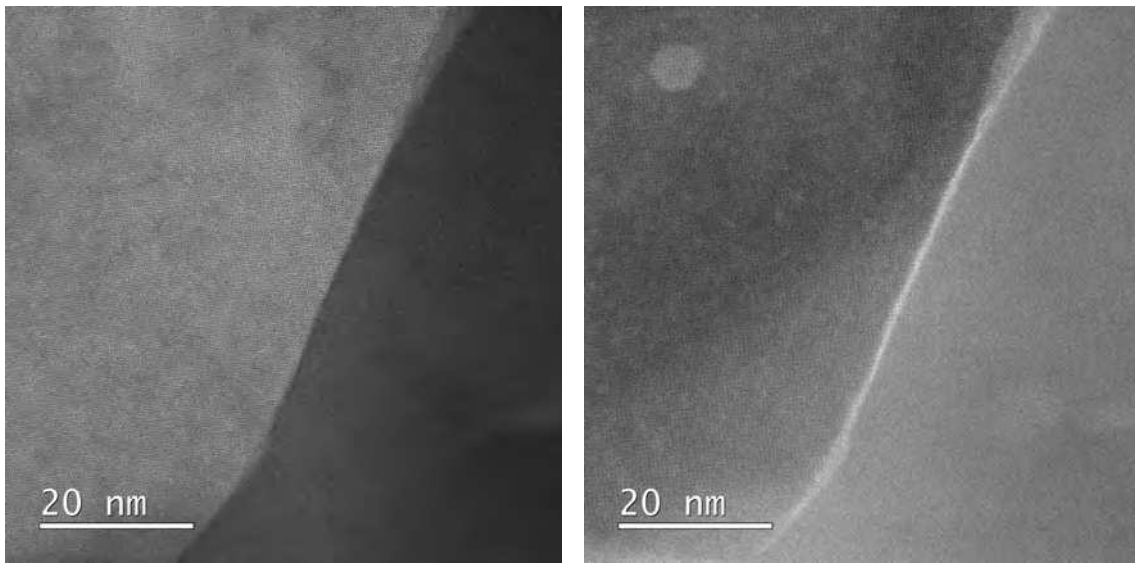
Figure 7.30: HRSTEM images of un-irradiated sample taken in a ⟨100⟩ zone axis showing largely undistorted lattice regions. Z-contrast (left) and diffraction contrast (right).
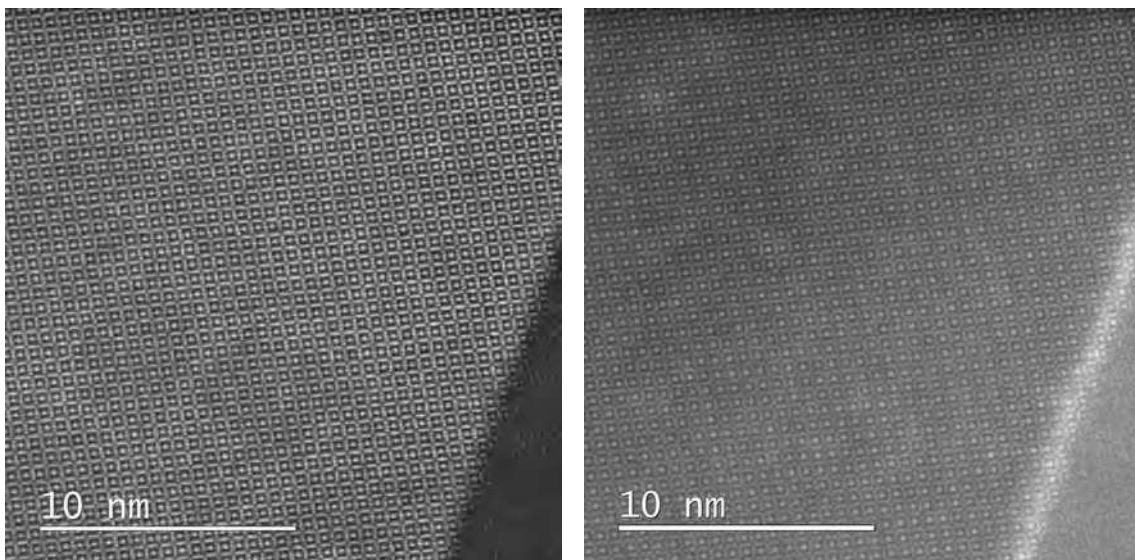
Figure 7.31: HRSTEM images of un-irradiated sample taken in a ⟨100⟩ zone axis showing largely undistorted lattice regions. Z-contrast (left) and diffraction contrast (right).
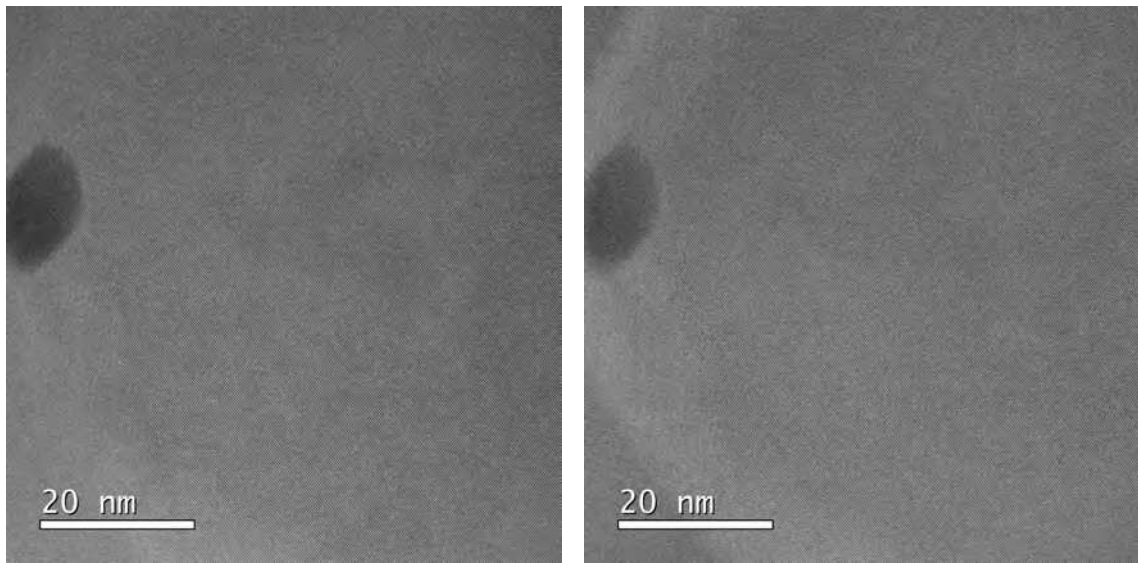
Figure 7.32: HRSTEM images of un-irradiated sample taken in a $\langle 110 \rangle$ zone axis showing largely undistorted lattice regions. Z-contrast (left) and diffraction contrast (right).
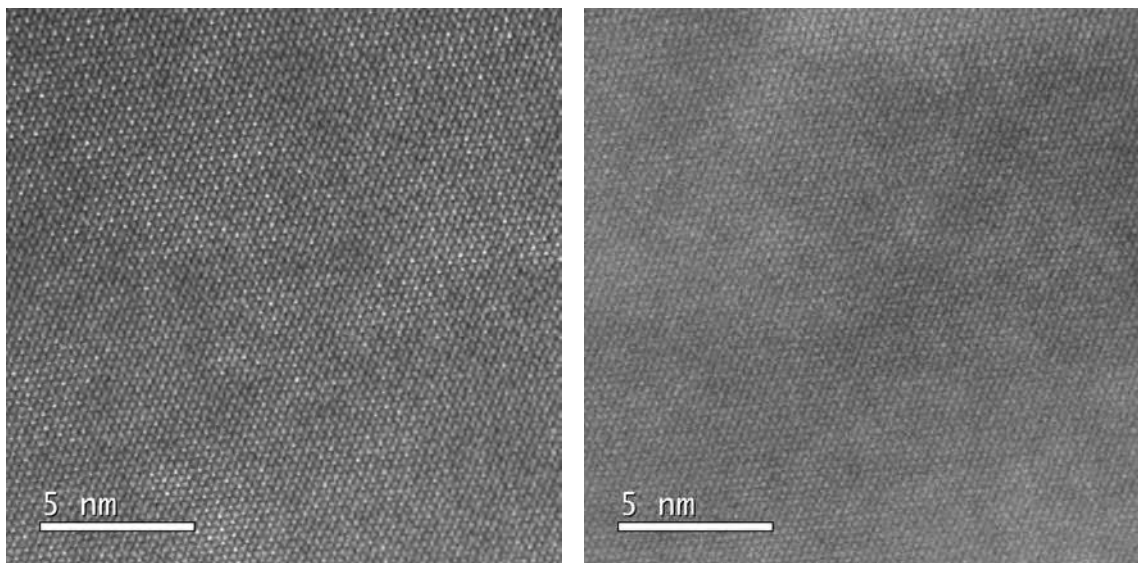
Figure 7.33: HRSTEM images of un-irradiated sample taken in a $\langle 111 \rangle$ zone axis showing largely undistorted lattice regions. Z-contrast (left) and diffraction contrast (right).

7.5.2 Irradiated samples

The analysis of RRP-Ti-108 wire samples that were irradiated at a fast neutron fluence of $2.82 \times 10^{22}\,\mathrm{m}^{-2}$ using high resolution STEM imaging revealed defects in the crystal structure that were likely caused by neutron irradiation.

Figure 7.34 shows images of an irradiated sample that was prepared only by FIB and without post-processing using ion milling. Disordered regions become apparent, that likely stem from ion damage induced during FIB preparation, as already described in Section 7.4.3. All the remaining images in this section were cleaned after FIB preparation using low energy ion milling.

The STEM image in Figure 7.35 was taken under dark field conditions, where the (400) reflection was strongly excited and used to form the image by shifting it onto the bright field detector. As already mentioned due to overlapping diffraction disks this image might contain contributions from the nearby reflections. A rather large grain was chosen in order to set the desired diffraction conditions more easily, where the corresponding diffraction pattern is shown in the same figure. The contrast of this image was inverted for a better visibility of the defects. The image shows small defects with black-white contrast resulting from strain fields around defects that are caused by a deformed lattice around the neutron impact sites. The imaged defects are presumably disordered regions resulting from collision cascades, in accordance with the literature review presented in Section 7.1. The dislocations seen at the top of the image were supposedly already present in the pristine sample and can not be related to the irradiation.
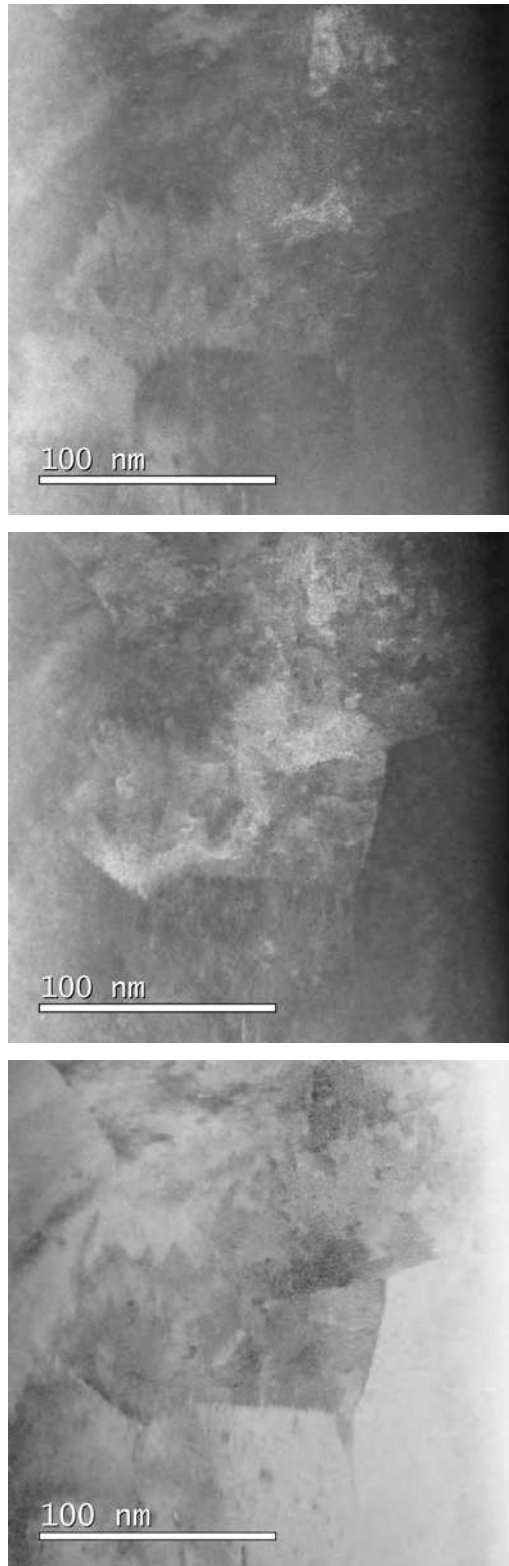
Figure 7.34: STEM images of irradiated sample showing small disordered regions likely induced by ions during preparation. Z-contrast (top), diffraction contrast (middle) and bright field (bottom).
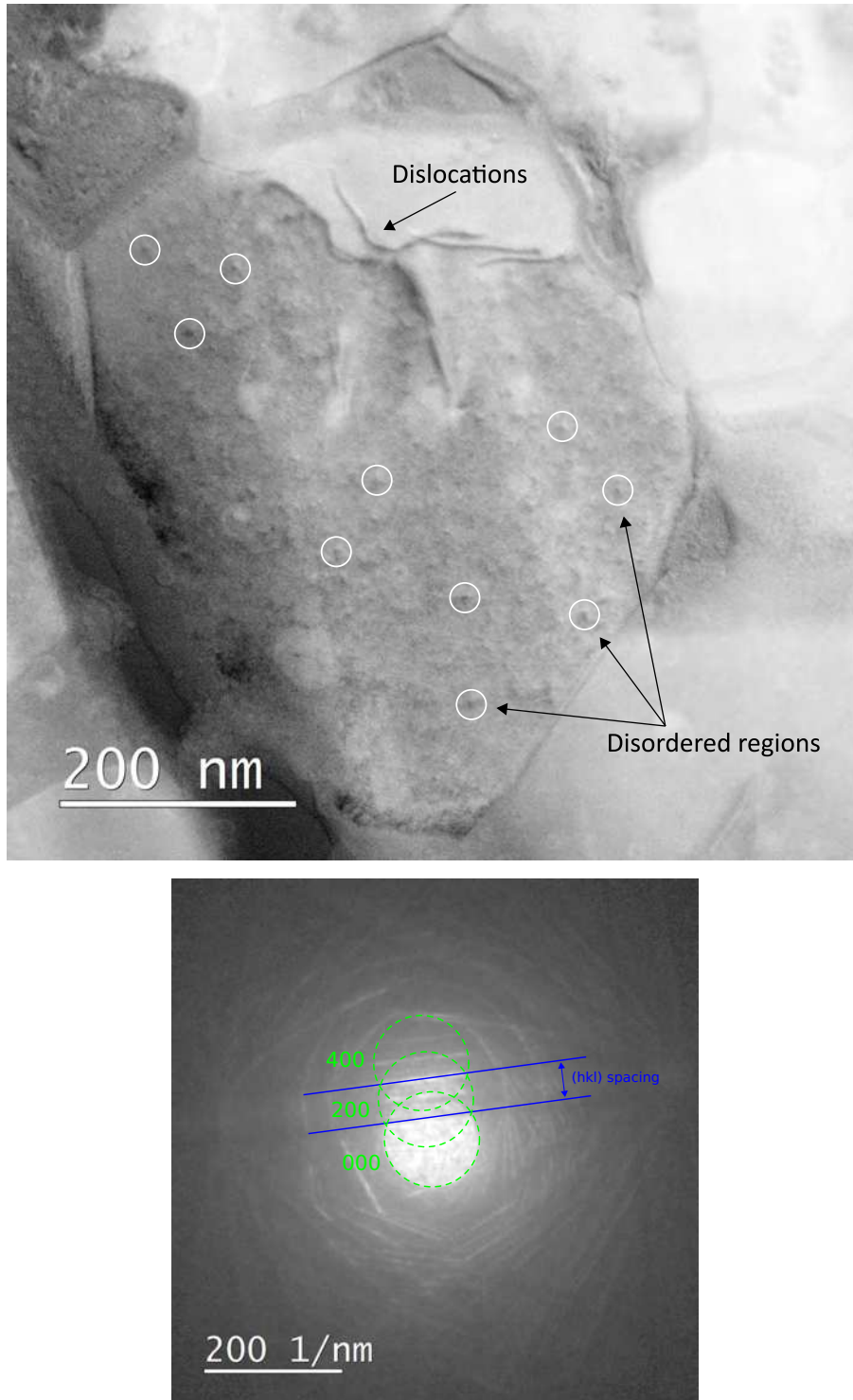
Figure 7.35: Inverted dark field STEM image of irradiated sample showing small disordered regions with black-white contrast resulting from the neutron irradiation (top) and corresponding diffraction pattern (bottom).

Figure 7.36 shows inverted dark field STEM images the same grain as investigated in Figure 7.35 where the corresponding diffraction conditions are displayed in the same figure, which show the used beam conditions. The (400) reflection was used for imaging in all cases. The condition of the first image in Figure 7.36 was the same as in Figure 7.35, except the diffraction pattern was moved slightly with respect to the detector, resulting in a weaker image due to less contribution from nearly reflections. For the second image in Figure 7.36, the weak (400) reflection was used for imaging, resulting in a weak-beam image. The same defects can be observed in all images, but their visibility and contrast changes depending on the diffraction conditions. The defects are frequently exhibiting black-white contrast, where the connection between the black and white area often points roughly in the direction of the $\vec{g}$-vector, which would indicate symmetrical strain fields and therefore isotropic defects as discussed in Section 1.8.
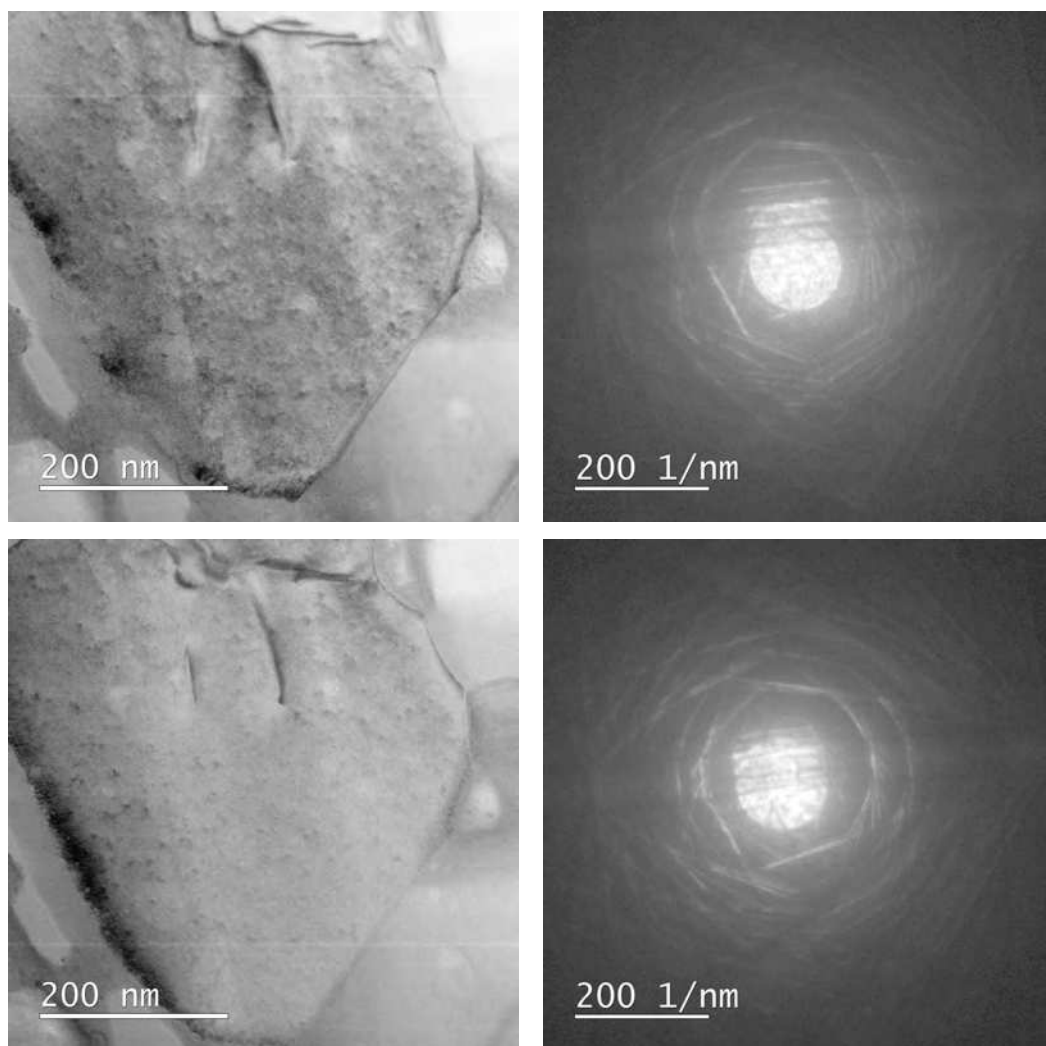
Figure 7.36: Inverted dark field STEM images of irradiated sample showing small disordered regions (left) and corresponding diffraction conditions (right).

A HAADF STEM image of the same grain of the irradiated sample in Figure 7.35 taken near a ⟨110⟩ zone axis is displayed in Figure 7.37, where small defects are visible in black under Z-contrast. Some defects also show white contrast lobes, hinting towards a vacancy rich and interstitial rich region, where the vacancy rich region is darker in Z-contrast due to the lower total atomic number.
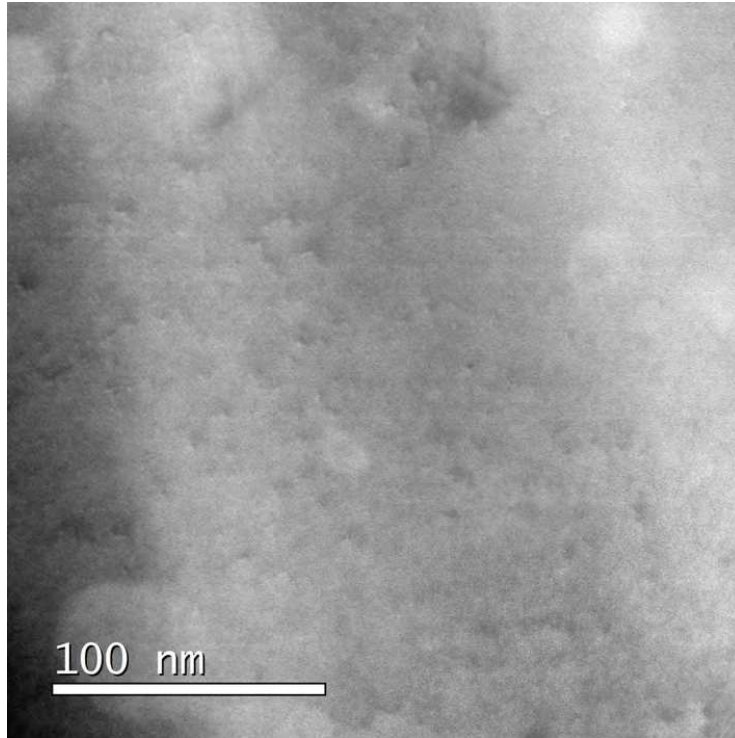
Figure 7.37: HAADF STEM image of irradiated sample taken near a ⟨110⟩ zone axis showing small disordered regions under Z-contrast.

Figure 7.38 shows HAADF, ADF and BF images of the same area taken near a ⟨110⟩ zone axis. The same types of images are displayed for a different sample area in Figure 7.39, in which case the sample was oriented in a ⟨110⟩ zone axis. The 20 nm large contrast in the central region of these images likely results from carbon contamination during acquisition of higher magnification images. Z-contrast as well as diffraction contrast becomes apparent, indicating strain fields that are accompanying the regions with displaced atoms.

High resolution STEM images of the same grain as shown in Figure 7.35 taken in a ⟨110⟩ zone axis are displayed in Figure 7.40, from which it becomes apparent that the defects caused by neutron irradiation are the size of around 3.5 nm in diameter. The first image in this figure is a HAADF image that shows Z-contrast, where the defect appears dark, indicating the regions being of type vacancy. Since the defect is also visible in the ADF image showing diffraction contrast and in BF, it can be said that the defect is accompanied with distortions in the lattice surrounding it.
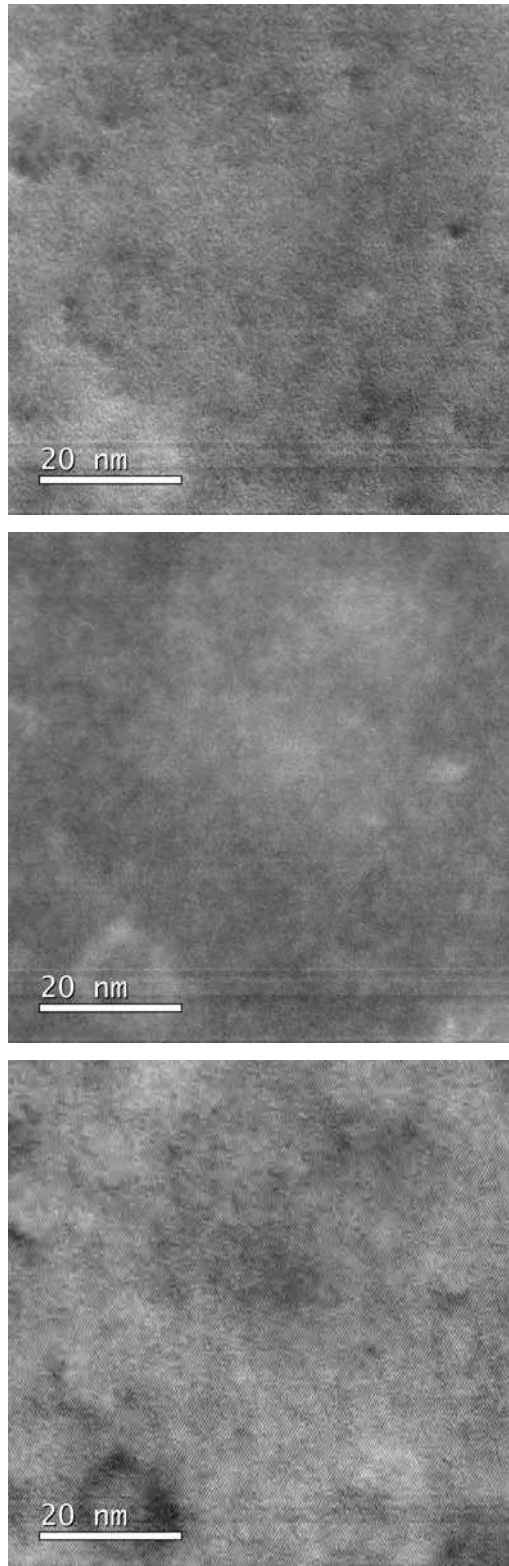
Figure 7.38: High resolution STEM images of irradiated sample showing small disordered regions. Z-contrast (top), diffraction contrast (middle) and bright field (bottom).
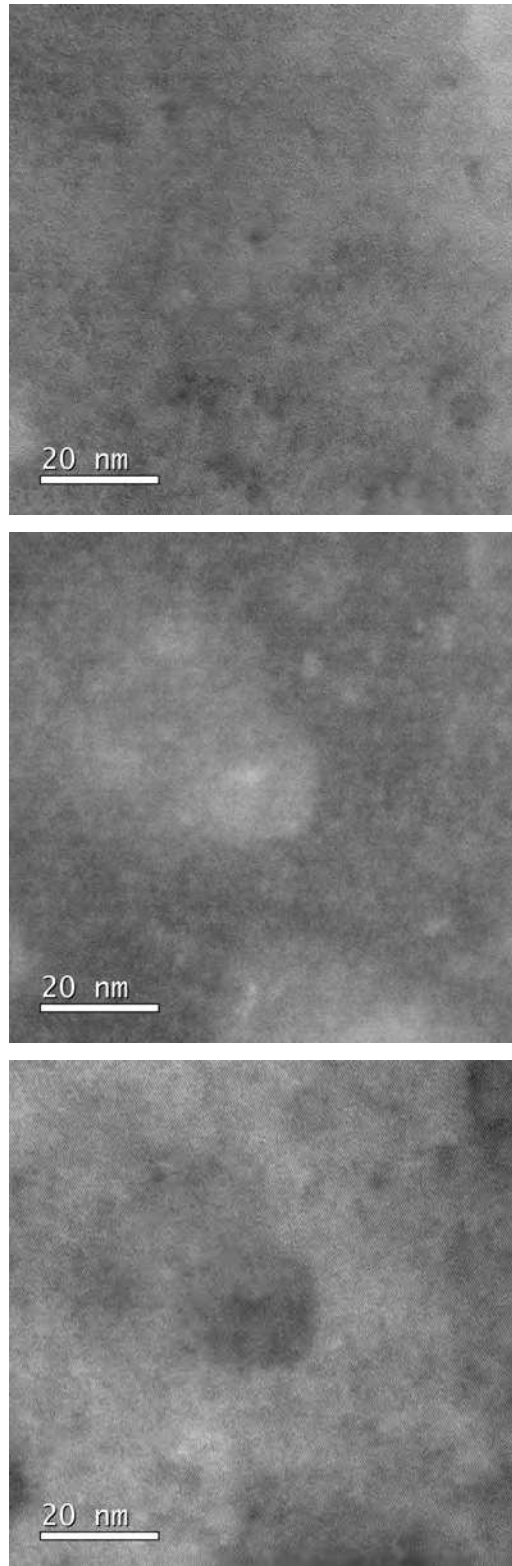
Figure 7.39: High resolution STEM images of irradiated sample taken in a $\langle 110 \rangle$ zone axis showing small disordered regions. Z-contrast (top), diffraction contrast (middle) and bright field (bottom).
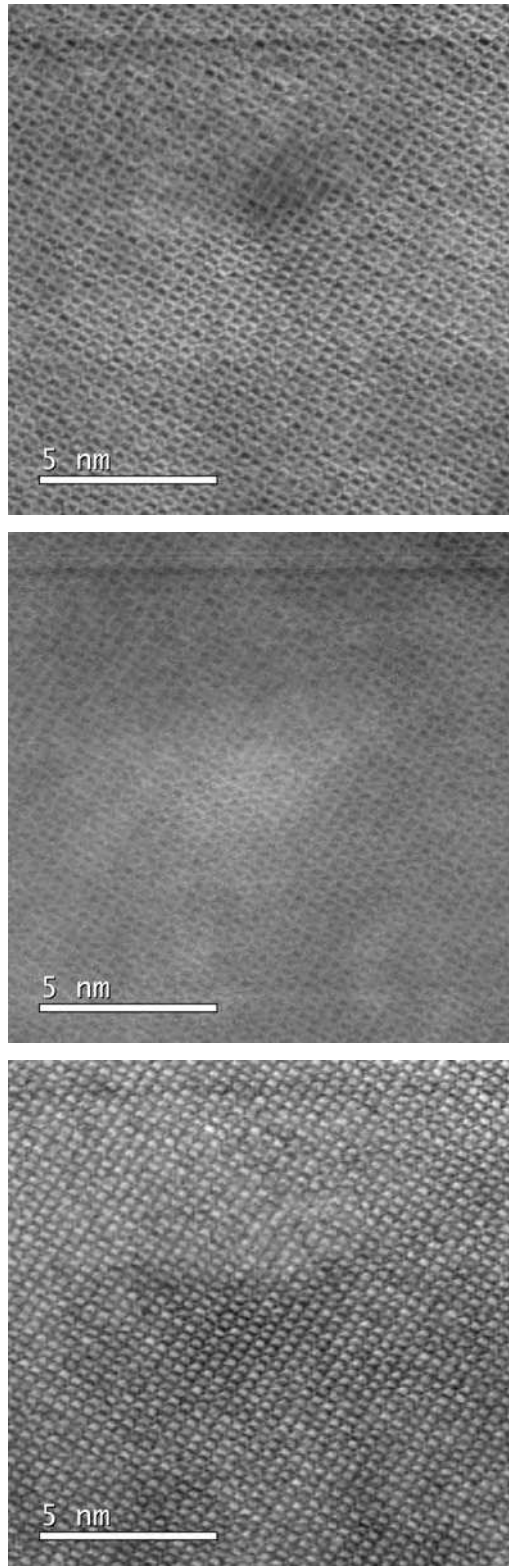
Figure 7.40: High resolution STEM images of irradiated sample taken in a ⟨110⟩ zone axis showing small disordered regions. Z-contrast (top), diffraction contrast (middle) and bright field (bottom).

In Figure 7.41, a high resolution STEM image taken in a $\langle 100 \rangle$ zone axis can be found, where the Nb$_3$Sn unit cells are visible. The marked locations show hints of displaced atoms and deformed unit cells. It can not be said with certainty that these defects originate from the irradiation with neutrons, albeit the simulations conducted in Section 7.2 have shown that the expected displacements per atom (dpa) at this fluence of $2.82 \times 10^{22}\,\mathrm{m}^{-2}$ is 2.2×10^{-3}, leading to the conclusion that 1.18×10^{8} vacancies are produced per µm^3. This amount of vacancies can therefore lead to the image contrast that was simulated in the same section and shows similarities to the experimentally acquired images.
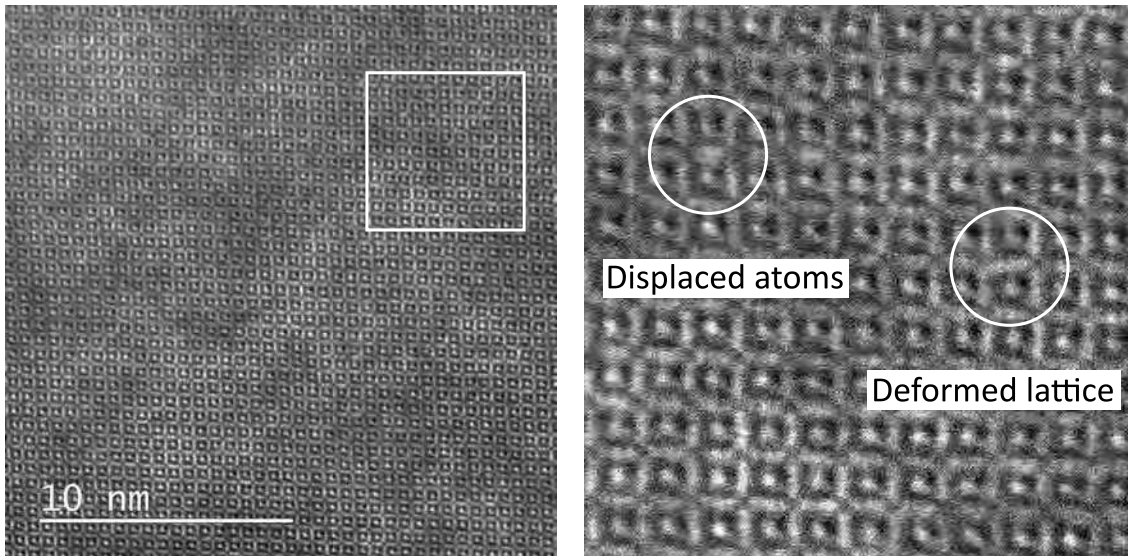
Figure 7.41: High resolution STEM images of irradiated sample taken in a $\langle 100 \rangle$ zone axis showing point defects. Original image (left) and magnification of the boxed area (right).

7.6 Evaluation of the defect density and size distribution

The HRSTEM images shown in Figure 7.42 and Figure 7.43 were used to evaluate the density of the observed defects. The results are displayed in Table 7.6 and Table 7.7, respectively.

The analysis of the first investigated area shown in Figure 7.42 led to 133 counted defects. The sample thickness of this region was determined by EELS measurements in different points. The average sample thickness in the investigated grain was determined at 62 nm. The amount of counted defects together with the estimated sample thickness leads to a defect density of $11\,589\,\mu\mathrm{m}^{-3}$. In the second investigated area, in Figure 7.43, 75 defects were counted, leading to a defect density of $16\,594\,\mu\mathrm{m}^{-3}$. The observed defect density thus can be stated to be in the order of roughly $1.16 \times 10^{22}\,\mathrm{m}^{-3}$–$1.66 \times 10^{22}\,\mathrm{m}^{-3}$, where the higher value was obtained from the higher magnification image and should therefore be more accurate.

The estimation of the volume defect density is afflicted with a number of factors that potentially increase the error and affect the resulting value, which have been outlined in Section 1.8 and in Section 7.1. It was explained how the diffraction conditions, the location of the defect in the sample and the sample thickness affect the visibility of the defects, where about half of the produced defects are possibly not visible by TEM imaging. Taking these factors into account, an estimation of the real present density of the defects leads to a value that might potentially be over $30\,000\,\mu\mathrm{m}^{-3}$. Aggravating the evaluation is furthermore the presence of dislocations and other forms of damage in the material originating from the manufacturing process and the sample preparation as well as the small grain size of the investigated Nb_3Sn wires. Additionally, the determination of the sample thickness by EELS might also be afflicted with errors and thus affecting the calculated defect density.

The evaluation of the defect density conduced on the samples that were irradiated at a fluence of $2.82 \times 10^{22}\,\mathrm{m}^{-2}$ led to a density of around $1.16 \times 10^{22}\,\mathrm{m}^{-3}$–$1.66 \times 10^{22}\,\mathrm{m}^{-3}$. Assuming that the defect density scales linearly with fluence, a fast neutron fluence of $10^{22}\,\mathrm{m}^{-2}$ therefore corresponds to a defect density of $4.11 \times 10^{21}\,\mathrm{m}^{-3}$–$5.89 \times 10^{21}\,\mathrm{m}^{-3}$.

Even though a number of studies about neutron irradiation damage in Nb_3Sn are available as presented in Section 7.1, neither of them states a value for the determined defect density. In the study presented in [1], neutron irradiated Bi-2212 single crystals were investigated. The cascade size was stated to be 3.5 nm and their density $3.7 \times 10^{22}\,\mathrm{m}^{-3}$ per neutron fluence of $10^{22}\,\mathrm{m}^{-2}$ ($E > 0.1\,\mathrm{MeV}$), which corresponds to $1.4 \times 10^{23}\,\mathrm{m}^{-3}$ at a fast fluence of $2.82 \times 10^{22}\,\mathrm{m}^{-2}$. This results of the defect density is higher than the one in the present study of $1.4 \times 10^{22}\,\mathrm{m}^{-3}$. In [1], however, the obtained values were calculated by applying a multiplication factor to the experimentally determined defect density in order to account for the

defects that were not visible in the TEM images during the evaluation at the used diffraction conditions. Aside from that, the investigated materials differ from each other, potentially behave different under irradiation and might therefore lead to different defect densities after irradiation with fast neutrons.

In [13], the same RRP type Nb_3Sn wire with Ti addition as investigated here was irradiated and the increase in J_c was determined by SQUID magnetometry. A fluence of $2.5 \times 10^{22} \, m^{-2}$ led to an increase in J_c by over 50% at $4.2\,K$ and $6\,T$. In the present study, the maximum neutron fluence was close to that value at $2.82 \times 10^{22}\,m^{-2}$ and it was determined that this fluence corresponds to the introduction of additional pinning centres with the density of $16\,600\,\mu m^{-3}$. Contrary to the defect density, which scales linearly with the fluence, the increase in J_c generally does not show a linear dependence on the fluence, for which reason it is not reasonable to establish a general correlation between the number of defects and the increase in J_c. Additionally, different wire types might behave differently under irradiation, therefore the values of the J_c increase might also differ between wires irradiated to the same fluence.
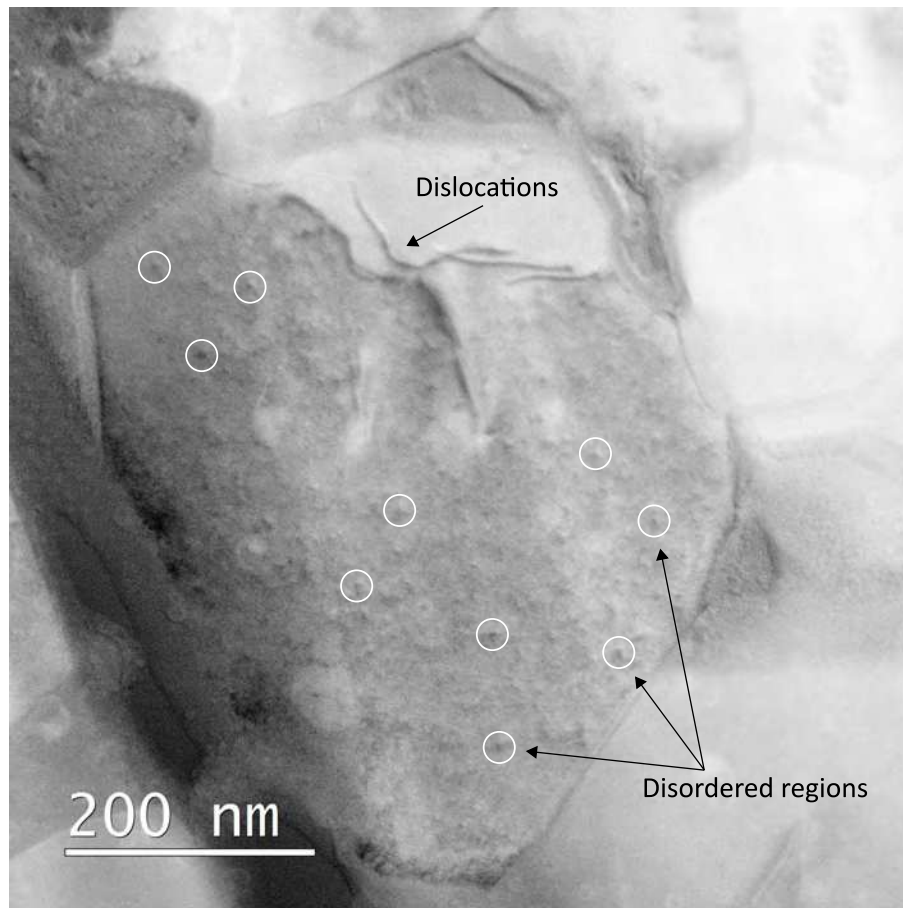
Figure 7.42: HRSTEM image of irradiated sample used for the evaluation of the defect density.

Parameter	Value	Unit
Investigated area	185 108	nm^2
Measured sample thickness	62	nm
Investigated volume	11 476 696	nm^3
Counted defects	133	
Defect density per area	718	μm^{-2}
Defect density per volume	11 589	μm^{-3}
Modal defect diameter	3–4	nm

Table 7.6: Results of the evaluation of the defect density of the irradiated sample.
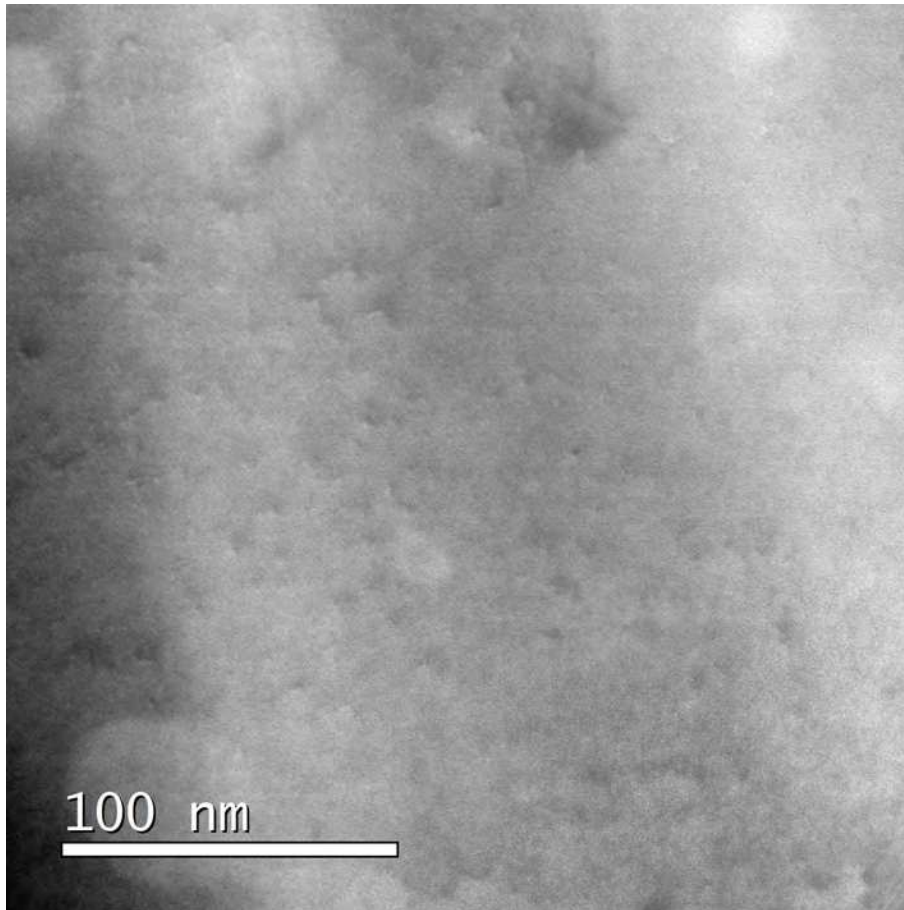
Figure 7.43: HRSTEM image of irradiated sample used for the evaluation of the defect density.

Parameter	Value	Unit
Investigated area	72 900	nm^2
Measured sample thickness	62	nm
Investigated volume	4 519 800	nm^3
Counted defects	75	
Defect density per area	1029	μm^{-2}
Defect density per volume	16 594	μm^{-3}
Modal defect diameter	2–3	nm

Table 7.7: Results of the evaluation of the defect density of the irradiated sample.

The size distribution of the defects that were analysed in Figure 7.42 and Figure 7.43 was evaluated in the same manner as for the precipitates in the APC wires, by drawing lines across their diameters as described in Chapter 4 and the corresponding distributions are displayed in Figure 7.44. It becomes apparent that the defects induced by fast neutron irradiation are most frequently in the order of 2 nm–4 nm, with a total range of 1 nm–10 nm. The modal interval for the first investigated area is 3 nm–4 nm with a mean value of (3.6 ± 1.4) nm, the second investigated area shows a modal interval of 2 nm–3 nm and a mean value of (3.3 ± 1.4) nm. The statistics resulting from the analysis of the second area resulted in slightly lower values of the defect diameters and also a higher defect density. These circumstances likely result from a higher image resolution due to a higher magnification at which the second image was acquired, which should therefore result in a more accurate statistics. Additionally, the defects are frequently not of circular shape and the contrast does often not show well defined edges, leading to errors in the determination of their diameter.
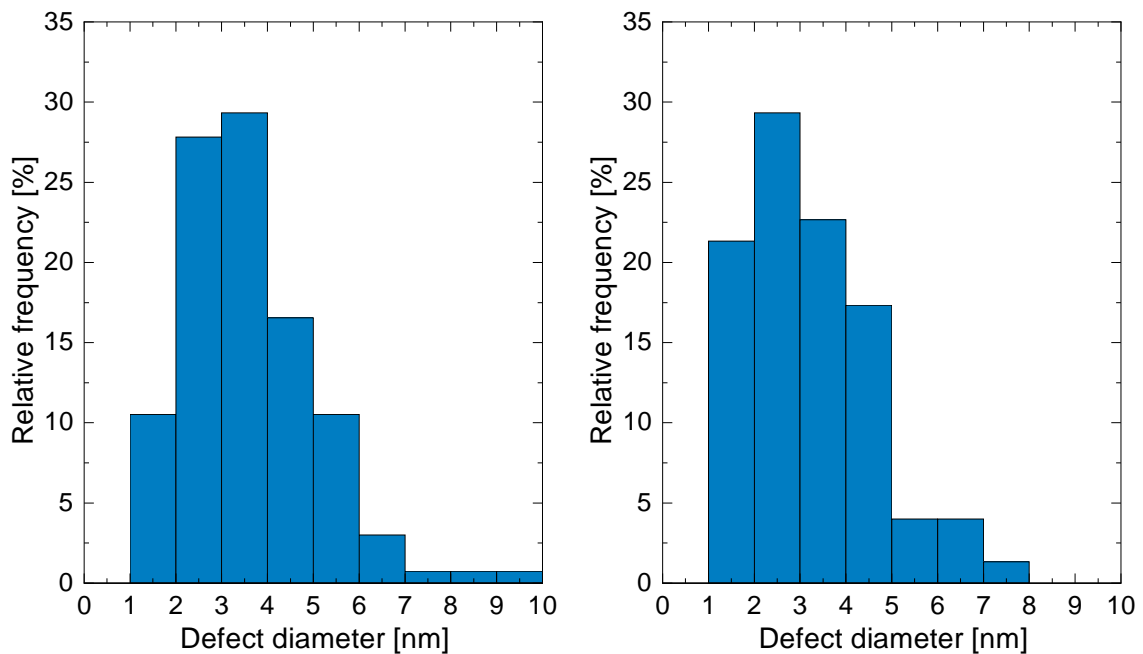
Figure 7.44: Size distribution of investigated neutron defects.

The obtained size distributions of the neutron irradiation defects in Nb$_3$Sn displayed in Figure 7.44 show a remarkable similarity with the distributions presented by Pande [102], confirming the validity of the results.

7.7 Correlation of irradiation experiments and simulations

The calculated *dpa* value described by Equation 7.1 yields information about the amount of produced Frenkel defects, but does not yield information about the number of defects that are observable by TEM, since a fraction might recombine.

In order to estimate the fraction of observed defects compared to the produced defects, the experimentally observed defect size and density presented in the previous section was correlated with the FISPACT-II simulation results, which can be found in Table 7.2. For this, the assumption was made that an observed defect exclusively consists of displaced atoms. All disordered regions therefore were approximated with spherical volumes in which all atoms are displaced. This assumption might naturally lead to errors in the calculation, since in reality the disordered regions might not exclusively consist of displaced atoms.

The results of this calculation are displayed in Table 7.8, where the defects were approximated with spheres of 3.5 nm in diameter. In this case it can be concluded that the vacancies inside the observed disordered regions with a density of $16\,600\,\mu m^{-3}$ amount to $16.9\,\%$ of the calculated *dpa* value and therefore the total produced vacancies in this volume.

Since the size of the defects exhibit a distribution as seen in Figure 7.44, the same calculations were conducted with the use of different defect diameters and the results are shown in Table 7.9 for defects with a spherical shape. The ratio of the observed to the produced defects varies between $10.7\,\%$ and $25.3\,\%$, depending on the used geometric approximation for the defects.

These results appear realistic when considering that the calculated *dpa* describes the amount of produced defects in the form of Frenkel pairs as described by Equation 7.1, where a large number of those can remain as single displaced atoms or be unstable and lead to recombination. The remaining vacancies either did not accumulate to observable defect clusters or relaxed to their original position in the crystal lattice. Additionally, it is likely that not all produced defects were observed by TEM as described earlier.

Parameter	Value	Unit
Atoms in 3.5 nm sphere	1.21×10^3	atoms
Defects of 3.5 nm counted	16 600	μm^{-3}
Total vacancies in counted defects	2×10^7	μm^{-3}
Ratio observed/produced vacancies	16.9	$\%$

Table 7.8: Results of the calculated ratio of observed to produced defects.

Defect diameter [nm]	Ratio observed/ produced vacancies [%]
3.0	10.7
3.5	16.9
4.0	25.3

Table 7.9: Results of the calculated ratio of observed to produced defects for different geometric approximations.

7.8 Geometric phase analysis

Geometric phase analysis (GPA) was originally described in [72]. GPA is a method of visualizing strain and displacement fields from high resolution TEM images. It can be used to quickly produce maps of lattice deformations in regard to a reference lattice. GPA is based on filtering of the Fourier transform of a TEM image by centring a mask around a strong Bragg reflection and calculating the inverse Fourier transform. The resulting complex phase image contains informations about atomic displacements. Through application of this method on two non-collinear reciprocal lattice vectors the two-dimensional displacement field can be calculated. Deriving this displacement field yields information about local strain and distortion. All deviations are then referred to the two-dimensional lattice that is defined by the two reciprocal lattice vectors. Variations in the lattice spacing lead to diffuse intensities of the Bragg spots while a perfect lattice results in sharp peaks of the Bragg spots. If an image is formed by the use of strong reflections and diffuse frequencies, local variations of the imaged structure can be imaged. GPA thus yields quantitative information about lattice deformation with regard to the reference lattice. Additionally, Fourier filtering can be used to improve the image contrast through applying masks around the Bragg spots of the Fourier transform [74].

The local lattice distortion e is defined by the gradient of the displacement field u, which originates from the phase differences of an image [74]:

$$e = \begin{pmatrix} e_{xx} & e_{xy} \\ e_{yx} & e_{yy} \end{pmatrix} = \begin{pmatrix} \frac{\partial u_x}{\partial x} & \frac{\partial u_x}{\partial y} \\ \frac{\partial u_y}{\partial x} & \frac{\partial u_y}{\partial y} \end{pmatrix}. \tag{7.2}$$

The local strain ε and the dilatation Δ are then given by [109]:

$$\varepsilon = \frac{1}{2}\left(e + e^T\right), \quad \Delta = Trace[e]. \tag{7.3}$$

The strain determination based on Fourier analysis has the advantage of a lower dependency on the imaging conditions compared to conventional methods that rely on establishing the positions of peaks in HRTEM images. However, precautions have to be made in respect to thickness variations of the sampled area which can lead to artefacts due to additional phase shifts. Noise in the image can furthermore result in a lowering of the resolution of the displacement field image and an unusable strain map [133].

Recently the technique of GPA has been applied to high resolution images acquired by an aberration corrected TEM allowing deformation maps of nanometre scale resolution with an accuracy of 0.1 % [73].

In the present study, GPA was conducted on HRSTEM images of irradiated samples using the Strain++ program [109], which implements the algorithm described in [74]. The result of the GPA analysis conducted on a HRSTEM image of an irradiated sample can be found in Figure 7.45, where the areas with defects are marked by circles and from which it becomes apparent that neutron impacts lead to dilatation in the crystal lattice. The noise in the top left corner of the image likely results from overlapping crystal lattices near a grain boundary or inhibited image quality. The central neutron impact site is additionally surrounded by a strain field that is much larger than the defect itself and over 20 nm in size, which is likely not related to the irradiation as already observed in Figure 7.39.
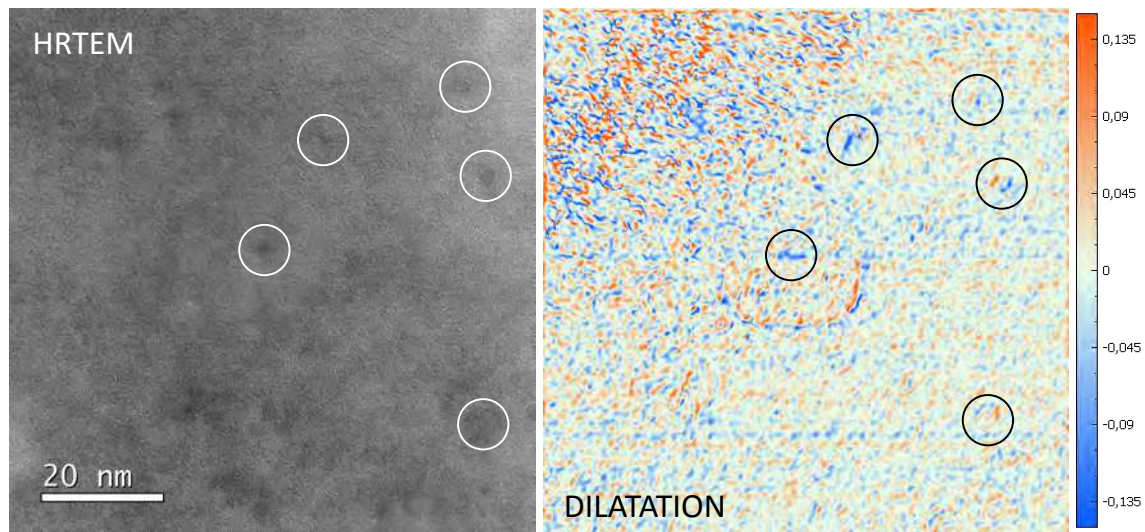
Figure 7.45: GPA analysis of an irradiated Nb_3Sn wire. HRSTEM image (left) and resulting dilatation map (right).

7.9 Comparison of defects by irradiation and internal oxidation

The results of the investigation of defect clusters in wires irradiated at a fluence of $2.82 \times 10^{22}\,\text{m}^{-2}$ in this chapter were compared with the results of the precipitate analysis of the ternary internal oxidized wires that was presented in Section 4.2. The comparison of the relevant parameters can be found in Table 7.10.

	Neutron irradiation	Internal oxidation
Pinning mechanisms	Disordered regions Displaced atoms	Grain refinement Nano-precipitates
Modal defect size	$\sim$2 nm–4 nm	$\sim$2 nm–4 nm
Pinning site density	$\sim$16 600 µm^{-3}	$\sim$25 000 µm^{-3}
FCC J_c target reached	✓ [13]	✓ [169]

Table 7.10: Comparison of the properties of neutron irradiated and internal oxidized wires.

A comparison of the size distributions between ZrO_2 precipitates in the APC-3912-084 wire and neutron irradiation induced defects is shown in Figure 7.46, where all measured defects of the respective type were included. The distributions are plotted up to a defect diameter of 20 nm for a better comparability, where outliers of the APC wire are not included and the complete statistics were presented in Chapter 4.

It becomes apparent that both the density of the defects as well as their modal size in the ternary APC-3912-084 wire show remarkably similar values to the defects in the wires that were irradiated with a fast neutron fluence of $2.82 \times 10^{22}\,\text{m}^{-2}$. The density of the defects is of the same magnitude and they share their three most frequent intervals of their size distributions at 2 nm–3 nm, 3 nm–4 nm and 4 nm–5 nm. A difference is observed for their maximum diameters, which is around 10 nm for neutron irradiation defects and over 20 nm for ZrO_2 precipitates in APC wires. However, it has to be noted that the size distributions vary also between different APC wires and the comparison of neutron irradiation defects with other APC wires might lead to different conclusions.

A comparison between the artificial pinning centres produced by high energy irradiation and by nano-inclusions was done in [137]. The enhancement of the critical current density J_c in irradiated wires is based on point pinning and depends on the number of Frenkel pairs that are described by the *dpa* value. In wires containing nano-inclusions, both point pinning and grain boundary pinning are contributing factors due to a refinement of the grain size and the importance of grain boundaries for a high pinning force in Nb_3Sn. The J_c enhancement as a function of the magnetic field B was found to show a similar behaviour for neutron irradiated wires and those
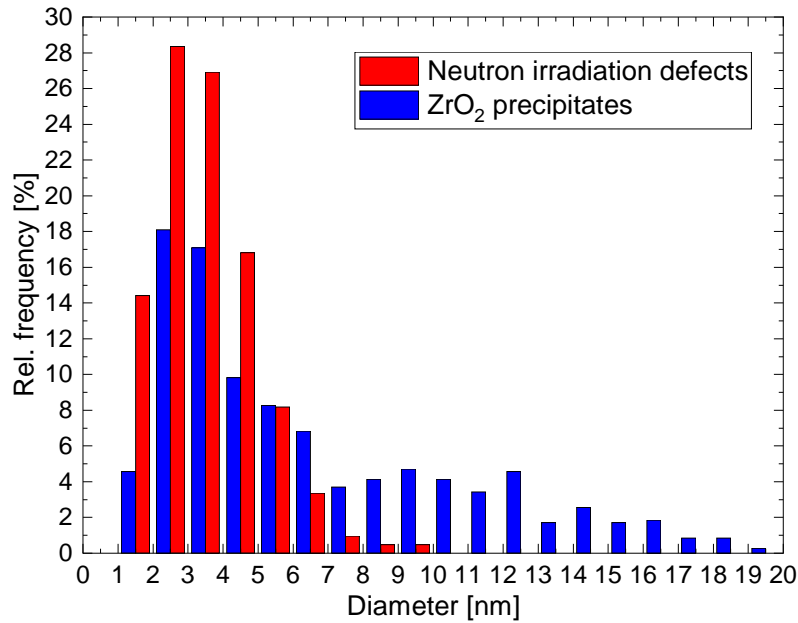
Figure 7.46: Comparison of the size distributions between ZrO_2 precipitates in the APC-3912-084 wire and neutron irradiation induced defects.

containing nano-precipitates. In both cases, a strong J_c enhancement was observed at low fields, while it decreased at increasing applied fields. For irradiated Nb_3Sn wires, the enhancement was stated to become zero at the upper critical field B_{c2}.

In summary, it is remarkable that both types of wires containing different forms of artificial pinning centres not only showed similarities in the behaviour of the J_c enhancement, but also in the microstructure.

7.10 Conclusions of irradiation experiments

The most relevant results of the investigations of the defect structure in neutron irradiated Nb_3Sn wires can be summarized as follows:

1. The simulation of the expected *dpa* in Nb_3Sn due to the irradiation showed that a fast (E>0.1 MeV) fluence of $2.82 \times 10^{22} \, \text{m}^{-2}$ leads to a total *dpa* of 2.2×10^{-3}. The amount of displaced atoms per grain was estimated at 1.18×10^5 at this fluence.

2. The direct comparison of the same sample regions before and after irradiation have proven to be challenging due to the deterioration of the sample surface quality during the irradiation process.

3. The interpretation of acquired images has shown to be challenging due to the influence of ion damage that results from the preparation process. This influence could be reduced through cleaning using low-energy ion milling.

4. The direct comparison of the same sample regions before and after irradiation at a fluence of $3.9 \times 10^{21}\,\mathrm{m}^{-2}$ have not led to noticeable differences in the defect structure.

5. The investigation of specimens that were prepared post irradiation at low fluences of $3.68 \times 10^{21}\,\mathrm{m}^{-2}$ and $3.83 \times 10^{21}\,\mathrm{m}^{-2}$ have shown sparsely distributed defects with a few nm in diameter.

6. The investigation of samples irradiated at a high fluence of $2.82 \times 10^{22}\,\mathrm{m}^{-2}$ that were prepared using only FIB revealed a high density of defects which were attributed to ion damage resulting from the preparation procedure.

7. The investigation of samples irradiated at a high fluence of $2.82 \times 10^{22}\,\mathrm{m}^{-2}$ that were prepared using FIB followed by low-energy ion milling resulted in the finding of nano-meter sized regions in which the crystal lattice is distorted.

8. The investigation of samples irradiated at a high fluence of $2.82 \times 10^{22}\,\mathrm{m}^{-2}$ using high resolution STEM imaging revealed defects that led to black-white contrast under dark field conditions, indicating strain contrast, and appeared dark under Z-contrast in HAADF images, indicating vacancy rich regions.

9. High resolution images taken in a zone axis revealed hints of displaced atoms, which simulations have predicted to occur at a density of $1.18 \times 10^{8}\,\mathrm{\mu m}^{-3}$ at this fluence.

10. The evaluation of the defect density from dark field and HAADF images resulted in about $16\,600\,\mathrm{\mu m}^{-3}$. The size distribution of the defects was determined, which showed modal values of $2\,\mathrm{nm}$–$4\,\mathrm{nm}$.

11. Assuming an observed defect of $3.5\,\mathrm{nm}$ in size exclusively consists of displaced atoms, the observed defect density of $16\,600\,\mathrm{\mu m}^{-3}$ amounts to about $16.9\,\%$ of the calculated *dpa*.

12. Geometric phase analysis of HRTEM images of irradiated wires revealed dilatation and strain fields accompanying the neutron impact sites.

13. The comparison of the parameters of neutron irradiation induced defects at a fluence of $2.82 \times 10^{22}\,\mathrm{m}^{-2}$ with those of the nano-precipitates in ternary wires manufactured by the internal oxidation process revealed that both their size and their density are very comparable. The modal sizes of the precipitates in a new generation ternary APC wire were found to be the same as the ones of the irradiation defects, while also their density is of the same magnitude.

8 SHPM analysis of the magnetic properties

While this thesis mainly addresses the microstructure of Nb$_3$Sn wires, the ultimate goal of the conductor development programme within the FCC study is to enhance their performance through refining the microstructure. For that reason an understanding of the correlation between the microstructure and the macroscopic magnetic properties is highly relevant. This chapter describes magnetic measurements that were performed at the Atominstitut of TU Wien. In particular, scanning Hall probe microscopy (SHPM) was employed, from which information about inhomogeneities in T_c and J_c can be derived. SHPM was used to determine distributions of the critical temperature T_c as well as remanent fields, from which the critical current density J_c can be estimated by the inversion of the Biot-Savart law. This chapter mainly described the employed techniques and the acquired measurements on the different samples. The correlations between the assessed magnetic properties and the microstructure will be discussed in Chapter 9.

8.1 Scanning Hall probe microscopy

Scanning Hall probe microscopy (SHPM) is a characterization method that enables the investigation of local superconducting properties resulting in spacial resolved maps [8]. The advantage of SHPM compared to other methods that aim to measure the magnetic flux profile at the sample surface is its noninvasiveness while simultaneously providing a good spatial resolution [25, 100]. The principle of magnetic mapping using Hall probes is described in [56] and [57], although the scanning system used in the present work is operating at a much finer resolution. The authors have further shown that it is possible to obtain the distribution of the critical current density by inversion of the Biot-Savart law. The calculation of the critical current distribution in thin samples from measurements of the magnetic flux density profile by inversion of the Biot-Savart law was also demonstrated in [141].

The magnetic flux density B can be measured by scanning over the surface of the superconductor with a Hall probe at a distance of a few µm after cooling it to temperatures below T_c and applying an external magnetic field. There are different

modifications of the SHPM technique in existence, including the use of a small permanent magnet that magnetizes the sample locally [34].

By conducting SHPM in the Meißner state at low applied fields of a few mT, it is possible to visualize the T_c distribution inside the sub-elements. Another method by specific heat measurements has confirmed the existence of T_c distributions in Nb$_3$Sn [160].

SHPM is more time-consuming and related to a higher effort compared to investigations by AC magnetometry, but has the advantage of the ability to investigate local properties of individual sub-elements and compare their resulting values [14].

In [28], a mathematic model is described that allows the computation of the measured magnetic field B from the critical current density J_c. Here the sub-element geometry is approximated by a hollow cylinder, in the case of Nb$_3$Sn sub-elements corresponding to the A15 area that carries a current. The model includes a surface current density J_s and a volume current density J_v. Since only assuming a constant J_v is equivalent to the critical state model developed by Bean, the term containing J_s is disregarded for the calculations in this chapter. The formula can then be inverted in order to determine the critical current density from SHPM measurements of the remanent magnetic field B. At the centre of a sub-element the formula then simplifies to:

$$J_c = \frac{2B_z}{\mu_0 \left[(z+t) \ln \left(\frac{r_o + \sqrt{r_o^2 + (z+t)^2}}{r_i + \sqrt{r_i^2 + (z+t)^2}} \right) + z \ln \left(\frac{r_i + \sqrt{r_i^2 + z^2}}{r_o + \sqrt{r_o^2 + z^2}} \right) \right]}. \tag{8.1}$$

where J_c is the critical current density, B_z the measured remanent magnetic field in the sub-element centre, z the distance of the Hall probe from the sample surface, t the sample thickness, r_o the outer radius of the sub-element and r_i the inner radius of the A15 phase. Table 8.1 shows an overview of typical values of the described parameters when conducting remanent field Hall scans on Nb$_3$Sn. The resulting calculated J_c at these parameters is $5.315 \times 10^4 \, \text{A mm}^{-2}$.

Parameter	Symbol	Value	Unit
Remanent magnetic field	B_z	0.3	T
Hall probe distance from sample surface	z	2	μm
Sample thickness	t	3	mm
Outer sub-element radius	r_o	25	μm
Inner sub-element radius	r_i	15	μm

Table 8.1: Overview of typical parameters of remanent field Hall scans.

While it is obvious from Equation 8.1 that the calculated J_c depends linearly from the measured magnetic field B_z, the dependency from the other parameters may not

be as easily visible. Figure 8.1 shows the dependency of the result of J_c from z and t while the respectively other parameters remain constant, in regard to the standard values outlined in Table 8.1. While an uncertainty of a few µm in z can result of a J_c difference of 50 %, the sample thickness t only significantly impacts the result below a value of 100 µm.
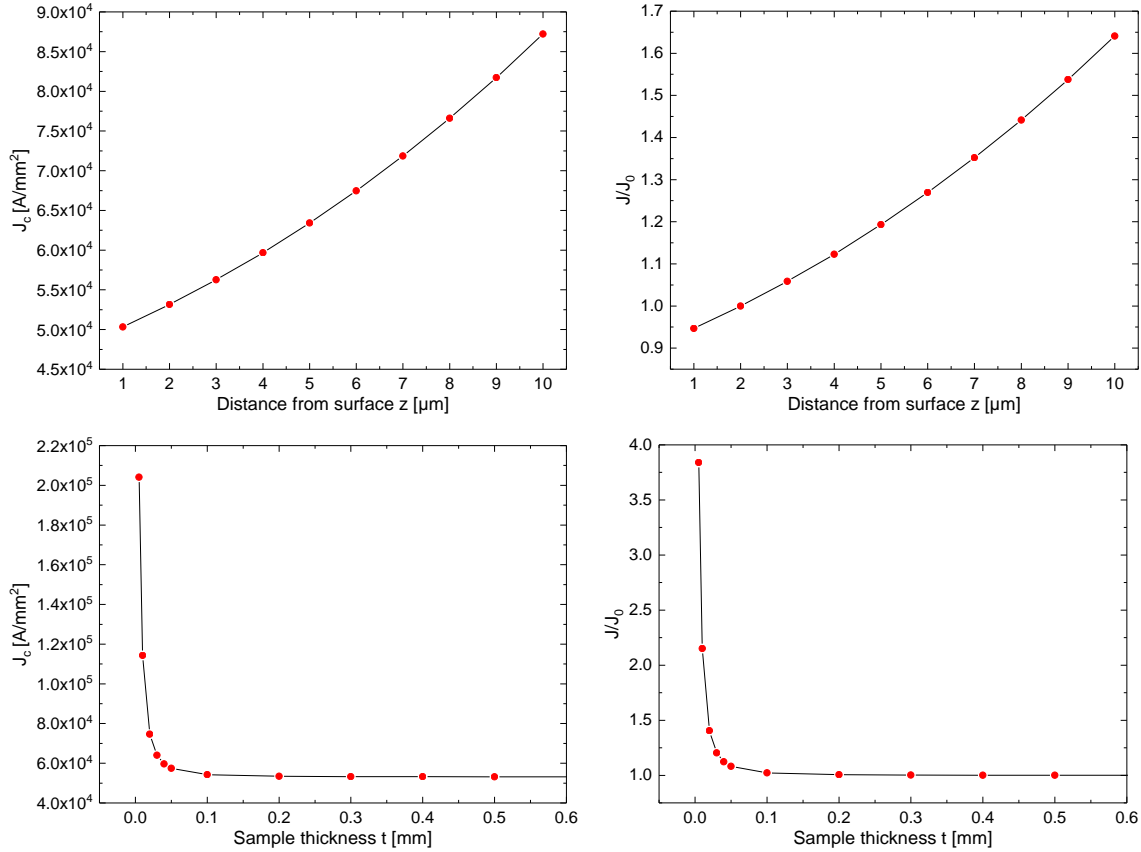
Figure 8.1: Dependency of the calculated J_c on the distance of the Hall probe from the sample surface z (top) and from the sample thickness t (bottom) while keeping the other parameters fixed.

The used micro Hall scanner at Atominstitut of TU Wien is capable of magnetizing samples of superconductors by applying fields up to 8 T as well as cooling them to low temperatures of 4.2 K using liquid nitrogen and liquid helium. A Hall probe scans over the surface of the sample at a distance of about 2 µm and measures the Hall voltage at different positions. From this data the prevalent magnetic flux distribution can be calculated using a separately recorded calibration file. The micro Hall scanner possesses a resolution of 1 µm and a scanning area of $3\,\mathrm{mm}^2 \times 3\,\mathrm{mm}^2$.

8.1.1 Applied techniques

In the following, the types of SHPM scans acquired on the Nb_3Sn samples as well as the conditions are described in detail:

- Remanent field scans: As described in Chapter 1, Bean [16] published a theory of magnetic hysteresis in high-field superconductors. In the remanent state, flux lines are trapped inside the conductor due to flux pinning, resulting in a field gradient which induces a current that flows at the value of J_c.

  For the remanent field scan, the samples were cooled to the final temperature followed by magnetizing them by applying an external field of at least $1\,T$. The field was then shut off and SHPM scans were acquired of the remanent flux profile that was trapped inside the samples. The applied field was large enough for the flux lines to fully penetrate the conductor volume. For this reason, the magnitude of the remanent field can be related to J_c, provided the geometry is considered.

- Infield scans: During infield scans, a field between B_{c1} and B_{c2} is applied externally, causing flux in the form of flux lines to enter the conductor to a varying depth. Currents are induced locally that flow at the value of J_c, which leads to the reduction of the applied field inside the sub-elements.

  After cooling, external fields of varying magnitude were applied at the same temperature in order to evaluate the shielding capabilities of the samples and compare areas of different flux penetration.

- Meißner scans: During the application of a low external field below B_{c1}, the conductor is able to shield the field, where Meißner currents are flowing at the surface. The field penetrates the conductor to the penetration depth λ.

  After cooling, a low external field below B_{c1} of around $5\,mT$ was applied to the samples that were at least partly still in the Meißner state due to gradients in the elemental composition and able to shield the small applied field. Scans at different temperatures were acquired and the shielded area was compared.

  The penetration depth λ of the applied field into the superconductor is in the order of $10\,nm$–$100\,nm$ for most pure metals at $0\,K$ and increases rapidly near T_c to a few hundred nm [130], for this reason the acquired contour plots reflect the T_c front sufficiently well.

  Due to the field expulsion caused by the superconducting sub-elements during the application of low external fields, the field values between the sub-elements are capable of extending beyond the value of the applied field. Simulations conducted by Thomas Baumgartner at ATI showed that the field between the sub-elements in the Meißner state can increase up to $35\,\%$ for the RRP-Ti-108 wire and up to $15\,\%$ for the PIT-Ta-114 wire. As example, when applying an

external field of 5 mT, the field value between the sub-elements can reach up to 6.75 mT between sub-elements of the RRP-Ti-108 wire.

The evaluation of the SHPM scan in the Meißner state was conducted by choosing two reference points that were chosen for the calibration of the measurements. The first one was located in the centre of a specific sub-element, where the field offset was corrected by setting the field value to zero according to the Meißner state. The other one was located farther away from the sub-elements, where the field value was set to the value of the applied field (or slightly above due to the mentioned field expulsion).

The technique of applying SHPM on cross sections of Nb$_3$Sn wires as well as the evaluation of the shielded area in the Meißner state and contours of the shielding currents is documented in [14]. A small external field of about 5 mT is applied and the contour lines at which the local field has decayed to a certain fraction of the applied field, for example 80 % or 50 %, is evaluated. The shielded area inside the contours is measured by pixel counting and radii of the shielded areas are calculated from this area assuming circular shape.

Two different wires were subjected to SHPM measurements, the RRP-Ti-108 and the PIT-Ta-114 wire, where polished cross sections were prepared by mechanically polishing in order to achieve a flat sample surface suited for the investigations of the magnetic properties. Additionally, one sample of the RRP-Ti-108 wire was prepared by polishing longitudinally along the wire axis to the centre of the wire in order to investigate longitudinal variations in the microstructure and the magnetic properties. SEM images of the prepared and investigated samples can be found in Figure 8.2. These samples possess a thickness of multiple mm, since it was found that reducing their thickness can lead to artefacts during the measurements, where the critical temperature T_c is suppressed, presumably due to longitudinal variations in the elemental composition along the wire axis as analysed in Chapter 5 or induced damage during the polishing procedure, as described in Chapter 2.
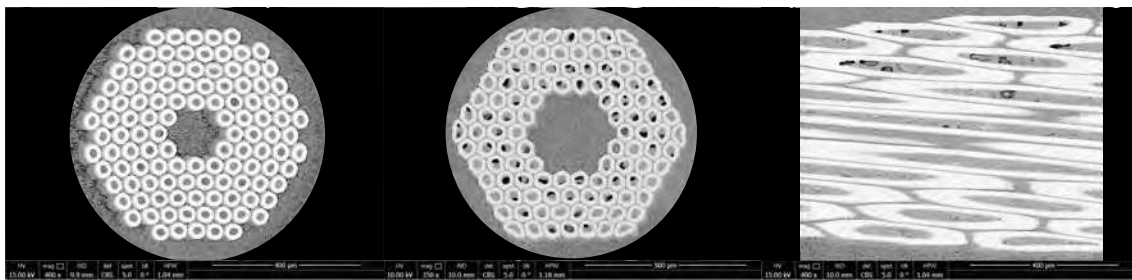
Figure 8.2: SEM images of polished samples for SHPM investigations: transversal cross sections of the PIT-Ta-114 wire (left) and the RRP-Ti-108 wire (middle) as well as the longitudinal cross section of the RRP-Ti-108 wire (right).

The samples were mounted into the scanner where the surfaces seen in Figure 8.2 correspond to the horizontal plane. The temperature was then reduced to the desired value, after which an external magnetic field was applied in the direction normal to the sample surface. Thereafter, the Hall probe was used to scan over the sample surface at a distance of a few µm and the Hall voltage was measured. By multiplying the measured Hall voltage with the so called Hall constant, the value of the magnetic field strength was calculated. This Hall constant was determined either by acquiring a calibration measurement at a large distance from the sample in the case of remanent scans, or by specifying known field values at certain positions in the case of Meißner and infield scans.

8.2 Results of the SHPM analyses

This section shows the results of the SHPM investigations of the different Nb_3Sn samples and is divided into the respective techniques. The SHPM maps are shown together with SEM images of the corresponding sample location in order to relate the magnetic signal to the sample geometry. The x-axis of the SHPM maps were inverted due to the scan direction originally being from right to left, thus the resulting maps and the SEM images possess the same orientation and can directly be compared.

8.2.1 RRP-Ti-108 transversal cross section

Scans in the remanent state

SHPM scans were conducted on the transversal cross section of the RRP-Ti-108 wire. Figure 8.3 shows an overview scan across the wire cross section and Figure 8.4 shows a scan taken of a few sub-elements at a higher resolution in the remanent state. The scans are displayed together with SEM images of the respective samples areas. Both scans were acquired after cooling the sample to a temperature of $10\,\mathrm{K}$ and applying and turning off an external field of $1\,\mathrm{T}$. The remanent field profile of the individual sub-elements is visible and was coloured according to its value. It already becomes apparent that there are differences in the shape and magnitude of the remanent field between different sub-elements. The correlation with the microstructure will be investigated in Chapter 9.

The overview SHPM scans in the remanent state across the whole wire cross sections often show a tendency for increasing signal strength between the outer and inner sub-elements for all investigated wires. This can likely be related to variations in the sub-element geometry as investigated in Chapter 3. Additional contributions could stem from a possible inter-filament coupling as well as a potential overlap of the signal from deeper samples layers due to the wire twist pitch. This effects becomes

especially apparent in the remanent scans of the longitudinally polished wire shown later in Figure 8.13 due to less sub-elements overlapping in the central wire region.
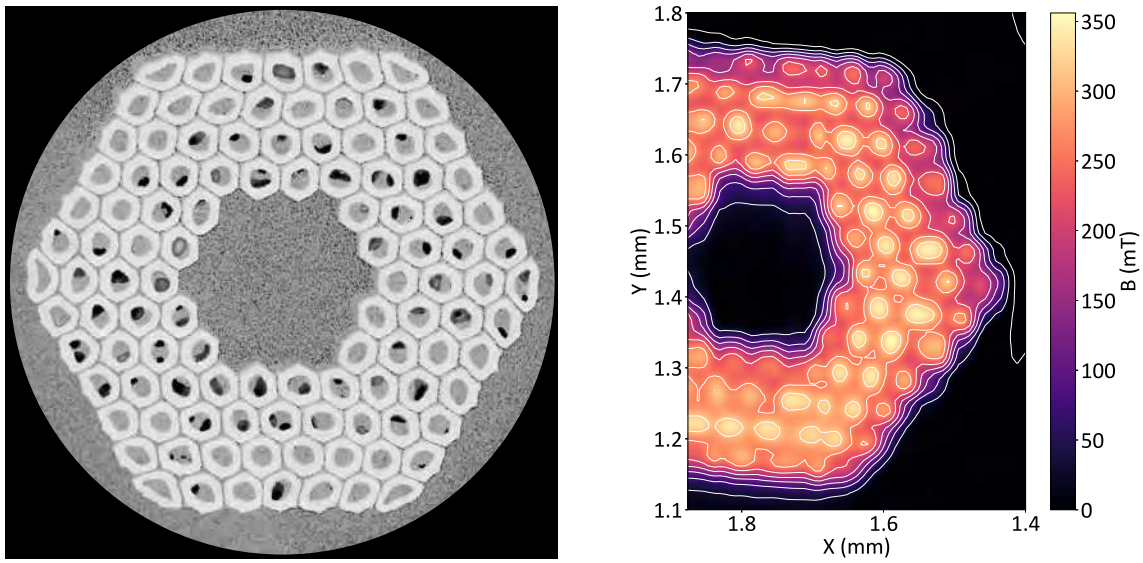
Figure 8.3: Remanent field scan of the RRP-Ti-108 wire at 10 K after applying 1 T (right) with SEM image of the cross section (left).
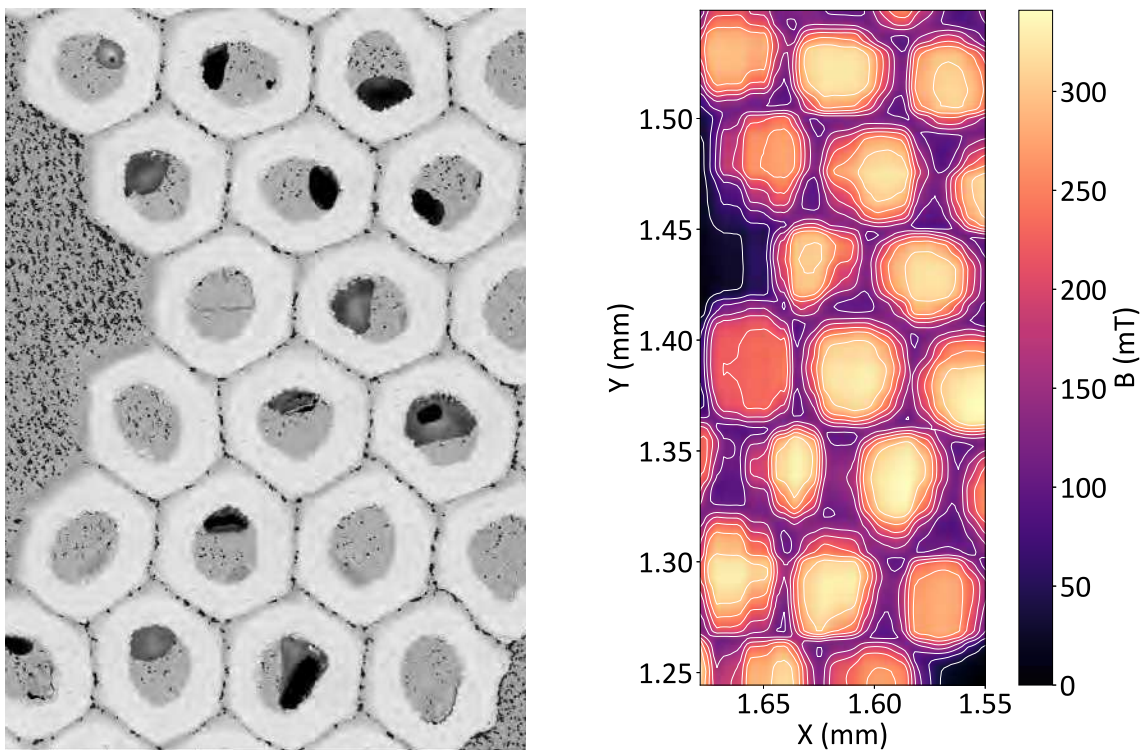
Figure 8.4: Remanent field scan of the RRP-Ti-108 wire at 10 K after applying 1 T (right) with SEM image of the investigated area (left).

Scans in the Meißner state

SHPM scans were acquired of RRP-Ti-108 sub-elements at different temperatures after cooling and applying a small external field of $5\,\mathrm{mT}$. The results are shown in Figure 8.5 and Figure 8.6, where it can be seen that at low temperatures the sub-elements are able to shield the applied field, while at increasing temperatures the applied field starts to increasingly penetrate the superconductor. The figures show the contour lines which connect points of equal field values. Especially in the scan that was acquired at a temperature of $16.5\,\mathrm{K}$, differences in the shielding capacity and therefore the critical temperature of individual sub-elements become apparent.

Figure 8.8 and Figure 8.9 show the same measurements for a different sample area, leading to comparable results. From the SHPM scan at $16.5\,\mathrm{K}$ in Figure 8.8, it becomes apparent that there are local inhomogeneities within individual sub-elements, which impact the current flow locally and lead to the deformation of the contour lines.

The contour lines at which the field has decayed to a certain value, for these measurements $1.84\,\mathrm{mT}$ which is $1/e$ of the applied field, were evaluated. The result is displayed in Figure 8.7 and Figure 8.10, where it can be seen that the shielded area decreases with increasing temperature. From this it becomes apparent that the sub-elements exhibit a radial gradient in the critical temperature T_{c}, which results from the gradient in the elemental composition investigated in Chapter 5 due to the diffusion mechanism during the heat treatment of the wires. The contour plots show that while for some sub-elements, contour plots at the evaluated field still exist at $16.5\,\mathrm{K}$, for other sub-elements this is not the case any more, which can be attributed to a lower T_{c}. A slight drift is observable in in the contours of the scans between different temperatures, resulting from thermal expansion of the scanner system, which leads to the overlap of some contour lines.
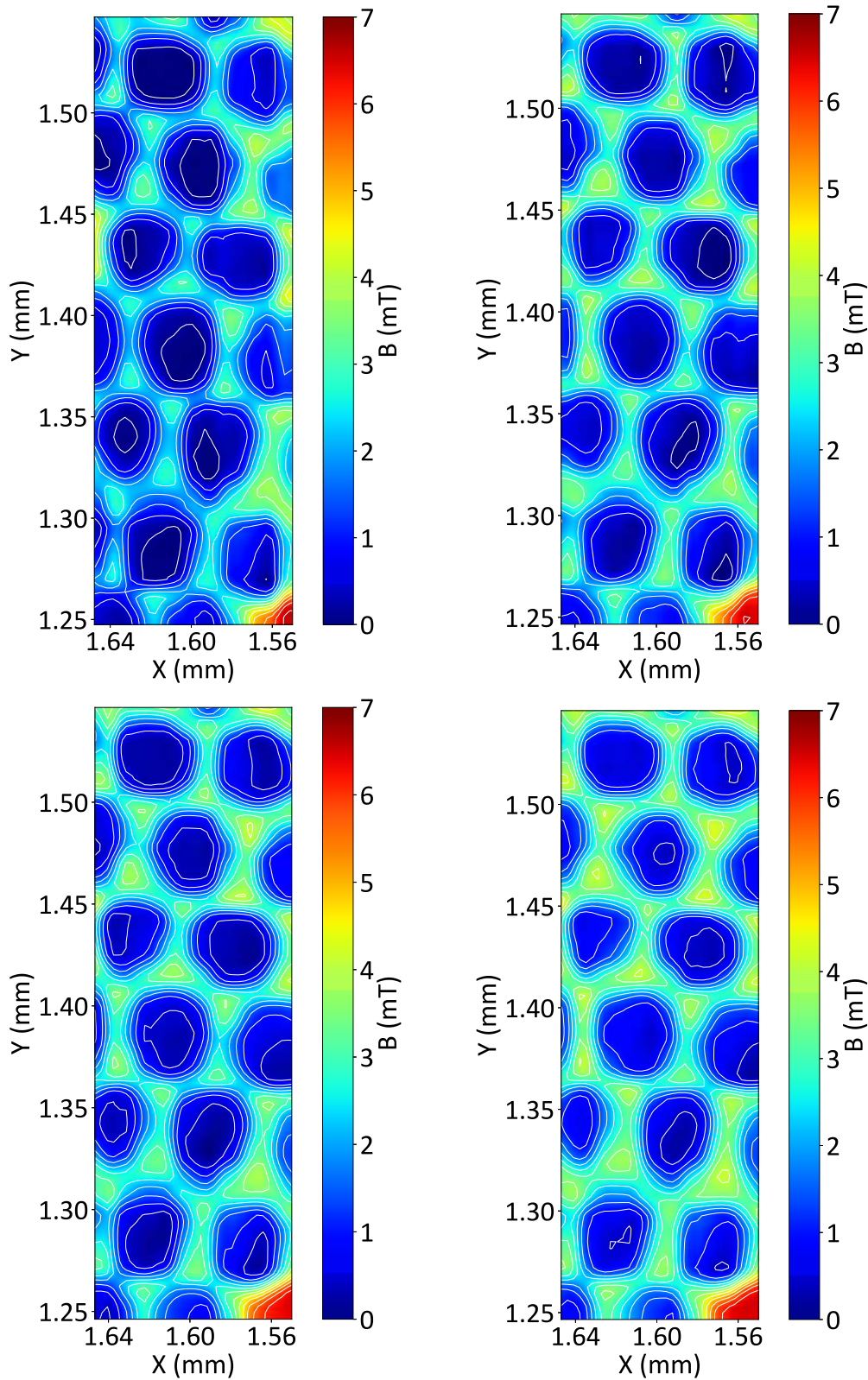
Figure 8.5: Meißner scans of the RRP-Ti-108 wire at $5\,\mathrm{mT}$ and $10\,\mathrm{K}$ (top left), $13\,\mathrm{K}$ (top right), $14\,\mathrm{K}$ (bottom left) and $15\,\mathrm{K}$ (bottom right).
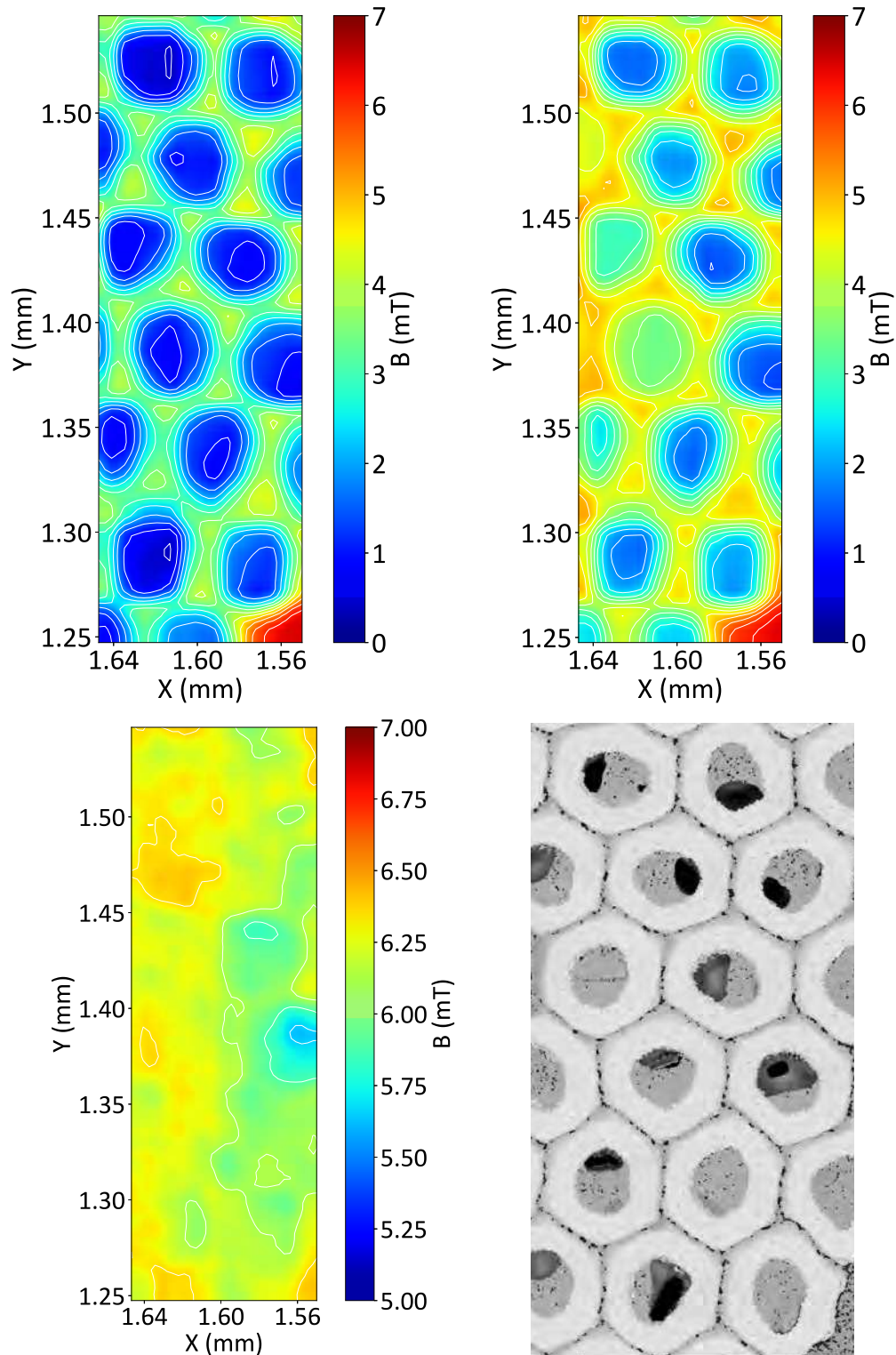
Figure 8.6: Meißner scans of the RRP-Ti-108 wire at 5 mT and 16 K (top left), 16.5 K (top right) and 17 K (bottom left) with SEM image of investigated area (bottom right).
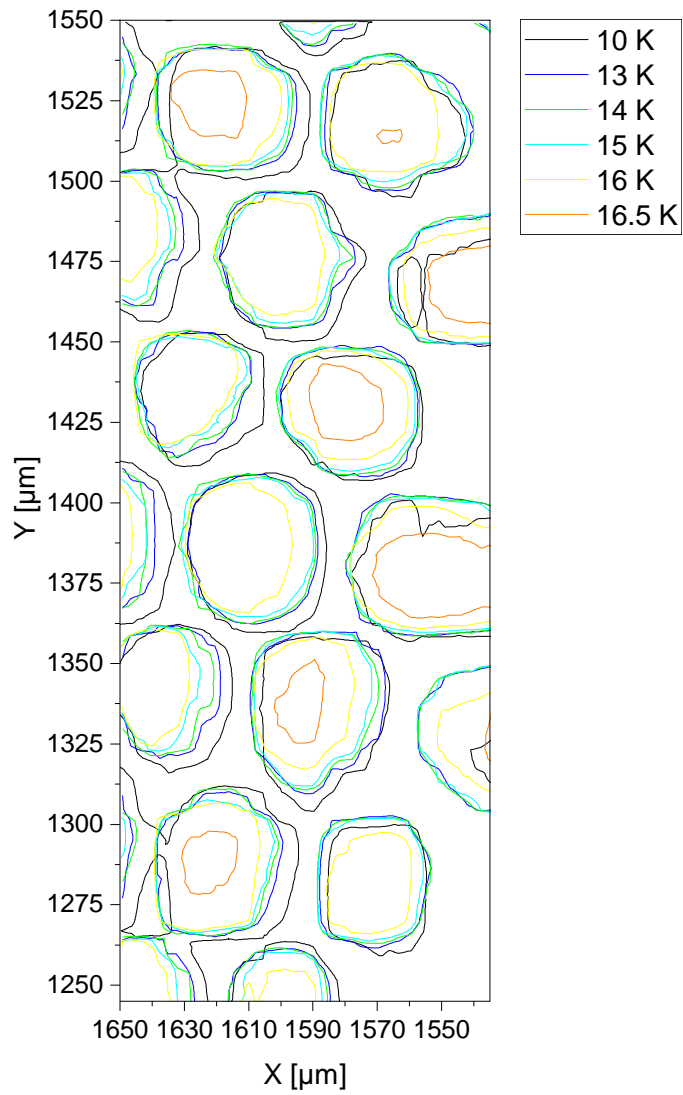
Figure 8.7: Contour plots of RRP-Ti-108 wire sub-elements at 1.84 mT and different temperatures.
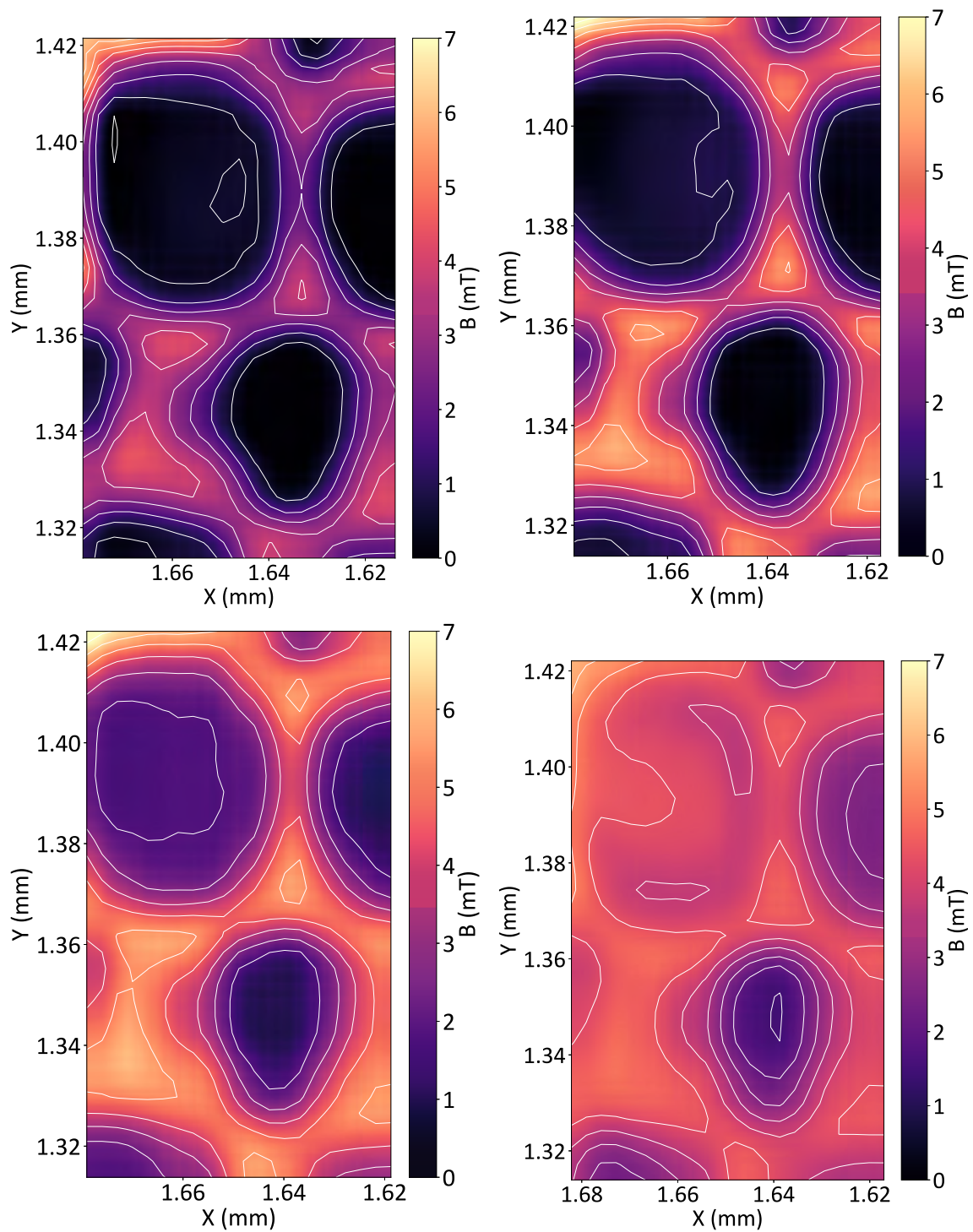
Figure 8.8: Meißner scans of the RRP-Ti-108 wire at 5 mT and 10 K (top left), 14 K (top right), 16 K (bottom left) and 16.5 K (bottom right).
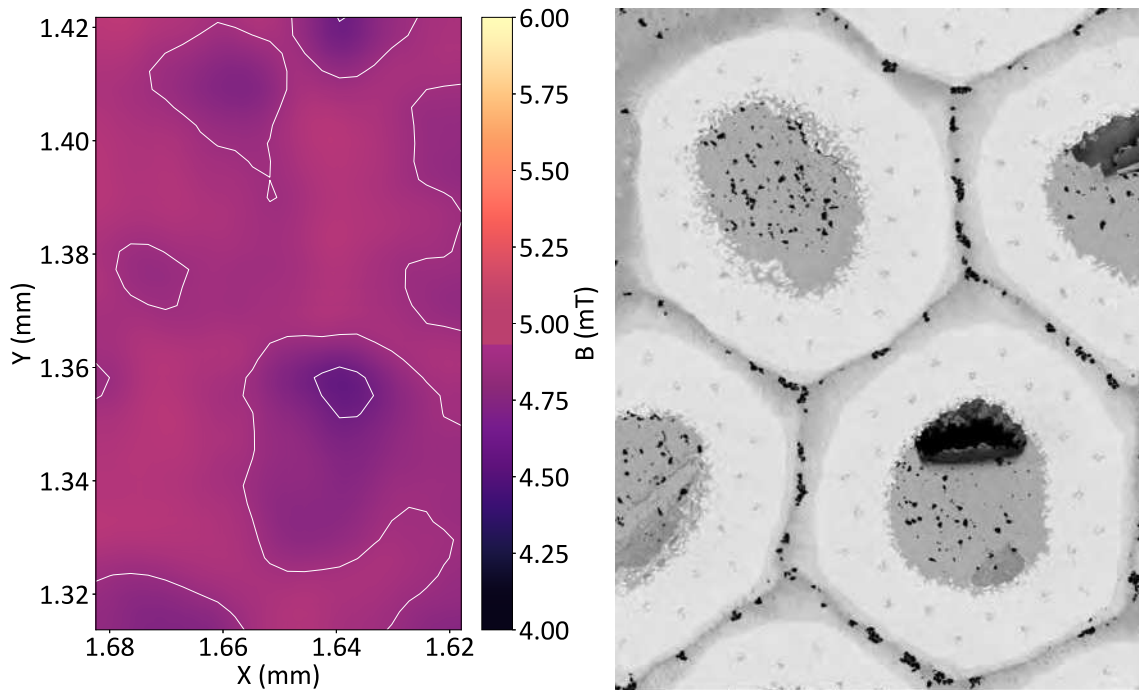
Figure 8.9: Meißner scan of the RRP-Ti-108 wire at 5 mT and 17 K (left) and corresponding sample area (right).
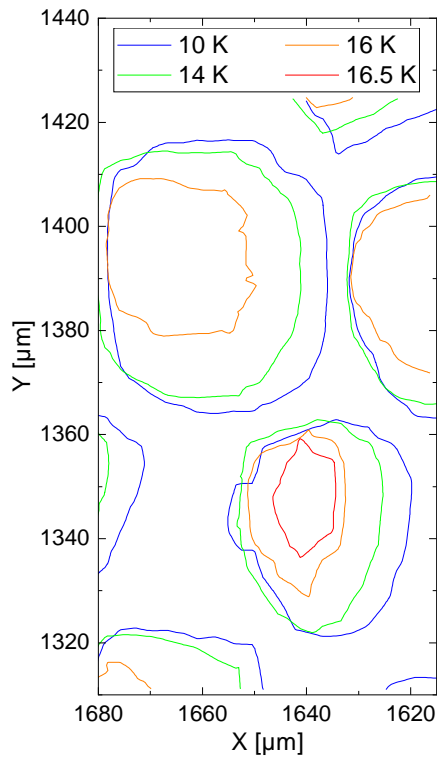
Figure 8.10: Contour plots of RRP-Ti-108 wire sub-elements at 1.84 mT and different temperatures.

Infield scans

SHPM scans were acquired after cooling to 10 K and applying external fields of different magnitudes. These scans yield information about the shielding capabilities of the sub-elements and potentially different field penetration due to inhomogeneities in the microstructure. The results are displayed in Figure 8.11 and Figure 8.12, which include the same sub-element that exhibited strong inhomogeneities in the remanent field in Figure 8.8. It can be seen that at increasing applied fields, the penetration by the applied magnetic field increases considerably. The forms of the contour lines show increasing deformation at increasing applied fields, making apparent that J_c seems to exhibit a higher dependency of the field in some areas. The reason for this is not directly visible from these scans, one possibly explanation could be an inhomogeneous Sn distribution within the sub-elements.
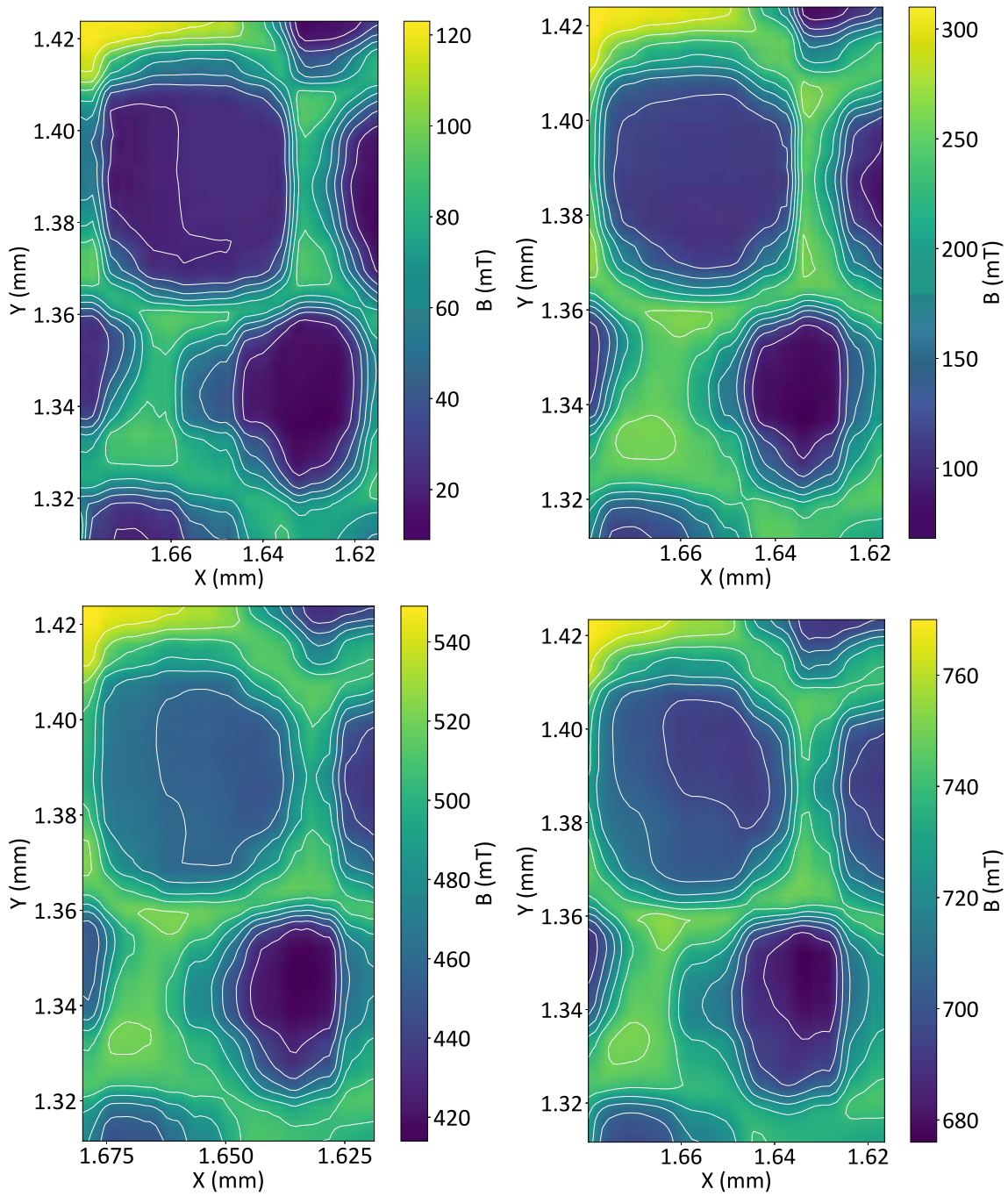
Figure 8.11: Infield scans of the RRP-Ti-108 wire at 10 K and 0.1 T (top left), 0.25 T (top right), 0.5 T (bottom left) and 0.75 T (bottom right).
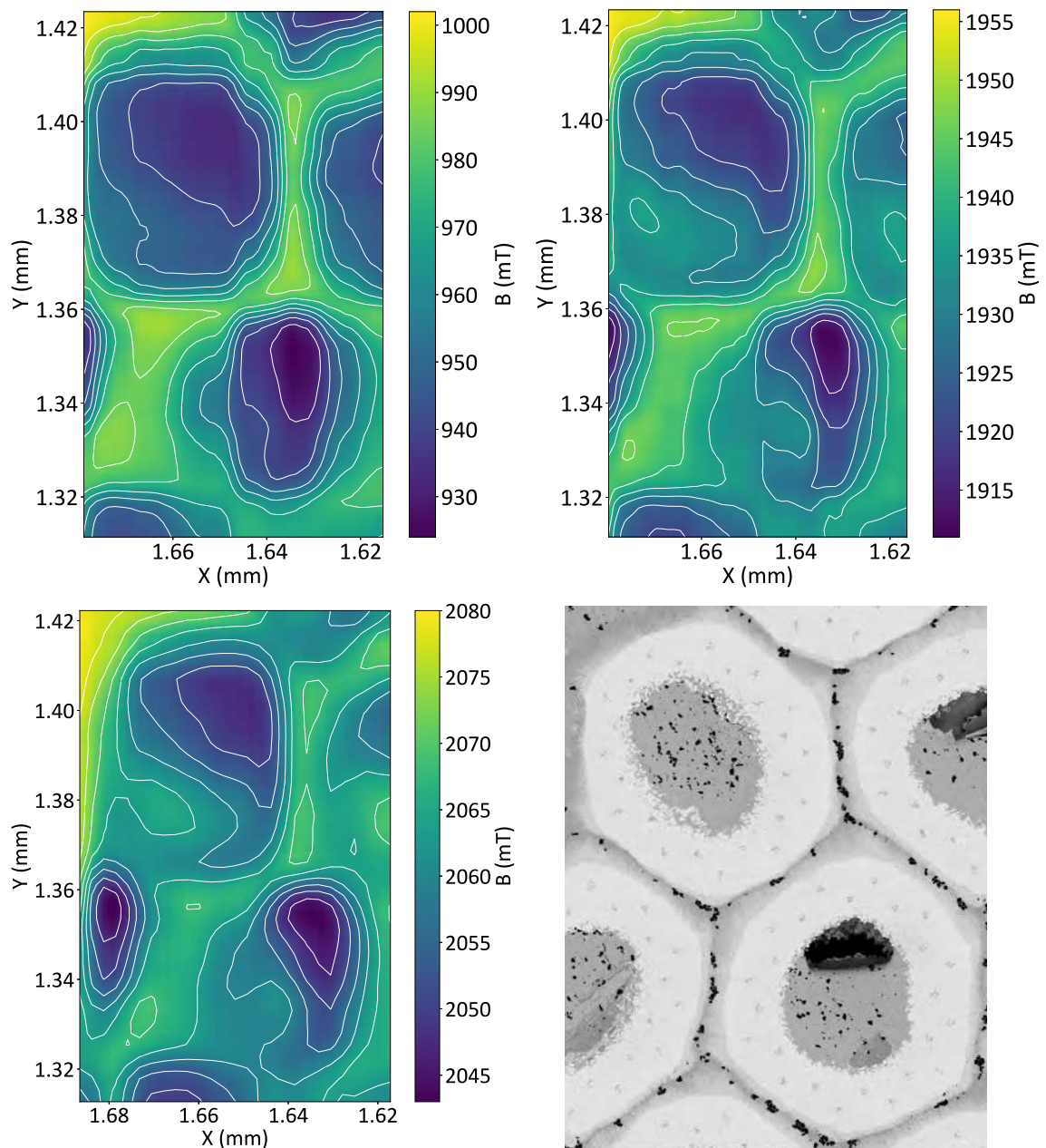
Figure 8.12: Infield scans of the RRP-Ti-108 wire at 10 K and 1 T (top left), 2 T (top right) and 2.5 T (bottom left) with SEM image of the investigated area (bottom right).

8.2.2 RRP-Ti-108 longitudinal cross section

The same measurements as on the transversal cross section of the RRP-Ti-108 wire were applied to the longitudinal cross section, which was polished to the wire centre. Figure 8.13 shows a SEM image of the finalized sample, where the outer sub-elements appear elliptically due to their heavy twisting around the wire axis, while the sub-element near the wire centre practically shows no twisting and parallel A15 phases.

Scans in the remanent state

A remanent field Hall scan of the longitudinal cross section of the RRP-Ti-108 wire at 10 K and after applying and turning off 1 T is shown in Figure 8.13, together with a SEM image of the cross section. The scan in Figure 8.14 was taken in the centre of the sample, where the sub-elements did not show considerable twisting and parallel A15 phases. From the scan it becomes apparent that the shape of the remanent field shows considerable variations along the wire axis. This result can likely be attributed to longitudinal variations of the A15 layer thickness as investigated in Chapter 3 as well as compositional changes along the wire axis as investigated in Chapter 5.
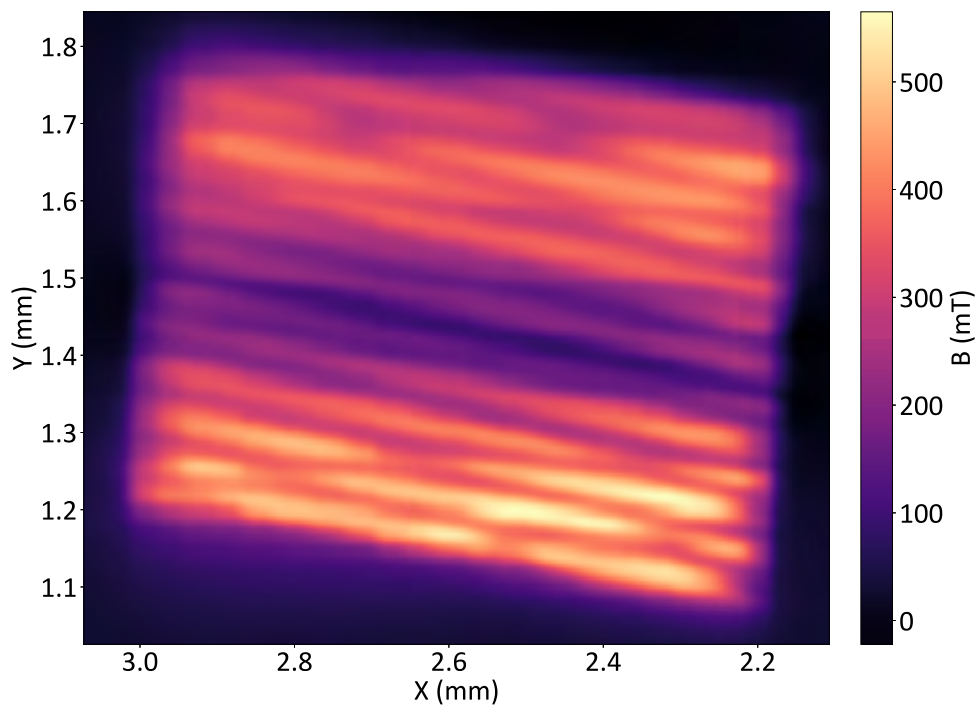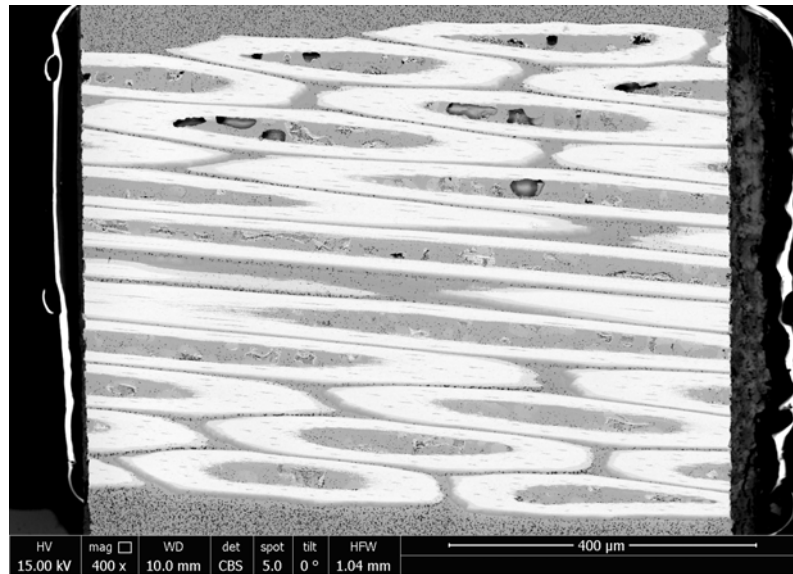
Figure 8.13: Remanent field Hall scan of the longitudinal cross section of the RRP-Ti-108 wire at 10 K and after applying 1 T (bottom), together with a SEM image of the cross section (top).
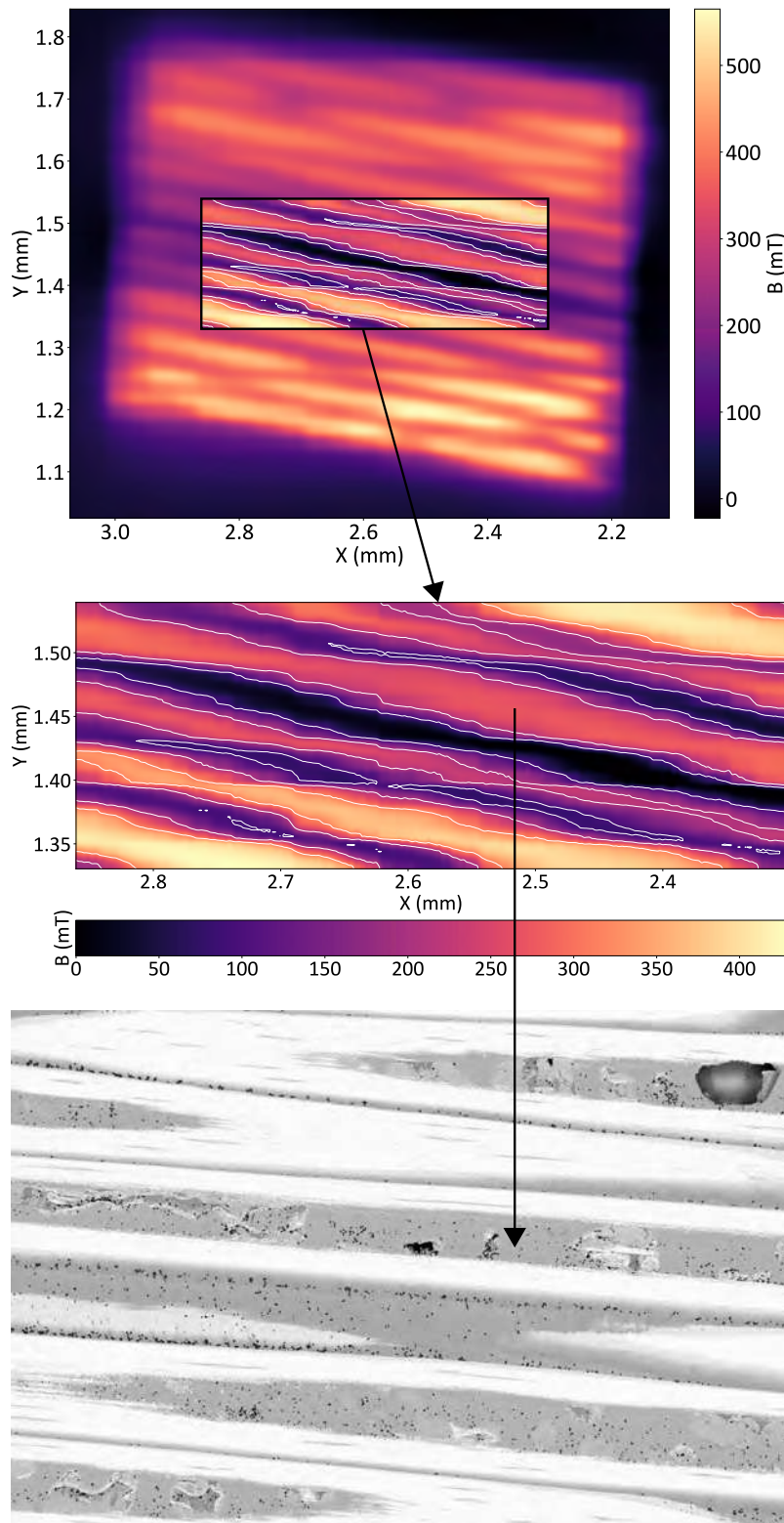
Figure 8.14: Remanent field Hall scan of the longitudinal cross section of the RRP-Ti-108 wire at 10 K and after applying 1 T (top and middle), together with a SEM image of the investigated area (bottom).

Scans in the Meißner state

SHPM scans on the longitudinal cross section of the RRP-Ti-108 wire in the Meißner state are shown in Figure 8.16 and Figure 8.17, which were taken at an applied field of 5 mT. The corresponding location within the sample cross section is shown in Figure 8.15. The central area exhibits a gap in the magnetic field values, which likely can attributed to a reduced A15 thickness in this area, but possibly also to irregularities in the positioning system of the Hall probe. The effect of a reduced shielded area at increasing temperatures can also be observed in these scans, where the evaluation of the contour plots at 2.5 mT is shown in Figure 8.18.
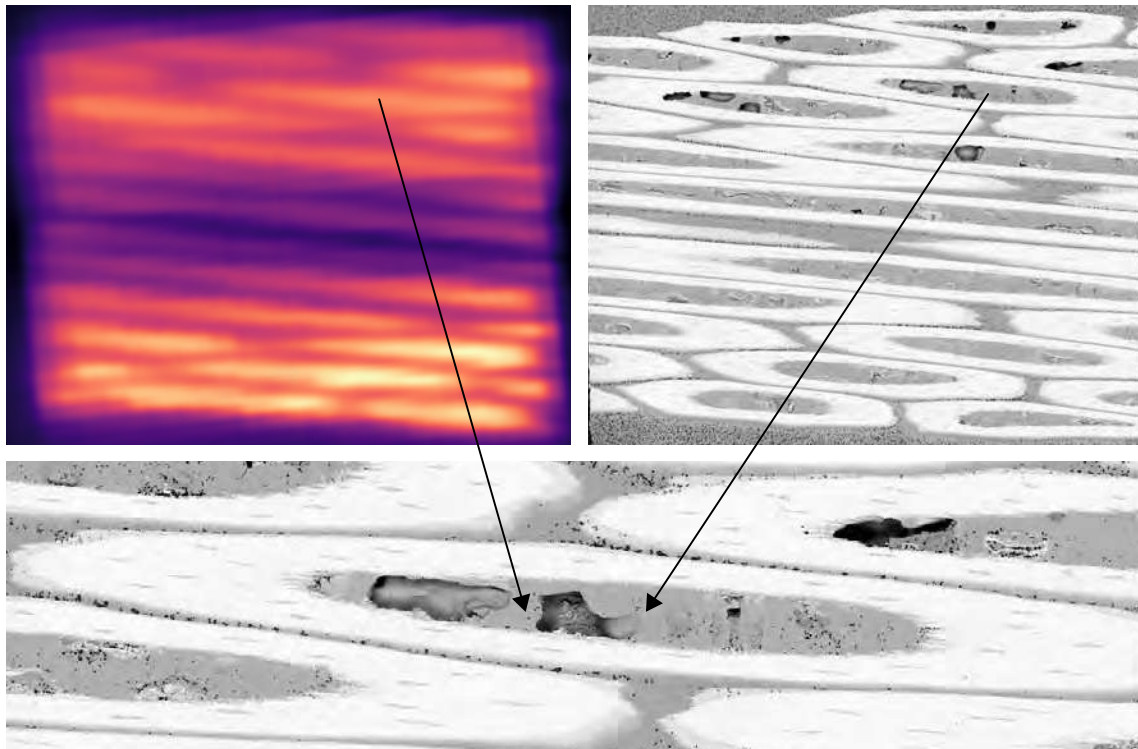
Figure 8.15: Remanent field Hall scan of the longitudinal cross section of the RRP-Ti-108 wire at 10 K and after applying 1 T, together with SEM images of the investigated area.
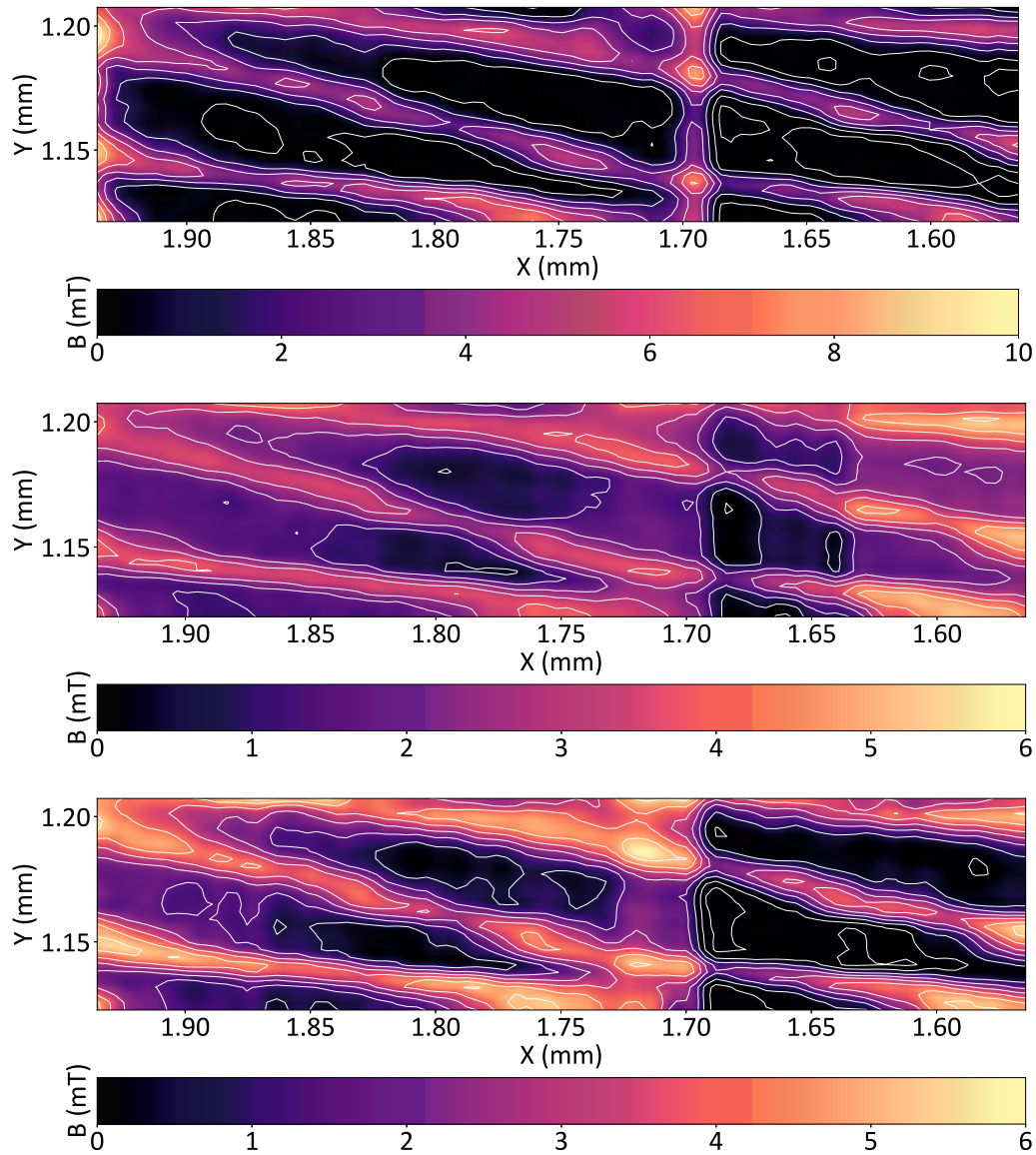
Figure 8.16: Meißner scans of the longitudinal RRP-Ti-108 wire cross section at 5 mT and 10 K (top), 14 K (middle) and 15 K (bottom).
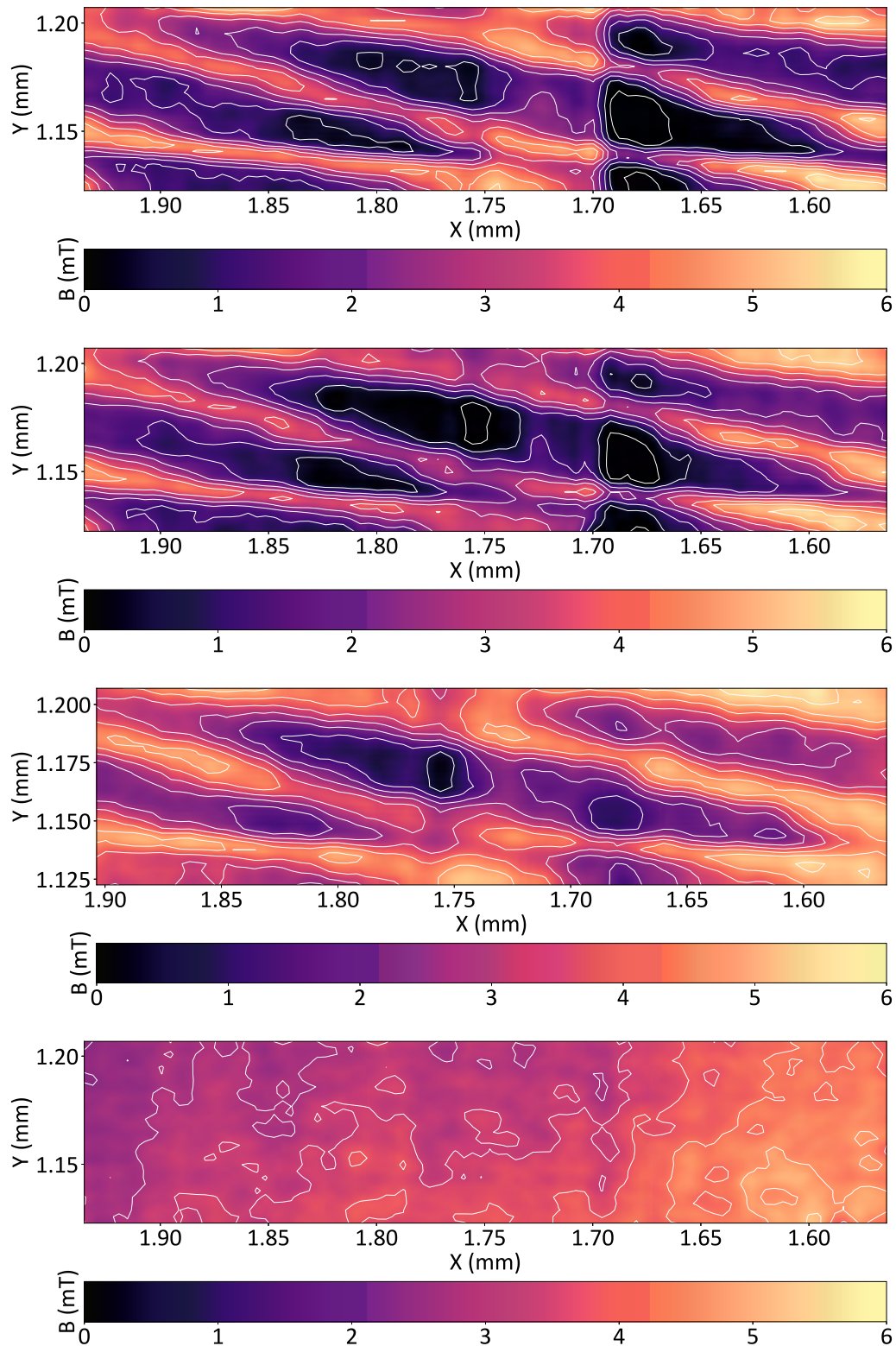
Figure 8.17: Meißner scans of the longitudinal RRP-Ti-108 wire cross section at 5 mT and different temperatures. From top to bottom: 16 K, 16.5 K, 17 K and 17.5 K.
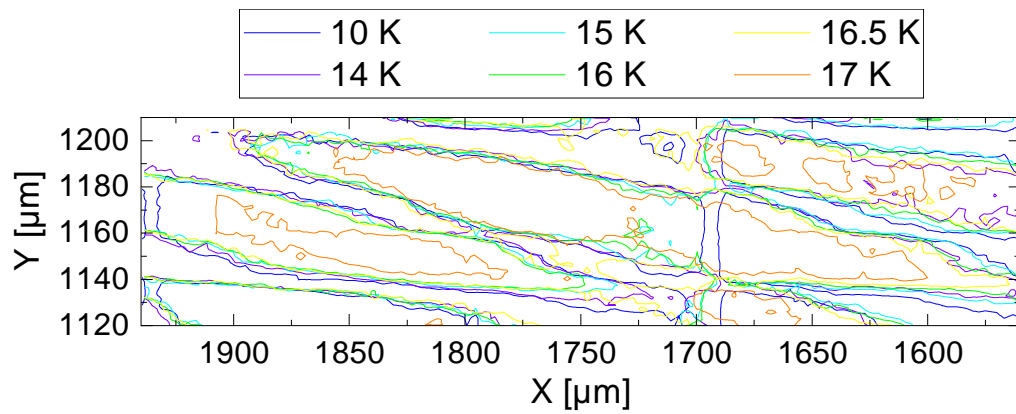
Figure 8.18: Contour plots of the longitudinal RRP-Ti-108 wire cross section at 2.5 mT and different temperatures.

Infield scans

Figure 8.20 shows in-field scans of the longitudinally polished RRP-Ti-108 wire at 5 K and different applied fields, ranging from 0.1 T to 3 T, that were performed at the wire location marked in Figure 8.19. It can be seen that a field of 0.1 T can fully be shielded at this temperature, while at higher fields it can only partly be shielded.
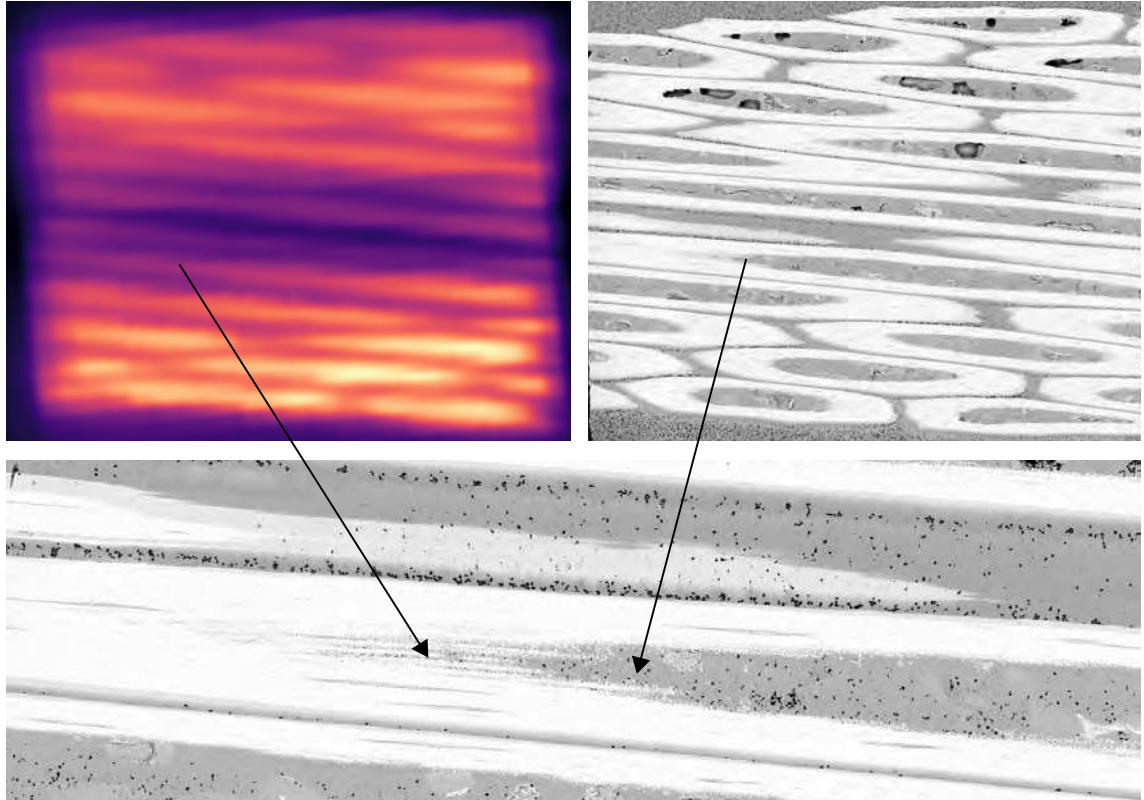
Figure 8.19: Remanent field Hall scan of the longitudinal cross section of the RRP-Ti-108 wire at 10 K and after applying 1 T, together with SEM images of the investigated area.
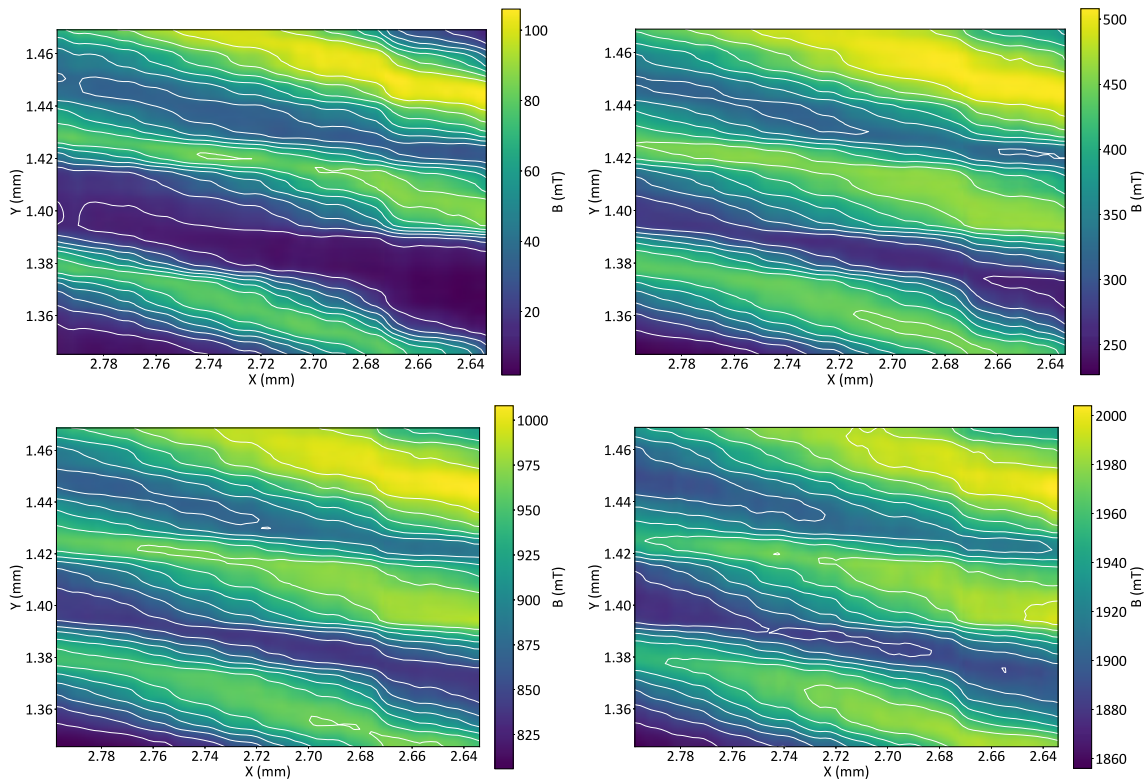
Figure 8.20: Infield scans of the longitudinal RRP-Ti-108 wire cross section at 5 K and 0.1 T (top left), 0.5 T (top right), 1 T (bottom left) and 2 T (bottom right).

8.2.3 PIT-Ta-114 transversal cross section

The previously described investigations by SHPM were furthermore applied to a polished transversal cross section of the PIT-Ta-114 wire. Figure 8.21 shows overview SEM images of the whole sample and the investigated areas.
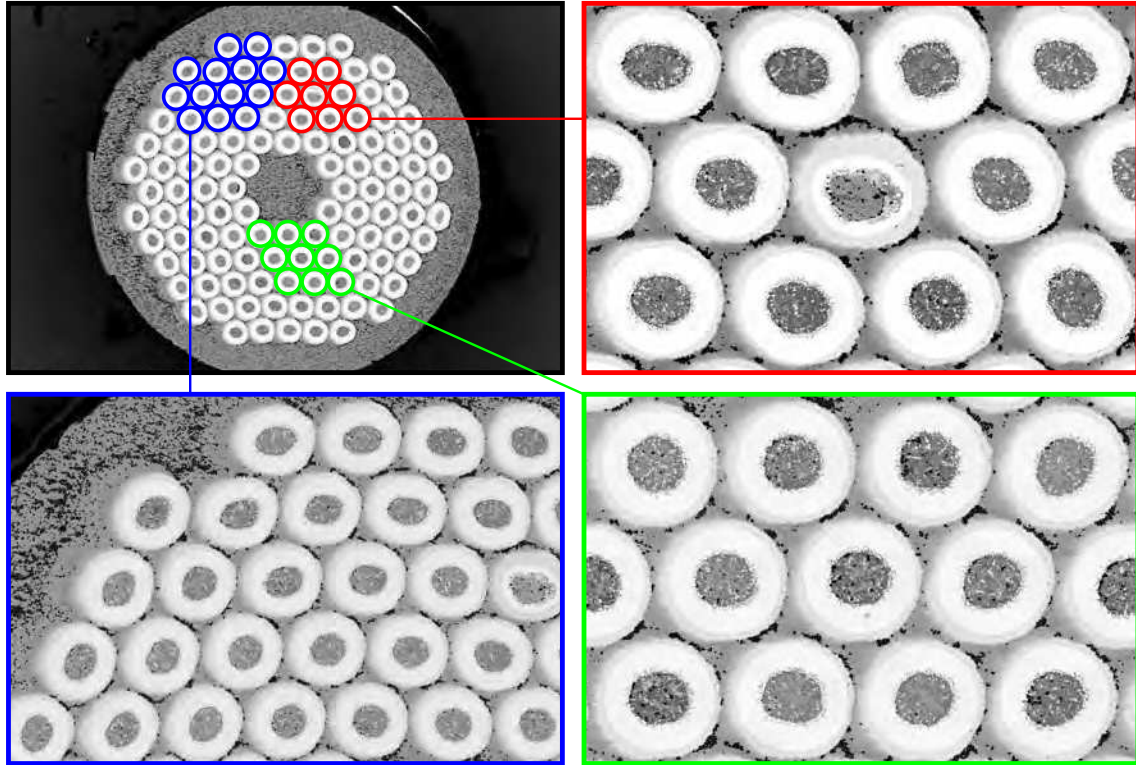
Figure 8.21: Overview SEM images of the investigated sub-elements of the PIT-Ta-114 wire.

Scans in the remanent state

Figure 8.22 shows a SHPM scan of the entire transversal cross section of the PIT-Ta-114 in the remanent state. A scan taken of a few sub-elements at a higher resolution is displayed in Figure 8.23. The scans were acquired after cooling the sample to a temperature of 7 K and 5 K, respectively, and applying and shutting off an external field of 1 T. Differences in the shape and magnitude of the remanent field between different sub-elements become apparent.
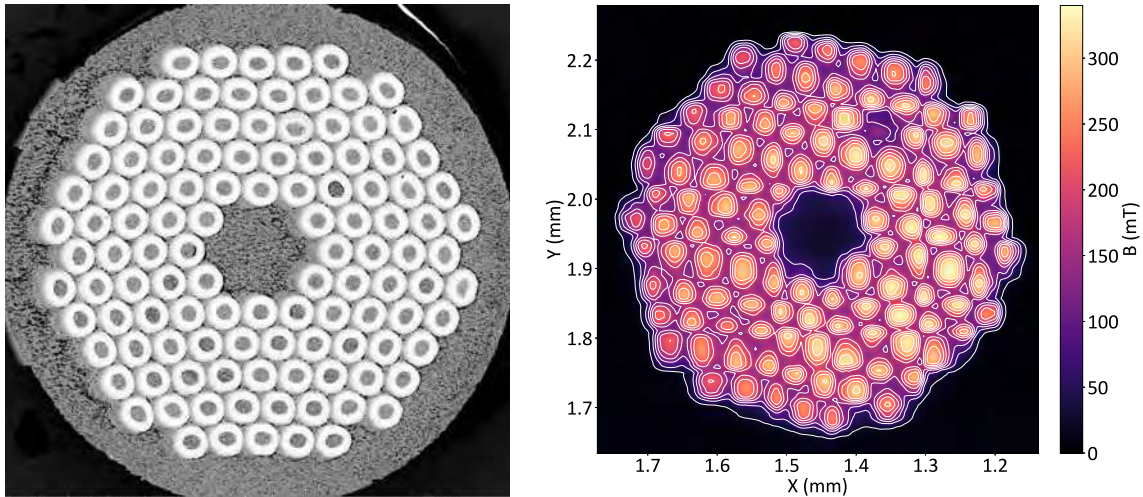
Figure 8.22: Remanent field scan of the PIT-Ta-114 wire 7 K and after magnetising at 1 T (right), together with SEM image of the cross section (left).
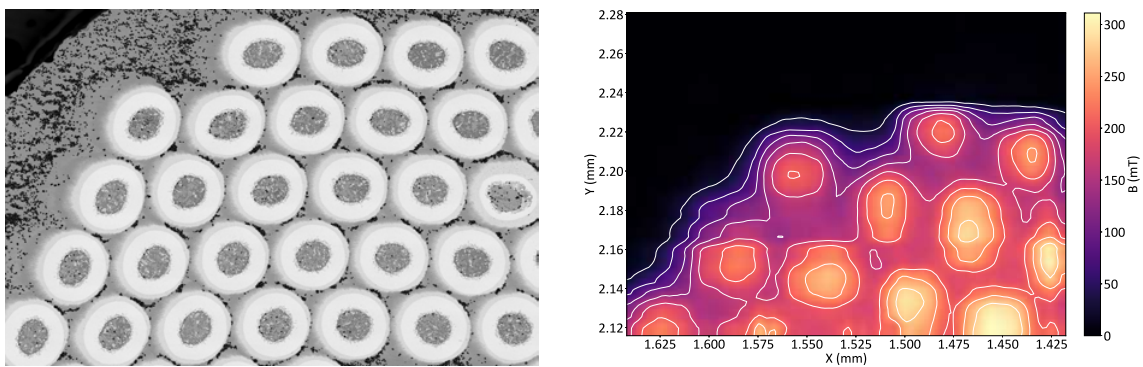
Figure 8.23: Remanent field scan of the PIT-Ta-114 wire 5 K and after magnetising at 1 T (right), together with SEM image of the investigated area (left).

Scans in the Meißner state

SHPM scans taken in the Meißner state on the transversal PIT-Ta-114 wire cross section at an applied field of 5 mT are displayed in Figure 8.25 and Figure 8.26, which were acquired on the sample area shown in Figure 8.24. The contour lines that were evaluated at 2.5 mT, which is 50 % of the applied field, are shown in Figure 8.27. The reduction of the shielded area at increasing temperatures due to the radial gradient of the critical temperature T_c can be clearly seen.
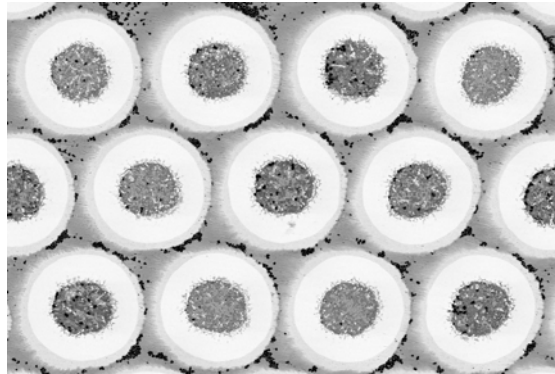
Figure 8.24: SEM image of the sample area of the PIT-Ta-114 wire subjected to SHPM scans in the Meißner state.

Additionally, one scan in the Meißner state was taken of the sub-element in the PIT-Ta-114 wire that did not react properly during the heat treatment as already investigated in Chapter 3 in order to evaluate its shielding capability. The Meißner scans of the poorly reacted sub-element is shown in Figure 8.28, which clearly exhibits less shielding capabilities than the surrounding sub-elements.
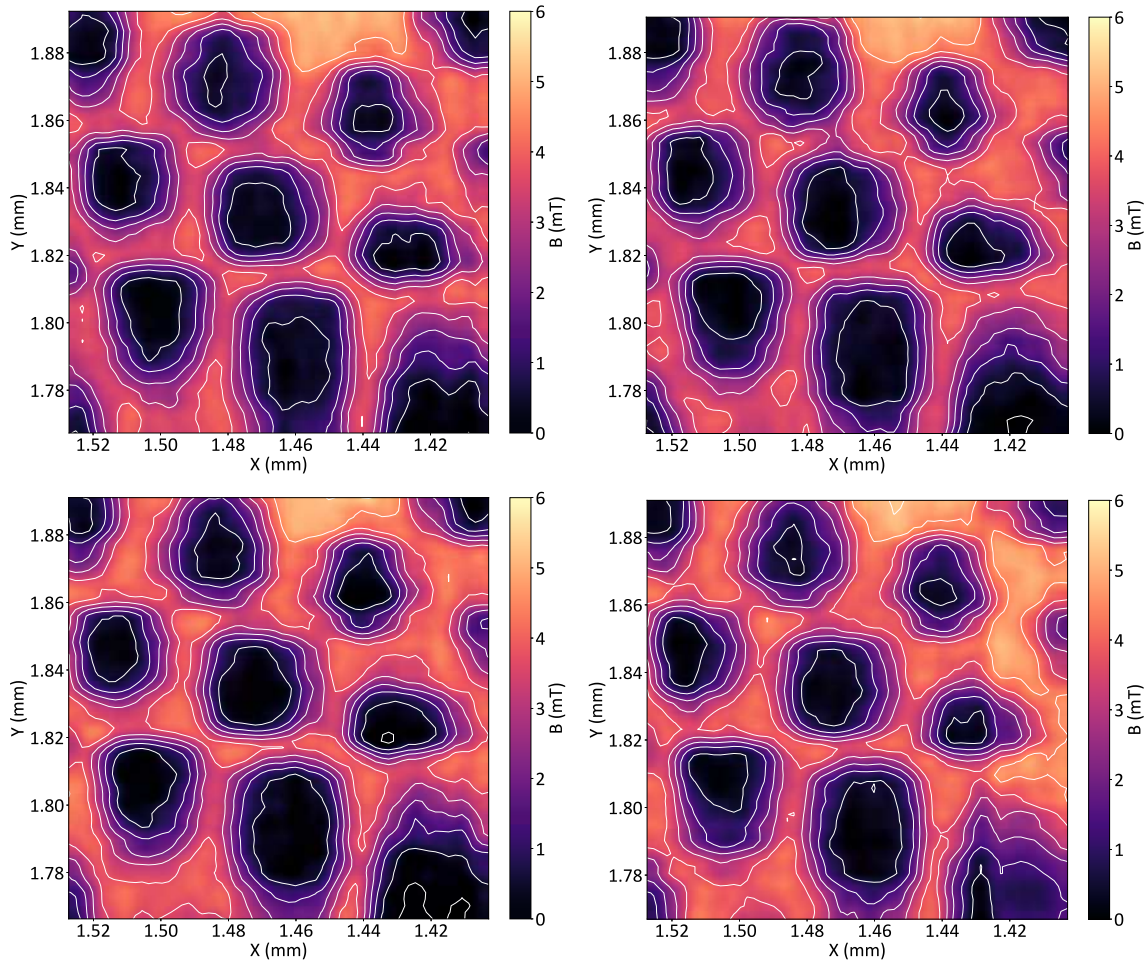
Figure 8.25: Meißner scans of the transversal PIT-Ta-114 wire cross section at 5 mT and 10 K (top left), 12 K (top right), 14 K (bottom left) and 15 K (bottom right).
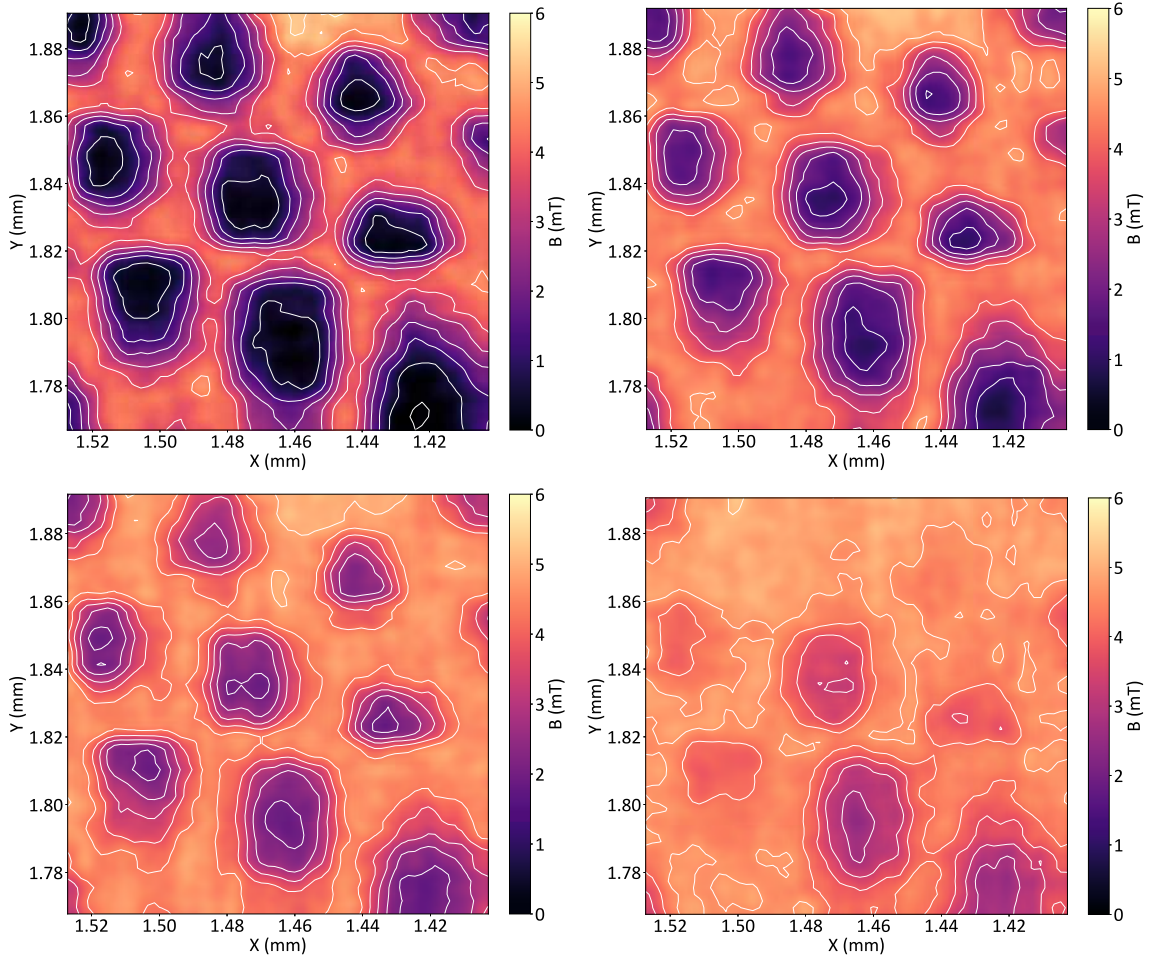
Figure 8.26: Meißner scans of the transversal PIT-Ta-114 wire cross section at 5 mT and 16 K (top left), 17 K (top right), 17.4 K (bottom left) and 17.8 K (bottom right).
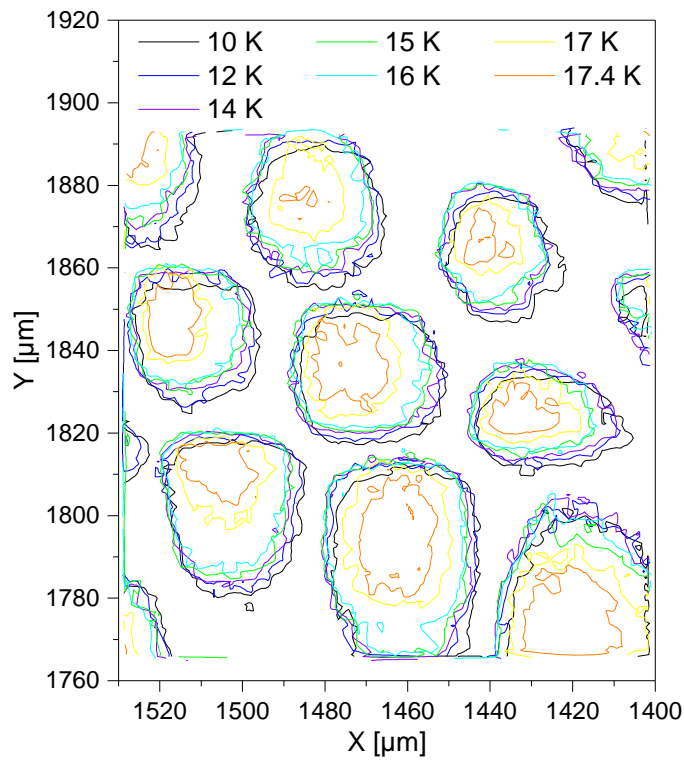
Figure 8.27: Contour plots of the transversal PIT-Ta-114 wire cross section at 2.5 mT and different temperatures.
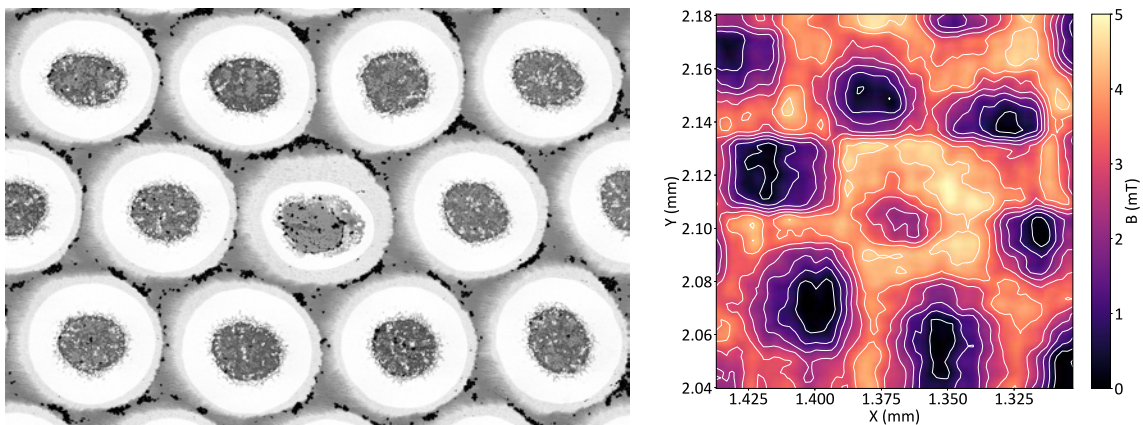
Figure 8.28: Meißner scan of a poorly reacted PIT-Ta-114 sub-element at 5 mT and 10 K (right), together with SEM image of the investigated area (left).

Infield scans

Figure 8.29 shows an infield SHPM scan that was taken on sub-elements of the PIT-Ta-114 wire after cooling to 10 K and applying an external field of 1 T. The sub-elements are able to reduce the penetrating field by about 40 mT.
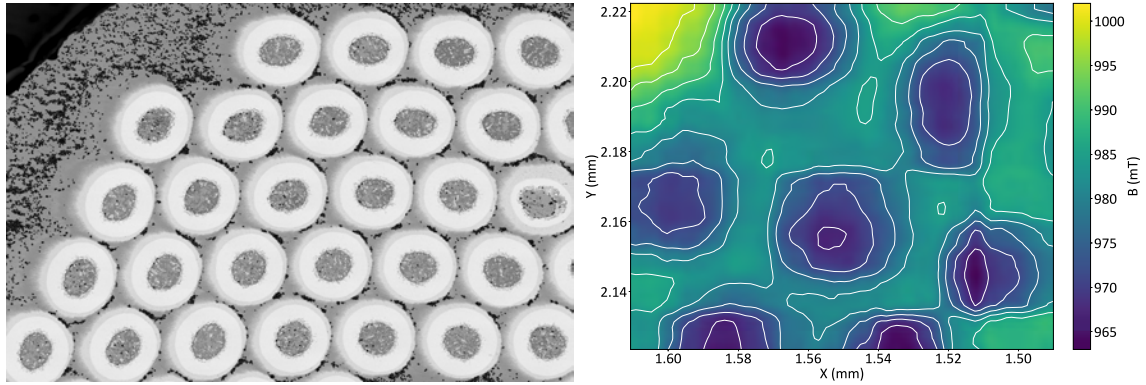
Figure 8.29: Infield scan of the PIT-Ta-114 wire at 10 K and 1 T (right), together with SEM image of the investigated area (left).

8.3 Conclusions of the SHPM analyses

The SHPM scans performed on different wire samples in this chapter yielded information about inhomogeneities between sub-elements and inside sub-elements, as well as their behaviour at increasing applied fields and increasing temperatures.

The results of this the SHPM investigations on different Nb_3Sn wire cross sections can be summarized as follows:

1. The remanent field strength of the sub-elements was assessed by SHPM scans in the remanent sample state, which can be related to their critical current density J_c, which, together with geometric information acquired by SEM, will be calculated in Chapter 9.

2. SHPM mapping performed on the transversal wire cross sections in the remanent and Meißner state revealed considerable differences in the remanent field strength and shielding capabilities between different sub-elements.

3. Through scans performed on the longitudinally polished wire cross section, variations in the remanent field along the wire axis became apparent, likely resulting from variations in the A15 geometry described in Chapter 3 and elemental composition described in Chapter 5.

4. The scans in the Meißner state and the evaluation of the shielded areas revealed the existence of a radial gradient in the critical temperature T_c, which results from the radial gradient of the Sn content that was assessed by EDX in Chapter 5.

5. Especially the Meißner scans at $16.5\,\text{K}$ led to the conclusion of differing T_c values between sub-elements as well as local inhomogeneities inside individual sub-elements.

6. The infield scans acquired at differing applied fields led to the conclusion of an asymmetric field penetration at increasing field strengths due to inhomogeneities inside the sub-elements.

In the following chapter, the obtained results will be compared with investigations of the microstructure in order to obtain a correlation between local variations in the geometry and elemental composition of the sub-elements and the resulting shape and magnitude of the magnetic fields assessed by SHPM.

9 Correlation of microstructure and superconducting properties

This chapter demonstrates the combined use of SEM and SHPM to analyse inhomogeneities in Nb$_3$Sn wires. Inhomogeneities of the A15 phase in Nb$_3$Sn sub-elements of the RRP-Ti-108 wire and the PIT-Ta-114 wire were investigated. Microstructural features were examined by SEM, elemental concentration gradients by EDX and the local superconducting properties J_c and T_c by SHPM. Correlations between the results were analysed to gain information about the impact of inhomogeneities in the microstructure on the superconducting properties.

Considerable differences in geometry and performance between sub-elements as well as compositional and geometric inhomogeneities of the A15 phase inside single sub-elements were found. Additionally, simulations of the influence of Sn concentration gradients on the critical current density J_c were performed. The viability of scanning Hall probe microscopy and energy-dispersive X-ray spectroscopy for determining the dependence of the critical temperature T_c on the Sn concentration is demonstrated and it is discussed how performance gains might be achieved by a reduction of inhomogeneities in Nb$_3$Sn wires.

9.1 Introduction

Simulations in past studies have shown that compositional inhomogeneities in Nb$_3$Sn wires can have a great influence on the superconducting properties [15, 29], hence their investigation in industrial wires is important to assess potential performance gains. In the present chapter, inhomogeneities are examined using experimental methods on state-of-the-art wires in order to gain a better understanding of their impact on the superconducting properties of real wires. The nature of these inhomogeneities are multifold and include geometric and compositional inhomogeneities as well as those in the local superconducting properties. The microstructure was investigated by SEM, elemental concentration gradients by EDX and J_c and T_c were analysed by SHPM. The combination of these methods allows a direct comparison and correlation between microstructural features and their influence on the local superconducting properties.

The goals of the study are twofold: on the one hand the conceptual introduction of the combined use of the given methods, on the other hand the demonstration of the acquisition of data of two different wire architectures and its discussion. These methods of analysing inhomogeneities yield information about local properties and are not designed for analysing the global properties, which might show considerably different values. Additionally, the combined investigation by SHPM and SEM of multiple sub-elements as well as the correlation between the results of both methods is extremely time-consuming and can therefore not easily be conducted on multiple cross sections per wire.

A part of the results shown in this chapter was already presented in previous chapters, most notably in Chapter 3, Chapter 5 and Chapter 8. Specific results will be shown again in addition to further analyses, which are necessary to establish a correlation between the different methods of investigation.

9.2 Experiments and simulations

Inhomogeneities of sub-elements in two types of Nb_3Sn wires were investigated, the Ti-alloyed Restacked Rod Process wire with 108 sub-elements, denoted as RRP-Ti-108, and the Ta-alloyed Powder-In-Tube wire with 114 sub-elements, denoted as PIT-Ta-114. The term sub-element is not entirely accurate for the PIT-Ta-114 wire, where filament would be the correct denotation, but for reasons of clarity and comprehensibility the term sub-element was used for all wires in this study. PIT and RRP type wires are currently the best candidates of standard wires for the use in future accelerator dipole magnets as discussed in Chapter 1, hence the investigations were carried out on these wire types. An overview over the relevant properties of the investigated wires can be found in Table 1.3. The RRP-Ti-108 wire possesses a Cu/non Cu ratio of 1.02 and a Ti content of 2 at.%, the Cu/non Cu ratio of the PIT-Ta-114 wire is 1.21 with a Ta content of 5 at.%.

One transversal cross sections of each of the two different types of Nb_3Sn wires were polished for SEM and SHPM analysis, of which multiple sub-elements were investigated. Additionally, one sample of the RRP-Ti-108 wire was prepared by polishing along the wire axis to the centre of a sub-element in order to examine longitudinal variations of the geometry and composition. Overview SEM images of all prepared and investigated samples can be found in Figure 9.1.

9.2.1 SEM analysis

SEM imaging was performed using a Quanta 250 FEG SEM to gain information about geometric variations of the A15 phase inside individual sub-elements and between different sub-elements. SEM images taken with the backscattered electron
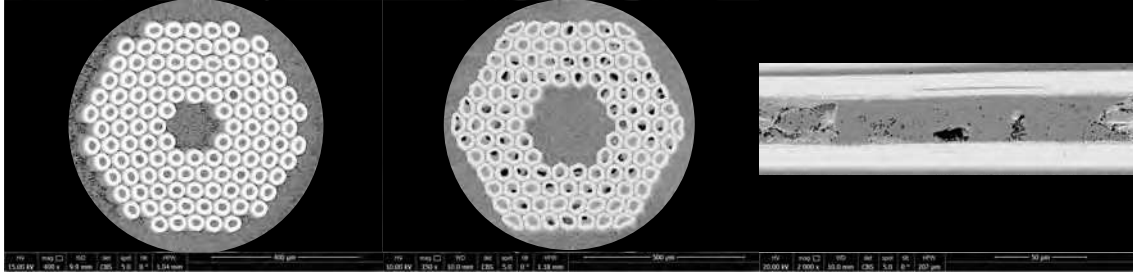
Figure 9.1: Overview SEM images of the prepared and investigated samples. Polished transversal cross sections of the PIT-Ta-114 wire (left) and the RRP-Ti-108 wire (middle) as well as the longitudinal cross section of an RRP-Ti-108 sub-element (right).

(BSE) detector were used to quantify the size distributions and aspect ratios of the sub-elements. The BSE detector yields high contrast between the Cu, Nb and A15 phases due to their differing atomic numbers. Based on the high contrast, the total area of the A15 phase and the inner parts of sub-elements of the RRP-Ti-108 and PIT-Ta-114 wires was evaluated by pixel counting as described in Chapter 3.

9.2.2 EDX analysis

EDX analyses were carried out on the A15 layers of the sub-elements to gain information about the distribution of the elements. EDX line scans from the outside to the inside of the sub-elements were performed on the transversal cross sections with a step width of 100 nm to determine the radial variations of the Sn concentration as described in Chapter 5. Additionally, the elemental composition of the A15 phase was measured along the wire axis with a step width of 200 nm to assess possible longitudinal variations of the Sn content. An accelerating voltage of 10 kV was used for the EDX analyses. In Nb_3Sn, this corresponds to a penetration depth of a few hundred nm [113], therefore the information acquired stems from the region between the sample surface and this depth.

9.2.3 SHPM analysis

SHPM allows spatially resolved mapping of a magnetic field above a superconductor and was performed on the polished transversal cross sections of the RRP-Ti-108 and the PIT-Ta-114 wire in the remanent and Meißner states as described in Chapter 8. The employed scanner is able to analyse a sample area of $3\,mm \times 3\,mm$ with a resolution of 1 μm. The remanent field scans performed at 10 K after applying and deactivating a field of 1 T were used for calculating the critical current density J_c of the A15 layer of different sub-elements and comparing the resulting values. In addition, SHPM was also used to analyse differences in the critical temperature

T_c between individual sub-elements by acquiring scans in the Meißner state at an applied external field of 5 mT. These scans were also used to evaluate the shielded area of the sub-elements at different temperatures. The SHPM scans were acquired without current injection to the samples. The pattern of currents and fields during current injection would differ from the employed setup.

9.2.4 Correlation of the SEM, EDX and SHPM results

The correlations between the results of the SEM, EDX and SHPM investigations were analysed; in particular Hall scans of the remanent field in the RRP-Ti-108 wire were compared with geometric information acquired by SEM. The area of each sub-element measured was determined by pixel counting from SEM images and the inner and outer radius were calculated based on circles with equivalent area. The critical current density J_c of the A15 layer was calculated from the central value of the remanent field above each sub-element.

Differences in the critical temperature T_c between different sub-elements of the RRP-Ti-108 wire were determined by SHPM and compared with the Sn distribution in the A15 phase that was acquired by EDX in order to investigate the correlation between T_c and the Sn content in specific sub-elements.

The radii of the shielded areas of the PIT-Ta-114 and RRP-Ti-108 wires in the Meißner state at different temperatures were combined with EDX measurements of the Sn gradient across the A15 phase, yielding the general dependence of the critical temperature T_c on the Sn content.

The methods applied on the RRP-Ti-108 wire focus on evaluating differences between sub-elements across the wire cross section, while the analysis focused on the PIT-Ta-114 wire aims to establish a statistics of multiple sub-elements, and is thus representative for the average value of each sub-element across the wire section. The reason for the difference in preferred methods applied to the two different wire types can be related to their better suitability for each method, since PIT wires inherently exhibit a greater homogeneity due to their manufacturing process of using Nb tubes instead of stacked filaments as described in Chapter 1.

9.2.5 Simulations

Simulations were performed in order to evaluate the influence of the Sn gradient inside the A15 phase on the critical current density J_c. The A15 inhomogeneity was modelled based on the properties of the real RRP-Ti-108 wire used in this study as described in [15], where elemental concentration profiles obtained by EDX and grain size data of the RRP-Ti-108 wire were used. The simulations of influence of the Sn gradient on the critical current density were performed by Thomas Baumgartner.

9.3 Results and discussion

9.3.1 Sub-element area and aspect ratio distribution

The results of the sub-element area distribution of the RRP-Ti-108 and PIT-Ta-114 wire obtained using SEM imaging are shown together with their respective statistics and the aspect ratios in Figure 9.2 and Figure 9.3, where the sub-element area is defined as the total area of the A15 phase and the central area. The sub-elements were colour coded according to the measured values using the ROI Colour Coder plugin for the ImageJ program [40], where the colour bar ranges from the minimum to the maximum of the measured values, except for the aspect ratio of the RRP-Ti-108 wire, where the upper limit was set to 1.35 due to the 6 outermost sub-elements being outliers. The opacity of the overlay was set to 80 %, allowing the spatial extent of the A15 phase to be visible in the background. The colour in the central area of each sub-element corresponds to the value displayed by the colour bar. The sub-element area distributions of both wires can be approximated by Gaussian fits. The fits are marked by the red lines and the insets show the minimum, maximum, mean value and standard deviation of the experimental data.

It is clearly visible that there are significant variations of the sub-element areas and aspect ratios over the wire cross section. While no apparent correlation between location and geometry of the sub-elements can be found in the RRP-Ti-108 wire, the outmost sub-elements are generally more elliptical than the ones near the wire centre in the PIT-Ta-114 wire. One sub-element in the PIT-Ta-114 wire is worth mentioning as it has not reacted properly during heat treatment and exhibits only a very limited A15 fraction. This sub-element can be seen near the top of the wire cross section in Figure 9.3 and was not included in the analysis.
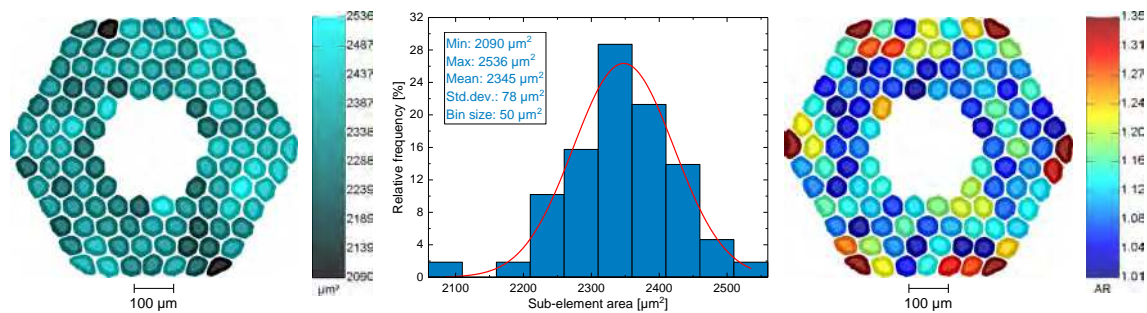
Figure 9.2: Areas of sub-elements in the RRP-Ti-108 wire (left), statistics of sub-element area distribution of RRP-Ti-108 wire (middle) and aspect ratios of sub-elements (right).
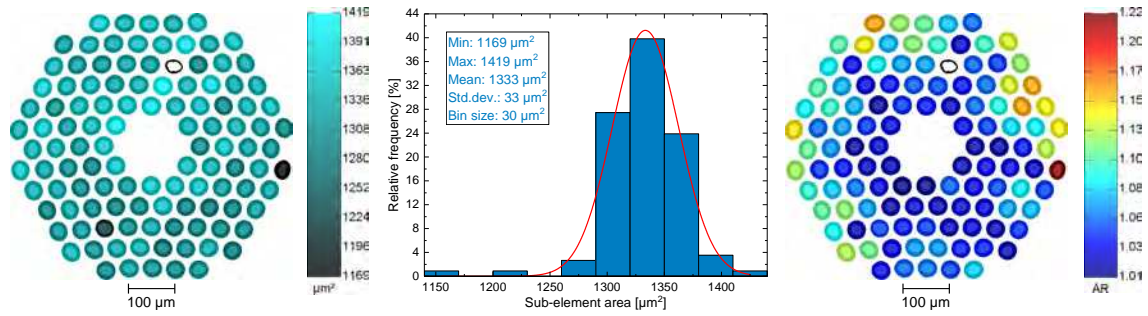
Figure 9.3: Areas of sub-elements in the PIT-Ta-114 wire (left) and statistics of sub-element area distribution of PIT-Ta-114 wire (middle) and aspect ratios of sub-elements (right).

9.3.2 Remanent fields and correlation with the microstructure

A remanent field Hall scan of the RRP-Ti-108 wire was acquired at 10 K after applying and deactivating an external field of 1 T. The result can be found in Figure 9.4, where a unique number was allocated to each sub-element. It becomes apparent that there are considerable differences in the magnitude and shape of the remanent fields between sub-elements.

After examination of the sub-elements by SHPM as shown in Figure 9.4, SEM images of the same area were taken in order to investigate a possible correlation between the remanent field and the geometry. This understanding is important for calculating J_c of the sub-elements as described in Subsection 9.3.3. Figure 9.5 shows an overview image of the investigated sub-elements together with the evaluation of their area and aspect ratio. All relevant parameters of the investigated sub-elements are summarized in Table 9.1.

As examples, sub-elements number 1, 4, 8 and 15 show low remanent fields as seen in Figure 9.4 and rather small areas, while the aspect ratio seems to have no considerable impact on the remanent field, since these sub-elements show small values. Sub-elements number 10 to 14 show the highest remanent fields but simultaneously a large variation in area and aspect ratio. Sub-element number 8 exhibits an exceptionally low remanent field. When looking at Figure 9.5, it becomes apparent that this sub-element seems to possess a smaller minimum thickness of the A15 phase than the remaining sub-elements. This suspicion was confirmed by analysing the minimum distance between the outer and inner border of all sub-elements using the layer thickness and line colour plugins for ImageJ [86]. The results of sub-elements number 8 and 9 are are displayed in Figure 9.6, where lines of the closest distance were drawn from each pixel at the outer border of the A15 layer to the inner border and coloured according to their length. The inner border of the A15 phase is often
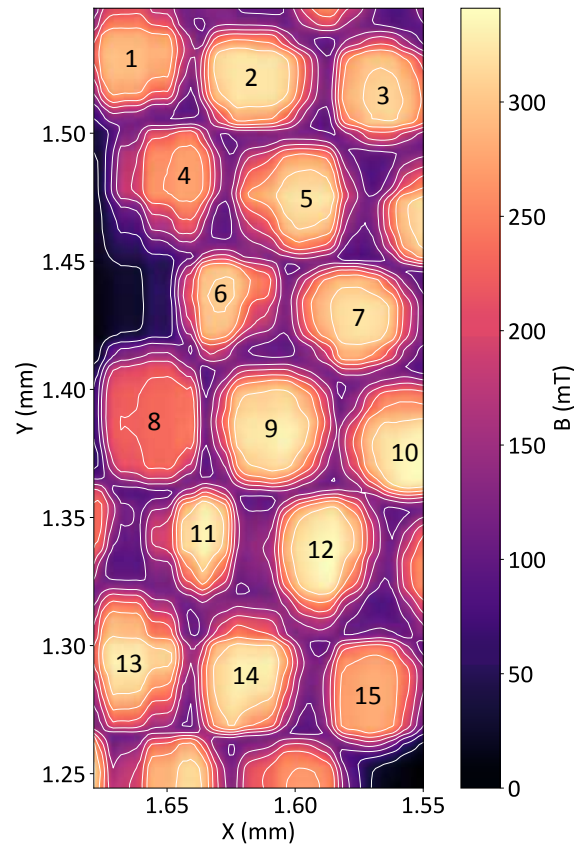
Figure 9.4: Remanent field Hall scan of the RRP-Ti-108 wire at 10 K after applying and deactivating an external field of 1 T.
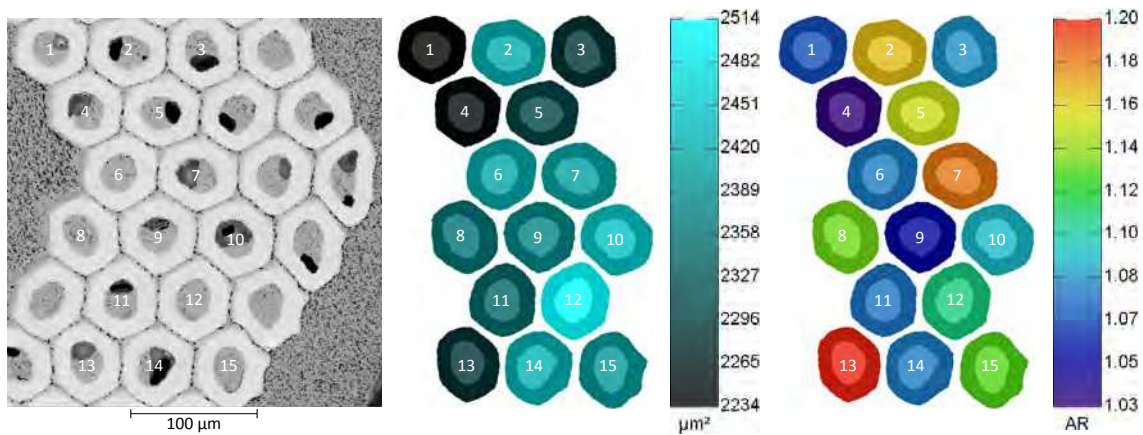
Figure 9.5: SEM image of investigated sub-elements of RRP-Ti-108 wire (left), their areas (middle) and their aspect ratios (right). The colour in the sub-element centre corresponds to the value in the colour bar.

not clearly defined due to weakly connected grains, which complicates the evaluation of the A15 layer thickness.
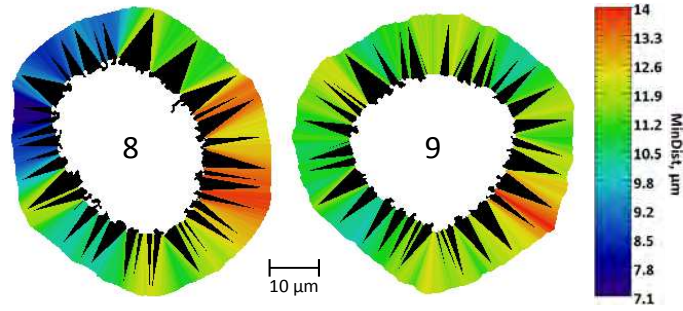
Figure 9.6: Minimum thickness of the A15 layer of two sub-elements of the RRP-Ti-108 wire.

It can be seen that the A15 layer thickness of sub-element number 8, which showed the lowest remanent field, at some locations only measures about 7.2 µm, which is 50 % lower than the maximum value of the same sub-element. For comparison, sub-element number 9 shows a much more uniform distribution of the A15 layer thickness, which for the most part stretches over 10 µm with a minimum of 9.7 µm. These findings show evidence that the minimum A15 layer thickness, further denoted as d_{A15}, has a major impact on the resulting remanent field, since it limits the circular current locally, which needs to be considered for calculating J_c. In practical wires, where the current flows in the longitudinal direction, such thickness reductions of the A15 phase limit the current by reducing the superconducting cross section.

9.3.3 Determination of the sub-element J_c

The SHPM scan of the RRP-Ti-108 wire in Figure 9.4 was used to evaluate the critical current density J_c of the A15 layer of each sub-element, which can be calculated from the measured remanent magnetic flux profile by the inversion of the Biot-Savart law. For this, the sub-element geometry is approximated by a hollow cylinder as derived from [28].

As shown in Chapter 8, an uncertainty of a few µm in the distance of the Hall probe from the sample surface z can have a large impact on the result of J_c, while the sample thickness t only significantly impacts the result below a value of 50 µm for the present geometry. The Hall probe distance from the sample surface z was measured at multiple points to ensure a flat sample surface and an accurate determination of its value. For the SHPM measurements of the RRP-Ti-108 wire the sample thickness t was about 3 mm and the Hall probe distance from the sample surface z was 2 µm. In the present case of large t and given the above assumptions, Equation 8.1 for calculating J_c along the cylinder axis simplifies to

$$J_{\mathrm{c}} = \frac{2B_z}{\mu_0 \left[r_{\mathrm{o}} - r_{\mathrm{i}} + z \ln \left(\frac{r_{\mathrm{i}} + \sqrt{r_{\mathrm{i}}^2 + z^2}}{r_{\mathrm{o}} + \sqrt{r_{\mathrm{o}}^2 + z^2}} \right) \right]} . \tag{9.1}$$

In Equation 9.1, B_z denotes the measured remanent magnetic field in the sub-element centre, z the distance of the Hall probe from the sample surface, r_{o} the outer radius of the A15 phase and r_{i} the inner radius of the A15 phase.

In Subsection 9.3.2, it was shown that the A15 layer thickness d_{A15} has a major influence on the remanent field of the sub-elements. For that reason, r_{o} was determined by pixel counting of SEM images, while r_{i} was defined as the difference between the outer radius and the minimum A15 thickness, $r_{\mathrm{i}} = r_{\mathrm{o}} - d_{A15}$. The measured values of B_z, r_{o}, d_{A15} and the calculated critical current density J_{c} of the A15 layer of the investigated sub-elements can be found together with the measured values of their areas and aspect ratios in Table 9.1.

Sub	B_z [mT]	r_{o} [μm]	d_{A15} [μm]	r_{i} [μm]	Area [μm^2]	AR	J_{c} [A mm^{-2}]
1	295	26.7	8.5	18.2	2234	1.07	6.10×10^4
2	325	27.8	9.5	18.3	2422	1.16	5.98×10^4
3	311	27.0	9.3	17.7	2288	1.08	5.85×10^4
4	274	26.7	8.9	17.8	2243	1.03	5.39×10^4
5	323	27.1	9.5	17.6	2308	1.15	5.96×10^4
6	306	27.7	9.1	18.6	2414	1.08	5.85×10^4
7	320	27.7	8.7	18.9	2408	1.18	6.38×10^4
8	234	27.4	7.2	20.2	2359	1.13	5.65×10^4
9	328	27.5	9.7	17.8	2378	1.05	5.89×10^4
10	335	27.9	9.7	18.3	2447	1.09	6.05×10^4
11	335	27.3	9.8	17.6	2347	1.08	6.00×10^4
12	337	28.3	9.3	18.9	2514	1.11	6.28×10^4
13	330	27.0	9.1	17.8	2286	1.20	6.31×10^4
14	331	27.8	8.7	19.1	2426	1.08	6.62×10^4
15	284	27.6	9.0	18.6	2398	1.13	5.50×10^4

Table 9.1: Comparison of the properties of the investigated RRP-Ti-108 sub-elements.

It becomes apparent that individual sub-elements show considerable differences in geometry and remanent field values, resulting in different calculated J_{c} values, ranging from 5.39×10^4 A mm^{-2} to 6.62×10^4 A mm^{-2}. Sub-element number 4 possesses the lowest calculated J_{c} value and one of the smallest measured areas. Sub-element number 14 exhibits a high remanent field but a rather small d_{A15}, resulting in the highest calculated J_{c} value. The average value is 5.99×10^4 A mm^{-2} with a standard deviation of 0.32×10^4 A mm^{-2}. Therefore the maximum J_{c} value of

$6.62 \times 10^4 \, \mathrm{A \, mm^{-2}}$ differs from the average value by about $10\,\%$ and by the minimum value by about $20\,\%$.

Part of the variations of the calculated J_c can be attributed to the fact that Equation 9.1 assumes a circular shape of the sub-elements and therefore might lead to errors in the calculation of J_c of elliptical sub-elements. On the other hand, no considerable influence of the aspect ratio on the resulting remanent field was determined, therefore not affecting the calculation.

The average longitudinal self-field J_c of 8 pieces cut from the RRP-Ti-108 wire was obtained from SQUID magnetometry at the same temperature of $10\,\mathrm{K}$ by Thomas Baumgartner at ATI and evaluated as described in [11]. It is quite remarkable that this analysis leads to $(6.18 \pm 0.16) \times 10^4 \, \mathrm{A \, mm^{-2}}$; thus the circular currents assessed by SHPM seem quite representative for the longitudinal currents.

Despite this good agreement it has to be noted that the obtained values by SHPM are based on local evaluations, and the ones from SQUID from samples a few mm in length. It should not be expected that these values coincide with transport J_c values over km of length, therefore the determined local properties are not representative of the global properties.

9.3.4 Differences in the sub-element T_c

Differences in the critical temperature T_c of individual sub-elements of the RRP-Ti-108 wire were assessed by applying scans in the Meißner state at an applied external field of $5\,\mathrm{mT}$. Figure 9.7 shows a Meißner scan of the RRP-Ti-108 wire at $5\,\mathrm{mT}$ and $16.5\,\mathrm{K}$, where the sub-elements are numbered in the same manner as in Figure 9.4.

From these results, it becomes apparent that different sub-elements also show variations in the shielding capacity which can be related to differences in T_c, where as example sub-elements number 9 and 11 show exceptionally low shielding capacities, while sub-element number 7 shows a better performance. Differences in T_c can generally be understood as differences in the local Sn content in the inner parts of the A15 layer of the sub-elements, where the Sn content and T_c reach their maximum values.

9.3.5 Correlation between sub-element T_c and the microstructure

Differences in T_c that became apparent in Figure 9.7 can be related to variations in the elemental composition. In [140] it was shown that increasing the Ta content led to a decrease in T_c, while an increase in the duration of the heat treatment led to an increase in T_c. The addition of $10\,\mathrm{at.\%}$ Ta to bronze processed Nb_3Sn wires
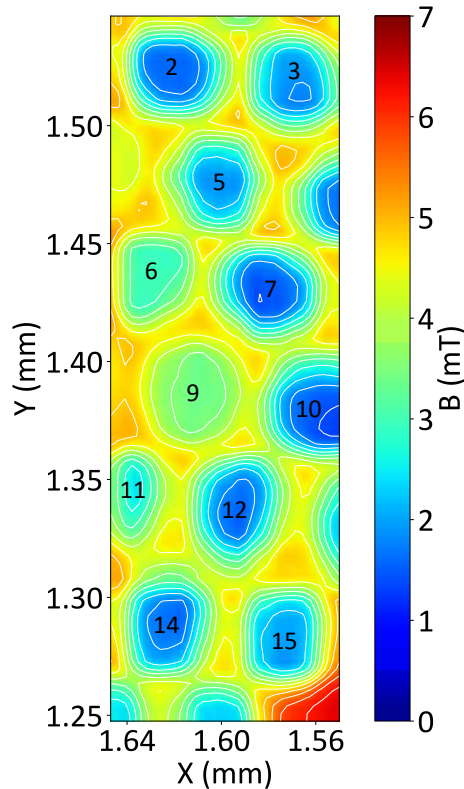
Figure 9.7: Meißner scan of the RRP-Ti-108 wire at 5 mT and 16.5 K.

reduced the T_c by about 1.5 K, depending on the heat treatment. An increase in J_c by a factor of two was observed at 16 T due to a Ta addition of 7 wt.%. A reduction to the original J_c value occurred when the Ta addition reached 20 wt.%.

The T_c measured by SHPM is limited by local minima of the Sn content near the sub-element centre which inhibit continuous shielding currents at higher temperatures. Due to this dependence, EDX line scans were carried out on sub-elements number 7, 9 and 11 in order to confirm a difference in the Sn content, which was suspected from Figure 9.7. On each sub-element, multiple line scans were performed in the radial direction and averaged. The results are summarized in Figure 9.8, where the Cu content was factored out for an accurate comparison of the Sn contents.

A correlation between the Sn content and differences in T_c between the sub-elements was found. The sub-elements number 9 and 11, which showed a poor T_c performance in the Meißner scans, showed a lower average Sn content than the better performing sub-element number 7 and indications of locations with exceptionally low values. Especially towards the inner parts, sub-element 7 shows higher Sn contents, while the Ti content shows lower values compared to the other sub-elements. It is furthermore possible that the EDX line scans did not even capture all the points of impactful local minima of the Sn content, since there might be considerable angular variations.

The EDX signal of Nb_3Sn at an accelerating voltage of 10 kV originates from only up
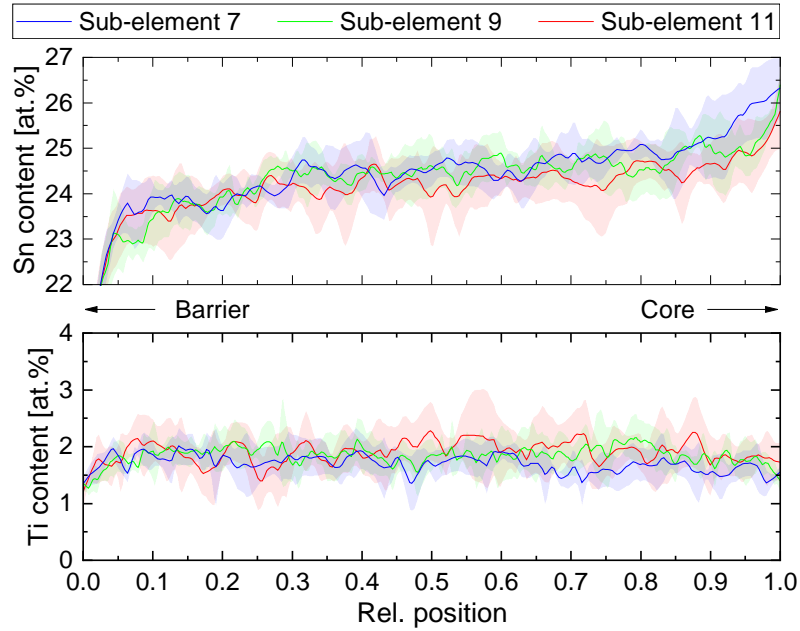
Figure 9.8: Comparison of the Sn and Ti content of different sub-elements of the RRP-Ti-108 wire. The standard deviations are indicated by the shaded areas.

to a few hundred nm below the sample surface [113] and differences in the measured T_c between sub-elements could also be attributed to longitudinal variations of the Sn content over a larger distance along the wire axis. Such longitudinal variations could impact the magnetic signal measured by SHPM due to current flow in deeper sample layers.

In order to examine possible longitudinal gradients of the Sn concentration, an EDX analysis was performed on a longitudinally polished RRP-Ti-108 wire sub-element close to the wire centre which shows practically no twisting, contrary to the outer sub-elements, as already described in Chapter 5. The EDX data are shown in Figure 9.9, where variations in the Sn content can be seen that are clearly larger than the noise. Additionally, much care was taken to measure parallel to the wire axis to obtain information of the change in Sn content along the wire axis only, without any influence from radial gradients. From these results, it can be concluded that there are significant changes of the A15 Sn content along the wire axis of over 1.5 at.%, in this case within a distance of less than 30 µm. Furthermore, the validation of radial and longitudinal variations reinforce the hypothesis of angular variations, all of which impact the distribution of T_c.

Aside from variations of the Sn content, longitudinal variations of the A15 geometry could also impact the superconducting properties. An evaluation of geometric variations along the wire axis is shown in Figure 9.10, where the distance between the outer and the inner border of the A15 layer was measured at multiple points of a SEM
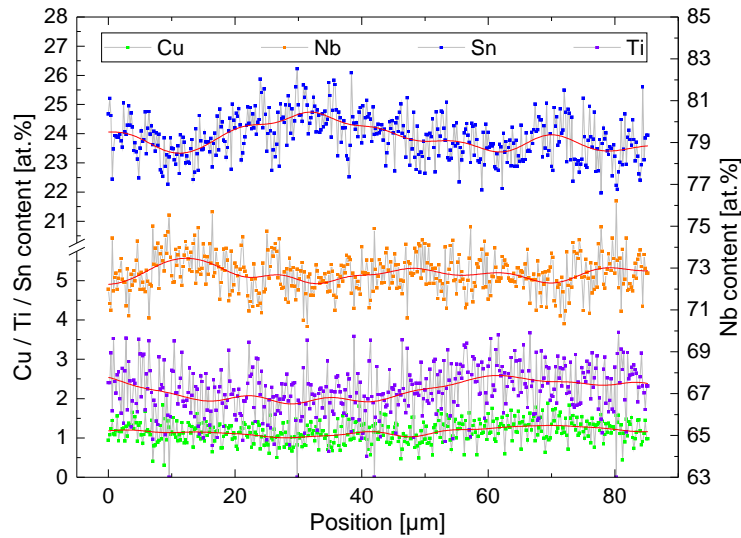
Figure 9.9: EDX line scan along the RRP-Ti-108 wire axis showing longitudinal variations of the Sn content. The data were smoothed by FFT filtering as marked by the red line in order to reduce the noise of the signal.

image of the transversal cross section of an RRP-Ti-108 sub-element. Longitudinal variations of the A15 layer thickness up to 2 μm were observed within the longitudinal distance of 60 μm, which equals a reduction of the maximum thickness by 16 %. It is furthermore visible that the A15 phase is partly interrupted by the inclusion of residual Cu that stretches over a distance of more than 50 μm, which might inhibit the current flow.
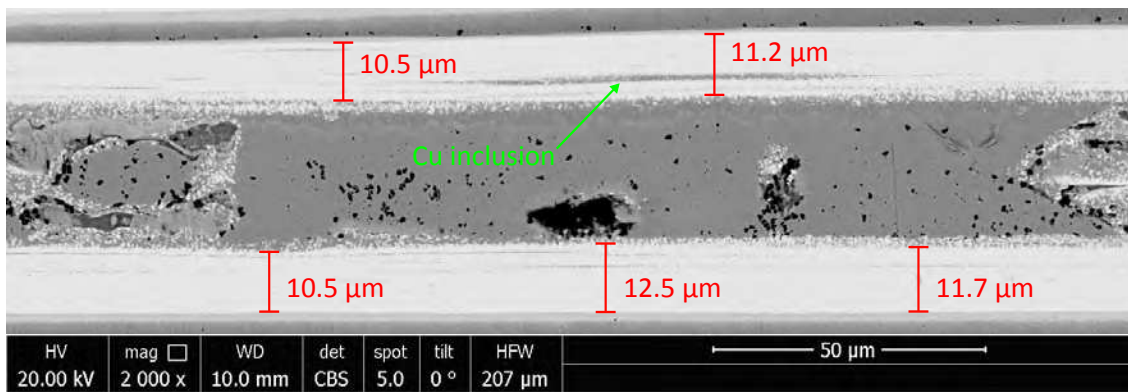
Figure 9.10: SEM image of the longitudinal cross section of the RRP-Ti-108 wire showing variations of the A15 thickness along the wire axis.

The determined longitudinal variations of the Sn content and geometry along the wire axis can have an impact on the performance of the wire by limiting the superconducting properties locally. It is obvious that no conclusions can be made about the entire wire over a long distance from only measuring a few μm along the axis.

However, given that in this study, considerable inhomogeneities in wires of small lengths up to 3 mm were determined, it can be expected that in practical wires of longer lengths the superconducting properties might be even more inhibited, since they are determined by the worst performing region. If such large variations were present in multiple sub-elements within short distances along the axis, it would have a significant impact on the wire performance.

9.3.6 Correlation of T_c and Sn content

This section aims to establish a statistics that is valid for the entire wire cross section by averaging multiple sub-elements, contrary to the investigations of the RRP-Ti-108 wire, were differences between sub-elements are compared. For the investigations described in this section, the PIT-Ta-114 wire was focused on since it exhibits a greater homogeneity of geometry and Sn content between different sub-elements compared to the RRP-Ti-108 wire, which results in a lower standard deviation of the EDX statistics and the values of the sub-element diameters being more comparable.

SHPM scans were performed on a transversal cross section of the PIT-Ta-114 wire in the Meißner state at different temperatures and a small applied magnetic field of 5 mT. The scans of the PIT-Ta-114 wire were used in combination with radial EDX line scans of this wire in order to determine the dependence of T_c on the Sn content. The shielded area was analysed at each temperature as described in [14], where the contour lines at 50 % of the applied field were evaluated. Figure 9.11 shows the contour plots of the PIT-Ta-114 sub-elements at 2.5 mT and different temperatures. The size of the shielded areas decrease with increasing temperature and confirm a T_c distribution due to the radial gradient of the Sn concentration, which past studies have determined using magnetic and calorimetric methods on various Nb_3Sn wires [128, 127, 147].

The average radii of the shielded areas assuming circular shape were correlated with the Sn content at each position which was acquired by EDX line scans. Due to the Nb barrier being superconducting below about 9 K [14], the lower temperature limit of the measurements was set to 10 K. In [52], a Boltzmann function is presented which accurately describes the experimentally determined dependence of T_c on the Sn content. For the evaluation of these measurements, a reference point had to be chosen. The assumption was made that a T_c of 10 K corresponds to a Sn content of 21.35 at.% as described by the Boltzmann function, therefore the values of the shielding radii at this temperature correspond to the position of the given Sn content in the A15 layers of the sub-elements.

Figure 9.12 shows statistics of the Sn content across the A15 area of the PIT-Ta-114 wire derived from 10 EDX line scans and the corresponding critical temperature at different points that was obtained through correlation with the shielding radii. The radii were acquired by scaling the contour plots at 2.5 mT to the value at 5 mT,
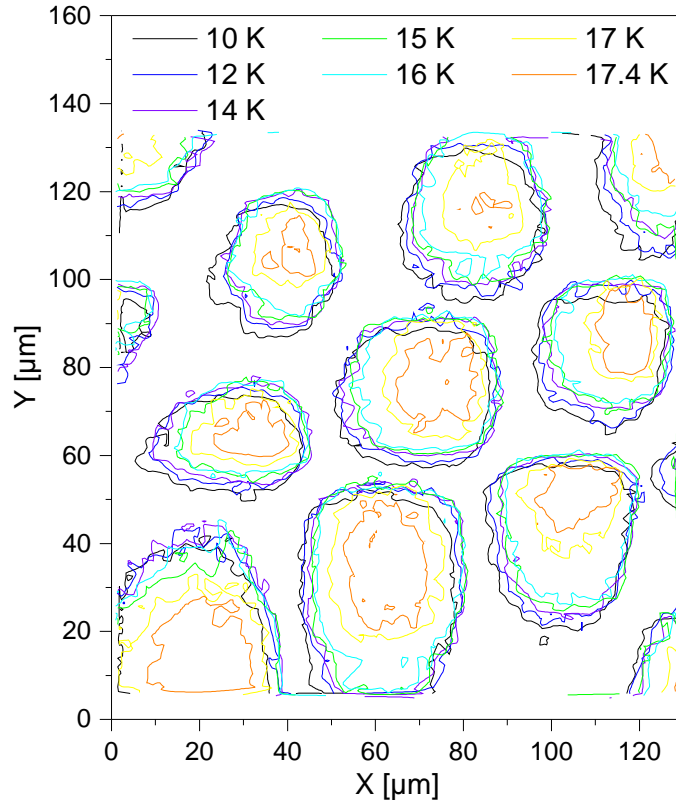
Figure 9.11: Shielding currents of PIT-Ta-114 sub-elements at 2.5 mT and different temperatures.

which defines the outer border of the shielded area. This was achieved by extending the average values of the radii at all temperatures by the same constant value so that the radius at 10 K corresponds to a Sn content of 21.35 at.%. Since the lower phase limit of Nb$_3$Sn is an atomic Sn content of 18 %, this value corresponds to the outer A15 layer radius. The same analysis is shown for the RRP-Ti-108 wire in the same figure.

Through correlating the Sn content that was obtained using EDX with the distribution of the critical temperature T_c that was obtained using SHPM scans in the Meißner state, it is possible to assess the dependence of the critical temperature T_c on the Sn content as shown in Figure 9.13, which is displayed for both investigated wire types. The resulting dependence shows good agreement with the Boltzmann function found in [52]. Additionally, the linear function found in the same publication was included in Figure 9.13, which also shows a good fit to the acquired data. One thing to note is the fact that the dependences in [52] describe the binary Nb$_3$Sn system, while the here investigated samples contain Ta and Ti, respectively. The influence of Ta and Ti on the dependence of T_c is not well known, but due to the good agreement between the present data and the literature, there is no reason to assume that the addition of Ta and Ti is drastically altering the established dependence.
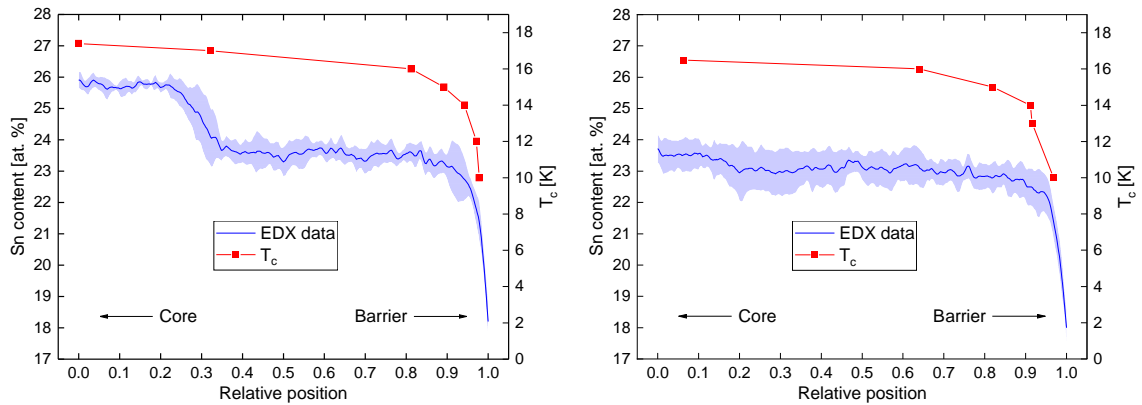
Figure 9.12: Statistics of EDX line scans across A15 phase of PIT-Ta-114 (left) and RRP-Ti-108 (right) sub-elements and position of shielding radii at different temperatures. The shaded area indicates the standard deviation.
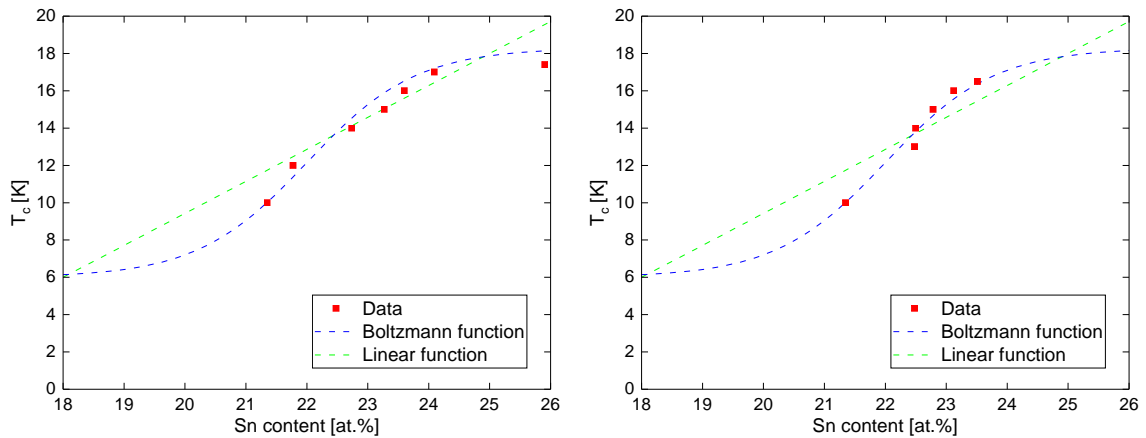
Figure 9.13: Dependence of T_c on the Sn content in the PIT-Ta-114 wire (left) and RRP-Ti-108 wire (right), together with the functions described in [52].

9.3.7 Influence of Sn gradients on J_c

Simulations were performed in order to evaluate the influence of the Sn gradient inside the sub-elements on the critical current density J_c. For that, a radial Sn distribution profile was chosen that emulates the experimentally determined properties of the RRP-Ti-108 wire as described in [15]. The Sn content used for the simulations was slightly altered from the experimental data in order to achieve a better agreement in J_c between the simulations and the real wire, since the influence of Ti is not well known and therefore not included in the simulation. The maximum Sn content was set at 24.4 at.% and the Sn gradient in the linear region, which spans most of the A15 area except for a steep fall-off at the barrier, was initially set at 0.1 at.% µm^{-1}. The Sn gradient was then varied between 0 % and double the value of the original profile while keeping the maximum Sn content fixed. For these profiles, the average transport J_c at 4.2 K and 16 T as well as at 10 K in self-field was calculated. The simulations of the influence of the Sn gradient on the critical current density were performed by Thomas Baumgartner, who also visualised the data.
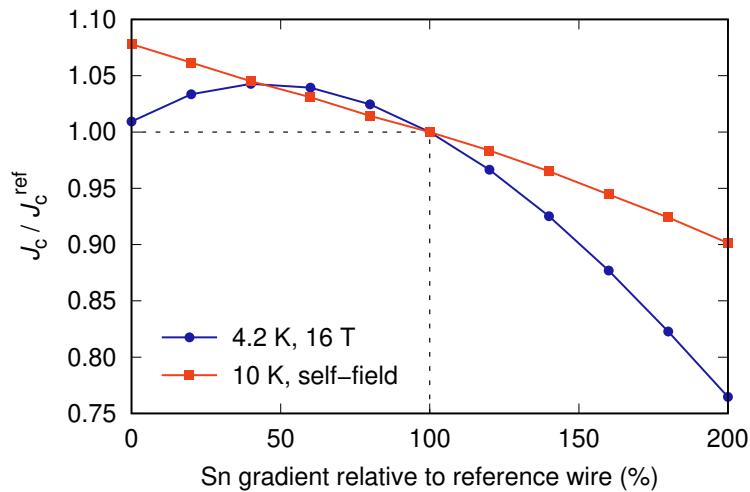
Figure 9.14: Simulation of the impact of different Sn gradients on J_c. Graphic drawn by Thomas Baumgartner.

The results of the simulations can be found in Figure 9.14, which shows the relative variation of J_c when the Sn gradient is altered. The reason for the decline of J_c for small gradients at 4.2 K and 16 T is that the maximum Sn content is slightly above the Sn content where B_{c2} is maximized, which has a high impact at high fields.

It becomes apparent that a reduction of the radial Sn gradient by 50 % alone could lead to an increase in J_c by almost 5 %, which is without considering all the other inhomogeneities present. From these simulations it furthermore can be seen that even a small J_c decrease measured by SHPM can signify a substantial reduction in J_c at the higher fields required for application in future particle accelerators.

9.4 Conclusions of the correlated analyses

In this chapter, the combined use of SEM and SHPM to determine inhomogeneities in Nb_3Sn wires was demonstrated. Information was acquired about sub-element area and aspect ratio distribution, remanent fields and their correlation with the microstructure, differences of the J_c values between sub-elements, variations of the sub-element T_c, longitudinal variations in the elemental composition and geometry, correlation of T_c and Sn content and the influence of Sn gradients on J_c.

The results of the correlated investigations of microstructure and the superconducting properties can be summarized as follows:

1. Inhomogeneities of sub-elements in multifilamentary Nb_3Sn wires were investigated by SEM, EDX and SHPM. Differences were found in geometry, J_c and T_c between sub-elements in the RRP-Ti-108 wire.

2. The remanent field values of a Hall scan were used in combination with geometric data acquired by SEM in order to calculate J_c of the A15 phase of each sub-element. The resulting J_c values show variations of up to around 20 % between sub-elements.

3. Differences in the shielding capacities and therefore T_c were observed in the Meißner scans of the RRP-Ti-108 wire. The variations in T_c arise due to compositional inhomogeneities of the A15 phase, which were confirmed by EDX analyses.

4. Longitudinal variations of the Sn content of the A15 layer along the RRP-Ti-108 wire axis up to 1.5 % were investigated and confirmed that can contribute to differences in T_c between sub-elements. Considerable longitudinal variations of the A15 geometry along the wire axis up to 2 μm were found that can inhibit the current locally.

5. SHPM scans in the Meißner state at different temperatures confirmed a radial T_c gradient inside the sub-elements due to a radial Sn gradient. The correlation of the shielding radii with the Sn content obtained by EDX analysis yielded the dependence of T_c on the Sn content, which was found to be consistent with existing literature data.

6. Simulations of the influence of Sn gradients on J_c showed that an optimization of the radial Sn gradient inside sub-elements can result in a J_c increase, especially at high fields.

Aside from demonstrating the methods to analyse such inhomogeneities, from this study it furthermore becomes apparent that there are geometric and compositional inhomogeneities between different sub-elements as well as inside single sub-elements, which can not be neglected. Given the magnitude of longitudinal inhomogeneities found within short distances in this study, it is to be expected that they have

a significant impact on the performance in practical wires. The performance of Nb₃Sn wires to be used in FCC magnets could benefit from the reduction of these inhomogeneities.

10 Conclusions and outlook

This chapter aims to summarise the main results of this thesis and provide an outlook for potentially useful experiments in the future.

10.1 Conclusions

This work dealt with the analysis of the microstructure of various state-of-the-art Nb_3Sn wires, which are required at CERN for new generation dipole magnets of the Future Circular Collider. Mainly three ways of increasing the performance were discussed in detail and corresponding microstructural analyses were presented:

1. The reduction of inhomogeneities inside sub-elements, particularly those in the elemental composition.

2. The refinement of the grain size through novel manufacturing techniques such as internal oxidation.

3. The introduction of artificial pinning centres that were present in the examined wires in the form of nano-precipitates and neutron irradiation induced defects.

In Chapter 1, the Future Circular Collider project was introduced, which aims to design a future particle accelerator with centre of mass collision energies of up to 100 TeV, accommodated in a new 100 km long tunnel, for which dipole magnets are required that operate at a field of 16 T. An extensive literature review about the properties of Nb_3Sn superconductors was presented, including the present state-of-the-art performance and the targets of the conductor development programme, which includes the increase in the critical current density J_c to $1500\,A\,mm^{-2}$ at 16 T and 4.2 K. The theory behind performance enhancement capabilities was introduced, in particular how J_c performance gains can be achieved, which are mainly based upon optimising the elemental composition, increasing the flux pinning force through grain refinement and the introduction of artificial pinning centres. The chapter concluded with an overview of the investigated wires types and the introduction of the applied experimental techniques including scanning electron microscopy (SEM) and transmission electron microscopy (TEM).

Chapter 2 described the findings and procedures related to the sample preparation for structural investigations by electron microscopy and magnetic characterizations

by scanning Hall probe microscopy (SHPM). The preparation processes were listed for thin samples of pristine and irradiated wires for TEM investigations by focused ion beam as well as whole cross sections for SEM and SHPM examinations by mechanical polishing. Additionally, alternative methods for sample preparation that were explored were described, such as the use of the assembled flash electro-polishing setup, which might be beneficial for future studies.

Chapter 3 dealt with the examination of inhomogeneities between sub-elements and inside individual sub-elements by scanning electron microscopy. In particular, variations in the geometry between sub-elements over the wire cross sections were analysed by evaluating the distributions of their areas and aspect ratios. It was found that the area distributions can be approximated by fits using Gaussian functions and the results were compared between the investigated wires. The APC wires showed the largest relative standard deviations of the sub-element areas, while PIT wires showed the smallest absolute and relative deviations. The outmost sub-elements were found to be generally more elliptical than the ones near the wire centre. The mean aspect ratios showed comparable values between all types of wires, while the maximum values differed considerably. At the end of the chapter, the observation of additional inhomogeneities was reported, which potentially can have a significant impact on the superconducting properties, such as longitudinal variations of the A15 geometry along the wire axis and leakage of Sn into the Cu matrix.

The local microstructure of the Nb_3Sn wires was analysed in Chapter 4 by transmission electron microscopy, where the finding of frequent Nb inclusions was reported and the microstructure of the A15 phase and precipitates was presented. A special focus was laid upon the determination of the size and density of the ZrO_2 and HfO_2 nano-precipitates in the APC wires, which form during the manufacturing process by internal oxidation in binary and ternary wires and likely contribute to an increase in the pinning force. The newer generation ternary APC wires showed much higher densities of precipitates, frequently in the order of $25\,000\,\mu m^{-3}$, compared to about $5000\,\mu m^{-3}$ in the older generation binary wires. The precipitates also showed smaller sizes in the ternary wires with modal diameters of around $2\,nm$–$4\,nm$, compared to frequently over $6\,nm$ in binary wires.

The analysis of the distribution of the chemical elements was conducted in Chapter 5 by the use of energy-dispersive X-ray spectroscopy (EDX), which plays a fundamental role in determining the local superconducting properties. EDX mapping revealed information about inhomogeneities in the elemental distribution in sub-elements as well as the accumulation of Cu at grain boundaries. Line scans across the A15 phases of the wires revealed gradients between the outer barrier and the core of the sub-elements, which are generally below $0.08\,at.\%\,\mu m^{-1}$ for the Sn content in the linear regions. The new generation ternary APC wires showed the highest Sn contents in the A15 phase of up to $26\,at.\%$. The contents of the additives Ti and Ta were found to decrease slightly towards the inside of the sub-elements of the ternary wires. The analysis of elemental the composition inside individual grains

revealed the existence of additional gradients inside the grains, where the highest Sn content can generally be found near grain boundaries and the minimum values near the grain centres. The Sn gradient inside grains was found to frequently cover the entire Nb_3Sn phase range between about 18 at.% and 26 at.%. In ternary wires, the Ti content was found to decrease towards the centre of the grains, while the Ta content showed the opposite behaviour. A higher Ta content was found in grains that exhibited higher Sn gradients and lower Sn contents. The EDX investigation of a longitudinal wire cross section furthermore revealed the presence of considerable longitudinal variations in the composition, where the Sn content varied by around 1.5 at.% within short distances of 30 μm.

The investigation of the grain geometry and orientation by the use of transmission Kikuchi diffraction (TKD) was presented in Chapter 6. The advantages and disadvantages compared to other conventional methods were discussed and the results compared. It was suggested that the use of area fractions instead of number fractions for the evaluation of grain size distributions yields the more relevant statistics, since it reveals information about the fine grain fraction of the sample area. While the older generation binary APC wires showed only a minor grain refinement, the newer generation ternary APC wires showed a substantial refinement of the average grain sizes, where the area weighted values were found to be in the order of 100 nm, compared to about 150 nm–200 nm in standard wires. Phase analysis confirmed the frequent inclusion of Cu between the grains of the A15 phase. The investigation of the grain shape orientation showed that the major axis of most of the elliptical grains with average aspect ratios of around 0.5 is oriented along the radial direction of the sub-elements. The analysis of grain boundary misorientations showed a preferential orientation of 27° between grains, which deviates from the random distribution and was mainly attributed to the $\Sigma\,17a$ coincidence site lattice boundary. The pole figures resulting from the analysis of the textures revealed that the majority of the grains in the ternary APC wires is oriented along a $\langle 111 \rangle$ direction with respect to the wire axis, which differs from the results of standard RRP and PIT wires.

Chapter 7 revolved around the evaluation of the impact of fast neutron irradiation on the microstructure. After a comprehensive literature review about previously determined irradiation effects on the superconducting properties and comparable studies on the microstructure, simulations were conducted of the expected *dpa* values and image contrast. The irradiation procedure as well as requirements for a suitable sample quality were described in detail. A variety of imaging techniques using transmission electron microscopy, including weak-beam dark field and HRSTEM imaging, was applied to samples prepared by different techniques and compared. The investigation of the defect structure after the irradiation with fast (E>0.1 MeV) neutrons to the fluence of $2.82 \times 10^{22}\,\mathrm{m}^{-2}$ revealed defects frequently in the size of around 2 nm–4 nm, which occurred at a density of up to $16\,600\,\mathrm{\mu m}^{-3}$. Through correlation with the simulations, this observed defect density was attributed to about 16.9 %–25.3 % of the calculated *dpa* value. The nature of the defects was discussed through evidence from Z-contrast, diffraction contrast and a comparison

with literature data and suspected to be disordered regions with a high density of vacancy type defects. Geometric phase analysis conducted on high resolution STEM images revealed information about dilatation and strain fields in the crystal lattice that accompany the neutron impact sites. The sizes and densities of neutron irradiation induced defects were found to be very comparable to those of the nano-precipitates found in the ternary APC wires, where both types of wires were reported to also show similarities in the behaviour of the J_c enhancement in the literature, leading to the achievement of the FCC J_c target in short samples.

The examination of the local magnetic properties by scanning Hall probe microscopy was presented in Chapter 8, where inhomogeneities between sub-elements and inside individual sub-elements became apparent. Scans were conducted in the Meißner state at different temperatures and the contour plots evaluated, which confirmed differences in the shielding capabilities between individual sub-elements as well as a radial gradient in the critical temperature T_c in all sub-elements, which originates from the variation in the elemental Sn content across their A15 layer. Particularly the scans at a temperature of 16.5 K made differences in T_c between the sub-elements apparent. Scans were furthermore acquired in the remanent state, where the remanent field strength can be related to the critical current density J_c.

The correlations between the microstructure and the superconducting properties were analysed in Chapter 9 through the combined use of SEM, EDX and SHPM. The critical current density J_c of individual sub-elements was estimated from the remanent field values acquired by SHPM, which showed variations of up to 20 %. Differences in the critical temperature T_c between sub-elements that became apparent from the scans in the Meißner state were related to compositional variations that were assessed by EDX. A correlation was confirmed, where the better performing sub-element showed slightly higher values of the Sn content and lower values of the Ti content. Differences in the performance between sub-elements were furthermore attributed to longitudinal variations in the composition and A15 geometry, which were confirmed by EDX and SEM. The correlation of shielding radii acquired by SHPM scans in the Meißner state with local analyses of the elemental composition by EDX yielded the global dependency of T_c on the Sn content.

10.2 Outlook

1. The TEM investigations of neutron irradiated Nb_3Sn wires revealed information about the size and density of neutron irradiation defects. The determination of the optimal sample preparation process and diffraction conditions in the TEM proved to be very challenging. It furthermore became apparent that for reliable results, the use of a C_s-corrected TEM is advantageous. For these reasons, only a limited amount of samples and grains could be examined under optimal conditions. For future works, it would be interesting to apply the acquired insights on samples irradiated at different fluences, especially higher fluences than the wires that were investigated in this work. Particularly the comparison of the same exact sample before and after irradiation at a high dose was not possible within this work and could potentially offer further insights.

2. The investigation of the defect structure of neutron irradiated Nb_3Sn wires using TEM should be complemented using different analytical techniques. Particularly changes in the elemental distribution after irradiation is not possible using EDX, since the spacial resolution is too sparse. Positron annihilation spectroscopy (PAS), extended X-Ray absorption fine structure (EXAFS) and atom probe tomography (APT) are techniques that can determine point defects and displacements of single atoms and should be applied to neutron irradiated Nb_3Sn wires in order to gain information about the processes during irradiation at an atomic scale, especially in ternary wires.

3. The preparation of thin slices of wires for SHPM investigations should be explored further. So far the inversion of the Biot-Savart law on remanent scans to gain information about local current distributions inside sub-elements did not lead to satisfactory results. The investigation of 3 mm thick slices led to uncertainties originating from deeper sample layers, while 10 µm thin slices led to a degradation of the superconducting properties due to induced damage during the preparation or longitudinal variations in the composition. The preparation and investigation of wire slices with varying thicknesses should be explored, where a thickness of around 50 µm could potentially be a good compromise.

4. In this work, it was shown that there are considerable longitudinal variations of the A15 layer thickness and elemental composition along the wire axis. A very tedious but interesting project would be the fabrication of multiple slices of a wire and subsequent analysis of the geometry, elemental composition, T_c and current distributions of each slice. This experiment could yield further information about longitudinal changes in the microstructure and their limiting effect on the performance of the wire. Additionally, single etched sub-elements could be investigated and compared by SQUID magnetometry in order to analyse performance differences between different sub-elements further.

Given the rapid progress of the Nb$_3$Sn wire optimisation in the recent years, coupled with the worldwide effort in the course of the conductor development programme, one can be optimistic that the FCC targets for Nb$_3$Sn will be achieved in the future, with this work hopefully contributing to the knowledge that is required to do so.

Bibliography

[1] M. Aleksa, P. Pongratz, O. Eibl, F. M. Sauerzopf, H. W. Weber, T. W. Li, and P. H. Kes. TEM observation of neutron-induced collision cascades in Bi-2212 single crystals. *Physica C: Superconductivity*, 297(3-4):171–175, mar 1998. doi: 10.1016/s0921-4534(97)01898-4.

[2] Giorgio Ambrosio. Nb$_3$Sn High Field Magnets for the High Luminosity LHC Upgrade Project. *IEEE Transactions on Applied Superconductivity*, 25(3):1–7, jun 2015. doi: 10.1109/tasc.2014.2367024.

[3] Toshihisa Asano, Yasuo Iijima, Kikuo Itoh, and Kyoji Tachikawa. Effects of Titanium Addition to the Niobium Core on the Composite-Processed Nb$_3$Sn. *Transactions of the Japan Institute of Metals*, 27(3):204–214, 1986. doi: 10. 2320/matertrans1960.27.204.

[4] Shreyas Balachandran, Chiara Tarantini, Peter J. Lee, Fumitake Kametani, Yi-Feng Su, Benjamin Walker, William L. Starch, and David C. Larbalestier. Beneficial influence of Hf and Zr additions to Nb4at%Ta on the vortex pinning of Nb$_3$Sn with and without an O source. *Superconductor Science and Technology*, 32(4):044006, feb 2019. doi: 10.1088/1361-6668/aaff02.

[5] A. Ballarino. Superconducting Materials for High Field Applications. Presentation at EASISchool 1 / ESAS Summer School in Vienna, 6.9.2018. URL https://indico.cern.ch/event/663949/sessions/275484/ attachments/1711937/2760652/Lecture_Amalia.pdf.

[6] A. Ballarino and L. Bottura. Targets for R&D on Nb$_3$Sn Conductor for High Energy Physics. *IEEE Transactions on Applied Superconductivity*, 25(3):1–6, jun 2015. doi: 10.1109/tasc.2015.2390149.

[7] Amalia Ballarino, Simon C. Hopkins, Bernardo Bordini, David Richter, Davide Tommasini, Luca Bottura, Michael Benedikt, Michinaka Sugano, Toru Ogitsu, Shinya Kawashima, Kazuyoshi Saito, Yoshito Fukumoto, Hisaki Sakamoto, Hitoshi Shimizu, Victor Pantsyrny, Ildar Abdyukhanov, Michael Shlyakov, Sergey Zernov, Florin Buta, Carmine Senatore, Iksang Shin, Jimam Kim, Jonas Lachmann, Andreas Leineweber, Stephan Pfeiffer, Thomas Baumgartner, Michael Eisterer, Johannes Bernardi, Andrea Malagoli, Valeria Braccini, Maurizio Vignolo, Marina Putti, and Carlo Ferdeghini. The CERN FCC Conductor Development Program: A Worldwide Effort for the Future Generation

of High-Field Magnets. *IEEE Transactions on Applied Superconductivity*, 29 (5):1–9, aug 2019. doi: 10.1109/tasc.2019.2896469.

[8] E. Bartolomé, X. Granados, B. Bozzo, S. Iliescu, T. Puig, and X. Obradors. In-field magnetic Hall probe microscopy studies of $YBa_2Cu_3O_7$ based superconductors. *Journal of Physics and Chemistry of Solids*, 67(1-3):403–406, jan 2006. doi: 10.1016/j.jpcs.2005.10.146.

[9] E. Barzi and S. Mattafirri. Nb_3Sn phase growth and superconducting properties during heat treatment. *IEEE Transactions on Appiled Superconductivity*, 13 (2):3414–3417, jun 2003. doi: 10.1109/tasc.2003.812338.

[10] Emanuela Barzi and Alexander V. Zlobin. Research and Development of Wires and Cables for High-Field Accelerator Magnets. *IEEE Transactions on Nuclear Science*, 63(2):783–803, apr 2016. doi: 10.1109/tns.2015.2500440.

[11] T. Baumgartner, M. Eisterer, H. W. Weber, R. Flükiger, B. Bordini, L. Bottura, and C. Scheuerlein. Evaluation of the Critical Current Density of Multifilamentary Nb_3Sn Wires From Magnetization Measurements. *IEEE Transactions on Applied Superconductivity*, 22(3):6000604–6000604, jun 2012. doi: 10.1109/tasc.2011.2175350.

[12] T. Baumgartner, M. Eisterer, H. W. Weber, R. Flükiger, C. Scheuerlein, and L. Bottura. Effects of neutron irradiation on pinning force scaling in state-of-the-art Nb_3Sn wires. *Superconductor Science and Technology*, 27(1):015005, nov 2013. doi: 10.1088/0953-2048/27/1/015005.

[13] T. Baumgartner, M. Eisterer, H. W. Weber, R. Flükiger, C. Scheuerlein, and L. Bottura. Performance Boost in Industrial Multifilamentary Nb_3Sn Wires due to Radiation Induced Pinning Centers. *Scientific Reports*, 5(1), jun 2015. doi: 10.1038/srep10236.

[14] T. Baumgartner, J. Hecher, J. Bernardi, S. Pfeiffer, C. Senatore, and M. Eisterer. Assessing composition gradients in multifilamentary superconductors by means of magnetometry methods. *Superconductor Science and Technology*, 30(1): 014011, nov 2016. doi: 10.1088/0953-2048/30/1/014011.

[15] T. Baumgartner, S. Pfeiffer, J. Bernardi, A. Ballarino, and M. Eisterer. Effects of inhomogeneities on pinning force scaling in Nb_3Sn wires. *Superconductor Science and Technology*, 31(8):084002, jun 2018. doi: 10.1088/1361-6668/aac87e.

[16] Charles P. Bean. Magnetization of High-Field Superconductors. *Reviews of Modern Physics*, 36(1):31–39, jan 1964. doi: 10.1103/revmodphys.36.31.

[17] M. Benedikt, A. Ballarino, T. Baumgartner, J. Bernardi, A. Doblhammer, M. Eisterer, M. Hofer, S. Holleis, J. Keintzel, A. Moros, M. Ortino, S. Pfeiffer,

E. Renner, M. Stöger-Pollach, J. Gutleber, C. Senatore, A. Saba, V. Völkl, C. Köberl, H. Kritscher, T. Hoehn, M. Aburaia, A. Kollegger, M. Lackner, P. Keinz, M. Putti, H. Humer, et al. FCC-ee: The Lepton Collider. *The European Physical Journal Special Topics*, 228(2):261–623, jun 2019. doi: 10.1140/epjst/e2019-900045-4.

[18] M. Benedikt, A. Ballarino, T. Baumgartner, J. Bernardi, A. Doblhammer, M. Eisterer, M. Hofer, S. Holleis, J. Keintzel, A. Moros, M. Ortino, S. Pfeiffer, E. Renner, M. Stöger-Pollach, J. Gutleber, C. Senatore, A. Saba, V. Völkl, C. Köberl, H. Kritscher, T. Hoehn, M. Aburaia, A. Kollegger, M. Lackner, P. Keinz, M. Putti, H. Humer, et al. FCC-hh: The Hadron Collider. *The European Physical Journal Special Topics*, 228(4):755–1107, jul 2019. doi: 10.1140/epjst/e2019-900087-0.

[19] M. Benedikt, A. Ballarino, T. Baumgartner, J. Bernardi, A. Doblhammer, M. Eisterer, M. Hofer, S. Holleis, J. Keintzel, A. Moros, M. Ortino, S. Pfeiffer, E. Renner, M. Stöger-Pollach, J. Gutleber, C. Senatore, A. Saba, V. Völkl, C. Köberl, H. Kritscher, T. Hoehn, M. Aburaia, A. Kollegger, M. Lackner, P. Keinz, M. Putti, H. Humer, et al. HE-LHC: The High-Energy Large Hadron Collider. *The European Physical Journal Special Topics*, 228(5):1109–1382, jul 2019. doi: 10.1140/epjst/e2019-900088-6.

[20] M. Benedikt, A. Ballarino, T. Baumgartner, J. Bernardi, A. Doblhammer, M. Eisterer, M. Hofer, S. Holleis, J. Keintzel, A. Moros, M. Ortino, S. Pfeiffer, E. Renner, M. Stöger-Pollach, J. Gutleber, C. Senatore, A. Saba, V. Völkl, C. Köberl, H. Kritscher, T. Hoehn, M. Aburaia, A. Kollegger, M. Lackner, P. Keinz, M. Putti, H. Humer, et al. FCC Physics Opportunities. *The European Physical Journal C*, 79(6), jun 2019. doi: 10.1140/epjc/s10052-019-6904-3.

[21] Luca Bottura and Arno Godeke. Superconducting Materials and Conductors: Fabrication and Limiting Parameters. *Reviews of Accelerator Science and Technology*, 05:25–50, jan 2012. doi: 10.1142/s1793626812300022.

[22] M. Brown, C. Tarantini, W. Starch, W. Oates, P. J. Lee, and D. C. Larbalestier. Correlation of filament distortion and RRR degradation in drawn and rolled PIT and RRP Nb_3Sn wires. *Superconductor Science and Technology*, 29(8): 084008, jul 2016. doi: 10.1088/0953-2048/29/8/084008.

[23] R. D. Burbank, R. C. Dynes, and J. M. Poate. X-ray study of atomic displacements in Nb_3Sn induced by radiation damage. *Journal of Low Temperature Physics*, 36(5-6):573–585, sep 1979. doi: 10.1007/bf00116986.

[24] M. Cantoni, C. Scheuerlein, P.-Y. Pfirter, F. de Borman, J. Rossen, G. Arnau, L. Oberli, and P. Lee. Sn concentration gradients in Powder-in-Tube superconductors. *Journal of Physics: Conference Series*, 234(2):022005, jun 2010. doi: 10.1088/1742-6596/234/2/022005.

[25] A. M. Chang, H. D. Hallen, L. Harriott, H. F. Hess, H. L. Kao, J. Kwo, R. E. Miller, R. Wolfe, J. van der Ziel, and T. Y. Chang. Scanning Hall probe microscopy. *Applied Physics Letters*, 61(16):1974–1976, oct 1992. doi: 10.1063/1.108334.

[26] J. P. Charlesworth, I. Macphail, and P. E. Madsen. Experimental work on the niobium-tin constitution diagram and related studies. *Journal of Materials Science*, 5(7):580–603, jul 1970. doi: 10.1007/bf00554367.

[27] N. Cheggour, P. J. Lee, L. F. Goodrich, Z.-H. Sung, T. C. Stauffer, J. D. Splett, and M. C. Jewell. Influence of the heat-treatment conditions, microchemistry, and microstructure on the irreversible strain limit of a selection of Ti-doped internal-tin Nb_3Sn ITER wires. *Superconductor Science and Technology*, 27 (10):105004, sep 2014. doi: 10.1088/0953-2048/27/10/105004.

[28] In-Gann Chen, Jianxiong Liu, Roy Weinstein, and Kwong Lau. Characterization of $YBa_2Cu_3O_7$, including critical current density J_c, by trapped magnetic field. *Journal of Applied Physics*, 72(3):1013–1020, aug 1992. doi: 10.1063/1.351826.

[29] L. D. Cooley, C. M. Fischer, P. J. Lee, and D. C. Larbalestier. Simulations of the effects of tin composition gradients on the superconducting properties of Nb_3Sn conductors. *Journal of Applied Physics*, 96(4):2122–2130, aug 2004. doi: 10.1063/1.1763993.

[30] D. E. Cox, A. R. Sweedler, S. Moehlecke, L. R. Newkirk, and F. A. Valencia. Superconductivity and atomic ordering in neutron-irradiated Nb_3Ge. In *Superconductivity in D- and F-Band Metals*, pages 335–347. Elsevier, 1980. doi: 10.1016/b978-0-12-676150-4.50041-x.

[31] P. N. Degtyarenko, A. Ballarino, L. Bottura, S. Y. Gavrilkin, R. Flukiger, I. A. Karateev, V. S. Kruglov, S. T. Latushkin, C. Scheuerlein, A. I. Ryazanov, E. V. Semenov, S. V. Shavkin, T. Spina, V. N. Unezhev, and A. L. Vasiliev. Influence of fast proton irradiation with energies of 12.4 and 12.8 MeV on magnetic characteristics and microstructure changes of superconducting intermetallic compound Nb_3Sn. *Journal of Physics: Conference Series*, 747:012030, sep 2016. doi: 10.1088/1742-6596/747/1/012030.

[32] D. Dew-Hughes. Flux pinning mechanisms in type II superconductors. *Philosophical Magazine*, 30(2):293–305, aug 1974. doi: 10.1080/14786439808206556.

[33] D. R. Dietderich and A. Godeke. Nb_3Sn research and development in the USA – Wires and cables. *Cryogenics*, 48(7-8):331–340, jul 2008. doi: 10.1016/j.cryogenics.2008.05.004.

[34] M. Eisterer, S. Haindl, T. Wojcik, and H. W. Weber. Magnetoscan : a modified Hall probe scanning technique for the detection of inhomogeneities in bulk

high temperature superconductors. *Superconductor Science and Technology*, 16(11):1282–1285, oct 2003. doi: 10.1088/0953-2048/16/11/005.

[35] J. W. Ekin. Unified scaling law for flux pinning in practical superconductors: I. Separability postulate, raw scaling data and parameterization at moderate strains. *Superconductor Science and Technology*, 23(8):083001, jul 2010. doi: 10.1088/0953-2048/23/8/083001.

[36] Jack W. Ekin, Najib Cheggour, Loren Goodrich, Jolene Splett, Bernardo Bordini, and David Richter. Unified Scaling Law for flux pinning in practical superconductors: II. Parameter testing, scaling constants, and the Extrapolative Scaling Expression. *Superconductor Science and Technology*, 29(12): 123002, nov 2016. doi: 10.1088/0953-2048/29/12/123002.

[37] Jack W. Ekin, Najib Cheggour, Loren Goodrich, and Jolene Splett. Unified Scaling Law for flux pinning in practical superconductors: III. Minimum datasets, core parameters, and application of the Extrapolative Scaling Expression. *Superconductor Science and Technology*, 30(3):033005, feb 2017. doi: 10.1088/1361-6668/30/3/033005.

[38] H. H. Farrell, G. H. Gilmer, and M. Suenaga. Grain boundary diffusion and growth of intermetallic layers: Nb_3Sn. *Journal of Applied Physics*, 45(9): 4025–4035, sep 1974. doi: 10.1063/1.1663907.

[39] Alberto Fasso, Alfredo Ferrari, George Smirnov, Florian Sommerer, and Vasilis Vlachoudis. FLUKA Realistic Modeling of Radiation Induced Damage. *Progress in Nuclear Science and Technology*, 2(0):769–775, oct 2011. doi: 10.15669/pnst. 2.769.

[40] Tiago Ferreira, Mark Hiner, Curtis Rueden, Kota Miura, Jan Eglinger, and Bitdeli Chef. Bar scripts 1.5.1, 2017. URL https://zenodo.org/record/ 495245.

[41] M. Fähnle. The influence of fast neutron irradiation on the critical current densities in Nb3Sn I. Low neutron doses ($\Phi < 2 \times 10^{18}$ neutrons/cm^2). *physica status solidi*, 1977. doi: 10.1002/pssb.2220840127.

[42] M. Fähnle. The influence of fast neutron irradiation on the critical current densities in Nb3Sn. II. High neutron doses ($\Phi > 2 \times 10^{18}$ neutrons/cm^2). *physica status solidi*, 1977.

[43] H. Fillunger, M. Foitl, K. Hense, I. Kajgana, A. Kasztler, H. Kirchmayr, R. Lackner, J. Leoni, R. Maix, T. Matthias, and J. Fidler. Influence of the annealing time of internal tin Nb_3Sn strands on the critical current and the magnetization losses. *Physica C: Superconductivity*, 372-376:1758–1761, aug 2002. doi: 10.1016/s0921-4534(02)01119-x.

[44] R. Flükiger, C. Senatore, M. Cesaretti, F. Buta, D. Uglietti, and B. Seeber. Optimization of Nb$_3$Sn and MgB$_2$ wires. *Superconductor Science and Technology*, 21(5):054015, mar 2008. doi: 10.1088/0953-2048/21/5/054015.

[45] R. Flükiger, D. Uglietti, C. Senatore, and F. Buta. Microstructure, composition and critical current density of superconducting Nb$_3$Sn wires. *Cryogenics*, 48 (7-8):293–307, jul 2008. doi: 10.1016/j.cryogenics.2008.05.005.

[46] R. Flükiger, T. Spina, F. Cerutti, A. Ballarino, C. Scheuerlein, L. Bottura, Y. Zubavichus, A. Ryazanov, R. D. Svetogovov, S. Shavkin, P. Degtyarenko, Y. Semenov, C. Senatore, and R. Cerny. Variation of T_c, lattice parameter and atomic ordering in Nb$_3$Sn platelets irradiated with 12 MeV protons: correlation with the number of induced Frenkel defects. *Superconductor Science and Technology*, 30(5):054003, mar 2017. doi: 10.1088/1361-6668/aa64ee.

[47] R. Flukiger, T. Baumgartner, M. Eisterer, H. W. Weber, T. Spina, C. Scheuerlein, C. Senatore, A. Ballarino, and L. Bottura. Variation of $(J_c/J_{c0})_{max}$ of Binary and Ternary Alloyed RRP and PIT Nb$_3$Sn Wires Exposed to Fast Neutron Irradiation at Ambient Reactor Temperature. *IEEE Transactions on Applied Superconductivity*, 23(3):8001404–8001404, jun 2013. doi: 10.1109/tasc.2012.2237492.

[48] Rene Flukiger, Tiziana Spina, Francesco Cerutti, Maria Ilaria Besana, Christian Scheuerlein, Amalia Ballarino, and Luca Bottura. Impact of the Number of dpa on the Superconducting Properties in HiLumi-LHC and FCC Accelerators. *IEEE Transactions on Applied Superconductivity*, 28(4):1–5, jun 2018. doi: 10.1109/tasc.2018.2810215.

[49] M. C. Frischherz, M. A. Kirk, J. Farmer, L. R. Greenwood, and H. W. Weber. Defect cascades produced by neutron irradiation in YBa$_2$Cu$_3$O$_{7-\delta}$. *Physica C: Superconductivity*, 232(3-4):309–327, nov 1994. doi: 10.1016/0921-4534(94) 90790-0.

[50] A. K. Ghosh, L. D. Cooley, J. A. Parrell, M. B. Field, Y. Zhang, and S. Hong. Effects of Reaction Temperature and Alloying on Performance of Restack-Rod-Process Nb$_3$Sn. *IEEE Transactions on Applied Superconductivity*, 17(2): 2623–2626, jun 2007. doi: 10.1109/tasc.2007.898165.

[51] A. K. Ghosh, E. A. Sperry, J. D. Ambra, and L. D. Cooley. Systematic Changes of the Nb-Sn Reaction With Time, Temperature, and Alloying in Restacked-Rod-Process (RRP) Nb$_3$Sn Strands. *IEEE Transactions on Applied Superconductivity*, 19(3):2580–2583, jun 2009. doi: 10.1109/tasc.2009.2018075.

[52] A. Godeke. A review of the properties of Nb$_3$Sn and their variation with A15 composition, morphology and strain state. *Superconductor Science and Technology*, 19(8):R68–R80, jun 2006. doi: 10.1088/0953-2048/19/8/r02.

[53] A. Godeke, M. C. Jewell, C. M. Fischer, A. A. Squitieri, P. J. Lee, and D. C. Larbalestier. The upper critical field of filamentary Nb$_3$Sn conductors. *Journal of Applied Physics*, 97(9):093909, may 2005. doi: 10.1063/1.1890447.

[54] A. Godeke, B. ten Haken, H. H. J. ten Kate, and D. C. Larbalestier. A general scaling relation for the critical current density in Nb$_3$Sn. *Superconductor Science and Technology*, 19(10):R100–R116, sep 2006. doi: 10.1088/0953-2048/19/10/r02.

[55] A. Godeke, A. den Ouden, A. Nijhuis, and H. H. J. ten Kate. State of the art powder-in-tube niobium–tin superconductors. *Cryogenics*, 48(7-8):308–316, jul 2008. doi: 10.1016/j.cryogenics.2008.04.003.

[56] X. Granados, S. Sena, E. Bartolome, A. Palau, T. Puig, X. Obradors, M. Carrera, J. Amoros, and H. Claus. Characterization of superconducting rings using an in-field hall probe magnetic mapping system. *IEEE Transactions on Appiled Superconductivity*, 13(2):3667–3670, jun 2003. doi: 10.1109/tasc.2003.812426.

[57] X. Granados, S. Iliescu, B. Bozzo, E. Bartolome, T. Puig, X. Obradors, J. Amorós, and M. Carrera. Magnetic Mapping, a way to test and understand current flows in thin and bulk superconductors. *Advances in Science and Technology*, 47:1–6, 2006.

[58] E. Gregory, M. Tomsic, M. D. Sumption, X. Peng, X. Wu, E. W. Collings, and B. A. Zeitlin. The Introduction of Titanium into Internal-Tin Nb$_3$Sn by a Variety of Procedures. *IEEE Transactions on Appiled Superconductivity*, 15(2):3478–3481, jun 2005. doi: 10.1109/tasc.2005.849067.

[59] E. Gregory, B. A. Zeitlin, M. Tomsic, X. Peng, M. D. Sumption, and E. W. Collings. Some Factors Involved in the Development of a Tubular Process for Nb$_3$Sn Conductors. *IEEE Transactions on Applied Superconductivity*, 17(2):2664–2667, jun 2007. doi: 10.1109/tasc.2007.899990.

[60] E. Gregory, M. Tomsic, X. Peng, R. Dhaka, V. R. Nazareth, and M. D. Sumption. Niobium Tin Conductors for High Energy Physics, Fusion, MRI and NMR Applications Made by Different Techniques. *IEEE Transactions on Applied Superconductivity*, 18(2):989–992, jun 2008. doi: 10.1109/tasc.2008.920569.

[61] E. Gregory, M. Tomsic, Xuan Peng, M. D. Sumption, and A. Ghosh. Nb$_3$Sn Superconductors Made by an Economical Tubular Process. *IEEE Transactions on Applied Superconductivity*, 19(3):2602–2605, jun 2009. doi: 10.1109/tasc.2009.2018152.

[62] H. Grimmer, W. Bollmann, and D. H. Warrington. Coincidence-site lattices and complete pattern-shift in cubic crystals. *Acta Crystallographica Section A*, 30(2):197–207, mar 1974. doi: 10.1107/s056773947400043x.

[63] X.-F. Gu, T. Furuhara, and W.-Z. Zhang. PTCLab: free and open-source software for calculating phase transformation crystallography. *Journal of Applied Crystallography*, 49(3):1099–1106, may 2016. doi: 10.1107/s1600576716006075.

[64] P. A. Hahn, M. W. Guinan, L. T. Summers, T. Okada, and D. B. Smathers. Fusion neutron irradiation effects in commercial Nb$_3$Sn superconductors. *Journal of Nuclear Materials*, 1991.

[65] S. Haindl, M. Eisterer, R. Muller, R. Prokopec, H. W. Weber, M. Muller, H. Kirchmayr, T. Takeuchi, and L. Bargioni. Neutron Irradiation Effects on A15 Multifilamentary Wires. *IEEE Transactions on Appiled Superconductivity*, 15(2):3414–3417, jun 2005. doi: 10.1109/tasc.2005.848950.

[66] D. A. Harvey, N. A. Fellows, J. F. Durodola, and A. Twin. The influence of the reaction heat-treatment process on the mechanical properties of multi-filamentary composite Nb$_3$Sn superconducting wires at 77 and 300 K. *Superconductor Science and Technology*, 19(1):79–84, dec 2005. doi: 10.1088/0953-2048/19/1/014.

[67] Y. S. Hascicek, S. Nourbakhsh, and M. J. Goringe. On the preparation of specimens from multifilamentary Nb$_3$Sn superconducting wires for transmission electron microscopy. *Journal of Microscopy*, 131(1):55–61, jul 1983. doi: 10.1111/j.1365-2818.1983.tb04230.x.

[68] C. D. Hawes, P. J. Lee, and D. C. Larbalestier. Measurements of the microstructural, microchemical and transition temperature gradients of A15 layers in a high-performance Nb3Sn powder-in-tube superconducting strand. *Superconductor Science and Technology*, 19(3):S27–S37, jan 2006. doi: 10.1088/0953-2048/19/3/004.

[69] Steve M. Heald, Chiara Tarantini, Peter J. Lee, Michael D. Brown, ZuHawn Sung, Arup K. Ghosh, and David C. Larbalestier. Evidence from EXAFS for Different Ta/Ti Site Occupancy in High Critical Current Density Nb$_3$Sn Superconductor Wires. *Scientific Reports*, 8(1), mar 2018. doi: 10.1038/s41598-018-22924-3.

[70] P. Holdway and R. D. Rawlings. Microstructure and radiation damage of commercially produced Nb$_3$Sn tapes. *Cryogenics*, 24(3):137–142, mar 1984. doi: 10.1016/0011-2275(84)90101-2.

[71] Barbara Horvath, Yong Dai, and Yongjoong Lee. Annealing effect on the microstructure of tungsten irradiated in SINQ target. *Journal of Nuclear Materials*, 506:19–25, aug 2018. doi: 10.1016/j.jnucmat.2017.12.020.

[72] M. J. Hÿtch. Geometric Phase Analysis of High Resolution Electron Microscope Images. *Scanning Microscopy*, 11:53–66, 1997.

[73] M. J. Hÿtch and F. Houdellier. Mapping stress and strain in nanostructures by high-resolution transmission electron microscopy. *Microelectronic Engineering*, 84(3):460–463, mar 2007. doi: 10.1016/j.mee.2006.10.062.

[74] M. J. Hÿtch, E. Snoeck, and R. Kilaas. Quantitative measurement of displacement and strain fields from HREM micrographs. *Ultramicroscopy*, 74(3): 131–146, aug 1998. doi: 10.1016/s0304-3991(98)00035-7.

[75] ASTM International. ASTM E112-13, Standard Test Methods for Determining Average Grain Size. ASTM International, West Conshohocken, PA, 2013, www.astm.org. URL https://www.astm.org/Standards/E112.htm.

[76] Hiroyuki Iwata and Hiroyasu Saka. Resolving individual Shockley partials of a dissociated dislocation by STEM. *Philosophical Magazine Letters*, 97(2):74–81, jan 2017. doi: 10.1080/09500839.2017.1282634.

[77] M. L. Jenkins. Characterisation of radiation-damage microstructures by TEM. *Journal of Nuclear Materials*, 216:124–156, oct 1994. doi: 10.1016/0022-3115(94)90010-8.

[78] M. L. Jenkins, G. Roller, K.-H. Katerbau, and M. Wilkens. TEM studies of displacement cascades in Nb_3Sn. *Journal of Nuclear Materials*, 108-109: 603–613, jul 1982. doi: 10.1016/0022-3115(82)90532-3.

[79] Matthew C. Jewell, Peter J. Lee, and David C. Larbalestier. The influence of Nb_3Sn strand geometry on filament breakage under bend strain as revealed by metallography. *Superconductor Science and Technology*, 16(9):1005–1011, aug 2003. doi: 10.1088/0953-2048/16/9/308.

[80] A. E. Karkin, V. E. Arkhipov, B. N. Goshchitskii, E. P. Romanov, and S. K. Sidorov. Radiation effects in the superconductor Nb_3Sn. *Physica Status Solidi (a)*, 38(2):433–438, dec 1976. doi: 10.1002/pssa.2210380202.

[81] Michael B. Kerber, Michael J. Zehetbauer, Erhard Schafler, Florian C. Spieckermann, Sigrid Bernstorff, and Tamas Ungar. X-ray line profile analysis - An ideal tool to quantify structural parameters of nanomaterials. *JOM*, 63(7): 61–70, jul 2011. doi: 10.1007/s11837-011-0115-1.

[82] G. H. Kinchin and R. S. Pease. The Displacement of Atoms in Solids by Radiation. *Reports on Progress in Physics*, 18(1):1–51, jan 1955. doi: 10.1088/0034-4885/18/1/301.

[83] Edward J. Kramer. Scaling laws for flux pinning in hard superconductors. *Journal of Applied Physics*, 44(3):1360–1370, mar 1973. doi: 10.1063/1.1662353.

[84] J.-W. Lee, H. S. Lessure, D. E. Laughlin, M. E. McHenry, S. G. Sankar, J. O. Willis, J. R. Cost, and M. P. Maley. Observation of proposed flux pinning

sites in neutron-irradiated YBa$_2$Cu$_3$O$_{7-x}$. *Applied Physics Letters*, 57(20): 2150–2152, nov 1990. doi: 10.1063/1.104159.

[85] P. J. Lee and D. C. Larbalestier. Microstructure, Microchemistry and the Development of Very High Nb$_3$Sn Layer Critical Current Density. *IEEE Transactions on Appiled Superconductivity*, 15(2):3474–3477, jun 2005. doi: 10.1109/tasc.2005.849064.

[86] Peter J. Lee. ImageJ Utilities: Applied Superconductivity Center, NHMFL. URL https://fs.magnet.fsu.edu/~lee/asc/ImageJUtilities/ASC_ImageJ_Utils.html.

[87] Peter J. Lee and David C. Larbalestier. Microstructural factors important for the development of high critical current density Nb$_3$Sn strand. *Cryogenics*, 48 (7-8):283–292, jul 2008. doi: 10.1016/j.cryogenics.2008.04.005.

[88] Yingxu Li and Yuanwen Gao. GLAG theory for superconducting property variations with A15 composition in Nb$_3$Sn wires. *Scientific Reports*, 7(1), apr 2017. doi: 10.1038/s41598-017-01292-4.

[89] Xi Feng Lu and Damian P. Hampshire. The field, temperature and strain dependence of the critical current density of a powder-in-tube Nb$_3$Sn superconducting strand. *Superconductor Science and Technology*, 23(2):025002, dec 2009. doi: 10.1088/0953-2048/23/2/025002.

[90] J. K. Mackenzie. The distribution of rotation axes in a random aggregate of cubic crystals. *Acta Metallurgica*, 12(2):223–225, feb 1964. doi: 10.1016/0001-6160(64)90191-9.

[91] S. Martin, A. Walnsch, G. Nolze, A. Leineweber, F. Leaux, and C. Scheuerlein. The crystal structure of (Nb$_{0.75}$Cu$_{0.25}$)Sn$_2$ in the Cu-Nb-Sn system. *Intermetallics*, 80:16–21, jan 2017. doi: 10.1016/j.intermet.2016.09.008.

[92] A. Martinelli, C. Tarantini, E. Lehmann, P. Manfrinetti, A. Palenzona, I. Pallecchi, M. Putti, and C. Ferdeghini. Direct TEM observation of nanometric-sized defects in neutron-irradiated MgB$_2$ bulk and their effect on pinning mechanisms. *Superconductor Science and Technology*, 21(1):012001, dec 2007. doi: 10.1088/0953-2048/21/01/012001.

[93] J. K. Mason and C. A. Schuh. The generalized Mackenzie distribution: Disorientation angle distributions for arbitrary textures. *Acta Materialia*, 57(14): 4186–4197, aug 2009. doi: 10.1016/j.actamat.2009.05.016.

[94] Teruo Matsushita. *Flux pinning in superconductors*. Springer, Berlin, 2007. ISBN 9783540445142.

[95] M. G. T. Mentink, M. M. J. Dhalle, D. R. Dietderich, A. Godeke, W. Goldacker, F. Hellman, H. H. J. ten Kate, M. D. Sumption, and M. A. Susner. The Effect of Ta and Ti Additions on the Strain Sensitivity of Bulk Niobium-Tin. *Physics Procedia*, 36:491–496, 2012. doi: 10.1016/j.phpro.2012.06.223.

[96] J. Miao, S. Singh, J. Tessmer, M. Shih, M. Ghazisaeidi, M. DeGraef, and M. J. Mills. Dislocation Characterization using Weak Beam Dark Field STEM Imaging. *Microscopy and Microanalysis*, 24(S1):2202–2203, aug 2018. doi: 10.1017/s1431927618011492.

[97] M. Di Michiel and C. Scheuerlein. Phase transformations during the reaction heat treatment of powder-in-tube Nb_3Sn superconductors. *Superconductor Science and Technology*, 20(10):L55–L58, aug 2007. doi: 10.1088/0953-2048/20/10/l01.

[98] L. R. Motowidlo, P. J. Lee, C. Tarantini, S. Balachandran, A. K. Ghosh, and D. C. Larbalestier. An intermetallic powder-in-tube approach to increased flux-pinning in Nb_3Sn by internal oxidation of Zr. *Superconductor Science and Technology*, 31(1):014002, nov 2017. doi: 10.1088/1361-6668/aa980f.

[99] V. R. Nazareth, M. D. Sumption, X. Peng, E. Gregory, M. J. Tomsic, and E. W. Collings. Characterization of the A15 Layer Growth and Microstructure for Varying Heat Treatments in Nb_3Sn Tube Type Composites. *IEEE Transactions on Applied Superconductivity*, 18(2):1005–1009, jun 2008. doi: 10.1109/tasc.2008.922464.

[100] A. Oral. Scanning Hall probe microscopy of superconductors and magnetic materials. *Journal of Vacuum Science & Technology B: Microelectronics and Nanometer Structures*, 14(2):1202, mar 1996. doi: 10.1116/1.588514.

[101] C. S. Pande. Effect of nuclear irradiation on the superconducting transition temperatures of A-15 materials. *Solid State Communications*, 24(3):241–245, oct 1977. doi: 10.1016/0038-1098(77)91206-6.

[102] C. S. Pande. Transmission electron microscopy of radiation damage in Nb_3Sn. *Physica Status Solidi (a)*, 52(2):687–696, apr 1979. doi: 10.1002/pssa.2210520241.

[103] C. S. Pande. Direct Observation of Defects in A15 Compounds Produced by Fast Neutron Irradiation. In *Superconductivity in D- and F-Band Metals*, pages 349–353. Elsevier, 1980. doi: 10.1016/b978-0-12-676150-4.50042-1.

[104] C. S. Pande and R. Viswanathan. Scattering of X-rays in irradiated A15 compounds. *Journal of the Less Common Metals*, 62:119–126, nov 1978. doi: 10.1016/0022-5088(78)90021-8.

[105] C.S. Pande. Imaging of small distortions in a15 "lattice" by electron microscopy. *Solid State Communications*, 37(9):753–756, mar 1981. doi: 10.1016/0038-1098(81)91093-0.

[106] J. A. Parrell, Youzhu Zhang, M. B. Field, P. Cisek, and Seung Hong. High field Nb$_3$Sn conductor development at oxford superconducting technology. *IEEE Transactions on Appiled Superconductivity*, 13(2):3470–3473, jun 2003. doi: 10.1109/tasc.2003.812360.

[107] X. Peng, M. D. Sumption, R. Dhaka, M. Bhatia, M. Tomsic, E. Gregory, and E. W. Collings. Composition Profiles and Upper Critical Field Measurement of Internal-Sn and Tube-Type Conductors. *IEEE Transactions on Applied Superconductivity*, 17(2):2668–2671, jun 2007. doi: 10.1109/tasc.2007.899443.

[108] X. Peng, E. Gregory, M. Tomsic, M. D. Sumption, A. Ghosh, X. F. Lu, N. Cheggour, T. C. Stauffer, L. F. Goodrich, and J. D. Splett. Strain and Magnetization Properties of High Subelement Count Tube-Type Nb$_3$Sn Strands. *IEEE Transactions on Applied Superconductivity*, 21(3):2559–2562, jun 2011. doi: 10.1109/tasc.2010.2100013.

[109] Jon Peters. Strain++: Implementation of geometric phase analysis (GPA) in C++. URL https://jjppeters.github.io/Strainpp/.

[110] P. J. Phillips, M. C. Brandes, M. J. Mills, and M. De Graef. Diffraction contrast STEM of dislocations: Imaging and simulations. *Ultramicroscopy*, 111(9-10): 1483–1487, aug 2011. doi: 10.1016/j.ultramic.2011.07.001.

[111] I. Pong, S. C. Hopkins, X. Fu, B. A. Glowacki, J. A. Elliott, and A. Baldini. Microstructure development in Nb$_3$Sn(Ti) internal tin superconducting wire. *Journal of Materials Science*, 43(10):3522–3530, mar 2008. doi: 10.1007/s10853-008-2522-4.

[112] Ian Pong, Luc-Rene Oberli, and Luca Bottura. Cu diffusion in Nb$_3$Sn internal tin superconductors during heat treatment. *Superconductor Science and Technology*, 26(10):105002, aug 2013. doi: 10.1088/0953-2048/26/10/105002.

[113] P. J. Potts. *A Handbook of Silicate Rock Analysis*. Springer Netherlands, 1987. doi: 10.1007/978-94-015-3988-3.

[114] E. Ravaioli, B. Auchmann, G. Chlachidze, M. Maciejewski, G. Sabbi, S. E. Stoynev, and A. Verweij. Modeling of Interfilament Coupling Currents and Their Effect on Magnet Quench Protection. *IEEE Transactions on Applied Superconductivity*, 27(4):1–8, jun 2017. doi: 10.1109/tasc.2016.2636452.

[115] D. Rodrigues, C. L. H. Thieme, D. G. Pinatti, and S. Foner. Grain boundary compositions, transport and flux pinning of multifilamentary Nb$_3$Sn wires. *IEEE Transactions on Appiled Superconductivity*, 5(2):1607–1610, jun 1995. doi: 10.1109/77.402881.

[116] M. J. R. Sandim, H. R. Z. Sandim, S. Zaefferer, D. Raabe, S. Awaji, and K. Watanabe. Electron backscatter diffraction study of Nb₃Sn superconducting multifilamentary wire. *Scripta Materialia*, 62(2):59–62, jan 2010. doi: 10.1016/j.scriptamat.2009.10.002.

[117] M. J. R. Sandim, D. Tytko, A. Kostka, P. Choi, S. Awaji, K. Watanabe, and D. Raabe. Grain boundary segregation in a bronze-route Nb₃Sn superconducting wire studied by atom probe tomography. *Superconductor Science and Technology*, 26(5):055008, mar 2013. doi: 10.1088/0953-2048/26/5/055008.

[118] R. M. Scanlan, W. A. Fietz, and E. F. Koch. Flux pinning centers in superconducting Nb₃Sn. *Journal of Applied Physics*, 46(5):2244–2249, may 1975. doi: 10.1063/1.321816.

[119] C. Scheuerlein, U. Stuhr, and L. Thilly. In situ neutron diffraction under tensile loading of powder-in-tube Cu/b₃Sn composite wires: Effect of reaction heat treatment on texture, internal stress state, and load transfer. *Applied Physics Letters*, 91(4):042503, jul 2007. doi: 10.1063/1.2766685.

[120] C. Scheuerlein, M. Di Michiel, and F. Buta. Synchrotron Radiation Techniques for the Characterization of Nb₃Sn Superconductors. *IEEE Transactions on Applied Superconductivity*, 19(3):2653–2656, jun 2009. doi: 10.1109/tasc.2009.2019101.

[121] C. Scheuerlein, G. Arnau, P. Alknes, N. Jimenez, B. Bordini, A. Ballarino, M. Di Michiel, L. Thilly, T. Besara, and T. Siegrist. Texture in state-of-the-art Nb₃Sn multifilamentary superconducting wires. *Superconductor Science and Technology*, 27(2):025013, jan 2014. doi: 10.1088/0953-2048/27/2/025013.

[122] C. Scheuerlein, M. Di Michiel, F. Buta, B. Seeber, C. Senatore, R. Flükiger, T. Siegrist, T. Besara, J. Kadar, B. Bordini, A. Ballarino, and L. Bottura. Stress distribution and lattice distortions in Nb₃Sn multifilament wires under uniaxial tensile loading at 4.2 K. *Superconductor Science and Technology*, 27 (4):044021, mar 2014. doi: 10.1088/0953-2048/27/4/044021.

[123] Christian Scheuerlein, Marco Di Michiel, Gonzalo Arnau Izquierdo, and Florin Buta. Phase Transformations During the Reaction Heat Treatment of Internal Tin Nb₃Sn Strands With High Sn Content. *IEEE Transactions on Applied Superconductivity*, 18(4):1754–1760, dec 2008. doi: 10.1109/tasc.2008.2006912.

[124] Daniel Schoerling and Alexander V. Zlobin, editors. *Nb₃Sn Accelerator Magnets*. Springer International Publishing, 2019. doi: 10.1007/978-3-030-16118-7.

[125] Daniel Schoerling, Diego Arbelaez, Bernhard Auchmann, Marta Bajko, Amalia Ballarino, Emanuela Barzi, Giovanni Bellomo, Michael Benedikt, Susana Izquierdo Bermudez, Bernardo Bordini, Luca Bottura, Lucas Brouwer, Pierluigi Bruzzone, Barbara Caiffi, Shlomo Caspi, Ananda Chakraborti, Eric

Coatanea, Gijs DeRijk, Marc Dhalle, Maria Durante, Pasquale Fabbricatore, Stefania Farinon, Helene Felice, Alejandro Fernandez, Inigo Sancho Fernandez, Peng Gao, Barbara Gold, Thodoris Gortsas, Steve Gourlay, Mariusz Juchno, Vadim Kashikhin, Charilaos Kokkinos, Sotiris Kokkinos, Kari Koskinen, Friedrich Lackner, Clement Lorin, Konstantinos Loukas, Alexandre Louzguiti, Kari Lyytikainen, Samuele Mariotto, Maxim Marchevsky, Giuseppe Montenero, Javier Munilla, Igor Novitski, and Toru Ogitsu. The 16 T Dipole Development Program for FCC and HE-LHC. *IEEE Transactions on Applied Superconductivity*, pages 1–1, 2019. doi: 10.1109/tasc.2019.2900556.

[126] Christopher Segal, Chiara Tarantini, Zu Hawn Sung, Peter J. Lee, Bernd Sailer, Manfred Thoener, Klaus Schlenga, Amalia Ballarino, Luca Bottura, Bernardo Bordini, Christian Scheuerlein, and David C. Larbalestier. Evaluation of critical current density and residual resistance ratio limits in powder in tube Nb_3Sn conductors. *Superconductor Science and Technology*, 29(8):085003, jun 2016. doi: 10.1088/0953-2048/29/8/085003.

[127] C. Senatore, V. Abächerli, M. Cantoni, and R. Flükiger. Distribution of Tc from calorimetry and the determination of Sn gradients in bronze Nb_3Sn wires with an internal and external Ti source. *Superconductor Science and Technology*, 20(9):S217–S222, aug 2007. doi: 10.1088/0953-2048/20/9/s16.

[128] C. Senatore, D. Uglietti, V. Abacherli, A. Junod, and R. Flukiger. Specific Heat, A Method to Determine the Tc Distribution in Industrial Nb_3Sn Wires Prepared by Various Techniques. *IEEE Transactions on Applied Superconductivity*, 17 (2):2611–2614, jun 2007. doi: 10.1109/tasc.2007.897928.

[129] Carmine Senatore and René Flükiger. Formation and upper critical fields of the two distinct A15 phases in the subelements of powder-in-tube Nb_3Sn wires. *Applied Physics Letters*, 102(1):012601, jan 2013. doi: 10.1063/1.4773490.

[130] R. G. Sharma. *Superconductivity*. Springer International Publishing, 2015. doi: 10.1007/978-3-319-13713-1.

[131] Takuma Shibata and Shin ichiro Sakai. Passive Micro Vibration Isolator Utilizing Flux Pinning Effect for Satellites. *Journal of Physics: Conference Series*, 744:012009, sep 2016. doi: 10.1088/1742-6596/744/1/012009.

[132] Glenn C. Sneddon, Patrick W. Trimby, and Julie M. Cairney. Transmission Kikuchi diffraction in a scanning electron microscope: A review. *Materials Science and Engineering: R: Reports*, 110:1–12, dec 2016. doi: 10.1016/j.mser.2016.10.001.

[133] E. Snoeck, B. Warot, H. Ardhuin, A. Rocher, M. J. Casanove, R. Kilaas, and M. J. Hÿtch. Quantitative analysis of strain field in thin films from HRTEM micrographs. *Thin Solid Films*, 319(1-2):157–162, apr 1998. doi: 10.1016/s0040-6090(97)01113-9.

[134] T. Spina, C. Scheuerlein, D. Richter, L. Bottura, A. Ballarino, and R. Flükiger. Critical current density of Nb$_3$Sn wires after irradiation with 65MeV and 24GeV protons. *Journal of Physics: Conference Series*, 507(2):022035, may 2014. doi: 10.1088/1742-6596/507/2/022035.

[135] T. Spina, C. Scheuerlein, D. Richter, B. Bordini, L. Bottura, A. Ballarino, and R. Flukiger. Variation of the Critical Properties of Alloyed Nb-Sn Wires After Proton Irradiation at 65 MeV and 24 GeV. *IEEE Transactions on Applied Superconductivity*, 25(3):1–5, jun 2015. doi: 10.1109/tasc.2014.2379116.

[136] T. Spina, C. Scheuerlein, D. Richter, A. Ballarino, F. Cerutti, L. S. Esposito, A. Lechner, L. Bottura, and R. Flukiger. Correlation Between the Number of Displacements Per Atom and After High-Energy Irradiations of Nb$_3$Sn Wires for the HL-LHC. *IEEE Transactions on Applied Superconductivity*, 26(3):1–5, apr 2016. doi: 10.1109/tasc.2016.2549858.

[137] Tiziana Spina, Amalia Ballarino, Luca Bottura, Christian Scheuerlein, and Rene Flukiger. Artificial Pinning in Nb$_3$Sn Wires. *IEEE Transactions on Applied Superconductivity*, 27(4):1–5, jun 2017. doi: 10.1109/tasc.2017.2651583.

[138] J.-Ch. Sublet, J. W. Eastwood, J. G. Morgan, M. R. Gilbert, M. Fleming, and W. Arter. FISPACT-II: An Advanced Simulation System for Activation, Transmutation and Material Modelling. *Nuclear Data Sheets*, 139:77–137, jan 2017. doi: 10.1016/j.nds.2017.01.002.

[139] M. Suenaga and W. Jansen. Chemical compositions at and near the grain boundaries in bronze-processed superconducting Nb$_3$Sn. *Applied Physics Letters*, 43(8):791–793, oct 1983. doi: 10.1063/1.94457.

[140] M. Suenaga, K. Aihara, K. Kaiho, and T. S. Luhman. Superconducting Properties of (Nb, Ta)$_3$Sn Wires Fabricated by the Bronze Process. In *Advances in Cryogenic Engineering Materials*, pages 442–450. Springer US, 1980. doi: 10.1007/978-1-4613-9859-2_51.

[141] Akira Sugimoto, Tetsuji Yamaguchi, and Ienari Iguchi. Evaluation of supercurrent distribution in high-Tc superconductor by scanning SQUID microscopy. *Physica C: Superconductivity*, 357-360:1473–1477, aug 2001. doi: 10.1016/s0921-4534(01)00590-1.

[142] A. R. Sweedler and D. E. Cox. Superconductivity and atomic ordering in neutron-irradiated Nb$_3$Al. *Physical Review B*, 12(1):147–156, jul 1975. doi: 10.1103/physrevb.12.147.

[143] A. R. Sweedler, D. G. Schweitzer, and G. W. Webb. Atomic Ordering and Superconductivity in High-T_c A-15 Compounds. *Physical Review Letters*, 33 (3):168–172, jul 1974. doi: 10.1103/physrevlett.33.168.

[144] K. Tachikawa, H. Sasaki, M. Yamaguchi, Y. Hayashi, K. Nakata, T. Takeuchi, and U. (Balu) Balachandran. Processing of high-performance Nb$_3$Sn wires through a new diffusion reaction using Sn based alloys. In *AIP Conference Proceedings*. AIP, 2010. doi: 10.1063/1.3402297.

[145] T. Takeuchi, K. Tsuchiya, M. Saeda, N. Banno, A. Kikuchi, and Y. Iijima. Electron backscatter diffraction analysis of Nb$_3$Al multifilamentary strands prepared by rapid heating, quenching and transformation annealing. *Superconductor Science and Technology*, 23(12):125001, oct 2010. doi: 10.1088/0953-2048/23/12/125001.

[146] C. Tarantini, P. J. Lee, N. Craig, A. Ghosh, and D. C. Larbalestier. Examination of the trade-off between intrinsic and extrinsic properties in the optimization of a modern internal tin Nb$_3$Sn conductor. *Superconductor Science and Technology*, 27(6):065013, apr 2014. doi: 10.1088/0953-2048/27/6/065013.

[147] C. Tarantini, C. Segal, Z. H. Sung, P. J. Lee, L. Oberli, A. Ballarino, L. Bottura, and D. C. Larbalestier. Composition and connectivity variability of the A15 phase in PIT Nb$_3$Sn wires. *Superconductor Science and Technology*, 28(9):095001, jul 2015. doi: 10.1088/0953-2048/28/9/095001.

[148] C. Tarantini, Z.-H. Sung, P. J. Lee, A. K. Ghosh, and D. C. Larbalestier. Significant enhancement of compositional and superconducting homogeneity in Ti rather than Ta-doped Nb$_3$Sn. *Applied Physics Letters*, 108(4):042603, jan 2016. doi: 10.1063/1.4940726.

[149] Chiara Tarantini, Shreyas Balachandran, Steve M. Heald, Peter J. Lee, Nawaraj Paudel, Eun Sang Choi, William L. Starch, and David C. Larbalestier. Ta, Ti and Hf effects on Nb$_3$Sn high-field performance: temperature-dependent dopant occupancy and failure of Kramer extrapolation. *Superconductor Science and Technology*, 32(12):124003, nov 2019. doi: 10.1088/1361-6668/ab4d9e.

[150] David M. J. Taylor and Damian P. Hampshire. The scaling law for the strain dependence of the critical current density in Nb$_3$Sn superconducting wires. *Superconductor Science and Technology*, 18(12):S241–S252, nov 2005. doi: 10.1088/0953-2048/18/12/005.

[151] B. ten Haken, A. Godeke, and H. H. J. ten Kate. The strain dependence of the critical properties of Nb$_3$Sn conductors. *Journal of Applied Physics*, 85(6):3247–3253, mar 1999. doi: 10.1063/1.369667.

[152] K. Togano and K. Tachikawa. Textures in diffusion-processed superconducting Nb$_3$Sn and V$_3$Ga layers. *Journal of Applied Physics*, 50(5):3495–3499, may 1979. doi: 10.1063/1.326345.

[153] Davide Tommasini, B. Auchmann, Hugues Bajas, Marta Bajko, Amalia Ballarino, Giovanni Bellomo, Michael Benedikt, Susana Izquierdo Bermudez,

Bernardo Bordini, Luca Bottura, Marco Buzio, Marc Dhalle, Maria Durante, Gijs de Rijk, Pasquale Fabbricatore, Stefania Farinon, Paolo Ferracin, Peng Gao, Friedrich Lackner, Clement Lorin, Vittorio Marinozzi, Teresa Martinez, J. Munilla, Toru Ogitsu, Rafal Ortwein, Juan Perez, M. Prioli, Jean-Michel Rifflet, Etienne Rochepault, Stephan Russenschuck, Tiina Salmi, Frederic Savary, Daniel Schoerling, Michel Segreti, Carmine Senatore, Massimo Sorbi, Antti Stenvall, Ezio Todesco, Fernando Toral, Arjan P. Verweij, Giovanni Volpini, Sander Wessel, and Felix Wolf. The 16 T Dipole Development Program for FCC. *IEEE Transactions on Applied Superconductivity*, 27(4):1–5, jun 2017. doi: 10.1109/tasc.2016.2634600.

[154] Patrick W. Trimby. Orientation mapping of nanostructured materials using transmission Kikuchi diffraction in the scanning electron microscope. *Ultramicroscopy*, 120:16–24, sep 2012. doi: 10.1016/j.ultramic.2012.06.004.

[155] D. Turrioni, E. Barzi, M. Bossert, V. V. Kashikhin, A. Kikuchi, R. Yamada, and A. V. Zlobin. Study of Effects of Deformation in Nb_3Sn Multifilamentary Strands. *IEEE Transactions on Applied Superconductivity*, 17(2):2710–2713, jun 2007. doi: 10.1109/tasc.2007.899352.

[156] T. Ungár. Microstructural parameters from X-ray diffraction peak broadening. *Scripta Materialia*, 51(8):777–781, oct 2004. doi: 10.1016/j.scriptamat.2004.05. 007.

[157] T. Ungár and A. Borbély. The effect of dislocation contrast on x-ray line broadening: A new approach to line profile analysis. *Applied Physics Letters*, 69(21):3173–3175, nov 1996. doi: 10.1063/1.117951.

[158] T. Ungár, Á. Révész, and A. Borbély. Dislocations and Grain Size in Electrodeposited Nanocrystalline Ni Determined by the Modified Williamson-Hall and Warren-Averbach Procedures. *Journal of Applied Crystallography*, 31(4): 554–558, aug 1998. doi: 10.1107/s0021889897019559.

[159] J. van Nugteren, D. Schoerling, G. Kirby, J. Murtomaki, G. de Rijk, L. Rossi, L. Bottura, H. ten Kate, and M. Dhalle. Layout study for the dipole magnets of the future circular collider using nb-ti and nb3sn. *IEEE Transactions on Applied Superconductivity*, 26(4):1–6, jun 2016. doi: 10.1109/tasc.2016.2530042.

[160] Y. Wang, C. Senatore, V. Abächerli, D. Uglietti, and R. Flükiger. Specific heat of Nb_3Sn wires. *Superconductor Science and Technology*, 19(4):263–266, jan 2006. doi: 10.1088/0953-2048/19/4/003.

[161] H. W. Weber, H. Böck, E. Unfried, and L. R. Greenwood. Neutron dosimetry and damage calculations for the TRIGA MARK-II reactor in Vienna. *Journal of Nuclear Materials*, 137(3):236–240, feb 1986. doi: 10.1016/0022-3115(86) 90225-4.

[162] David B. Williams and C. Barry Carter. *Transmission electron microscopy: a textbook for materials science.* Plenum Press, New York, 1996.

[163] G. K. Williamson and W. H. Hall. X-ray line broadening from filed aluminium and wolfram. *Acta Metallurgica*, 1(1):22–31, jan 1953. doi: 10.1016/0001-6160(53)90006-6.

[164] X. Wu, X. Peng, M. D. Sumption, M. Tomsic, E. Gregory, and E. W. Collings. Ti and Sn Diffusion and Its Influence on Phase Formation in Internal-Tin Nb_3Sn Superconductor Strands. *IEEE Transactions on Appiled Superconductivity*, 15 (2):3399–3402, jun 2005. doi: 10.1109/tasc.2005.848921.

[165] X. Xu, M. D. Sumption, S. Bhartiya, X. Peng, and E. W. Collings. Critical current densities and microstructures in rod-in-tube and tube type Nb_3Sn strands—present status and prospects for improvement. *Superconductor Science and Technology*, 26(7):075015, may 2013. doi: 10.1088/0953-2048/26/7/075015.

[166] X. Xu, M. D. Sumption, and E. W. Collings. A model for phase evolution and volume expansion in tube type Nb_3Sn conductors. *Superconductor Science and Technology*, 26(12):125006, oct 2013. doi: 10.1088/0953-2048/26/12/125006.

[167] X. Xu, M. Sumption, X. Peng, and E. W. Collings. Refinement of Nb_3Sn grain size by the generation of ZrO2 precipitates in Nb_3Sn wires. *Applied Physics Letters*, 104(8):082602, feb 2014. doi: 10.1063/1.4866865.

[168] X. Xu, M. D. Sumption, and E. W. Collings. Influence of heat treatment temperature and Ti doping on low-field flux jumping and stability in (Nb-Ta)$_3$Sn strands. *Superconductor Science and Technology*, 27(9):095009, aug 2014. doi: 10.1088/0953-2048/27/9/095009.

[169] X. Xu, X. Peng, J. Rochester, M. Sumption, and M. Tomsic. Achievement of FCC specification in critical current density for Nb_3Sn superconductors with artificial pinning centers. *arXiv:1903.08121 [cond-mat.supr-con]*, 2019. URL https://arxiv.org/abs/1903.08121.

[170] X. Xu, J. Rochester, X. Peng, M. Sumption, and M. Tomsic. Ternary Nb_3Sn superconductors with artificial pinning centers and high upper critical fields. *Superconductor Science and Technology*, 32(2):02LT01, jan 2019. doi: 10.1088/1361-6668/aaf7ca.

[171] Xingchen Xu. A review and prospects for Nb_3Sn superconductor development. *Superconductor Science and Technology*, 30(9):093001, aug 2017. doi: 10.1088/1361-6668/aa7976.

[172] Xingchen Xu, Edward Collings, Michael Sumption, Chris Kovacs, and Xuan Peng. The Effects of Ti Addition and High Cu/Sn Ratio on Tube Type Nb_3Sn Strands, and a New Type of Strand Designed to Reduce Unreacted Nb Ratio.

IEEE Transactions on Applied Superconductivity, 24(3):1–4, jun 2014. doi: 10.1109/tasc.2013.2291159.

[173] Xingchen Xu, Michael D. Sumption, and Xuan Peng. Internally Oxidized Nb_3Sn Strands with Fine Grain Size and High Critical Current Density. *Advanced Materials*, 27(8):1346–1350, jan 2015. doi: 10.1002/adma.201404335.

[174] Xingchen Xu, Xuan Peng, Michael Sumption, and E. W. Collings. Recent Progress in Application of Internal Oxidation Technique in Nb_3Sn Strands. *IEEE Transactions on Applied Superconductivity*, 27(4):1–5, jun 2017. doi: 10.1109/tasc.2016.2625780.

[175] H. W. Zandbergen, J. Kulik, and B. Nieuwendijk. Limitations on the monitoring with electron microscopy of the formation of defects in $YBa_2Cu_3O_7$ by neutron irradiation. *Physica C: Superconductivity*, 179(1-3):43–51, aug 1991. doi: 10.1016/0921-4534(91)90009-n.

[176] M. Zehetmayer. How the vortex lattice of a superconductor becomes disordered: a study by scanning tunneling spectroscopy. *Scientific Reports*, 5(1), mar 2015. doi: 10.1038/srep09244.

[177] Y. Zhai, L. D. Hauthuille, C. Barth, and C. Senatore. Finite-Element Analysis of Transverse Compressive and Thermal Loads on Nb_3Sn Wires With Voids. *IEEE Transactions on Applied Superconductivity*, 26(4):1–5, jun 2016. doi: 10.1109/tasc.2016.2535784.

[178] P. X. Zhang, Y. Feng, X. H. Liu, C. G. Li, K. Zhang, X. D. Tang, and Y. Wu. Microstructure and superconducting properties comparison of bronze and internal tin process Nb_3Sn strands for ITER. *Physica C: Superconductivity*, 469(15-20):1536–1540, oct 2009. doi: 10.1016/j.physc.2009.05.236.

Acknowledgements, Danksagung

An dieser Stelle möchte ich mich bei meinem Chef Johannes Bernardi sowie bei meinem Betreuer Michael Stöger-Pollach für die gute Betreuung bedanken, sowie für das angenehme Arbeitsklima und die Möglichkeit, meine Forschungsergebnisse auf zahlreichen internationalen Konferenzen präsentieren zu können.

Bei Michael Eisterer und Thomas Baumgartner möchte ich mich für die gute Zusammenarbeit im Rahmen des Projektes bedanken, welche auch stets bereit waren, meine zahlreichen Fragen zum Thema Supraleitung bestmöglich zu beantworten.

Einen besonderen Dank möchte ich meinen Kollegen Stefan Löffler und Thomas Schachinger aussprechen, welche immer für interessante Dikussionen bereit waren und mit zahlreichen Anregungen zur Entstehung meiner Arbeit beigetragen haben.

Weiters möchte ich allen Mitarbeitern des USTEM und der Forschungsgruppe Tieftemperaturphysik und Supraleitung des ATI sowie Tomasz Wojcik danken, welche durch unzählige Gespräche mein Wissen in den verschiedensten Bereichen erweitert haben.

Danken möchte ich auch Jack Haley vom Department of Materials der University of Oxford für die Zusammenarbeit im Rahmen eines Forschungsaufenthaltes, die Bedienung des JEOL JEM-ARM 200F TEMs und des FISPACT-II Programmes sowie die Hilfe bei der Auswertung der Ergebnisse.

Ein Dank gebührt natürlich auch unseren Projektpartnern am CERN, welche das Projekt ins Leben gerufen und für die finanzielle Unterstützung gesorgt haben.

Zuletzt möchte ich mich bei meiner Familie und Freunden bedanken, welche durch ihre moralische Unterstützung zur Entstehung dieser Arbeit beigetragen haben.

Curriculum Vitae

Name	Stephan Pfeiffer
Date of birth	3rd January 1991
Place of birth	Vienna, Austria
Address	Ferdinand-Raimund-Gasse 401, 3034 Maria Anzbach, Austria

Education and experience

2016 − 2020	Doctoral programme in Engineering Sciences, dissertation field Technical Physics and project assistant at USTEM, TU Wien
2013 − 2015	Master's programme in Physical Energy and Measurement Engineering at TU Wien
2009 − 2013	Bachelor's programme in Technical Physics at TU Wien
2001 − 2009	Realgymnasium Sacré Coeur Pressbaum (secondary education)
1997 − 2001	Volksschule Maria Anzbach (primary education)

Publications

1. Amalia Ballarino, Simon C. Hopkins, Bernardo Bordini, David Richter, Davide Tommasini, Luca Bottura, Michael Benedikt, Michinaka Sugano, Toru Ogitsu, Shinya Kawashima, Kazuyoshi Saito, Yoshito Fukumoto, Hisaki Sakamoto, Hitoshi Shimizu, Victor Pantsyrny, Ildar Abdyukhanov, Michael Shlyakov, Sergey Zernov, Florin Buta, Carmine Senatore, Iksang Shin, Jimam Kim, Jonas Lachmann, Andreas Leineweber, Stephan Pfeiffer, Thomas Baumgartner, Michael Eisterer, Johannes Bernardi, Andrea Malagoli, Valeria Braccini, Maurizio Vignolo, Marina Putti, and Carlo Ferdeghini. **The CERN FCC Conductor Development Program: A Worldwide Effort for the Future Generation of High-Field Magnets.** IEEE Transactions on Applied Superconductivity, 29(5):1-9, aug 2019.
doi: 10.1109/tasc.2019.2896469.

2. T. Baumgartner, J. Hecher, J. Bernardi, S. Pfeiffer, C. Senatore, and M. Eisterer. **Assessing composition gradients in multifilamentary superconductors by means of magnetometry methods.** Superconductor Science and Technology, 30(1):014011, nov 2016.
doi: 10.1088/0953-2048/30/1/014011.

3. T. Baumgartner, S. Pfeiffer, J. Bernardi, A. Ballarino, and M. Eisterer. **Effects of inhomogeneities on pinning force scaling in Nb3Sn wires.** Superconductor Science and Technology, 31(8):084002, jun 2018.
doi: 10.1088/1361-6668/aac87e.

4. M. Benedikt, A. Ballarino, T. Baumgartner, J. Bernardi, A. Doblhammer, M. Eisterer, M. Hofer, S. Holleis, J. Keintzel, A. Moros, M. Ortino, S. Pfeiffer, E. Renner, M. Stöger-Pollach, J. Gutleber, C. Senatore, A. Saba, V. Völkl, C. Köberl, H. Kritscher, T. Hoehn, M. Aburaia, A. Kollegger, M. Lackner, P. Keinz, M. Putti, H. Humer, et al. **FCC Physics Opportunities.** The European Physical Journal C, 79(6), jun 2019.
doi: 10.1140/epjc/s10052-019-6904-3.

5. M. Benedikt, A. Ballarino, T. Baumgartner, J. Bernardi, A. Doblhammer, M. Eisterer, M. Hofer, S. Holleis, J. Keintzel, A. Moros, M. Ortino, S. Pfeiffer, E. Renner, M. Stöger-Pollach, J. Gutleber, C. Senatore, A. Saba, V. Völkl, C. Köberl, H. Kritscher, T. Hoehn, M. Aburaia, A. Kollegger, M. Lackner, P. Keinz, M. Putti, H. Humer, et al. **FCC-ee: The Lepton Collider.** The European Physical Journal Special Topics, 228(2):261-623, jun 2019.
doi: 10.1140/epjst/e2019-900045-4.

6. M. Benedikt, A. Ballarino, T. Baumgartner, J. Bernardi, A. Doblhammer, M. Eisterer, M. Hofer, S. Holleis, J. Keintzel, A. Moros, M. Ortino, S. Pfeiffer, E. Renner, M. Stöger-Pollach, J. Gutleber, C. Senatore, A. Saba, V. Völkl, C. Köberl, H. Kritscher, T. Hoehn, M. Aburaia, A. Kollegger, M. Lackner, P.

Keinz, M. Putti, H. Humer, et al. **FCC-hh: The Hadron Collider.** The European Physical Journal Special Topics, 228(4):755-1107, jul 2019. doi: 10.1140/epjst/e2019-900087-0.

7. M. Benedikt, A. Ballarino, T. Baumgartner, J. Bernardi, A. Doblhammer, M. Eisterer, M. Hofer, S. Holleis, J. Keintzel, A. Moros, M. Ortino, S. Pfeiffer, E. Renner, M. Stöger-Pollach, J. Gutleber, C. Senatore, A. Saba, V. Völkl, C. Köberl, H. Kritscher, T. Hoehn, M. Aburaia, A. Kollegger, M. Lackner, P. Keinz, M. Putti, H. Humer, et al. **HE-LHC: The High-Energy Large Hadron Collider.** The European Physical Journal Special Topics, 228(5):1109-1382, jul 2019. doi: 10.1140/epjst/e2019-900088-6.

Awards

ESAS (European Society for Applied Superconductivity)
Young Researcher Award at EUCAS 2019